U. Salvolini · T. Scarabino (Eds.)

High Field Brain MRI

Use in Clinical Practice

With 156 Figures in 553 Parts

Springer

Ugo Salvolini
Neuroradiology and Department of Radiology
University of Marche, Ancona, Italy

Tommaso Scarabino
Department of Neuroradiology, Scientific Institute "Casa Sollievo della Sofferenza"
San Giovanni Rotondo (Fg), Italy
Department of Radiology, ASL BA/1, Hospital of Andria (Ba), Italy

ISBN 3-540-31775-9 Springer-Verlag Berlin Heidelberg New York

Library of Congress Control Number: 2006921045

Springer is a part of Springer Science+Business Media
http://www.springer.com

Printed in Germany

Editor: Dr. Ute Hesemann
Desk Editor: Meike Stoeck
Production Editor: Joachim W. Schmidt

Cover design: eStudio Calamar, Spain

Typesetting: FotoSatz Pfeifer GmbH, D-82166 Gräfelfing
Printed on acid-free paper – 24/3151 – 5 4 3 2 1 0

Preface

Since the advent of magnetic resonance (MR) imaging, systems with a magnetic field intensity of 1.5 tesla (T) have been deemed the gold standard for different clinical applications in all body areas. Ongoing advances in hardware and software have made these MR systems increasingly compact, powerful and versatile, leading to the development of higher magnetic field strength MR systems (3.0 T) for use in clinical practice and for research purposes. As usually occurs with a new technology, 3.0 T MR imaging units will probably follow the same development trends in the years to come.

These new systems are currently in routine use mainly in the United States, but despite their high cost they are increasingly being adopted for research in much broader fields than those of conventional MR systems, and also in daily clinical practice for new, more sophisticated applications, bringing major practical benefits.

Results to date have been encouraging with respect to previous experience with lower field strength MR systems and show that the many advantages of 3.0 T imaging (high signal, high resolution, high sensitivity, shorter imaging times, additional more advanced study procedures and enhanced diagnostic capacity) will ensure it becomes the future standard for morphofunctional study of the brain.

When future technological advances have resolved some of the shortcomings of the new 3.0 T systems (inhomogeneity of the field, artefacts caused by susceptibility and chemical shift, elevated SAR, high costs), the current MR units will gradually be replaced by higher field strength MR imaging systems.

The 3.0 T MR systems of the future will offer morphological investigation with high spatial, temporal and contrast resolution (essential for diagnosis) and will also yield physiological, metabolic and functional information, enhancing the diagnostic power of routine MR imaging in terms of sensitivity and specificity both in clinical practice and for applied research purposes.

This volume includes papers on the techniques and semeiotics of morphofunctional cerebral imaging at 3.0 T (including reference to the advantages and drawbacks with respect to lower field strength MR systems) and the main clinical applications in neuroradiology.

We are grateful to Dr. Silvia Modena for the language revision.

Ugo Salvolini
Tommaso Scarabino

Contents

List of Contributors

Raffaele Agati
Servizio di Neuroradiologia, Ospedale Bellaria, Bologna, Italy

Adriana Aragri
Department of Neurological Sciences, II University of Naples, Naples, Italy

Michele Armillotta
Neuroradiologia, Dipartimento di Scienze Radiologiche, Istituto Scientifico „Casa Sollievo della Sofferenza“, San Giovanni Rotondo (Fg), Italy

Antonella Bacci
Servizio di Neuroradiologia, Ospedale Bellaria, Bologna, Italy

Alessandro Carriero
Radiologia, Università di Novara, Novara, Italy

Domenico Catapano
Department of Neurosurgery, Scientific Institute „Casa Sollievo della Sofferenza“, San Giovanni Rotondo (Fg), Italy

Daniela Cevolani
Servizio di Neuroradiologia, Ospedale Bellaria, Bologna, Italy

Arnaud Charil
Neuroimaging Research Unit, Scientific Institute and University H San Raffaele, Milan, Italy

Andrea Cherubini
Department of Radiology and Neuroimaging Laboratory, IRCCS Fondazione Santa Lucia, Rome, Italy

Mario Cirillo
Department of Neurological Sciences, II University of Naples, Naples, Italy

Sossio Cirillo
Department of Neurological Sciences, II University of Naples, Naples, Italy

Valentina d'Alesio
Fisica Sanitaria, IRCCS „Casa Sollievo della Sofferenza“, San Giovanni Rotondo (Fg), Italy

Vincenzo A. d'Angelo
Department of Neurosurgery, Scientific Institute „Casa Sollievo della Sofferenza“, San Giovanni Rotondo (Fg), Italy

Alfonso Di Costanzo
Department of Health Sciences, University of Molise, Campobasso, Italy

Francesco Di Salle
Department of Radiology, University of Pisa, Pisa, Italy

Andrea Elefante
Department of Neurological Sciences, II University of Naples, Naples, Italy

Raffaele Elefante
Department of Neurological Sciences, II University of Naples, Naples, Italy

Fabrizio Esposito
Department of Radiology, University of Pisa, Pisa, Italy

Andrea Falini
CERMAC, Scientific Institute and University H San Raffaele, Milan, Italy

Fabrizio Fasano
Department of Radiology and Neuroimaging Laboratory, IRCCS Fondazione Santa Lucia, Rome, Italy

Massimo Filippi
Neuroimaging Research Unit, Scientific Institute and University H San Raffaele, Milan, Italy

Giuseppe M. Giannatempo
Neuroradiologia, Dipartimento di Scienze Radiologiche, Istituto Scientifico „Casa Sollievo della Sofferenza“, San Giovanni Rotondo (Fg), Italy

Elisabetta Giugni
U.O. Diagnostica per Immagini e Laboratorio di neuroimmagini funzionali, IRCCS Fondazione Santa Lucia, Rome, Italy

Gisela E. Hagberg
Department of Radiology and Neuroimaging Laboratory, IRCCS Fondazione Santa Lucia, Rome, Italy

Marco Leonardi
Servizio di Neuroradiologia, Ospedale Bellaria, Bologna, Italy

Giacomo Luccichenti
Department of Radiology and Neuroimaging Laboratory, IRCCS Fondazione Santa Lucia, Rome, Italy

Alberto Maggialetti
Radiologia, AUSL BA/1, Andria (Ba), Italy

Nicola Maggialetti
Medical Student, University of Bari, Bari, Italy

Alberto Maiorana
Servizio di Fisica Sanitaria, IRCCS „Casa Sollievo della Sofferenza“, San Giovanni Rotondo (Fg), Italy

Francesco Nemore
Radiologia, AUSL BA/1, Andria (Ba), Italy

Patrice Péran
Department of Radiology and Neuroimaging Laboratory, IRCCS Fondazione Santa Lucia, Rome, Italy

Saverio Pollice
Department of Radiology, University of Novara, Novara, Italy

Teresa Popolizio
Neuroradiologia, Dipartimento di Scienze Radiologiche, Istituto Scientifico „Casa Sollievo della Sofferenza“, San Giovanni Rotondo (Fg), Italy

Umberto Sabatini
Department of Radiology and Neuroimaging Laboratory, IRCCS Fondazione Santa Lucia, Rome, Italy

Ugo Salvolini
Neuroradiologia, Università Politecnica delle Marche, Ancona, Italy

Ornella Santopaolo
Department of Neurological Sciences, University of Pisa, Pisa, Italy

Tommaso Scarabino
Neuroradiologia, Dipartimento di Scienze Radiologiche, Istituto Scientifico „Casa Sollievo della Sofferenza", San Giovanni Rotondo (Fg), Italy; and Dipartimento di Radiologia, AUSL BA/1, Andria (Ba), Italy

Timo Schirmer
G2 Healthcare Technologies, Applied Science Laboratory Europe, Monaco

Anna Simeone
Neuroradiologia, Dipartimento di Scienze Radiologiche, Istituto Scientifico „Casa Sollievo della Sofferenza", San Giovanni Rotondo (Fg), Italy

Alessandra Stranieri
Neuroradiologia, Dipartimento di Scienze Radiologiche, Istituto Scientifico „Casa Sollievo della Sofferenza", San Giovanni Rotondo (Fg), Italy

Gioacchino Tedeschi
Department of Neurological Sciences, II University of Naples, Naples, Italy

Michela Tosetti
MR Laboratory, Stella Maris Scientific Institute, Calabrone, Pisa, Italy

Francesca Trojsi
Department of Neurological Sciences, II University of Naples, Naples, Italy

Techniques and Semeiotics

High-Field MRI and Safety: I. Installation

1

A. Maiorana, T. Scarabino, V. d'Alesio, M. Tosetti, M. Armillotta, U. Salvolini

High-field magnetic resonance (MR), originally developed in the framework of spectroscopy and functional neuroradiology, is set to become an important diagnostic tool not only in research but also in advanced clinical practice.

High magnetic fields afford a better signal/noise ratio (SNR) and consequently better spatial resolution in a shorter acquisition time, even though the diagnostic outcome is then subject to the dependence on the magnetic field of other factors that variously contribute to image quality.

The rationale for the utilization of high magnetic fields in MR diagnostic imaging is obvious.

The distribution of the population into two spin levels is statistically determined:

$$\frac{n_f}{n_e} = e^{\left(\frac{\Delta E}{kT}\right)}$$

where $\Delta E = h \cdot \gamma \cdot B_0$ depends on the static magnetic field, h and γ are constants, n_f is the spin population in the fundamental state and n_e is the population in excited state.

An increase in B_0 values results in an inversion of the states of the two populations, and therefore in a stronger MR signal.

In fact, the signal intensity is proportional to the square of the static magnetic field, since:

$$S \cong (N_{spin} \cdot V_{spin})$$

where the number of N_{spin} and V_{spin} and the voltage induced by each spin both depend linearly on B_0 [1, 2].

However, if the signal is proportional to the square of the static field B_0 and the noise is proportional to B_0, then from 1.5 T to 3.0 T the SNR doubles. This allows an acceptable image quality to be obtained even with increased spatial resolution or reduced time of acquisition.

Clearly, achieving greater spatial resolution while minimizing undesired partial volume effects requires increasing the gradient steepness G_z and reducing the encoding frequency bandwidth $\Delta\omega$, since the slice thickness is defined as:

$$\Delta z = \frac{\Delta\omega}{\gamma G_z} \quad (2)$$

In any case, shimming requires very strong field homogeneity. For instance, the first 3.0 T system installed in Italy achieves a field homogeneity of less than 1 ppm in a spherical volume of 33 cm, and of less than 0.3 ppm in a spherical volume of 24 cm, with a peak gradient ramp of 50 mT/m and a slew rate of 150 mT/m/ms.

Another key principle is that the resonance frequency $\omega_0 = \gamma \cdot B_0$ depends on the static magnetic field. It therefore is 43 MHz at 1.0 T and 128 MHz at 3.0 T, resulting in greater radiofrequency (RF) absorption by biological tissues, whose conductivity increases with frequency. This poses problems when designing coils suitable for the greater power applied as well as for patient safety, as increased tissue temperature is one of the risks associated with RF electromagnetic fields [3, 4]. Finally, the increased susceptibility of tissues exposed to the magnetic field can result in local inhomogeneities that cannot be corrected, and eventually present as artefacts. This effect can be exploited in functional MR BOLD studies, which are based on the changes in blood oxygenation generated by magnetic susceptibility inhomogeneities [2, 4, 5].

Notwithstanding technical and cost problems, high-field MR offers very significant advantages, and recent human imaging studies at 340 MHz have demonstrated that safety margins still exist above 3.0 T and 4.0 T, while spectroscopic analysis has overcome the 1 GHz threshold [6].

The growing interest in 3.0 T and higher magnetic fields and their expected increasing diffusion in clinical practice have brought the safety issues back to the forefront.

When planning the installation of a high-field MR unit, the strength of the static magnetic field is one of the major problems to be addressed by those responsible for safety and technicians alike. In fact, this is but one, albeit the most apparent, element to be considered when estimating the associated risks and benefits. Patients in the tunnel of a high-strength imager are exposed to a magnetic field many thousands of times greater than the earth's, even though no special patient or operator safety precautions are required compared with low or medium magnetic fields. However, during scanning patients are also exposed to gradient switch-

on and to RF impulses for signal decoding and spin excitation, both of which are related to the intensity of the static magnetic field and carry different though acceptable patient risk.

Approval of high-field MR tomographs for diagnostic purposes dates from 1997, when the US Department of Health and Human Services Food and Drug Administration, Center for Devices and Radiological Health (FDA), classified as carrying a significant risk, and therefore subjected to specific authorization, all MR systems having: static magnetic fields exceeding 4.0 T; a specific absorption rate (SAR) exceeding 4 W/kg averaged over the whole body for any 15-min period, 3 W/kg averaged over the head for any 10-min period, 8 W/kg for any gram of body or chest tissue in any 15-min period, or 15 W/kg for any gram of tissue in the extremities in any 15-min period; field gradients sufficient to induce patient discomfort or pain; and acoustic noise reaching sound pressure levels of 99 dB(A) (with reference to the response curve of the human ear, A curve) or peak values exceeding 140 dB(A). Based on these conditions, a 3.0 T MR unit meeting SAR, gradient and noise requirements is substantially equivalent to a 1.5 T unit and does not carry a significantly greater risk, hence further restrictions [7].

At that time, the components of the early high-field tomographs available on the market were substantially similar to those of the 1.5 T machines from which they had been derived. They thus presented a number of drawbacks, such as poor homogeneity of the static magnetic field, insufficient gradient slew rate, inadequate coil structure in relation to the greater resonance frequency, excessive fringe field extension, noise and weight, and were also extremely expensive. All such factors hampered the diffusion of the technique, which remained confined to specific research fields for a long time.

By contrast, last-generation units have been conceived as high-field diagnostic machines and are equipped with technical features that allow operation with a degree of safety comparable to the conventional low- and medium-field scanners [3, 8]. The passive-shield 3.0 T prototype was bulky and heavy and its 0.5 mT line (or 5 gauss limit) was an ellipsoid measuring 8.5 × 6.5 m in an axial radial direction. Adequate additional shielding of the fringe field in the magnet room would have required hundreds of tons of iron. The recent introduction of active shielding has significantly reduced magnet weight. The 3.0 T unit installed at the San Giovanni Rotondo Scientific Institution is still bulkier and heavier than the corresponding 1.5 T machine, but the 0.5 mT line occupies a 4.4 × 2.7 m area in the scan room compared with 3.9 × 2.4 m of the same type 1.5 T magnet installed 10 years previously [4]. In particular, the 200 mT line, which is crucial towards meeting current operator safety regulations, is practically contained in the tomograph's volume. This feature protects staff from excessive whole-body exposure even for long stays in the scan room, while also due to the presence of passive ferromagnetic barriers around the scan room perimeter, the 0.1 mT line barely exceeds the boundary of the magnet room

Due to the intrinsic weakness of the MR signal and to the high sensitivity of image reconstruction systems, the magnet room needs to be protected by a Faraday cage capable of attenuating the outside electromagnetic noise. The shielding must be able to attenuate signals by at least 80 dB, and it obviously also works the other way around, i.e. by shielding the operators from any type of exposure to the RF electromagnetic fields generated by the coils.

In 1999, the FDA approved for sale some high-field tomographs for clinical diagnostic imaging [4].

In July 2003 it replaced its 1997 guidelines and laid down new upper static magnetic field limits for MR diagnostic units. These new limits are 8.0 T for adults and 4.0 T for neonates less than 1 month old [9].

In Europe, particularly in Italy, the earliest reference technical regulation, CEI EN 60601 – 2-33/A11 of 1998 [10], was superseded by IEC 60601 1 – 2-33 Ed. 2.0 of 2002 [11], which later became CEI EN 60601 – 2-3 of 2004 [12].

Recently, the International Commission for Non-Ionizing Radiation Protection (ICNIRP) has issued patient safety guidelines for MR scanning [13].

In Italy, MR units with a static field strength of or exceeding 2.0 T are not approved for clinical use and are restricted to documented research applications [14]. Further legislation [15, 16] lays down SAR and field gradient limits substantially in line with the indications of the Comitato Elettrotecnico Italiano (CEI) [10]. In addition, MR machines with static magnetic fields exceeding 2.0 T, classified by the law as group B systems, can be installed only at major research institutions subject to ministerial authorization [14]. Such units also need to be involved in scientific or clinical research projects mandating the use of such high field strengths, whereas units with magnetic fields exceeding 4.0 T may be authorized only for specific, documented needs of scientific or clinical experimental research limited to the limbs. Authorization of group B tomographs by the Health Ministry is currently also subject to the prior technical opinion of the Istituto per la Sicurezza e la Prevenzione degli Incidenti sul Lavoro (ISPESL), the Istituto Superiore di Sanità (ISS) and the Consiglio Superiore di Sanità (CSS). In practice, meeting the requirements for the authorization of MR imagers, especially high-field ones, is hampered by an intricate and fragmentary legislation [17].

As regards staff safety and protection, limits for static magnetic fields were issued by the ICNIRP in 1994 [18]. Whereas the limits adopted in Italy [15] are sub-

stantially similar (save for those regarding the limbs), there are considerable differences in the time periods to which some of these limits are to be applied.

With high-field systems, correct dimensioning or upgrading of ventilation and helium venting pipes in relation to the type of magnet being installed and room size should be addressed at the design stage. Indeed, in the event of a quench, i.e. the sudden inactivation of the magnet, the liquid helium contained in a superconducting magnet (which is more abundant in a high-strength unit) rapidly turns to gas and may saturate the magnet room atmosphere.

References

1. Takahashi M, Uematsu H, Hatabu H (2003) MR imaging at high magnetic fields. Eur J Radiol 46:45 – 52
2. Duerk JL (1999) Principles of MR image formation and reconstruction. Magn Reson Im Clin NA, Physics of MR Imaging 7(4):629 – 659
3. Schenck JF (1999) MR safety at high magnetic fields. Magn Reson Im Clin NA, MR Safety 6(4):715 – 730
4. Frayne R, Goodyear BG, Dickhoff P, et al. (2003) Magnetic resonance imaging at 3.0 Tesla: Challenges and advantages in clinical neurological imaging. Invest Radiol 38(7):385 – 402
5. Uematsu H, Dougherty L, Takahashi M, et al. (2003) A direct comparison of signal behaviour between 4.0 and 1.5 T: a phantom study. Eur J Radiol 45:154 – 159
6. Kangarlu A, Robitaille PML (2000) Biological effects and health implications in magnetic resonance imaging. Concepts Magn Res 12:321 – 359
7. Food and Drug Administration Center for Devices and Radiological Health (1997) Guidance for magnetic resonance diagnostic devices – criteria for significant risk investigation.
8. Budinger TF (1999) MR safety, past, present and future from a historical perspective. Magn Reson Imaging Clin NA, MR Safety 6(4):701 – 714
9. Food and Drug Administration Center for Devices and Radiological Health (2003) Criteria for significant risk investigations of magnetic resonance diagnostic devices.
10. Comitato Elettrotecnico Italiano, Apparecchi Elettromedicali Parte 2 (1998) Prescrizioni particolari di sicurezza relative agli apparecchi a risonanza magnetica per diagnostica medica. CEI EN 60601 – 2-33/A11
11. International Electrotechnical Commission (2002) Medical electrical equipment, part 2 – 33: Particular requirements for the safety of magnetic resonance equipment for medical diagnosis. IEC 60601 1 – 2-33 Ed. 2.0
12. Comitato Elettrotecnico Italiano (2004) Apparecchi Elettromedicali Parte 2: Prescrizioni particolari di sicurezza relative agli apparecchi a risonanza magnetica per diagnostica medica. CEI EN 60601 – 2-33
13. The International Commission on Non-Ionizing Radiation Protection (ICNIRP) (2004) Medical magnetic resonance (MR) procedures: Protection of patients. Health Phys 87(2):197 – 216
14. D.P.R 542 (1994) Regolamento recante norme per la semplificazione del procedimento di autorizzazione all'uso diagnostico di apparecchiature a risonanza magnetica nucleare sul territorio nazionale. G.U. 219
15. D.M. 02/08/1991 (1991) Autorizzazione alla installazione ed uso di apparecchiature diagnostiche a risonanza magnetica. G.U. 194.
16. D.M. 03/08/1993 (1993) Aggiornamento di alcune norme concernenti l'autorizzazione all'installazione ed all'uso di apparecchiature a risonanza magnetica. G.U. 187
17. Campanella F, Mattozzi M, Panebianco AS, et al. (2004) Indicazioni operative e gestionali relative all'installazione ed uso di apparecchiature diagnostiche a Risonanza Magnetica. Indicazioni Operative ISPESL
18. The International Commission on Non-Ionizing Radiation Protection (ICNIRP) (1996) Guidelines on limits of exposure to static magnetic fields. Health Phys 66:100 – 106

2 High-Field MRI and Safety: II. Utilization

A. Maiorana, T. Scarabino, V. d'Alesio, M. Tosetti, M. Armillotta, U. Salvolini

The possible risks directly connected with magnetic resonance (MR) diagnostic imaging are mainly related to three components that are simultaneously active as the patient is being scanned: static magnetic field, magnetic field gradients and radiofrequency (RF) field.

No adverse effects of static magnetic fields lower than 4.0 T have yet been demonstrated in man [1 – 4]; in contrast, it is well established that attempts to improve the diagnostic performance by acting on the other two elements may lead to potentially hazardous situations. Although the electric and the magnetic field are commonly conceived of as separate entities, in fact they coexist and only rarely can they be considered separately. Several effects ascribed to variable magnetic fields are in fact due to changes in the associated electric field.

Two possible sources of indirect risk can be magnified by the intrinsic working characteristics of fast superconducting MR imagers: cryogenic gases and the noise produced by coil vibration during sequence performance.

Some of the main risks directly or indirectly connected with high magnetic fields are discussed below.

2.1 Static Magnetic Field

The suspicion that exposure to high magnetic fields could be associated with some kind of risk dates from 1970, when MR diagnostic imaging was first introduced. However, unofficial data indicate that about 150,000,000 MR diagnostic examinations have been performed in the world from 1980 to 1999 (ca. 20,000,000 a year, or 50,000 a day) with very few accidents. The few documented cases of severe injury directly ascribable to the static magnetic field were due to magneto-mechanical effects on patient implants or devices introduced into the scan room by mistake [3, 5].

2.1.1 Translation and Rotation Forces

All materials that magnetize transiently have a susceptibility value χ_m other than 0; in particular, materials whose values range from –1 and 0, designated as diamagnetic, are repelled by the magnetic field. In fact, although all materials have a diamagnetic field, in some of them the presence of ions of transition elements tends to raise the susceptibility value. Materials with positive values are attracted to the magnetic field and are called paramagnetic. Ferromagnetism is an extreme form of paramagnetism and characterizes some materials having high levels of susceptibility, which are strongly attracted to magnetic fields. The presence of such objects in the magnet room is extremely dangerous and must be avoided. Diamagnetic and paramagnetic materials, whose susceptibility is about 0.01, respond weakly to the magnetic field and are often considered non-magnetic. To this group belong biological tissues, whose susceptibility is in the range of $-9 \times 10^{-6} \pm 20\,\%$, i.e. the susceptibility of water. For instance, when patients are slid into the tunnel, the magnet exerts a force that contrasts this movement, although it is so weak as to be negligible [5].

The magnetic flow density B, expressed as tesla (T), represents the magnetic induction deriving from exposure to a magnetic field H, according to the relationship:

$$B = \mu_0 (1 + \chi_m) H$$

where the magnetic susceptibility $\chi_m = \frac{M}{H}$ is the ratio of induced magnetization to the source field, and μ_0 is the magnetic permeability in vacuum.

Although the distinction between source and induced magnetic field tends to be neglected in practice, in MR diagnostic imaging it has an important role when the susceptibility has an appreciable positive value, as is the case of paramagnetic contrast agents and ferromagnetic objects.

When an object, such as the human body, a metal prosthesis or an erythrocyte, is introduced into an MR tomograph, it is subjected to translation forces in the gradient zones and to rotation forces with respect to the direction of the static field B. Such forces depend on the susceptibility of the material from which the object is made, on its shape and volume, and on the intensity of the magnetic field, and in relation to them they may be negligible or have potentially lethal effects.

The force of translation $F_{trasl} \approx \frac{\chi_m V}{\mu_0} \cdot B \cdot \frac{dB}{dz}$ depends on the volume V, the susceptibility value and the mag-

netic field gradient, whereas the force of rotation required to oppose the object's rotation $F_{rot} \approx \frac{\chi_m^2 V}{2L\mu_0} \cdot B^2$ also depends on its length L and volume, thus on its shape.

In general, $F_{\text{rot}} >> F_{\text{trasl}}$; thus the tissue damage induced by the rotation force generated by the field of an implanted metal object will be greater than the damage caused by the force of translation, especially in the presence of high magnetic fields, due to its quadratic dependence on B [5].

In human tissues the magneto-mechanical effects are negligible due to their weak susceptibility; for instance, the alignment of erythrocytes parallel to the magnetic field due to their ellipsoid shape is negligible because of the quadratic dependence of the torque on susceptibility. The force acting on 100 g of water in an 8.0 T magnetic field with a peak gradient of 7.9 T/m and a product $B \cdot \frac{dB}{dz}$, equalling 43 T^2/m, is negative and equal to -3.4×10^{-3} N.

By contrast, a 100 g stainless steel tool with susceptibility 0.01 and a volume of 12.5 cm^3 will be attracted to the same field with a force of 4.3 N and an acceleration of 43 m/s^2, i.e. more than four times the force of gravity, turning it into a projectile [3, 5]. The magnitude of the force acquired by the paramagnetic and ferromagnetic objects would be greater by a factor of 10^2 to 10^5, posing serious hazards for workers and patients in the magnet area.

People with splinters lodged in their bodies or wearing metal prostheses are also at high risk, since the movement of these objects, induced by the magnetic field, may cause tissue or vessel tears.

Inside the magnet the field gradient is zero and so is the force of translation exerted on a ferromagnetic object, which will thus remain trapped in the tunnel. Attempts to extract it forcibly in case of an accident are often vain and can impair the magnet's stability in the cryostat. Recovery of the object usually requires inactivation of the magnet. By contrast, the rotation forces, which depend solely on B^2, continue to be active. To prevent this type of risk, metal objects must never be introduced into the scan room. This is clearly stated in notices and is prevented from happening by taking an accurate patient history.

Since most of the data on the compatibility of several implanted devices and prostheses concern 1.5 T static magnetic fields, MR investigations of such patients at higher fields are to be avoided.

However, information on the safety and compatibility of 26 aortic aneurysm clips tested at 8.0 T and of 109 implants and devices tested at 3.0 T has recently been published. With regard to safety the objects have been shown to carry no additional patient risk save a reduction in image quality, whereas compatibility demonstrates the property of not interfering with image quality. The distinction between long- and short-bore magnets of equal field intensity lies in the differences in the respective position and height of gradient peaks at the tunnel aperture [6–9].

In general, patients wearing pacemakers should avoid undergoing MR imaging, especially at a high magnetic field. The several effects that may derive from exposure are due to the static magnetic field (e.g. pacemaker shifting, remote control switch-off and ECG changes), to the RF field (e.g. heating, alteration of pace frequency and device reset), and to the gradients (e.g. induction of voltage, heating and remote control switch-off). However, these effects still present controversial aspects because on the one hand early compatibility studies assessed models that are no longer in use, and on the other, recent data indicate that small groups of patients underwent MR imaging for vital reasons without experiencing adverse effects [10, 11].

In most materials, the magnetization induced is parallel to H; in such cases M, B and H all point in the same direction and the material is said to have isotropic susceptibility. If, however, the susceptibility varies within the volume of the material exposed to the magnetic field, the object becomes magnetized along directions that may not be parallel to the magnetic field; in anisotropic cell structures, this may lead to structure reorientation or distortion. In such cases this effect, which has been documented in vitro, is stronger than the one induced by object shape [5].

Another biological effect connected with a potential risk, which in the past has been attributed to abnormal myocardial repolarization, is in fact induced by the blood flow in the large vessels within a strong magnetic field. The Lorentz force, F, induces on vessel walls an electric field $E = \frac{F}{q} = vBsen\theta$, where v is blood velocity, θ the angle between the flow direction and the direction of the magnetic field, and q the charge of the ions in the blood.

This induced electric field causes a reversible increment in T-wave amplitude in the ECG. In vivo investigation of this effect at fields greater than 8.0 T has demonstrated that the induced potentials are below the threshold of nerve or muscle stimulation. The migration of opposite charges to vessel walls induced by the magnetic field also causes a current in a direction perpendicular to the flow velocity in vessels and thus an additional Lorentz force in a direction opposite to the blood flow that could contrast it appreciably. However, it has been demonstrated that this effect is negligible even in the presence of magnetic fields exceeding 10 T [12].

2.2 Varying Electric and Magnetic Fields

During scanning patients are also exposed to the activation of magnetic field ramps or gradients for spatial localization of the signal and to RF impulses for signal generation and decoding. Specific effects that may constitute a source of patient risk during scanning have been documented in their connection.

2.2.1 Magnetic Field Gradients

Many of the effects ascribed to magnetic fields that vary over time are in fact related to the associated electric field. Switching the magnetic field gradients on and off may induce electric currents capable of affecting the cell membrane potential and, if sufficiently intense, of stimulating the peripheral nervous system and the cardiac muscle. The stimulation threshold of peripheral nerves may be painful but is reversible and is used as a safety reference indicator for cardiac stimulation, which in contrast carries the risk of fibrillation. In fact, with ramp durations of less than 1 ms, the former threshold is always lower than, and is reached before, the latter [13].

The intensity of these currents is proportional to the induced electric field and depends on the conductivity of biological tissues. The other critical factor of gradients, besides their amplitude, is the slew rate; the value of the induced electric field can be calculated using a model represented by a cylindrical object with radius r as follows:

$$E = \frac{r}{2} \cdot \frac{\mathrm{d}B}{\mathrm{d}t}$$

For instance, if during an examination a localization ramp from 0 to 20 mT/m in 200 μs is launched from a 1 m coil, then the temporal variation of the magnetic field will be 100 T/s, and for an abdomen 0.4 m in diameter the value of the electric field calculated using the above model will be 10 V/m, which exceeds the 6 V/m threshold of peripheral nerve stimulation [4, 13].

An ability to excite 20 mT/m gradients is shared by several last-generation MR units with static fields of 1.0 or 1.5 T; 30 mT/m gradients with ramps shorter than 100 μs have also been developed to improve acquisition time and spatial resolution.

At high magnetic fields, spatial resolution can be improved by strengthening the gradients; this results in an increased induced electric field that may easily exceed the safety threshold. To avoid this effect, the electric field increase could be offset by increasing gradient duration; however, an increase for instance from 0 to 40 mT/m in 400 μs would result in a value of $\frac{dB}{dt}$ of 100 T/s, while based on the model mentioned above the electric field would still be 10 V/m. In addition, increasing gradient duration leads too close to the values where the thresholds of peripheral and cardiac stimulation converge, preventing peripheral nerve stimulation from being used as a safety indicator.

2.2.2 Radiofrequency Electromagnetic Fields

The RF impulses applied in MR imaging are always accompanied by an RF electric field, which in turn induces RF electric currents in patients.

Due to the Joule effect, these currents may induce a potentially adverse heating of tissues, or burns caused by conducting loops accidentally generated by the contact between the patient's limbs or by leads of auxiliary devices inadvertently left on the patient's skin [14, 15].

At 3.0 T, the resonance frequency of protons is 128 MHz, i.e. twice the value at 1.5 T, the spatial distribution of the RF field generated by the coils becomes more complex with increasing frequency, and the temperature rise may become localized, generating hot spots.

At very high frequencies, the wavelength of the field is comparable to the size of the anatomical structure being scanned, a situation that may lead to generation of stationary waves that impair RF field homogeneity. In addition, as the frequency increases so do tissue conductivity and consequently the density of the induced current, resulting in greater power density being deposited in tissues.

Greater conductivity also involves impaired RF signal penetration, requiring greater power to obtain the same signal.

Prevention of accidental tissue heating requires careful evaluation of the energy deposited per unit of mass in unit of time, or specific absorption rate (SAR), which is measured in W/kg of exposed tissue. Between 1.5 and 3.0 T, this rate increases with B^2, making the safety threshold more likely to be reached in the course of the same sequence performed with a 3.0 T than with a 1.5 T unit [2].

2.3 Cryogenic Gases

With high-field systems, correct dimensioning or upgrading of ventilation and helium venting pipes in relation to the type of magnet being installed and room size should be addressed at the design stage, given that 700 l of gas is produced from 1 l of liquid helium. The cryostat of a 3.0 T superconducting magnet contains approximately 3 m^3 helium, i.e. roughly three times the content of a 1.0 T magnet. In normal boil-off, i.e. gradual, controlled evaporation conditions, the gas is channelled outside through a dedicated exhaust pipe. In

case of a quench, i.e. a sudden increase in coil temperature and violent, uncontrolled evaporation of the helium in which the coils are immersed, the oxygen concentration in the scan room may drop to levels likely to cause asphyxia. In case of an emergency, the forced ventilation plant therefore needs to guarantee at least 20 air changes/h to restore safety conditions in the room as quickly as possible. In particular, the design of the ventilation plant inlet and outlet points must ensure against a short circuit of the air flow, and inlet and outlet fluxes need to be proportionate.

To ensure helium outflow in normal as well as emergency conditions, the quench pipe diameter must be correctly dimensioned in relation to pipe length and the number of bends. Finally, the oxygen monitor, which activates the ventilation plant in case of an emergency, needs to be placed at an appropriate height in the room (since helium is lighter than air and tends to rise) and close to the likeliest point of leakage, which is the limiting pressure valve fitted on the quench pipe.

To avoid introducing cryogenic gas containers into the hospital, an insulated pipe allowing the helium to be refilled from the outside should be envisaged.

2.3.1 Acoustic Noise

In an MR unit, field gradients are the main source of acoustic noise, which is produced by the rapid current changes inside the coils. In the presence of a strong magnetic field, these currents are subject to the Lorentz force acting on the coils. Changes in gradient amplitude and steepness connected with different sequences may affect noise levels, which tend to increase with decreasing slice thickness, field of view, TR and TE [16].

There is growing interest in high-field functional MR using fast gradients exceeding 30 mT/m; these, however, involve a noise level close to 120 dB(A), which varies in relation to the sequences performed but is consistently higher than the noise produced by a 1.5 T unit.

At present, the simplest and least expensive means to reduce noise is passive patient protection using earplugs or earphones, even though this impairs communication with the operator and may cause discomfort.

„Silent“ coils made from new materials with new assembly techniques or active noise cancellation systems are being developed. In addition, optimization of the choice of imaging parameters should enable less noisy sequences to be obtained [16].

References

1. Schenck JF (1999) MR safety at high magnetic fields. Magn Reson Imaging Clin NA, MR Safety 6(4):715 – 730
2. Frayne R, Goodyear BG, Dickhoff P, et al. (2003) Magnetic resonance imaging at 3.0 Tesla: Challenges and advantages in clinical neurological imaging. Invest Radiol 38(7):385 – 402
3. Kangarlu A, Robitaille PML (2000) Biological effects and health implications in magnetic resonance imaging. Concepts Magn Reson 12:321 – 359
4. Budinger TF (1999) MR safety, past, present and future from a historical perspective. Magn Reson Imaging Clin NA, MR Safety 6(4):701 – 714
5. Schenck JF (2000) Safety of strong, static magnetic fields. J Magn Reson Imaging 12:2 – 19
6. Shellock FG (2002) Magnetic resonance safety update 2002: Implants and devices. J Magn Reson Imaging 16: 485 – 496
7. Kangarlu A, Shellock FG (2000) Aneurysm clips: evaluation of magnetic field interactions with an 8.0 T MR system. J Magn Reson Imaging 12:107 – 111
8. Shellock FG (2002) Biomedical implants and devices: Assessment of magnetic field interactions with a 3.0 Tesla MR System. J Magn Reson Imaging 16:721 – 732
9. Shellock FG, Tkach JA, Ruggeri PM, et al. (2003) Aneurysm clips: Evaluation of magnetic field interactions and translational attraction by use of „long-bore“ and „short bore“ 3.0-T MR imaging systems. Am J Neuroradiol 24:463 – 471
10. Duru F, Luechinger R, Scheidegger MB, et al. (2001) Pacing in magnetic resonance imaging environment: clinical and technical considerations on compatibility. Eur Heart J 22:113 – 124
11. Shellock FG, Tkach JA, Ruggeri PM, et al. (2003) Cardiac pacemakers, ICDs, and loop recorder: evaluation of translational attraction using conventional („long bore“) and „short bore“ 1.5 and 3.0 Tesla MR systems. J Cardiovasc Magn Reson 5(2):387 – 397
12. Kangarlu A, Burgess RE, Zhu H, et al. (1999) Cognitive, cardiac, and physiological safety studies in ultra high field magnetic resonance imaging. Magn Reson Imaging 17(10): 1407 – 1416
13. Schaefer DJ, Bourland JD, Nyenhuis JA (2000) Review of patient safety in time – varying gradient field. J Magn Reson Imaging 12:20 – 29
14. Shellock FG (2000) Radiofrequency energy-induced heating during MR procedures: A review. J Magn Reson Imaging 12:30 – 36
15. Dempsey MF, Condon B (2000) Thermal injuries associated with MRI. Clin Radiol 56:457 – 465
16. McJury M, Shellock FG (2000) Auditory noise associated with MR procedures: A review. J Magn Reson Imaging 12:37 – 45

3 3.0 T MRI Diagnostic Features: Comparison with Lower Magnetic Fields

T. Scarabino, G. M. Giannatempo, T. Popolizio, A. Simeone, A. Maggialetti, N. Maggialetti, U. Salvolini

3.0 T magnetic resonance (MR) units are optimized for high-resolution morphological and functional imaging, especially of the head and neck, and offer a number of advantages over lower-field systems, such as a higher signal/noise ratio (SNR) and greater spatial and temporal resolution (Fig. 3.1) [1–4]. Drawbacks include greater specific absorption rates (SAR), acoustic noise, and dielectric resonance, although in the more recent imagers these problems have largely been resolved by improvements in hardware and software.

MR scans acquired at 3.0 T and 1.5 T exhibit different diagnostic features that need to be taken into consideration when images are being interpreted and also to optimize sequence parameters. These same differences prevent transfer of 1.5 T study protocols to 3.0 T systems.

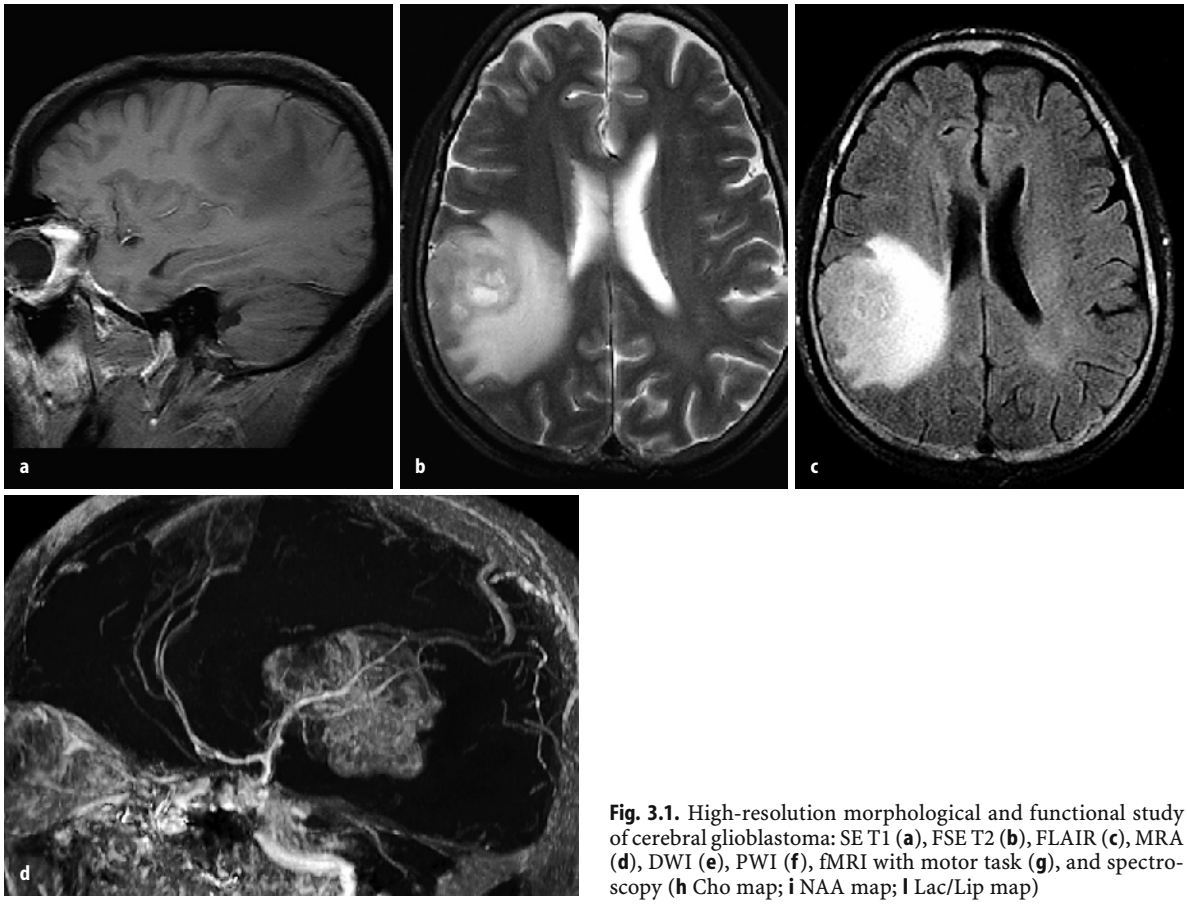

Fig. 3.1. High-resolution morphological and functional study of cerebral glioblastoma: SE T1 (**a**), FSE T2 (**b**), FLAIR (**c**), MRA (**d**), DWI (**e**), PWI (**f**), fMRI with motor task (**g**), and spectroscopy (**h** Cho map; **i** NAA map; **l** Lac/Lip map)

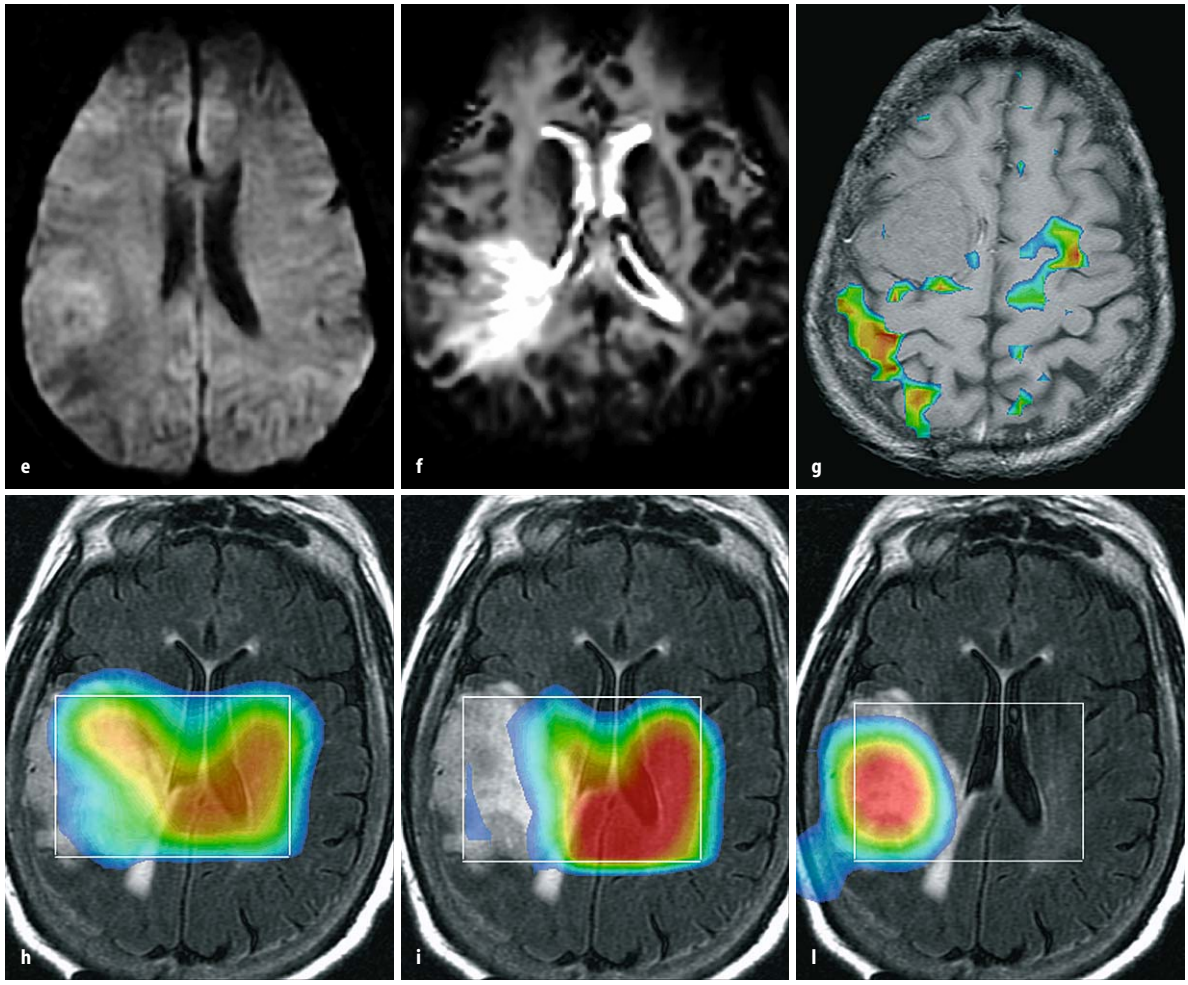

Fig. 3.1. (Cont.)

3.1 Comparison of 3.0 T and 1.5 T MR Imaging

3.1.1 Advantages

3.1.1.1 High SNR

This is undoubtedly the main advantage of high-field MR systems [5–8]. The stronger magnetic field is associated with a proportional increase in the percentage of hydrogen protons oriented parallel to the static magnetic field (B_0), resulting in increased macroscopic longitudinal magnetization (MLM) and thus in a better SNR. In particular, signal intensity increases with the square of B_0, whereas the noise is linearly proportional to it.

In principle, the linear dependence of SNR on magnetic field strength should result in its doubling from 1.5 T to 3.0 T. In practice, this is true only of some tissues such as cerebrospinal fluid (CSF). In white and grey matter and in the grey nuclei the increase is much smaller (30–60%) because the signal reduction induced by changes in relaxation times is associated with a greater signal loss due to susceptibility (related to the very low iron concentrations in some of these areas) and to chemical shift artefacts. Moreover, despite major advances in software and hardware directed at improving image quality and reducing imaging time, acquisition parameters can also be modified to an extent where a lower SNR can be obtained at 3.0 T than 1.5 T (Fig. 3.2). However, use of 3.0 T systems in clinical settings requires great care to avoid compromising image quality.

3.1.1.2 High Spatial Resolution

The greater SNR allows increased spatial resolution to be achieved and a reduction of partial volume effects, thereby depicting structures that are difficult to visualize at 1.5 T (e.g. blood vessels measuring 200–300 μm).

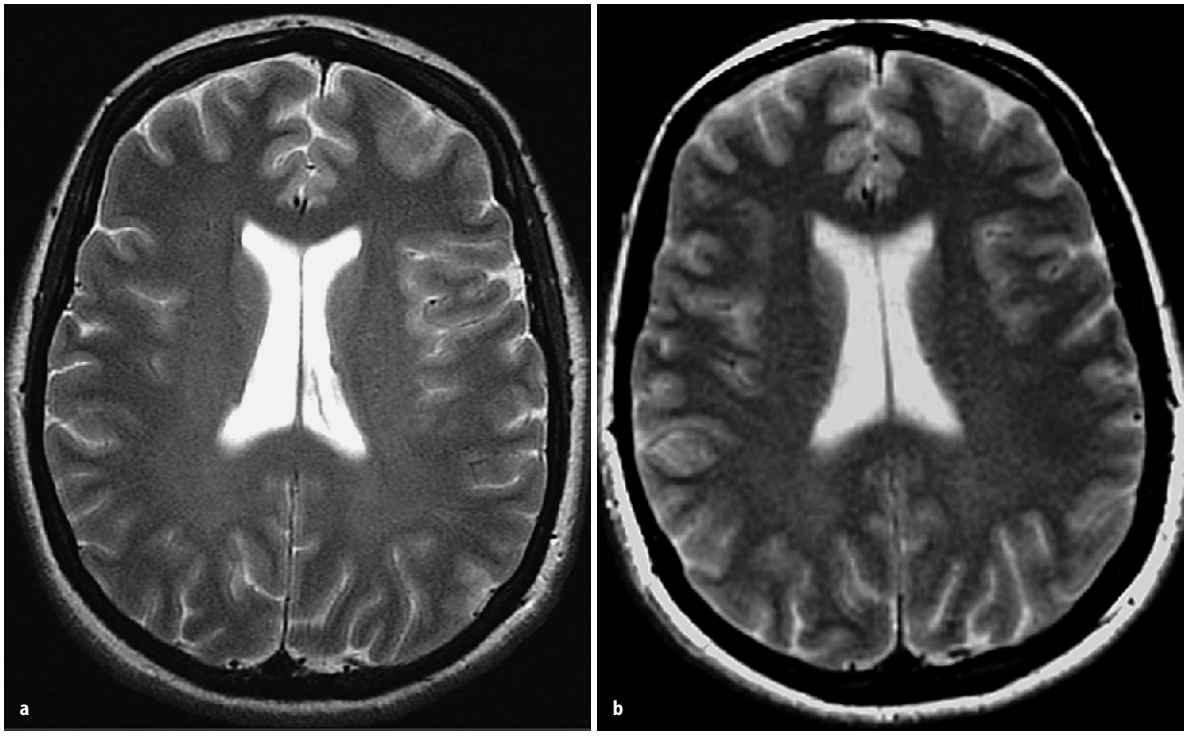

Fig. 3.2. FSE T2 study: comparison of 3.0 T (TR/TE/ETL 4850/81/15, slice thickness 4 mm, FOV 22 cm, matrix 448×320, 2 NEX, 2:39) (**a**) with 1.5 T (TE/TE/ETL 3000/88/8, slice thickness 6 mm, FOV 24×18, 2 NEX, 256×224, 2:24) (**b**). At 3.0 T (**a**) an FSE T2 study takes a similar amount of time as at 1.5 T (**b**) but achieves greater definition (thinner and more numerous slices, broader matrices and smaller FOV)

In addition, the resulting greater spatial resolution makes 3.0 T imaging more accurate when fine morphological detail is required, as in volumetric studies like hippocampal volumetry, which is performed to analyse the extent of hippocampal damage in patients with epilepsy and other diseases involving the brain such as Alzheimer's [9].

3 T MRI also provides accurate stereotactic data sets [10].

3.1.1.3 High Temporal Resolution

Temporal resolution is also enhanced at higher field intensity due to greatly reduced acquisition time. Indeed, the fast gradients of 3.0 T units allow scanning times to be drastically shortened, resulting in a reduction of motion artefacts.

Using a 3.0 T MR system, morphological investigations of the brain, including a standard high-definition study before and after contrast administration, can be performed in 20–30 min and yield greater detail than using a 1.5 T unit. If diffusion and perfusion studies, spectroscopy and functional MR imaging (fMRI) are also performed, acquisition and processing times do not exceed 50–60 min.

Since intrinsically fast techniques like echoplanar sequences obviously involve similar acquisition times with both low and high field strengths, the greater SNR of the latter is exploited to achieve enhanced spatial resolution (Fig. 3.3).

High-strength magnetic fields are therefore indicated for fast imaging of patients in poor conditions, for long protocols (including structural, metabolic and functional imaging), and for novel applications such as continuous EEG recording and functional fMRI for the detection of seizure foci [11].

Reduced times of acquisition are also useful with uncooperative and paediatric patients. In the latter, this feature is especially valuable in the case of non-sedated children who may have difficulties in lying still, or in sedated neonates in poor conditions: short examination times are thus crucial in both cases [12].

3.1.2 Disadvantages

3.1.2.1 Increased SAR

A major drawback of high magnetic fields is an increased SAR, i.e. the radiofrequency (RF) energy deposited per kilogram of tissue in unit of time. The resonance frequency of the hydrogen protons, hence the

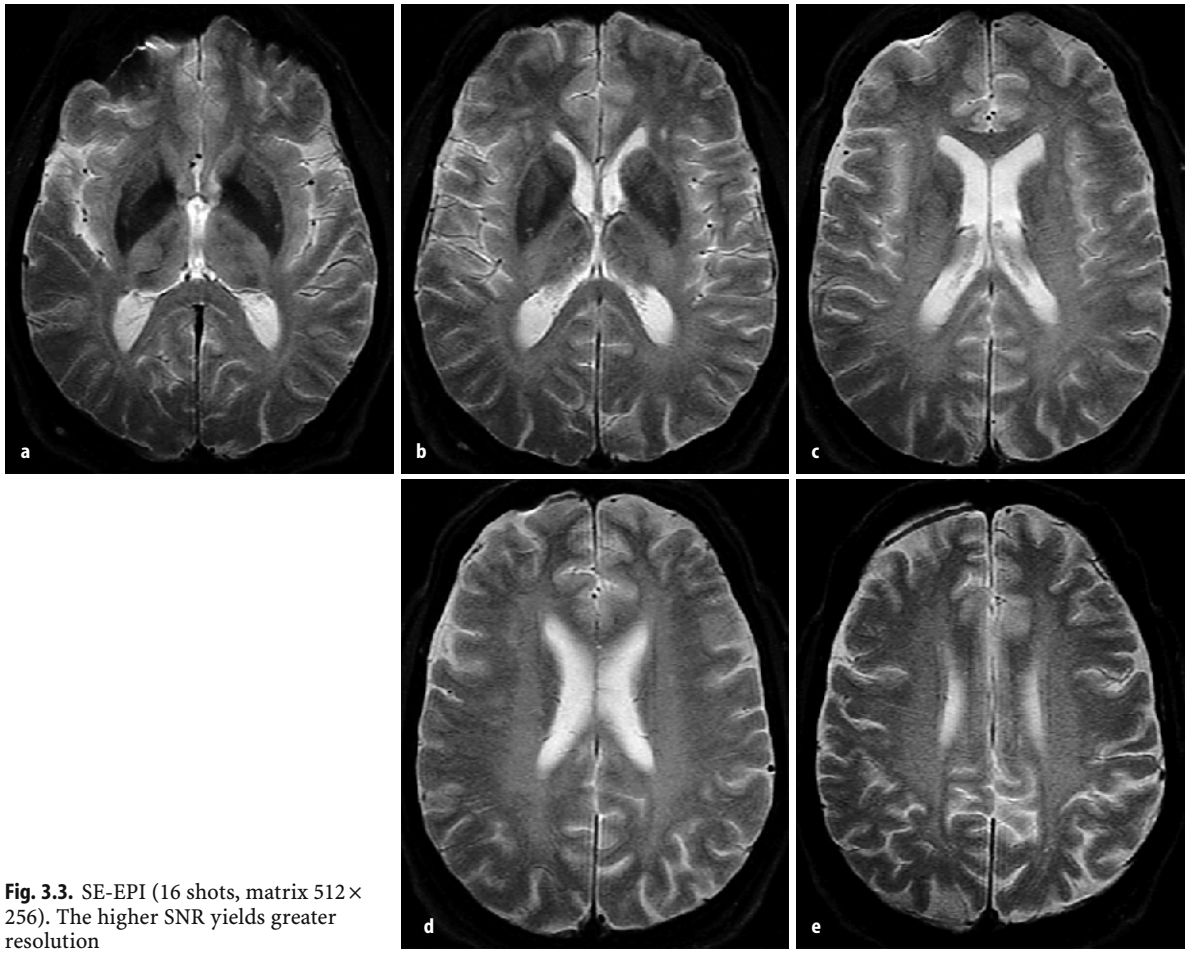

Fig. 3.3. SE-EPI (16 shots, matrix 512 × 256). The higher SNR yields greater resolution

RF signal, grows proportionally with magnetic field strength, resulting in more energy being deposited in tissues. As a consequence the SAR limits are reached sooner with 3.0 T than 1.5 T units, the SAR increasing fourfold from 1.5 T to 3.0 T [13, 14]. Because the SAR increases with the square of the field strength, RF deposition is more limiting at higher field strengths.

Moreover, as the SAR is also proportional to pulse duration and pulse and slice number, its increment at higher magnetic field strengths entails a number of drawbacks, limiting the number of slices, the use of fast spin echo (FSE) sequences, selection of the flip angle (FA), and speed of acquisition. Therefore sequences such as FSE, which employ a large number of closely spaced RF pulses with large FA, are those most likely to cause increased energy deposition at higher fields and to be affected by SAR level limitations. Unfortunately, as FSE sequences rely on T2- rather than T2*-weighted echo trains, they are the least sensitive to susceptibility-induced image distortion and would be extremely useful at higher magnetic fields.

High magnetic field strength therefore requires a new approach to reduce the SAR, especially when using FSE. Several different strategies have been devised to do this. The most obvious one is to reduce acquisition time via an increase in echo spacing and a reduction in echo train length, or by employing partial FA (e.g. 150° instead of 180°). However, these methods impair scanning efficiency (due to longer examination times or to reduced anatomical coverage) or the contrast/noise gain per unit of time. An interesting technique that is not affected by these limitations is the one using hyperechoes, which for tissues with $T1 >> T2$ provides greater signal intensity. Using the hyperecho as the centre *k*-space line for the image, a greater SNR is achieved with respect to comparable conventional FSE sequences with a marked reduction in SAR.

With T1 sequences, use of longer TR partially resolves the SAR problem but entails longer imaging times as well as a decrease in the T1 weighting of sequences, which is not necessarily desirable.

By contrast, in gradient echo imaging lower FA for given TR are used to reduce the SAR.

To prevent accidental heating of tissues during scan-

ning, the SAR must always be closely monitored to avoid exceeding the limits laid down by the FDA (Food and Drug Administration) (less than 1°C in any tissue). This threshold is rarely reached at 1.5 T even using FSE sequences.

Therefore, since sequences can be modified and still yield high-quality images, the SAR is not an insurmountable problem for brain scanning at 3.0 T with the exception of foetal imaging; high-field imagers are thus unlikely to be used for the latter applications in the foreseeable future [12].

The newer MR system designs are inherently more SAR-efficient. While the earlier units were so RF-intense as to require „patient cooling" intervals between sequences in some cases, the more modern, units and their protocols do not normally carry this risk. Limitations in the rate of RF energy deposition continue to place minor restrictions on the number of sections that can be acquired per TR period, thus some of the efficiency gains afforded by the potentially doubled signal intensity of 3.0 T units. The problem is much less severe with newer systems, and section reduction is currently a relatively minor concern also thanks to the increasing diffusion of parallel imaging with multichannel receiver coil arrays, which is becoming an integral part of high-field MR neuroimaging. This technique reduces the effects of SAR by means of a decreased RF exposure achieved by reducing the number of pulses required to obtain a given image with a set resolution. Although this entails an increase in dead time, it is partly offset by the greater SNR of 3.0 T systems. For this reason, high-field imaging is the ideal platform for parallel imaging because it helps to offset the low SNR of parallel imaging.

Finally, modifications in pulse sequence design by several manufacturers should in the near future lead to RF limitations and section acquisition efficiency equal to or even slightly greater than those currently available with 1.5 T units [15, 16].

3.1.2.2 Increased Acoustic Noise

The acoustic noise generated by rapid gradient switching within the main magnetic field, which increases with field strength, is another considerable disadvantage of 3.0 T units. The noise is twice that generated in a 1.5 T MR system and may exceed 119 dB, especially with fast sequences like fast SE, fast gradient echo (FGE) and echoplanar imaging (EPI).

However, this disadvantage can also be overcome relatively easily by using parallel imaging.

3.1.2.3 Dielectric Resonance Effect

This phenomenon is connected with the distortion of the B_1 field by the body of the subject in the tunnel when volume coils are used at high fields. In particular, as the field strength, and therefore the Larmor frequency, increases – while the wavelength decreases – body size becomes significant with respect to the wavelength of the radiation transmitted, particularly in the presence of a high dielectric constant of the body. This results in a change in the intensity of the signal, which will often exhibit a bright centre and relatively hypointense borders [17, 18].

3.2 Diagnostic Features of 3.0 T MR Imaging

The main differences compared with lower field strength systems are: (1) changes in tissue contrast, (2) increased magnetic susceptibility, and (3) increased chemical shift.

3.2.1 Changes in Tissue Contrast

Whereas proton density is clearly a magnetic field-independent parameter, T1 and T2 relaxation times are field-dependent, usually increasing and, respectively, decreasing at higher magnetic fields.

The rates at which excited protons relax are a function of magnetic field strength. In general, the longitudinal or spin-lattice relaxation rate (R1 = 1/T1) of certain tissues (e.g. semisolids) decreases with field strength, whereas the transverse relaxation rate (R2 = 1/T2) is scarcely affected [5, 19]. This leads to a 25 – 40 % increase in T1 relaxation time in tissues on passing from 1.5 T to 3.0 T fields. By contrast, for biological fluids (like CSF and blood) the longitudinal rate is weakly affected, so that R1 and R2 are basically equal at both field intensities. As a result, given the same TR, T1 weighting is greater at 3.0 T than at 1.5 T. Good T1 contrast can also be achieved using relatively long TR.

The increase in T1 relaxation time is a major drawback in high-field SE T1 imaging, as the reduction in T1 differences between tissues results in loss of contrast (Fig. 3.4).

T1 lengthening with increasing magnetic field also applies to blood. Blood T1 is insensitive to the level of oxygenation and increases linearly with field strength. This is particularly valuable in MR angiography (especially in time-of-flight sequences), as it involves greater background suppression due to a lower R1 of stationary tissues and a greater flow enhancement given the broadly constant R1 of blood, thus yielding better vessel-tissue contrast (Fig. 3.5) [20, 21].

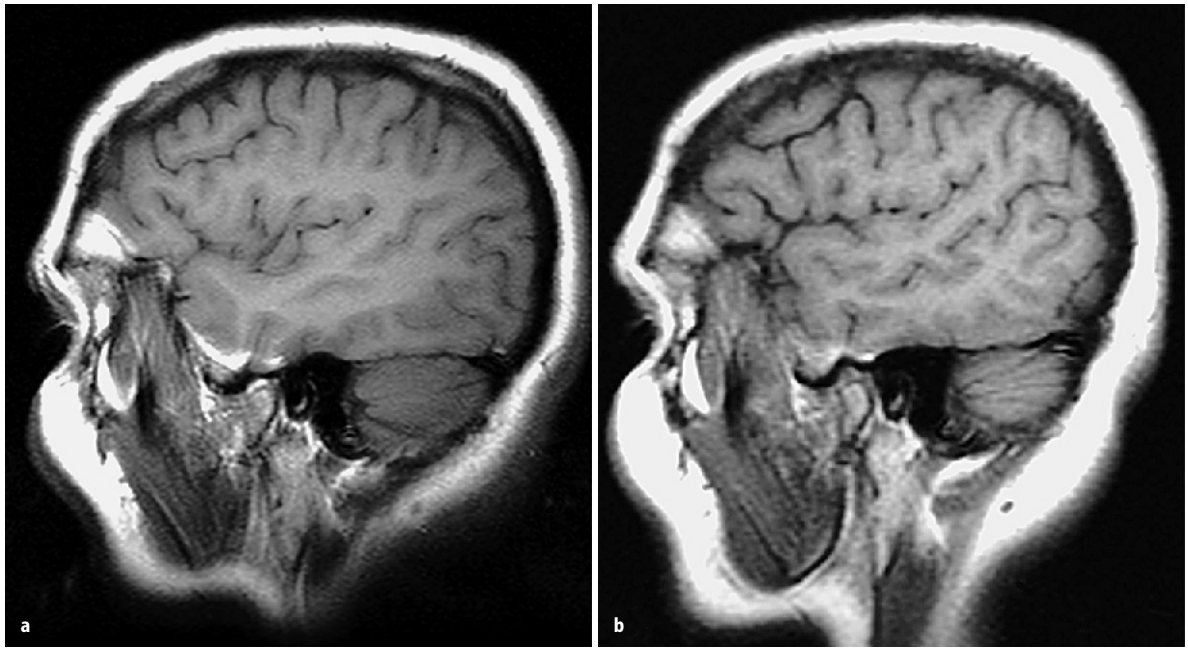

Fig. 3.4. T1 imaging: SE T1 sequence acquired at 3.0 T (TR/TE 500/min, slice thickness 5 mm, FOV 24, matrix 320×224, 1 NEX, 2:00) (**a**) and 1.5 T (TR/TE 500/min, slice thickness 5 mm, FOV 24 cm, matrix 256×192, 1 NEX, 1:23) (**b**). The increased T1 involves reduced contrast at 3.0 T with respect to 1.5 T

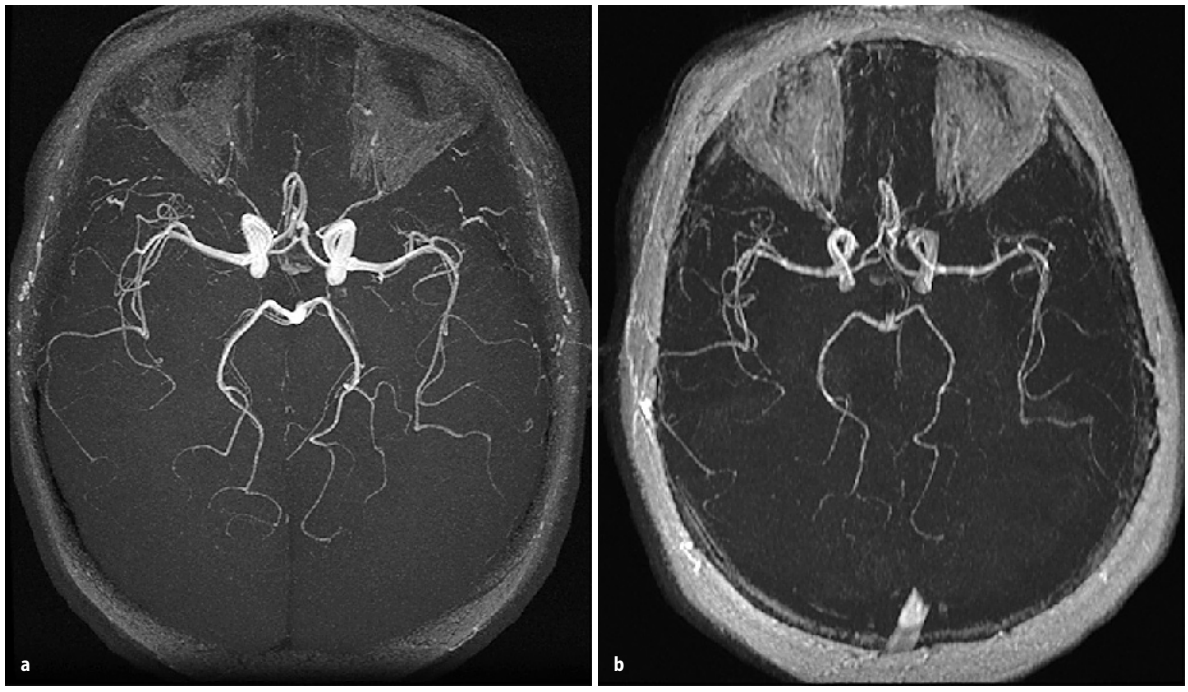

Fig. 3.5. Normal arterial circulation: 3D TOF study at 3.0 T (**a**) and 1.5 T (**b**). Vascular conspicuity and background are greater in **a** (TOF SPGR TE/TE/FA 30/min/20, slice thickness 1.4 mm, matrix 512×320, ZIP 1024, ZIP 2, 1 NEX, 50 locations per slab, 6:18) than in **b** (TOF SPGR TE/TE/FA 45/4/20, slice thickness 1.4 mm, FOV 24×18, matrix 512×224, 1 NEX, 50 locations per slab, 6:22) resulting in greater vessel-tissue contrast

The long T1 is also useful in perfusion studies, as spin tags persist over a longer time, boosting sensitivity.

As regards brain tissue T2 relaxation time, it diminishes with increasing magnetic field, albeit not linearly. In fact, T2 contrast is largely unaffected by field

strength, probably due to the action of other mechanisms (like exchange and/or diffusion during gradient activation).

T2* is also shorter at 3.0 T. This may be useful when studying the deoxyhaemoglobin-containing vasculature (i.e. the venous system) and can also yield brain tissue contrast, for instance between grey and white matter. Indeed, the shorter T2* relaxation times enhance the differences in the T2* of different tissues, resulting in greater distortion and in a larger number of artefacts due to signal loss. Indeed, changes in R2* are sensitive to changes in B_0 and are therefore related to differences in field susceptibility and homogeneity. Optimal B_0 field homogeneity, improved high-order coil shimming and broader reconstruction bandwidths are essential to improve the signal in such circumstances.

3.2.2 Increased Magnetic Susceptibility

Susceptibility effects increase with field strength. Increased magnetic susceptibility enhances the BOLD (blood oxygenation level dependent) effect, making clinical BOLD imaging more practical and informative as a result. BOLD contrast is the result of small magnetic susceptibility effects also responsible for the MR signal changes caused by changes in blood oxygenation under 3 %.

3.0 T fMR images reflect greater signal changes (up to 7 %) (Figs. 3.6 – 3.8) [22 – 25].

The increased static MR signal can be used to reduce the cortical volume needed for signal averaging to

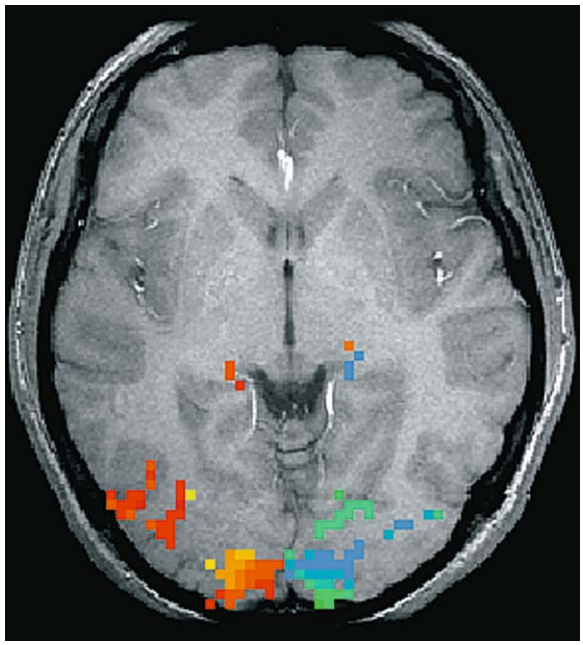

Fig. 3.7. Visual fMRI at 3.0 T: the enhanced BOLD effect maps additional areas at the millimetre and submillimetre levels (*arrows*)

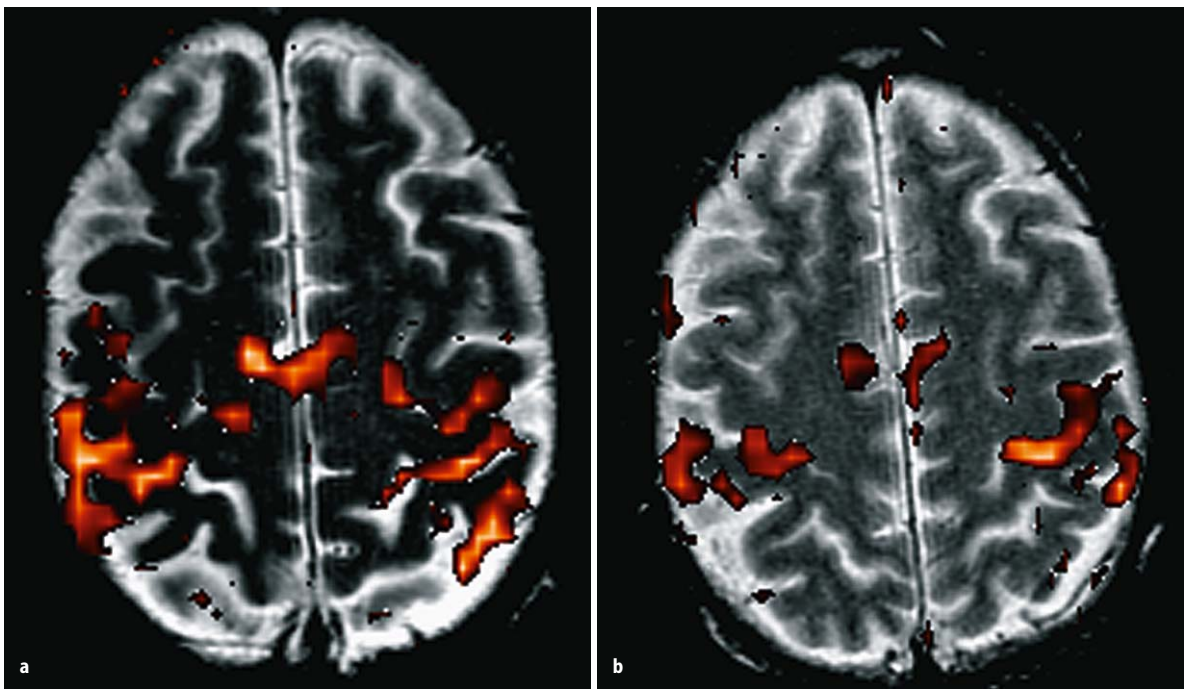

Fig. 3.6. Motor fMRI with bilateral finger tapping: study at 3.0 T (**a**) and 1.5 T (**b**). The enhanced sensitivity to blood oxygenation and reduced background noise of the 3.0 T system (**a**) affords more reliable localization of motor areas compared with the 1.5 T imager (**b**)

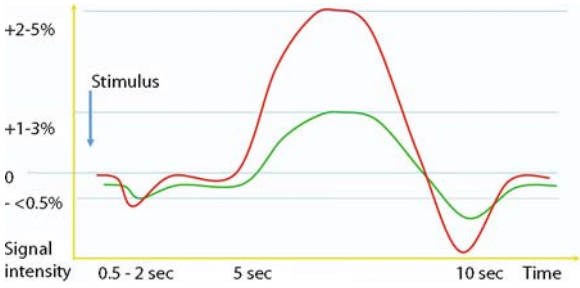

Fig. 3.8. Visual fMRI: the signal level obtained with the 1.5 T system is 1 – 3 % (green) compared with 2 – 5 % with the 3.0 T system (*red*)

achieve sufficient SNR. Another, potentially more important advantage of the higher B_0 is that as the field strength increases, the field gradient around the capillaries becomes larger and extends further into the parenchyma, thus involving a greater amount of brain tissue in producing the functional signal. In field gradients, the magnetization vectors inside voxels attain different phases and the effective transverse relaxation time T2* decreases as a result. Concurrently, the shortened T2* of blood at high B_0 reduces the relative contribution from the large veins. So the weighting of capillary signal contributions becomes more significant and the functional signal is more closely coupled with neuronal activity [26].

The BOLD contrast increases as a result, becoming more sensitive to the susceptibility effects in and around the smaller vessels rather than in and around larger draining vessels. GE-EPI are usually preferred to SE-EPI sequences because they afford better discrimination of small from large vessels. SE-EPI are the sequences of choice for the study of small vessels on which the BOLD effect depends with the increase in magnetic field strength. In addition, because SE-EPI sequences are less sensitive to magnetic susceptibility effects, they are preferred for fMRI in areas where differences in susceptibility at the air-tissue interface (e.g. paranasal sinuses) are more difficult to depict at high-field strengths, resulting in marked SNR reductions.

The greater sensitivity of high-strength magnetic fields to magnetic susceptibility can also be exploited to boost the sensitivity of contrast-enhanced perfusion studies and to improve the sensitivity of FSE sequences to haemorrhagic lesions (Figs. 3.9 – 3.11) [19, 27, 28].

However, 3.0 T MR systems have two potential disadvantages with respect to 1.5 T scanners. Firstly, EPI sequences are usually noisier due to switching of the usually more powerful gradients, even more so when EPI sequences are acquired with GE sequences, because using SE sequence refocalization prevails over phase dispersion, thereby reducing the noise. Secondly, high-field systems are characterized by a larger number of magnetic susceptibility artefacts, especially when us-

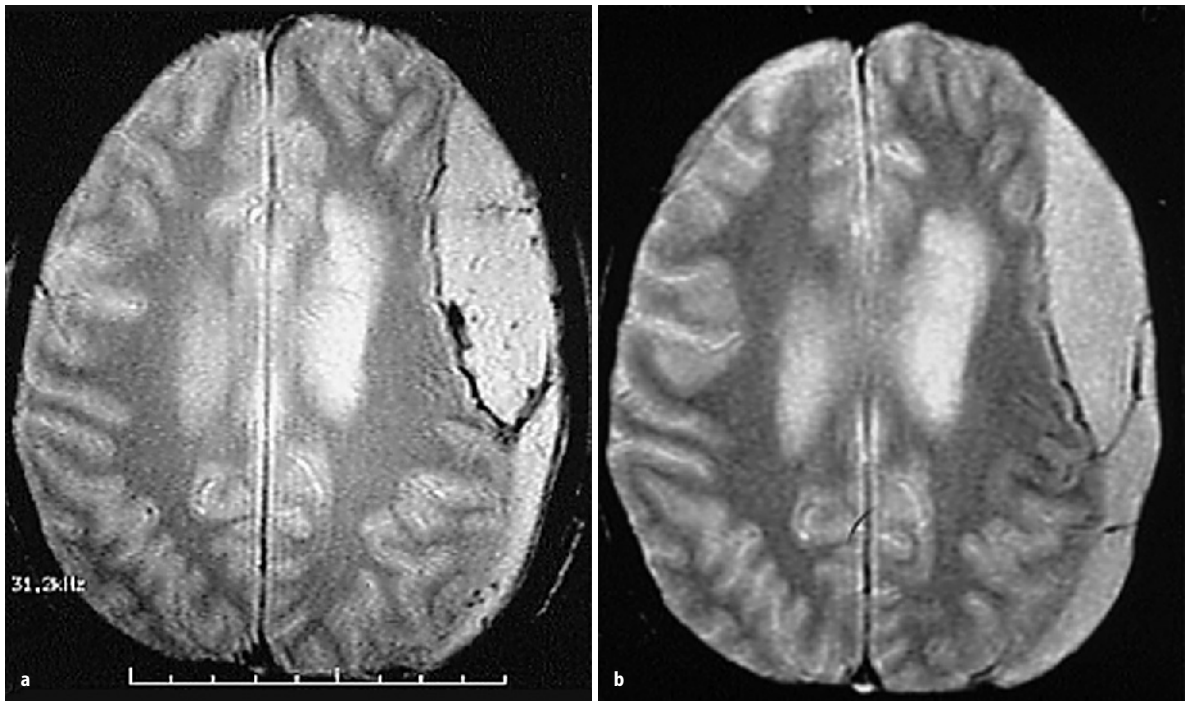

Fig. 3.9. Arachnoid cysts complicated by haemorrhage in subacute-chronic stage after surgery. Study with GRE T2 sequences at 3.0 T (TR/TE/FA 525/9.8/20, slice thickness 5 mm, FOV 24 × 18, matrix 512 × 224, 2 NEX, 2:60) (**a**) and 1.5 T (TR/TE/FA 500/15/20, slice thickness 5 mm, FOV 24 × 18, matrix 320 × 192, 2 NEX, 2:28) (**b**). The greater sensitivity of 3.0 T MRI to the effects of magnetic susceptibility affords better depiction of haemosiderin deposits

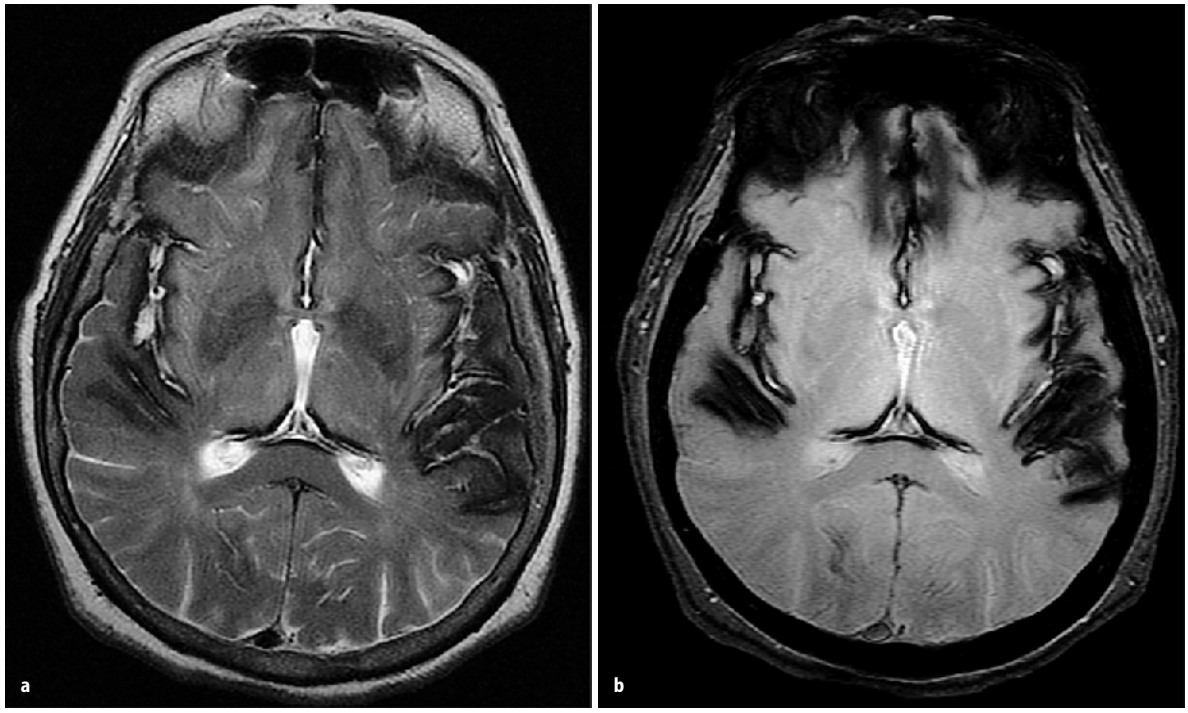

Fig. 3.10. Leptomeningeal haemosiderosis studied with FSE (**a**) and GRE (**b**). Despite the intrinsically lower sensitivity of FSE to magnetic susceptibility, the 3.0 T imager affords excellent depiction of the low haemosiderin signal, which is visualized even more clearly in the GRE sequence

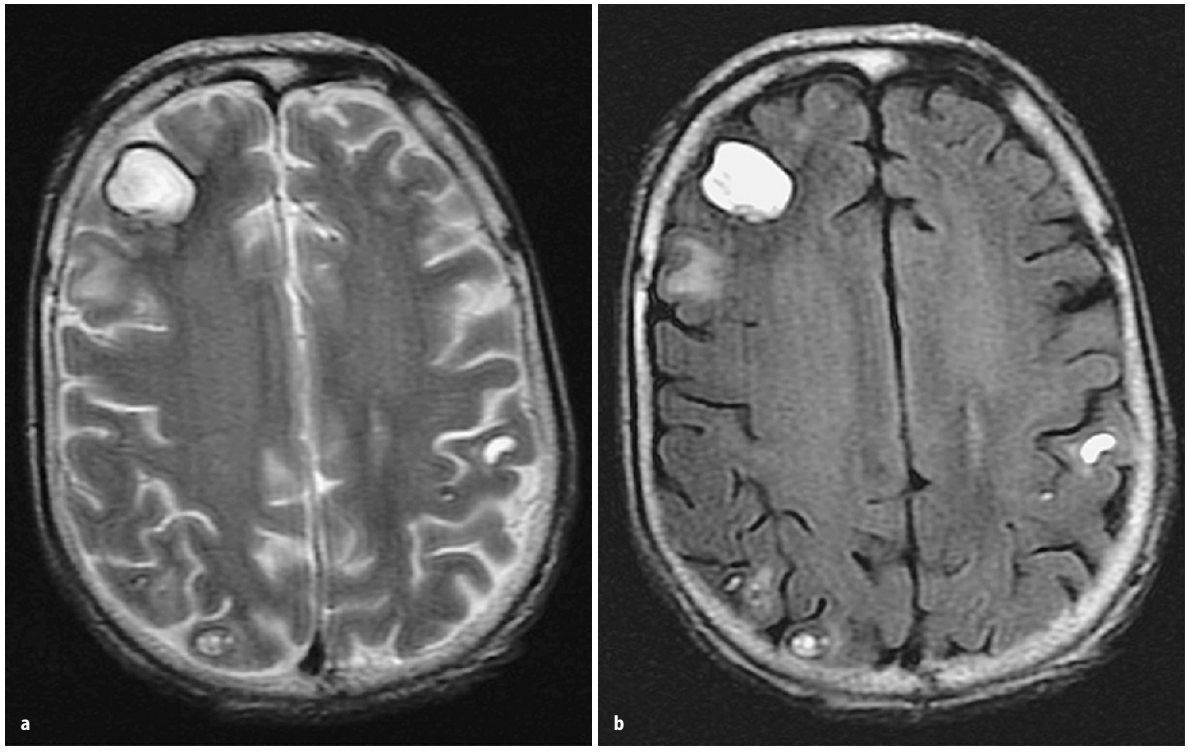

Fig. 3.11. Multiple recent haemorrhagic foci studied with FSE (**a**) and FLAIR (**b**). Suppression of the CSF signal improves detection of the smaller lesions in the FLAIR sequence

ing GE and EPI sequences (mainly in the areas that most commonly generate artefacts, such as the temporal lobes), and from blurring when FSE sequences are performed, which often yield unsatisfactory images. In both cases, experience and use of correction systems (phase map correction) and techniques such as radial array orientation of *k*-space data and propeller CD help dispel diagnostic doubts. Finally, by reducing effective echo spacing and TE at the expense of SNR, parallel imaging allows images to be obtained with an artefact incidence comparable to that of 1.5 T units [29].

3.2.3 Increased Chemical Shift

Chemical shift effects also increase with magnetic field strength. The increased chemical shift enhances spectroscopic investigations via an increased chemical shift resolution, which affords wider separation of the absolute frequencies of different metabolites (Fig. 3.12) [30–32]. However, a larger number of artefacts is generated at the interfaces between tissues with different chemical bonds (fat/water) due to erroneous signal attribution within the reconstruction matrix, resulting in diagnostic limitations in standard anatomical imaging.

At 3.0 T, the water/fat chemical shift is around 440 Hz; this leads to the use of FSE sequences, in which more 180° pulses (greater echo train length), fewer TE and reduced slice thickness compensate for the susceptibility artefacts at the interfaces of tissues with different susceptibility constants. In addition, broader receiver bandwidths (32–125 kHz) are applied to keep the chemical shift within limits that do not impair diagnostic quality. Indeed, to reduce these artefacts to levels seen at 1.5 T, since the chemical shift frequency between water and fat doubles at 3.0 T, the receiver bandwidth needs to be doubled too, with a consequent reduction in SNR by approximately 40 %. All other imaging parameters being equal, the images obtained at 3.0 T, which show a roughly 60 % improvement in SNR over those acquired at 1.5 T, will therefore have 20 % better SNR. Attempts to enhance spatial resolution by increasing the in-plane matrix, reducing section thickness, or both will further compromise the SNR [33]. The reduced SNR associated with the receiver bandwidth is, however, partly compensated for by the higher SNR of 3.0 T systems and by last generation multichannel coils.

One alternative to reducing chemical shift artefacts that does not entail image degradation is fat saturation, which however will further reduce the number of sections that can be acquired because it increases the SAR. Another is water excitation, which does not increase the SAR significantly, improves image resolution and has an SNR similar to that at 1.5 T [33].

3.3 Conclusions

High-field MR, with its intrinsically higher SNR, can be a platform for new diagnostic applications or can serve to improve existing methods. However, its use is not unfettered by limitations.

In fact, the very high spatial resolution and shorter acquisition times permitted by the greater SNR result in a loss of image quality to a level below that which can be achieved with 1.5 T systems. Given the high SNR of 3.0 T MR systems, neuroradiologists can choose between imaging the brain in the same time taken with a 1.5 T unit, thus obtaining better quality images (by increasing the matrix and/or reducing slice thickness and/or FOV) and generating images of the same quality

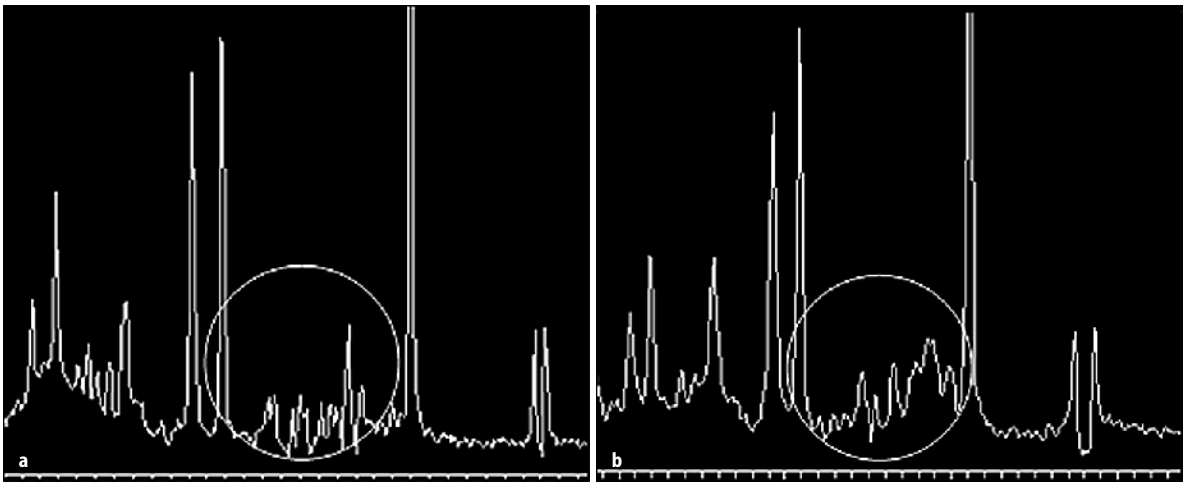

Fig. 3.12. Single volume spectroscopy (PRESS TR/TE 2000/30) acquired at 3.0 T (**a**) and 1.5 T (**b**). In **a** the increased chemical shift improves spectroscopic resolution, resulting in broader separation of the peaks of the different metabolites in the Glx area

as those of a 1.5 T system in a shorter time, thus increasing patient comfort or reducing the dose of contrast medium administered.

Resolution quality tends to be privileged in clinical practice, with acquisition of a larger number of slices of reduced thickness, use of smaller FOV and broader matrices, and acquisition times similar to those of 1.5 T systems (Fig. 3.3).

A compromise is generally sought between resolution and speed (e.g. by reducing the number of excitations) depending on the clinical problem and the type of patient [34].

The high SNR of high-strength magnetic fields can also be obtained with 1.5 T devices using the latest hardware (surface receiver coils used singly or in arrays; high-yield gradients to reduce TE) and software (new sequences able to optimize the contrast/noise ratio) or longer examination times. However, this cannot be done in the case of unstable or poorly cooperative patients, or it may be impossible for reasons of cost (reduced patient flow). In addition, although matrix size can be increased within 1.5 T systems, the attendant reduction in voxel size yields a more granular image.

Lastly, the higher SNR of high-field MR systems is a resource that the neuroradiologist can exploit in clinical practice, since the higher the SNR, the greater the scope for adjusting protocols.

References

1. Scarabino T, Giannatempo GM, Nemore F, et al. (2003) RM 3.0 Tesla. II parte: L'imaging morfo-funzionale cerebrale. Radiol Med 105:150 – 161
2. Scarabino T, Nemore F, Giannatempo GM, et al. (2003) Risonanza Magnetica 3.0 Tesla. Riv Neuroradiol 16 (Suppl): 314 – 315
3. Scarabino T, Nemore F, Giannatempo GM, et al. (2004) 3.0 T imaging. Riv Neuroradiol 17:765 – 776
4. Scarabino T, Nemore F, Giannatempo GM, et al. (2003) 3.0 T magnetic resonance in neuroradiology. Eur J Radiol 48: 154 – 164
5. Frayne R, Goodyear BG, Dickhoff P, et al. (2003) Magnetic resonance imaging at 3.0 Tesla: challenges and advantages in clinical neurological imaging. Invest Radiol 38(7): 385 – 402
6. Norris DG (2003) High field human imaging. J Magn Reson Imag 18:519 – 529
7. Scarabino T, Nemore F, Giannatempo GM, et al. (2004) Semeiological features of 3.0 T MR imaging: what changes at high magnetic field. Riv Neuroradiol 17:755 – 764
8. Takahashi M, Uematsu H, Hatabu H (2003) MR imaging at high magnetic fields. Eur J Radiol 46:45 – 52
9. Briellmann RS, Pell GS, Wellard RM, et al. (2003) MR imaging of epilepsy: state of the art at 1.5 T and potential of 3 T. Epileptic Disord 5(1):3 – 20
10. Azmi H, Schulder M (2003) Stereotactic accuracy of a 3 T magnetic resonance unit. Stereotact Funct Neurosurg 80(1 – 4):140 – 145
11. Briellmann RS, Syngeniotis A, Jackson GD (2001) Comparison of hippocampal volumetry at 1.5 Tesla and at 3 Tesla. Epilepsia 42(8):1021 – 1024
12. Rutherford M, Malamateniou C, Zeka J, et al. (2004) MR imaging of the neonatal brain at 3 Tesla. Eur J Paediat Neurol 8:281 – 289
13. Price RR (1999) MR imaging safety considerations. Radiographics 19:1641 – 1651
14. Schenck JF (1998) MR safety at high magnetic fields. MRI Clinics North Am 6:715 – 730
15. Ross JS (2004) The high field strength curmudgeon. AJNR 25:168 – 169
16. Tanenbaum LN (2004) 3-T MR imaging: ready for clinical practice (letters). AJNR 25:1626 – 1627
17. Tropp J (2004) Image brightening in samples of high dielectric constant. J Magn Reson 167:12 – 24
18. Yang QX, Wang J, Zhang X (2002) Analysis of wave behaviour in lossy dielectric samples at high field. Magn Reson Med 47:982 – 989
19. Wansapura JP, Holland SK, Dunn RS, et al. (1999) NMR relaxation times in the human brain at 3.0 T. JMRI 9:531 – 538
20. Bernstein MA, Huston J 3rd, Lin C, et al. (2001) High-resolution intracranial and cervical MRA at 3.0 T: technical considerations and initial experience. Magn Reson Med 46:955 – 962
21. Reichenbach JR, Barth M, Haacke EM, et al. (2000) High-resolution MR venography at 3.0 Tesla. Comput Assist Tomogr 24:949 – 957
22. Di Salle F, Esposito F, Elefante A, et al. (2003) High field functional MRI. Eur J Radiol 48:138 – 145
23. Chen W, Ugurbil K (1999) High spatial resolution functional magnetic resonance imaging at very-high-magnetic field. Top Magn Reson Imaging 10:63 – 78
24. Thulborn KR (1999) Clinical rationale for very-high-field (3.0 Tesla) functional magnetic resonance imaging. Top Magn Reson Imaging 10:37 – 50
25. Thulborn KR, Chang SY, Shen GX, et al. (1997) High resolution echo-planar imaging of human cortex at 3.0 T. NMR Biomed 10:183
26. Kim D-S, Garwood M (2003) High field magnetic resonance techniques for brain research. Curr Opin Neurobiol 13:612 – 619
27. Sugahara T, Korogi Y, Kochi M, et al. (2001) Perfusion-sensitive MR imaging of glioma: comparison between gradient-echo and spin-echo echo-planar imaging techniques. AJNR 22:1306 – 1315
28. Wang J, Alsop DC, Li L, et al. (2002) Comparison of quantitative perfusion imaging using arterial spin labeling at 1.5 T and 4.0 Tesla. Magn Reson Med 48:242 – 254
29. Heidelmann RM, Griswold MA, Muller M, et al. (2004) Feasibility and limitations of high field parallel MRI. Radiologe 44(1):49 – 55
30. Polonara G, Scarabino T, Salvolini U (2003) Basics and new frontiers of MR spectroscopy with high Tesla. Riv Neuroradiol 16 (Suppl):144 – 148
31. Barker PB, Hearshen DO, Boska MD (2001) Single-voxel proton MRS of the human brain at 1.5 T and 3.0 T. Magn Reson Med 45:765 – 769
32. Di Costanzo A, Trojsi F, Giannatempo GM, et al. (2003) High-field proton MRS of human brain. Eur J Radiol 48:146 – 153
33. Pattany PM (2004) 3 T MR imaging: the pros and cons (editorial). AJNR 25:1455 – 1456
34. Shapiro MD (2004) The time for 3 T clinical imaging is now (letter). AJNR 25:1628 – 1629

Standard 3.0 T MR Imaging

4

T. Scarabino, F. Nemore, G. M. Giannatempo, A. Simeone, A. Maggialetti, N. Maggialetti, U. Salvolini

Magnetic resonance imaging (MRI) studies of the brain can be classified into two general categories based on the type of information that is being collected: morphological or functional. Standard morphological studies are performed to depict tissue, cerebrospinal fluid (CSF) spaces, vessels and fibre bundles; functional studies include mapping of brain function (fMRI), perfusion and diffusion imaging, and metabolic studies by means of spectroscopy.

Standard 3.0 T MR scanning offers better quality images than lower-strength systems, thereby providing superb detail of the brain. Its increased spatial resolution is a major advantage in investigating certain diseases, such as brain tumours requiring tissue characterization, spatial work-up and pre-surgical planning, and difficult to identify congenital abnormalities.

4.1 Pulse Sequences

Anatomical brain scanning essentially relies on proton density, differences in T1 and T2 between regions (e.g. cortex vs. subcortical nuclei), and tissue type (white matter, grey matter and CSF). Brain images can be acquired using different pulse sequences. A 3.0 T MR system implements all the pulse sequences commonly applied in clinical practice, including SE (normal, fast 2D and 3D); GE (GRASS/fast GRASS 2D and 3D, SPGR/fast SPGR 2D and 3D); EPI (single shot/multishot 2D and 3D); and IR (STIR, FLAIR, normal, fast) using common imaging parameters like flow and respiratory compensation, cardiac and peripheral gating, graphic prescription, graphic saturation, fat/water saturation, variable bandwidth and asymmetric field of view.

Since the user interface and sequence parameters are the same as those employed with 1.5 T systems, at 3.0 T one should in theory obtain the same images with the advantage of high-field strength, i.e. a double signal intensity. In practice, much depends on tissue relaxation times (T1 and T2) and the specific absorption rate (SAR) [1–6]. Since relaxation times are field-dependent and affect image contrast, 1.5 T imaging sequences cannot be transferred to 3.0 T systems. In addition, the excessive RF energy that is deposited on tissues at 3.0 T needs to be taken into account when adapting and optimizing clinical imaging protocols for use with such systems.

The technical parameters of the main sequences applied with 1.5 and 3.0 T systems are reported in Table 4.1. Higher-field systems afford greater resolution quality by allowing the acquisition of a larger number of slices (usually 25–27 vs. 18–20) of smaller thickness (4 mm vs. 5–6 mm), with narrower fields of view (20–22 vs. 24), broader matrices (512×512 vs. 256×256), and acquisition times similar to those of 1.5 T systems.

Lastly, two factors that depend on magnetic field strength need to be taken into consideration: the influence of the signal loss caused by the stronger susceptibility effects and the potentially diminished sensitivity of the radiofrequency coils at higher field intensity.

4.1.1 T1 Imaging

Since T1 relaxation times are longer at higher magnetic fields, entailing a reduction in the relative differences among different tissue types, it is generally difficult to obtain T1-weighted images with sufficient contrast when using a 3.0 T unit [2]. In fact, not only T1 increases, but the T1 values of different tissue types actually converge, giving rise to a narrower range of distribution. For this reason, optimization of the signal/noise ratio (SNR) in the same sample using a higher field unit requires longer TR (and a smaller flip angle), resulting in longer scanning times. Using longer TR, the gain in signal intensity in unit of time afforded by the higher magnetic field is therefore lost. T1 saturation for a given TR is greater at 3.0 T, resulting in reduced signal gain. In other words, the SNR per unit of time would be optimized with the shortest possible TR/T1. The possibility that the SNR gain connected with the high magnetic field may substantially be offset by a longer T1 highlights the importance of optimizing the imaging parameters [3].

The increased T1 is the main problem in 3.0 T brain imaging using SE T1-weighted sequences, which afford very unsatisfactory T1 contrast (Fig. 4.1) [7–10]. In-

Table 4.1. Technical parameters of the main sequences applied with 1.5 and 3.0 T systems

Sequence	TR (ms)	TE (ms)	Other parameters (TI, FA, ETL)	Slice thickness (mm)	No. of slices	FOV	Matrix	NEX	Examination time (min:s)
SE T1 1.5 T	500	Min	–	6	16	24	256×192	1	1:23
SE T1 3.0 T	500	Min	–	5	18	24	320×224	1	2:00
FGE T1 3.0 T	225	Min	FA 75	4	20	24	512×256	1	1:57
IR T1 3.0 T	2,075	24	TI auto	4	11×2	24	256×256	1	2:49
TSE T2 1.5 T	3,000	88	ETL 12	6	21	24	256×224	2	2:24
TSE T2 3.0 T	4,850	81	ETL 15	4	25	22	448×320	2	2:39
TSE T2 HD 3.0 T	4,975	85	ETL 15	3	25	20	512×320	4	7:20
FLAIR 1.5 T	8,800	120	TI 2200	5	14×2	26	256×192	2	4:24
FLAIR 3.0 T	11,000	130	TI 2250	4	16×2	22	288×192	2	5:52

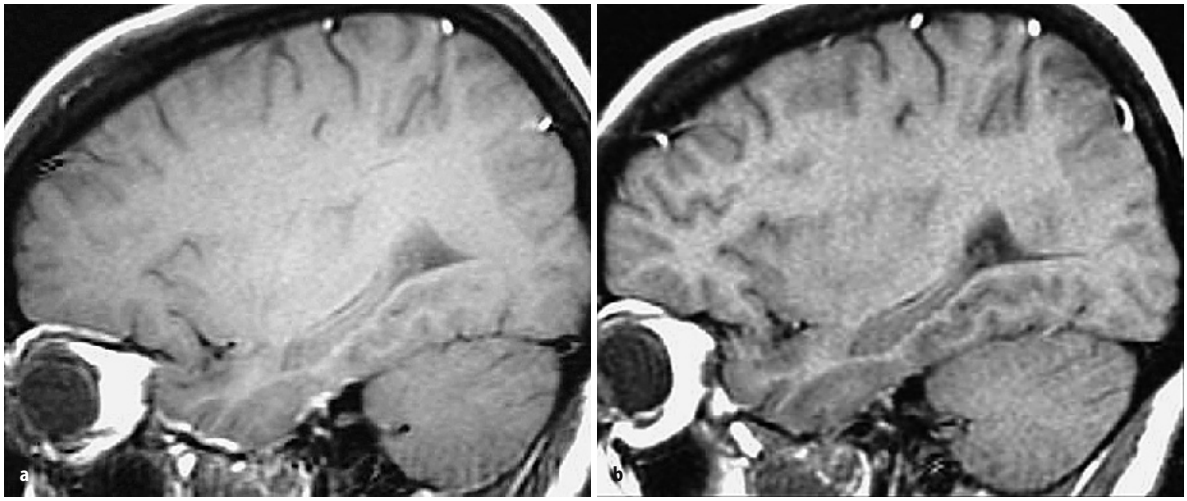

Fig. 4.1. T1 imaging: comparison of the same SE T1 sequence (TR 500, 0.5 NEX, 1:00) acquired at 3.0 T (**a**) and 1.5 T (**b**). Note the less satisfactory white/grey matter contrast in **a**

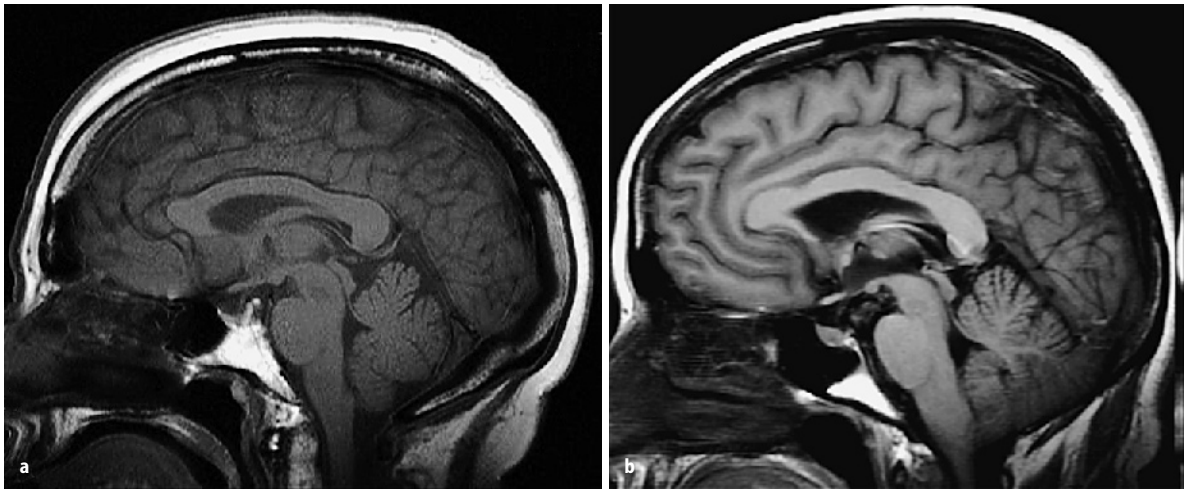

Fig. 4.2. T1 imaging with SE T1 (**a**), FLAIR T1 (**b**) and FGRE T1 (**c**)

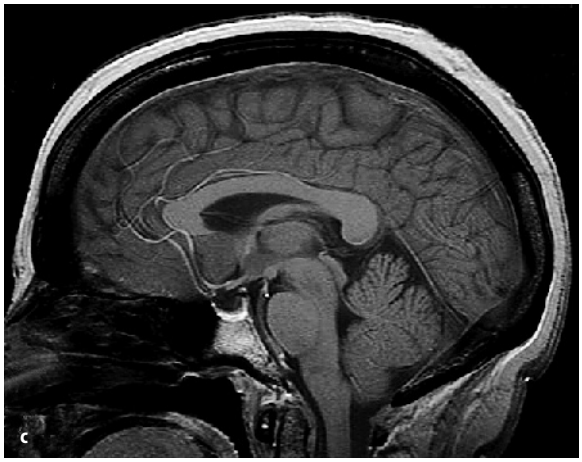

Fig. 4.2. (Cont.) The poor white/grey matter contrast of the SE T1 sequence (**a**) required performance of the other two high-contrast sequences. Note the typical high signal of the larger arterial vessels in **c** (*arrow*)

deed, the reduction in T1 differences among different types of tissues entails a loss of contrast between white and grey matter. For T1 contrast, this has led to the application of sequences other than SE which yield high T1 contrast irrespective of field strength, i.e. fast GE T1 (spoiled gradient echo, SPGR, or MP-RAGE) and fast IR or fast FLAIR T1-weighted (Figs. 4.2–4.4) [7–9].

Fast SPGR allows thinner slices to be obtained in a shorter time and provides images suitable for reformatting in all three planes using a single volumetric acquisition of the whole brain, thus disclosing a larger number of lesions than can be depicted using SE T1-weighted sequences acquired in a single plane. In addition, large arterial vessels appear hyperintense on fast SPGR sequences, although this does not impair image interpretation.

In contrast, fast IR entails longer scanning times because chained acquisitions are required to image the whole brain; this can be a problem when multiple unenhanced and contrast-enhanced studies, or different views, need to be performed.

Unlike IR T1-weighted sequences, which are less satisfactory and take longer to perform, a typical FLAIR T1-weighted study of the brain coupled with parallel imaging allows higher spatial resolution protocols to be applied in a shorter acquisition time.

Greater inflow contrast and enhanced background suppression make contrast-enhanced T1 imaging a definite advantage of 3.0 T systems. For instance, when studying primary and secondary brain tumours, administration of a both single- and multiple-dose gadolinium yields greater contrast between tumour and normal brain tissue and allows the detection of more metastases, and demonstrates different patterns of enhance-

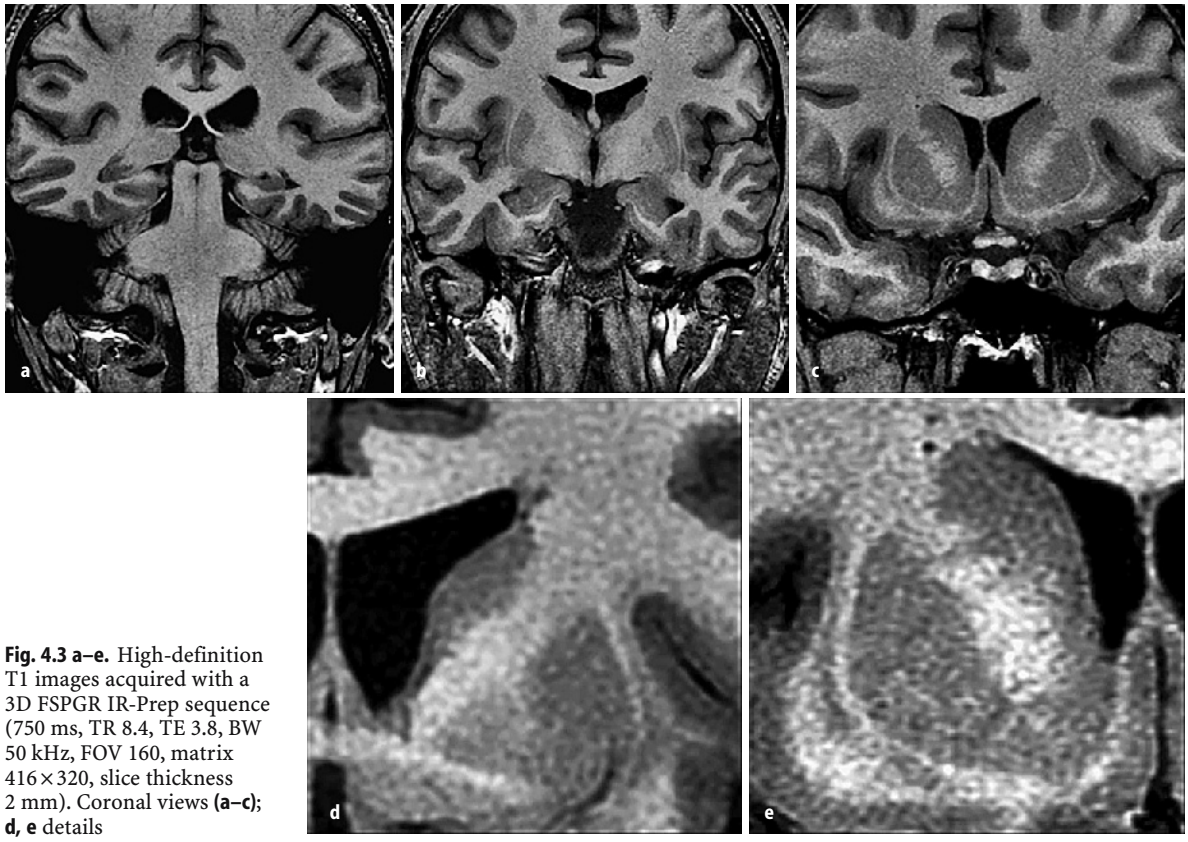

Fig. 4.3 a–e. High-definition T1 images acquired with a 3D FSPGR IR-Prep sequence (750 ms, TR 8.4, TE 3.8, BW 50 kHz, FOV 160, matrix 416×320, slice thickness 2 mm). Coronal views **(a–c)**; **d, e** details

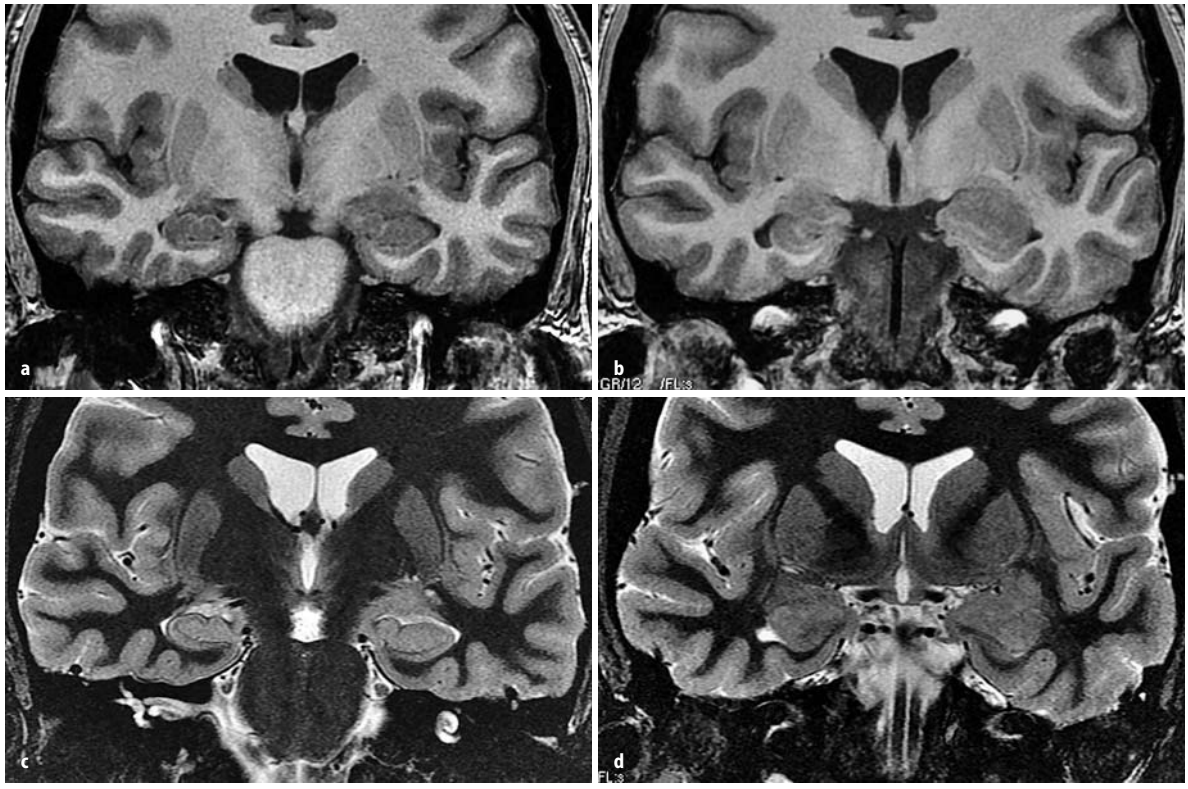

Fig. 4.4. High-definition images: comparison of a 3D FSPGR IR-Prep sequence **(a, b)** (TR 9.1, TE 4.0, FOV 170, slice thickness 2 mm, matrix 320 × 288) with an FSE-IR sequence **(c, d)** (TI 250 ms, FOV 160, slice thickness 3 mm, matrix 512 × 256). Note the optimum anatomical depiction of the cortico-subcortical junction on both sequences

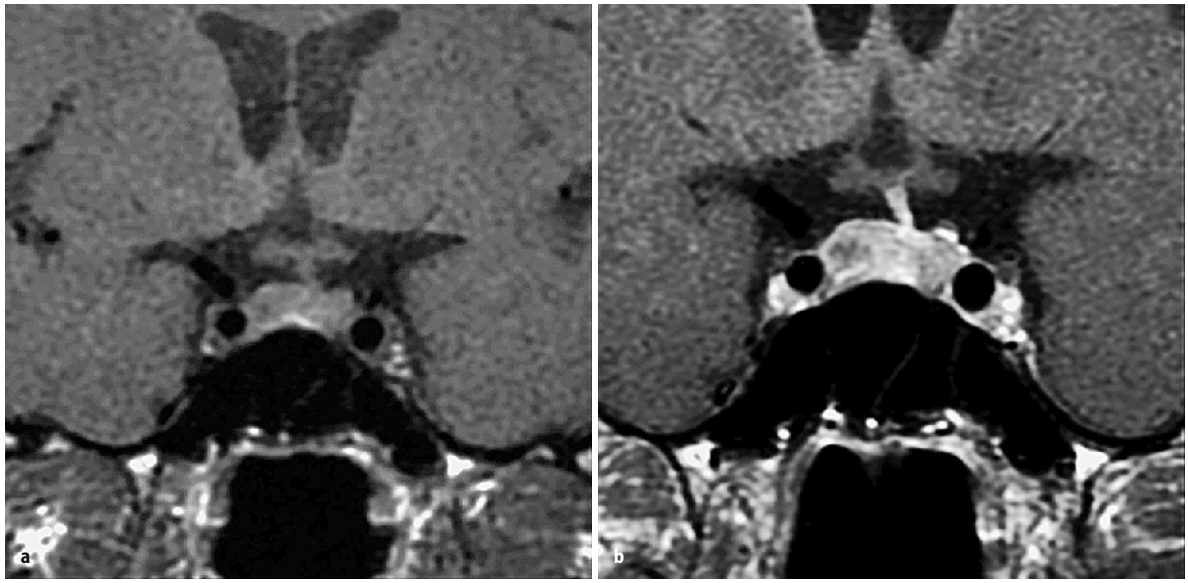

Fig. 4.5. Unenhanced (**a**) and contrast-enhanced (**b**) hypophyseal microadenoma acquired with FSE-XL T1 (TR 600, TE 12, ETL 5, FOV 180 mm, slice thickness 2.5 mm/0.5, matrix 224 × 192, ZIP 512, 29"/phase). PEI processing using Functool 2 (**c**)

ment that may be useful to assess the degree of malignancy and to monitor response to therapy [11 – 13].

The greater sensitivity of 3.0 T contrast-enhanced investigations has also been demonstrated in multiple sclerosis, with a 21 % increase in the number of enhancing lesions detected, a 30 % increase in enhancing lesion volume and a 10 % increase in total lesion volume relative to scanning at 1.5 T [14].

Contrast-enhanced imaging also improves the evaluation of hypophyseal macro- and microadenomas (Figs. 4.5, 4.6). 3.0 T MR venography is another valuable technique that provides increased spatial resolution, and thus more detailed information, in the same time of acquisition as a 1.5 T system [15].

However, contrast-enhanced T1 semeiotics requires adjustments in TR and TE and a reduction in the dose of contrast agent [3]. The usual dosage of 0.1 mmol/kg can be halved without affecting image quality. Using a standard dose, the contrast/noise ratio (CNR) is two and a half times greater than with 1.5 T systems [15]. Double or triple doses can result in meningeal contrast uptake, a common non-pathological finding at 3.0 T which at lower field strengths may, however, mimic carcinomatosis or meningitis, and should thus be avoided.

To enhance sensitivity or highlight minimal changes in the blood brain barrier, a double dose of contrast agent may be employed in selected investigations of brain metastases or inflammatory disease [16, 17]. In such cases, greater lesion enhancement with respect to normal brain parenchyma results in improved sensitivity and resolution.

Fast GE T1, rather than standard SE sequences, are preferred for contrast-enhanced T1 imaging, as they offer better contrast in the same acquisition time. SE T1 sequences are, however, consistently improved by contrast administration (Fig. 4.7).

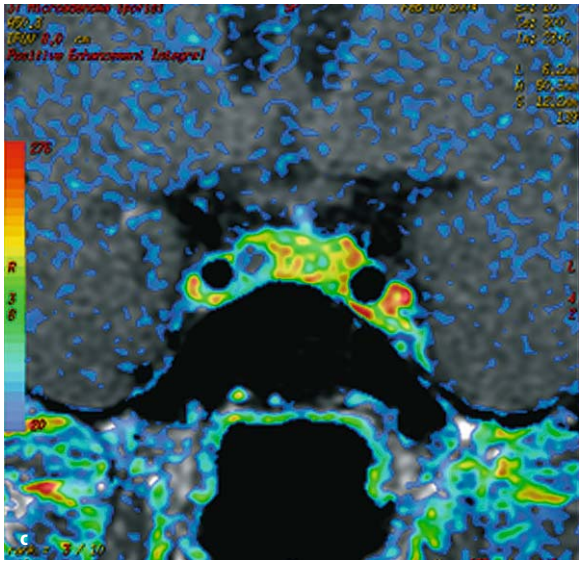

Fig. 4.5. (Cont.)

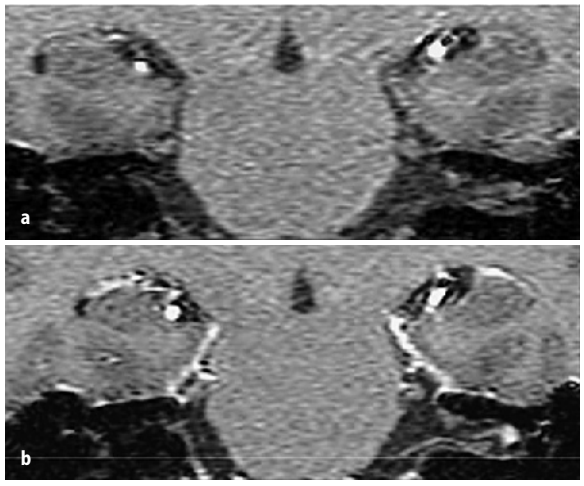

Fig. 4.7 a, b. Small left acoustic neurinoma: high-definition SE T1 sequence (matrix 512, thickness 1.5 mm). Unenhanced (**a**) and contrast-enhanced (**b**) images

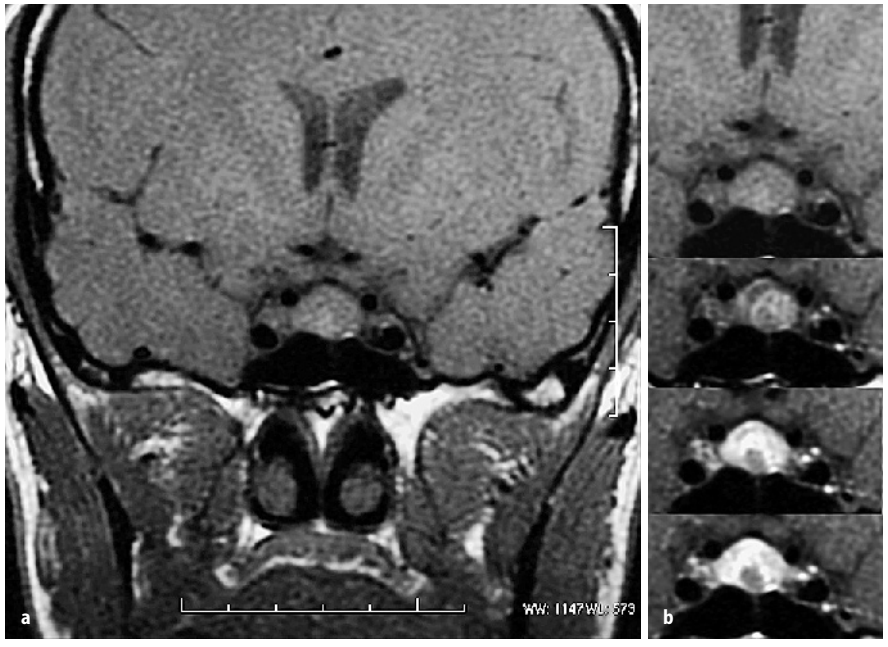

Fig. 4.6. Hypophyseal macroadenoma: dynamic contrast-enhanced image (unenhanced image in **a**)

4.1.2 T2 Imaging

In T2 contrast imaging the advantages of high magnetic field strength are best exploited by performing fast SE sequences acquired using the same technique as with 1.5 T, imagers but with shorter TR and TE due to the shorter T2 relaxation times (Fig. 4.8). High spatial resolution FSE-weighted images are especially effective at 3.0 T as they provide more anatomical detail and better contrast due to the greater SNR, which allows to employ thinner slices and broader matrices (Figs. 4.9–4.13) [7–9, 18]. Even better images are obtained with inverted contrast FSE T2 sequences (Fig. 4.14).

In practice, the greater SNR may be attenuated by

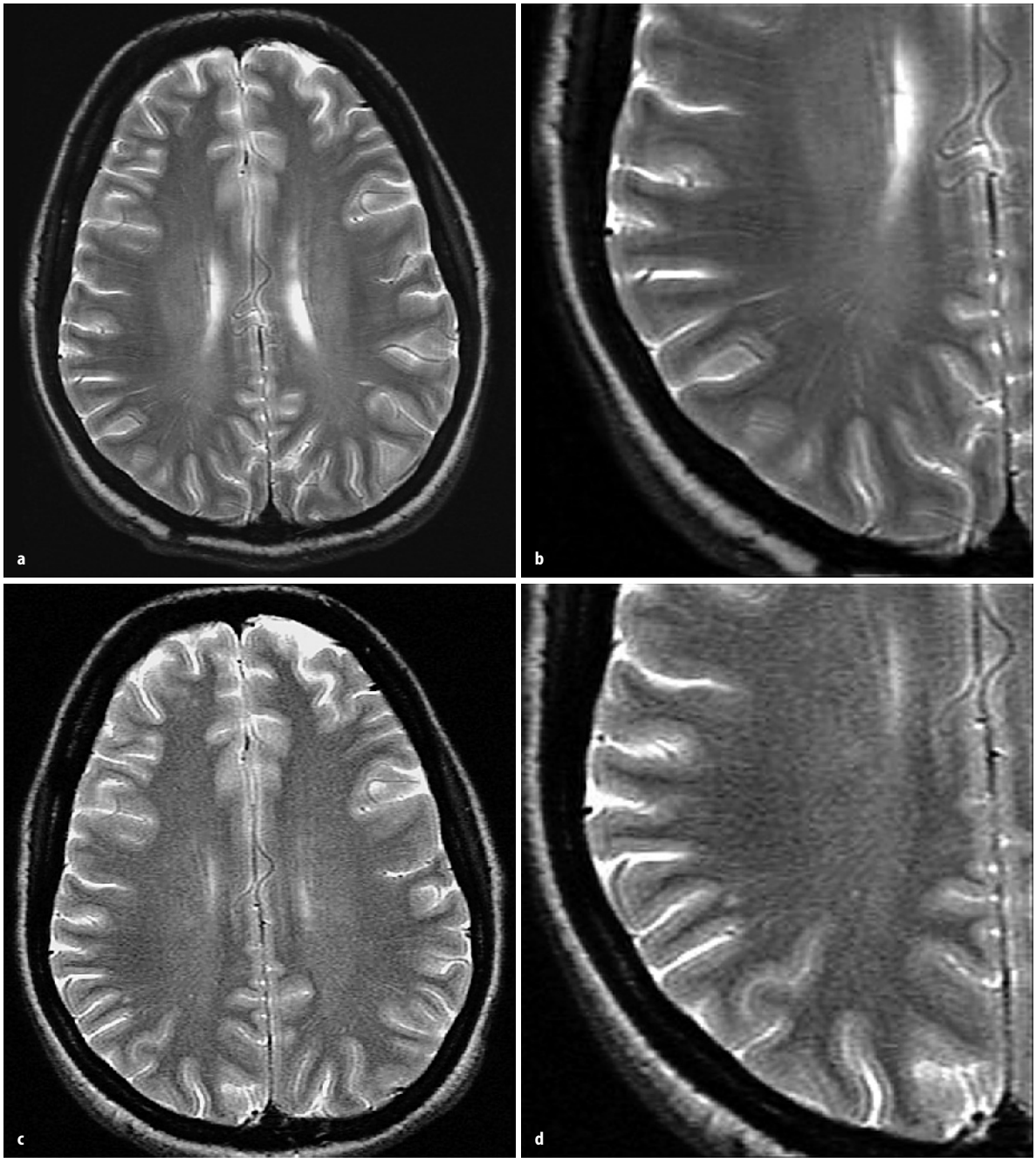

Fig. 4.8. T2 imaging: comparison between the same FSE T2 sequence at 3.0 T (**A, B** zoom) and 1.5 T (**C, D** zoom). Anatomical detail and contrast resolution are greater in **a** and **b**

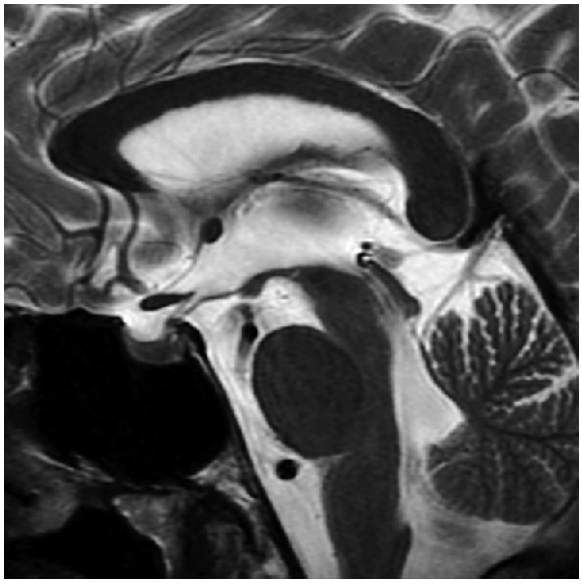

Fig. 4.9. High-definition FSE T2 image of the median sections of the brain

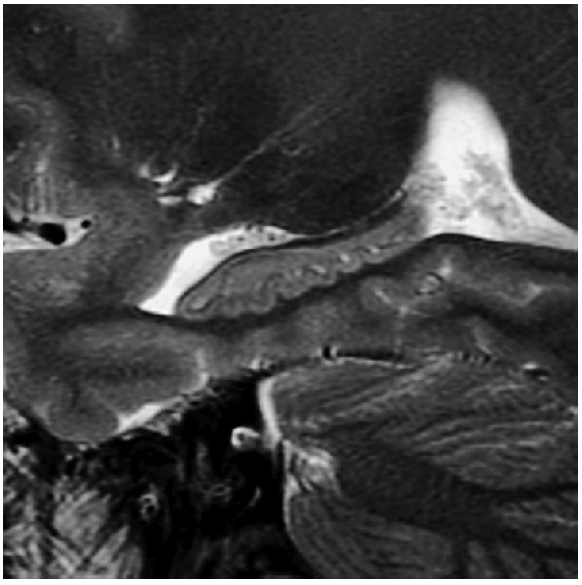

Fig. 4.10. High-definition FSE T2 image of the hippocampus

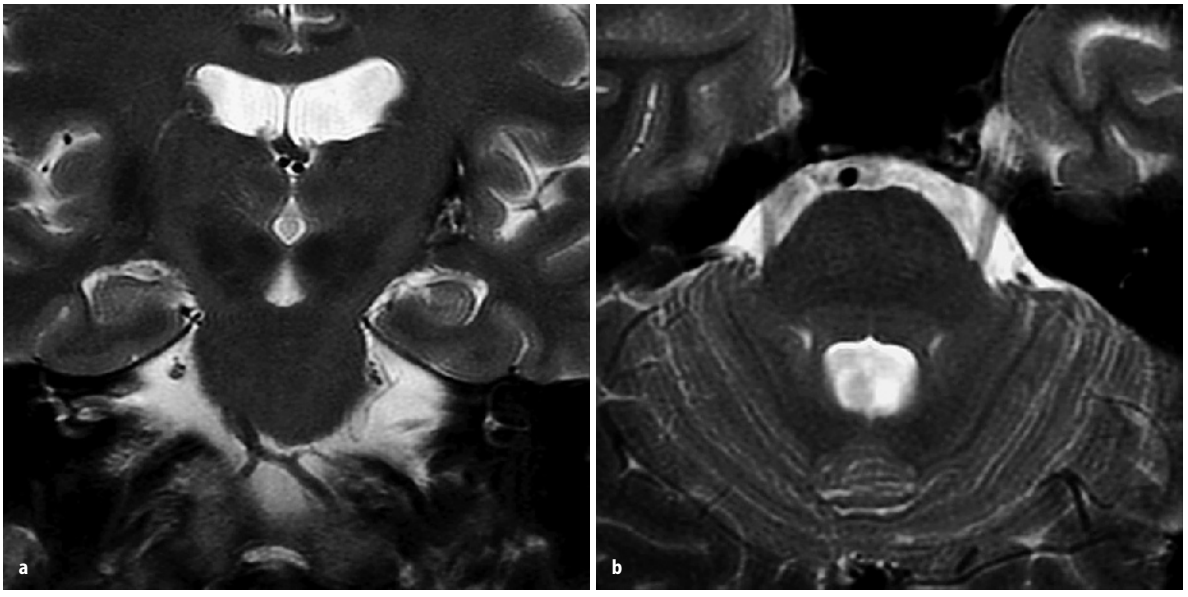

Fig. 4.11. High-definition FSE T2 image of the fifth cranial nerve in coronal (**a**), axial (**b**) and parasagittal (**c**) section

the increased deposition of RF energy, which in turn requires long TR or pulse refocalization angles well below 180°. This lower SNR can, however, be compensated for by the higher field strength. In addition, the broader bandwidth, smaller echo space, shorter minimum TR and TE, and shorter FSE sequences employed at higher field strengths result in improved image quality, artefact reduction, and enhanced diagnostic performance in much shorter examination times, to the benefit of patients.

These sequences allow excellent visualization of the basal or mesencephalic nuclei, by virtue of their iron content, despite the intrinsically lower sensitivity of FSE to magnetic susceptibility in 3.0 T compared with 1.5 T systems [3].

Different signal features are also seen in brain haemorrhage, which at 3.0 T is characterized by greater hypointensity in the acute and early subacute phases [19]. SNR and signal intensity being roughly similar at both field intensities, correct dating of the haemorrhage is

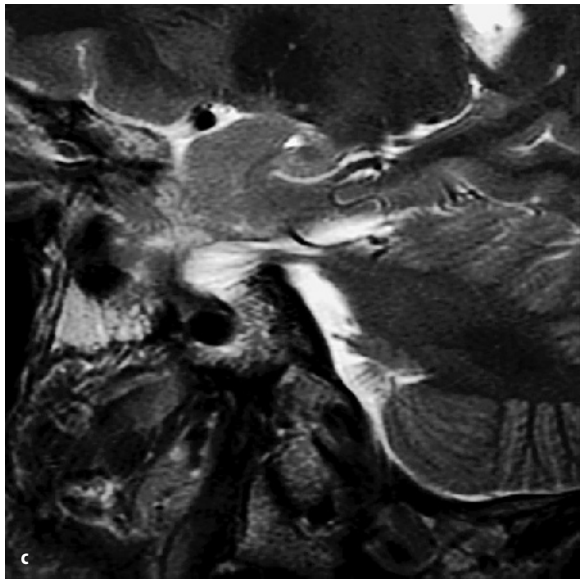

Fig. 4.11. (Cont.)

usually feasible. Only in the acute phase can bleeding be erroneously construed as early subacute haemorrhage [19].

T2 images can also be acquired with GE (T2*) sequences like CISS (constructive interference in the steady state), which is particularly suited to investigations of the inner ear. 3D CISS offers high-resolution images of the inner ear and labyrinth with greater SNR than other T2-weighted sequences used to study this area (e.g. fast recovery FSE) (Fig. 4.15) [20].

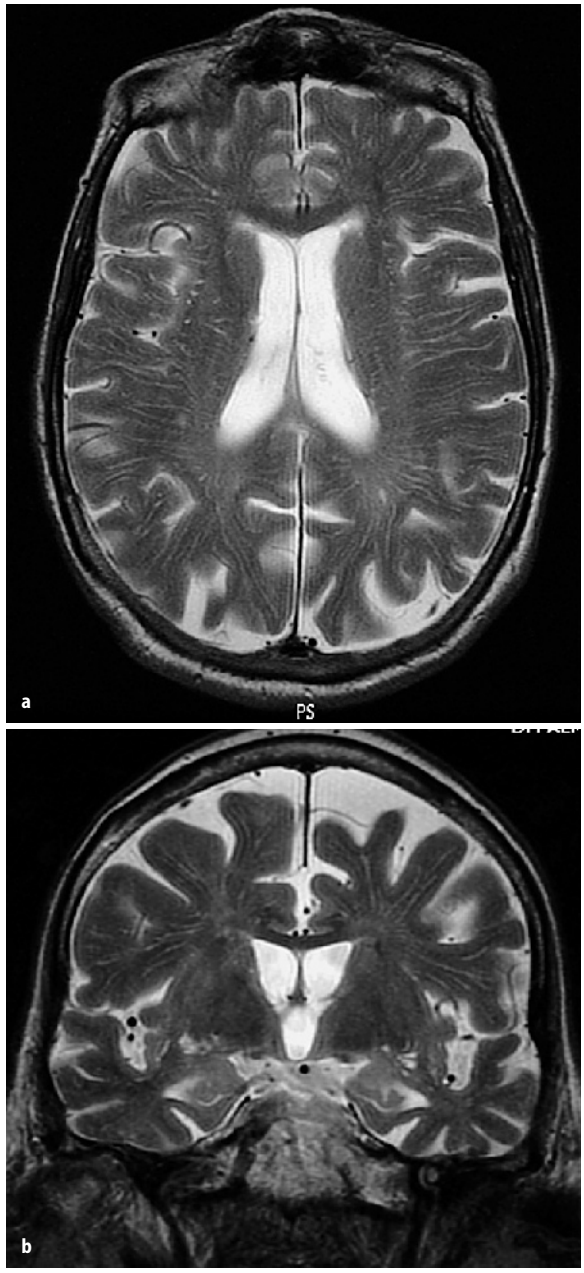

▷
Fig. 4.12 a, b. FSE T2 imaging. The excellent detail of this sequence allows visualization of the perivascular (Virchow-Robin) spaces at the level of the bi-hemispheric cortico-subcortical junction. Axial (**a**) and coronal (**b**) views

Fig. 4.13. Multiple sclerosis: FSE T2 sequence

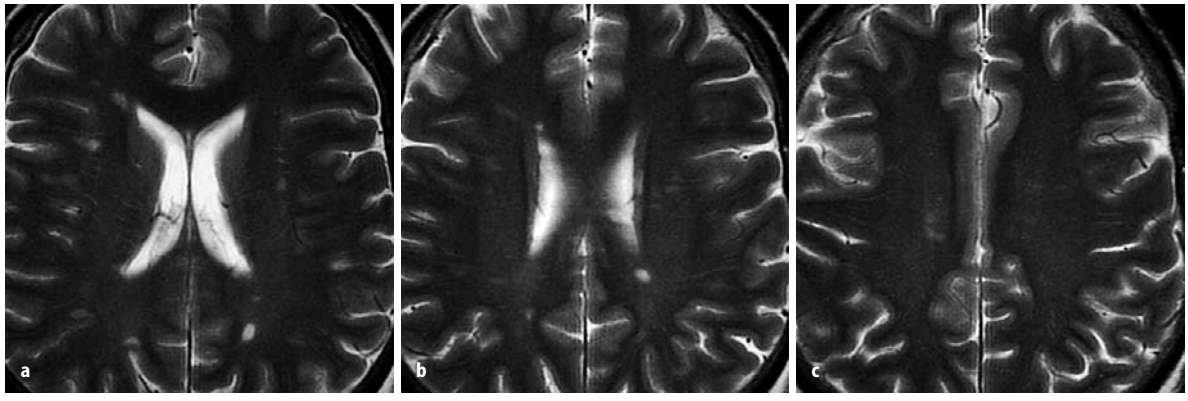

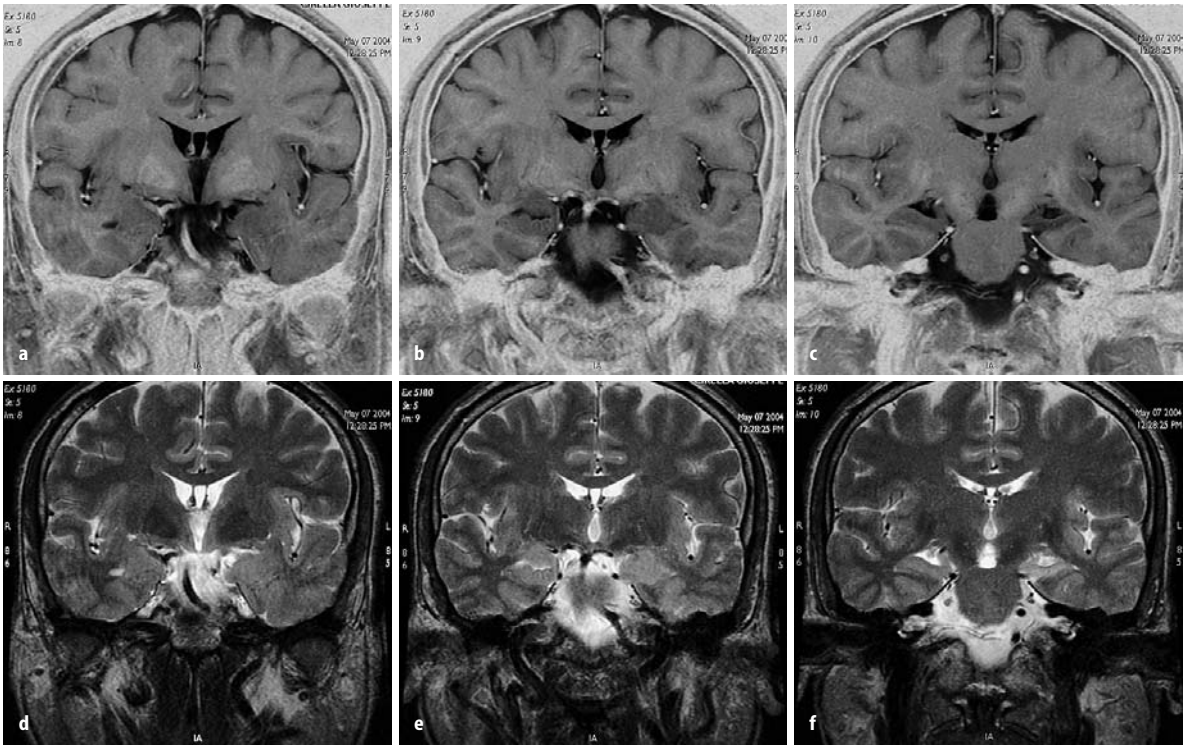

Fig. 4.14. High-definition FSE T2 sequence (matrix 512×320, thickness 3 mm, ZIP 1024) acquired with **(a–c)** and without **(d–f)** inverted contrast: coronal view. Note the excellent anatomical detail of both hippocampi

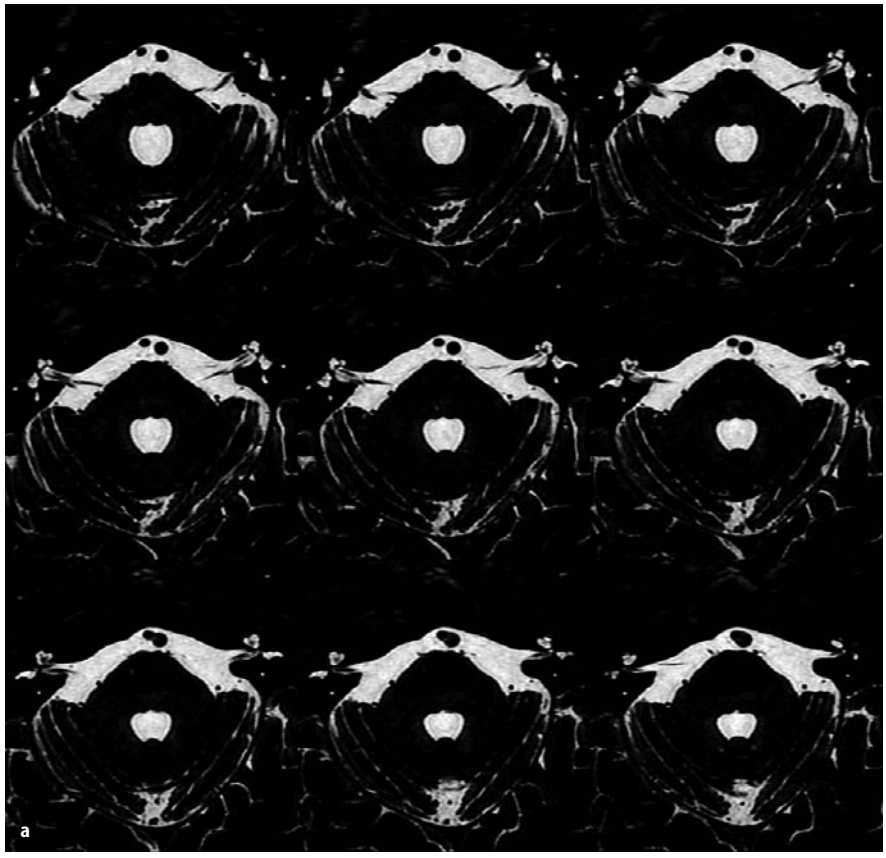

Fig. 4.15a. High-definition study of the inner ear using a 3D FIESTA sequence (TR 4.3, TE 1.5, flip angle 50°, BW 62 kHz, FOV 170, slice thickness 0.6 mm, matrix 256×256, ZIP 512, 2 NEX, 4:43). Single partitions (**a**)

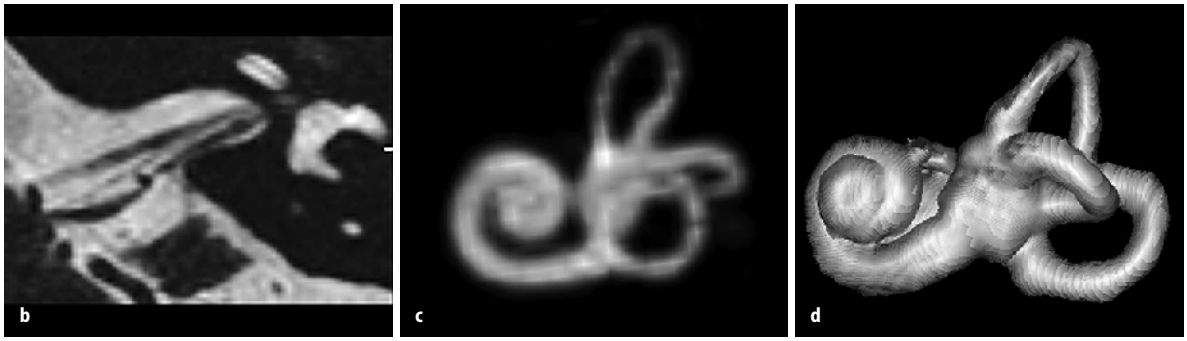

Fig. 4.15 b–d. (Cont.) Detail (**b**); MIP image (**c**); post-processing with volume rendering (**d**)

4.1.3 FLAIR Imaging

FLAIR sequences, which are generally included in all imaging protocols, are also sharper and more sensitive at 3.0 T by virtue of their reduced slice thickness and broader matrices, especially in detecting small lesions. Greater sensitivity is also afforded by the longer TE required in relation to 3.0 T relaxation times, allowing good contrast and acceptable noise levels (Figs. 4.16–4.18). Indeed, detection of small lesions requires CNR, rather than SNR, optimization, which is obtained using longer TE (120 ms).

The basic lack of difference in CSF T1 between 1.5 T and 3.0 T entails that a similar inversion time (IT) is required to suppress the fluid signal (around 2,250 ms) at both field strengths [3]. This does not apply to other IR sequences, neither those that seek to enhance contrast between different tissues (e.g. between white and grey matter), nor those using fat suppression, where T1 must be increased by 25–40 %.

The white matter, especially periventricular, areas that are physiologically hyperintense at 1.5 T enhance even more strongly on 3.0 T images, requiring great caution in distinguishing them from diseases like amyotrophic lateral sclerosis [7].

The semeiological features described for grey nuclei and recent haemorrhage also apply to FLAIR sequences (Figs. 4.19, 4.20) [3, 19].

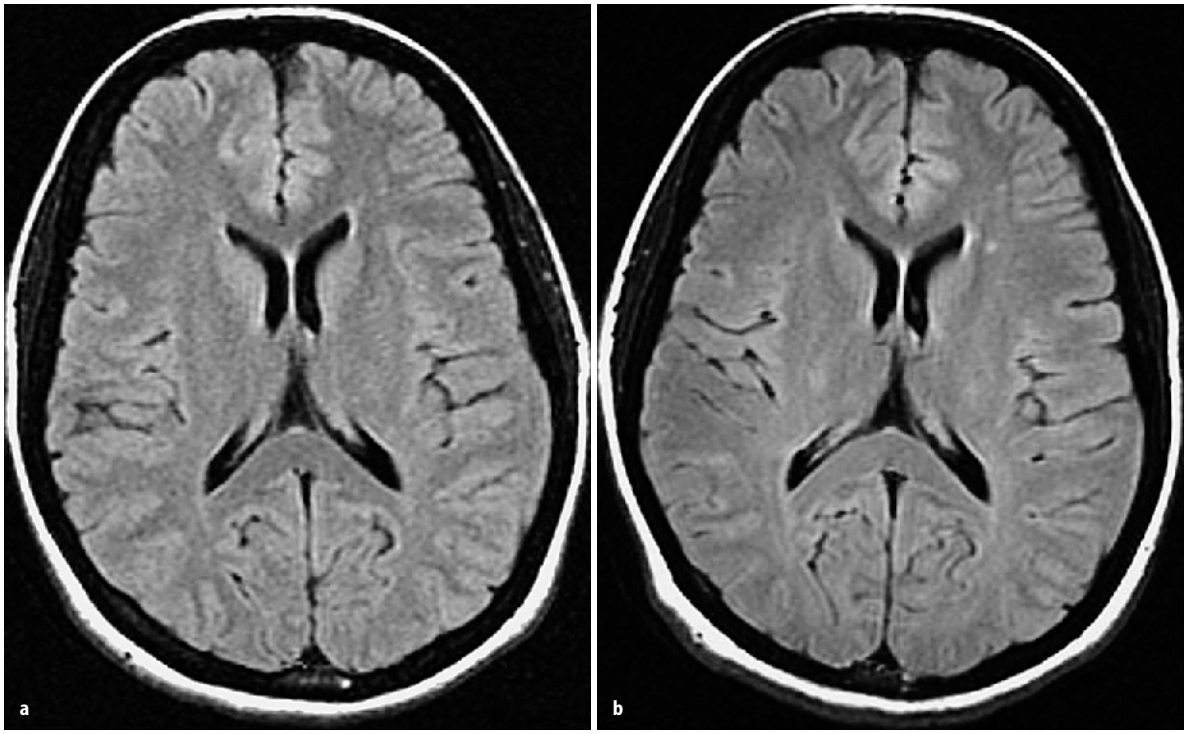

Fig. 4.16. FLAIR T2 image acquired at 3.0 T (**a**) and 1.5 T (**b**). Use of broader matrices and thinner slices at 3.0 T (**a**) disclosed small lesions difficult to identify at 1.5 T (**b**)

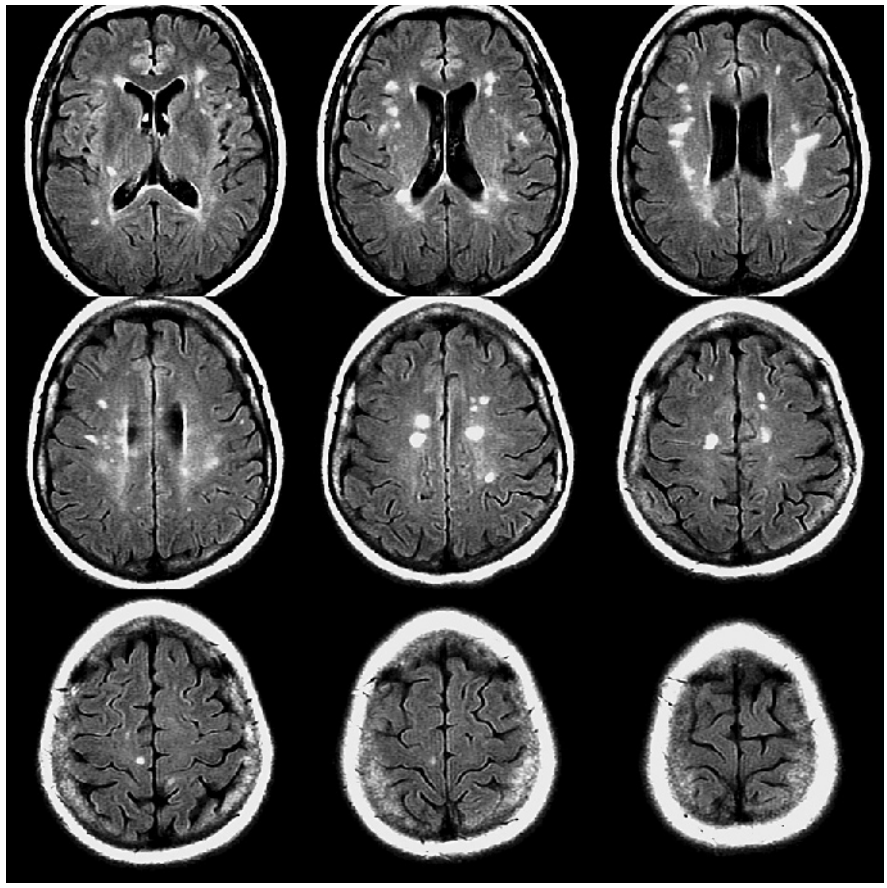

Fig. 4.17. Multiple sclerosis: image acquired using a FLAIR T2 sequence

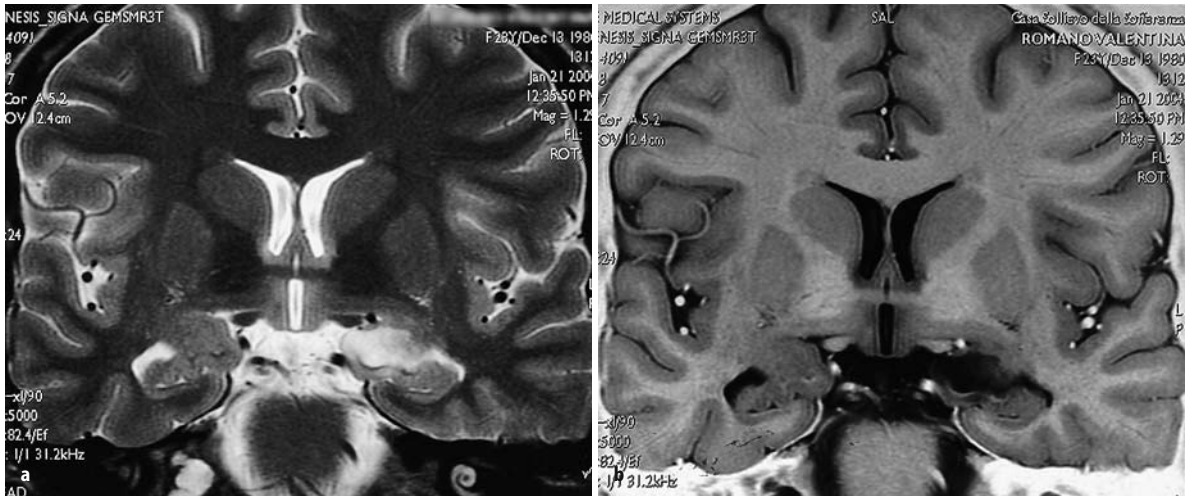

Fig. 4.18. Left hippocampal lesion on FSE T2 (**a**), „inverted contrast" FSE T2 (**b**), and FLAIR (**c**) sequences. The signal alteration is best appreciated in **c**. Optimum anatomical cortical-subcortical detail in **b**

A major drawback of high-field imaging is a larger number of pulsation artefacts, especially in the posterior fossa, probably due to higher blood flow magnetization. The adoption of broader saturation bands does not address the problem because of difficulties with the head coil, but recently developed new coils or new software (parallel imaging) are expected to diminish its impact.

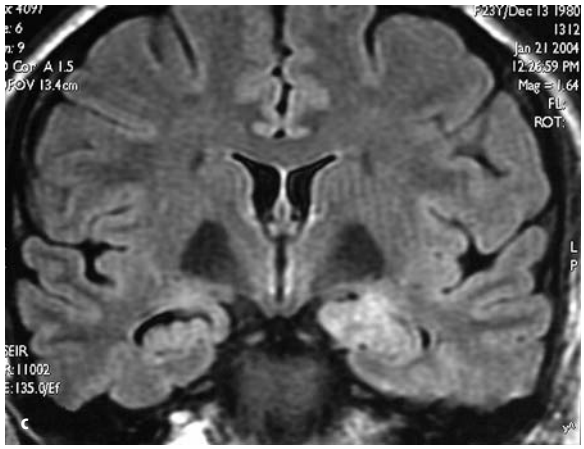

Fig. 4.18. (Cont.)

References

1. Schwindt W, Kugel H, Bachmann R, et al. (2003) Magnetic resonance imaging protocols for examination of the neurocranium at 3 T. Eur Radiol 13:2170 – 2179
2. Wansapura JP, Holland SK, Dunn RS, et al. (1999) NMR relaxation times in the human brain at 3.0 T. JMRI 9:531 – 538
3. Frayne R, Goodyear BG, Dickhoff P, et al. (2003) Magnetic resonance imaging at 3.0 Tesla: challenges and advantages in clinical neurological imaging. Invest Radiol 38(7):385 – 402
4. Scarabino T, Nemore F, Giannatempo GM, et al. (2004) Semeiological features of 3.0 T MR imaging: what changes at high magnetic field. Riv Neuroradiol 17:755 – 764
5. Scarabino T, Nemore F, Giannatempo GM, et al. (2004) 3.0 T imaging. Riv Neuroradiol 17:765 – 776

▽ **Fig. 4.19.** FLAIR sequence: note the low signal of mesencephalic nuclei (**a**, zoom in **b**) and brain base (**c**, zoom in **d**) due to their iron content

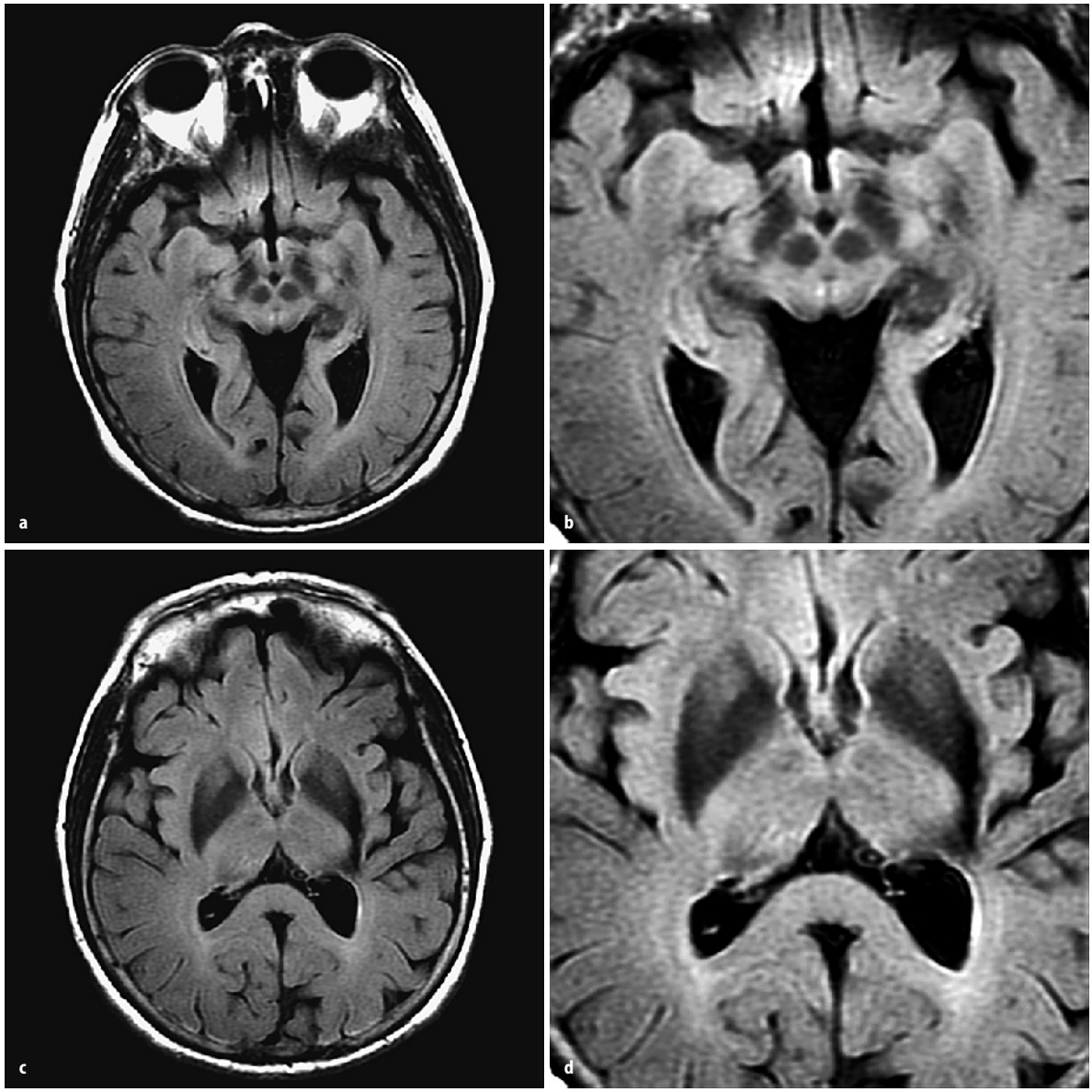

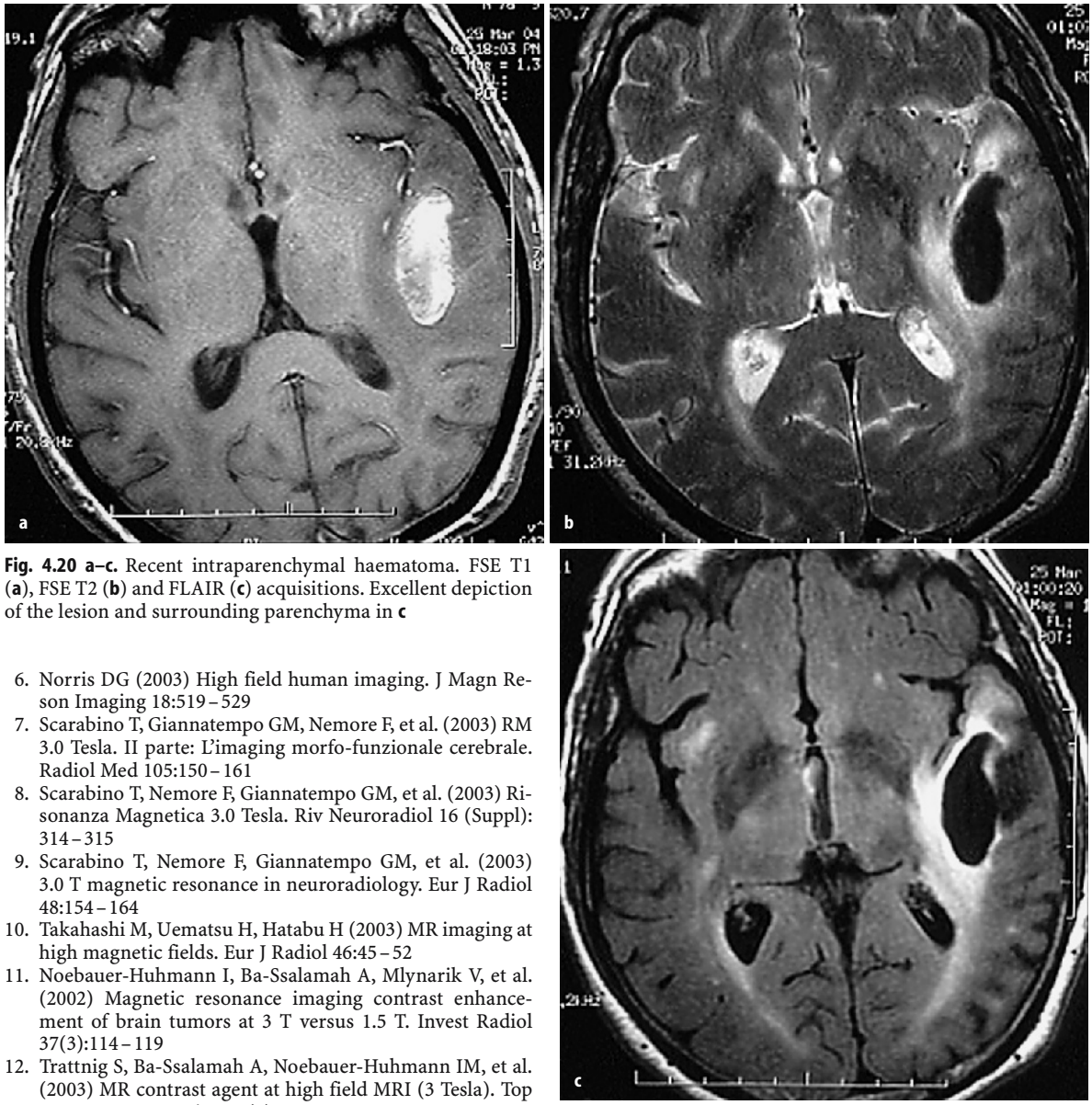

Fig. 4.20 a–c. Recent intraparenchymal haematoma. FSE T1 (**a**), FSE T2 (**b**) and FLAIR (**c**) acquisitions. Excellent depiction of the lesion and surrounding parenchyma in **c**

6. Norris DG (2003) High field human imaging. J Magn Reson Imaging 18:519 – 529
7. Scarabino T, Giannatempo GM, Nemore F, et al. (2003) RM 3.0 Tesla. II parte: L'imaging morfo-funzionale cerebrale. Radiol Med 105:150 – 161
8. Scarabino T, Nemore F, Giannatempo GM, et al. (2003) Risonanza Magnetica 3.0 Tesla. Riv Neuroradiol 16 (Suppl): 314 – 315
9. Scarabino T, Nemore F, Giannatempo GM, et al. (2003) 3.0 T magnetic resonance in neuroradiology. Eur J Radiol 48:154 – 164
10. Takahashi M, Uematsu H, Hatabu H (2003) MR imaging at high magnetic fields. Eur J Radiol 46:45 – 52
11. Noebauer-Huhmann I, Ba-Ssalamah A, Mlynarik V, et al. (2002) Magnetic resonance imaging contrast enhancement of brain tumors at 3 T versus 1.5 T. Invest Radiol 37(3):114 – 119
12. Trattnig S, Ba-Ssalamah A, Noebauer-Huhmann IM, et al. (2003) MR contrast agent at high field MRI (3 Tesla). Top Magn Reson Imaging 14(5):365 – 375
13. Buerk BM, Pulido JS, Chiong I, et al. (2004) Vascular perfusion of choroidal melanoma by 3.0 Tesla magnetic resonance imaging. Trans Am Ophthalmol Soc 102:209 – 215
14. Sicotte NL, Voskuhl RR, Bouvier S, et al. (2003) Comparison of multiple sclerosis lesions at 1.5 T and 3.0 Tesla. Invest Radiol 38(7):423 – 427
15. Kim DS, Garwood M (2003) High field magnetic resonance techniques for brain research. Curr Opin Neurobiol 13:612 – 619
16. Krautmacher C, Tschamps H, Traeber F, et al. (2003) 3.0 T MR imaging of contrast-enhancing brain tumors: intra-individual study comparing standard and half standard dose at 3.0 T with standard dose at 1.5 T. Eur Radiol 1381:222
17. Karlberg M, Annertz M, Magnusson M (2004) Acute vestibular neuritis visualized by 3-T magnetic resonance imaging with high-dose gadolinium. Arch Otolaryngol Head Neck Surg 130(2):229 – 232
18. Nakada T (2003) Clinical experience on 3.0 T systems in Niigata, 1996 to 2002. Invest Radiol 38(7):377 – 384
19. Allkemper T, Tombach B, Schwindt W, et al. (2004) Acute and subacute intracerebral hemorrhages: comparison of MR imaging at 1.5 T and 3.0 T – initial experience. Radiology 232(3):874 – 881
20. Lane JI, Ward H, Witte RJ, et al. (2004) 3-T imaging of the cochlear nerve and labyrinth in cochlear-implant candidates: 3 D fast recovery fast spin echo versus 3 D constructive interference in the steady state techniques. Am J Neuroradiol 25(4):618 – 622

5 3.0 T MR Angiography

T. Scarabino, T. Popolizio, A. Stranieri, A. Maggialetti, A. Carriero, N. Maggialetti, U. Salvolini

Magnetic resonance angiography (MRA) is a well-established non-invasive technique for imaging the intracranial vasculature, particularly large calibre arteries and veins, and detecting changes in vessel calibre and/or course (Figs. 5.1, 5.2). It is generally performed without administration of paramagnetic contrast media.

Drawbacks with respect to conventional angiography are lower spatial and, above all, temporal resolution.

The quality of MR angiographic images has recently been improved even in lower field systems by the advent of surface or phased array coils with a higher signal/noise ratio (SNR) and shorter echo times (TE) made possible by stronger gradients, new pulse sequences with optimized SNR, and longer acquisition times (given that a fourfold increase in examination time doubles the SNR).

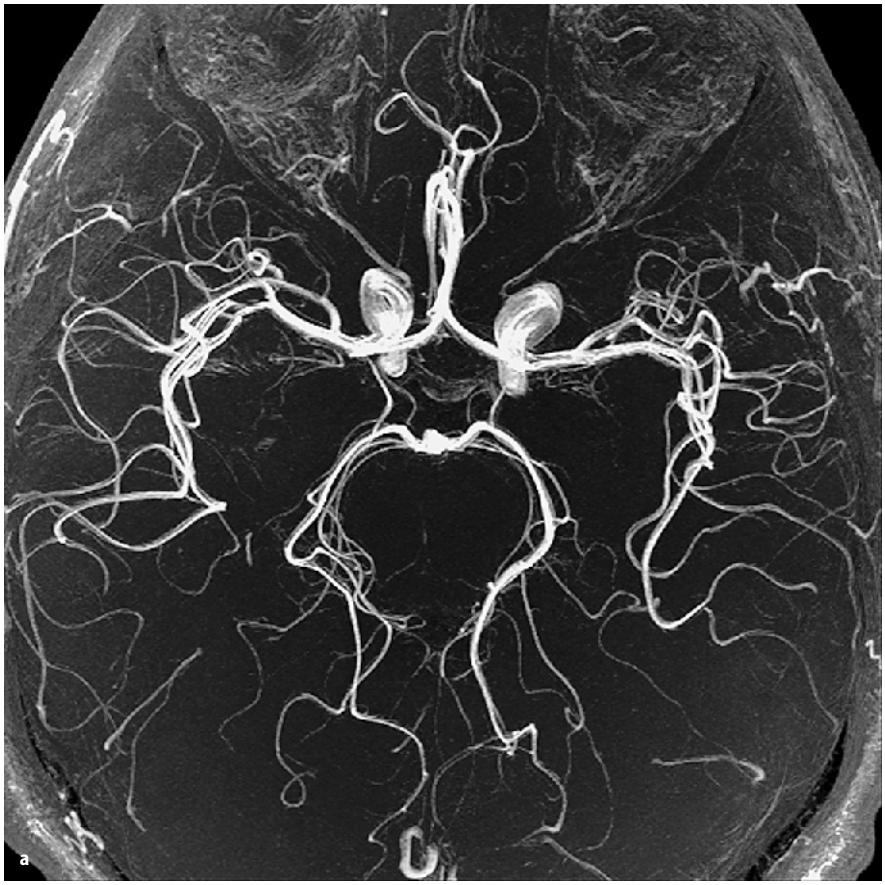

Fig. 5.1. Normal arterial circulation: high-definition 3D TOF image at 3.0 T (matrix 1,024 × 512, FOV 240 mm, slice thickness 1 mm) (**a**); detail of the circle of Willis, especially of the posterior circle (**b**); also note detail of the right middle cerebral artery branches (**c**)

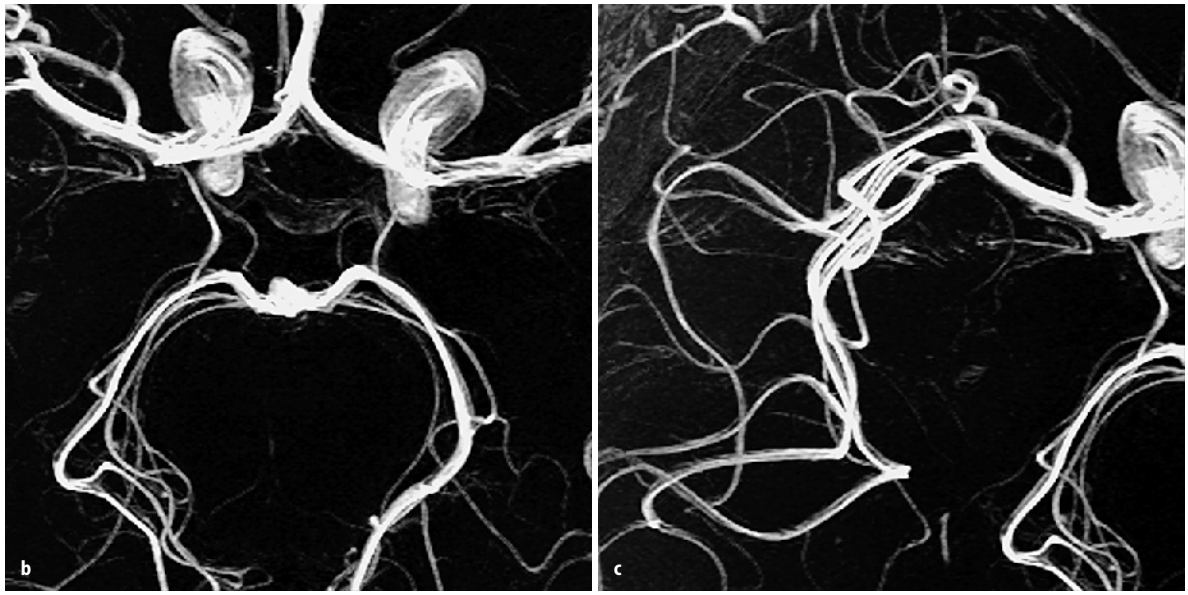

Fig. 5.1. (Cont.)

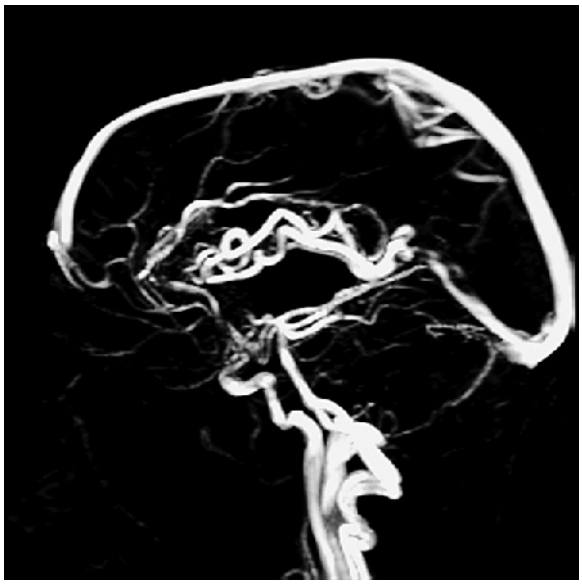

Fig. 5.2. Normal venous cerebral circulation: 3D PC study at 3.0 T

5.1 MRA Techniques

Although there are several approaches to visualizing the intracranial vessels with MR, the two most widely used techniques are time of flight (TOF) and phase contrast (PC) MRA.

In TOF MRA, which is usually performed using a flow compensated gradient refocused sequence, stationary tissues are saturated and thus have low signal intensity. However, blood upstream of the imaging volume is unsaturated. When this blood flows into the imaging volume, it is bright compared with the stationary background tissue [1].

For vessels coursing within the acquired section the inflow effect becomes less effective, reducing intravascular signal to the level of the surrounding stationary spins. Potential difficulties in TOF MRA may therefore arise in situations where larger sections of vessels lie within a section, and also in situations where turbulent flow is present, as this also suppresses bright intravascular signal.

In TOF MRA, vessels appear bright independent of the flow direction. Hence, arteries and veins cannot be differentiated. Flow in a particular direction can, however, be saturated using spatial flow presaturation bands. Spins being washed into the slice from the presaturation area will not carry any magnetization and no inflow enhancement occurs [2]. These saturation bands can thus be used to obtain selective TOF angiograms or venograms.

Unlike TOF MRA, PC MRA utilizes phase shifts as blood flows in the presence of flow encoding bipolar gradients. On phase difference images, the signal phase intensity is proportional to velocity, resulting in suppression of the stationary background tissue. The flow encoding gradients can be applied in any one or multiple directions depending on the desired flow sensitivity [1]. This technique is thus a direct velocity map, where the voxel intensity values are proportional to the actual flow velocity in a particular flow direction.

Because the typical imaging time of these conventional MRA techniques is between 2 and 8 min, neither technique is able to demonstrate the dynamics of cerebral blood flow. Moreover, both techniques are prone

to artefacts resulting from slow, turbulent or complex blood flow.

Most of the problems associated with TOF MRA and PC MRA can be overcome with contrast enhanced MRA (CE-MRA) [1, 3]. Three dimensional CE-MRA fundamentally differs from other vascular MR imaging strategies in that it is not flow dependent. Blood signal is derived from the T1 shortening effect of the dynamically infused paramagnetic contrast. Hence, arterial contrast is based on the difference in T1 relaxation between blood and surrounding tissue [4]. As a result, problems associated with slow flow and turbulence induced signal voids are overcome. The technique allows a small number of slices oriented in the plane of the vessels of interest to image an extensive region of vascular anatomy in a short period of time [5]. With this technique, a temporal resolution of about one image in 20 s has become possible, enabling selective demonstration of the early arterial and late venous phase [5–7].

MRA images are best interpreted on an independent workstation with 3D reconstruction capabilities. In addition to perusal of the original sections, diagnoses should be based on a combination of maximum intensity projection (MIP) images and interactive 3D multiplanar reformations (MPR). The MPR technique permits cross sectional visualization of the vessels in any plane. Venous overlap can effectively be compensated and the course of tortuous vessels can easily be reconstructed. This represents an advantage even over conventional catheter angiography. Surface rendering algorithms as well as virtual angioscopic reconstructions are useful mainly for demonstration purpose.

5.2 3.0 T MRA

3.0 T MRA offers significant advantages (Figs. 5.3–5.6) [8–11].

First of all, it allows to perform all the angiographic sequences applied routinely in clinical practice with lower field systems, such as 2D and 3D TOF and PC, as well as ultrafast dynamic sequences after administration of a bolus of contrast agent (CE-MRA).

Similarly to standard brain MRI, the technical parameters of MRA sequences also need to be optimized at higher magnetic fields (Table 5.1).

The higher SNR improves scan quality largely through wider acquisition matrices (up to 1,024) without giving rise to significantly grainy images [12–15]. In addition, the change in T1 relaxation time, i.e. the increased T1, yields greater background stationary tissue suppression due to decreased R1 (the rate of longitudinal or spin-lattice relaxation), and greater flow enhancement since blood R1 is roughly constant, thus improving vessel-tissue contrast [12, 16, 17].

This advantage makes the application of magnetization transfer less effective than it is with 1.5 T systems [18, 19] and is mainly evident when using 3D TOF sequences, since the short TR usually saturates stationary tissue but not circulating blood [20], and the tag per-

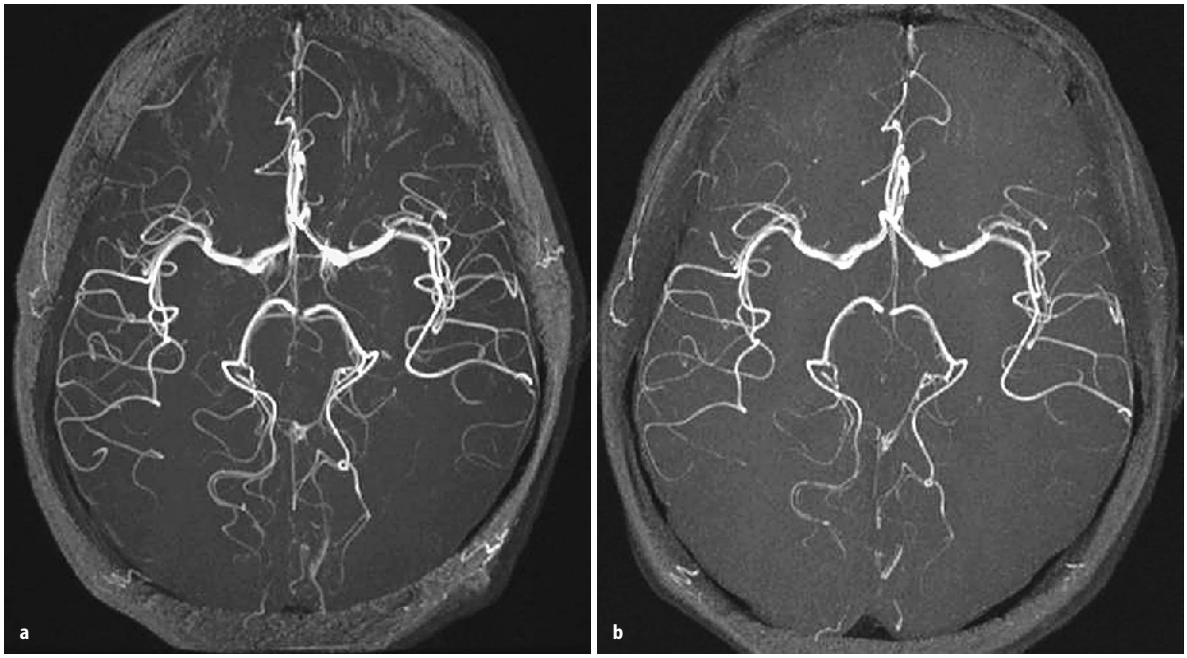

Fig. 5.3. Normal arterial cerebral circulation imaged using the same 3D TOF sequence at 3.0 T (**a**) and 1.5 T (**b**). In **a**, vessel conspicuity is greater than in **b**, yielding better and more detailed depiction of superficial, smaller calibre vessels

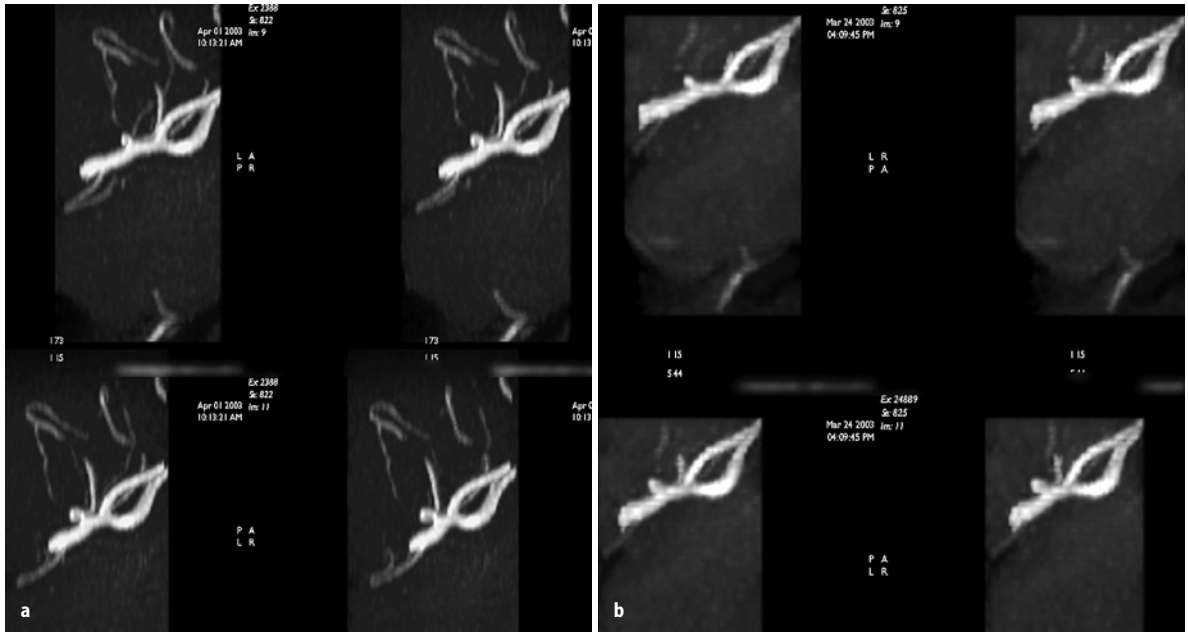

Fig. 5.4. Coiling of a branch of the right middle cerebral artery studied with a 3D TOF sequence at 3.0 T (**a**) and 1.5 T (**b**). The coil is better depicted in **a** than in **b**, where the image mimics a small aneurysm

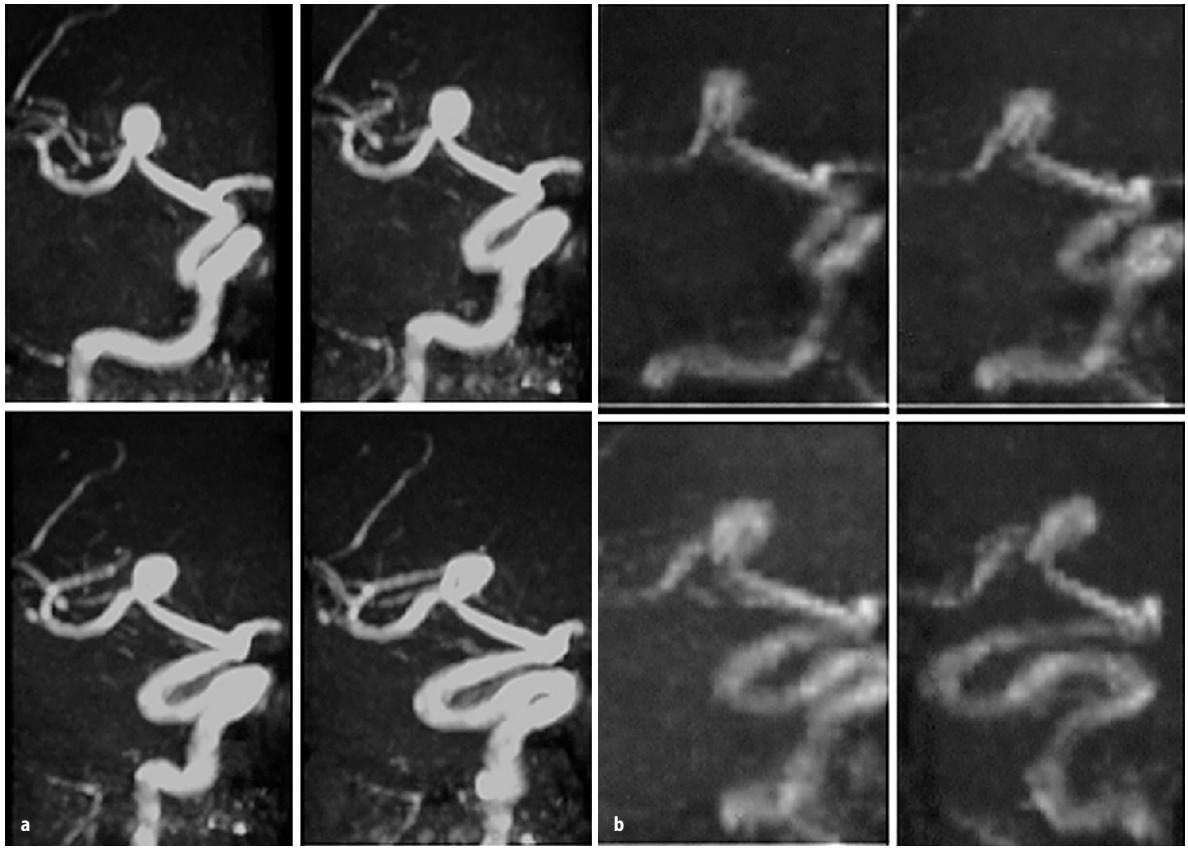

Fig. 5.5. Sacciform aneurysm of middle cerebral artery imaged using the same 3D TOF sequence performed at 3.0 T (**a**) and 1.5 T (**b**). The sacciform vascular dilatation is depicted in greater detail and exhibits a more intense signal in **a** than in **b**

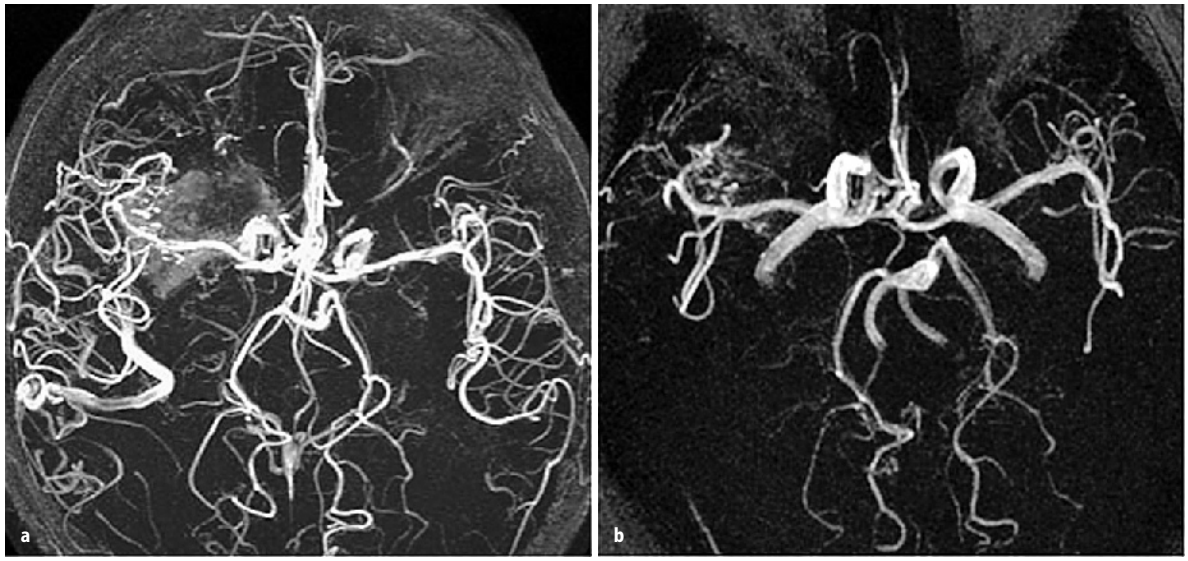

Fig. 5.6. Large right arteriovenous malformation: unenhanced 3D TOF images acquired at 3.0 T (**a**) and 1.5 T (**b**). Greater background suppression and flow enhancement afford better spatial depiction of the malformation at 3.0 T

Table 5.1. Optimization of technical parameters of MRA sequences at higher magnetic fields

Sequence	TR (ms)	TE (ms)	Other parameters (TI, FA, ZIP)	Slice thickness (mm)	No. of slices	FOV	Matrix	NEX	Examination time (min:s)
3D TOF 1.5 T	30	6.9	FA 30	1.2	32	24	352×224	1	3:08
3D TOF 3.0 T	26	Min	FA 20 ZIP 512 ZIP 2	1.4	60	16	288×224	1	5:53
HD 3D TOF 3.0 T	30	Min	FA 20 ZIP 1,024 ZIP 2	1.4	48	19	384×320	1	6:18
2D TOF 1.5 T	Min	Min	70	1.5		23	256×224	1	Variable in relation to number of slices
2D TOF 3.0 T	Min	Min	50	1.4		22	256×192	1	Variable in relation to number of slices
3D PC 1.5 T	33		20	50		20	256×192	8	3:23
3D PC 3.0 T	30		20	35		22	256×224	6	2:41

sists over a longer time. These effects afford greater vessel detail and conspicuity, especially with regard to small calibre structures, including surface vessels not clearly depicted on 1.5 T images (Figs. 5.7–5.12) [21, 22].

For the same reasons, 3.0 T MRA appears to be a promising technique to enhance vessel conspicuity in neonatal intracranial vessels or to further reduce scanning time [23]. Neonatal brain vessels are small, they exhibit lower blood flow velocity than adult vessels, and frequently have a turbulent flow. MRA protocols therefore need to be adapted to the specific needs and features of these patients, e.g. by reducing acquisition time to prevent motion artefacts, by using low flip angles and out-of-phase imaging better to saturate subcutaneous fat (which sometimes masks vessels on 3D MIP sequences), and by implementing ramped RF pulse and multiple thin volume strategies to visualize the intravascular signal at distal cortical branches.

Since the relaxivity of paramagnetic contrast media remains largely unchanged at higher magnetic field strengths, contrast administration further improves 3.0 T imaging given that its high SNR can be transformed into spatial resolution: resolution of 300 µm on the plane of section and of 400 µm on the slice thick-

ness, i.e. 300 × 300 × 400 interpolated voxels (ZIP 4 and ZIP 1,024) (Fig. 5.13).

Dynamic techniques, which afford shorter acquisition times, further contribute to improving contrast-enhanced MRA.

Additional gains are obtained with parallel imaging, which significantly reduces examination times and increases anatomical coverage providing the same image quality. In this case, a TOF sequence is usually applied with a wide matrix and hence greater spatial resolution [24].

(*Continued on p. 41*)

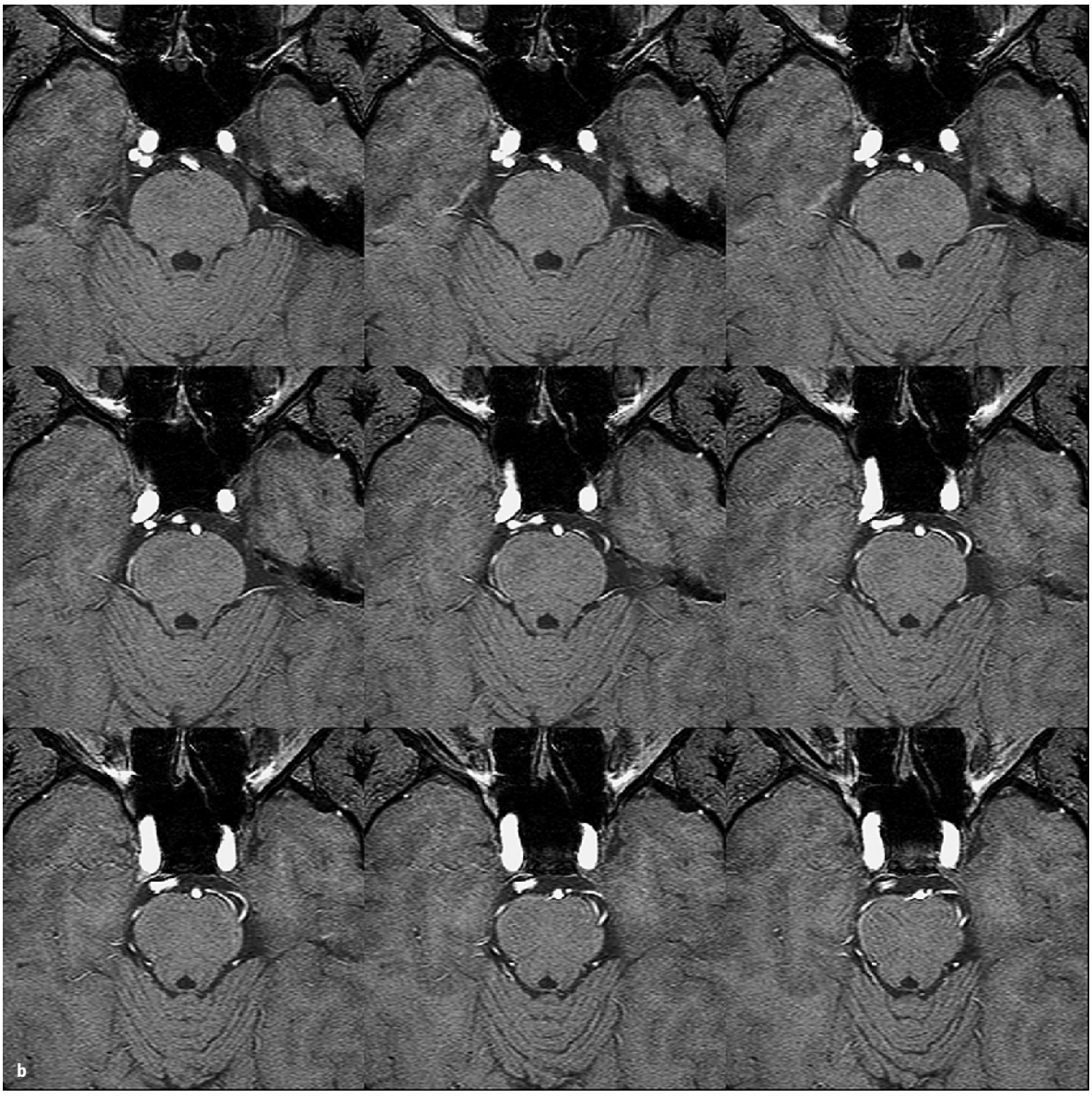

Fig. 5.7. Vestigial artery: unenhanced 3D TOF study at 3.0 T. MIP image (**a**); single partitions (**b**)

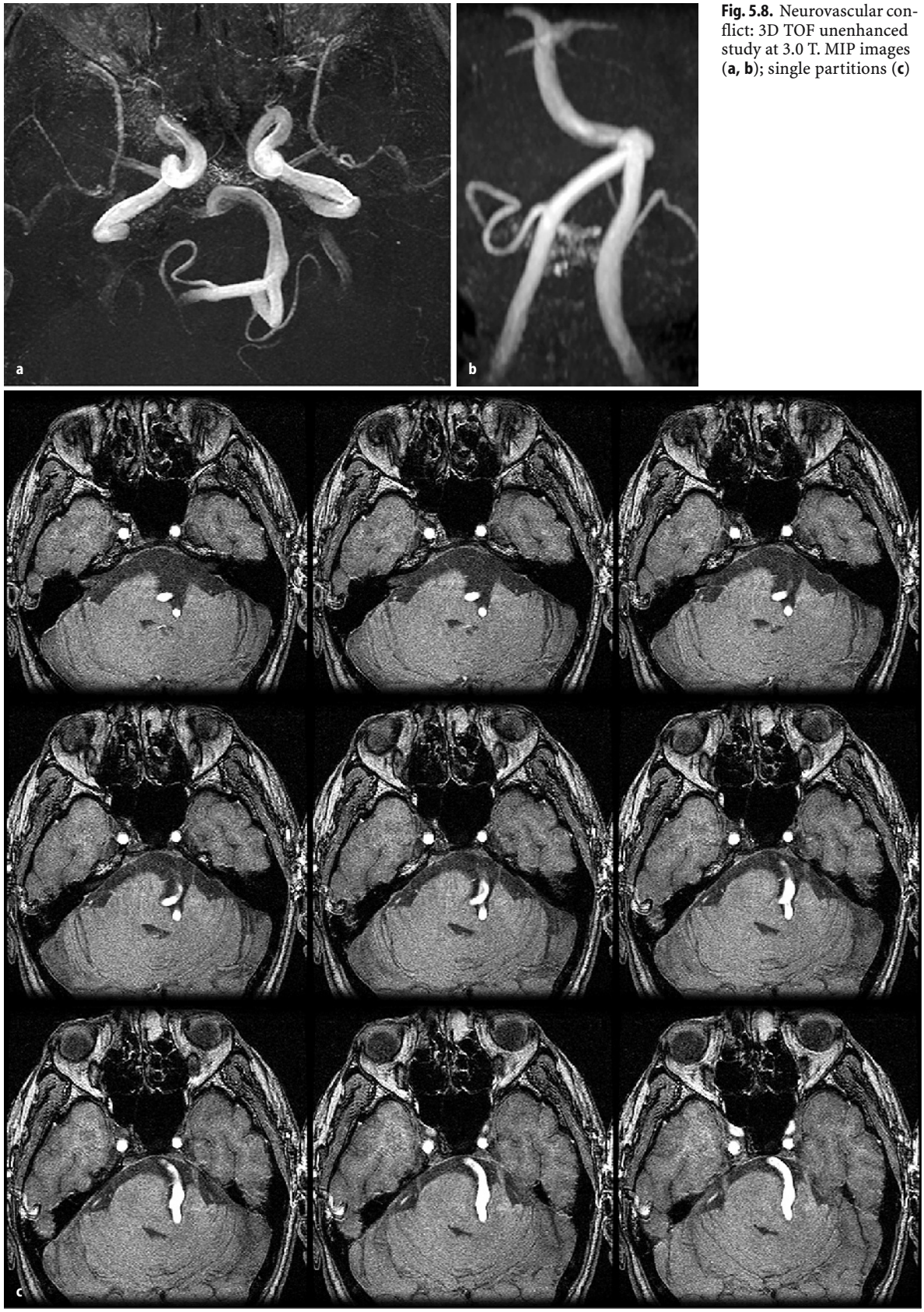

Fig. 5.8. Neurovascular conflict: 3D TOF unenhanced study at 3.0 T. MIP images (**a, b**); single partitions (**c**)

Finally, although the deflection and torsion movements of biomedical devices (such as the aneurysm clips commonly used in interventional and therapeutic neuroradiological procedures) and resulting susceptibility artefacts increase at higher magnetic field strength, the newer devices appear to entail no particular safety or compatibility risk [25, 26]. Patients with tested biomedical implants can therefore safely undergo 3.0 T MRA [27, 28].

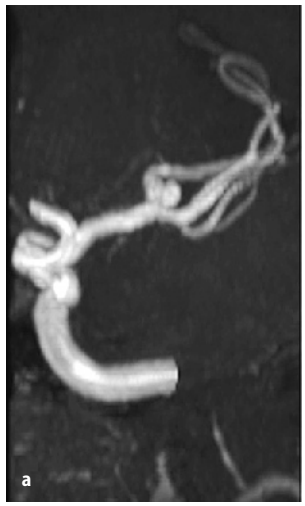

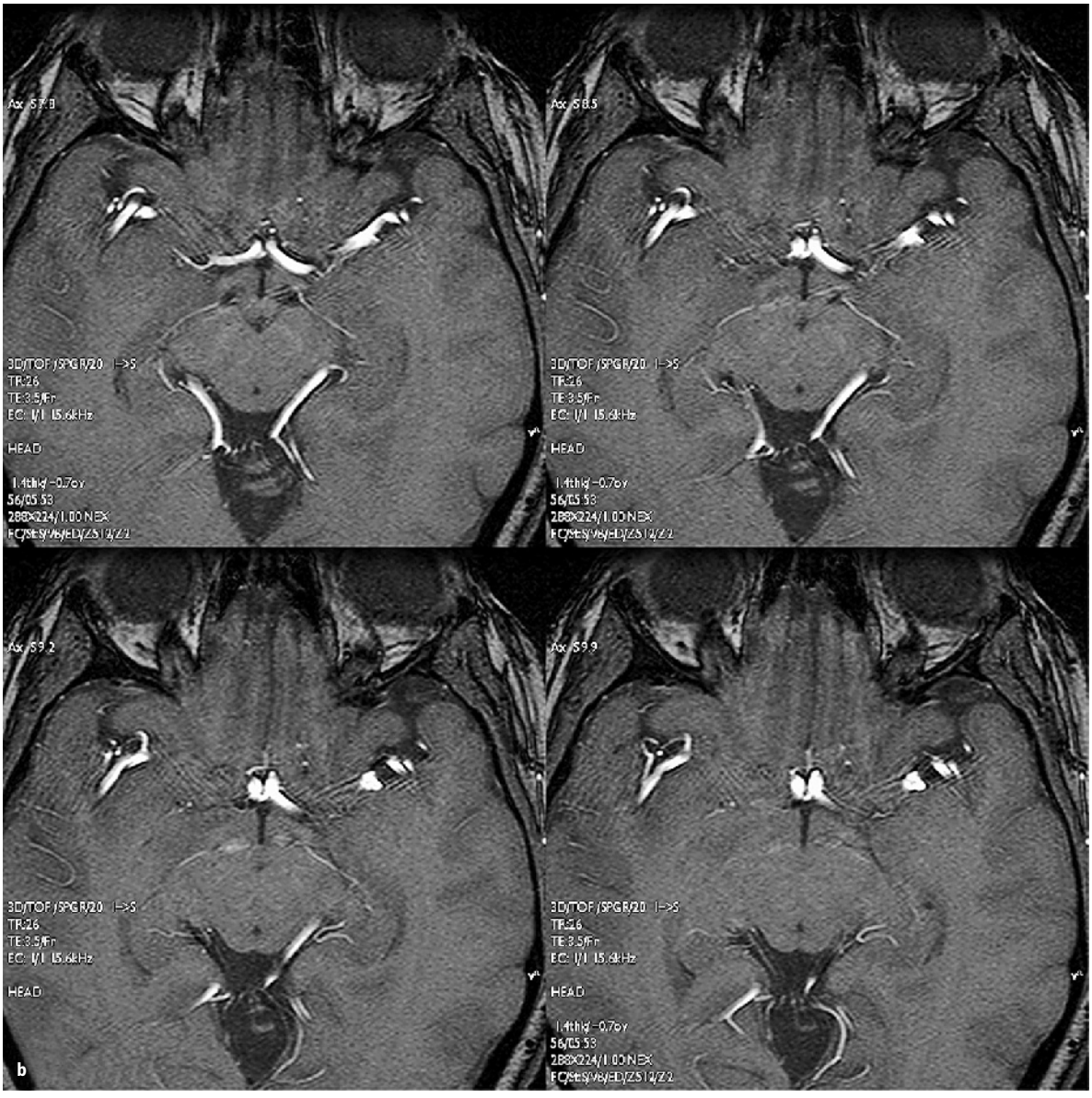

Fig. 5.9. Small berry aneurysm of left middle cerebral artery: 3D TOF study at 3.0 T. MIP image (**a**); single partitions (**b**)

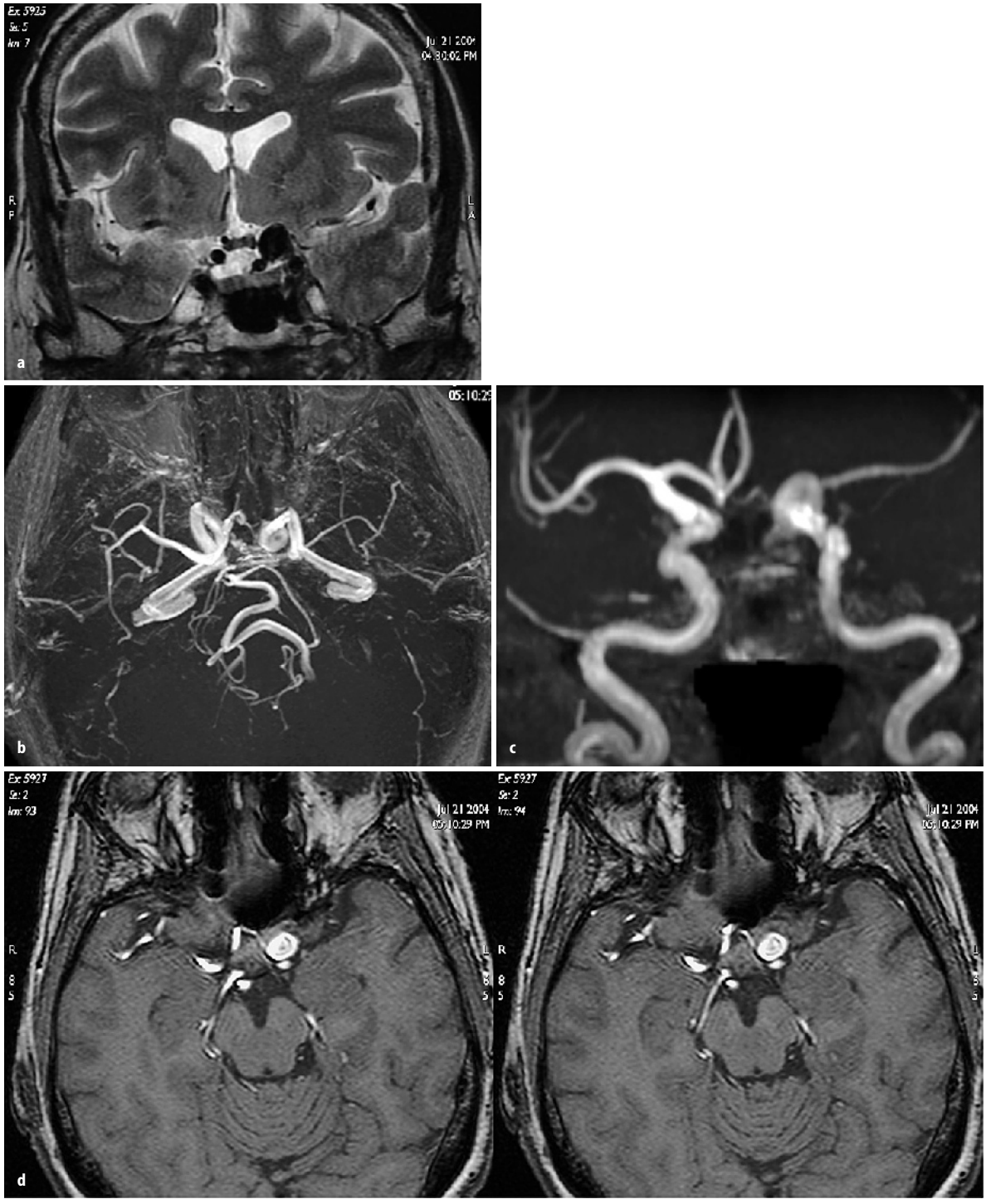

Fig. 5.10. Small berry aneurysm of the supraclinoid stretch of the left carotid siphon. Standard MRI: FSE T2 sequence (**a**), 3D TOF: axial and coronal MIP images (**b, c**), single partitions (**d**)

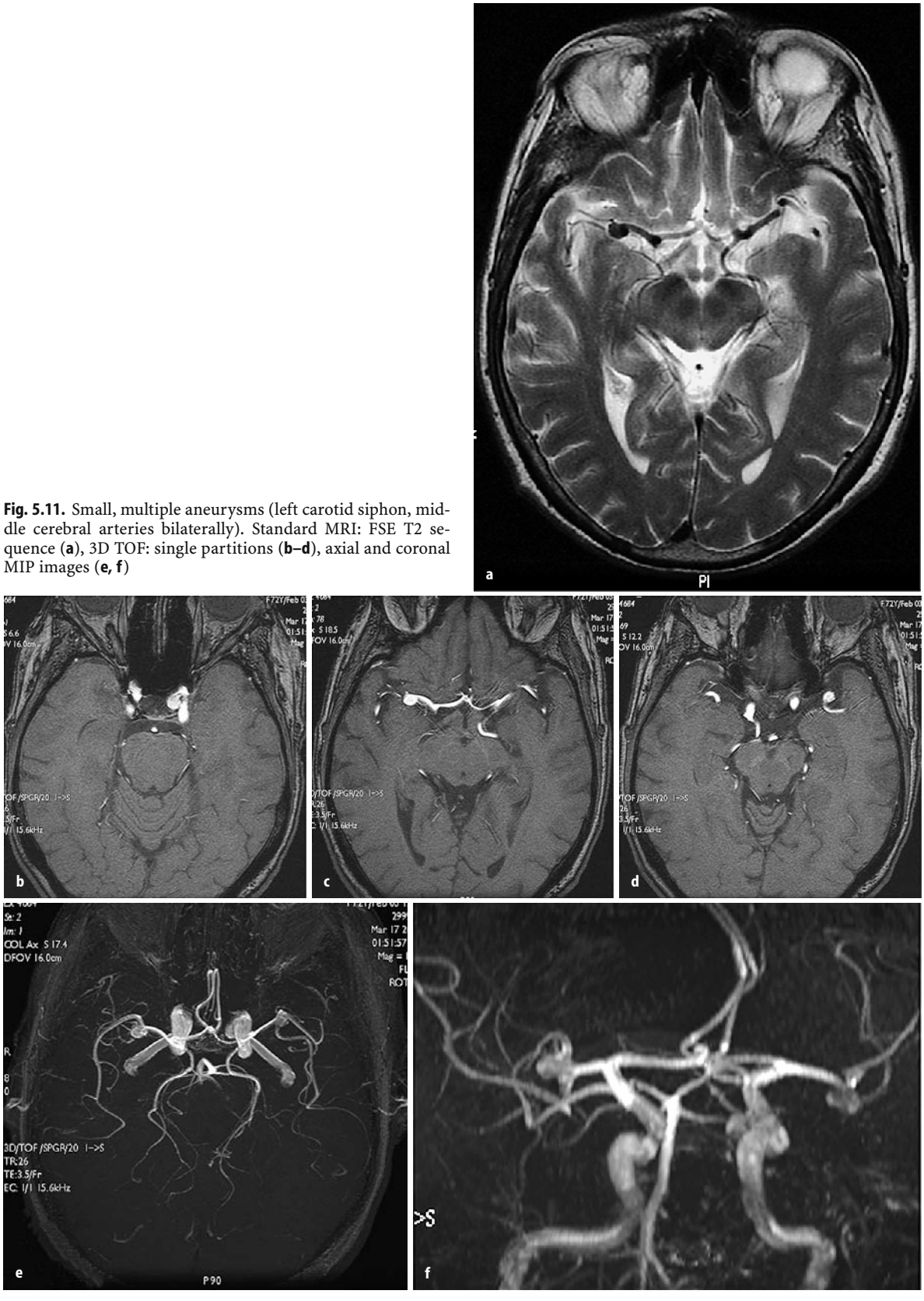

Fig. 5.11. Small, multiple aneurysms (left carotid siphon, middle cerebral arteries bilaterally). Standard MRI: FSE T2 sequence (**a**), 3D TOF: single partitions (**b–d**), axial and coronal MIP images (**e, f**)

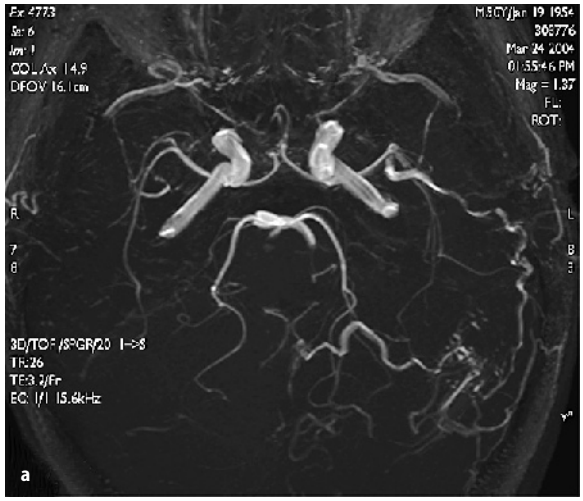

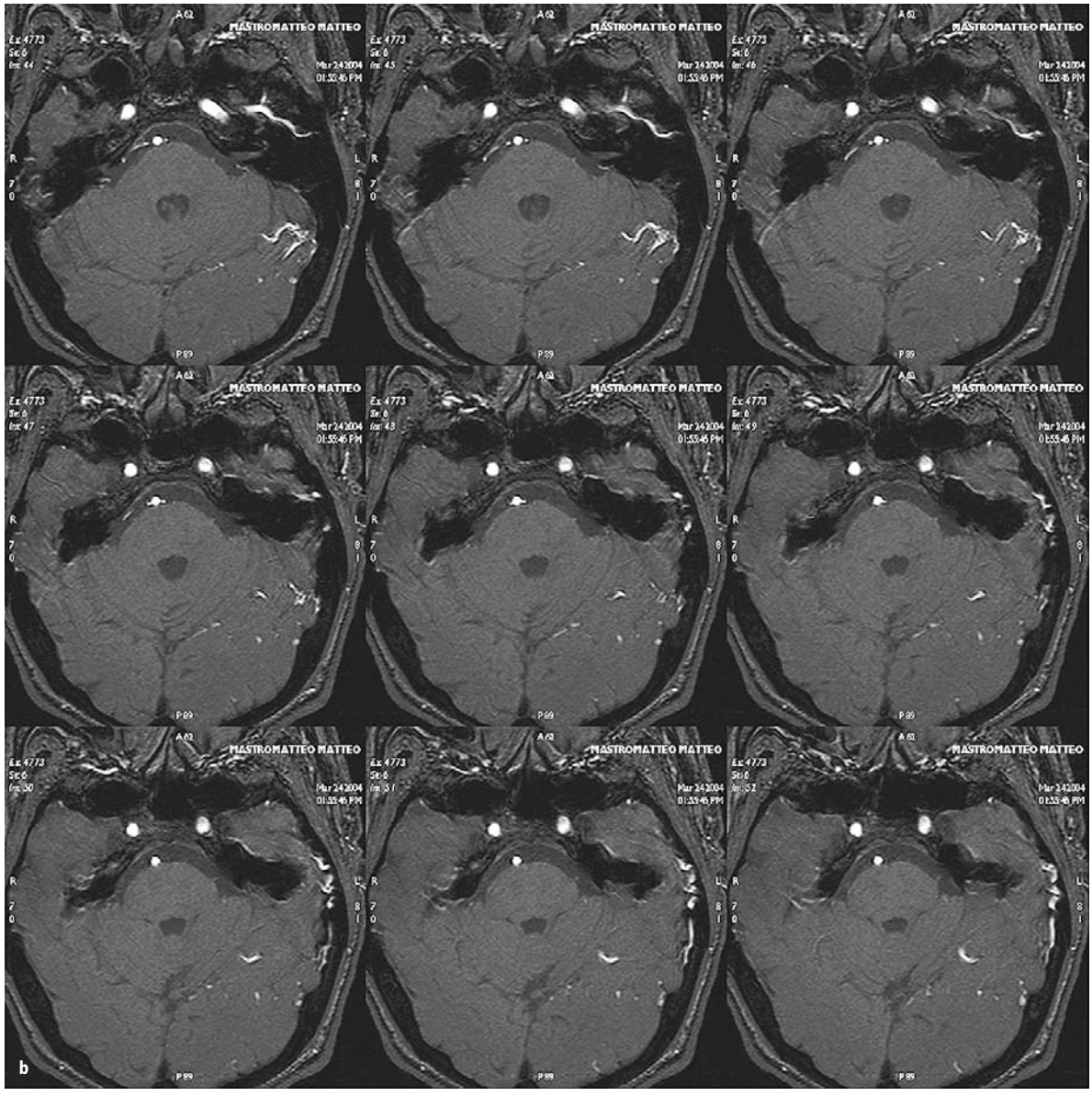

Fig. 5.12. Left arteriovenous malformation at the convexity: unenhanced 3D TOF study at 3.0 T. MIP image (**a**); single partitions (**b**)

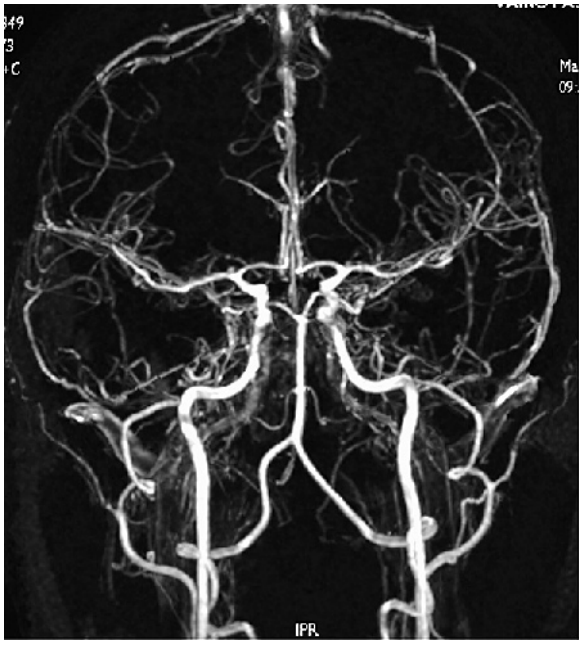

Fig. 5.13. Normal arterial cerebral circulation: contrast-enhanced coronal view at 3.0 T

5.3 Conclusions

The advantages offered by 3.0 T systems make MRA superior even to digital subtraction angiography, especially for studying atherosclerotic disease and vascular malformations like aneurysms, despite its lower spatial resolution. Digital angiography is increasingly being reserved for interventional and therapeutic rather than diagnostic applications (Figs. 5.14 – 5.18) [29].

Fig. 5.14. Giant aneurysm with turbulent flow in the intracavernous segment of the left internal carotid artery: 3D TOF study at 3.0 T. MIP images (**a–c**); single partitions (**d, e**); digital angiography (**f**)

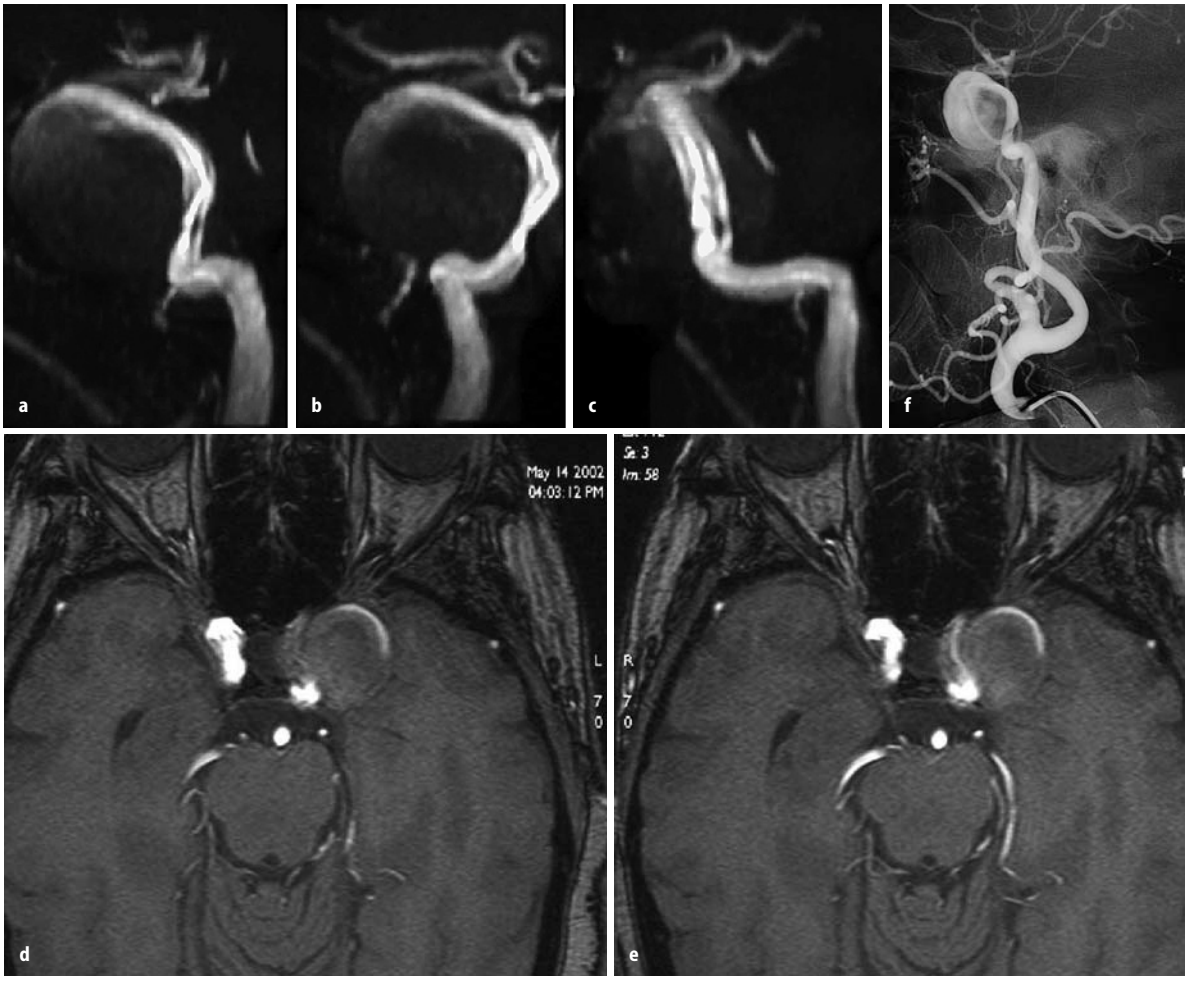

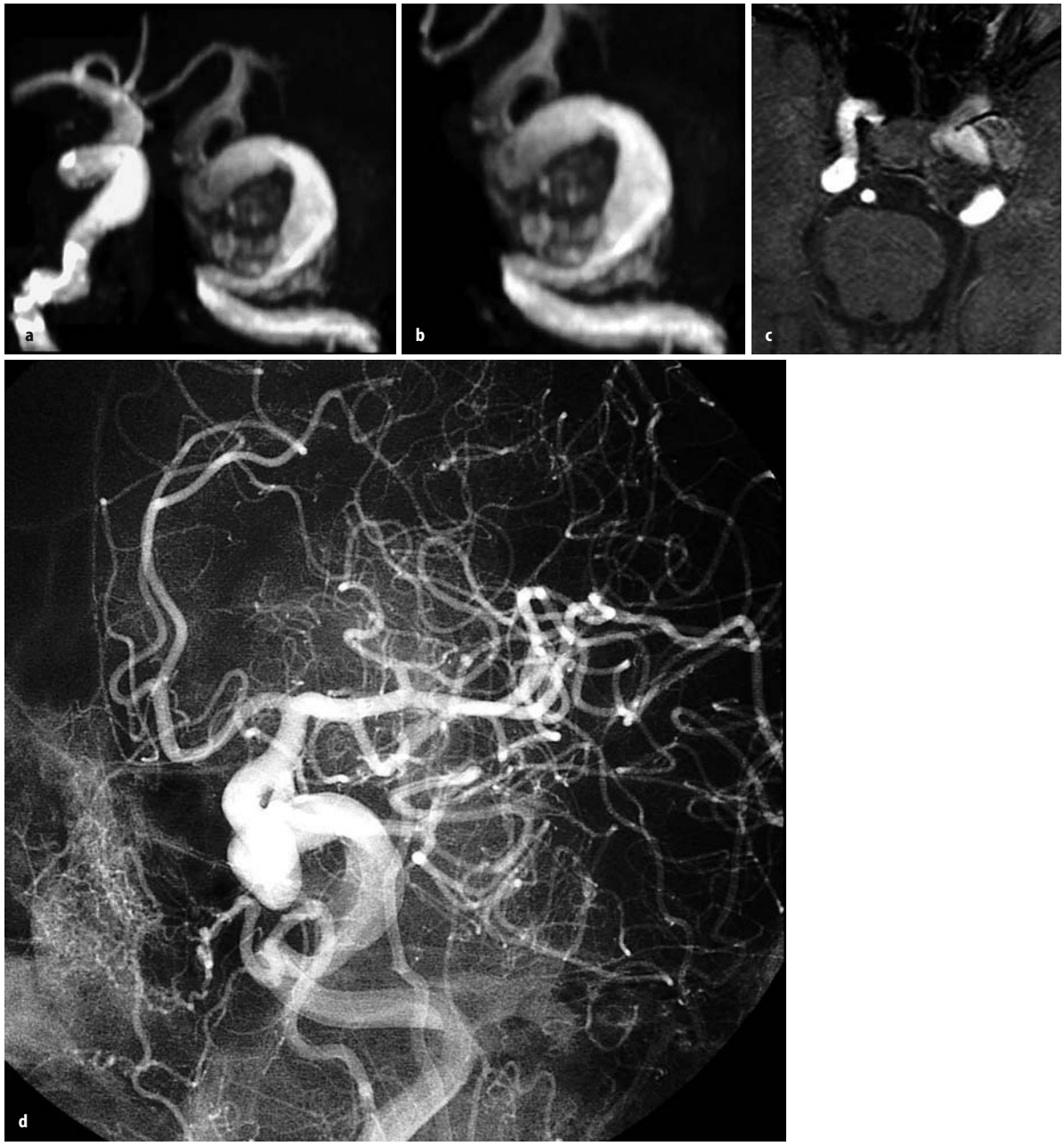

Fig. 5.15. Partially thrombosed giant aneurysm of the intracavernous segment of the left internal carotid artery. 3D TOF study at 3.0 T: coronal MIP image (**a**, detail in **b**); single partition (hyperintense signal inside the true lumen, mixed signal intensity of the thrombus) (**c**); digital angiography (**d**)

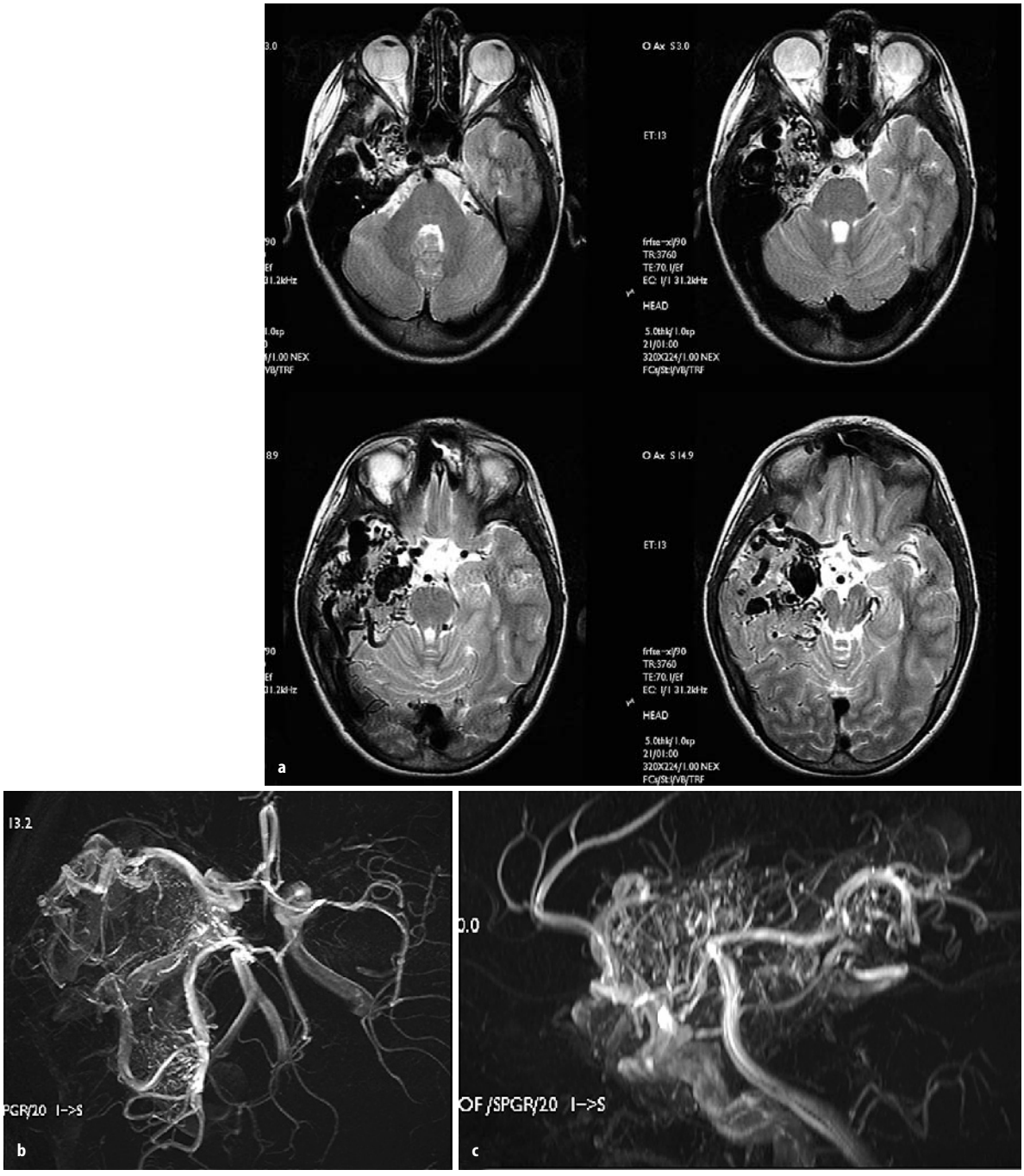

Fig. 5.16. Bulky right temporal arteriovenous malformation: standard MRI T2 FSE study (**a**), 3D TOF axial and sagittal MIP images (**b, c**)

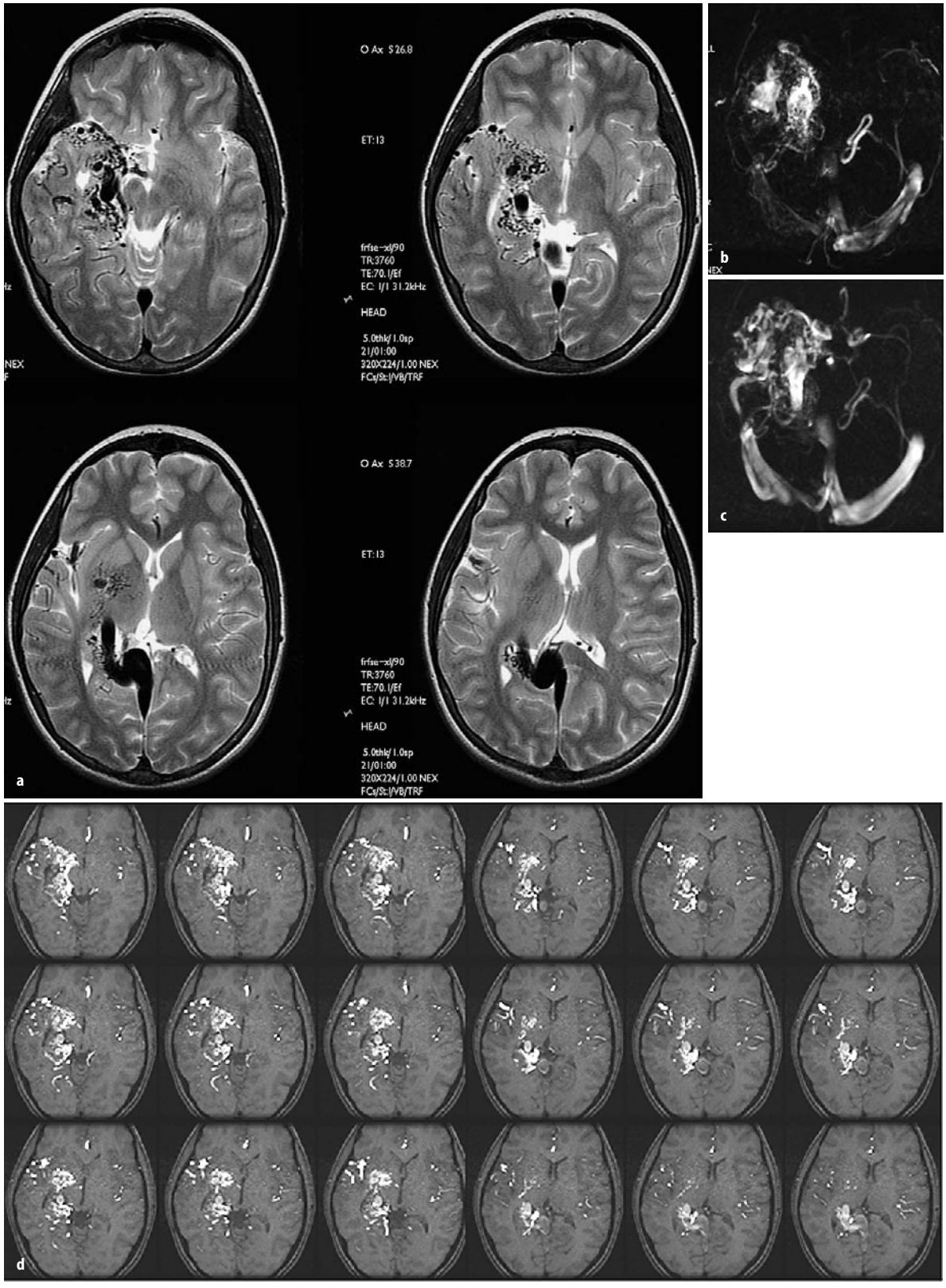

Fig. 5.17. Right arteriovenous malformation: 3D PC and TOF obtained at 3.0 T. T2 FSE image (**a**); MIP PC image with 20 cm/s (**b**); with 90 cm/s (**c**); single 3D TOF partitions (**d**)

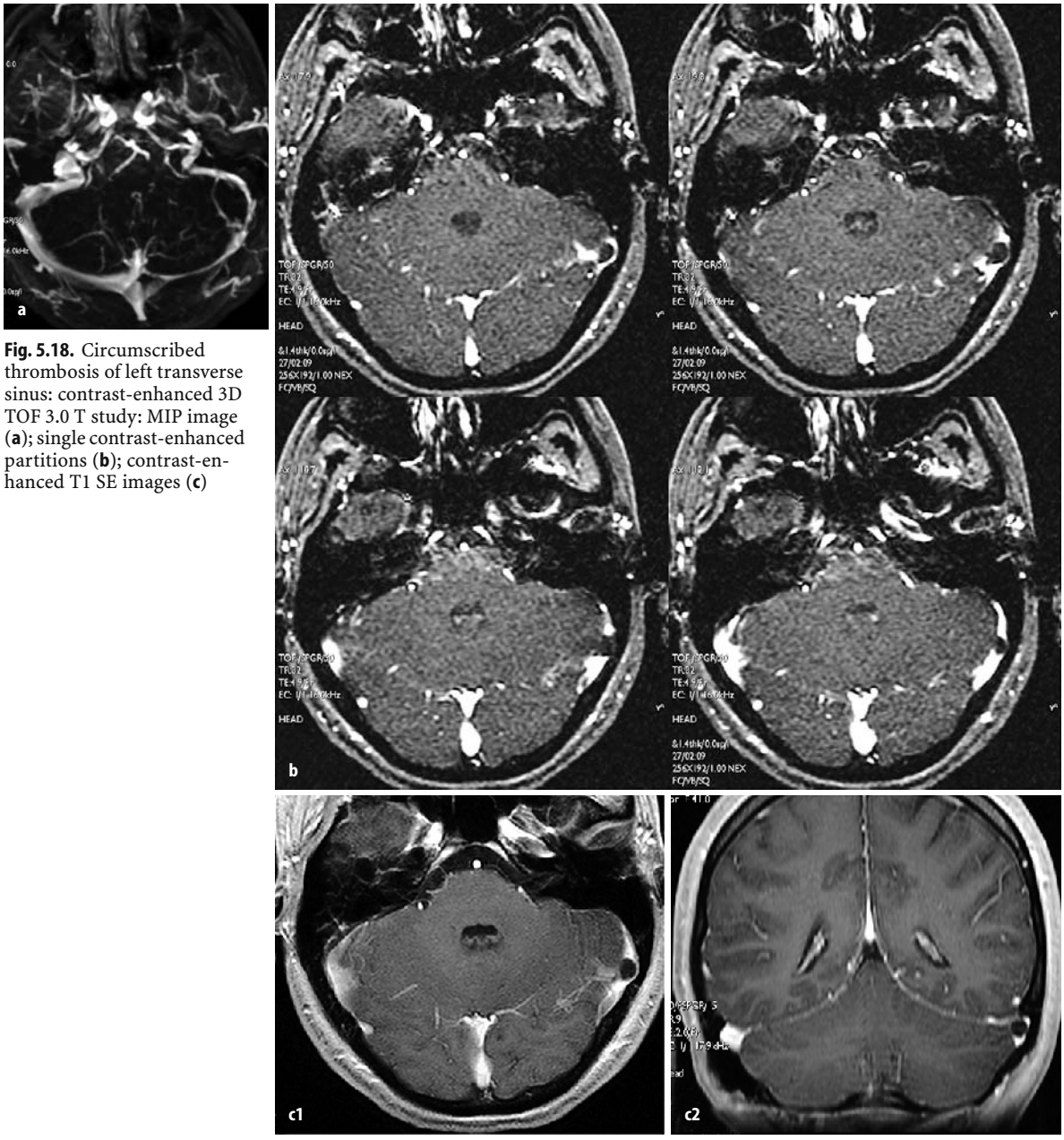

Fig. 5.18. Circumscribed thrombosis of left transverse sinus: contrast-enhanced 3D TOF 3.0 T study: MIP image (**a**); single contrast-enhanced partitions (**b**); contrast-enhanced T1 SE images (**c**)

References

1. Krings T, Hans FJ, Moeller-Hartmann W, et al. (2002) Time of flight, phase contrast and contrast enhanced magnetic resonance angiography for pre-interventional determination of aneurysm size, configuration, and neck morphology in an aneurysm model in rabbits. Neurosci Lett 326:46 – 50
2. Lenz GW, Haacke E, Masaryk TJ, et al. (1988) In plane vascular imaging: pulse sequences design and strategy. Radiology 166:876 – 882
3. Prince MR (1988) Contrast enhanced MR angiography: theory and optimization. Magn Reson Imaging Clin N Am 6:257 – 267
4. Prince MR, Yucel EK, Kaufmann JA, et al. (1993) Dynamic gadolinium-enhanced three dimensional abdominal MR arteriography. J Magn Reson Imaging 3:877 – 881
5. Leung DA, Mckinnon GC, Davis CP, et al. (1996) Breathhold contrast-enhanced 3 D MR angiography. Radiology 201: 569 – 571
6. Prince MR, Narasimhan DL, Jacoby WT (1996) Three-dimensional gadolinium-enhanced MR angiography of the thoracic aorta. Am J Roentgenol 166:1387 – 1397
7. Prince MR, Narasimham DL, Stanley JC (1995) Breath-hold gadolinium-enhanced MR angiography of the abdominal aorta and its major branches. Radiology 197:785 – 792
8. Scarabino T, Giannatempo GM, Nemore F, et al. (2003) RM 3.0 Tesla. II parte: L'imaging morfo-funzionale cerebrale. Radiol Med 105:150 – 161
9. Scarabino T, Nemore F, Giannatempo GM, et al. (2003) Risonanza Magnetica 3.0 Tesla. Riv Neuroradiol 16 (Suppl): 314 – 315

10. Scarabino T, Nemore F, Giannatempo GM, et al. (2003) 3.0 T magnetic resonance in neuroradiology. Eur J Radiol 48:154 – 164
11. Scarabino T, Nemore F, Giannatempo GM, et al. (2004) 3.0 T MR angiography. Riv Neuroradiol 17:777 – 783
12. Campeau NG, Huston J, Bernstein MA, et al. (2001) Magnetic resonance angiography at 3.0 T: clinical experience. Top Magn Reson Imag 12:183 – 203
13. Frayne R, Goodyear BG, Dickhoff, et al. (2003) Magnetic resonance imaging at 3.0 tesla: challenges and advantages in clinical neurological imaging. Invest Radiol 38(7): 385 – 402
14. Scarabino T, Nemore F, Giannatempo GM, et al. (2004) Semeiological features of 3.0 T MR imaging: what changes at high magnetic field. Riv Neuroradiol 17:755 – 764
15. Takahashi M, Uematsu H, Hatabu H (2003) MR imaging at high magnetic fields. Eur J Radiol 46:45 – 52
16. Norris DG (2003) High field human imaging. J Magn Reson Imag 18:519 – 529
17. Wansapura JP, Holland SK, Dunn RS, et al. (1999) NMR relaxation times in the human brain at 3.0 T. JMRI 9:531 – 538
18. Thomas SD, Al-Kwifi O, Emery DJ, et al. (2002) Application of magnetization transfer at 3.0 T in three-dimensional time-of-flight magnetic resonance angiography of the intracranial arteries. J Magn Reson Imaging 15:479 – 483
19. Parker DL, Buswell HR, Goodrick KC, et al. (1995) The application of magnetization transfer to MR angiography with reduced total power. Magn Reson Med 34:283 – 286
20. Al-Kwifi O, Emery DJ, Wilman AH (2002) Vessel contrast at 3.0 T in time-of-flight magnetic resonance angiography of the intracranial and carotid arteries. Magn Reson Imaging 20:181 – 187
21. Bernstein MA, Huston J 3rd, Lin C, et al. (2001) High-resolution intracranial and cervical MRA at 3.0 T: technical considerations and initial experience. Magn Reson Med 46:955 – 962
22. Reichenbach JR, Barth M, Haacke EM, et al. (2000) High-resolution MR venography at 3.0 Tesla. Comput Assist Tomogr 24:949 – 957
23. Rutherford M, Malamateniou C, Zeka J, et al. (2004) MR imaging of the neonatal brain at 3 Tesla. Eur J Paediat Neurol 8:281 – 289
24. Willinek WA, Gieseke J, von Falkenhausen M, et al. (2004) Sensitivity encoding (SENSE) for high spatial resolution time-of-flight MR angiography of the intracranial arteries at 3.0 T. Rofo 176:21 – 26
25. Hennemeyer CT, Wicklow K, Feinberger DA, et al. (2001) In vitro evaluation of platinum Guglielmi detachable coils at 3 T with a porcine model: safety issues and artifacts. Radiology 219:732 – 737
26. Sommer T, Maintz D, Schmiedel A, et al. (2004) High field MR imaging: magnetic field interactions of aneurysm clips, coronary artery stents and iliac artery stents with a 3.0 Tesla MR system. Rofo 176(5):731 – 738
27. Shellock FG (2002) Biomedical implants and devices: assessment of magnetic field interaction with a 3.0 Tesla MR system. J Magn Reson Imaging 16:721 – 732
28. Shellock FG, Gounis M, Wakhloo A (2005) Detachable coil for cerebral aneurysms: in vitro evaluation of magnetic field interaction, heating, and artifacts at 3 T. AJNR 26: 363 – 366
29. Gibbs GF, Huston J 3rd, Bernstein MA, et al. (2004) Improved image quality of intracranial aneurysms: 3.0-T versus 1.5-T time-of-fight MR angiography. Am J Neuroradiol 25(1):84 – 87

3.0 T MR Spectroscopy

6

M. Tosetti, T. Schirmer, V. d'Alesio, A. Di Costanzo, T. Scarabino

Magnetic resonance spectroscopy (MRS) is a non-invasive technique that can be used to measure the concentrations of different low-molecular weight chemicals. The technique is based on the same physical principles as magnetic resonance imaging (MRI), i.e. the detection of energy exchanges between external magnetic fields and specific nuclei within atoms. The principal differences between MRI and MRS lie in the different use of frequency, phase and signal amplitude as carriers of information:

- In MRI, frequency and phase are used to encode the spatial coordinates, while the signal amplitude of the signal is translated into a grey value of the resulting image (Fig. 6.1a).
- In MRS, phase and frequency are used to identify spectral patterns unique to specific metabolites, while the amplitude is used as a scale for the concentration of these metabolites (Fig. 6.1b).

The information obtained during MRS experiments, usually acquired as a series of FIDs, spin echoes or stimulated echoes in the time domain, is displayed graphically as a spectrum in the frequency domain with individual peaks representing the various chemical compounds. The diagnostic ability of MRS can be increased by improving the spectral quality through changes in hardware and software, and/or by improving the analytical approach aiming for objective absolute concentration measurements.

MRS should be performed as an adjunct to MRI gain additional information for a reliable clinical diagnosis: while conventional MRI provides anatomical images of the brain, MRS provides functional information related to its underlying dynamic physiology.

6.1 Spectroscopy Basics

MRS has been demonstrated in vivo for different nuclei, including ^{1}H, ^{31}P, ^{13}C, ^{15}N, ^{19}F and ^{23}Na. While most of these nuclei are very difficult to detect, ^{1}H and ^{31}P are available in the human brain in significant concentra-

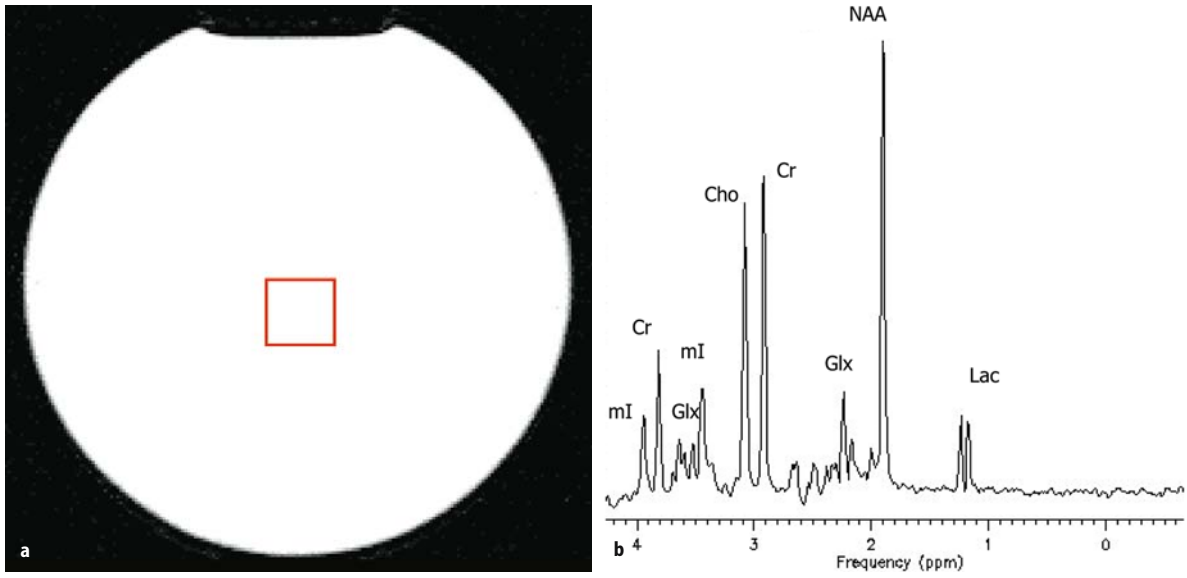

Fig. 6.1. a MRI of a phantom containing main brain metabolites dissolved in a water-based, Ph-buffered stock solution. **b** Spectrum acquired from the VOI prescribed in **a** using volume selective spectroscopy sequence with PRESS excitation (TR: 2,000 ms, TE: 35 ms)

tions and have the appropriate physical configuration to be detected by MRS. Besides the technical prerequisites, ^{1}H and ^{31}P are prominent candidates for clinical studies also from a biochemical viewpoint, as they allow in vivo investigation of some of the processes involved in brain metabolism. For instance, ^{31}P-MRS has been the first to be applied to medicine in vivo, and can be used to evaluate brain energy metabolism by directly and non-invasively measuring ATP, PCr or Pi concentrations. While ^{31}P-MRS was the first spectroscopic technique to be applied in vivo, the main nucleus studied today in neuospectroscopy is ^{1}H, which provides information on markers of neurons, myelin, energy metabolism and other metabolically active compounds. Besides its important clinical role, ^{1}H spectroscopy is also less technically demanding as it uses hardware employed for standard MRI, and provides a higher signal/noise ratio (SNR) [1, 3].

6.1.1 Proton MRS in Neuroradiology

Proton magnetic resonance spectroscopy of the brain reveals specific biochemical information about cerebral metabolites, which may support clinical diagnosis and enhance the understanding of neurological disorders. Analysis of the resonance signals of low-molecular weight brain metabolites (concentrations in mmol) provides information on metabolite concentrations and makes it possible to correlate their modifications with various pathological conditions. The high diagnostic specificity of MRS enables the biochemical changes that accompany various diseases to be detected, as well as disease characterization, sometimes diagnosis, and monitoring. At 1.5 T the main metabolites detected vary according to the acquisition parameters (TR, TE) and type of pulse sequence adopted (STEAM, PRESS). 1.5 T brain MRS currently has a number of clinical applications, including the characterization of cerebral tumours and the monitoring of their treatment (e.g., radiation necrosis versus recurrence tumour), epilepsy, infection, stroke, multiple sclerosis (MS), trauma, neurodegenerative processes, such as Alzheimer's and Parkinson's diseases [2–4], and allows to diagnose several hereditary and acquired brain metabolic disorders such as Canavan's disease [5], brain creatine deficiency syndromes [6, 7], adrenoleukodystrophy [8] and hepatic encephalopathy [9].

However, despite the demonstrated ability of MRS to detect neurochemical changes and to be technically feasible to study the brain in vivo, there are no standardized techniques for acquiring and interpreting MRS spectra, and little high-quality direct evidence of its influence on diagnosis and therapeutic decision-making is available. Its specificity, diagnostic and prognostic value needs to be improved, and especially its sensitivity to disease markers, all of which can be achieved at higher magnetic field.

In the recent past, high magnetic field MR systems, particularly 3 T instruments, have proliferated with FDA „non-significant risk" clearance [10] and are expected to replace 1.5 T in many clinical and research applications now performed with these magnets [11]. 1.5 T fields have long been seen as the standard, but the development of 3 T and higher field technology suggests that the concept of "high field" may be a moving target. Indeed, NMR spectrographs operating at magnetic fields of 14–21 T, are routinely used for in vitro structural studies of complex molecules. The development of in vivo high-field MRS has however been delayed by safety considerations, hardware limitations (such as the availability of wide-bore magnets), high-performance gradients and methods to correct magnetic field inhomogeneity [11, 13]. MRS like other advanced MR techniques to study the brain (e.g. angiography, diffusion, perfusion and functional imaging) should considerably benefit from the greater SNR and contrast/noise ratio and the increased spatial and temporal resolution provided by high-field systems [10–12].

Several studies comparing brain ^{1}H-MRS at different field strengths in the same subjects using the same experimental parameters, and have demonstrated the usefulness of high-field ^{1}H-MRS [13–19]. Its advantages rest on greater SNR and spectral resolution, which afford greater spatial and temporal resolution and enable the acquisition of high-quality, easily quantifiable spectra in acceptable acquisition times. In addition to improved measurement precision of common metabolites, such as *N*-acetylaspartate (NAA), choline (Cho), creatine/phosphocreatine (Cr/PCr), *myo*-inositol (mI) and when present lactic acid (Lac) and lipids (Lip), high-field systems allow the high-resolution measurement of other metabolites, such as glutamate (Glu), glutamine (Gln), glutathione (GSH), γ-aminobutyric acid (GABA), scyllo-inositol (ScyI), aspartate (Asp), taurine (Tau), *N*-acetylaspartylglutamate (NAAG) and glucose (Glc), thus extending the range of metabolic information. However, these advantages may be hampered by intrinsic field-dependent technical difficulties, such as increased T2 signal decay, chemical shift dispersion errors, J-modulation anomalies, increased magnetic susceptibility, eddy current artefacts, limitations in the design of homogeneous and sensitive radiofrequency coils, magnetic field instabilities and safety issues. Several studies have demonstrated that these limitations can be overcome, suggesting that optimization of high-field ^{1}H-MRS can lead to its broader application in clinical research and diagnosis.

Table 6.1 summarizes several metabolites involved in brain biochemistry detectable with ^{1}H-MRS. Beside

Table 6.1. Some of the primary resonances found in ^{1}H brain spectroscopy and corresponding chemical shifts (in ppm)

Brain metabolites detected on ^{1}H MRS Compound	Abbreviation	Frequency (ppm)
Alanine	Ala	1.48, 3.78
Aspartate	Asp	3.9, 2.69, 2.82
Choline	Cho	3.22 (4.05, 3.54)
Creatine/phosphocreatine	Cr/PCr	3.03, 3.95
γ-Aminobutyric acid	GABA	2.31, 1.91, 3.01
Glucose	Glc	3.43, 3.84 (...)
Glutamate	Glu	3.77, 2.06, 2.38
Glutamine	Gln	3.71, 2.15, 2.46
Glycine	Gly	3.56
Lactate	Lac	1.33
Myo-Inositol	mI	3.56, 4.06
N-Acetylaspartate	NAA	2.02
Scyllo-inositol	ScyI	3.35
Taurine	Tau	3.44, 3.38, 3.32, 3.27

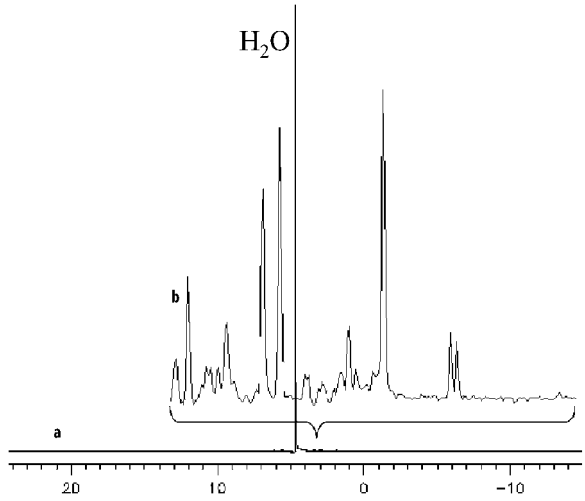

Fig. 6.2. a Full water signal of a phantom spectrum containing the main brain metabolites compared to the metabolite signal (**b**) several orders of magnitude smaller than the water signal

the most prominent resonances of NAA, choline and creatine, a variety of other resonances might or might not be present in a spectrum depending on its type and quality as well as disease. This list is not complete, in that several metabolites are only observed in the rare cases when their concentrations are several times higher than normal, while metabolites such as alcohol and propylene glycol are not present in normal brain metabolism but may be found in certain patients. For a full list of detectable metabolites the reader required to interpret spectra with unusual resonances is referred to the literature.

6.1.2 MR Spectroscopy – Quality and Resolution

While the ^{1}H protons bound to the H_2O molecule provide basically the whole signal used for MR imaging, the high water signal is one of the most disrupting elements in MRS, since the molecules of interest are found at much lower concentrations, yielding signal amplitudes more than 1,000-fold smaller than the signal of water (Fig. 6.2). Thus the quality of a spectrum, which is usually measured as SNR, and its resolution, which includes the spectral, spatial and temporal dimensions, play a major role in the applicability and acceptance of MR spectroscopy.

6.1.2.1 Signal to Noise Ratio

The SNR is based on several variables, the most important of which are of course signal intensity (where Cr is often used as the reference) and the underlying noise of a spectroscopy experiment. The dependencies of signal intensity and noise can be divided into two categories:

1. Dependencies which cannot be affected by the user and which are given by fixed natural constants. The corresponding SNR shall be called SNR_{int}.
2. Dependencies that can be altered by modifying the acquisition parameters. The corresponding SNR shall be called SNR_{Exp}.

The most important factors for SNR_{int} in a ^{1}H-MRS experiment are to be aware of are the number of protons contributing to the total signal N, the field strength of the static magnetic field B_0 and the relaxation properties of a specific metabolite. With a direct, linear proportionality of SNR_{int} to N and B_0 these parameters define the intrinsic SNR available for the spectroscopy experiment, which means that an increase in B_0 from 1.5 T to 3.0 T will theoretically boost the SNR by a factor of two. This achievable SNR will always be degraded by the natural phenomena of relaxation, expressed as an exponential signal decay after full excitation with the relaxation constants T2 and exponential return of the spin system into thermal equilibrium with the time constant T1.

For a given sample in a specific MR scanner, the value of SNR_{int} is fixed, and its limitations cannot be overcome. Beside these factors, there are others which can be optimized by the user, and which contribute to the final SNR. The main parameters to be considered by the user are the type of sequence, the number of signal averages N, the sample volume (VOI), and the echo and repetition times (TE, TR).

The SNR gain obtained from the intensity increase from 1.5 to 3.0 T can for instance be used to decrease the acquisition volume by a factor of two. On the other hand, reduction of the acquisition volume by a factor of two at a constant field strength would require to in-

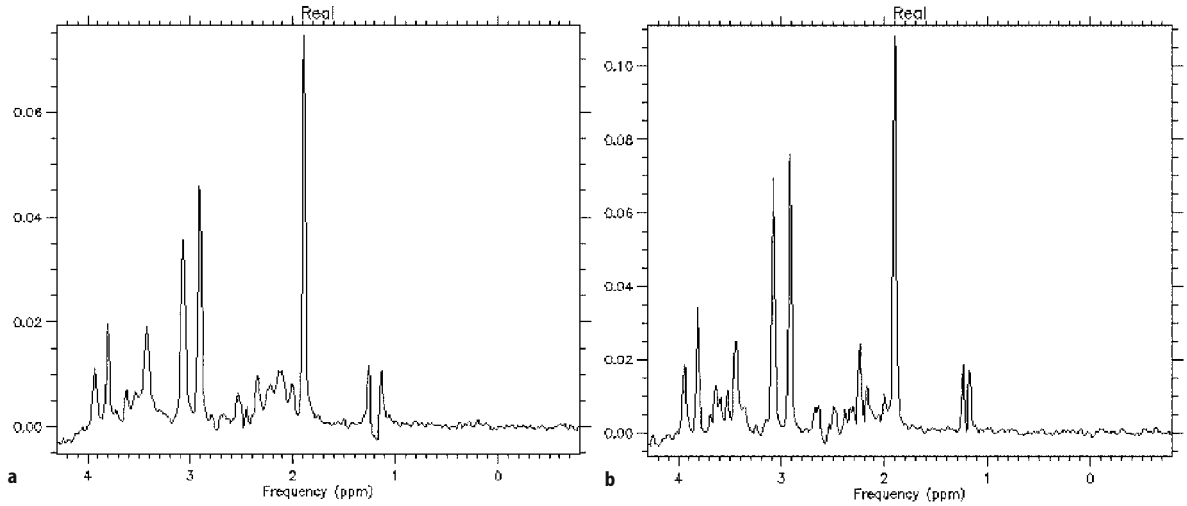

Fig. 6.3. Spectra acquired on the same phantom containing the main brain metabolites at 1.5 T (**a**) and at 3.0 T (**b**) using the same sequence parameters (PRESS: TR: 2000 ms, TE: 35 ms), showing the increased SNR, the improved spectral resolution, in particular between 2 ppm and 2.6 ppm, and the different peak ratio between the main metabolites due to the different relaxation times of individual metabolites at different field strengths

crease the number of averages by factor of four to maintain the SNR. In addition, T1 relaxation times increase with higher field strength, leading to increased signal saturation for a given repetition time, and T2 relaxation times decrease. Therefore, the theoretical doubling of SNR cannot be achieved, due to the use of repetition times (TR) in the order of the T1 decay times (and not infinitely long) and echo times (TE) in the order of the metabolite T2 decay times [19–22].

Comparison of different experimental settings thus requires careful analysis of all parameters to avoid errors and misinterpretations (Fig. 6.3).

6.1.2.2 Spatial and Temporal Resolution

The achievable quality of a spectrum identified by its SNR is directly related to the size of the sample volume (VOI) and the acquisition time, defined by the number of signal averages *N* multiplied by the repetition time (TR), as described in the paragraph above. Thus the SNR is usually the limiting factor for spatial and temporal resolution in a clinical setting, where the time of acquisition is usually restricted by logistical, technical, financial and ethical aspects.

Spectra can be acquired from a single-voxel or a multidimensional grid of spectra, which are generally referred to as chemical shift or spectroscopic images (CSI, SI) (Fig. 6.4). Unlike the ca. 1 mm^3 resolution that can be achieved with routine MRI, ^{1}H-MRS studies have been performed with a spatial resolution of 8 ml and an acquisition time of 3–5 min per single-voxel acquisition and 2–4 ml for CSI in 5–10 min [23].

The greater ability to detect smaller lesions afforded by advanced MRI technologies can involve an increased need for greater spatial resolution of single-voxel spectroscopy and CSI experiments. Whereas the poor SNR of 1.5 T magnets prevented the acquisition of single-voxel spectra with a spatial resolution significantly below 4–8 ml or chemical shift images with a spatial resolution of less than 2 ml, lower spatial resolutions are becoming feasible at 3 T.

The direct matching of metabolic and anatomical information would obviously be of clinical importance since it could improve the sensitivity and specificity of diagnosis. Higher-resolution SI can enable to distinguish between different anatomical structures, between normal and pathological tissue, or between different pathological structures (e.g. heterogeneous tumours, SM plaques, etc.). In patients with brain tumour, for example, high-resolution SI could differentiate healthy oedematous from affected tissue as well as normal from normal-appearing hippocampus in patients with temporal lobe epilepsy. At 3 T and higher field intensities, voxel volumes of 1 cm^3 and lower can be obtained with still good intrinsic SNR and acceptable acquisition times [23, 24].

Higher field strengths have also considerably ameliorated resolution time reducing examination times which had limited the application of ^{1}H-MRS to clinical research. The advantages of shorter examinations for patients, radiologists, technicians and hospital administrators are obvious. At high magnetic fields, larger brain volumes can be studied over times similar to current single-voxel protocols using multivoxel 2D or 3D ^{1}H-SI sequences. In multivoxel 3D spectroscopy ex-

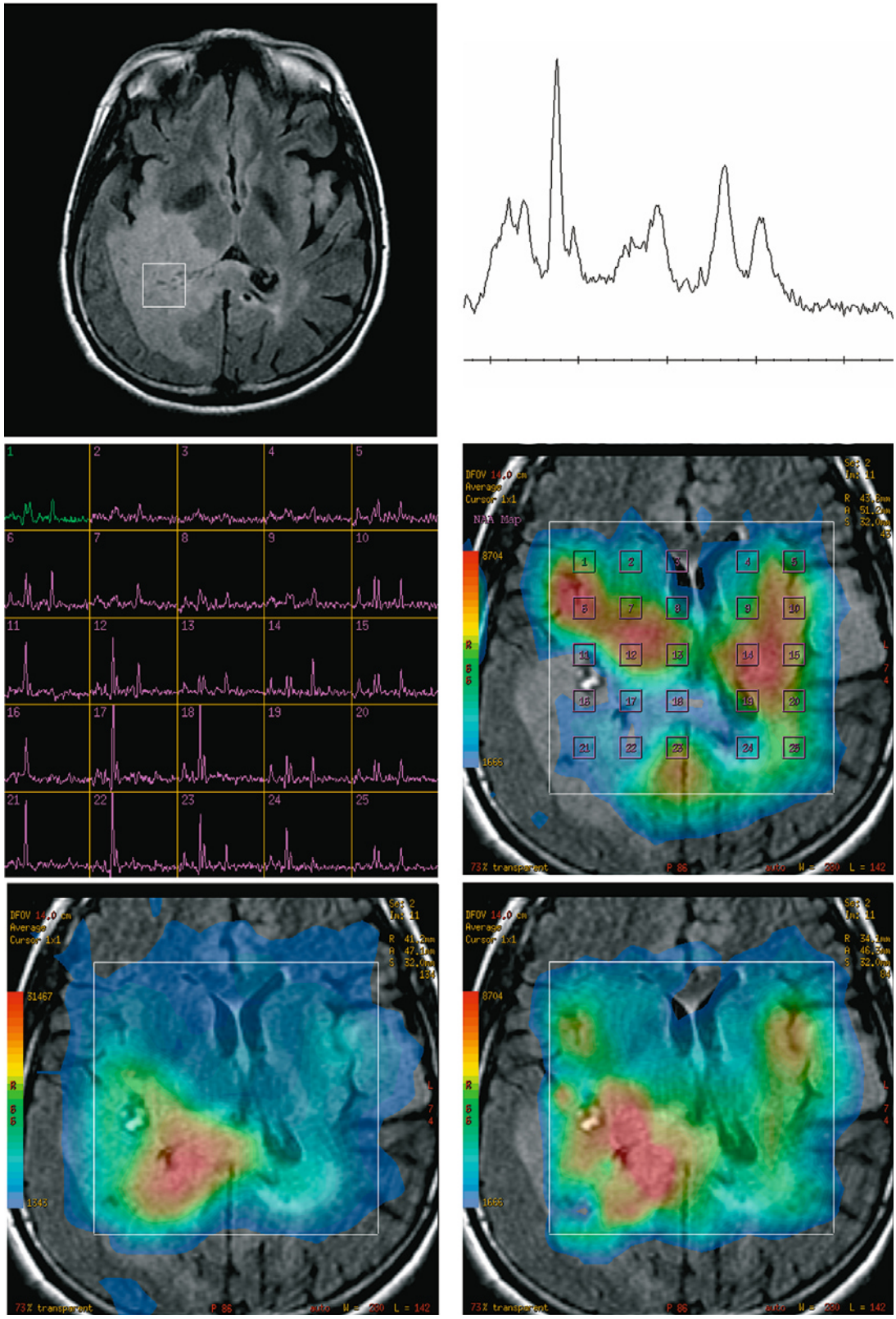

Fig. 6.4. Whereas a single-voxel spectrum usually provides good quality, high SNR data but limited to a small region, a CSI acquisition will yield a grid of spectra, which are often prone to artefacts or low SNR, which can be translated into metabolite maps. (Images courtesy of Charité, Virchow Clinic, Berlin, Germany)

periments, the time of acquisition has been reduced 25%, retaining the lowest SNR of 1.5 T at 3T [18, 22, 23]. Shorter times allow multinuclear MRS to determine the metabolic changes coupled to neuronal activity.

Beside the clinical advantages, high spatial and temporal resolution also have some striking technical features. Next to the SNR, the linewidths of the individual peaks are responsible for the qualitative appearance of a spectrum. The linewidth is defined by the T2 relaxation time of the metabolite and the local field inhomogeneities, where the inhomogeneities can be the dominating factor of a resulting T2*. As local inhomogeneities will decrease with smaller voxel volumes, T2* increases, resulting in a noticeable decrease of linewidths, improving spectral quality, especially for voxels with a volume smaller than 0.75 cm^3 [24].

Another factor degrading spectral quality is the stability of the consecutively acquired signal averages. Patient motion, magnet drifts and the instability of other system components can interfere with the acquisition of MRS data, yielding broadened metabolite peaks or other artefacts. Thus keeping the acquisition times as short as possible spectral quality can significantly be improved.

6.1.2.3 Spectral Resolution

Spectral resolution essentially refers to the ability to distinguish adjacent peaks in a spectrum of individual peaks. The resonance frequency ω of a specific metabolite is defined by the static magnetic field B_0 and a shielding factor σ, defined by the geometric structure of the molecule shielding the nuclei from the external magnetic field and referred to as chemical shift. The chemical shift is field-independent, for every metabolite characteristic unit measured as parts per million (ppm). The resonance frequency $\omega(\sigma, B_0)$ of a specific metabolite is defined by:

$$\omega = \gamma \cdot B_0 \cdot (1 - \sigma)$$

where γ is the gyromagnetic ratio of the nucleus studied. The spectral distance $\Delta\omega$ between two peaks with chemical shifts σ_1 and σ_2 can be expressed using the above equation as:

$$\Delta\ \omega = \gamma \cdot B_0 \cdot (\sigma_2 - \sigma_1)$$

This means that the spectral distance $\Delta\omega$ for two identical metabolites will be twice as much at 3.0 T compared to 1.5 T (Fig. 6.5a).

This gain in spectral resolution with higher field strengths will allow for improved differentiation between peaks that might overlap at lower field strengths. It is necessary to adjust some sequence parameters to make full use of this gain in spectral resolution. The achieved resolution of the raw data acquired is defined by the sampling scheme used. A given number of points are sampled with a specific sampling rate to get a good digital representation of the MR signal. Typically at 1.5 T, a spectroscopy signal is sampled with 2,048 points and a sampling rate of 2,500 Hz, which is equivalent to a sampling interval of 0.4 ms between each point, yielding a total sampling time of 819.2 ms in which the acquisition window is opened. This kind of resolution is recommended at

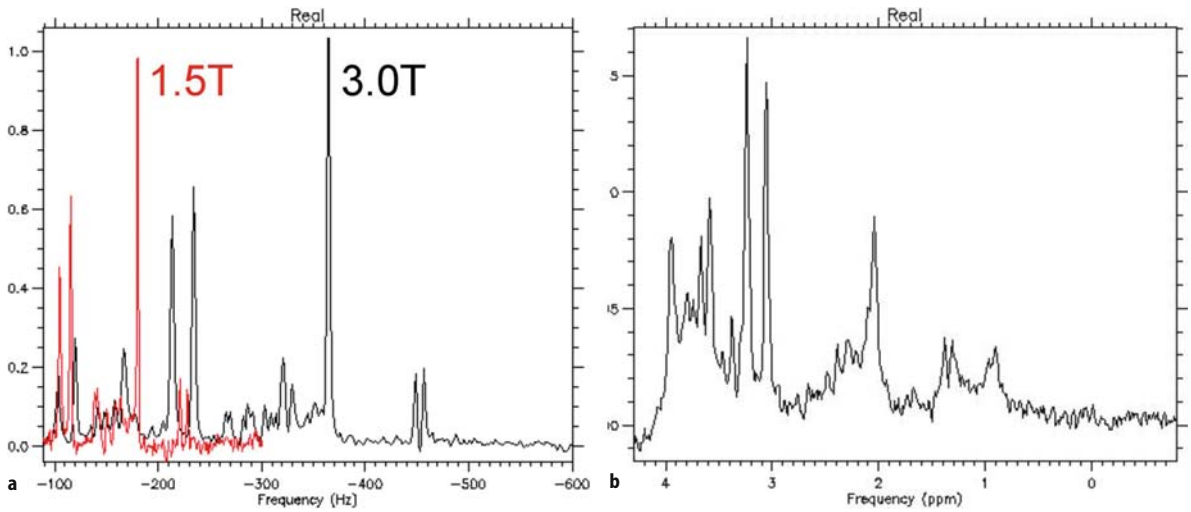

Fig. 6.5. The frequency resolution between individual peaks increases as a proportion of field strength. This means that the spectral distance $\Delta\omega$ for two identical metabolites will be twice as much at 3.0 T compared to 1.5 T (**a**) and therefore in abnormal tissue it is possible to resolve different close resonance signals such as glycine at 3.56 ppm from *myo*-inositol at 3.55 ppm and to achieve a better detection of scyllo-inositol (3.35 ppm) (**b**)

1.5 T to cover most of the spectral information, and sample long enough to see the signal decay down to the noise level. To cover exactly the same spectral information at 3.0 T, it is necessary to double the sampling rate to 5,000 Hz, which for these settings is equivalent to a sampling interval of 0.2 ms between points. At a constant number of 2,084 points sampled the acquisition window is open for an overall 409.6 ms of sampling time. This sampling window can be so short, especially for phantom experiments, that a significant amount of signal is left at the end of the sampling interval. This can cause artefacts, known as ringing artefacts, in the reconstructed spectrum.

Even though the above considerations are usually of minor importance to the clinical user, they show that a direct one-to-one comparison of MR spectroscopy experiments at different field strengths can be misleading. If exactly the same parameters for sampling rate and number of points are used, the quality of the spectrum acquired at higher field strength is always degraded. If the parameters are adjusted the comparison is no longer one-to-one anymore.

Spectral resolution also depends on the attainable linewidths, which are a function of field-dependent T2 relaxation times and field homogeneity. However, higher-field MR scanners can improve the resolution between peaks as shown above, allowing a more accurate identification and quantification of each metabolite [16–19, 21]. Despite shorter T2 relaxation times and increased field inhomogeneity, the chemical shift doubling at 3 T yields better spectral resolution. At 1.5 T, the quantification of NAA, Cho, Cr, Lac, and other metabolites such as mI has been feasible [1–4], while Glu and Gln are closely coupled and present extensive spectral overlap at this field intensity, making peak assignments and quantitative measurements difficult and subject to considerable uncertainty. At 3.0 T the increase in chemical shift is reflected, for instance, in improved baseline separation of Cho and Cr, which are only 0.2 ppm apart, and in slightly better resolution of Glu/Gln region, between 2.05 and 2.5 ppm. Furthermore the presence of abnormal metabolites such as Phe at 7.36 ppm (Fig. 6.6) or the differentiation of glycine at 3.56 ppm from *myo*-inositol at 3.55 ppm (Fig. 6.5b) can be confirmed with more confidence.

Significantly improved spectral resolution was also demonstrated in the quantification of J-coupled metabolites, such as glutamate, glutamine and GABA and the detection of glucose at 3.48 ppm and 5.23 ppm, without using glucose infusion [16, 17, 21, 25].

The previous paragraphs have shown that spectral quality is always a compromise between SNR and the spatial, spectral and temporal resolutions. The relations cannot be expressed in a simple formula, and even though systems with higher field strength provide the required basis for a trend to higher resolutions or

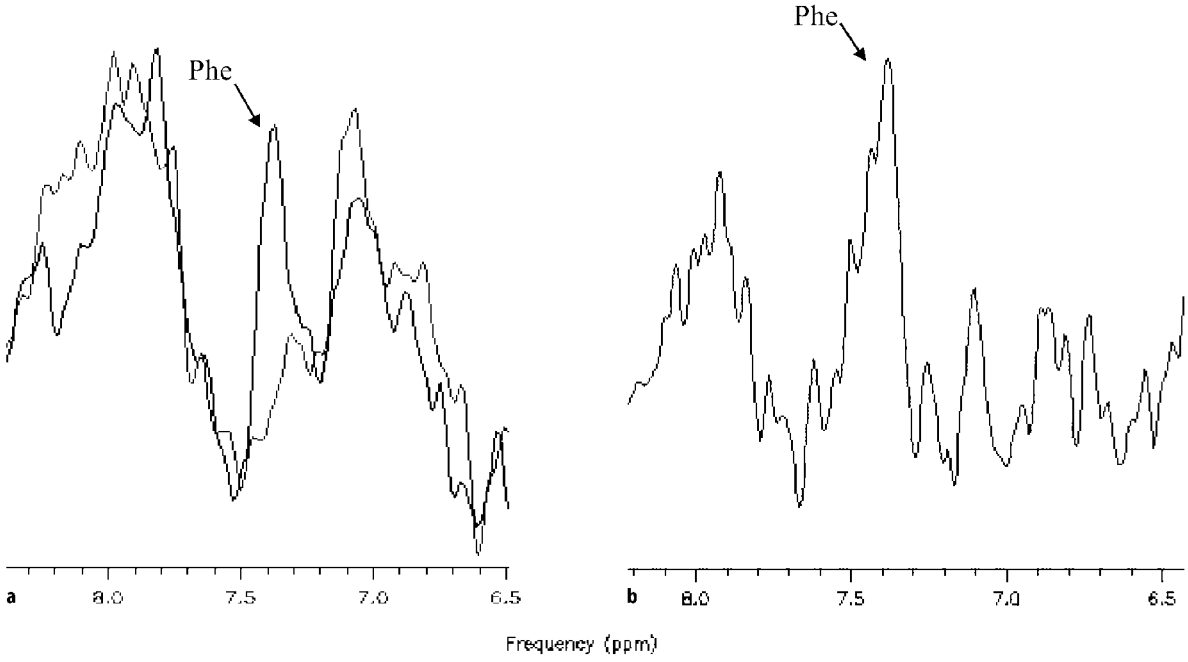

Fig. 6.6. Detection of phenylalanine (Phe) at 7.36 ppm in a patient affected by phenylketonuria (PKU). With respect to the MRS study conducted with the 1.5 T system (**a**) to detect the Phe signal it is mandatory to use a VOI of 32 cc and to compare two signals in a follow-up therapeutic study. At 3 T, the Phe signal is detectable and can be analysed due to the increased SNR and the better spatial resolution. In fact, use of a smaller VOI (8 cc) reduced the line-broadening effects, allowing Phe to be better resolved with respect to histidine and homocarnosine at 7.05, 7.8 and 8.02 ppm, to the amide proton of NAA at 7.9 ppm and due to the reduction in the macromolecular contributions (MM) at 7.3 ppm

SNR, experimental settings have to be carefully weighted against each other to provide the optimum raw data required for further analysis.

6.2 Spectroscopy Artefacts and Pitfalls

6.2.1 Magnetic Susceptibility and B_0 and B_1 Inhomogeneities

Different materials placed in a homogeneous magnetic field (e.g. in an MR scanner), affect the magnetic field in different ways according to their magnetic susceptibility. For instance, water has weak negative susceptibility, namely it develops a small magnetization that acts to counteract the external field, while bone and air have near zero susceptibility with little effect on the magnetic field. When a structure composed of materials of different susceptibility, such as the head, is placed in the bore, the magnetic field becomes distorted and inhomogeneous [26]. At higher magnetic fields, microscopic susceptibility from paramagnetic substances and blood products, and macroscopic susceptibility at the level of air-tissue and tissue-bone interfaces, such as near the air-filled sinuses and skull base, are sensibly increased. Consequently, magnetic field inhomogeneity and susceptibility artefacts will make it more difficult to obtain good-quality spectra, especially from lesions near the skull base or close to the calvaria. These problems can be alleviated mainly by the following expedients: using higher spatial resolution, optimizing RF pulse and coil designs [27, 28], improving automatic local shimming methods [29, 30], and undistorting the images using magnetic field maps [26]. Spectral distortion and loss in SNR may also be caused by eddy currents, which are more apparent at higher field strength due to increased speed and power of gradient coils. These eddy currents can create an additional magnetic field of duration much longer than the original gradient pulse that generated them [31], even though these effects can be reduced by dedicated hardware and software designs [32].

Field inhomogeneity, measured in Hz, has been found to be similar at 1.5 T and 3.0 T in phantom studies, but comparison of the linewidth and T2 values in vivo shows that the inhomogeneity contribution to the linewidth is greater at 3.0 T than at 1.5 T. For all three main metabolites (NAA, Cr and Cho), the average of the difference between the experimental linewidth and the estimated natural linewidth was 0.95 Hz at 1.5 T and 2.66 Hz at 3 T [33]. Improved high-order shimming techniques may help to minimize this term at higher field strengths [34].

Another important effect found at 3.0 T is related to B_1 inhomogeneities, usually referred to as dielectric resonance. As soon as the sample size approaches the dimension of the RF wavelength, the RF field becomes inhomogeneous. This can be observed as bright spots in the central area of head, body or phantom images acquired at 3.0 T and above. In MRS experiments, this effect makes it difficult or impossible to define the appropriate transmitter gain going along with the required flip angle, which will locally vary significantly, to apply the reciprocity theorem for spectrum quantification.

6.2.2 Chemical Shift Misregistration and J-Modulation Artefacts

The spatial location of a signal is usually encoded by a volume-selective excitation. With three consecutive excitation pulses, the signal is first selectively excited in a slice, with a second pulse focused on a row inside the slice and finally selectively excited inside the volume of interest with a last, third pulse. The excitation performed by 90° and 180° excitation pulses used in a PRESS or STEAM sequence suffers from a frequency-dependent spatial misregistration known as the chemical shift error. While ideally all spins of every metabolite inside a VOI would be excited by the same pulse angle, the excitation varies across the metabolites and their localization. As a compromise NAA is often used as the reference for the VOI, so that all NAA protons are fully excited inside the selected VOI, while, for instance, the excited volume of metabolites right of the NAA would be shifted by a few millimetres to the right and upwards (Fig. 6.7). The size and location of chemical shift errors are influenced by a number of factors, including the field strength [35]. At higher magnetic fields, the selective pulses used for MRS volume localization go along with increased volume misregistration. This problem can be minimized by several techniques, where the use of outer volume suppression techniques with very selective saturation pulses has shown to be very promising [36].

J-Modulation anomalies for homonuclear-coupled resonances represent another difficulty more frequently encountered at higher magnetic fields. For molecules such as lactate, the extreme separation of the coupled resonances (a doublet at 1.33 ppm due to methyl protons and a quartet at 4.1 due to methine protons) will result in incomplete inversion of the coupled spin over a large portion of the selected volume, resulting in anomalous intensity losses, which are a function of position. This effect can be overcome by some methods, each presenting advantages and disadvantages [37].

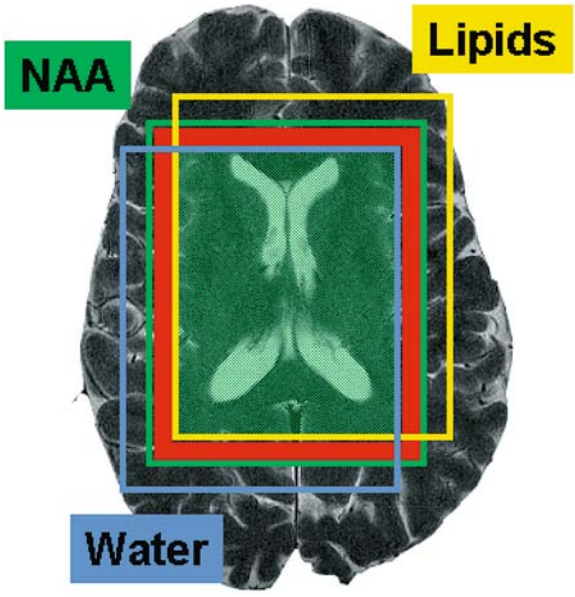

Fig. 6.7. Voxel misregistration due to chemical shift error caused by spatially varying, frequency-dependent differences of excitation. The different metabolites are only in a subset of the whole excitation volume (*red plus green area*) and equally excited (*green area*), while certain metabolites are or are not excited in- or outside the ROI, which can have a significant impact on the achieved qualitative and quantitative results

6.2.3 Magnetic Field Stability and Radiofrequency Coil Efficiency

The temporal variation of the metabolite signal, especially during long examinations, strongly impairs the quality of the resulting spectra. Beside the usual patient motion, the reason for this instability can be found in the drift of the main magnetic field, which particularly affects high-field systems due to the higher technical demands for these magnets. The observable magnet drift over a long spectroscopy experiment can be within the order of the linewidth that can be achieved in ^{1}H-MRS. Spectral distortions due to temporal signal instabilities can be efficiently compensated for by the use of a correction algorithm on the basis of phase and frequency post-correction of the time-resolved raw data or by using additional signals from interleaved acquisition with a navigator scan [38].

A further hurdle for clinical spectroscopy at high-field is the difficulty in building high-sensitivity, high-homogeneity volume coils. Since RF penetration into tissues becomes more demanding [39]. The problems become striking for large structures, where achieving satisfactory field homogeneity is difficult. An inadequate RF coil may sacrifice the SNR gained with the greater field strength. To address these problems, some technical strategies have been proposed leading to a second generation of head coils for 3.0 T and 4.0 T systems [39–41]. Further improvements can be expected with the development of new multi-element coil arrays, low temperature coils and new concepts of coil designs for volume resonators.

6.3 MR Spectroscopy Quantification and Analysis

Quantification of metabolites is one of the major challenges in current clinical MR spectroscopy. At higher field strength, the increase in SNR and spectral resolution helps to improve the reliability and reproducibility of the quantitative results. The improvement has been striking for some metabolites, such as Glu, Gln and GABA, suggesting that multiplet resolution is as important in spectral quantification as SNR [17]. Still, all the difficulties and pitfalls known from quantitative analysis of spectra acquired at 1.5 T, especially when trying to determine absolute concentrations, apply to spectra acquired at 3.0 T. The challenges of quantitative spectroscopy are twofold, as in a first step a variety of methods can be used to determine the integral under the individual peaks, which is known to be proportional to the concentrations, and then to translate the value of the integral thus determined into true concentration. While the first is more of a statistical and mathematical problem, albeit quite a large one, where all methods applied should yield similar results, the second step can adopt conceptually different approaches that can yield very different results. Apart from the statistical methods, there are two conceptually different techniques to approach a quantitative output MR spectroscopy:

1. The use of a reference as a standard to normalize the results
2. The use of the so-called reciprocity theorem to translate signal intensity directly into an absolute concentration value

There is no agreement on which method should be employed in which cases, but use of a reference has become an established method, at least as a significant set of results. There are several signals that can be used as a reference: historically, creatine has been used as a reference, as in the majority of the neurological diseases studied with ^{1}H-MRS the Cr concentration has been shown to be constant up to the reliability of the method. On the other hand, a mounting body of findings where Cr is not constant is leading to the exploration of further reference markers. One of these markers is the internal water signal. Since the mmol concentration of water from healthy brain tissue is known, the metabolite signal can be normalized using the water signal as a reference. This method has disadvantages, as it does not take atrophy into consideration, even though there

are methods to correct, for instance, for CSF contamination. If no internal signal is available, an external reference like a small phantom close to the sample volume has been suggested. This requires good B_0 and also RF homogeneity, which is not always given. While the use of internal references works as well for 1.5 T and 3.0 T, the use of an external signal is more difficult. Due to the properties of wave propagation, it is nearly impossible to achieve homogeneous RF excitation over a large FOV with 3.0 T systems. It would be necessary to acquire the spectrum of the VOI inside the patient followed by an acquisition of an external reference while keeping all acquisition parameters constant.

This also yields to a problem related to the second conceptual approach using the reciprocity theorem to quantify in absolute units. The use of the theorem requires knowing the exact transmitter gain, e.g. defined by the RF energy needed to apply a 90° pulse, and receiver gains used to amplify and digitize the signal. Whereas this works well at 1.5 T, acquisitions at higher field strengths are impaired by dielectric resonance due to B_1 inhomogeneities.

Additional to the analytical approach, the decrease in the intrinsic individual metabolic T1 and T2 relaxation times have to be well thought out [42], particularly if metabolite concentrations are to be expressed as absolute concentrations. The „normal" metabolite ratios observed at 1.5 T are, therefore, different at higher magnetic fields and it is essential to gather new normative data when switching to a different field strength.

Despite all the qualitative arguments speaking for MR systems with higher field strength, the quantification of the resulting spectra can be much more demanding, and some of the methods well established at 1.5 T might not even be applicable at all.

6.4 Advanced Spectroscopy Sequences and Applications

6.4.1. Spectral Editing

Even though their concentration levels limit the number of detectable metabolites with in vivo spectroscopy, there are still a dozen or more metabolites contributing to the total spectrum. Due to signal overlaps and complicated spectral patterns, most of these metabolites cannot easily be differentiated from each other, and have to be treated as metabolite groups like the Glx-components glutamine, glutamate and GABA, or just as baseline disturbances like most of the macromolecules.

Any technique simplifying or selectively changing the appearance of a spectrum can be considered a spectral editing technique. Most clinical ^{1}H spectroscopy sequences have several of these techniques in common like CHESS water or lipid suppression, or spatially selective excitation. In this chapter, all the techniques that allow to simplify a spectrum by focusing on a subset of specific metabolites will be discussed under spectral editing. Increasing the echo time TE is the simplest approach, where only metabolites with long T2 relaxation times will contribute to the spectrum.

Most of the advanced spectral editing techniques rely on the phenomenon of either homonuclear or heteronuclear spin coupling. Spin coupling, also known as J-coupling, is responsible for several of the spectral patterns of individual metabolites observable in spectroscopy, like the doublet of lactate or the multiplet of GABA. Even though J-coupling itself is independent of the field-strength B_0, several of the editing sequences cannot be applied with clinical 1.5 T scanners. A sufficient spectral resolution and usually high signal when aiming for low concentrated metabolites are prerequisites for successful spectral editing.

In vivo measurements of cerebral GABA for example are limited by its low concentration and by the presence of the significantly overlapping resonances at GABA-2 (2.3 ppm) from Glx, at GABA-3 (1.9 ppm) from NAA and at GABA-4 (3.0 ppm) from the methyl group of creatine. Fortunately, the methyl group of creatine is not subject to the effects of J-coupling. This allows it to be suppressed or separated using a variety of spectroscopic techniques, such as J-editing [43 – 47], 2D J-resolved spectroscopy [48], longitudinal scalar order difference editing [49], and multiple quantum filtering [50, 51]. These methods selectively prepare GABA-3 and GABA-4 into a steady state while suppressing the dominant overlapping creatine signal at 3.0 ppm. The GABA-4 can be made visible by further advanced processing, which can include signal averaging or subtraction. The result is a single signal assigned to GABA as shown in Fig. 6.8, even though a significant amount of co-edited resonances from macromolecules, such as glutathione at 2.87 – 2.94 ppm, are included.

Another application of the J-coupled editing technique is in the detection of glutamate (Glu), which gives rise to a complex proton spectrum characterized by the coupled spins of the C2–C4 hydrogen nuclei. At the moderate field strength of 1.5 T, the in vivo brain spectrum in the respective spectral ranges exhibits poor resolution and, despite the relatively high brain Glu concentration of 7 – 12 mmol/l, low sensitivity due to substantial contributions by glutamine (Gln). In conventional spectroscopy sequences, the resonances in this range are therefore mostly assigned to a mixture of Glu and Gln (and sometimes GABA), summarized as Glx-components. A method to accurately measure the tissue level of brain glutamate at 3 T is based on a TE-averaged PRESS data acquisition, which gives an unobstructed single line response for glutamate at 2.38 ppm

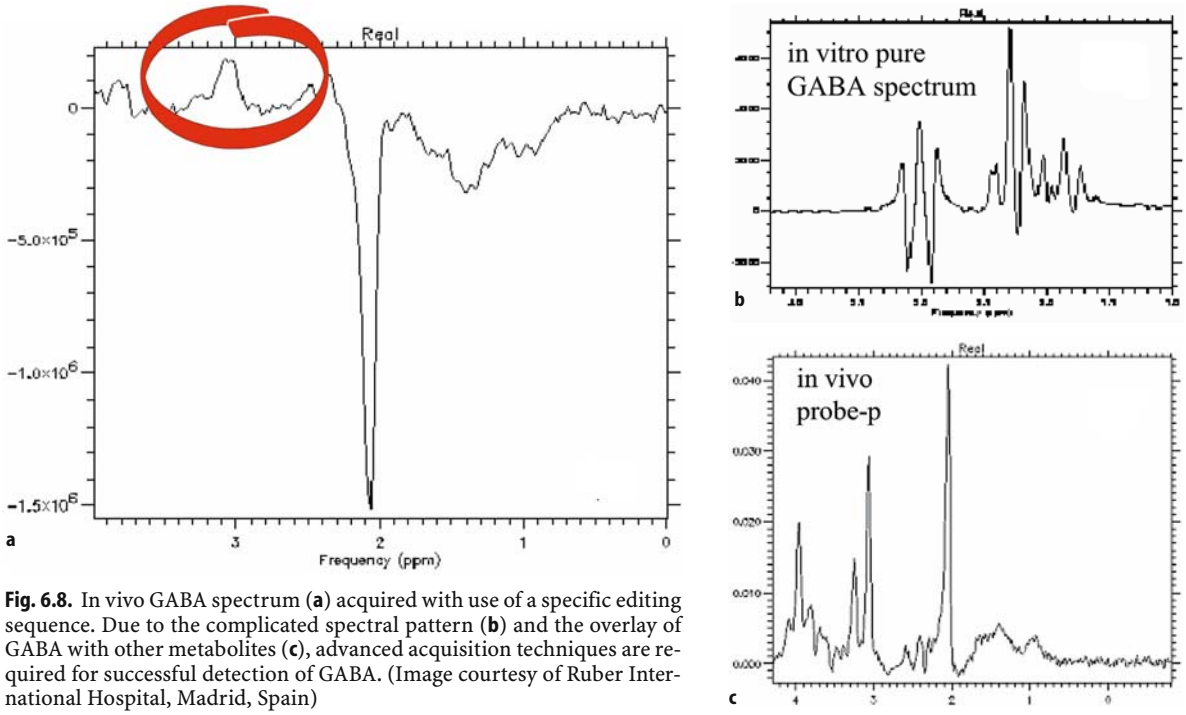

Fig. 6.8. In vivo GABA spectrum (**a**) acquired with use of a specific editing sequence. Due to the complicated spectral pattern (**b**) and the overlay of GABA with other metabolites (**c**), advanced acquisition techniques are required for successful detection of GABA. (Image courtesy of Ruber International Hospital, Madrid, Spain)

(Fig. 6.9). The sequence is based on a modification of the standard asymmetric single-voxel PRESS sequence with equidistant TE increments ranging from 35 to 195 ms [52]. This sequence also provides a sensitive method to measure the other metabolites and their effective T2 relaxation rates for uncoupled spins [53, 54].

6.4.2 Fast Acquisition Techniques

Fast acquisition techniques are usually restricted to techniques for multidimensional spectroscopic imaging (CSI). While the acquisition time in a CSI experiment is mainly defined by the number of phased-encoding steps used for encoding the spatial information, the time for a single-voxel experiment is proportional to the number

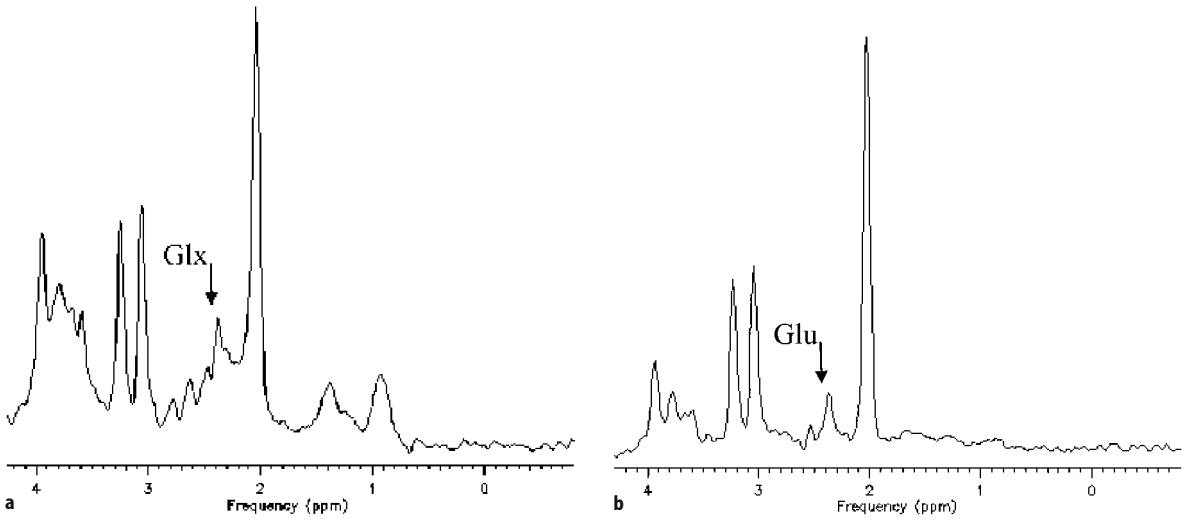

Fig. 6.9. Spectra obtained from grey matter in a healthy subject using PRESS (**a**) and TE-averaged PRESS (**b**) sequences. In conventional spectroscopy sequences (**a**), the resonances between 2 and 2.6 ppm are assigned to a mixture of glutamate (Glu) and glutamine (Gln), designated Glx. At 3 T, a TE-averaged PRESS data acquisition gives an unobstructed single line response for glutamate at 2.38 ppm (**b**)

of signal averages and the repetition time TR. None of the techniques used to decrease the time needed to cover the *k*-space for spectroscopic imaging can be directly applied to single-voxel spectroscopy.

Different fast CSI acquisition techniques make use of increased gradient performance and specific *k*-space trajectories to acquire the full spatial and spectral information in a reduced amount of time. These techniques utilize approaches initially developed for conventional fast imaging methods and include echoplanar spectroscopic imaging (EPSI, PEPSI) [55, 56], spiral acquisitions [57] or recently developed flyback techniques [58].

Some of the techniques described above are very hardware-demanding, and an alternative approach, with very little or no extra hardware requirements, uses a method commonly known as parallel imaging. These techniques work with dedicated coil arrays, using the known B_1 field distribution of every coil element to reduce the number of required phased-encoding steps for full encoding of the required spatial information. Parallel imaging techniques have successfully been applied to spectroscopic imaging, even though post-processing is very demanding, and the complex nature of the spectroscopic data makes the resulting spectra prone to artefacts or quality losses.

Even though all the techniques enable a significant reduction in acquisition time, down to less than 15 min for a full brain metabolite map, the resulting spectra always suffer from reduced SNR compared for instance to conventional PRESS chemical shift imaging. To regain this SNR, multiple averaging would be required, preventing the acceptance of these approaches for clinical applications. Greater field strengths with higher intrinsic SNR may in the future open new prospects for the use of these methods.

6.4.3 High Spatial Resolution Spectroscopy

The ability of improved MRI technologies to detect smaller lesions may involve a greater need for higher spatial resolution in single-voxel spectroscopy and CSI experiments. Whereas the poor SNR of 1.5 T magnets prevented the acquisition of single-voxel spectra with a spatial resolution significantly below 4 – 8 ml or chemical shift images with a spatial resolution of less than 2 ml, lower spatial resolutions are becoming feasible at 3.0 T.

A specific application requiring lower resolution is the MR spectroscopic study of small animals. These studies are usually performed on dedicated animal systems, which offer ideal conditions. However, given their increasing diffusion, researchers are interested in using whole-body high-field MR systems for animal studies both for reasons of cost reduction and to perform direct comparisons of animal and human data. This requires new techniques that allow to achieve the highest possible spatial resolution and obtain conclusive data from brain structures that are several orders of magnitude smaller than the human brain while keeping examination times short to minimize animal mortality [59].

Recent studies have shown that proton spectroscopy, for instance of newborn rat brain in a 3.0 T whole-body scanner using a standard clinical spectroscopy protocol is feasible. Irrespective of field strength, the RF resonator for signal transmission and reception plays a major role in the quality that can be achieved. A coil with a size close to that of the object to be studied is usually appropriate, like the small birdcage resonator shown in Fig. 6.10 designed for brain studies of new-

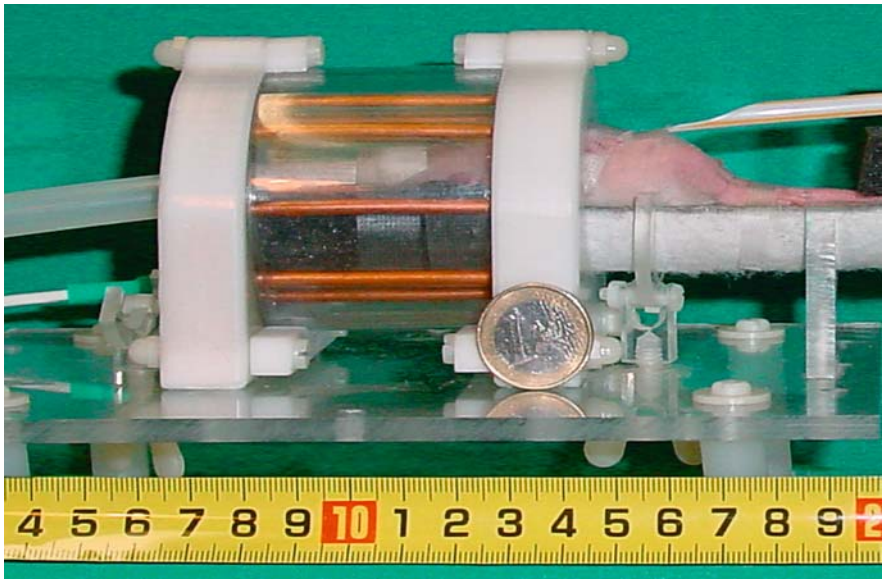

Fig. 6.10. Dedicated linear volume resonator (Flick Engineering Solutions, The Netherlands) designed for newborn rat brain MR studies in a conventional clinical 3.0 T MR scanner. (Image courtesy of University Children's Hospital, Zurich, Switzerland)

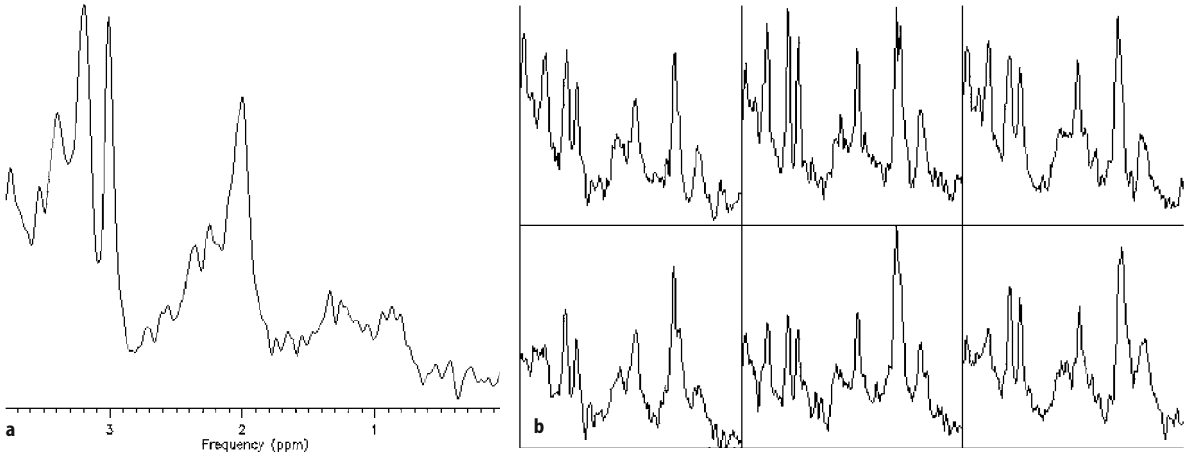

Fig. 6.11. High-resolution single-voxel spectrum (**a**) with a spatial resolution of 0.2 ml and high-resolution CSI (**b**) with a spatial resolution of 0.04 ml acquired from a newborn rat brain in a conventional clinical whole-body 3.0 T scanner

born rats. If the transfer of results from animal experiments to human in vivo studies is going to be explored, similar acquisition protocols would be appropriate to achieve comparable results. While maintaining these prerequisites, single-voxel spectra can be acquired of volumes as small as about 0.2 ml, or CSI spectra with a spatial resolution of 0.04 ml, both with an acquisition time of less than 10 min (Fig. 6.11).

6.5 Conclusions

The utilization of high-field MR systems for clinical spectroscopy studies involves a variety of improvements and advantages which anable the use of new and advanced acquisition techniques that raise the diagnostic accuracy of MR spectroscopy above the desired threshold. At the same time, the higher field strength can also carry disadvantages and limitations that may degrade its usefulness. At the time of the introduction of clinical 3.0 T scanners, results were often unsatisfactory and performances for some applications were poorer than those obtained with the well-optimized clinical 1.5 T scanners. However, most problems with 3 T systems have been or are being addressed by the research community and the manufacturers with the development of sophisticated technical strategies, pulse sequences and/or processing algorithms.

Higher field strength will improve MR imaging thanks to the greater SNR, but will also experience some image degradation due to the increased frequency distance between fat and water. By contrast, MR spectroscopy will gain from both the increased SNR and the increased spectral resolution. Thus spectroscopy is and will be one of the key applications of MR systems with field strength of 3.0 T and above, despite the current problems. The various strategies illustrated above should allow these problems to be overcome and make higher magnetic field scanners the workhorse for all brain MR applications in the near future.

References

1. Smith ICP, Stewart LC (2002) Magnetic resonance spectroscopy in medicine: clinical impact. Progr Nucl Magn Reson Spectroscopy 40(1):1 – 34
2. Bonavita S, Di Salle F, Tedeschi G (1999) Proton MRS in neurological disorders. Eur J Radiol 30(2):125 – 131
3. Ross B, Bluml S (2001) Magnetic resonance spectroscopy of the human brain. Anat Rec 265(2):54 – 84
4. Burtscher IM, Holtås S (2001) Proton MR spectroscopy in clinical routine. J Magn Reson Imaging 13(5):732 – 737
5. Grodd W, Krageloh-Mann I, et al. (1990) In vivo assessment of *N*-acetylaspartate in brain spongy degeneration (Canavan's disease) by proton spectroscopy. Lancet 336: 437 – 438
6. Stöckler S, Hanefeld F, Frahm J (1996) Creatine replacement therapy in guanidinoacetate methyltransferase deficiency, a novel inborn error of metabolism. Lancet 348: 789 – 790
7. Bianchi MC, Tosetti M, Fornai F, et al. (2000) Reversible brain creatine deficiency in two sisters with normal blood creatine level. Ann Neurol 47:511 – 513
8. Kruse B, Barker PB, Van Zijl PC, et al. (1994) Multislice proton magnetic resonance spectroscopic imaging in X-linked adrenoleukodystrophy. Ann Neurol 36:595 – 608
9. Ross BD, Jacobson S, Villamil F, et al. (1994) Subclinical hepatic encephalopathy: proton MR spectroscopic abnormalities. Radiology 193:457 – 463
10. Guidance for significant risk investigations. US CDRH, FDA, DHHS. September 29, 1997
11. Takahashi M, Uematsu H, Hatabu H (2003) MR imaging at high magnetic fields. Eur J Radiol 46(1):45 – 52
12. Kangarlu A, Burgess RE, Zhu H, et al. (1999) Cognitive, cardiac, and physiological safety studies in ultra high field magnetic resonance imaging. Magn Reson Imaging 17(10): 1407 – 1416
13. Vaughan JT, Garwood M, Collins CM, et al. (2001) 7T vs 4T: RF power, homogeneity and signal-to-noise comparison in head images. Magn Reson Med 46(1):24 – 30

14. Uematsu H, Dougherty L, Takahashi M, et al. (2003) A direct comparison of signal behavior between 4.0 and 1.5 T: a phantom study. Eur J Radiol 45(2):154 – 159
15. Posse S, Cuenod CA, Risinger R, et al. (1995) Anomalous transverse relaxation in ^{1}H spectroscopy in human brain at 4 Tesla. Magn Reson Med 33(2): 246 – 252
16. Gruetter R, Weisdorf SA, Rajanayagan V, et al. (1998) Resolution improvements in in vivo ^{1}H NMR spectra with increased magnetic field strength. J. Magn Reson 135(1): 260 – 264
17. Bartha R, Drost DJ, Menon RS, Williamson PC (2000) Comparison of the quantification precision of human short echo time ^{1}H spectroscopy at 1.5 and 4.0 Tesla. Magn Reson Med 44(2):185 – 192
18. Gonen O, Gruber S, Li BSY, et al. (2001) Multivoxel 3D proton spectroscopy in the brain at 1.5 versus 3.0 T: signal-to-noise ratio and resolution comparison. Am J Neuroradiol 22(9):1727 – 1731
19. Barker PB, Hearshen DO, Boska MD (2001) Single-voxel proton MRS of the human brain at 1.5T and 3.0T. Magn Reson Med 45(5):765 – 769
20. Ocali O, Atalar E (1998) Ultimate intrinsic signal-to-noise ratio in MRI. Magn Reson Med 39(3):462 – 473
21. Tká I, Andersen P, Adriany G, et al. (2001) In vivo ^{1}H NMR spectroscopy of the human brain at 7 T. Magn Reson Med 46(3):451 – 456
22. Hetherington HP, Pan JW, Chu WJ, et al. (1997) Biological and clinical MRS at ultra-high field. NMR Biomed 10(8): 360 – 371
23. Gruber S, Mlynárik V, Moser E (2003) High-resolution 3D proton spectroscopic imaging of the human brain at 3 T: SNR issues and application for anatomy-matched voxel sizes. Magn Reson Med 49(2):299 – 306
24. Li BSY, Regal J, Gonen O (2001) SNR versus resolution in 3D ^{1}H MRS of the human brain at high magnetic fields. Magn Reson Med 46(6):1049 – 1053
25. Kim DS, Garwood M (2003) High-field magnetic resonance techniques for brain research. Curr Opin Neurobiol 13(5):612 – 619
26. Cusack R, Brett M, Osswald K (2003) An evaluation of the use of magnetic field maps to undistort echo-planar images. Neuroimage 18(1):127 – 142
27. Stenger VA, Boada FE, Noll DC (2000) Three-dimensional tailored RF pulses for the reduction of susceptibility artifacts in T^*_2-weighted functional MRI. Magn Reson Med 44(4):525 – 531
28. Alecci M, Collins CM, Smith MB, Jezzard P (2001) Radio frequency magnetic field mapping of a 3 Tesla birdcage coil: experimental and theoretical dependence on sample properties. Magn Reson Med 46(2):379 – 385
29. Pfeuffer J, Tká I, Provencher SW, Gruetter R (1999) Toward an in vivo neurochemical profile: quantification of 18 metabolites in short-echo-time ^{1}H NMR spectra of the rat brain. J Magn Reson 141(1):104 – 120
30. Gu H, Feng H, Zhan W, et al. (2002) Single-shot interleaved z-shim EPI with optimized compensation for signal losses due to susceptibility-induced field inhomogeneity at 3 T. Neuroimage 17(3):1358 – 1364
31. Klose U (1990) In vivo proton spectroscopy in presence of eddy currents. Magn Reson Med 14(1):26 – 30
32. Gach HM, Lowe IJ, Madio DP, et al. (1998) A programmable pre-emphasis system. Magn Reson Med 40(3):427 – 431
33. Mlynárik V, Gruber S, Moser E (2001) Proton T_1 and T_2 relaxation times of human brain metabolites at 3 Tesla. NMR Biomed 14(5):325 – 331
34. Michaeli S, Garwood M, Zhu XH, et al. (2002) Proton T2 relaxation study of water, *N*-acetylaspartate, and creatine in human brain using Hahn and Carr-Purcell spin echoes at 4T and 7T. Magn Reson Med 47(4):629 – 633
35. Parizel PM, van Hasselt BA, van den Hauwe L, et al. (1994) Understanding chemical shift induced boundary artefacts as a function of field strength: influence of imaging parameters (bandwidth, field-of-view, and matrix size). Eur J Radiol 18(3):158 – 164
36. Hood MN, Ho VB, Smirniotopoulos JG, Szumowski J (1999) Chemical shift: the artifact and clinical tool revisited. Radiographics 19(2):357 – 371
37. Kelley DAC, Wald LL, Star-Lack JM (1999) Lactate detection at 3T: compensating J coupling effects with BASING. J Magn Reson Imaging 9(5):732 – 737
38. Thiel T, Czisch M, Elbel GK, Hennig J (2002) Phase coherent averaging in magnetic resonance spectroscopy using interleaved navigator scans: compensation of motion artifacts and magnetic field instabilities. Magn Reson Med 47(6):1077 – 1082
39. Zhang X, Uurbil K, Chen W (2001) Microstrip RF surface coil design for extremely high-field MRI and spectroscopy. Magn Reson Med 46(3):443 – 450
40. Alecci M, Collins CM, Wilson J, et al. (2003) Theoretical and experimental evaluation of detached endcaps for 3 T birdcage coils. Magn Reson Med 49(2):363 – 370
41. Wright AC, Song HK, Wehrli FW (2001) In vivo MR micro imaging with conventional radiofrequency coils cooled to 77 degrees K. Magn Reson Med 43(2):163 – 169
42. Mlynárik V, Gruber S, Moser E (2001) Proton T_1 and T_2 relaxation times of human brain metabolites at 3 Tesla. NMR Biomed 14(5):325 – 331
43. Rothman DL, Petroff OAC, Behar KL, Mattson RH (1993) Localized 1H NMR measurement of γ-aminobutyric acid in human brain in vivo. Proc Natl Acad Sci USA 90: 5662 – 5666
44. Keltner JR, Wald LL, Christensen JD, et al. (1996) A technique for detecting GABA in the human brain with PRESS localization and optimized refocusing spectral editing radiofrequency pulses. Magn Reson Med 36:458 – 461
45. Hetherington HP, Newcomer BR, Pan JW (1998) Measurement of human cerebral GABA at 4.1 T using numerically optimized editing pulses. Magn Reson Med 39:6 – 10
46. Mescher M, Merkle H, Kirsch J, et al. (1998) Simultaneous in vivo spectra editing and water suppression. NMR Biomed 11:266 – 272
47. Henry PG, Dautry C, Hantraye P, Bloch G (2001) Brain GABA editing without macromolecule contamination. Magn Reson Med 45(3):517 – 520
48. Ke Y, Cohen BM, Bang JY, et al. (2000) Assessment of GABA concentration in human brain using two-dimensional proton magnetic resonance spectroscopy. Psychiatr Res 100:169 – 178
49. de Graaf RA, Rothman DL (2001) Detection of gamma-aminobutyric acid (GABA) by longitudinal scalar order difference editing. J Magn Reson 152(1):124 – 131
50. Keltner JR, Wald LL, Frederick B, Renshaw P (1997) In vivo detection of GABA in human brain using a localized double-quantum filter technique. Magn Reson Med 37:366 – 371
51. Shen J, Shungu DC, Rothman DL (1999) In vivo chemical shift imaging of γ-aminobutyric acid in the human brain. Magn Reson Med 41:35 – 42
52. Hurd R, Sailasuta N, Srinivasan R, et al. (2004) Measurement of brain glutamate using TE-averaged PRESS at 3T. Magn Reson Med 51(3):435 –440
53. Hancu I, Zimmerman EA, Sailasuta N, Hurd RE (2005) 1H MR spectroscopy using TE averaged PRESS: a more sensitive technique to detect neurodegeneration associated with Alzheimer's disease. Magn Reson Med 53(4):777 – 782
54. Srinivasan R, Sailasuta N, Hurd R, et al. (1994) Evidence of elevated glutamate in multiple sclerosis using magnetic resonance spectroscopy at 3 T. Brain 128(5):1016 – 1025

55. Posse S, DeCarli C, Le Bihan D (1994) Three-dimensional echo-planar MR spectroscopic imaging at short echo times in the human brain. Radiology 192(3):733 – 738
56. Guimaraes AR, Baker JR, Jenkins BG, et al. (1999) Echoplanar chemical shift imaging. Magn Reson Med 41(5):877 – 882
57. Adalsteinsson E, Spielman DM (1999) Spatially resolved two-dimensional spectroscopy. Magn Reson Med 41(1): 8 – 12
58. Dydak U, Pruessmann KP, Weiger M, et al. (2003) Parallel spectroscopic imaging with spin-echo trains. Magn Reson Med 50(1):196 – 200
59. Dydak U, Weiger M, Pruessmann KP, et al. (2001) Sensitivity-Encoded Spectroscopic Imaging. Magn Reson Med 46: 713 – 722

7 3.0 T Diffusion Studies

T. Scarabino, F. Di Salle, F. Esposito, M. Tosetti, M. Armillotta, R. Agati, U. Salvolini

Diffusion magnetic resonance imaging (DWI) studies the diffusivity of water, i.e. the random microscopic movement of water molecules, or Brownian motion, induced by thermal energy.

MR is the only imaging technique enabling non-invasive observation of diffusion in vivo, and provides high-resolution images of deep-seated organs without interfering with the diffusion process itself.

Although intriguing, this description still does not however explain the strong and growing interest raised by DWI in the scientific community and among clinicians in the last decade. The reason for its success lies in the astonishing detail of the data provided. In fact, based on the diffusion-driven incoherent motion detected with DWI, the water molecules probe tissue structures on a microscopic scale that is well beyond the resolution commonly achieved with other techniques, providing information on the microscopic and even the molecular structure of brain tissue that is virtually unobtainable using conventional MRI. In the diffusion times typically used in DWI acquisitions (in the order of tens of milliseconds), water molecules diffuse in the brain over distances of microns or tens of microns, interacting with microscopic tissue components such as cell membranes, myelin and macromolecules.

Since the typical voxel size of a DWI image is a few cubic millimetres, DWI analyses an overall diffusion effect representing statistically the distribution of the Brownian motion of water molecules, and provides unique data about the structural organization of tissues at the microscopic level [1].

Furthermore, mounting evidence indicates that accurate selection of sequence parameters will allow DWI to become sensitive to specific subcompartments of brain tissue, providing hitherto inaccessible tissue dynamics information.

Unlike most tissue parameters that can be studied with MRI, such as T1 and T2, the physical process of DWI is totally independent of the MR effect or the magnetic field. For this reason DWI acquisitions entail no specific requirements in terms of magnetic field strength. Nonetheless, since the diffusion-weighting effect basically consists of an attenuation of the MR signal, DWI poses peculiar demands in terms of signal to noise ratio (SNR), thus warranting the use of high-field MR units. High-field magnets are essential for advanced applications of DWI, such as tensor imaging (DTI) and tractography (TI).

Although most soluble molecules exhibit Brownian diffusion, water is by far the most convenient molecular species to be studied with DWI, due to its concentration in biological tissue, the highest natural abundance of its MRI visible nucleus (^{1}H), its small dimension permitting easy access to most biological compartments, and the water-based organization of biological tissues, where most molecules show some degree of hydrophilicity.

Other metabolites may also be investigated through the study of diffusion of ^{1}H and other nuclei. Despite their much lower intrinsic SNR, non-water and non-^{1}H studies can provide valuable and interesting information about specific biological compartments governed by different principles to those regulating water diffusion [2]. However, such unfavourable SNR mandates the use of high-field MR units for non-water diffusion studies.

The basic principles of diffusion MRI were introduced in the mid-1980s [1], combining MR strategies with earlier concepts applied to encode molecular diffusion effects in the NMR signal by using bipolar magnetic field gradient pulses [1]. The movement of water molecules is affected by various tissue components (cell walls, membranes, intracellular organs, macromolecules). Diffusion may be restricted in all directions (isotropic diffusion) or in one particular direction within voxels (anisotropic diffusion), as in structured tissues (e.g. cerebral white matter).

Molecular diffusion can be evaluated using MR techniques with ultrafast sequences sensitized to movement. In particular, diffusion weighting is often combined with spin-echo echoplanar sequences. The sensitization to molecular diffusion is implemented using two strong and fast bipolar diffusion gradients applied symmetrically before and after the 180° radiofrequency (RF) refocusing pulse, resulting in proton dephasing and subsequent rephasing. The water molecules diffusing freely during and after application of the first dephasing gradient are not completely repha-

sed by the second gradient, unlike what is seen in stationary tissues. This process results in a signal intensity attenuation that is proportional to the amount of molecular displacement.

7.1 Diffusion Studies

The random diffusion of water molecules in the presence of a strong magnetic gradient results in a reduction of the MR signal caused by the loss of spin coherence.

As mentioned above diffusion sensitization, or diffusion weighting, consists of the application of a pair of strong gradients to elicit differences in the diffusion of water molecules within different biological compartments [3]. The application of a second gradient oriented in the same spatial direction but with inverse polarity, or with the same polarity but applied on the other side of the 180° refocusing pulse, restores the phase coherence of stationary protons, while the randomly diffusing molecules lose phase coherence proportionally to their displacement in the gradient direction.

The degree of diffusion weighting is given by the *b* value, a parameter that is determined by the mode of application of the diffusion-sensitizing gradient scheme. The most commonly implemented modality in clinical MR scanners is the Stejskal-Tanner spin-echo scheme [3], which consists of a pulsed pair of approximately rectangular gradients before and after a 180° RF pulse. In this case, the *b* value depends on the duration (*d*) and strength (*G*) of the sensitizing pulsed gradients, and on the time interval between the two pulsed gradients (Δ), according to the equation:

$$b = \gamma^2 G^2 d^2 (\Delta - d/3)$$

where γ is the gyromagnetic ratio. Thus, the *b* value, and so the diffusion sensitization, can be increased by using stronger (*G*) and longer (*d*) pulsed gradients or by increasing the time between the pulsed gradients (*D*) [3].

Adding diffusion-sensitizing gradients to an imaging sequence constitutes the basis for diffusion weighted MRI. In these MR images, the signal intensity (*S*) of each voxel is influenced by two sequence parameters, *b* value and echo time, and by two parameters intrinsic to biological tissues: the apparent diffusion coefficient (ADC) and the transverse relaxation time (T2). ADC is a measure of molecular diffusion and reflects the presence of restrictions, such as viscosity and spatial barriers.

The following formula [3] describes the relationship between signal intensity in a diffusion-weighted MR image and molecular diffusivity:

$$S = S_0 e^{-b(ADC)}$$

where S_0 is the signal intensity at $b = 0$; or using the natural logarithm:

$$Ln\ (S/S_0) = -b(\mathrm{ADC})$$

Given the mixed dependence of the signal intensity on tissue ADC and T2, it is necessary to use an acquisition strategy to highlight the effect of diffusion. Indeed, acquiring images with at least two different *b* values (commonly 0 – 20 and 1,000 s/mm^2) to vary the diffusion weighting, but with the same TE so as to obtain a stable T2 weighting, allows determination of the ADC value of each voxel. The lower *b* value is often selected to be slightly greater than zero to eliminate the effects of large vessels and flow [3].

Molecular diffusion within a given voxel is generally assumed to have a single diffusion coefficient. In fact, most tissues contain multiple subcompartments. At least the intra- and extracellular compartment are always present, whose contribution is estimated to be respectively 82.5 % and 17.5 % of the brain tissue; they have basically different intrinsic ADC values, the extracellular diffusion being much faster. The measured ADC can depend on the *b* value used, as data obtained with low *b* values (up to 1,000 s/mm^2) would be more sensitive to fast diffusion components and thus to extracellular compartment dynamics. In clinical studies and most animal experiments, especially when data are fitted with a single exponent, the diffusion patterns observed in tissues thus need to be explained in terms of extracellular space dynamics, even though this compartment is physically the smaller one. Changes in ADC calculated in this way should thus be interpreted as changes in ADC of the extracellular space (tortuosity) and in its fractional variation relative to the intracellular volume. This explains why diffusion studies have immediately been recognized as sensitive probes of the changes taking place in the extracellular/intracellular volume ratio, as observed in brain ischaemia, spreading depression [1 – 4, 6] and status epilepticus [1 – 7].

It is important to note that diffusion imaging is a quantitative method. The diffusion coefficient is a physical parameter that reflects directly the physical properties of tissues in terms of random molecular translation. This entails that, in principle, diffusion coefficients obtained at different times in a given patient, in different patients, or even at different hospitals can be compared without need for normalization [1].

MR measurement of the Brownian movement of water molecules can be applied at different, increasingly complex levels: (1) DWI, (2) ADC maps, (3) DTI and TI (Fig. 7.1).

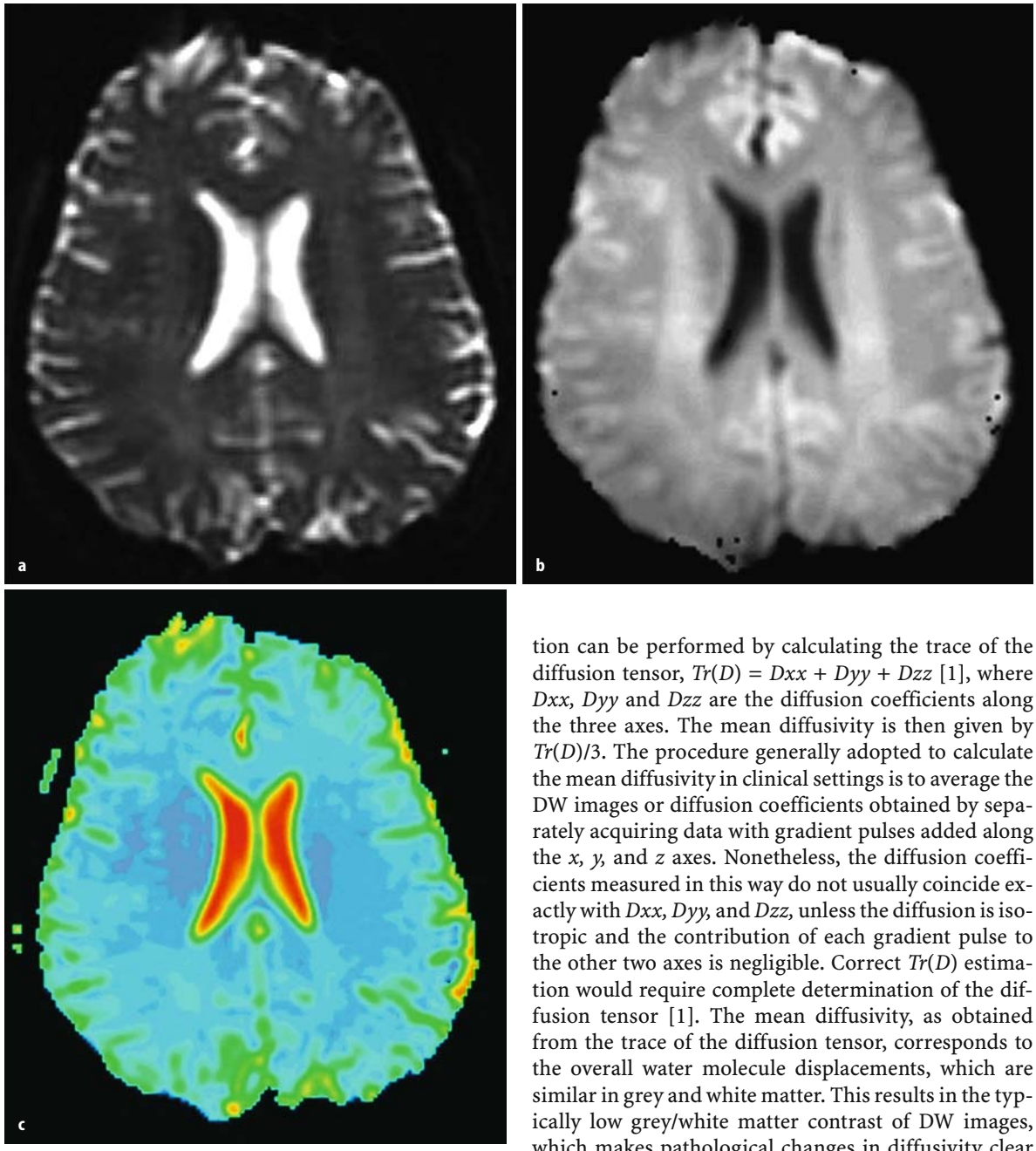

Fig. 7.1. Different MR diffusion imaging techniques. **a** EPI T2 with *b* value = 0. **b** Diffusion weighted imaging (TR/TE 11,000/ min, matrix 164×192, 1 Nex, FOV 32 cm, thickness 5 mm, *b* value = 1,000, 0:44). **c** ADC map

7.1.1 DWI

DWI evaluates the mean molecular diffusivity from the average diffusion coefficients in all directions. Evaluation of the mean diffusivity must avoid anisotropic diffusion effects and make the results independent of the orientation of the reference frame [1]. Such an evaluation can be performed by calculating the trace of the diffusion tensor, $Tr(D) = Dxx + Dyy + Dzz$ [1], where *Dxx*, *Dyy* and *Dzz* are the diffusion coefficients along the three axes. The mean diffusivity is then given by $Tr(D)/3$. The procedure generally adopted to calculate the mean diffusivity in clinical settings is to average the DW images or diffusion coefficients obtained by separately acquiring data with gradient pulses added along the *x, y,* and *z* axes. Nonetheless, the diffusion coefficients measured in this way do not usually coincide exactly with *Dxx*, *Dyy,* and *Dzz,* unless the diffusion is isotropic and the contribution of each gradient pulse to the other two axes is negligible. Correct $Tr(D)$ estimation would require complete determination of the diffusion tensor [1]. The mean diffusivity, as obtained from the trace of the diffusion tensor, corresponds to the overall water molecule displacements, which are similar in grey and white matter. This results in the typically low grey/white matter contrast of DW images, which makes pathological changes in diffusivity clear and easy to detect. Tissue components with free or elevated diffusion, like cerebrospinal fluid, exhibit hypointense signal, whereas those restricting diffusion are hyperintense.

Potential clinical applications of water-diffusion MRI were suggested very early after its introduction [8]. DWI is widely used in clinical practice, its most successful application being in the study of brain ischaemia [9]; in particular, it has a fundamental role in the diagnosis of hyperacute ischaemia, where no other MR imaging modality provides comparable results (Fig. 7.2).

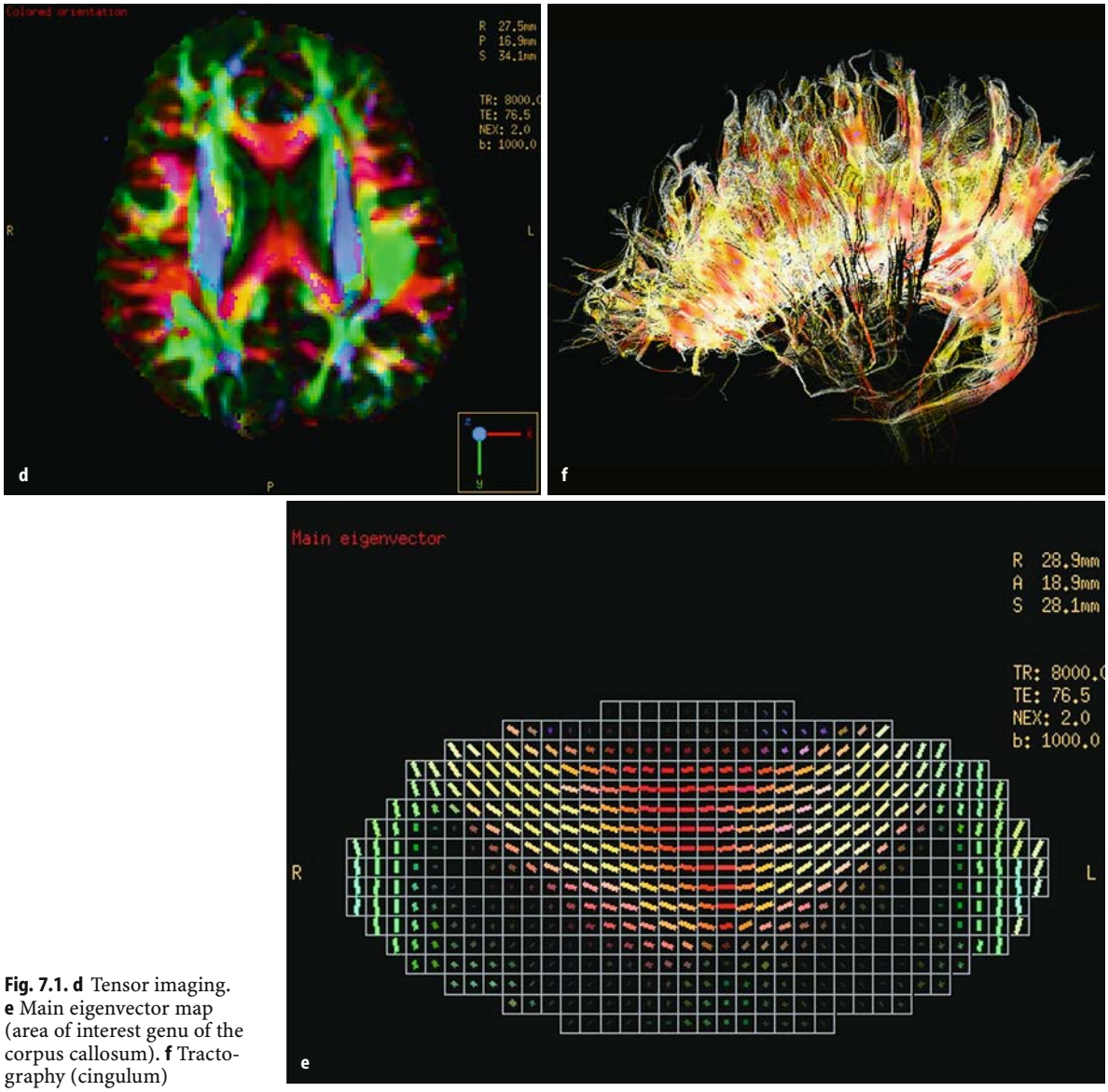

Fig. 7.1. d Tensor imaging. **e** Main eigenvector map (area of interest genu of the corpus callosum). **f** Tractography (cingulum)

Moseley et al. reported that in cat brain water diffusion decreases in a very early phase of the ischaemic event [10], and that it can drop to 50 % of the normal value [11]. This finding is related to the cytotoxic oedema, which in turn is induced by the energy failure of the cell membrane Na/K pump system, although the exact mechanism underpinning such decreased diffusion at the molecular level is still unclear. Changes in water compartmentalization in brain tissue determined by the cytotoxic oedema, with a reduction of the fast extracellular compartment and an increase of the slow-diffusion intracellular volume fraction might explain it. While changes in membrane permeability [12] are a prerequisite for changes in water compartmentalization, two events concur to reduce molecular diffusion. The first is the volume increase of the slower intracellular compartment at the expense of the faster extracellular one, resulting in reduced average water diffusion; the second is the reduced water diffusion in the faster compartment itself, through the shrinkage of the extracellular space, resulting in increased tortuosity and impairment the Brownian displacement of water molecules [1 – 14]. The results from animal studies have been confirmed in human stroke, where DWI has been able to detect the ischaemic regions within the first few hours, or even minutes, of the ischaemic event. In this very early phase, well before standard MRI can depict the vasogenic oedema, the ischaemic tissue may still be rescued [1 – 16] with appropriate therapies. DWI appears to be particularly useful in combination with perfusion MRI, making it possible to distinguish the ischaemic tissue from the penumbra, optimize the therapeu-

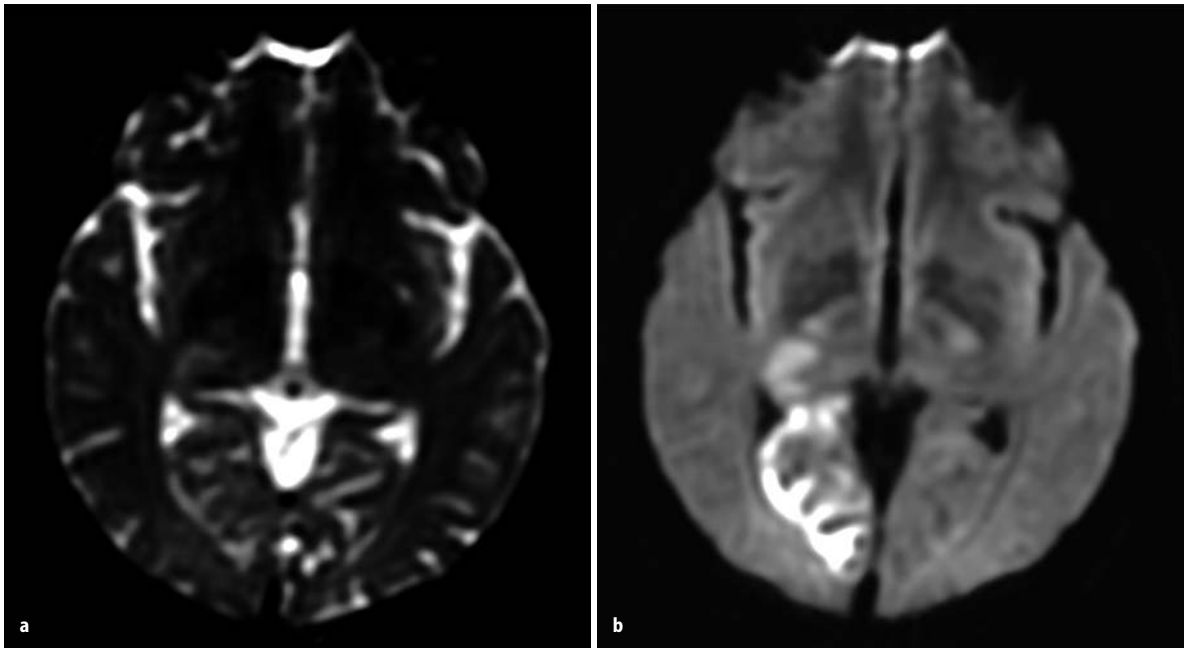

Fig. 7.2. Right occipital hyperacute cerebral ischaemia: DWI (in **a** *b* value = 0; in **b** *b* value = 1,000)

tic approach [17], monitor patient progress and predict outcome [18, 19].

Despite the high sensitivity and specificity of DWI for ischaemia, anisotropic diffusion effects may sometimes mimic ischaemic regions, especially near ventricular cavities. In fact, if diffusion sensitization is applied in only one direction, the compact white matter bundles that run perpendicular to the gradient sensitization direction will appear artefactually brighter due to restriction of diffusion by membranes and myelin. It is, therefore, necessary to use mean diffusivity or the trace of the diffusion tensor to remove these artefacts [20].

7.1.2 ADC Studies

DW images are also T2-weighted due to the long probe time of the magnetic field gradients. Difficulties in the interpretation of DWI semeiology can arise due to this double weighting. For instance, a hyperintense focus can be both an area with restricted diffusion and one with increased T2, since a T2 increase is a common feature of many brain lesions that are not necessarily accompanied by diffusion abnormalities. To avoid losing much of the diagnostic ability of DWI, a map of ADC values (in s/mm^2) must thus be calculated to separate diffusion-induced signal changes from those caused by T2 weighting.

Changes in ADC values seem to occur before morphological changes become apparent, thereby playing an important role in in vivo tissue characterization (as in tumours) and in monitoring response to treatment [21–23] (Fig. 7.3).

As mentioned above, a pair of DWI acquisitions with low and high diffusion weighting and the same TE make it possible to calculate ADC maps.

7.1.3 Diffusion Tensor Imaging and Tractography

When six or more gradients are used (gradient orientation is not only along the three main axes, but also in different, diagonal, directions: *zx, zy, xy,* ...), DTI and TI are obtained.

Tensor imaging follows the multidirectional diffusion of water in tissues. To follow anisotropic diffusion, the DTI can be displayed as an ellipsoid whose three main axes constitute a system of orthogonal coordinates. The longest main axis of the diffusion ellipsoid is the value (eigenvalue) and direction (eigenvector) of peak diffusion (the longer the diffusion, the greater the anisotropy), whereas the shortest axis is the value and direction of minimum diffusion. If the three values are equal, the diffusion is called isotropic and the diffusion tensor will be sphere-shaped.

As discussed in detail below, DTI is used to depict structured water movements within tissues, especially in bundles of white matter fibres, whose orientation is of particular interest in stroke and tumours. This information can be processed to produce colour maps of white matter fibre bundles.

Tractography uses the main direction of diffusion measured by the tensor to calculate the pathways of white matter fibres. In TI, signal intensity represents the value of anisotropy (the greater the anisotropy, the

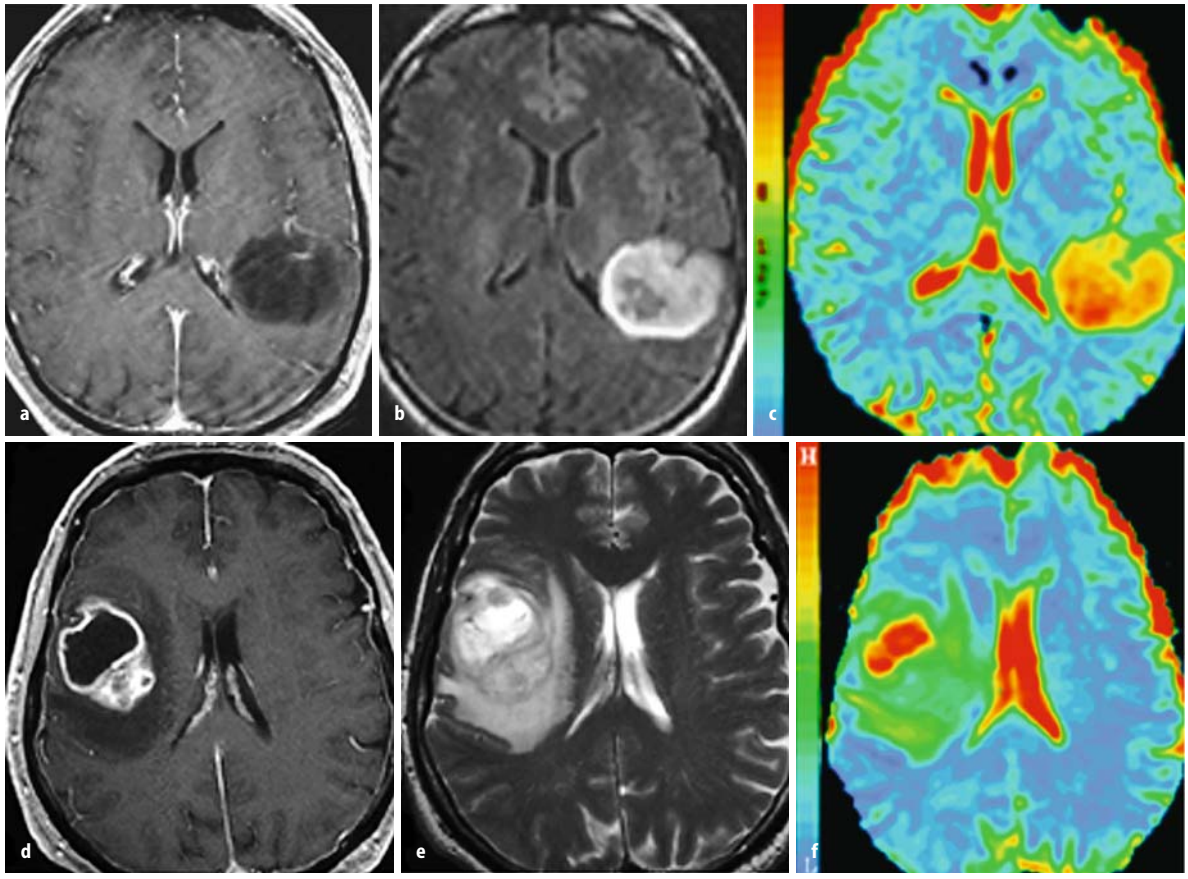

Fig. 7.3. ADC map acquired at 3.0 T. Low-grade astrocytoma: **a** SE T1 after contrast administration, **b** FLAIR image, **c** ADC map; compared with glioblastoma: **d** SE T1 after contrast administration, **e** FSE T2 image, **f** ADC map. The ADC is higher in the tumour compared with the surrounding parenchyma, in the oedema compared with the tumour, in the cystic areas compared to solid tumour components and in the low-grade compared to the high-grade solid tumour areas

whiter the image), while colour codifies the prevalent direction of the diffusion. Tracing is obtained first by defining the positions of interest in the white matter pathways and then, following the interpolated directions of peak diffusion, by drawing a continuous path through the initial position. These pathways, depicted by dedicated software in three dimensions, show the anatomy of white matter fibres.

The possibility of determining the anisotropy of each diffusion ellipsoid and then undertaking a more elaborate analysis of the relations between the diffusion ellipsoids enables non-invasive in vivo investigation of the connections between axonal fibres and the functions of different brain regions. In addition, fibre tracking with DTI could be used instead of, or in combination with, functional MRI (fMRI) [24]. For example, combined study with fMRI provides more consistent approaches for analysing brain function and anatomy [25].

7.2 3.0 T Diffusion Studies

DWI benefits from the higher SNR, spatial resolution and accuracy of 3.0 T magnetic fields [26–30] (Fig. 7.4), despite the greater image distortion due to increased magnetic susceptibility effects compared with 1.5 T magnets (especially in areas of high susceptibility such as the paranasal sinuses). In such cases, parallel imaging or new techniques like PROPELLER (Periodically Rotated Overlapping ParallEL Lines with Enhanced Reconstruction) and radial *k*-space filling can solve the problem of increased susceptibility (Fig. 7.5).

Diffusion studies adopt echoplanar techniques in which all phase-encoding steps are acquired with one RF excitation, thereby reducing the number of phase errors, which are responsible for susceptibility effects and image distortion. Parallel imaging reduces the number of phase errors by decreasing the number of phase encoding steps. Despite greater field inhomogeneity, it enables control of geometric distortion and enhancement of spatial resolution up to 0.8 mm in plane.

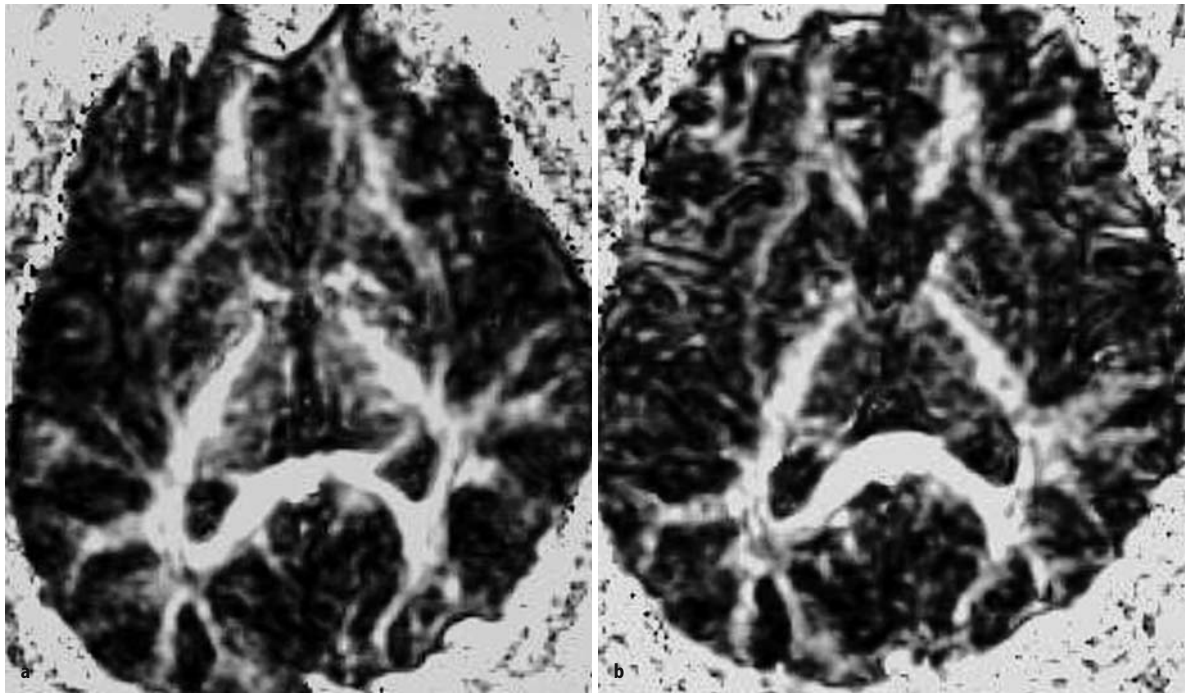

Fig. 7.4. Tensor imaging at 1.5 T (**a**) and 3.0 T (**b**). The greater resolution of the 3.0 T image also shows signs of image distortion close to the anterior cranial fossa

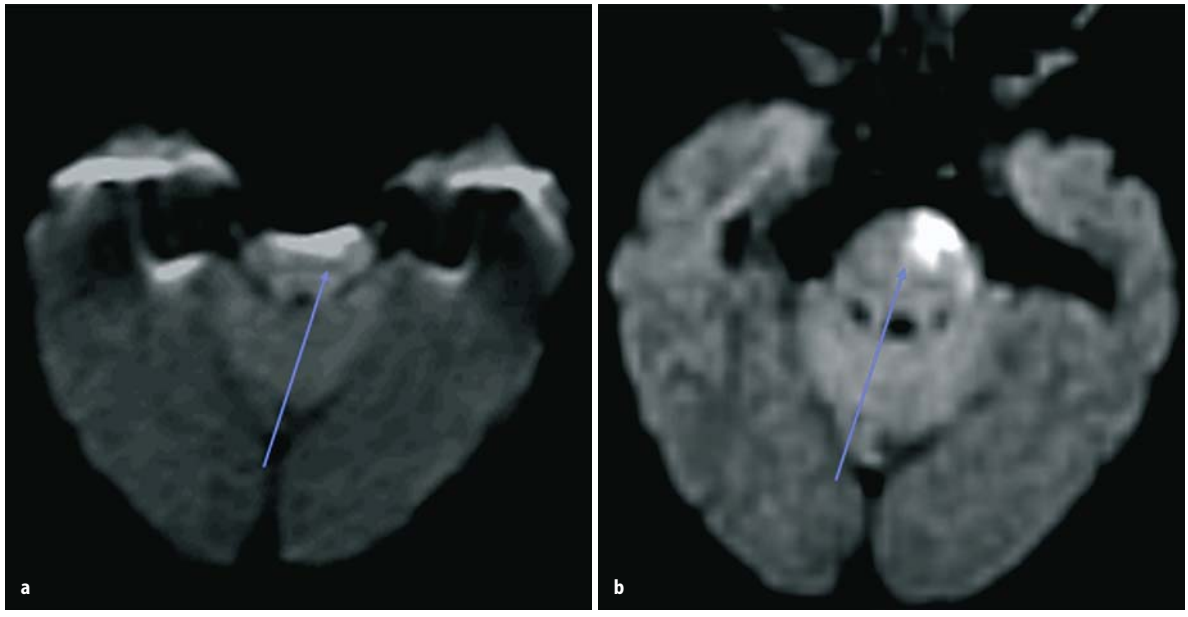

Fig. 7.5. DWI: conventional imaging (**a**) vs radial *k*-space filling (**b**). In **b** the susceptibility artefacts in the posterior cranial fossa (*arrows*) are almost completely eliminated due to the greater SNR and higher spatial and temporal resolution

Heightened SNR requirements are met in part by the higher sensitivity of 3.0 T magnets [31]. Using parallel imaging at 3.0 T, DTI data sufficient for brain fibre tracking in healthy subjects can be obtained in < 2 min with 2 mm slice thickness, 700 s/mm^2 *b* factor, six motion probing gradient directions, and no averaging (number of averages = 1) [32].

A diffusion sequence based on single-shot FSE has recently been proposed to address the problem of susceptibility, as this sequence is not affected by the spatial distortions which usually limit conventional acquisitions with EPI [33].

DTI with PROPELLER shows a significant potential to reduce the number of weighted acquisitions, avoid

ambiguity in reconstructing diffusion tensor parameters, increase SNR, and decrease the influence of signal distortion [34].

The linear increase of the MR signals with increased B_0, entailing a reduction of partial volume effects, is particularly beneficial for DTI-based fibre tracking. In fact, the reconstructed DTI trajectories reflect more accurately the underlying axonal fibres, particularly crossing or bifurcating bundles [24].

High-field strength MRI is very sensitive to hyperacute ischaemic lesions also at lower *b* values (500 instead of 1,000 as in 1.5 T systems) (Fig. 7.6) [35], whereas tumours must be investigated at high *b* values to distinguish the (hyperintense) lesion from the surrounding (hypointense) vasogenic oedema (Fig. 7.7).

The higher SNR makes it possible to increase the *b* value to enhance the anisotropic effect, thus improving the quality of more complex evaluations like anisotropy, DTI and TI, which are poorly displayed on 1.5 T images, even with multiple excitations, due to their insufficient SNR [26] (Figs. 7.8–7.11). Using a 3.0 T system, these diffusion techniques seem to provide more informative data for the study of brain tumours, especially to assess the involvement of peritumour white matter,

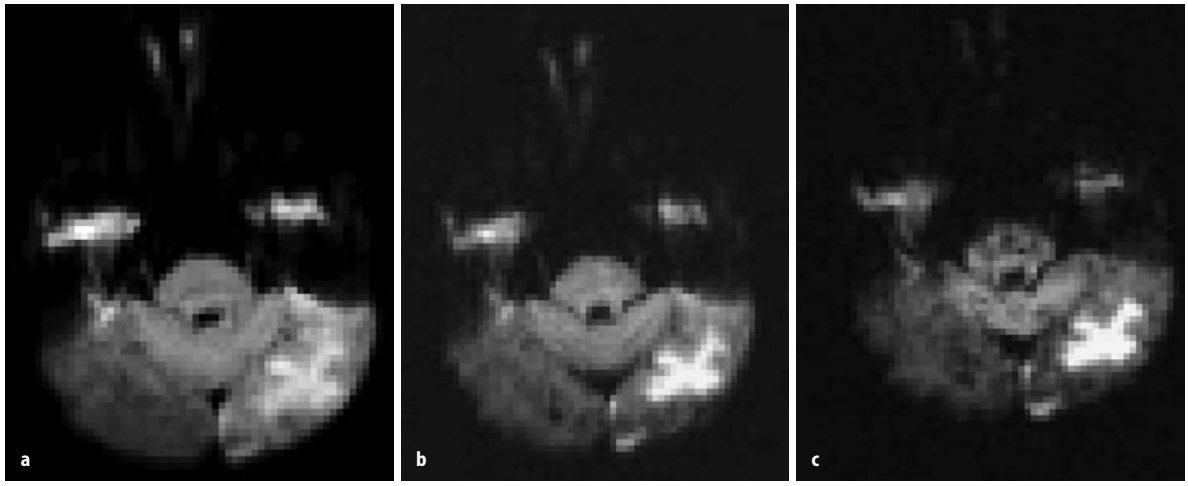

Fig. 7.6. Hyperacute cerebral ischaemia: DWI using different *b* values: 500 (**a**), 1,000 (**b**), 2,000 (**c**). The small ischemic lesion is already disclosed at low *b* values

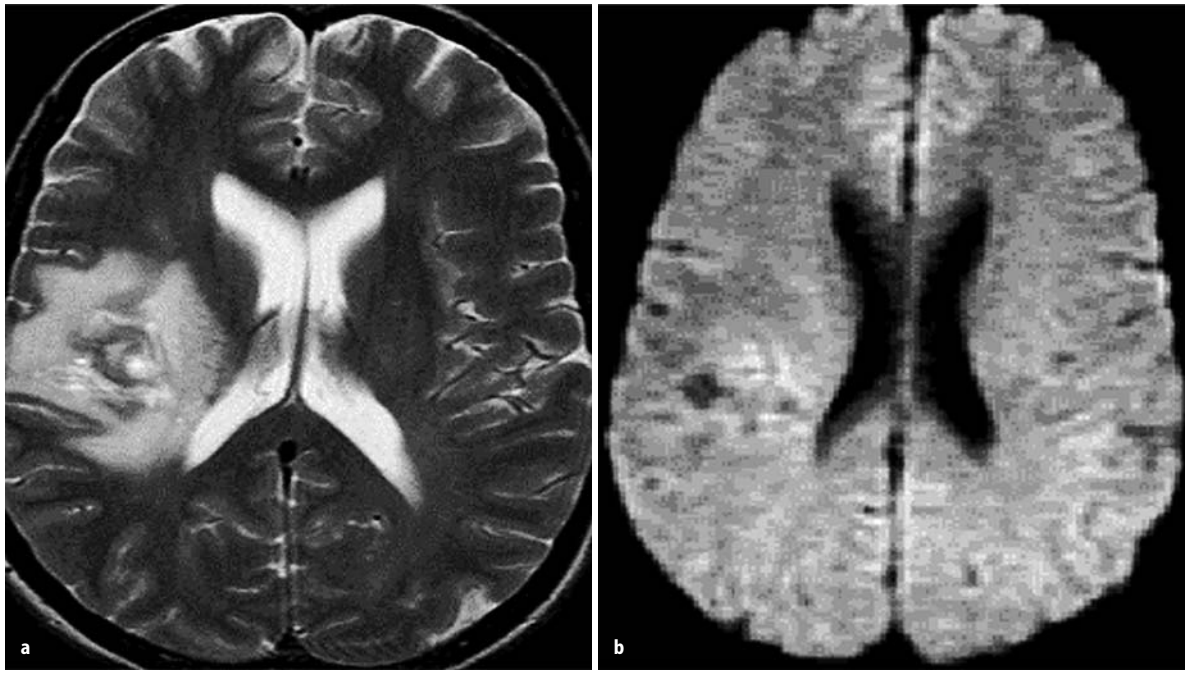

Fig. 7.7. Right frontal glioblastoma: DWI at different *b*-values. **a** FSE T2 image. **b** DWI with *b*-value = 1,000

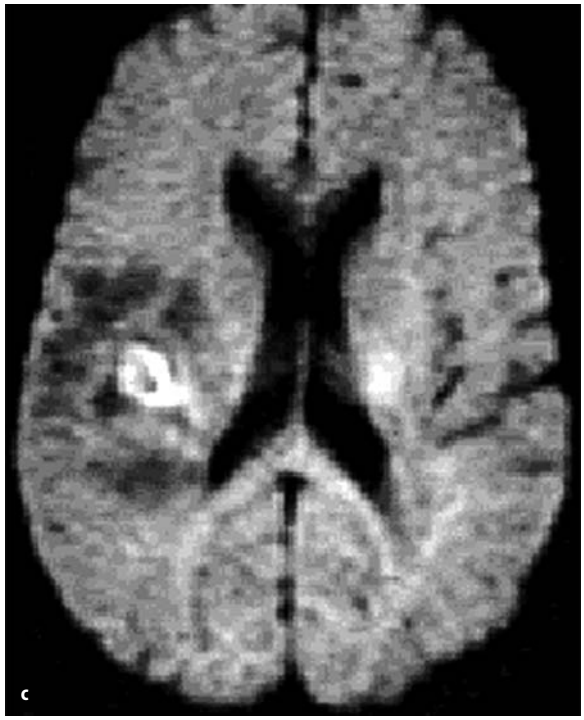

which may exhibit oedema and/or neoplastic infiltration. In particular, subtle white matter disruption can be identified using DTI in patients with high-grade gliomas. Such disruption is not seen in association with metastases or low-grade gliomas, despite the fact that these tumours produce significant mass effect and oedema. In the latter case, white matter fibres are merely compressed and dislocated, not infiltrated or disrupted as in high-grade gliomas. The changes detected on DTI may therefore be due to tumour infiltration. For this reason, DTI can be a valuable method for detecting occult white matter invasion by glioma, thus providing useful information for planning treatment [37].

◁

Fig. 7.7 c *b* value = 3,000. At the higher *b* value (**c**) the tumoral core (hyperintense) can be distinguished from the peripheral vasogenic oedema (hypointense)

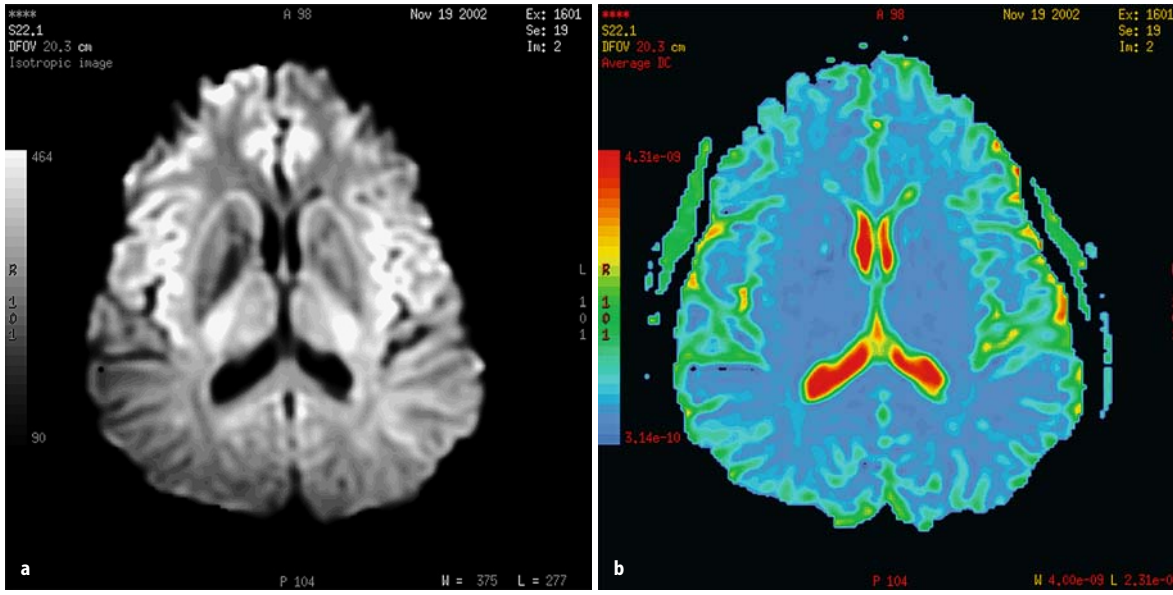

Fig. 7.8. Healthy control subject: DWI (**a**), ADC map (**b**), tensor imaging (**c**), main eigenvector map area of interest (**d**)

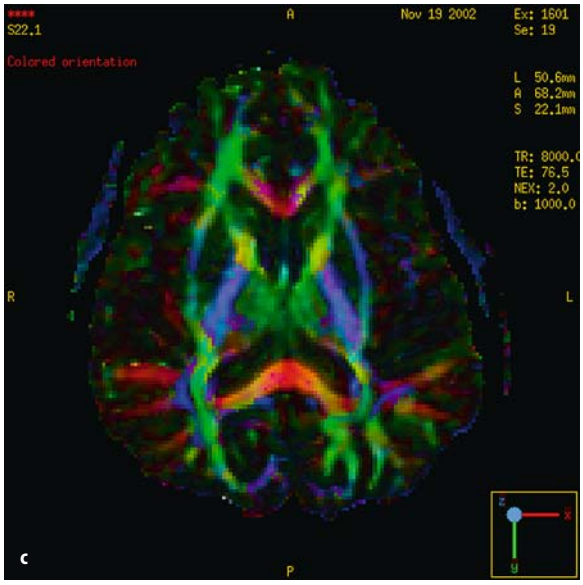

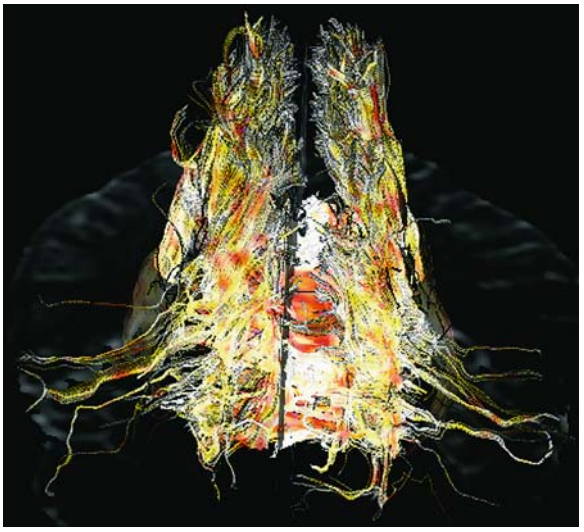

Fig. 7.9. Healthy control subject: tractography

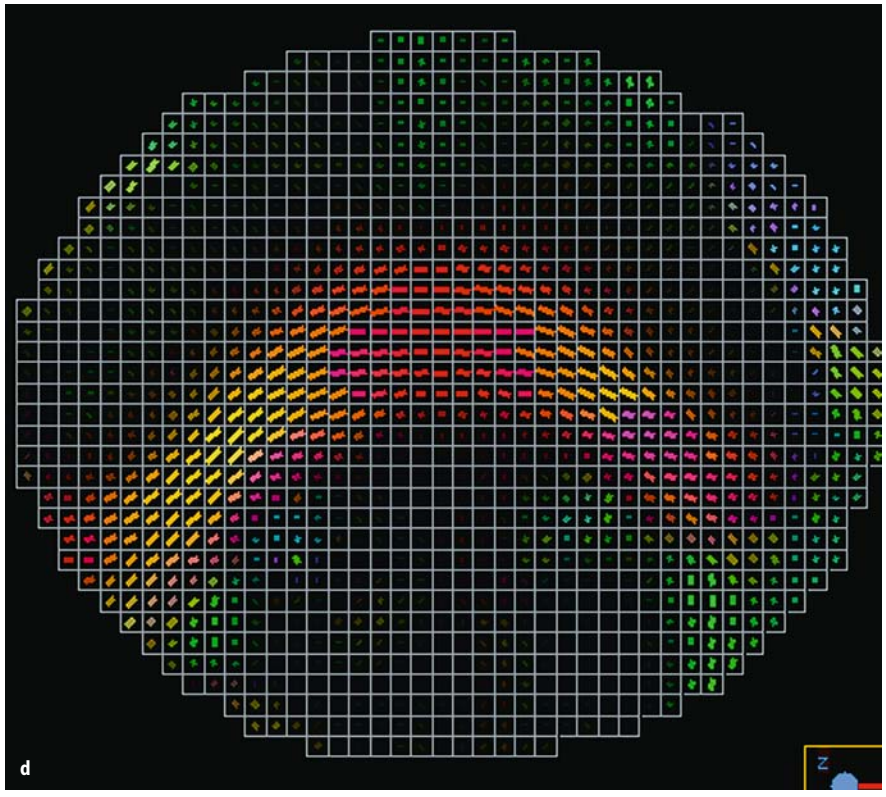

Fig. 7.8 d. (Cont.)

References

1. Le Bihan D, Mangin JF, Poupon C, et al. (2001) Diffusion tensor imaging: concepts and applications. J Magn Reson Imaging 13:534 – 546
2. Wick M, Nagatomo Y, Prielmeier F, Frahm J (1995) Stroke. Alteration of intracellular metabolite diffusion in rat brain in vivo during ischemia and reperfusion 26(10):1930 – 1933
3. Melhem ER, Mori S, Mukundan G, et al. (2002) Diffusion tensor MR imaging of the brain and white matter tractography. AJR 178:3 – 16
4. Latour LL, Hasegawa Y, Formato JE, et al. (1994) Spreading waves of decreased diffusion coefficient after cortical stimulation in the rat brain. Magn Reson Med 32:189 – 198
5. Hasegawa Y, Latour LL, Formato JE, et al. (1995) Spreading waves of a reduced diffusion coefficient of water in normal and ischemic rat brain. J Cereb Blood Flow Metab 15: 179 – 187

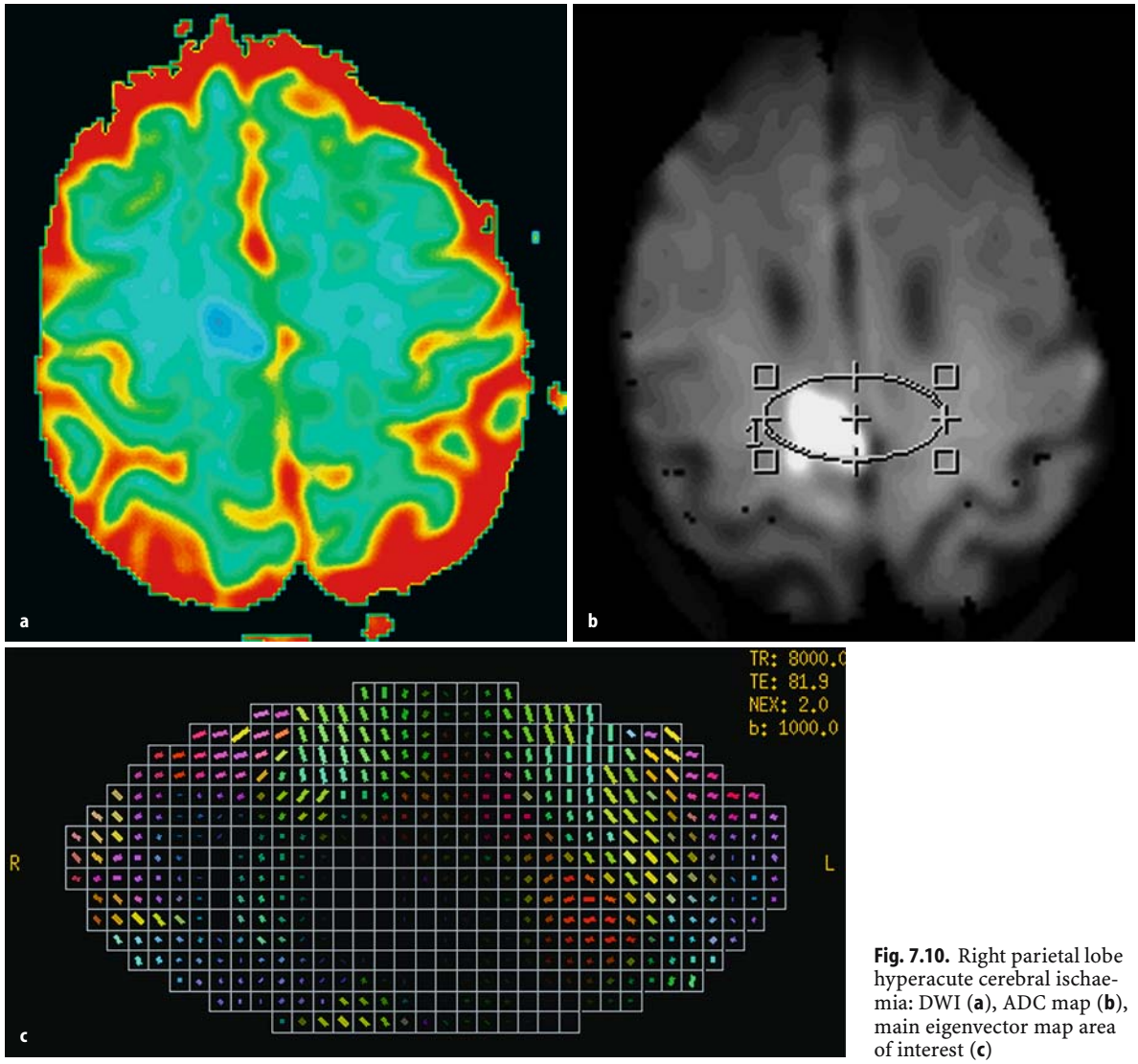

Fig. 7.10. Right parietal lobe hyperacute cerebral ischaemia: DWI (**a**), ADC map (**b**), main eigenvector map area of interest (**c**)

6. Busch E, Hoehn Berlage M, Eis M, et al. (1995) Simultaneous recording of EEG, DC potential and diffusion weighted NMR imaging during potassium induced spreading depression in rats. NMR Biomed 8: 59 – 64
7. Zhong J, Petroff OAC, Prichard JW, Gore JC (1993) Changes in water diffusion and relaxation properties of rat cerebrum during status epilepticus. Magn Reson Med 30:241 – 224
8. Le Bihan D, Breton E, Lallemand D, et al. (1986) MR imaging of intravoxel incoherent motions: application to diffusion and perfusion in neurologic disorders. Radiology 161:401 – 407
9. Warach S, Chien D, Li W, et al. (1992) Fast magnetic resonance diffusion-weighted imaging of acute human stroke. Neurology 42:1717 – 1723
10. Moseley ME, Cohen Y, Mintorovitch J (1990) Early detection of regional cerebral ischemic injury in cats: evaluation of diffusion and T2-weighted MRI and spectroscopy. Magn Reson Med 14:330 – 346
11. Moseley ME, Kucharczyk J, Mintorovitch J, et al. (1990) Diffusion weighted MR imaging of acute stroke: correlation with T2-weighted and magnetic susceptibility-enhanced MR imaging in cats. AJNR 11:423 – 429
12. Latour LL, Svoboda K, Mitra PP, Sotak CH (1994) Time-dependent diffusion of water in a biological model system. Proc Natl Acad Sci USA 91:1229 – 1233
13. Norris DG, Niendorf T, Leibfritz D (1994) Healthy and infarcted brain tissues studied at short diffusion times: the origins of apparent restriction and the reduction in apparent diffusion coefficient. NMR Biomed 7:304 – 310
14. Pfeuffer J, Dreher W, Sykova E, Leibfritz D (1998) Water signal attenuation in diffusion-weighted 1H NMR experiments during cerebral ischemia: influence of intracellular restrictions, extracellular tortuosity, and exchange. Magn Reson Imaging 16:1023 – 1032
15. Sorensen AG, Buonanno FS, Gonzalez RG, et al. (1996) Hyperacute stroke: evaluation with combined multisection diffusion-weighted and hemodynamically weighted echo-planar MR imaging. Radiology 199:391 – 401
16. Warach S, Boska M, Welch KMA (1997) Pitfalls and potential of clinical diffusion-weighted MR imaging in acute stroke. Stroke 28:481 – 482

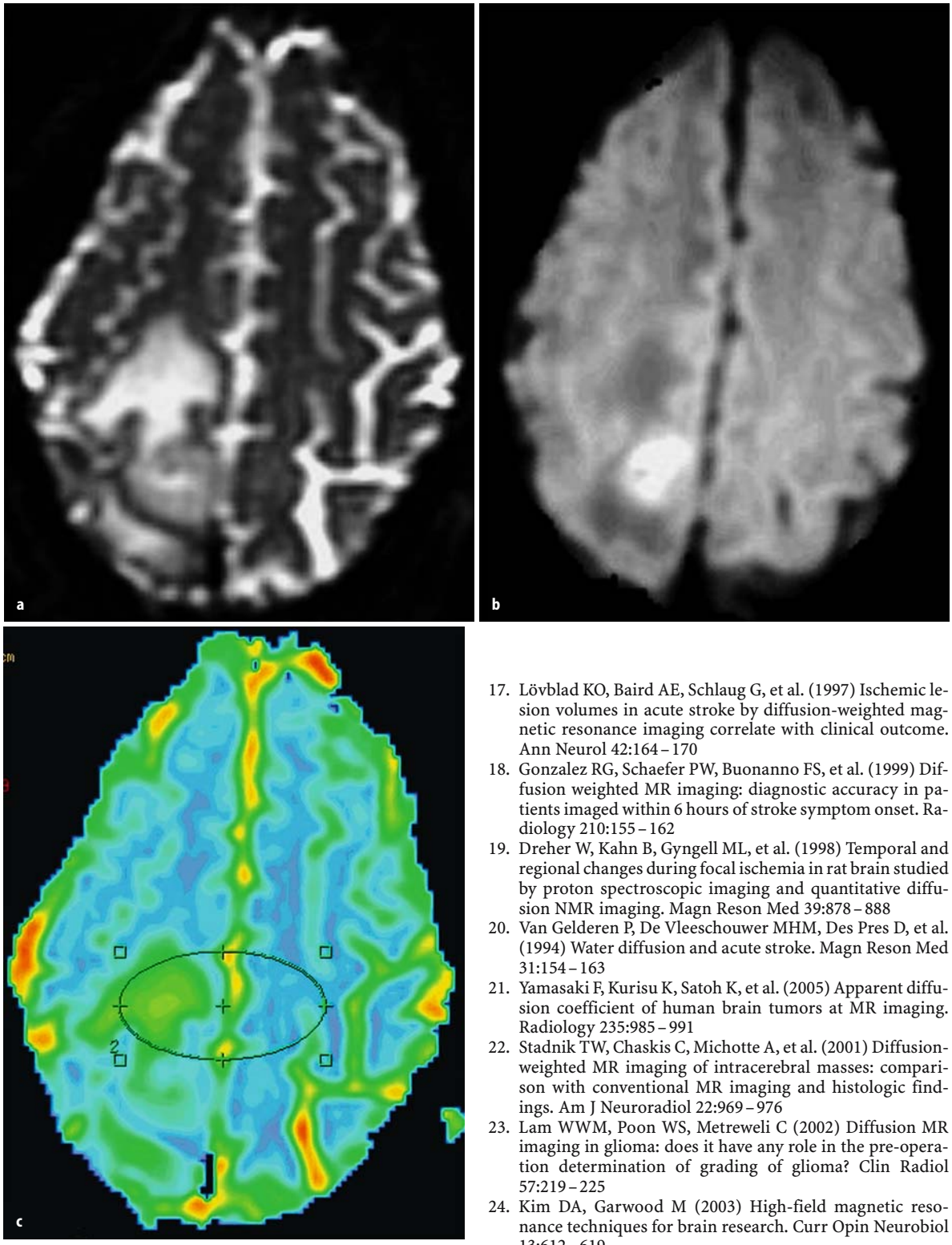

Fig. 7.11. Small right parietal lobe tumour: DWI (in **a** *b* value = 0, in **b** *b* value = 1,000), ADC map (**c**), main eigenvector map area of interest (**d**)

17. Lövblad KO, Baird AE, Schlaug G, et al. (1997) Ischemic lesion volumes in acute stroke by diffusion-weighted magnetic resonance imaging correlate with clinical outcome. Ann Neurol 42:164 – 170
18. Gonzalez RG, Schaefer PW, Buonanno FS, et al. (1999) Diffusion weighted MR imaging: diagnostic accuracy in patients imaged within 6 hours of stroke symptom onset. Radiology 210:155 – 162
19. Dreher W, Kahn B, Gyngell ML, et al. (1998) Temporal and regional changes during focal ischemia in rat brain studied by proton spectroscopic imaging and quantitative diffusion NMR imaging. Magn Reson Med 39:878 – 888
20. Van Gelderen P, De Vleeschouwer MHM, Des Pres D, et al. (1994) Water diffusion and acute stroke. Magn Reson Med 31:154 – 163
21. Yamasaki F, Kurisu K, Satoh K, et al. (2005) Apparent diffusion coefficient of human brain tumors at MR imaging. Radiology 235:985 – 991
22. Stadnik TW, Chaskis C, Michotte A, et al. (2001) Diffusion-weighted MR imaging of intracerebral masses: comparison with conventional MR imaging and histologic findings. Am J Neuroradiol 22:969 – 976
23. Lam WWM, Poon WS, Metreweli C (2002) Diffusion MR imaging in glioma: does it have any role in the pre-operation determination of grading of glioma? Clin Radiol 57:219 – 225
24. Kim DA, Garwood M (2003) High-field magnetic resonance techniques for brain research. Curr Opin Neurobiol 13:612 – 619
25. Masutani Y, Aoki S, Abe O, Hayashi N, Otomo K (2003) MR diffusion tensor imaging: recent advance and new techniques for diffusion tensor visualization. Eur J Radiol 46:53 – 66
26. Scarabino T, Giannatempo GM, Nemore F, et al. (2003) RM

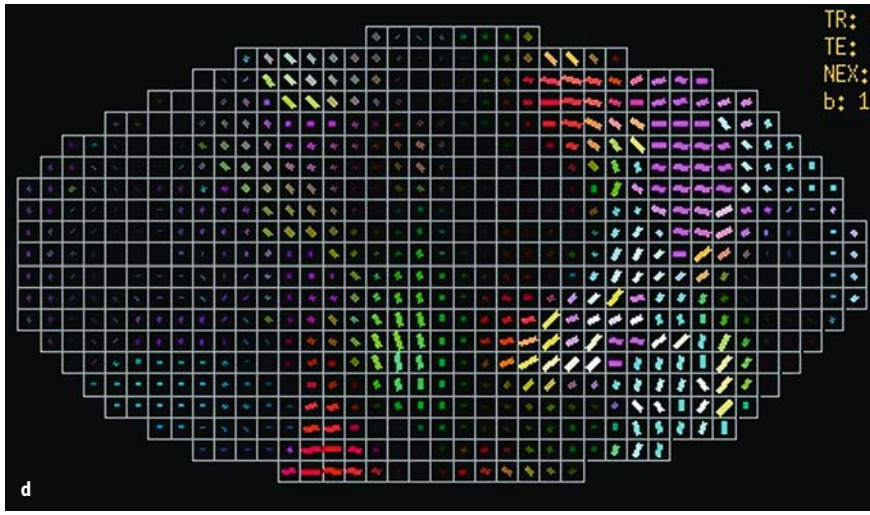

Fig. 7.11 d

3.0 Tesla. II parte: L'imaging morfo-funzionale cerebrale. Radiol Med 105:150 – 161
27. Scarabino T, Nemore F, Giannatempo GM, et al. (2003) Risonanza Magnetica 3.0 Tesla. Rivista di Neuroradiologia 16 (Suppl):314 – 315
28. Scarabino T, Nemore F, Giannatempo GM, et al. (2003) 3.0 T magnetic resonance in neuroradiology. Eur J Radiol 48:154 – 164
29. Frayne R, Goodyear BG, Dickhoff P, et al. (2003) Magnetic resonance imaging at 3.0 tesla: challenges and advantages in clinical neurological imaging. Invest Radiol 38(7): 385 – 402
30. Takahashi M, Uematsu H, Hatabu H (2003) MR imaging at high magnetic fields. Eur J Radiol 46:45 – 52
31. Jaermann T, Crelier G, Pruessmann KP, et al. (2004) SENSE-DTI at 3 T. Magn Reson Med 51(2):230 – 236
32. Naganawa S, Koshikawa T, Kawai H, et al. (2004) Optimization of diffusion-tensor MR imaging data acquisition for brain fiber tracking using parallel imaging at 3 T. Eur Radiol 14(2): 234 – 238
33. Xu D, Henry RG, Mukherjiee P, et al. (2004) Single-shot fast spin-echo diffusion tensor imaging of the brain and spine with head and phase array coils at 1.5 T and 3.0 T. Magn Reson Imaging 22(6):751 – 759
34. Cheryauka AB, Lee JN, Samsonov AA, et al. (2004) MRI diffusion tensor reconstruction with PROPELLER data acquisition. Magn Reson Imaging 22(2): 139 – 148
35. Kuhl CK, Textor HJ, Simon B, et al. (2002) Determine optimum b-value for diffusion imaging of acute ischemic stroke at high magnetic fields (3.0 T). Radiology 225:278
36. Hunskhe S, Moseley ME, Stoeter P, et al. (2001) Diffusion-tensor MR imaging at 1.5 and 3.0 T: initial observation. Radiol 221:550 – 556
37. Price SJ, Burnet NG, Donovan T, et al. (2003) Diffusion tensor imaging of brain tumours at 3 T: a potential tool for assessing white matter tract invasion? Clin Radiol 58:455 – 462

Nerve Pathways with MR Tractography

8

A. Cherubini, G. Luccichenti, F. Fasano, G. E. Hagberg, P. Péran, F. Di Salle, F. Esposito, T. Scarabino, U. Sabatini

The neuroradiological interpretation of magnetic resonance (MR) images relies on a complex semeiotics that is based on the morphological and signal characteristics of normal and pathological brain and on the detailed knowledge of the ultrastructural and functional organization of the central nervous system (CNS). The study of the brain's cortical organization is facilitated by the presence on its surface of fissures that divide it into lobes and sulci that circumscribe in each lobe a number of convolutions or gyri. Identification of the encephalic nuclei, grey matter formations lying deep in the hemispheres, is also facilitated by their characteristic morphology, their symmetric position with respect to the midline, and the presence of specialized white structures such as the internal, external and extreme capsule that mark their borders.

Detailed white matter evaluation is more challenging than the study of cortical organization, because it does not exhibit anatomical landmarks excepting the contiguous cortical gyri, the ventricular systems and the base nuclei; however, it does contain fibres with distinct anatomical courses and functional significance that include projection and association systems. Identification of nerve fibre bundles is essential in neurophysiology and to study CNS diseases, and knowledge of their spatial relationships with lesions requiring surgical treatment is crucial to preserve functional pathways and the activities they subserve.

Standard MR techniques provide an accurate representation of the brain's macroscopic anatomy, but not detailed information on white matter anatomy. By contrast, study of the anisotropic diffusion of water molecules (diffusion tensor imaging; DTI) [1] and tractography (fibre tracking) provide data on its microscopic organization and make it possible to reconstruct axonal tracts using diffusion-weighted MR images [2–6]. Since tractography is currently the sole method affording non-invasive study of the 3D architecture of axons in vivo, it has potential applications to several fields of neurophysiology, neurology and neurophysiology to visualize and quantify physiological mechanisms and pathological processes.

Herein we illustrate the main tractographic techniques and discuss their enormous potential and current limitations.

8.1 Basic Principles

A brief overview of the structural characteristics of nerve tissue is in order to help understand the rationale of diffusion studies. White matter is mainly composed of myelinated axons with a given orientation, whereas grey matter is made up of cells, principally neurons. Axons have a mean diameter of ~20 μm and may form parallel, sometimes thick bundles.

The rationale of tractography and DTI is that the random movement of water molecules in tissues (diffusion) is restricted by the presence of cell structures (Fig. 8.1). As a consequence, diffusion perpendicular to axon bundles is hindered by axonal cell membranes and myelin sheaths [7, 8] whereas it is unrestricted along them. Within axons water is surrounded by cell membranes and myelin sheaths; again, its diffusion will be greater parallel to the fibres. Longitudinally oriented axoplasmic neurofilaments do not seem to restrict diffusion [9]. Tissues like cerebral white matter, possessing a microscopic architecture with a specific spatial orientation, will thus exhibit different diffusion values in the different spatial directions. When diffusion exhibits a preferential direction, it is termed anisotropic.

The diffusion of water molecules in biological tissues can be measured using MR gradients and diffusion-weighted sequences. The acquisition technique consists of „tagging" the water molecules with a very short gradient. Tagged molecules acquire a magnetization and a phase that depend on their spatial position. The natural phenomenon of diffusion causes the displacement of these molecules to areas containing molecules with different magnetization and phase. The presence in a region of signals with different magnetization and phase results in an overall lower signal intensity, as the signal of the diffusing molecules reduces the one of local molecules. Therefore, increasing diffusion of the water molecules induces a reduction in tissue signal. The study of diffusion anisotropy uses the same image acquisition strategies as clinical diffusion studies. Indeed, water molecule diffusion data are actually generated as anisotropic data, because all acquisi-

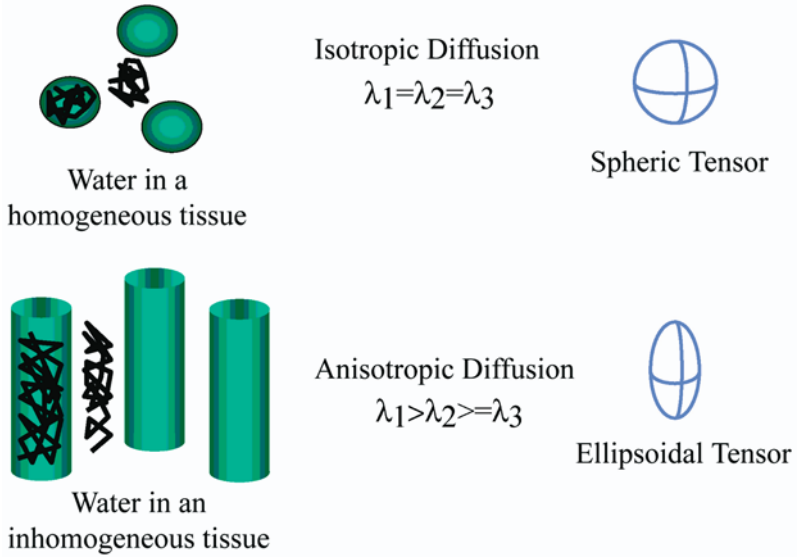

Fig. 8.1. Representation of the physical bases of the reconstruction of the diffusion tensor. In homogeneous tissues, the three eigenvalues have similar values and the tensor is spherical. In tissues where barriers restrict water diffusion in a particular direction, the tensor is an ellipsoid and the direction corresponding to the principal eigenvalue represents the direction of the fibres

tions read diffusion along a given spatial direction, coinciding with the direction of the magnetic field gradient used. In clinical diffusion studies, the direction information is lost through the averaging of diffusion values along the three spatial axes; this simplifies the detection of pathological changes in the diffusion coefficient, which are independent of fibre direction.

In DTI studies, this information is retained and the prevalence of diffusion along a direction, e.g. along a fibre bundle, can be expressed in terms of anisotropy. The degree of anisotropy can be quantified using the diffusion tensor [9–11]. A tensor is a complex mathematical entity [12]; when measured with MR, it may be represented in matrix form using data from diffusion-weighted images to obtain parameters like fractional anisotropy (FA) and the apparent diffusion coefficient (ADC) [13]. The diffusion tensor also contains much additional information. In particular, an algebraic procedure called diagonalization makes it possible to obtain for each image voxel three eigenvalues (λ_1, λ_2, λ_3) representing the values of diffusion along three spatial directions (eigenvectors). If in a given voxel the three values are similar ($\lambda_1 \sim \lambda_2 \sim \lambda_3$), as in grey matter, the water diffuses in a similar manner in all directions and its diffusion in the voxel is called isotropic. If, by contrast, one of the three eigenvalues is much greater than the other two, as in white matter, water diffuses more easily along the direction corresponding with that eigenvalue, and its diffusion in the voxel is termed anisotropic.

It may bear stressing that, unlike MR parameters such as relaxation times, those obtained from the diffusion tensor do not depend directly on the magnetic field and can thus be measured and directly compared between high- and low-field acquisitions. In practice, whereas T1 and T2, and thus the relevant images, change as a function of the magnetic field, water diffusion in a given space is the same at 1.5, 3.0 and even 7.0 T. Diffusion studies thus fully benefit from the greater signal/noise ratio (SNR) of high-field magnets.

8.2 Image Acquisition

Calculation of the diffusion tensor requires acquisition of a set of MR images using suitable diffusion-weighted sequences. Echo-planar sequences with different gradient directions and intensities are the more appropriate for these applications and are those used most commonly [1, 14, 15].

Diffusion weighting involves a general reduction in signal intensity, which is greater the greater the diffusion of water. This magnifies the SNR problems shared by all MR acquisitions and makes it difficult to obtain images with very high spatial resolution. Currently, the best spatial resolution that can be achieved is rarely less than 1 mm, particularly along the slice-encoding direction, but use of high magnetic fields (3.0 T or greater) and parallel imaging can further enhance resolution, thus fibre tracking [16]. Diffusion weighting depends on gradient intensity, which is usually denominated *b* factor and is measured as s/mm^2. In theory, increasing *b* values should be used to calculate the ADC; in practice, limitations in the gradients used in clinical practice, specific absorption rate, and times of acquisition result in the prevalent use of only two *b* values, one virtually null (no diffusion weighting), and the second high, 1,000 s/mm^2 or greater. A *b* value slightly greater than 0 (~20) is used to remove the effects of large vessels and flow. The minimum set of images to be acquired for a DTI study includes six different diffusion-weighted directions (with b = 1,000 or greater) and a non-diffusion-weighted scan (b = 0). The minimum set

may be acquired several times to improve the SNR, whereas acquisitions with different b values for each direction are unnecessary as well as inefficient in terms of SNR [11]. More accurate evaluation of the diffusion coefficient D from two acquisitions has been demonstrated using two values of b differing by ~1/D, which in the brain entails that $b2–b1 < 1{,}000 – 1{,}500$ s/mm^2 [11, 17]. If more than two acquisitions are performed to optimize the SNR, the theory of error propagation states that it is more convenient to obtain multiple acquisitions at the two b values selected than to use a broader range of b values [11].

Acquisitions in a range, rather than a pair ($b = 0$ and $b = 1{,}000$) of b values, can however provide interesting information [18, 19]. Although a single ADC value tends to be assigned to each tissue voxel, most tissues are in fact made up of separate compartments, each with a distinct ADC. Brain tissue comprises at least two compartments, a fast-diffusion intracellular compartment and a slower-diffusion extracellular compartment. The ADC depends on the range of b values used, because low values (1,000) are more sensitive to fast-diffusion components and thus to the structural features of the interstitium, than to those of axon fibres. Ideally, the different tissue compartments should be studied separately using several different b values and then fitted with a multiexponential function. However, since slow-diffusion compartments can be studied only with high b values and favourable SNRs, this is difficult to achieve.

The number of directions offering the best compromise between a reliably reconstructed tensor (multiple directions) and long acquisition times is still debated. While from a mathematical standpoint at least six different directions plus a low b value acquisition are required, most researchers use 6 to 90 different directions, with considerable differences in acquisition times and uncertain benefit. A sequence with 68 directions, $b = 100$ and 1,000 s/mm^2, and a cubic voxel of 2.3 mm lasts about 13 min, but actually takes much longer because image averaging to obtain an acceptable SNR requires multiple acquisitions. Here, a large role is played by acquisition conditions, particularly magnetic field intensity and the availability of parallel imaging to improve the SNR.

High angular resolution techniques (HARDI; see below), which require a much greater number of directions (even 252 or more), benefit from favourable conditions of field intensity and high coil sensitivity.

As mentioned above, the diffusion tensor basically provides two types of information: a quantitative estimate of diffusion anisotropy and the spatial orientation of fibres (Fig. 8.2). These data are interesting but „local“, i.e. they regard a single voxel. Tractography uses these microscopic data to obtain „global“ information and reconstruct macroscopic fibre tracts.

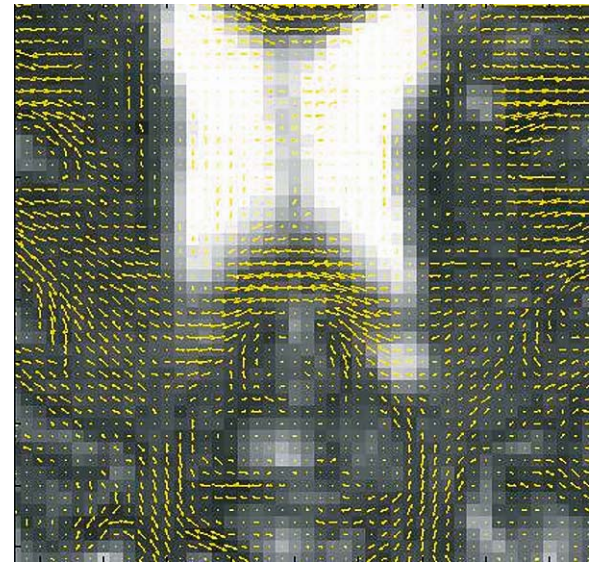

Fig. 8.2. Diffusion tensor. Projection in the image plane of the principal eigenvector. Vectors are represented by *double-headed arrows* because diffusion data provide the direction, not the orientation of diffusion

8.3 Fibre Tracking Techniques

The voxel grid of an MR image may be compared to a chessboard: selecting a number of adjacent voxels that form a trajectory is like drawing a line on the chessboard (Fig. 8.3). The algorithm used to draw this trajectory in most fibre tracking techniques involves selecting an initial point (seed point) that is highlighted on the image, and then moving to the next nearest voxel, which in turn is highlighted, along the prevalent anisotropic direction, until a condition that halts this process arises (stopping criterion). The differences among these, line propagation, algorithms lie in the way in

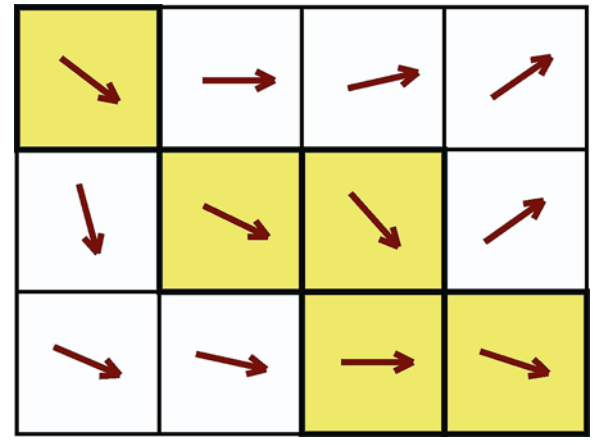

Fig. 8.3. Propagation of a fibre in a vector field. The *yellow pixels* represent the course of the reconstructed fibre

which the information contained in the voxels nearest to the one being examined with the algorithm (nearest neighbours approach) is used by the algorithm itself to draw the likeliest trajectories and minimize noise.

Since digital images are represented on discrete fields, the vector will often point to an area straddling at least two adjacent voxels, requiring a choice from one or more possible trajectories. In such cases, the selected tract will be a mere approximation of the information contained in the diffusion data, irrespective of the trajectory that has been selected.

The first researchers to reconstruct a white matter fibre tract successfully [20, 21] solved this problem using propagation in a continuous numerical field – where the coordinates can be expressed as decimal values – each time approximating the coordinates of the line to those of the nearest voxel. This simple but fairly rough method can be improved by applying a tract curvature threshold. Assuming that the course of a fibre tract exhibits only reasonably soft curves, whenever two possible trajectories present, the less curved one is selected, while sharp curves (e.g. $>60°$) are excluded. Line propagation algorithms may require vector interpolation (direction and eigenvalue) at the point of arrival of the previous step, which usually straddles two or more voxels and therefore does not directly correspond to a measured value. Interpolation is a mathematical operation that makes it possible to obtain the value of a point from those of surrounding points. In the simpler algorithms, the vectors corresponding to the neighbouring voxels are interpolated, while the more sophisticated ones directly interpolate the diffusion tensor and calculate a new vector [6]. Interpolation enables more uniform paths to be obtained with respect to the algorithms that do not employ them, and is less sensitive to noise, although the additional calculations considerably increase computation time.

8.3.1 Seed Point

A factor requiring careful consideration is the initial point of tract propagation, as this choice influences the relative effect of noise on the propagation itself. A frequently adopted solution is to use a number of equidistant seed points arranged on a grid space. This reduces the variance connected with the arbitrary choice of the seed point. However, a seed point acceptance criterion may be applied to avoid selecting voxels not containing fibres. One useful criterion is a minimum FA value ensuring the presence of a distinct fibre at the seed point. It is worth stressing that, since the directions identified in each voxel by the diffusion tensor do not have an orientation (see Fig. 8.2), a forward and a backward pathway, lying on the same straight line but running in opposite directions, are consistently generated at seed points.

8.3.2 Stopping Criteria

All fibre tracking algorithms that use a seed point require a stopping criterion to terminate the propagation process. The most intuitive criterion is the FA value itself; in grey matter FA is low (0.1 – 0.2 on a 0 – 1 scale), so the orientation of the principal eigenvector of the diffusion tensor is random and unrelated to that of the fibre tract. A useful stopping criterion may thus be an FA threshold (usually 0.2) below which the propagation is halted, preventing reconstruction of fibres that are not organized into bundles, like grey matter fibres. However, this criterion may also halt the elongation of a line in those white matter voxels which, albeit containing fibre tracts, have a low FA because of the lack of a main direction (see below).

Another possible stopping criterion is the curvature of the reconstructed fibre tract. The method used to calculate the diffusion tensor assumes the absence in the voxels of sharp curves, in line with the fundamental hypothesis of the Gaussian nature of the diffusion process in all directions. A criterion halting tract propagation in the presence of sharp angles is thus useful, but is difficult to apply to the shorter and more tortuous tracts, where the low spatial resolution of the image does not enable reconstruction of the real course of the fibres.

8.3.3 Global Algorithms

The algorithms of this class use a radically different approach. In fact, whereas the line propagation algorithms use only local information (i.e. the data contained in a voxel and in those nearest to it), these employ the information in a global way by applying a mathematical function that reproduces the structural characteristics of the fibre tracts. For instance, the physical analogy used for the Fast Marching Technique [22 – 24] is that of an ink drop falling on adsorbent tissue. The stain extends faster along the direction of the tissue fibres than perpendicular to them. Assuming a vector field indicating the directions in which the ink spreads, a speed function for front propagation can be defined on the basis of the fibres' anisotropy value. This function reflects the fact that propagation is fastest along fibres and slowest perpendicular to them, and makes it possible to calculate the „shape" of the stain from any point at any given time. Its contours may be compared to the isobars of meteorological charts and, in the case of a vector field of DTI data, they represent a sort of map of the likelihood of connection starting

from a given point. Using this technique, the course of the fibres coincides with the faster route, hence its name.

Another physical analogy, well known in the field of numerical simulations as the „travelling salesman problem", can help explain another class of methods. A travelling salesman needs to find the optimum route passing through all the towns where he will be calling. One solution is to define a function, e.g. petrol consumption or time, and find the route that minimizes it. Using DTI data, the function ensuring global energy minimization is related to paths along the direction of the field vectors, while those associated with greater energy expenditure are perpendicular to them [25]. Calculation of the value of the function for all possible trajectories makes it possible to identify the course that minimizes the energy function. However, methods like simulated annealing allow the solution to be found rapidly without calculating the energy for all the possible courses, while minimizing the effect of noise.

Halfway between line propagation and global algorithms are the Monte Carlo probabilistic methods [26–28]. With these techniques, thus named for their similarity to gambling, each time the tract is propagated from one voxel to the next, the various directions are given a probability value depending on the diffusion values measured. It is assumed that by repeating the line propagation a large number of times, the course that has been selected most often will correspond to the actual trajectory of the fibre.

Global methods have two main advantages. First, they can provide a semiquantitative estimate of the level of connectivity between two points or regions (Fig. 8.5). In fact, fibres like those shown in Fig. 8.4 provide a visual representation of the bundles, but not a „value" of the connection [29], for instance between two activation areas shown on functional MR. Secondly, they are less affected by the typical limitations of line propagation algorithms (addressed below). However, the level of calculation required to implement them is often close to the computational capacity of current processors, and they are still in an early phase of development compared with the more common line propagation algorithms.

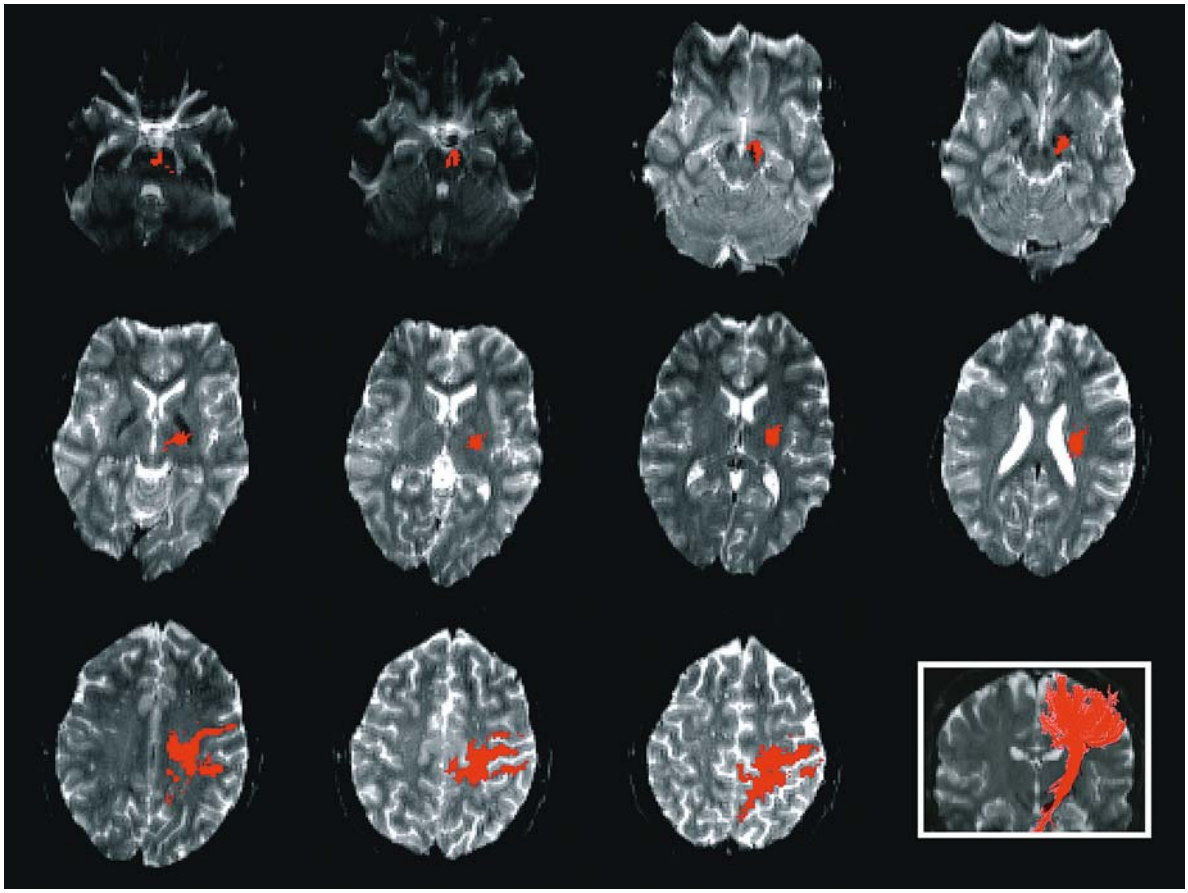

Fig. 8.4. Fibre reconstruction with a line propagation algorithm (left pyramidal tract in *red*), superimposed on axial T2-weighted images. *Lower right corner:* 3D reconstruction of the same tract overlaid on a coronal image

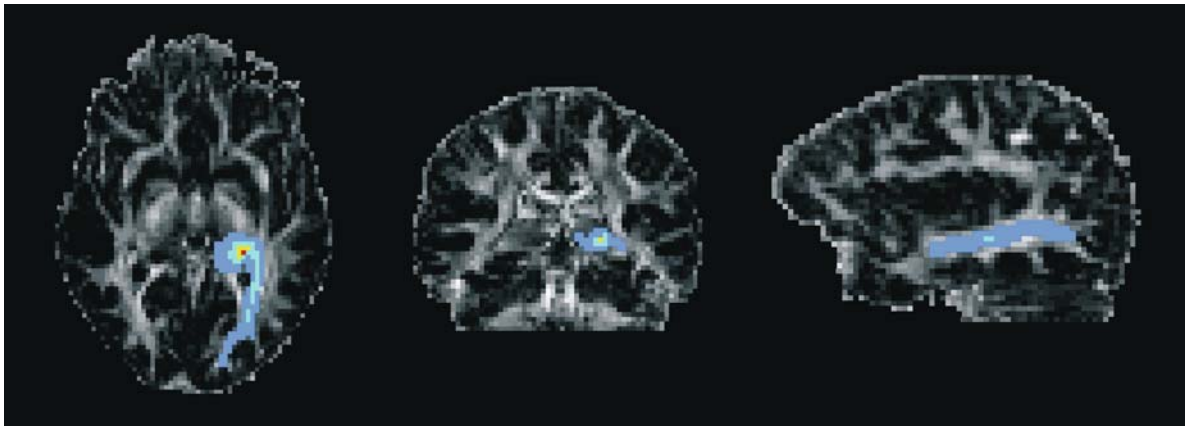

Fig. 8.5. Connectivity map generated using a Monte Carlo algorithm. Overlay on a fractional anisotropy map. Fractional anisotropy is derived from the diffusion tensor and represents white matter distribution. Colours represent the likelihood of connection with the seed point in the left lateral geniculate nucleus, according to an intensity scale

8.4 Limitations of Tractography Techniques and Their Solutions

Also due to their recent introduction, tractography techniques suffer from a number of drawbacks.

8.4.1 Noise

Owing to the frequent need for compromising between acquisition time and image quality, the three-dimensional vector field that is obtained using DTI data may contain a high level of noise. Several researchers have tried to quantify the effects of noise on tensor and tract reconstruction [30–35]. Unlike what takes place in standard MR, the noise present in the reconstructed tensor is not directly perceived on images like those of Fig. 8.2 and Fig. 8.4, because it affects only the direction of the tracts. Consequently, though exhibiting a consistent distribution of directions, the vectors may indicate slightly different trajectories with respect to the actual anatomy. This type of noise considerably affects fibre tracking, and one of the main problems of line propagation algorithms is that such errors accumulate with increasing distance from the seed point [28]. Therefore, the greater this distance, the higher the risk of deviation of the reconstructed fibre towards an adjacent, unconnected fibre tract. This possibility should always be taken into account when analysing DTI reconstructions, especially of long fibre tracts. SNR optimization is essential to obviate this and other, conceptually related problems. Here, too, the intensity of the magnetic field used and the availability of parallel imaging play a large role.

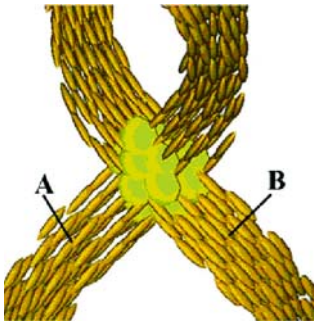

Fig. 8.6. The crossing of two fibre bundles may result in a spherical diffusion tensor, erroneously indicating an absence of fibres

8.4.2 Partial Volume

Different types of tissue may be found in a single voxel (partial volume effects), resulting in a reduction in the value of anisotropy [36]. Partial volume effects constitute a problem for fibre tracking techniques. The problem may be accentuated in short fibre tracts and in those close to grey matter, where white matter tends to thin out and anisotropy to diminish. Addressing partial volume effects requires spatial resolution to be increased, thus reducing the SNR. As in the previous case, the solution lies in defining the noise level tolerated by the algorithm used and in adjusting the resolution and acquisition time of the MR image.

8.4.3 Ultrastructure

DTI provides information on fibre bundles, not on individual axon branches. In addition, the diffusion tensor is unable to model adequately voxels containing more than one axon population with different directions [37]. For instance, if the relationship among the three eigenvalues of the diffusion tensor is of the type $\lambda_1 = \lambda_2 > \lambda_3$, the FA may still be sufficiently high as to

fail to halt a line propagation algorithm, even in the absence of a major direction with an eigenvalue greater than the other two. In this case, the plane defined by the *two* major eigenvectors contains several more or less equivalent directions, leading to error. This problem stems from the nature of the diffusion tensor itself, which being a mere second-order approximation of the diffusion process, cannot adequately represent complex situations like the one described. The tensorline technique partially obviates this problem by selecting, among the directions of the plane defined by the two main eigenvectors, the one minimizing the curvature of the trajectory according to the original direction [33].

These methods do not address the possibility that a dominant direction is not identified in a voxel due to crossing bundles giving rise to different directions. The inability to resolve a single direction within each voxel is a significant general limitation of DTI. In fact, in the millimetre scale of the MR voxel, voxels typically exhibit a number of fibre orientations. Common situations of intra-voxel orientational heterogeneity may be due to the intersection of different white matter bundles, or to the complex architecture of subcortical or junctional fibres. In the presence of fascicles with multiple directions within the same voxel, for example due to crossing or divergence, DTI will estimate the prevalent direction, which does not necessarily correspond to any actual direction. For instance, if in a voxel a vertical bundle branches off a horizontal bundle, DTI will show the presence of a single direction corresponding to their diagonal, thus failing to represent either.

The standard diffusion tensor reconstruction technique using DTI data cannot resolve this problem. Indeed, even using several different diffusion-weighting directions to reconstruct the tensor, its mathematical nature prevents it from identifying the different directions when, for instance, two or three different bundles cross. The inability of the DTI technique to resolve fibres with multiple directions derives from the assumption of the Gaussian nature of the tensor model, because a Gaussian function has a single directional peak, preventing the recognition of multidirectional diffusion by the tensor model.

Methods capable of using all the diffusion information are HARDI techniques [38–41], which measure diffusion in several directions with an equal distribution in the three-dimensional space but do not calculate the diffusion tensor. These approaches to the resolution of multiple fibre directions in voxels are based on much more complex models of diffusion in nerve tissue.

The most promising method is currently an approach that is independent of a priori models, does not require the prediction of a single diffusion direction, and can therefore recognize crossing or branching structures. The methods that measure diffusion independently of a model are called *q*-space techniques, i.e. *q*-space imaging, diffusion spectrum and *q*-ball imaging. *q*-Space imaging directly measures the microscopic diffusion function without making a priori assumptions. The diffusion function, $P(r)$, describes the likelihood of a water molecule undergoing a displacement r over a diffusion time t. *q*-Space imaging is based on the Fourier relationship between the diffusion function $P(r)$ and the MR signal $S(\gamma DI)$, where D and I indicate the duration and intensity of diffusion-sensitizing gradients and γ is the gyromagnetic ratio. The Fourier relationship $P(R) = F[S(\gamma DI)]$ enables direct reconstruction of the diffusion function through Fourier transform of the diffusion signal.

The degree of anisotropy can also be estimated directly using HARDI methods without calculating the tensor. In this case an anisotropy index, the spherical diffusion variance, is used instead of conventional FA. Given that, unlike the tensor, this method is not based on an a priori physical model of diffusion, it has the advantage of not losing any information contained in the data. HARDI and its future developments appear to be very promising, and the evolution of tractography is likely to be based on it even though it requires specialized acquisition sequences, generally longer acquisition times than tensor methods, more complex processing algorithms and, save for *q*-ball imaging, very powerful gradients [39].

8.4.4 Error Correction Methods

Tractography may yield anatomical reconstruction errors with any technique. These errors can be minimized using one of two methods of result analysis, one based on functional brain anatomy and one, a probabilistic method, using a standard space of brain coordinates. The first consists of using the anatomical data a priori by requiring a fibre tract to pass through at least two manually selected regions of interest (ROIs) [34, 42]. Using a single ROI, the reconstructed tract is more likely to contain different fibres, some representing trajectories belonging to the tract being studied and others generated by partial volume effects or noise. The latter can be eliminated by selecting multiple ROIs along the fibre tract being reconstructed so as to avoid an erroneous deviation of the reconstruction algorithm from the actual trajectory (Fig. 8.7). This method makes it possible to track simply and non-invasively the position of several tracts with a high level of confidence [34]. Its main drawback is that it cannot reconstruct bundles that are not well documented anatomically [42], and may also exhibit limitations in the presence of fibre deviations induced by brain disease.

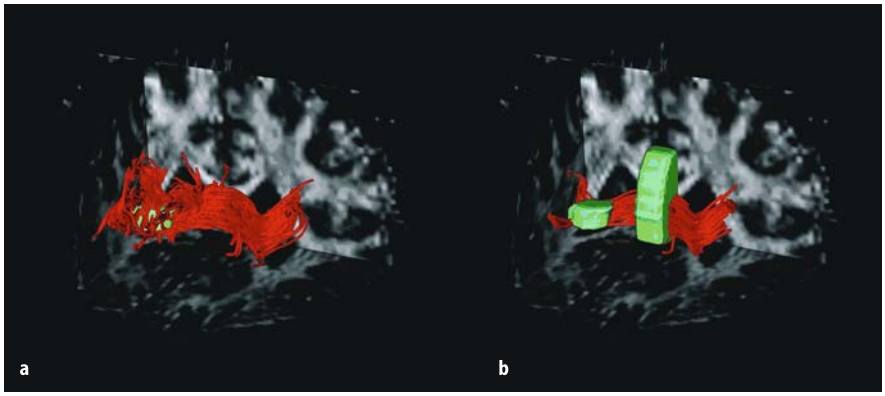

Fig. 8.7 a, b. Use of the multi-ROI approach improves tractographic reconstruction of white matter tracts. Above, the addition of a second ROI (**b**) specifically selects the fibre tract of interest

The second, probabilistic method is based on the assumption that errors induced by partial volume effects or low SNR have a random distribution and are not reproduced consistently if multiple studies of the same object are performed and their results are superimposed. The same principle underpins a method that uses data from a large sample of subjects in a standard space of brain coordinates (e.g. the Talairach atlas). The first studies applying this method of normalization have yielded a high level of reproducibility for the large fibre bundles, but greater intersubject variability for the smaller bundles [24, 44–46].

8.4.5 The Problem of Validation

One of the critical problems in the development of fibre tracking techniques is that there are no other available methods to assess the course of nerve fibres in vivo, or reference standards to which data can be compared. Indeed, knowledge of white matter fibre anatomy derives from postmortem studies, where even in the best conditions only the main fibre bundles can be followed and the resolution is insufficient to constitute a reference for validation [42].

Ablation studies of animal models make it possible to document the course of axons using specific tracers. Though representing the reference standard for connectivity studies, these data cannot however be extended to humans because tracer methods follow single axons at the cell level, and axons may cross different fibre bundles along their course. Owing to the practical impossibility of obtaining adequate statistics for 10^{11} neurons, these methods cannot be used to validate effectively data obtained using tractographic techniques.

Despite the limitations outlined above, a good agreement between fibre tracking and anatomy has however been demonstrated [24, 44].

8.5 Clinical Applications

The potential clinical applications of tractographic techniques are numerous [48, 49], first and foremost in physiological studies of human CNS, where they enable in vivo identification of the topographic distribution of circuits shown by anatomical primate research and surmised in man.

In neurophysiology, tractography has fostered the development of a new strategy to study brain activity patterns: anatomical connectivity. This technique is

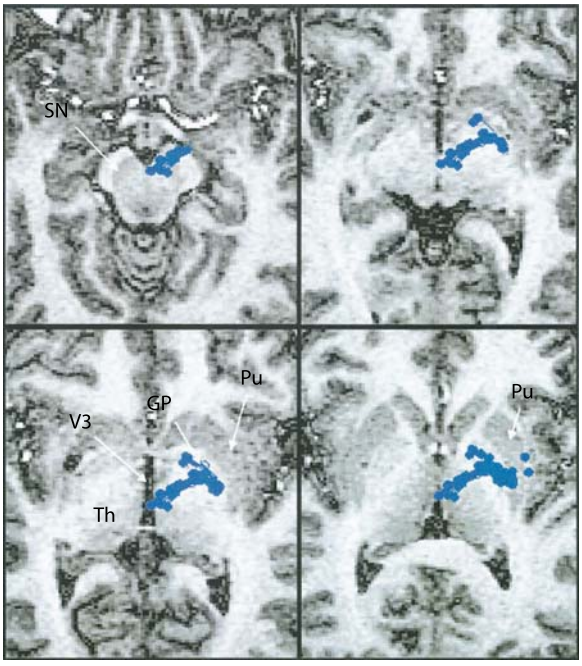

Fig. 8.8. Image from Lehéricy et al. [43]. T1-weighted axial images at the level of the mesencephalon (*upper left*), subthalamic area (*upper right*), and thalamus (*lower left and right*). *Blue points* represent the fibre tract reconstructed from the putamen through globus pallidus, subthalamic area, and medial substantia nigra (*GP* globus pallidus, *Pu* putamen, *SN* substantia nigra, *Th* thalamus, *V3* third ventricle)

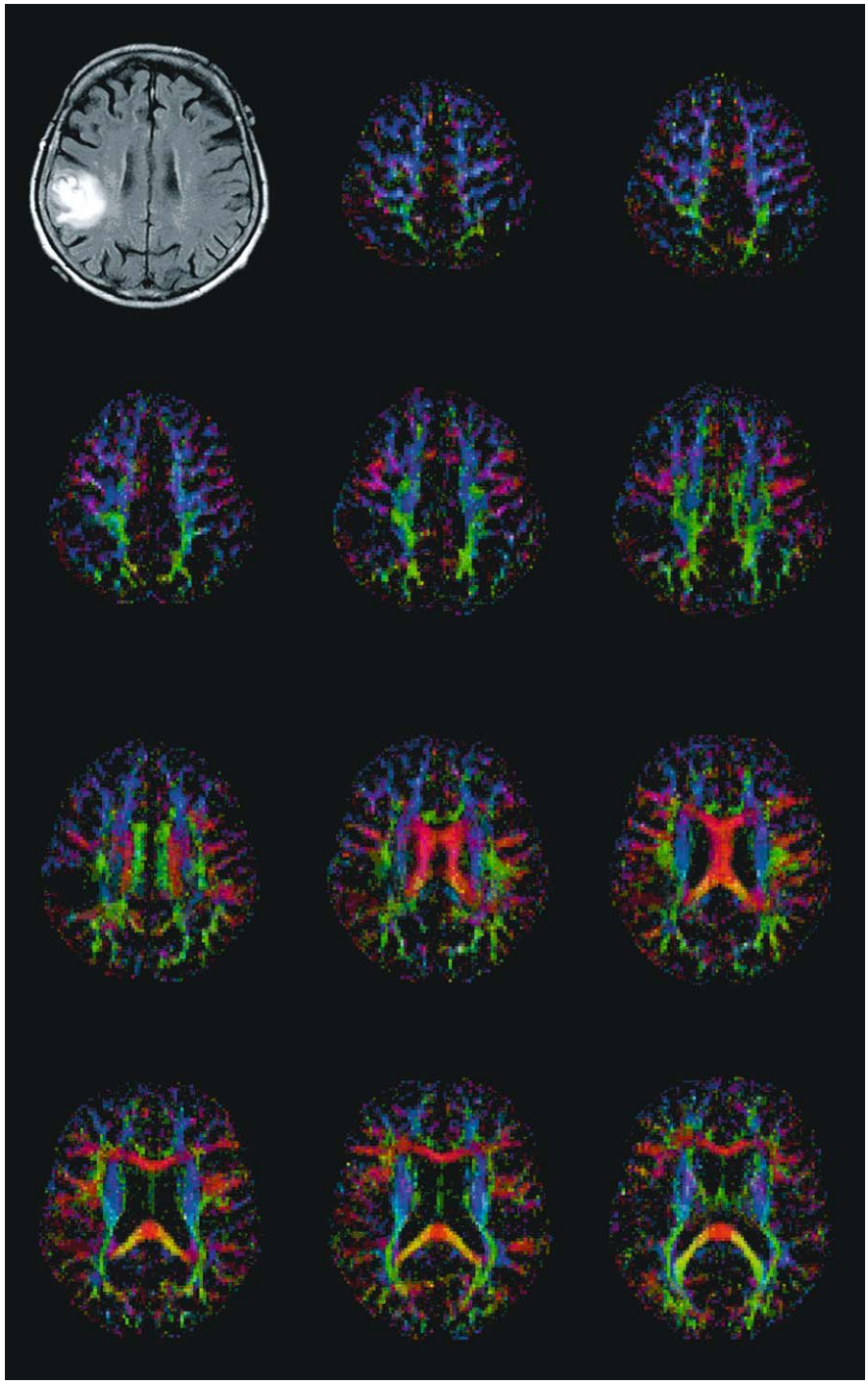

Fig. 8.9. Axial FLAIR image (*upper left*) compared with fractional anisotropy maps. DTI-based colour orientation map: *red* = *x* direction; *green* = *y* direction; *blue* = *z* direction. A tumour shown in the FLAIR image alters the course of surrounding fibres in several slices, as shown by the DTI data

based on the possibility of visualizing directly the connections among the brain areas activated during a given task and conceptually complements two other strategies that explore connectivity, i.e. functional connectivity (the study of how two cerebral areas tend to work in a correlated manner) and effective connectivity (the study of the information flow within an active pattern by identifying its direction and orientation). Anatomical connectivity is essential, because it provides evidence for the existence of anatomical connections, which are indispensable elements to confirm and validate the results of functional and effective connectivity studies. An example is the study of the connectivity of the dopaminergic system, which originates in substantia nigra neurons in the pars compacta of the mesencephalon. Tractography has recently made it possible to

identify the course of human dopaminergic fibres as far as the corpus striatum (nigro-striatal circuit) and their subsequent cortical distribution (cortico-striatal circuit) [43] (Fig. 8.8).

The utilization of this method in neurological investigations is obvious, especially in degenerative CNS disease. In Parkinson's disease, MR has a limited role except in the differential diagnosis from other diseases, since its diagnosis is essentially clinical and thus cannot be made early. By identifying the dopaminergic fibres at their origin, tractography can quantify the axonal depletion and thus provide an index of disease severity. Another common degenerative disease, Alzheimer's, is characterized already in its early phase by a depletion of temporo-mesial neurons, which can be identified with tractography [50 – 58].

In neurophysiology, electrophysiological data – indirect indicators of fibre integrity – could be better interpreted using tractography, which is capable of displaying fibre tracts directly. For instance, corticospinal fibres can be identified and reconstructed with tractography from their origin through the centrum semiovale, corona radiata, internal capsule and cerebral peduncle. Identification of this bundle is important in neurological diseases like multiple sclerosis, where demyelination and the consequent axon damage even at a distance from the lesion site can be documented and quantified using these techniques [59 – 74].

In neurosurgery, knowledge of the course of nerve fibre bundles (Fig. 8.9) and their relationships to the expanding lesion can preserve them from resection [75 – 85].

Finally, tractography should be applied to identify and describe the brain plasticity phenomena secondary to CNS lesions. Identification of the axonal loss and consequent impairment of further adjacent or distant circuits, normally not involved in a given function, can offer insights into the complex phenomena underpinning clinical recovery and enable better targeted pharmacological and rehabilitation therapy [86 – 98].

8.6 Conclusion

We have described the main MR tractographic techniques, which enable in vivo and non-invasive reconstruction of the anatomy of axon fibres, documenting the connections among grey matter areas. Tractography is the natural complement of functional MR, which can depict the activation of these areas. Combined use of these techniques is expected to be performed with increasing frequency in the future [80, 83, 99, 100], and to yield useful results in the study of physiological and pathological CNS mechanisms, enabling better planning and quantification of therapeutic interventions.

References

1. Basser PJ, Jones DK (2002) Diffusion-tensor MRI: theory, experimental design and data analysis – a technical review. NMR Biomed 15:456 – 467
2. Basser PJ, Pajevic S, Pierpaoli C, et al. (2000) In vivo fiber tractography using DT-MRI data. Magn Reson Med 44: 625 – 632
3. Bammer R, Acar B, Moseley ME (2003) In vivo MR tractography using diffusion imaging. Eur J Radiol 45:223 – 234
4. Mori S, van Zijl PC (2002) Fiber tracking: principles and strategies – a technical review. NMR Biomed 15:468 – 480
5. Habas C (2004) [Basic principles of diffusion tensor MR tractography]. J Radiol 85:281 – 286
6. Conturo TE, Lori NF, Cull TS, et al. (1999) Tracking neuronal fiber pathways in the living human brain. Proc Natl Acad Sci U S A 96:10422 – 10427
7. Beaulieu C (2002) The basis of anisotropic water diffusion in the nervous system – a technical review. NMR Biomed 15:435 – 455
8. Moseley ME, Cohen Y, Kucharczyk J, et al. (1990) Diffusion-weighted MR imaging of anisotropic water diffusion in cat central nervous system. Radiology 176:439 – 445
9. Le Bihan D, Mangin JF, Poupon C, et al. (2001) Diffusion tensor imaging: concepts and applications. J Magn Reson Imaging 13:534 – 546
10. Basser PJ, Mattiello J, LeBihan D (1994) MR diffusion tensor spectroscopy and imaging. Biophys J 66:259 – 267
11. Basser PJ, Mattiello J, LeBihan D (1994) Estimation of the effective self-diffusion tensor from the NMR spin echo. J Magn Reson B 103:247 – 254
12. Batchelor PG, Moakher M, Atkinson D, et al. (2005) A rigorous framework for diffusion tensor calculus. Magn Reson Med 53:221 – 225
13. Parker GJ (2004) Analysis of MR diffusion weighted images. Br J Radiol 77 Spec No 2:S176 – 185
14. Lori NF, Akbudak E, Shimony JS, et al. (2002) Diffusion tensor fiber tracking of human brain connectivity: acquisition methods, reliability analysis and biological results. NMR Biomed 15:494 – 515
15. Assaf Y, Freidlin RZ, Rohde GK, et al. (2004) New modeling and experimental framework to characterize hindered and restricted water diffusion in brain white matter. Magn Reson Med 52:965 – 978
16. Nagae-Poetscher LM, Jiang H, Wakana S, et al. (2004) High-resolution diffusion tensor imaging of the brain stem at 3 T. AJNR 25:1325 – 1330
17. Burdette JH, Elster AD, Ricci PE (1998) Calculation of apparent diffusion coefficients (ADCs) in brain using two-point and six-point methods. J Comput Assist Tomogr 22:792 – 794
18. Xing D, Papadakis NG, Huang CL, et al. (1997) Optimised diffusion weighting for measurement of apparent diffusion coefficient (ADC) in human brain. Magn Reson Imaging 15:771 – 784
19. Melhem ER, Mori S, Mukundan G, et al. (2002) Diffusion tensor MR imaging of the brain and white matter tractography. AJR 178:3 – 16
20. Xue R, van Zijl PC, Crain BJ, et al. (1999) In vivo three-dimensional reconstruction of rat brain axonal projections by diffusion tensor imaging. Magn Reson Med 42:1123 – 1127
21. Mori S, Crain BJ, Chacko VP, et al. (1999) Three-dimensional tracking of axonal projections in the brain by magnetic resonance imaging. Ann Neurol 45:265 – 269
22. Parker GJ, Stephan KE, Barker GJ, et al. (2002) Initial demonstration of in vivo tracing of axonal projections in the macaque brain and comparison with the human brain us-

ing diffusion tensor imaging and fast marching tractography. Neuroimage 15:797 – 809
23. Parker GJ, Wheeler-Kingshott CA, Barker GJ (2002) Estimating distributed anatomical connectivity using fast marching methods and diffusion tensor imaging. IEEE Trans Med Imaging 21:505 – 512
24. Ciccarelli O, Toosy AT, Parker GJ, et al. (2003) Diffusion tractography based group mapping of major white-matter pathways in the human brain. Neuroimage 19:1545 – 1555
25. Duncan JS, Papademetris X, Yang J, et al. (2004) Geometric strategies for neuroanatomic analysis from MRI. Neuroimage 23(1):S34 – 45
26. Parker GJ, Alexander DC (2003) Probabilistic Monte Carlo based mapping of cerebral connections utilising whole-brain crossing fibre information. Inf Process Med Imaging 18:684 – 695
27. Parker GJ, Haroon HA, Wheeler-Kingshott CA (2003) A framework for a streamline-based probabilistic index of connectivity (PICo) using a structural interpretation of MRI diffusion measurements. J Magn Reson Imaging 18: 242 – 254
28. Behrens TE, Woolrich MW, Jenkinson M, et al. (2003) Characterization and propagation of uncertainty in diffusion-weighted MR imaging. Magn Reson Med 50:1077 – 1088
29. Wu YC, Field AS, Chung MK, et al. (2004) Quantitative analysis of diffusion tensor orientation: theoretical framework. Magn Reson Med 52:1146 – 1155
30. Jones DK, Basser PJ (2004) „Squashing peanuts and smashing pumpkins“: how noise distorts diffusion-weighted MR data. Magn Reson Med 52:979 – 993
31. Jones DK (2003) Determining and visualizing uncertainty in estimates of fiber orientation from diffusion tensor MRI. Magn Reson Med 49:7 – 12
32. Anderson AW (2001) Theoretical analysis of the effects of noise on diffusion tensor imaging. Magn Reson Med 46:1174 – 1188
33. Lazar M, Weinstein DM, Tsuruda JS, et al. (2003) White matter tractography using diffusion tensor deflection. Hum Brain Mapp 18:306 – 321
34. Huang H, Zhang J, van Zijl PC, et al. (2004) Analysis of noise effects on DTI-based tractography using the brute-force and multi-ROI approach. Magn Reson Med 52:559 – 565
35. Heim S, Hahn K, Samann PG, et al. (2004) Assessing DTI data quality using bootstrap analysis. Magn Reson Med 52:582 – 589
36. Alexander AL, Hasan KM, Lazar M, et al. (2001) Analysis of partial volume effects in diffusion-tensor MRI. Magn Reson Med 45:770 – 780
37. Barrick TR, Clark CA (2004) Singularities in diffusion tensor fields and their relevance in white matter fiber tractography. Neuroimage 22:481 – 491
38. Ozarslan E, Mareci TH (2003) Generalized diffusion tensor imaging and analytical relationships between diffusion tensor imaging and high angular resolution diffusion imaging. Magn Reson Med 50:955 – 965
39. Tuch DS, Reese TG, Wiegell MR, Wedeen VJ (2003) Diffusion MRI of complex neural architecture. Neuron 40:885 – 895
40. Tuch DS (2004) Q-ball imaging. Magn Reson Med 52: 1358 – 1372
41. Tournier JD, Calamante F, Gadian DG, et al. (2004) Direct estimation of the fiber orientation density function from diffusion-weighted MRI data using spherical deconvolution. Neuroimage 23:1176 – 1185
42. Mori H, Masutani Y, Aoki S, et al. (2003) Simple visualization of the corticospinal pathway using tractography: one-ROI and two-ROI methods. Nippon Igaku Hoshasen Gakkai Zasshi 63:51 – 53
43. Lehericy S, Ducros M, Van de Moortele PF, et al. (2004) Diffusion tensor fiber tracking shows distinct corticostriatal circuits in humans. Ann Neurol 55:522 – 529
44. Ciccarelli O, Parker GJ, Toosy AT, et al. (2003) From diffusion tractography to quantitative white matter tract measures: a reproducibility study. Neuroimage 18:348 – 359
45. Catani M, Jones DK, Donato R, et al. (2003) Occipito-temporal connections in the human brain. Brain 126:2093 – 2107
46. Holodny AI, Gor DM, Watts R, et al. (2005) Diffusion-tensor MR tractography of somatotopic organization of corticospinal tracts in the internal capsule: initial anatomic results in contradistinction to prior reports. Radiology 234:649 – 653
47. Kier EL, Staib LH, Davis LM, et al. (2004) Anatomic dissection tractography: a new method for precise MR localization of white matter tracts. AJNR 25:670 – 676
48. Oppenheim C, Rodrigo S, Poupon C, et al. (2004) Diffusion tensor MR imaging of the brain. Clinical applications. J Radiol 85:287 – 296
49. Sundgren PC, Dong Q, Gomez-Hassan D, et al. (2004) Diffusion tensor imaging of the brain: review of clinical applications. Neuroradiology 46:339 – 350
50. Rose SE, Chen F, Chalk JB, et al. (2000) Loss of connectivity in Alzheimer's disease: an evaluation of white matter tract integrity with colour coded MR diffusion tensor imaging. J Neurol Neurosurg Psychiatry 69:528 – 530
51. Bozzali M, Franceschi M, Falini A, et al. (2001) Quantification of tissue damage in AD using diffusion tensor and magnetization transfer MRI. Neurology 57:1135 – 1137
52. Bozzali M, Falini A, Franceschi M, et al. (2002) White matter damage in Alzheimer's disease assessed in vivo using diffusion tensor magnetic resonance imaging. J Neurol Neurosurg Psychiatry 72:742 – 746
53. Horsfield MA, Jones DK (2002) Applications of diffusion-weighted and diffusion tensor MRI to white matter diseases – a review. NMR Biomed 15:570 – 577
54. Larsson EM, Englund E, Sjobeck M, et al. (2004) MRI with diffusion tensor imaging post-mortem at 3.0 T in a patient with frontotemporal dementia. Dement Geriatr Cogn Disord 17:316 – 319
55. Sugihara S, Kinoshita T, Matsusue E, et al. (2004) Usefulness of diffusion tensor imaging of white matter in Alzheimer disease and vascular dementia. Acta Radiol 45:658 – 663
56. Sun Y, Du XK, Zhang ZX, et al. (2004) Relationship between the data from MR-diffusion tensor imaging and the clinical cognitive evaluation in Alzheimer's disease. Zhongguo Yi Xue Ke Xue Yuan Xue Bao 26:134 – 138
57. Yoshida T, Shiga K, Yoshikawa K, et al. (2004) White matter loss in the splenium of the corpus callosum in a case of posterior cortical atrophy: a diffusion tensor imaging study. Eur Neurol 52:77 – 81
58. Sullivan EV, Pfefferbaum A (2003) Diffusion tensor imaging in normal aging and neuropsychiatric disorders. Eur J Radiol 45:244 – 255
59. Rovaris M, Gallo A, Valsasina P, et al. (2005) Short-term accrual of gray matter pathology in patients with progressive multiple sclerosis: an in vivo study using diffusion tensor MRI. Neuroimage 24:1139 – 1146
60. Hong YH, Lee KW, Sung JJ, et al. (2004) Diffusion tensor MRI as a diagnostic tool of upper motor neuron involvement in amyotrophic lateral sclerosis. J Neurol Sci 227:73 – 78
61. Yin H, Lim CC, Ma L, et al. (2004) Combined MR spectroscopic imaging and diffusion tensor MRI visualizes corticospinal tract degeneration in amyotrophic lateral sclerosis. J Neurol 251:1249 – 1254

62. Abe O, Yamada H, Masutani Y, et al. (2004) Amyotrophic lateral sclerosis: diffusion tensor tractography and voxel-based analysis. NMR Biomed 17:411 – 416
63. Cassol E, Ranjeva JP, Ibarrola D, et al. (2004) Diffusion tensor imaging in multiple sclerosis: a tool for monitoring changes in normal-appearing white matter. Mult Scler 10:188 – 196
64. Ulug AM, Grunewald T, Lin MT, et al. (2004) Diffusion tensor imaging in the diagnosis of primary lateral sclerosis. J Magn Reson Imaging 19:34 – 39
65. Rashid W, Hadjiprocopis A, Griffin CM, et al. (2004) Diffusion tensor imaging of early relapsing-remitting multiple sclerosis with histogram analysis using automated segmentation and brain volume correction. Mult Scler 10:9 – 15
66. Sach M, Winkler G, Glauche V, et al. (2004) Diffusion tensor MRI of early upper motor neuron involvement in amyotrophic lateral sclerosis. Brain 127:340 – 350
67. Ciccarelli O, Werring DJ, Barker GJ, et al. (2003) A study of the mechanisms of normal-appearing white matter damage in multiple sclerosis using diffusion tensor imaging – evidence of Wallerian degeneration. J Neurol 250:287 – 292
68. Cercignani M, Bozzali M, Iannucci G, et al. (2002) Intravoxel and inter-voxel coherence in patients with multiple sclerosis assessed using diffusion tensor MRI. J Neurol 249:875 – 883
69. Tench CR, Morgan PS, Wilson M, et al. (2002) White matter mapping using diffusion tensor MRI. Magn Reson Med 47:967 – 972
70. Guo AC, MacFall JR, Provenzale JM (2002) Multiple sclerosis: diffusion tensor MR imaging for evaluation of normal-appearing white matter. Radiology 222:729 – 736
71. Filippi M, Rocca MA, Falini A, et al. (2002) Correlations between structural CNS damage and functional MRI changes in primary progressive MS. Neuroimage 15:537 – 546
72. Assaf Y, Ben-Bashat D, Chapman J, et al. (2002) High b-value q-space analyzed diffusion-weighted MRI: application to multiple sclerosis. Magn Reson Med 47:115 – 126
73. Horsfield MA, Larsson HB, Jones DK, et al. (1998) Diffusion magnetic resonance imaging in multiple sclerosis. J Neurol Neurosurg Psychiatry 64(1):S80 – 84
74. Castriota Scanderbeg A, Tomaiuolo F, Sabatini U, et al. (2000) Demyelinating plaques in relapsing-remitting and secondary-progressive multiple sclerosis: assessment with diffusion MR imaging. AJNR 21:862 – 868
75. Nimsky C, Ganslandt O, Hastreiter P, et al. (2005) Intraoperative diffusion-tensor MR imaging: shifting of white matter tracts during neurosurgical procedures – initial experience. Radiology 234:218 – 225
76. Wu JS, Zhou LF, Hong XN, et al. (2003) Role of diffusion tensor imaging in neuronavigation surgery of brain tumors involving pyramidal tracts. Zhonghua Wai Ke Za Zhi 41:662 – 666
77. Clark CA, Barrick TR, Murphy MM, et al. (2003) White matter fiber tracking in patients with space-occupying lesions of the brain: a new technique for neurosurgical planning? Neuroimage 20:1601 – 1608
78. Akai H, Mori H, Aoki S, et al. (2005) Diffusion tensor tractography of gliomatosis cerebri: fiber tracking through the tumor. J Comput Assist Tomogr 29:127 – 129
79. Nimsky C, Ganslandt O, Hastreiter P, et al. (2005) Preoperative and intraoperative diffusion tensor imaging-based fiber tracking in glioma surgery. Neurosurgery 56:130 – 138
80. Parmar H, Sitoh YY, Yeo TT (2004) Combined magnetic resonance tractography and functional magnetic resonance imaging in evaluation of brain tumors involving the motor system. J Comput Assist Tomogr 28:551 – 556
81. Kier EL, Staib LH, Davis LM, et al. (2004) MR imaging of the temporal stem: anatomic dissection tractography of the uncinate fasciculus, inferior occipitofrontal fasciculus, and Meyer's loop of the optic radiation. AJNR 25:677 – 691
82. Barboriak DP (2003) Imaging of brain tumors with diffusion-weighted and diffusion tensor MR imaging. Magn Reson Imaging Clin N Am 11:379 – 401
83. Guye M, Parker GJ, Symms M, et al. (2003) Combined functional MRI and tractography to demonstrate the connectivity of the human primary motor cortex in vivo. Neuroimage 19:1349 – 1360
84. Holodny AI, Ollenschlager M (2002) Diffusion imaging in brain tumors. Neuroimaging Clin N Am 12:107 – 124
85. Holodny AI, Schwartz TH, Ollenschleger M, et al. (2001) Tumor involvement of the corticospinal tract: diffusion magnetic resonance tractography with intraoperative correlation. J Neurosurg 95:1082
86. Le TH, Mukherjee P, Henry RG, et al. (2005) Diffusion tensor imaging with three-dimensional fiber tractography of traumatic axonal shearing injury: an imaging correlate for the posterior callosal „disconnection" syndrome: case report. Neurosurgery 56:189
87. Naganawa S, Sato C, Ishihra S, et al. (2004) Serial evaluation of diffusion tensor brain fiber tracking in a patient with severe diffuse axonal injury. AJNR 25:1553 – 1556
88. Huisman TA, Schwamm LH, Schaefer PW, et al. (2004) Diffusion tensor imaging as potential biomarker of white matter injury in diffuse axonal injury. AJNR 25:370 – 376
89. Huisman TA, Sorensen AG, Hergan K, et. al. (2003) Diffusion-weighted imaging for the evaluation of diffuse axonal injury in closed head injury. J Comput Assist Tomogr 27:5 – 11
90. Arfanakis K, Haughton VM, Carew JD, et al. (2002) Diffusion tensor MR imaging in diffuse axonal injury. AJNR 23:794 – 802
91. Konishi J, Yamada K, Kizu O, et al. (2005) MR tractography for the evaluation of functional recovery from lenticulostriate infarcts. Neurology 64:108 – 113
92. Yamada K, Ito H, Nakamura H, et al. (2004) Stroke patients' evolving symptoms assessed by tractography. J Magn Reson Imaging 20:923 – 929
93. Munoz Maniega S, Bastin ME, Armitage PA, et al. (2004) Temporal evolution of water diffusion parameters is different in grey and white matter in human ischaemic stroke. J Neurol Neurosurg Psychiatry 75:1714 – 1718
94. Thomalla G, Glauche V, Koch MA, et al. (2004) Diffusion tensor imaging detects early Wallerian degeneration of the pyramidal tract after ischemic stroke. Neuroimage 22:1767 – 1774
95. Huisman TA (2003) Diffusion-weighted imaging: basic concepts and application in cerebral stroke and head trauma. Eur Radiol 13:2283 – 2297
96. Kunimatsu A, Aoki S, Masutani Y, et al. (2003) Three-dimensional white matter tractography by diffusion tensor imaging in ischaemic stroke involving the corticospinal tract. Neuroradiology 45:532 – 535
97. Sotak CH (2002) The role of diffusion tensor imaging in the evaluation of ischemic brain injury – a review. NMR Biomed 15:561 – 569
98. Huisman TA, Hawighorst H, Benoit CH, et al. (2001) Diffusion weighted MRI: ischemic and traumatic injuries of the central nervous system. Radiologe 41:1038 – 1047
99. Johansen-Berg H, Behrens TE, Sillery E, et al. (2005) Functional-anatomical validation and individual variation of diffusion tractography-based segmentation of the human thalamus. Cereb Cortex 15:31 – 39
100. Toosy AT, Ciccarelli O, Parker GJ, et al. (2004) Characterizing function-structure relationships in the human visual system with functional MRI and diffusion tensor imaging. Neuroimage 21:1452 – 1463

3.0 T Perfusion Studies

9

G. M. Giannatempo, T. Scarabino, A. Simeone, T. Popolizio, A. Stranieri, M. Armillotta, U. Salvolini

Cerebral perfusion is the process by which oxygen and glucose are supplied to the brain capillaries through the circulation. Disruption of brain perfusion is found in nearly all types of brain disease, most notably stroke, but also in neurodegenerative and neoplastic disorders [1–8].

Imaging the regional distribution of cerebral blood flow quantitatively is a diagnostic and technical challenge [3, 7, 9]. $H_2{}^{15}O$ positron emission tomography (PET), which uses a freely diffusible tracer and can quantitate blood flow with relative insensitivity to vascular transit time variations, is currently the gold standard of perfusion studies [7, 10].

However, it is an expensive examination entailing radioactive dosing and invasive monitoring, besides having low intrinsic spatial resolution. Moreover, $H_2{}^{15}O$ PET imaging centres are relatively few due to difficulties in staffing and maintaining an onsite cyclotron. Hence the interest in adapting more widespread imaging modalities, such as magnetic resonance imaging (MRI), to the quantitative measurement of blood flow.

MR perfusion imaging is increasingly being used for the assessment of brain perfusion in several different pathological conditions including ischaemic stroke [8, 11–15], neurovascular disease [16–19], brain tumours [20–28] and neurodegenerative disorders [29–35]. In brain tumours, perfusion MRI has been applied to grade gliomas [26, 27, 35], to distinguish between different tumour types, like primary tumour from solitary metastases or lymphoma [23, 28], to differentiate radiation necrosis from recurrent tumour [2], and to discriminate high-grade neoplasms from non-neoplastic lesions like abscess [24].

Perfusion MRI has been used in the diagnosis of dementia, including Alzheimer's disease, mild cognitive impairment and non-Alzheimer's dementia [29–34], epilepsy [35] and multiple sclerosis [36].

Unlike angiography, which depicts flow within large vessels, MR perfusion techniques are sensitive to perfusion at such microscopic levels as the capillary bed.

Measurement of tissue perfusion depends on the ability to measure serially the concentration of a tracer in a target organ. Tracers can be divided into exogenous and endogenous. The former include iced saline solution, iodinated radiographic contrast material and, more recently, paramagnetic contrast agents; magnetically labelled blood is currently the sole available endogenous tracer [1, 3]. Obtaining haemodynamic parameters from serial measurements of tissue tracer concentrations requires use of a general model of the way in which the tracer passes through or diffuses in the target organ that takes into account tracer diffusibility from intravascular to extravascular space, volume of distribution, equilibrium and half-life.

9.1 Exogenous Methods: Dynamic Susceptibility Contrast

Exogenous tracer methods for perfusion MRI use a model assuming that the tracer is confined to the intravascular compartment and does not diffuse to the extravascular space [1, 3–5].

Imaging can be obtained either dynamically (rapid imaging over time after a bolus injection) or, less frequently, in the steady state (after constant infusion has achieved an equilibrium concentration of the tracer in the blood) [1–5].

With steady-state techniques, a baseline image is acquired before injection and a post-infusion image is obtained up to 30 min after slow administration of the agent (i.e. during the steady state) [1]. Subtraction of the baseline from the post-contrast image allows a map of absolute blood volume to be obtained. This method is not very common due to its inherently low signal-to-noise ratio (SNR) and the fact that patient movement between scans can affect accuracy [1].

Dynamic susceptibility contrast perfusion MRI (DSC), also called dynamic contrast-enhanced perfusion MRI, dynamic susceptibility-weighted perfusion imaging, perfusion-weighted imaging, or first-pass bolus tracking perfusion MRI, is the most widespread, clinically applicable MR technique for estimating cerebral haemodynamic parameters, especially in stroke, but also for tumour imaging and other research applications.

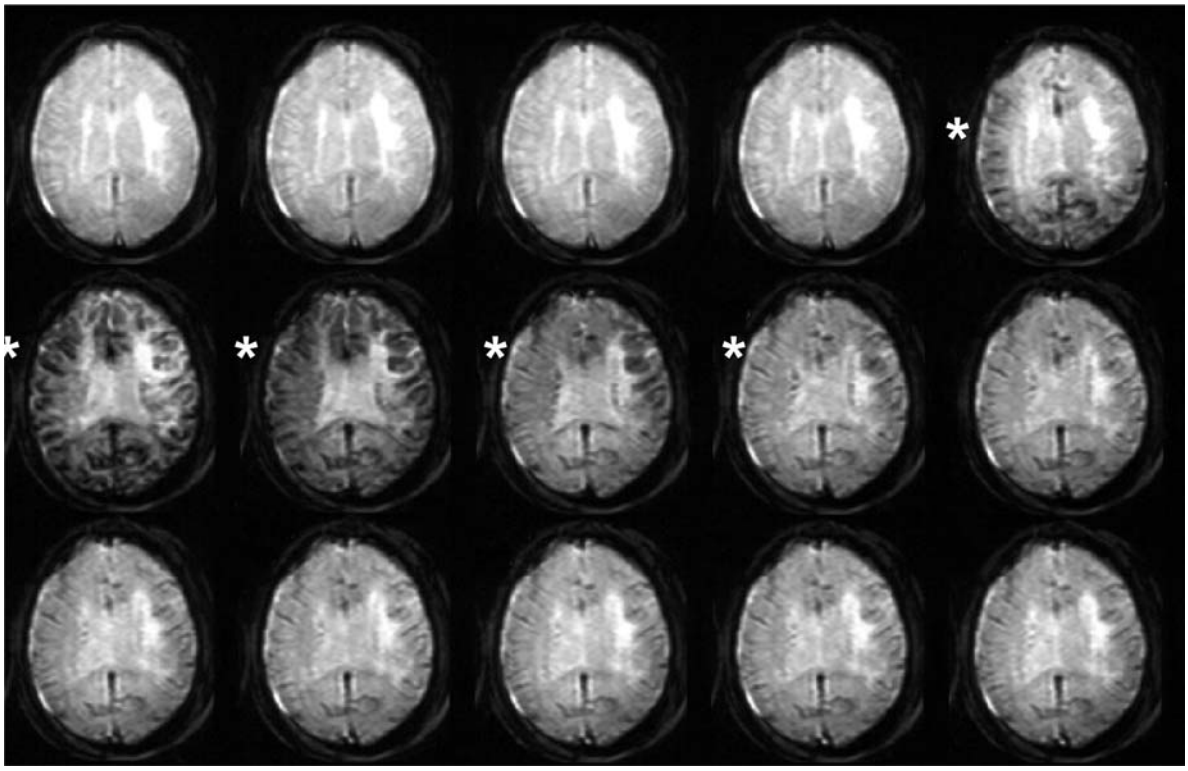

Fig. 9.1. Series of T2*-weighted images from a single axial slice during the passage of a bolus of contrast agent. When the bolus arrives it produces signal attenuation (*)

This technique is based on the passage of a bolus of contrast medium through the arterial and capillary circulation and on the transient changes it produces in vessels and surrounding tissues (Fig. 9.1).

Under normal perfusion conditions, in the presence of an intact blood brain barrier (BBB), the contrast medium remains confined within the vascular network and does not diffuse in the extravascular space. While passing through the cerebral vasculature, a short bolus of contrast material produces local magnetic field inhomogeneities that lead to a reduction in the transverse relaxation time of the tissue. This susceptibility effect can be recorded by a series of ultra-fast T2*- or T2-weighted sequences using gradient-echo and spin-echo sequences, respectively. The signal intensity-time curves can be converted to concentration-time curves, which allow the calculation of haemodynamic parameters such as blood volume, blood flow and transit time (Fig. 9.2).

In pathological perfusion conditions, e.g. hyperacute ischaemic lesion, the signal reduction is attenuated or delayed whereas in brain tumour the signal varies in relation to grade.

Perfusion imaging requires: (1) rapid administration of the contrast agent; (2) acquisition of ultra-fast sequences; and (3) post-processing of the native images to calculate the intensity-time curve and obtain perfusion maps.

1. Infusion of the gadolinium-chelated agent must be as rapid as possible to ensure correct mixing of the agent with blood and a sharp signal drop profile. This requires using a large intravenous line (18 or, preferably, 16 gauge), an automatic injector and high infusion velocity (5 ml/s) and doses of 0.2 mmol/kg (or less at 3.0 T, see below).
2. Imaging sequences must be sufficiently fast to allow accurate measurement of the rapidly changing signal from the first pass of the bolus and have adequate temporal resolution (< 2 s for the entire brain) [1]. The most widely applied imaging sequences for these studies are T2*-weighted gradient-echo single-shot echo-planar imaging (EPI) and T2-weighted spin-echo EPI.
Spin-echo EPI sequences display excellent sensitivity for the susceptibility effect produced by 5 μm capillaries. Gradient-echo EPI sequences are generally more sensitive up to a vessel diameter of 7 μm. Spin-echo sequences are thus inherently weighted towards the microvasculature and are therefore less sensitive to larger vessels.
Gradient-echo EPI sequences are currently those used most frequently [37 – 40]. They are characterized by superior sensitivity in detecting the signal change produced by the passage of the contrast material and therefore require smaller doses of the

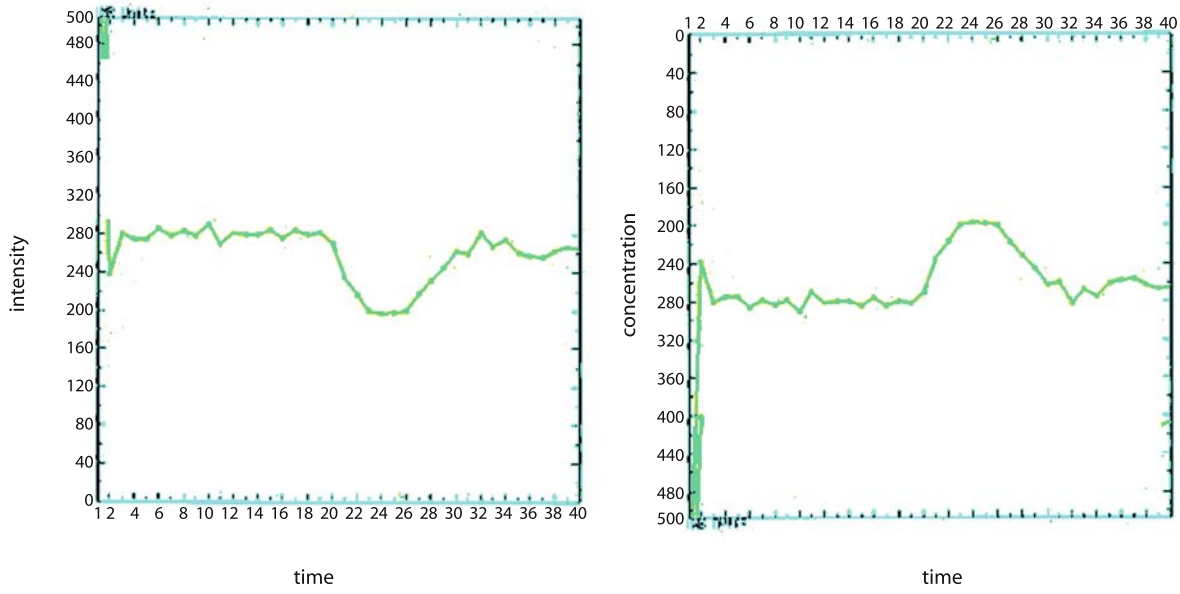

Fig. 9.2. The inversion proportion between signal drop and concentration of contrast agent permits the calculation of the relative concentration from the signal intensity curve

agent. Their drawback is their high sensitivity not only to the microvasculature but also to the macrovasculature, including large arteries and veins on the brain surface. Susceptibility effects are elicited not only by the passage of contrast material, but also by haemoglobin degradation products, the interfaces between different tissues and age-related iron accumulation in the extrapyramidal nuclei. These effects are much more pronounced at high field intensities [40].

An alternative to T2- or T2*-sequences are T1-weighted 3D spoiled gradient-echo sequences, which give rise to relaxivity, rather than susceptibility effects. The relaxivity effect of paramagnetic contrast agents results in a shortening of T1 relaxation time (yielding higher signal on T1), whereas the susceptibility effect shortens both T2 and T2* (giving lower signal on T2 or T2*) [1].

Because the relaxivity effects are much stronger than the susceptibility effects, T1-weighted sequences require a smaller amount of contrast agent (approximately 10 %) compared with T2 or T2* weighted sequences, allowing multiple repeated studies [1].

The main disadvantage of T1-weighted techniques is that the effects of BBB disruption are much greater than with T2- and T2*-weighted sequences [1, 3].

3. The decrease in signal intensity produced by the passage of a bolus of gadolinium chelate allows a signal intensity-time curve to be obtained by calculating the change in signal intensity in a single voxel (or in a single region of interest) as a function of time. This curve is then converted to an agent concentration-time curve.

The sum of all the concentration-time curves of all the voxels in a given slice generates perfusion maps from which various haemodynamic parameters can be calculated, including cerebral blood volume (CBV), cerebral blood flow (CBF), mean transit time (MTT) and time-to-peak (TTP) (Figs. 9.3, 9.4).

These parameters are dependent on the specific features of the bolus injection (injection rate, amount and concentration of contrast material) and on specific variables of the patient being imaged (total body vascular volume and cardiac output) [1, 3]. As a result, haemodynamic parameters cannot be directly compared between different subjects and may even differ between examinations of the same individual performed at different times [1, 3].

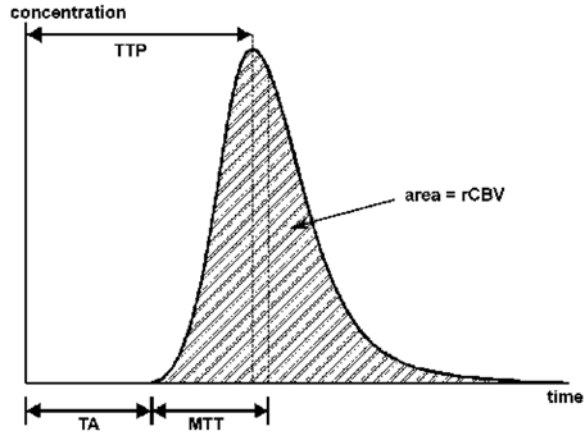

Fig. 9.3. Concentration-time curve (*rCBV* cerebral blood volume, *MTT* mean transit time, *TA* arrival time, *TTP* time-to-peak)

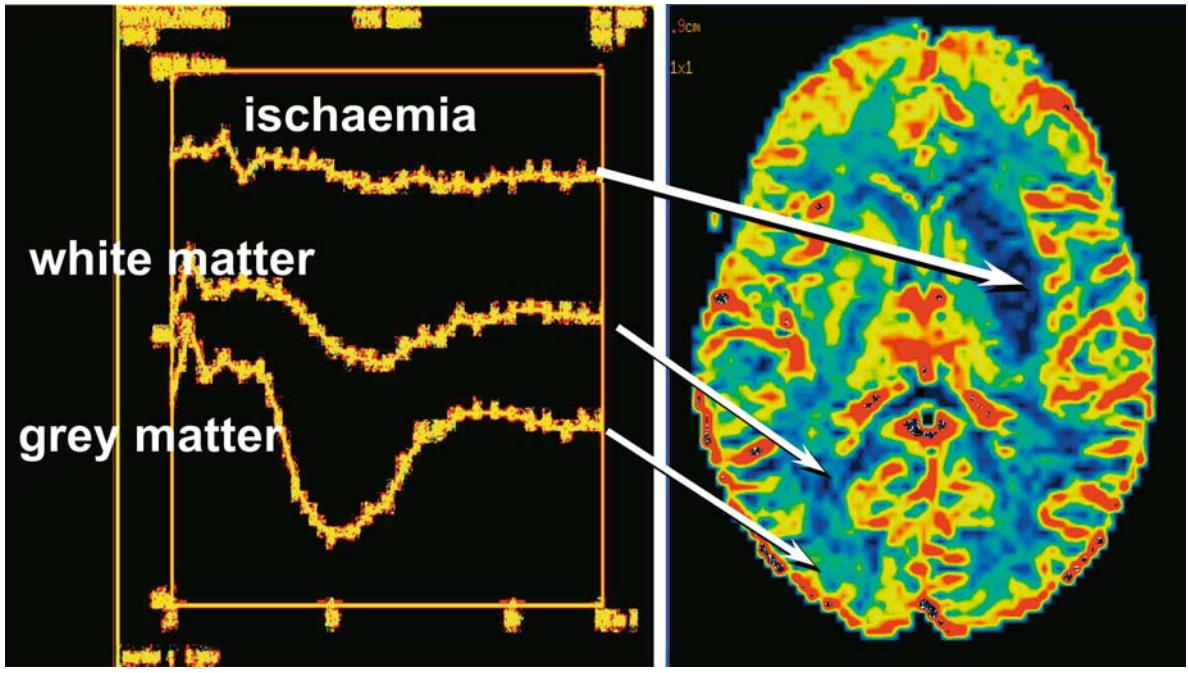

Fig. 9.4. CBV and MTT maps

Thus, relative values can be obtained using an internal standard of reference such as normal-appearing grey or white matter (Figs. 9.5, 9.6) [1, 3].

For diffuse processes, in which the internal reference may also be affected, absolute quantitation is required. Absolute quantitation of CBV and CBF has been attempted using methods that measure arterial input to the brain, but their accuracy is debated [1, 3].

9.1.1 Cerebral Blood Volume

Cerebral blood volume (CBV) is the fraction of each imaged voxel comprising the intravascular space, and therefore the volume of the blood vessels within a volume of brain tissue. It is measured as millilitres of blood per 100 g of tissue; since brain tissue approximates water in density (1 g/millilitre), this can also be expressed as a percent value.

Typical values for the brain are between 3% and 5%. Only a small fraction of CBV is arterial, most of it being divided between capillaries and veins, and its changes are related to autoregulatory vasodilatation of the capillaries and/or veins [6, 7, 38]. CBV is a potentially sensitive indicator of vascular endothelial response to changes in local CBF and tissue metabolism.

Relative CBV can be measured as the area under the curve of the voxel concentration versus time. Absolute CBV can be determined by dividing the area under the

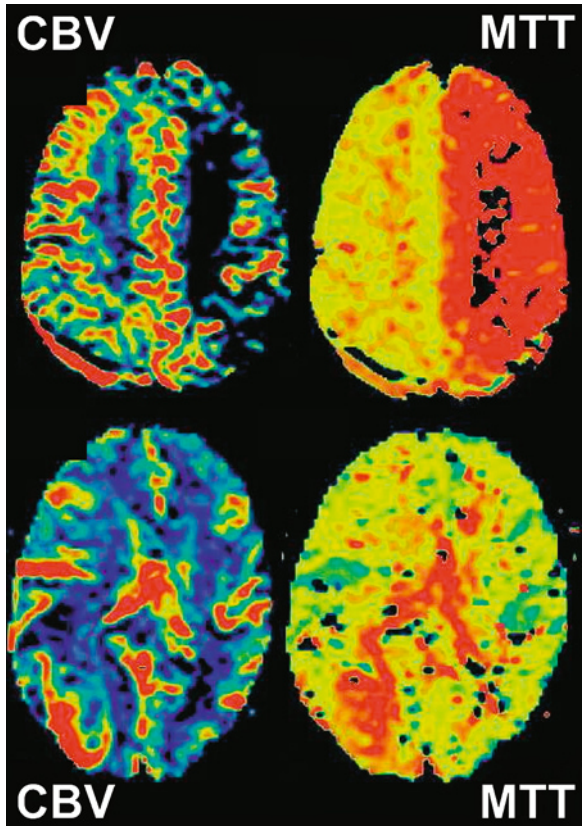

Fig. 9.5. Intensity-time curves are correlated to cerebral perfusion, better visualized in the CBV map: perfusion is greater in grey than in white matter and is reduced or absent in the ischaemic area

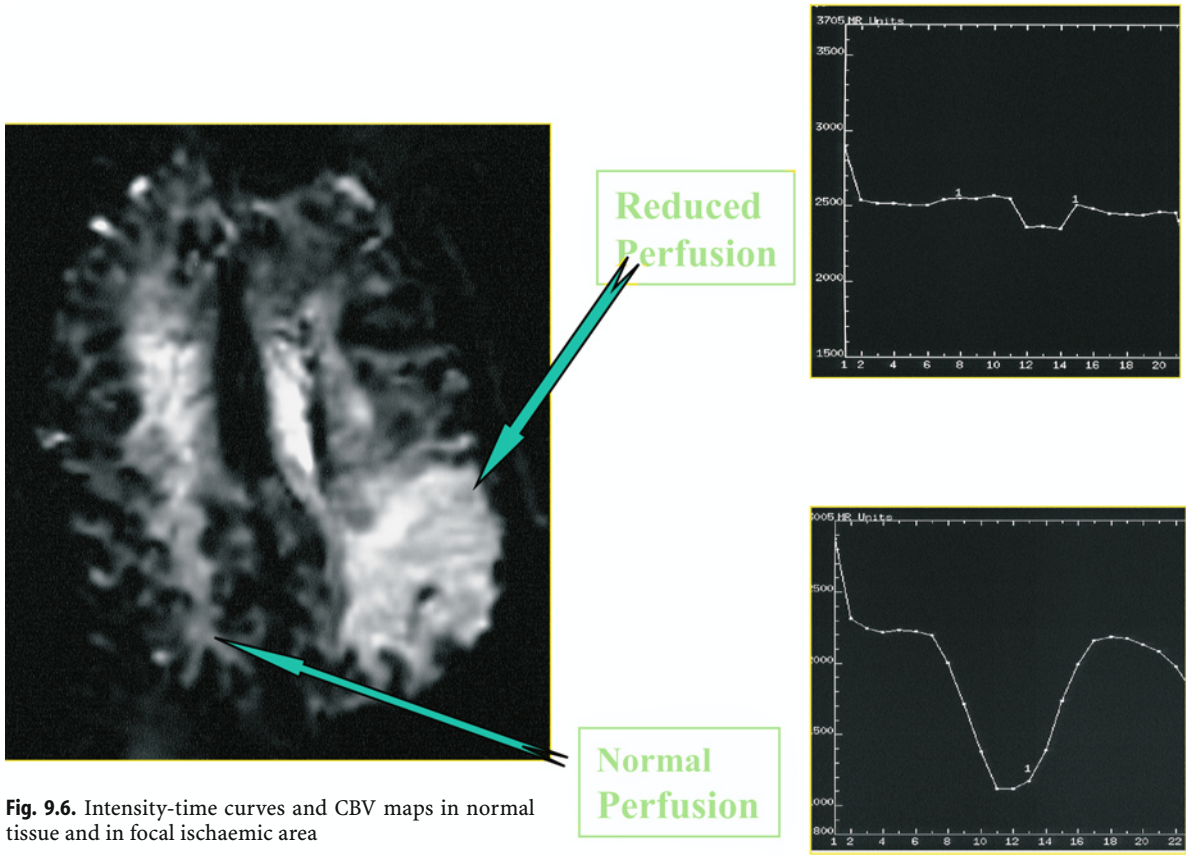

Fig. 9.6. Intensity-time curves and CBV maps in normal tissue and in focal ischaemic area

curve by a „reference" voxel known to contain 100% blood, such as the superior sagittal sinus [7, 39].

Unfortunately several technical factors can impair the accuracy of this relatively simple measurement [1, 3, 41]. The first is that dynamic susceptibility contrast arises from spin diffusion in the space surrounding the blood vessels, making it difficult to determine a reference 100% blood-filled voxel [41]. Secondly, the effects of contrast recirculation must be eliminated or minimized. Thirdly, CBV measurement can be erroneous if the gadolinium chelate leaks through a disrupted BBB. This is of particular concern when imaging tumours, since several tumours cause BBB disruption, yielding a bright signal on post-contrast T1 images [7, 42].

New molecules, such as superparamagnetic iron-oxide particles, dendritic compounds saturated with gadolinium atoms, or reversible protein-binding gadolinium-based agents have a longer half-life in blood [7, 43–45]. These so-called „blood pool" agents offer higher SNR for measuring CBV using steady-state susceptibility contrast that circumvents many of the problems outlined earlier.

9.1.2 Cerebral Blood Flow

Cerebral blood flow (CBF) is the amount of arterial blood delivered to brain tissue per unit of time. It is most commonly measured as millilitres of blood per 100 g of tissue per minute. Characteristic values for grey matter are 60 ml/min/100 g and 15 ml/min/100 g for white matter. CBF control is via control of the diameter of the feeding arterioles.

CBF is the primary rate constant controlling the supply of nutrients and removal of waste products from the brain. Below a threshold level, duration multiplied by the absolute CBF level can predict tissue infarction [7].

While CBV measurement with intravascular tracers is relatively straightforward, the measurement of CBF is more challenging [7, 46], as it requires delicate deconvolution methods.

In particular, one method tries to deconvolve the effects of a bolus of finite width (as estimated from the arterial signal near a large feeding vessel, such as the anterior communicating artery). This arterial input function is taken to represent the profile of the bolus at its point of entry into each individual voxel based on the assumption that every voxel has the same arterial input function. This is clearly an oversimplification, and un-

certainties about regional changes in the profile and timing of the bolus can cause significant errors in CBF evaluation [7, 47].

Good absolute CBF correlation with $H_2{}^{15}O$ PET has been shown in anaesthetized healthy pigs [48] and an excellent relative CBF correlation has been reported in an experimental model of ischaemia [49]. However, in diseased brain, where collateral pathways are more common, intravascular tracer CBF measurements that do not account for variations in bolus delay (caused by arterial stenoses and occlusions) and dispersion are inaccurate [7, 46, 59].

9.1.3 Mean Transit Time

Mean transit time (MTT) is the average amount of time the blood spends in the capillary bed. A capillary bed is made up of numerous capillaries of different lengths, so the time spent in the tissue has a distribution. The unit of measurement is seconds. Typical values for the normal brain are in the range of 3 – 5 s, whereas in acute cerebral infarction MTT is increased.

According to the central volume principle, it is important to note close relationship between the CBF, CBV, and MTT. This relationship is:

$$CBF = CBV/MTT$$

This relationship can easily be explained with the simple case of flow through a single capillary. Flow is defined as the motion of a volume of fluid over time and velocity as distance over time. If the distance is measured along the capillary vessel, and the velocity is the speed of the fluid in this vessel, this relationship can be multiplied by the cross-sectional area of the capillary. This converts the distance to a volume and the velocity to a flow.

9.1.4 Time-to-Peak

Time-to-peak (TTP) is the time the blood takes to reach the maximum intensity, from the start of the bolus injection to the peak concentration of contrast agent; it is defined as the time point of maximum intensity loss after the passage of the contrast agent. It is calculated in seconds and reveals any delays in transit time, enabling quick quantification of perfusion deficits. Ischaemic areas are characterized by a delay of tracer arrival and a TTP increase [6, 51, 52]. A study of patients with acute cerebral ischaemia postulated that TTP values of 0 – 3.5 s are related to normal perfusion, values ranging from 3.5 from 7 s may indicate a perfusion disorder, whereas values above 7 s indicate a high risk of ischaemic tissue injury and watershed infarcts in border zones [51].

Despite these difficulties in determining the absolute values of volume and flow, relative values of CBV and CBF are extremely useful in clinical practice, especially in stroke evaluation.

It is generally accepted that tissue with abnormalities on both perfusion and diffusion-weighted imaging has already undergone irreversible ischaemia.

However, tissue with perfusion abnormalities but normal diffusion is thought to be consistent with reversible ischaemia. This area of diffusion-perfusion mismatch, also called ischaemic penumbra, is a region of decreased perfusion that is potentially reversible because it is above the critical level for the maintenance of the Na^+ K^+-ATPase pump [1]. Exact evaluation of the tissue that can be rescued is critical in assessing the risk-benefit ratio of possible therapies, since patients with no mismatch are considered unlikely to benefit from thrombolytic therapy.

Time-dependent perfusion thresholds were first established using $H_2{}^{15}O$ PET to distinguish underperfused tissue evolving towards infarction (< 12 ml/min per 100 g) from penumbral flow with functionally compromised but viable tissue (12 – 20 ml/min per 100 g) [1 – 3].

The exact role of each haemodynamic parameter (CBV, CBF, MTT and TTP) in the correct evaluation of

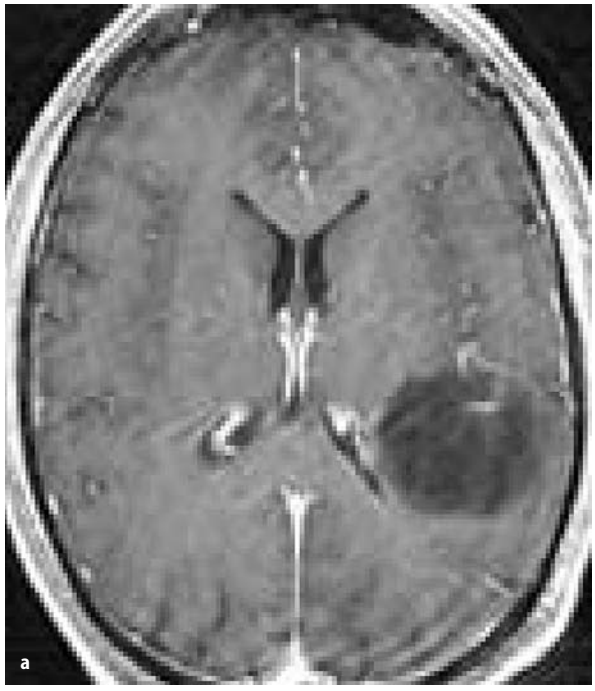

Fig. 9.7. a, b Low grade astrocytoma: SE T1 after contrast agent administration (**a**) and CBV map (**b**); **C, D** glioblastoma: SE T1 after contrast administration (**c**) and CBV map (**d**). The CBV is reduced in the low grade astrocytoma (**b**) and in the cystic component of the glioblastoma (**d**), whereas it is increased in the solid part of the glioblastoma (**d**)

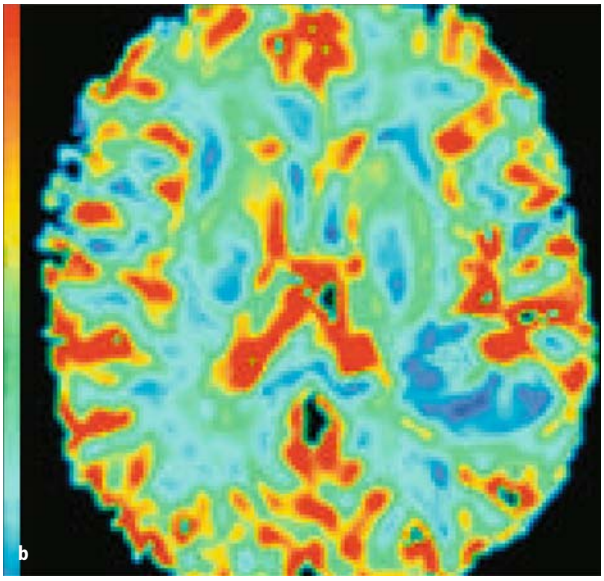

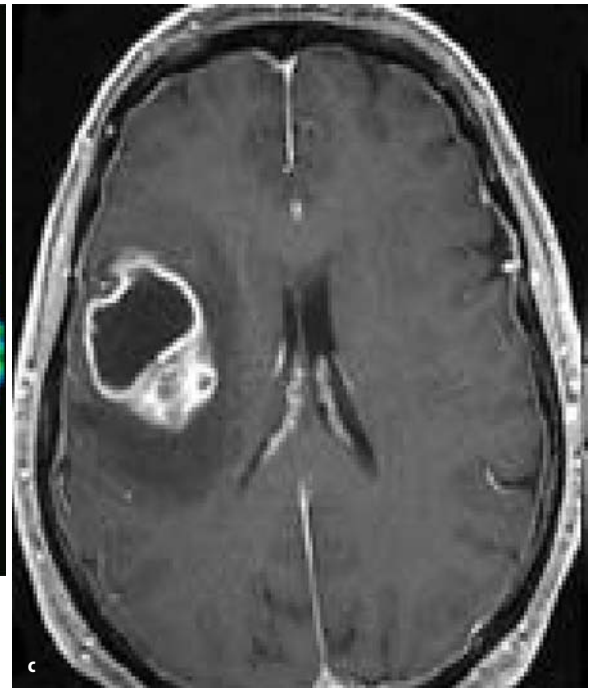

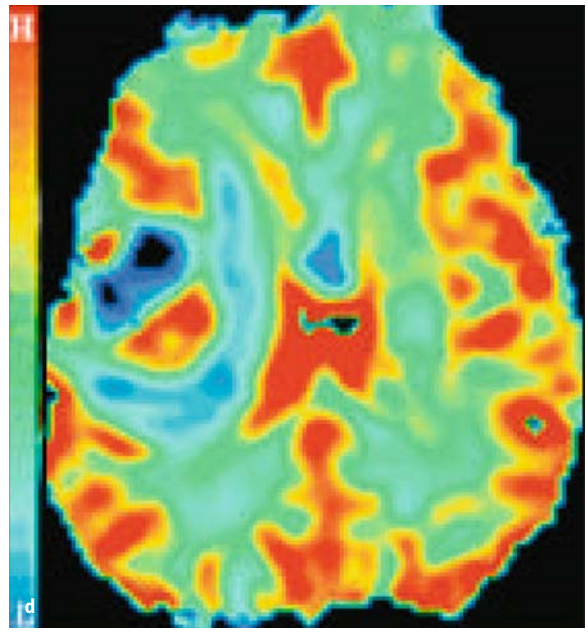

Fig. 9.7 (Cont.)

brain perfusion changes and which of them is more representative of salvageable tissue and predictive of final infarct size is still debated.

It appears that MTT maps generally show the largest area of abnormality and often overestimate final infarct size, while CBV maps tend to underestimate this size.

In one study comparing CBV maps, CBF maps, and MTT maps with change in size from initial infarct size to final infarct size, a mismatch between initial CBF maps and a diffusion abnormality predicted more often the growth of infarct than did a mismatch between initial CBV maps and diffusion abnormality [41]. In that study, however, CBV maps best correlated with change in infarct size from initial to follow-up imaging [41].

A recent study comparing TTP maps and thresholds in patients with acute ischaemia using CBF data acquired with PET, assumed as the gold standard, indicated that TTP is a useful estimate of ischaemic injury but entails considerable methodological limitations that have to be considered in routine use of MRI for stroke [52].

Relative TTP maps are only indirect surrogates of CBF and do not represent the best application of MRI perfusion imaging. They are used in clinical routine because they are simple, they clearly delineate haemodynamic alterations, yield satisfactory results compared with quantitative methods, and do not rely on deconvolution algorithms, calibration with PET data, or selection of adequate input functions [52].

However, TTP maps may be inappropriate, since simple visual analysis is more prone to errors related to individual subjectivity [52].

A quantitative observer-independent measure such as TTP thresholds has proved to be more indicative of underperfusion stated by PET for a CBF value of <20 ml/min per 100 g [52].

The best estimate of penumbral flow was found for a TTP delay of >4 s (sensitivity 84 %, specificity 77 %); it best identifies the volume of penumbra and should be used to define the mismatch volume. The volume of a TTP delay of >4 s correlated with clinical deficit, whereas the volume of a TTP delay between >5 and >8 s was strongly associated with infarct growth [52].

The lack of a complete match between PET and TTP thresholds is partly explained by method-specific properties. TTP only yields a relative estimation of CBF as it indicates the time point of maximum signal intensity loss during the passage of the tracer within several seconds. $H_2{}^{15}O$ PET assesses the „true" CBF as the concentration of a partly diffusible tracer integrated over a scanning time of several minutes. TTP data are therefore more prone to movement artefacts, collateral flow or individual haemodynamic properties [1, 52].

However, even the TTP threshold with the best sensitivity and specificity seems to include a large portion of tissue with only modest haemodynamic damage; particularly in small ischaemia TTP tends to overestimate the true extent of the „tissue at risk" [52].

9.2 High Field DSC

Currently, most MR perfusion studies are acquired on 1.5 T machines, but MR systems operating at higher field strengths are increasingly becoming available in clinical practice [4, 5, 8]. In general, imaging at higher magnetic field strengths offers at least a linear SNR increase, but its utilization is impaired by problems related to magnetic susceptibility artefacts.

Since magnetic susceptibility increases with field strength, at 3.0 T image distortion may be critical, particularly if EPI pulse sequences are used, as in most protocols for DSC perfusion studies. In fact, with EPI sequences the trade-off is increased B_0 inhomogeneity and magnetic susceptibility differences at air-tissue interfaces, leading to signal drop-out and geometric distortions, most notably in the phase encode direction [53].

Image quality may thus be severely impaired by distortion and blurring around tissues interfaces, especially in patients who have undergone neurosurgery, and assessment of signal intensity at the passage of a bolus of contrast agent may be inaccurate.

Other drawbacks inherent with T2* susceptibility are systematic overestimation of perfusion because of the different relaxivity of the paramagnetic contrast agent in the larger vessels (from which the input function is obtained) and in capillaries; problems in defining a good input function because of low spatial resolution on T2*-weighted EPI; and finally problems in assessing a damaged BBB. The latter is a critical element in the evaluation of brain tumour perfusion, because relaxivity is different when the contrast agent is confined to a small compartment as opposed to distributed in the interstitial space [54].

In order to minimize these negative effects, use of rapid 3D fast field-echo T1-weighted or 3D FLASH T1-weighted sequences has recently been proposed [54, 55]. Although acquisition is slower and yields less spatial and temporal resolution than EPI, FLASH seems to suffer less from spatial distortion than EPI, thus yielding a better arterial input function [55].

On the other hand, T2*-weighted contrast-enhanced perfusion imaging using 3.0 T systems offers some potential advantages. In particular, shorter T2 and T2* relaxation times and increased SNR [56, 57] may allow a greater T2* signal drop to be obtained for a given amount of contrast bolus during capillary passage [58].

A recent study of the feasibility of MR perfusion at 3.0 T demonstrated that image quality of the perfusion source images was not impaired, leading to rating distortion and blurring as minor in most images [8].

This was also true of critical anatomical areas, such as the posterior fossa and the regions close to the base of the skull (e.g. hippocampus and brainstem) [8]. This is probably due to use of a multi-shot echo-shifted three-dimensional gradient-echo echo-planar imaging sequence, in which the short echo train length may compensate for the field-dependent increase in susceptibility effects [8, 59–62].

Choice of correct echo time may also affect the performance of DSC perfusion imaging. A recent work comparing different echo times (ranging from 21 to 45 ms) in DSC perfusion in 17 patients demonstrated that the shortest echo time used yielded the best images [63].

Important benefits have recently been reported from using EPI sequences in DSC perfusion at 3.0 T with parallel imaging [37], also with the implementation of a multi-channel coil array [53], or with use of spin echo EPI, as an alternative to gradient echo EPI [64].

Parallel imaging (PI) techniques such as simultaneous acquisition of spatial harmonics (SMASH), sensitivity encoding (SENSE) or generalized autocalibrating partially parallel acquisition (GRAPPA) allow the shortening of scanning time by reducing the number of phase-encoding steps needed. Correct image reconstruction is achieved by inclusion of additional spatial information obtained from the spatial variation of coil sensitivity of multiple receiver coils. The reduction in encoding time can be used to achieve greater temporal resolution or to increase spatial resolution of the otherwise typically low-resolution dynamic scans [37].

The use of EPI sequences at 3.0 T is ideally suited for combination with PI techniques because the reduced echo train length results in several improvements.

The first benefit is reduction of image distortion and blurring from B_0 inhomogeneities produced by the interfaces between tissues and tissue boundaries or by haemorrhage products and surgical material after craniotomy. These image distortions are proportional to the off-resonance frequency produced by the inhomogeneities and inversely proportional to the time necessary to traverse the *k*-space. With PI the sensitivity of

EPI to any of these off-resonance artefacts, particularly significant at 3.0 T, can be reduced [37].

Another advantage is the reduction of the influence of T2* relaxation on spatial resolution, also referred to as *k*-space filtering. *k*-space filtering limits the resolution that can be achieved due to signal loss during spatial encoding. At 1.5 T a typical contrast agent reduces the T2* time of brain tissue to 20 – 40 ms. Therefore encoding steps performed after the actual T2* time contribute little to the *k*-space information and the image appears as if acquired at much lower resolution. Because of the shorter T2* relaxation at higher field intensities, this effect is even more pronounced at 3.0 T. This effect is also very important for the measurement of the arterial input function. With conventional EPI, the signal inside vessels vanishes completely and the arterial input function can be detected only around vessels.

Moreover, reduced shot duration in PI allows the acquisition of more slices in the same scanning time, enabling increased coverage of the region being investigated.

Finally, using interleaved EPI sequences, application of PI is also recommended for selecting an appropriate echo time.

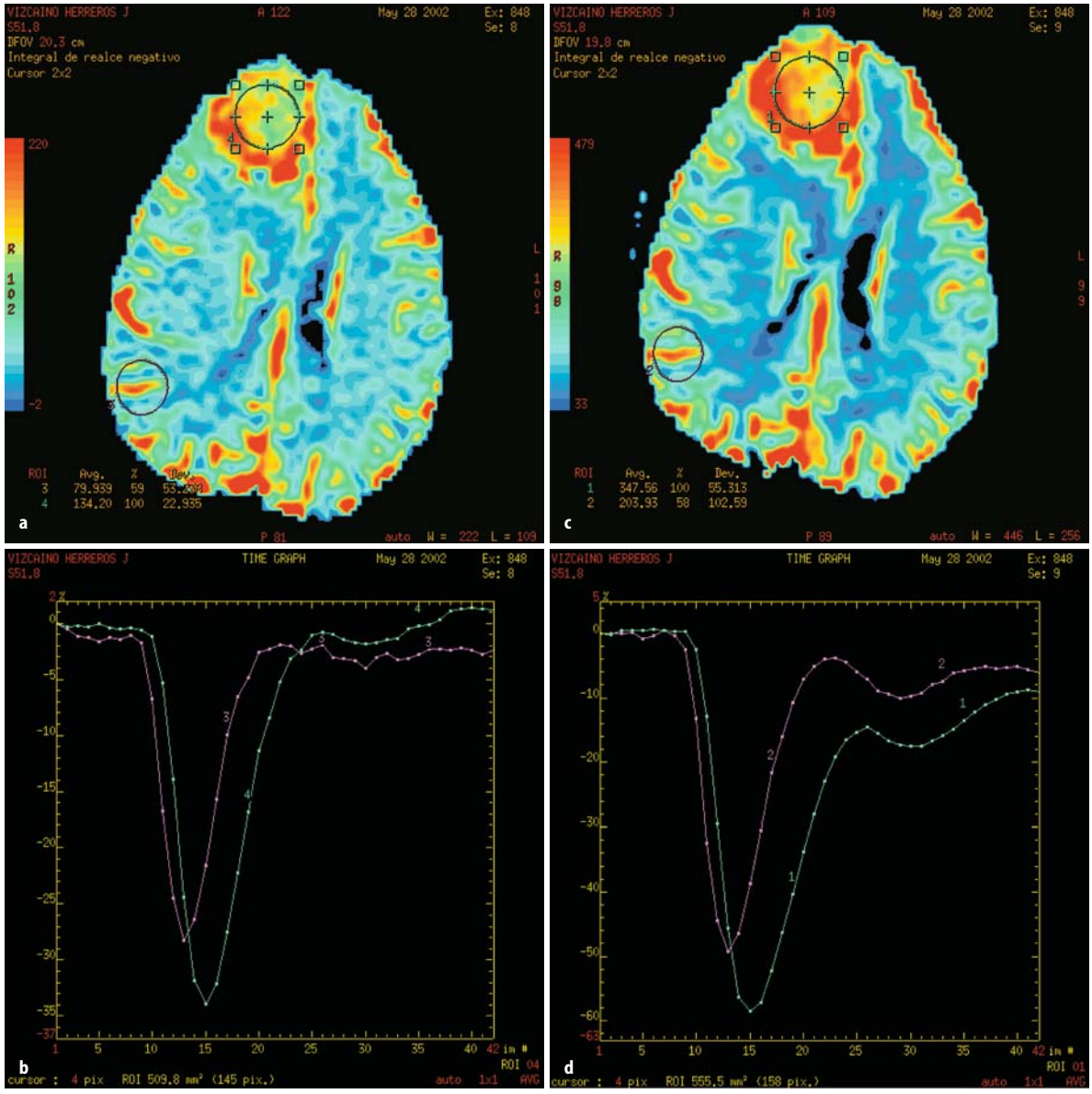

Fig. 9.8. DSC at 3.0 T. Comparison between two different concentrations of the same dose of contrast agent: 0.5 mmol (**a, c**) versus 1.0 mmol (**b, d**). At 3.0 T the enhanced magnetic susceptibility requires lower doses and/or lower concentrations than 1.5 T systems. (Courtesy of General Electric)

The dose of contrast agent also needs to be adjusted to the high-field strength setting. Although structural contrast-enhanced brain imaging at 1.5 T is usually performed with 0.1 mmol/kg of body weight, 0.2 mmol of gadolinium chelate is the most widely used dose and is considered optimal for DSC perfusion studies [65–71], also in case of higher concentrations of gadolinium-based contrast agents (e.g. gadobutrol, Gadovist; Schering, Berlin, Germany) [8, 72]. When this dose (0.2 mmol) was used for DSC perfusion at 3.0 T, the stronger susceptibility effects caused a complete signal void during the first pass of gadolinium, especially in grey matter, affecting the accuracy of signal drop calculation and impairing sensitivity to perfusion deficits [8]; for this reason, a dose of 0.2 mmol is not recommended for high-field perfusion imaging.

A recent 3.0 T study comparing different doses (0.05, 0.1 and 0.2 mmol) has recommended a dose of 0.1 mmol on the basis both of subjective analysis of the quality of the perfusion maps and of a quantitative assessment of perfusion variables [8] (Fig. 9.8).

9.3 Endogenous Methods: Arterial Spin Labelling

Endogenous tracer methods in perfusion MRI use a model that assumes that the tracer diffuses freely from the intravascular compartment into the tissue compartment. This model is similar to the one used in PET measuring the regional accumulation of the tracer, which is influenced by regional blood flow and its half-life [1].

Arterial spin labelling (ASL), also called arterial spin tagging, is an endogenous tracer perfusion method based on the measurement of the signal loss produced by magnetically labelled water protons flowing into the imaging plane and exchanging with tissue protons. Water protons within inflowing arterial blood are magnetically labelled (or „tagged“) by application of a special radiofrequency pulse designed to invert spins in a thick slab proximal to the slice of interest [1, 72–75]. By comparing tagged and untagged baseline images, qualitative or quantitative images can be obtained (Fig. 9.9).

The modelling of ASL is similar to that used in the analysis of PET perfusion imaging, since in ASL methods arterial blood water is labelled as an endogenous diffusible tracer that can detect functional deficiencies in a way similar to PET [33].

ASL has many advantages over PET as it is entirely non-invasive and does not entail exposure to ionizing radiation, intravenous contrast agents or radioactive isotopes.

It can be performed with most MR scanners in 10–15 min and can be rapidly repeated since labelled water is cleared after a few seconds because of T1 relaxation [33].

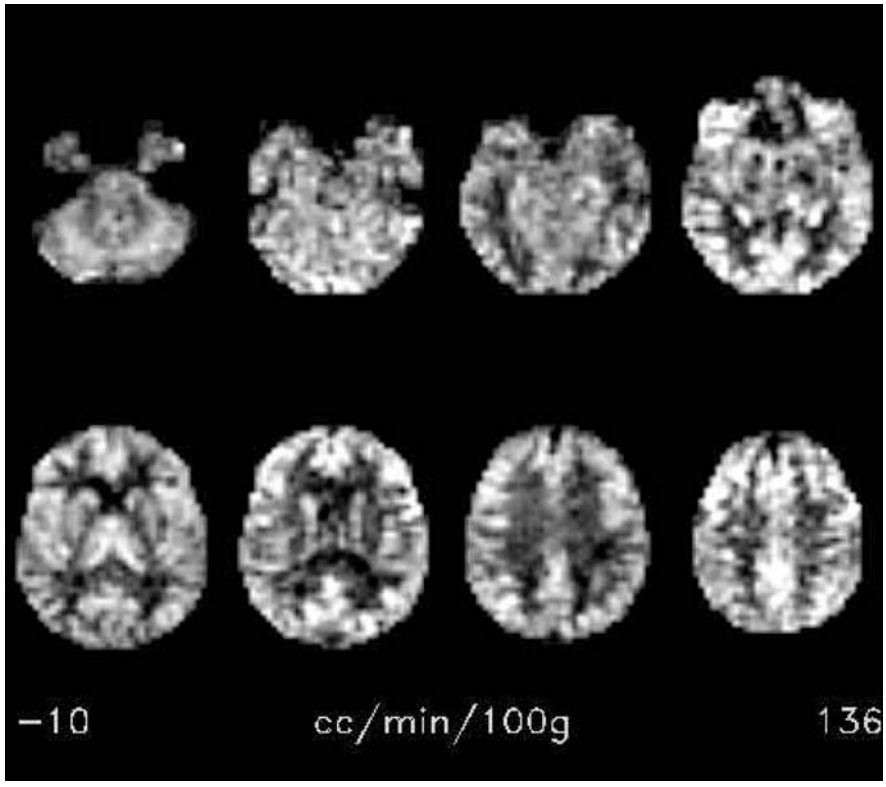

Fig. 9.9. ASL in normal subject

Compared with DSC methods, use of water as the label in ASL entails advantages over intravascular tracers, including the potential to be quantitative, repeatable, and independent of BBB status [7, 9].

Difficulties associated with CBF quantitation are related to the relatively short half-life of the tracer due to T1 of blood, low SNR (especially in slow flow areas) and uncertainties regarding the precise timing of the arrival of labelled water at different voxels [7, 74]. In normal subjects ASL has been favourably compared with $H_2{}^{15}O$ PET [76].

All current ASL methods are based on the collection of image pairs, which are subsequently subtracted, in which arterial magnetization entering the imaging slice during the repetition time (TR) interval varies. For maximum contrast, inflowing spins should have control image and be inverted during the label image. In practice, the signal difference between label and control images is a tiny fraction (0.5 – 2 %) of the source images, requiring collection of multiple image pairs and averaging of their small signal to provide adequate sensitivity [7].

Labelling can be achieved using either a short radiofrequency pulse to invert the spins, followed by a delay time to allow inflow (pulsed ASL – PASL) [77, 78], or by continuous adiabatic inversion of spins crossing a predefined plane, defined by off-resonance low-level continuous wave radiofrequency radiation in the presence of a magnetic field gradient (continuous ASL – CASL) [79].

In theory, CASL permits an approximately threefold increase in SNR, although this advantage is partially mitigated by imperfect adiabatic labelling and by a longer distance between the labelling plane and the imaged slices [79].

Because the magnetic label decays with blood T1 (1.2 – 1.4 s at 1.5 T), both methods suffer from CBF underestimation in regions with prolonged arterial arrival times, defined as the average time needed for labelled blood to reach the capillaries, which has been measured to be between 4,000 and 1,500 ms in the normal brain [80]. This problem can be minimized by inserting a post-labelling delay before imaging in CASL or by saturation pulses in PASL [74, 81].

However, in the diseased brain arterial arrival times may be markedly increased (by up to 5 s) if flow is provided by collateral networks; in this case, by the time the label arrives, its has relaxed back to equilibrium and an erroneously low CBF will be measured. Unless diffusion gradients are used to suppress the signal from large arteries, regions with a delayed arrival time often show several serpiginous bright spots with decreased flow signal distal to the supplying vessels. Recently, two different methods have been proposed to measure CBF more accurately in the presence of unknown regional changes in arterial arrival times.

Considering the water inflow at multiple post-label delay times, the movement of labelled blood from the arteries to the parenchyma can be detected, but this is generally not time-efficient.

However, if the full wash-in curve is measured, arrival time and CBF can be measured independently [82, 83].

In a different approach, called velocity-selective ASL (VS ASL), a 90°-gradient-180°-gradient-90° labelling pulse can be used to create a label independent of position and sensitive only to spin velocity [84, 85].

Moreover, with VS ASL not only arterial arrival time effects but also the slow-flow CSF artefacts in regions surrounding the ventricles may be reduced [86, 87].

9.4 High-Field ASL

High-field imaging machines may represent an ideal application for arterial spin labelling, due to the intrinsic SNR, the use of proton-density-weighted images, and the longer T1 of blood, which improve sensitivity to labelled spins and decrease sensitivity to uncertainties in arterial arrival time [4, 5]. For example, at 3.0 T, the SNR is about twice that at 1.5 T. At 3.0 T, blood T1, which determines the half-life of the label, is 1.6 – 1.8 s (vs 1.2 – 1.4 s at 1.5 T).

This results in a better SNR because the label decays more slowly, and, more importantly, in less sensitivity to arterial arrival time differences, because longer post-labelling delays are enabled. Such increased SNR sensitivity can be harnessed to decrease scanning time, to acquire higher resolution images, or to apply longer post-label delay times (Fig. 9.10).

Several recent papers have reported favourably on high-field ASL perfusion imaging [88 – 90]. Using CASL at 3.0 T with a 16-element phased-array receive coil and separate neck coil for labelling, Talagala et al. found a better SNR and obtained 3-mm isotropic resolution images in only 1 – 2 min [91]. Wang et al. showed a 33 % higher SNR at 3.0 T using a single coil and amplitude-modulated control pulse to reduce the effects of magnetization transfer [92].

Other recent applications of ASL are devoted to the study of regional perfusion territory imaging in order to visualize the vascular territory supplied by a specific labelled vessel.

Selective labelling may be useful in patients with high-grade or complete vascular occlusion to guide the choice between angioplasty and stenting, to evaluate cerebrovascular bypass grafts, or to estimate the likelihood of an embolic or atherothrombotic source in a patient with multiple bright regions on diffusion-weighted imaging.

Zaharchuk [93] first reported on this method by using continuous selective labelling at the level of the human carotid bifurcation with a separate labelling coil.

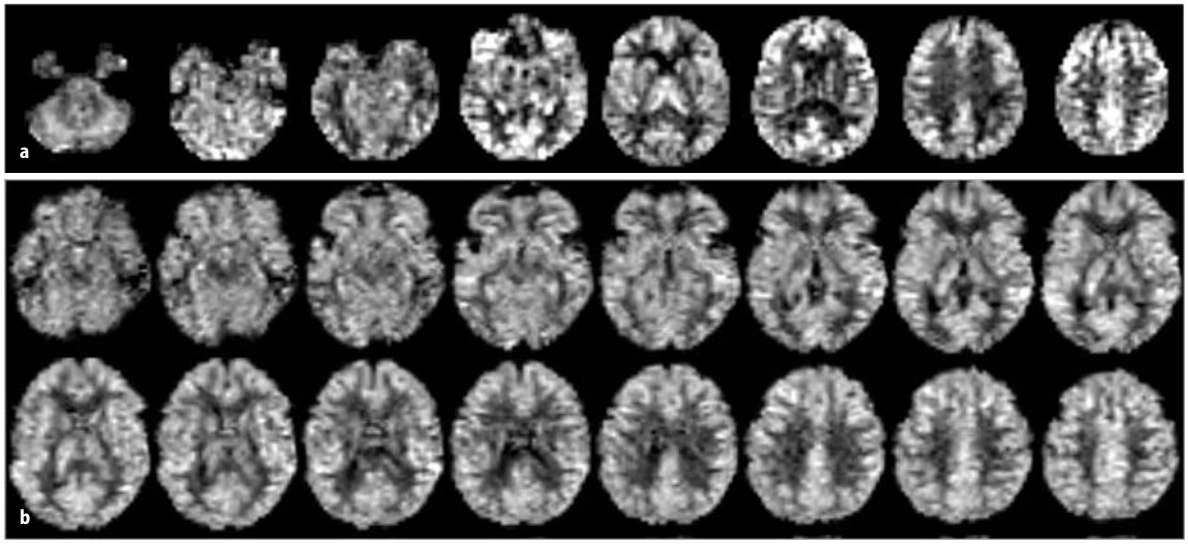

Fig. 9.10. Comparison between ASL acquired at 1.5 T (**a**) and 3.0 T (**b**). In **b** there is a higher S/N and better definition

Several investigations of regional perfusion territories using continuous [94] or pulsed [95–98] ASL methods have followed this first study.

Hendrikse et al., selecting a rectangular volume for labelling based on a previous MR angiogram, showed excellent visualization at 3.0 T of perfusion territories of isolated right carotid, left carotid and posterior circulation, demonstrating individual differences in vascular territories relating to different variants in the circle of Willis [96–98].

It is important to note that the only way to obtain such information used to be invasive catheter angiography. These data may be helpful to gain a better understanding of vascular dynamics in patients at high risk of stroke or being considered for corrective surgical procedures [99].

9.5 New Frontiers

There is increasing worldwide interest in developing new kinds of endogenous tracers based on molecules normally present in the human body that could be „labelled" in order to be detected on MRI. This would enable the same advantages to be obtained as for PET in terms of accurate quantitative evaluation of blood flow at lower cost without using radioactive isotopes.

Studies of these new endogenous tracers can be grouped under two major branches: research into oxygen-17 water ($H_2{}^{17}O$) and studies of hyperpolarized molecules [7, 100–103]. In both approaches, studies are currently limited to animals, but promising results have been obtained, encouraging their extension to human research.

Oxygen-17 is a non-radioactive isotope that occurs naturally at low concentrations (0.038%) [7, 100]. When enriched and incorporated into a water molecule ($H_2{}^{17}O$), it can be used as a weak MRI contrast agent, either imaged directly with a dedicated ^{17}O-receiver coil or through the decrease in T2 that it causes in protons [7, 100, 102]. This molecule has ideal physiochemical properties for monitoring blood flow since it is freely diffusible in the extravascular compartment, is stable and is non-radioactive.

It is important to note that the mathematical model used for $H_2{}^{15}O$ PET can be directly applied to the ^{17}O-method allowing true quantitative evaluation of CBF via a simple washout measurement, which is independent of delay and dispersion (measured in seconds), because the washout time is measured in minutes [7, 100].

Currently, a considerable limitation of this method is the high cost of enrichment even though it is likely to drop with increased demand. In order to reduce the costs some authors also proposed intra-arterial injection.

Another approach is based on hyperpolarized molecules. Conventional MRI depends on the high concentration of water protons because even at high field strengths the relative polarization (i.e. the number of excess spins directed along the main magnetic field) is very small, in the order of 1 in millions of spins.

Several methods can be adopted to create a non-equilibrium state in which polarization is so increased that imaging nuclei with far lower concentration than protons becomes feasible [7, 102]. Among these, the techniques based on electron-proton spin exchange rely on the concept that manipulation of electron spins using microwave energy can be transferred to the nu-

clear spins to create large non-equilibrium nuclear magnetization [7, 102].

Recently a system has been shown in which high degrees of polarization (up to 37%) of ^{13}C and ^{15}N nuclei can be created at an extremely low temperature in the solid state and then dissolved to liquid state at body temperature [7, 103]. This method offers a very high SNR (about 10,000) with a sensitivity equal or superior to conventional MRI. It has recently been applied to evaluate brain perfusion by using ^{13}C attached to an intravascularly confined small molecule [7, 103].

Advantages of these techniques include insensitivity to the static field (since the coils are tuned to the ^{13}C resonance frequency) and to contamination due to recirculation (as the hyperpolarization is completely destroyed at the end of the pulse sequence) [7].

9.6 Conclusions

Perfusion MRI is a valuable and flexible clinical tool enabling the assessment of regional cerebral haemodynamics using a variety of techniques and playing a relevant role in treatment strategies (e.g. in deciding which patient should undergo thrombolysis).

The most frequently applied technique uses rapid T2- or T2*-weighted EPI sequences to monitor the first pass of a bolus of gadolinium chelate to calculate semiquantitative maps of relative blood flow, blood volume and transit time.

The arterial spin labelling technique uses magnetically tagged blood as an endogenous tracer, allowing absolute CBF measurement using the same model as PET. Both techniques benefit from high-field imaging.

Despite disadvantages related to increased susceptibility to field inhomogeneities, use of high-field imaging, especially in combination with parallel imaging, affords higher SNR, greater sensitivity to the signal drop produced by exogenous tracers (thus permitting use of a smaller dose of contrast agent) and better performances of ASL methods, including greater sensitivity to labelled blood and lower sensitivity to uncertainties in arterial arrival time.

Finally, research is in progress to study and develop new endogenous tracers, such as $H_2{}^{15}O$ and hyperpolarized nucleus-based imaging.

References

1. Petrella JR, Provenzale JM (2000) MR perfusion imaging of the brain: techniques and applications. AJR Am J Roentgenol 175:207 – 220
2. Cha S (2003) Perfusion MR imaging: basic principles and clinical applications. Magn Reson Imaging Clin N Am 11(3):403 – 413
3. Provenzale JM, Jahan R, Naidich TP, Fox AJ (2003) Assessment of the patient with hyperacute stroke: imaging and therapy. Radiology 229(2):347 – 359
4. Scarabino T, Nemore F, Giannatempo GM, et al. (2003) 3.0 T magnetic resonance in neuroradiology. Eur J Radiol 48:154 – 164
5. Scarabino T, Giannatempo GM, Pollice S, et al. (2004) 3.0 T perfusion MR imaging. Riv Neuroradiol 17:807 – 812
6. Shimony JS (2005) Concepts in perfusion MRI. Syllabus. Intl Soc Mag Reson Med 13
7. Zaharchuk G (2005) Frontiers of cerebral perfusion magnetic resonance imaging. Appl Radiol (Suppl to January):100 – 111
8. Manka C, Traber F, Gieseke J, et al. (2005) Three-dimensional dynamic susceptibility-weighted perfusion MR imaging at 3.0 T: feasibility and contrast agent dose. Radiology 234(3):869 – 877
9. Barbier EL, Lamalle L, Decorps M (2001) Methodology of brain perfusion imaging. J Magn Reson Imaging 13(4): 496 – 520
10. Derdeyn CP, Videen TO, Yundt KD, et al. (2002) Variability of cerebral blood volume and oxygen extraction: stages of cerebral haemodynamic impairment revisited. Brain 125(3): 595 – 607
11. Flacke S, Urbach H, Folkers PJ, et al. (2000) Ultra-fast three-dimensional MR perfusion imaging of the entire brain in acute stroke assessment. J Magn Reson Imaging 11:250 – 259
12. Fiehler J, von Bezold M, Kucinski T, et al. (2002) Cerebral blood flow predicts lesion growth in acute stroke patients. Stroke 33:2421 – 2425
13. Liu Y, Karonen JO, Vanninen RL, et al. (2000) Cerebral hemodynamics in human acute ischemic stroke: a study with diffusion- and perfusion-weighted magnetic resonance imaging and SPECT. J Cereb Blood Flow Metab 20:910 – 920
14. Parsons MW, Yang Q, Barber PA, et al. (2001) Perfusion magnetic resonance imaging maps in hyperacute stroke: relative cerebral blood flow most accurately identifies tissue destined to infarct. Stroke 32:1581 – 1587
15. Latchaw RE, Yonas H, Hunter GJ, et al. (2003) Guidelines and recommendations for perfusion imaging in cerebral ischemia: a scientific statement for healthcare professionals by the writing group on perfusion imaging, from the Council on Cardiovascular Radiology of the American Heart Association. Stroke 34:1084 – 1104
16. Doerfler A, Eckstein HH, Eichbaum M, et al. (2001) Perfusion-weighted magnetic resonance imaging in patients with carotid artery disease before and after carotid endarterectomy. J Vasc Surg 34:587 – 593
17. Calamante F, Ganesan V, Kirkham FJ, et al. (2001) MR perfusion imaging in Moyamoya syndrome: potential implications for clinical evaluation of occlusive cerebrovascular disease. Stroke 32:2810 – 2816
18. Maeda M, Yuh WT, Ueda T, et al. (1999) Severe occlusive carotid artery disease: hemodynamic assessment by MR perfusion imaging in symptomatic patients. Am J Neuroradiol 20:43 – 51
19. Michel E, Liu H, Remley KB, et al. (2001) Perfusion MR neuroimaging in patients undergoing balloon test occlusion of the internal carotid artery. Am J Neuroradiol 22:1590 – 1596
20. Kassner A, Annesley DJ, Zhu XP, et al. (2000) Abnormalities of the contrast re-circulation phase in cerebral tumors demonstrated using dynamic susceptibility contrast-enhanced imaging: a possible marker of vascular tortuosity. J Magn Reson Imaging 11:103 – 113
21. Alexander E (2001) Optimizing brain tumor resection: midfield interventional MR imaging. Neuroimaging Clin N Am 11:659 – 672

22. Vonken EP, Van Osch MJ, Willems PW, et al. (2000) Repeated quantitative perfusion and contrast permeability measurement in the MRI examination of a CNS tumor. Eur Radiol 10:1447 – 1451
23. Chiang IC, Kuo YT, Lu CY, et al. (2004) Distinction between high-grade gliomas and solitary metastases using peritumoral 3T magnetic resonance spectroscopy, diffusion and perfusion imagings. Neuroradiology 46(8):619 – 627
24. Holmes TM, Petrella JR, Provenzale JM (2004) Distinction between cerebral abscesses and high-grade neoplasms by dynamic susceptibility contrast perfusion MRI. AJR 183: 1247 – 1252
25. Hakyemez B, Erdogan C, Ercan I, et al. (2005) High-grade and low-grade gliomas: differentiation by using perfusion MR imaging. Clin Radiol 60(4):493 – 502
26. Provenzale JM, Wang GR, Brenner T, et al. (2002) Comparison of permeability in high-grade and low-grade brain tumors using dynamic susceptibility contrast MR imaging. Am J Roentgenol 178:711 – 716
27. Law M, Yang S, Babb JS, et al. (2004) Comparison of cerebral blood volume and vascular permeability from dynamic susceptibility contrast-enhanced perfusion MR imaging with glioma grade. Am J Neuroradiol 25(5):746 – 755
28. Hartmann M, Heiland S, Harting I, et al. (2003) Distinguishing of primary cerebral lymphoma from high-grade glioma with perfusion-weighted magnetic resonance imaging. Neurosci Lett 338:119 – 122
29. Bozzao A, Floris R, Baviera ME, et al. (2001) Diffusion and perfusion MR imaging in cases of Alzheimer's disease: correlations with cortical atrophy and lesion load. Am J Neuroradiol 22:1030 – 1036
30. Firbank MJ, Colloby SJ, Burn DJ, et al. (2003) Regional cerebral blood flow in Parkinson's disease with and without dementia. Neuroimage 20:1309 – 1319
31. Chabriat H, Pappata S, Ostergaard L, et al. (2000) Cerebral hemodynamics in CADASIL before and after acetazolamide challenge assessed with MRI bolus tracking. Stroke 31:1904 – 1912
32. Brusa L, Bassi A, Pierantozzi M, et al. (2002) Perfusion-weighted dynamic susceptibility (DSC) MRI: basal ganglia hemodynamic changes after apomorphine in Parkinson's disease. Neurol Sci 23(Suppl 2):S61–S62
33. Johnson NA, Jahng GH, Weiner MW, et al. (2005) Pattern of cerebral hypoperfusion in Alzheimer disease and mild cognitive impairment measured with arterial spin label in MR imaging: initial experience. Radiology 234:851 – 859
34. Norfray JF, Provenzale JM (2004) Alzheimer's disease: neuropathologic findings and recent advances in imaging. Am J Radiol 182:3 – 13
35. Szabo K, Poepel A, Pohlmann-Eden B, et al. (2005) Diffusion-weighted and perfusion MRI demonstrates parenchymal changes in complex partial status epilepticus. Brain 128:1369 – 1376
36. Wuerfel J, Bellmann-Strobl J, Brunecker P, et al. (2004) Changes in cerebral perfusion precede plaque formation in multiple sclerosis: a longitudinal perfusion MRI study. Brain 127:111 – 119
37. Stollberger R, Fazekas F (2004) Improved perfusion and tracer kinetic imaging using parallel imaging. Top Magn Reson Imaging 15(4):245 – 254
38. Leenders KL, Perani D, Lammertsma AA, et al. (1990) Cerebral blood flow, blood volume and oxygen utilization. Normal values and effect of age. Brain 113:27 – 47
39. Lassen NA, Perl W (1979) Tracer kinetic methods in medical physiology. Raven Press, New York
40. Yamada K, Gonzalez RG, Ostergaard L, et al. (2002) Iron-induced susceptibility effect at the globus pallidus causes underestimation of flow and volume on dynamic susceptibility contrast-enhanced MR perfusion images. Am J Neuroradiol 23(6):1022 – 1029
41. Sorensen AG, Copen WA, Ostergaard L, et al. (1999) Hyperacute stroke: simultaneous measurement of relative cerebral blood volume, relative cerebral blood flow, and mean tissue transit time. Radiology 210:519 – 527
42. Weisskoff RM, Boxerman JL, Sorensen AG, et al. (1994) Simultaneous blood volume and permeability mapping using a single Gd-based contrast injection. In: Proceedings of the Society of Magnetic Resonance, 2nd Annual Meeting. San Francisco, CA, p 279
43. Shen T, Weissleder R, Papisov M, et al. (1993) Monocrystalline iron oxide nanocompounds (MION): physicochemical properties. Magn Reson Med 29(5):599 – 604
44. Wiener EC, Brechbiel MW, Brothers H, et al. (1994) Dendrimer-based metal chelates: a new class of magnetic resonance imaging contrast agents. Magn Reson Med 31(1):1 – 8
45. Cavagna FM, Maggioni F, Castelli PM, et al. (1997) Gadolinium chelates with weak binding to serum proteins. A new class of high-efficiency, general purpose contrast agents for magnetic resonance imaging. Invest Radiol 32(12):780 – 796
46. Lassen NA (1984) Cerebral transit of an intravascular tracer may allow measurement of regional blood volume but not regional blood flow. J Cereb Blood Flow Metab 4(4): 633 – 634
47. Calamante F, Gadian DG, Connelly A (2000) Delay and dispersion effects in dynamic susceptibility contrast MRI: simulations using singular value decomposition. Magn Reson Med 44(3):466 – 473
48. Ostergaard L, Smith DF, Vestergaard-Poulsen P, et al. (1998) Absolute cerebral blood flow and blood volume measured by magnetic resonance imaging bolus tracking: comparison with positron emission tomography values. J Cereb Blood Flow Metab 18(4):425 – 432
49. Sakoh M, Rohl L, Gyldensted C, et al. (2000) Cerebral blood flow and blood volume measured by magnetic resonance imaging bolus tracking after acute stroke in pigs: comparison with [(15)O]H(2)O positron emission tomography. Stroke 31(8):1958 – 1964
50. Mukherjee P, Kang HC, Videen TO, et al. (2003) Measurement of cerebral blood flow in chronic carotid occlusive disease: comparison of dynamic susceptibility contrast perfusion MR imaging with positron emission tomography. Am J Neuroradiol 24(5):862 – 871
51. Nasel C, Kronsteiner N, Schindler E, et al. (2004) Standardized time-to-peak in ischemic and regular cerebral tissue measured with perfusion MR imaging. Am J Neuroradiol 25(6):945 – 950
52. Sobesky J, Weber OZ, Lenhardt FG, et al. (2004) Which time-to-peak threshold best identifies penumbral flow? A comparison of perfusion-weighted magnetic resonance imaging and positron emission tomography in acute ischemic stroke. Stroke 35 (12):2843 – 2847
53. Lupo JM, Lee MC, Han ET, et al. (2005) Feasibility of dynamic susceptibility-weighted perfusion MRI at 3T using a standard head coil and 8-channel phased-array coil with and without SENSE reconstruction. Proc Intl Soc Mag Reson Med 13:741
54. Larsson HB, Berg HK, Vangberg T, et al. (2005) Measurement of CBF and PS product in brain tumor patients using T1 w dynamic contrast enhanced MRI at 3 tesla. Proc Intl Soc Mag Reson Med 13:2082
55. Morgan PS, George MS, Kozel FA, et al. (2005) Dynamic contrast enhanced whole brain perfusion using a rapid 3D T1-weighted sequence at 1.5T and 3T. Proc Intl Soc Mag Reson Med 13:1257

56. Wang J, Alsop DC, Li L, et al. (2002) Comparison of quantitative perfusion imaging using arterial spin labeling at 1.5 and 4.0 Tesla. Magn Reson Med 48:242 – 254
57. Kruger G, Kastrup A, Glover GH (2001) Neuroimaging at 1.5 T and 3.0 T: comparison of oxygenation-sensitive magnetic resonance imaging. Magn Reson Med 45:595 – 604
58. Heiland S, Kreibich W, Reith W, et al. (1998) Comparison of echo-planar sequences for perfusion-weighted MRI: which is best? Neuroradiology 40:216 – 221
59. Liu G, Sobering G, Duyn J, et al. (1993) A functional MRI technique combining principles of echo-shifting with a train of observations (PRESTO). Magn Reson Med 30:764 – 768
60. Mattay VS, Frank JA, Duyn JH, et al. (1996) Three-dimensional „BURST" functional magnetic resonance imaging: initial clinical applications. Acad Radiol 3(Suppl 2):S379–S383
61. van Gelderen P, Grandin C, Petrella JR, et al. (2000) Rapid three-dimensional MR imaging method for tracking a bolus of contrast agent through the brain. Radiology 216: 603 – 608
62. Grandin CB (2003) Assessment of brain perfusion with MRI: methodology and application to acute stroke. Neuroradiology 45:755 – 766
63. Thilmann O, Larsson EM, Bjorkman-Burtscher IM, et al. (2004) Effects of echo time variation on perfusion assessment using dynamic susceptibility contrast MR imaging at 3 Tesla. Magn Reson Imaging 22(7):929 – 935
64. Shin W, Sakaie K, Cashen TA, et al. (2005) High field (3.0T) CBF imaging using spin-echo EPI and parallel imaging. Proc Intl Soc Mag Reson Med 13:1124
65. Keston P, Murray AD, Jackson A (2003) Cerebral perfusion imaging using contrast-enhanced MRI. Clin Radiol 58: 505 – 513
66. Tombach B, Benner T, Reimer P, et al. (2003) Do highly concentrated gadolinium chelates improve MR brain perfusion imaging? Intraindividually controlled randomized crossover concentration comparison study of 0.5 versus 1.0 mol/L gadobutrol. Radiology 226:880 – 888
67. Warmuth C, Gunther M, Zimmer C (2003) Quantification of blood flow in brain tumors: comparison of arterial spin labeling and dynamic susceptibility-weighted contrast-enhanced MR imaging. Radiology 228:523 – 532
68. Flacke S, Urbach H, Block W, et al. (2002) Perfusion and molecular diffusion-weighted MR imaging of the brain: in vivo assessment of tissue alteration in cerebral ischemia. Amino Acids 23:309 – 316
69. Baird AE, Lovblad KO, Dashe JF, et al. (2000) Clinical correlations of diffusion and perfusion lesion volumes in acute ischemic stroke. Cerebrovasc Dis 10:441 – 448
70. Fiehler J, Knudsen K, Kucinski T, et al. (2004) Predictors of apparent diffusion coefficient normalization in stroke patients. Stroke 35:514 – 519
71. Hillis AE, Wityk RJ, Beauchamp NJ, et al. (2004) Perfusion-weighted MRI as a marker of response to treatment in acute and subacute stroke. Neuroradiology 46:31 – 39
72. Benner T, Reimer P, Erb G, et al. (2000) Cerebral MR perfusion imaging: first clinical application of a 1 M gadolinium chelate (Gadovist 1.0) in a double-blinded randomized dose-finding study. J Magn Reson Imaging 12:371 – 380
73. Detre JA, Leigh JS, Williams DS, Koretsky AP (1992) Perfusion imaging. Magn Reson Med 23(1):37 – 45
74. Alsop DC, Detre JA (1996) Reduced transit-time sensitivity in noninvasive magnetic resonance imaging of human cerebral blood flow. J Cereb Blood Flow Metab 16(6): 1236 – 1249
75. Jahng GH, Song E, Zhu XP, et al. (2005) Human brain: reliability and reproducibility of pulsed arterial spin-labeling perfusion MR imaging. Radiology 234(3):909 – 916
76. Ye FQ, Berman KF, Ellmore T, et al. (2000) H(2)(15)O PET validation of steady-state arterial spin tagging cerebral blood flow measurements in humans. Magn Reson Med 44(3):450 – 456
77. Edelman RR, Siewert B, Darby DG, et al. (1994) Qualitative mapping of cerebral blood flow and functional localization with echo-planar MR imaging and signal targeting with alternating radio frequency. Radiology 192(2):513 – 520
78. Kim SG (1995) Quantification of relative cerebral blood flow change by flow-sensitive alternating inversion recovery (FAIR) technique: application to functional mapping. Magn Reson Med 34(3):293 – 301
79. Wong EC, Buxton RB, Frank LR (1999) Quantitative perfusion imaging using arterial spin labeling. Neuroimaging Clin N Am 9(2):333 – 342
80. Wang J, Alsop DC, Song HK, et al. (2003) Arterial transit time imaging with flow encoding arterial spin tagging (FEAST). Magn Reson Med 50(3):599 – 607
81. Wong EC, Buxton RB, Frank LR (1998) Quantitative imaging of perfusion using a single subtraction (QUIPSS and QUIPSS II). Magn Reson Med 39(5):702 – 708
82. Buxton RB, Frank LR, Wong EC (1998) A general kinetic model for quantitative perfusion imaging with arterial spin labeling. Magn Reson Med 40(3):383 – 396
83. Guenther M, Oshio K, Feinberg D (2004) Very fast 3D perfusion measurement with high signal-to-noise ratio using single-shot 3D GRASE: Application to improve perfusion quantitation. Proc Intl Soc Mag Reson Med 12:714
84. Wong E, Liu T, Sidaros K, et al. (2002) Velocity selective arterial spin labeling. Proc Intl Soc Mag Reson Med 10:621
85. Wu WC, Won EC (2005) Intravascular effects in velocity-selective arterial spin labeling: the choice of transit delay and cutoff velocity. Proc Intl Soc Mag Reson Med 13:1156
86. Duhamel G, de Bazelaire C, Alsop DC (2003) Evaluation of systematic quantification errors in velocity-selective arterial spin labeling of the brain. Magn Reson Med 50(1): 145 – 153
87. Wong E (2004) Time efficient CSF suppressed velocity selective ASL using a T2-FLAIR preparation. Proc Intl Soc Mag Reson Med 12:711
88. Manka CA, Traeber F, Block W, et al. (2005) Continuous arterial spin labeling (CASL) in clinical practice at 3.0 T – results on reliability and quantification. Proc Intl Soc Mag Reson Med 13:1141
89. Fernandez-Seara MA, Wang J, Wang Z, et al. (2005) Continuous arterial spin labelling perfusion measurements using single shot 3D GRASE at 3T. Proc Intl Soc Mag Reson Med 13:1160
90. Last D, Alsop DC, Marquis RP, et al. (2005) Effects of type II diabetes on cerebral vasoregulation using continuous arterial spin labeling MRI at 3 Tesla. Proc Intl Soc Mag Reson Med 13:1139
91. Talagala S, Chuang KH, Chesnick S, et al. (2004) High sensitivity CASL perfusion MRI at 3T using a 16 channel receiver coil array. Proc Intl Soc Mag Reson Med 12:717
92. Wang J, Zhang Y, Wolf R, et al. (2004) Single coil amplitude modulated continuous arterial spin labeling perfusion MR at 3.0 T. Proc Intl Soc Mag Reson Med 12:1363
93. Zaharchuk G, Ledden PJ, Kwong KK, et al. (1999) Multislice perfusion and perfusion territory imaging in humans with separate label and image coils. Magn Reson Med 41(6):1093 – 1098
94. Werner R, Alfke K, Schaeffter T et al. (2004) Spatially selective perfusion imaging applying continuous arterial spin labeling. Proc Intl Soc Mag Reson Med 12:715
95. Song HK, Zhang Y, Wolf RL, et al. (2004) Unilateral labeling PASL technique for vascular territory perfusion imaging. Proc Intl Soc Mag Reson Med 12:1358

96. Hendrikse J, van Raamt AF, van der Graaf Y, et al. (2005) Distribution of cerebral blood flow in the circle of Willis. Radiology 235(1):184 – 189
97. Hendrikse J, van der Grond J, Lu H, et al. (2004) Flow territory mapping of the cerebral arteries with regional perfusion MRI. Stroke 35(4):882 – 887
98. Hendrikse J, van Osch MJ, van der Zwan A, et al. (2005) Altered flow territories after extracranial to intracranial bypass surgery: clinical implementation of selective arterial spin labeling MRI. Proc Intl Soc Mag Reson Med 13:1137
99. van Laar PJ, Hendrikse J, Golay X, et al. (2005) In-vivo flow territory mapping of major brain feeding arteries: a population study with selective arterial spin labeling MRI. Proc Intl Soc Mag Reson Med 13:1134
100. Nakatani A, Shiomi B, Oka S, et al. (2004) Measurement of cerebral blood flow in dogs: comparison of magnetic resonance imaging using $H_2{}^{17}O$ with positron emission tomography using $H_2{}^{15}O$. Proc Intl Soc Mag Reson Med 12:1404
101. Mazzanti M, Sun Y, Mansour J, et al. (2004) Functional brain imaging using hyperpolarized ^{129}Xe. Proc Intl Soc Mag Reson Med 12:768
102. Golman K, Aredenkjarer-Larsen JH, Petersson JS, et al. (2003) Molecular imaging with endogenous substances. Proc Natl Acad Sci USA 100:10435 – 10439
103. Johansson E, Mansson S, Wirestam R, et al. (2004) Cerebral perfusion assessment by bolus tracking using hyperpolarized carbon-13. Magn Reson Med 51:464 – 472

High-Field Strength Functional MRI

10

F. Di Salle, T. Scarabino, F. Esposito, A. Aragri, O. Santopaolo, A. Elefante, M. Cirillo, S. Cirillo, R. Elefante

Since its introduction in 1992, fMRI has proved so sensitive to the detection of functional phenomena, flexible in use and reliable in its results, and has evolved so rapidly in such a short period of time, that it has become by far the most widely used imaging technique for studying brain function in humans.

Among the main reasons for the astonishing success fMRI has enjoyed so far, a pivotal role has certainly been played by its high sensitivity in analysing brain functional phenomena and its lack of biological invasiveness, resulting in an unprecedented and unparalleled flexibility of use [1]. Within the few years since its introduction, fMRI has produced a huge amount of information on brain functional anatomy, contributing to the unravelling of many basic mechanisms of brain physiology, the clarification of details of the hierarchical organization of functional areas and the unveiling of the dynamics of parallel processing of information in the living brain.

In brief, the introduction of fMRI has had a revolutionary effect on neuroscience research, since most of the knowledge we have on the functional organization of the brain has been rewritten, modified or at least complemented by new concepts and innovative information coming from fMRI.

As an example, the detailed information we have concerning the functional organization of the human visual cortex has been largely gathered from fMRI experiments, which have enabled the occipital cortex to be divided into a complex constellation of functionally different activities segregated into multiple neighbouring visual areas [3].

Fundamental to the success of fMRI have been its high spatial and temporal resolution, which are clearly favourable compared to the other methods of functional neuroimaging. In fact, brain functional phenomena are analysed with higher spatial and temporal resolution by fMRI than by the neuroimaging methods using radioactive tracers [1, 2], and with a far higher spatial resolution, compared to electrophysiological measures.

Due to these advantages, fMRI can produce more localized information, and allows a better understanding of the neural dynamics at the level of single functional areas and of the neural constituents of functional patterns.

The spatial resolution of fMRI, which normally ranges within a few millimetres, can be increased to further improve its analytical potential. This is very simple to achieve, since it requires only a modification of the combination of field of view (FOV) and acquisition matrix in the direction of an increased matrix or a reduced FOV. Nonetheless, these changes as a side effect produce a linear decrease in the signal to noise ratio (SNR) paralleling the reduction of voxel dimension (and, thus, the quantity of protons per voxel), which in turn can greatly impairs image quality, practically nullifying the advantages of raising spatial resolutions above a reasonable compromise level.

While this practical limitation in the possibility of increasing spatial resolution is true for any application of MRI, it is especially evident and particularly detrimental for fMRI experiments. Here, the decrease in voxel SNR cannot be compensated for by increasing the number of signal averages, as is generally achieved in structural MR imaging, since this would produce a dramatic reduction in temporal resolution.

Furthermore, fMRI images are not considered in isolation, as is the case for structural imaging, but contribute collectively to a post-processing statistical analysis, which can be considerably impaired by a high level of noise. Since a low SNR thwarts the statistical analysis to such an extent that no reliable results are obtained at the commonly used statistical thresholds, a pre-processing step of spatial smoothing is usually applied in the presence of noisy data. Smoothing the data, in turn, practically implies a loss of the original spatial resolution.

Hence, especially in fMRI applications, the only real way to take advantage of the increase in spatial resolution is by the concurrent use of acquisition strategies able to improve SNR.

Besides the possibility of improving the intrinsic pulse sequence SNR, and the use of high SNR coils, the most successful solution for gaining SNR consists of using high magnetic field intensity fMRI units.

It can be claimed that the spread of high-field MRI units for human studies throughout the world has been appreciably stimulated, if not in fact determined, by the

need for an acceptable SNR in functional studies at high spatial resolution.

Furthermore, a number of ancillary reasons suggest the use of high-field units: many fMRI applications have been proposed that may lead to interesting and insightful perspectives in understanding fine neural mechanisms at the cost of decreasing the statistical power of the fMRI studies. It is the case, for instance, for single-trial event-related studies or other demanding fMRI paradigms, which can be beyond the reach of fMRI studies at lower field intensity due to the insufficient statistical power when carried out in unfavourable conditions of SNR [3].

An important reason for pursuing higher spatial resolution fMRI examinations also comes from neurophysiological considerations. In order to gain a comprehensive understanding of brain functions, the observation of the behaviour of single neurons, as permitted by the recording of the electrical activity of single neuronal units, is not enough. Nor can it be fully satisfactory to study the functional properties of large macroscopic structures such as whole cytoarchitectonic areas. The study of the primary sensory areas of primates has taught us that many fundamental neural dynamics take place at a dimensional scale intermediate between the level of single neurons and the level of functional areas, dwelling in specific laminar, columnar and multicolumnar domains. Hence, much key information about brain functions is contained in the spatial dimensions ranging beyond the level of a single neuron, where the dynamics are fragmented and incomplete, and below the level of Brodmann's areas, where many neural dynamics can be blurred and confused.

fMRI has a very high potential for analysing brain functional phenomena at this intermediate level, which are thoroughly accessible only by increasing spatial resolution up to and beyond the millimetre range.

Nevertheless, as with any imaging method, fMRI has intrinsic limitations in spatial and temporal resolution, which are due to different factors but which are intimately interdependent.

10.1 Effects of Field Strength on Spatial Resolution

Conditioned by the existing MRI technologies and by the available magnets, generally with a field strength of 1.5 T, in most human fMRI studies performed so far spatial resolution has ranged between 3 and 5 mm in plane, and between 3 and 10 mm along the *z*-axis [7]. Functional temporal series with higher spatial resolution are compatible with fMRI experimental designs, but generally at the cost of partially sacrificing temporal resolution or SNR. On the other hand, higher spatial resolution has been achieved by many groups in human and animal studies [6–14]. Recently, even a submillimetre resolution in space has been reached without dramatically impairing resolution in time and SNR [6].

Nevertheless, further overwhelming difficulties exist, beyond the concerns about the SNR worsening, in the attempt to improve the spatial resolution. In fact, the main limitation in the spatial resolution of fMRI is not actually dependent on technical limitations but resides in the very nature of the fMRI phenomena. Indeed, since the fMRI signal arises from vascular phenomena requiring local modifications in the vascular tone, it may be expected that spatial resolution had as a physical limit the minimal dimension of the vascular territory able to vary its blood flow independently from the neighbouring regions. This consideration has led to the hypothesis that the ultimate spatial resolution of fMRI coincides with the vascular territory of the pre-capillary arterioles, the smallest afferent vascular structures having a distinct muscular wall and so being capable of autonomous vasoregulation. Hence, the smallest functional unit visible in fMRI has been proposed to have a volume in the order of 1 mm^3, and this supposed to represent the theoretical limit in spatial resolution of functional vascular phenomena [15].

Nevertheless, alternative hypotheses propose that an amount of capillary autoregulation is also possible through the function of pre-capillary sphincters or through an autonomous contractile function of the capillary wall. Either way, the result is a vasoregulation carried out by both the „capillary recruitment", regulating the number of capillaries open to blood flow, and by a variation in capillary diameter. While the former operates in a discrete way, in a binary „yes or no" fashion at the level of the single capillary, the latter is probably capable of a continuous regulation of the blood flow operating in a „more or less" fashion [15]. In either case, the effect on blood flow seen above the capillary level possibly consists of a continuous variation depending on the local vascular tone.

The ancillary role of the capillary bed in regulating functional brain haemodynamics seems to be confirmed by optical spectroscopy, which produces functional maps of working mammal cortex with a precision higher than 100 μm. In these maps, functional effects have been demonstrated far beyond the resolution (1 mm^3) possibly compatible with the hypothesis of the vasoregulation being operated only at the arteriolar level [15].

Additional evidence for this discussion arises from the analysis of the temporal dynamics of optical measurements and of blood oxygenation level dependent (BOLD) fMRI signal. While the optical spectroscopy is performed on the exposed cortex of experimental animals, the near infrared spectroscopy can be applied to humans and allows the evaluation of haemoglobin oxygenation dynamics through the intact skull. This latter technique has documented a transient rise in deoxy-

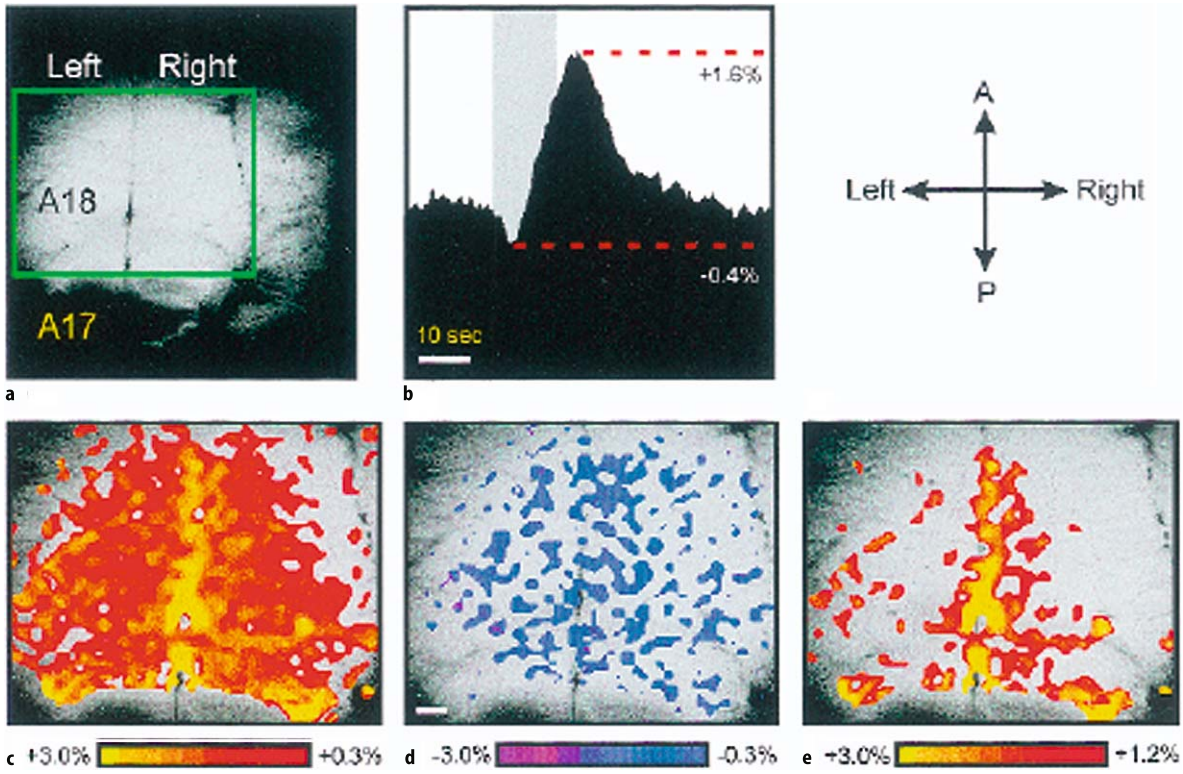

Fig. 10.1 a–e. Increased fMRI spatial specificity using the initial dip (reprinted from [10] with permission). In **a** the anatomical image of cat area 18 on the lateral gyrus (image size 2 × 2 cm) is depicted. The *green box* indicates the field of view of the activation maps displayed in this study. **b** The biphasic fMRI signal time course following 10 s of visual stimulation (marked in *grey*). **c** Pattern of increased positive (conventional) BOLD activity in response to moving 45° gratings. **d** Functional map for which only negative BOLD percentage changes occurring within the first 2 s after stimulus onset were used. **e** The pattern of positive BOLD responses after raising the threshold to match the number of activated pixels to that in **d**. It is easy to appreciate the improvement in spatial resolution in the negative BOLD functional map

genated haemoglobin (Hb) accompanied by a rise in oxy-Hb, which suggests an early increase in oxygen metabolism, possibly associated with an early increase in vascular volume, taking place at the capillary level, before a substantial rise in blood flow.

These data converge with the information coming from time-resolved BOLD fMRI experiments in indicating the existence of BOLD phenomena dwelling at the capillary level. Indeed, if the BOLD dynamics following a short stimulation is analysed, one can often observe an early signal deflection known as the „initial dip" phenomenon, which has recently stimulated a large body of research. The interest in the initial dip has been mainly determined by its presumed origin. Without questions, if the hypotheses concerning the dip hold true, then the phenomenon is generated by an early increase in oxygen consumption without a corresponding increase in blood flow. The occurrence of the binomial of an early metabolic increase uncoupled by a resting level regional cerebral blood flow (rCBF) is of particular interest since it is intrinsically well localized in space. In fact, an isolated increase in regional cerebral glucose metabolism (rCMRglu) is not affected by the spreading effect due to the increase in regional flow, which tends to distribute over a much more extended territory the phenomena originally circumscribed to a small cortical region.

Consequently, the use of the initial dip of the haemodynamic response, instead of the large later positive BOLD signal for the statistical evaluation of functional phenomena, has increased dramatically the spatial specificity of BOLD fMRI. In fact, the combined use of very high in-plane resolution (156 μm) and of the initial dip as input to the statistical analysis, has allowed researchers to demonstrate neural activation at the columnar level in the visual cortex (V2) of anaesthetized cats at very high magnetic field strength (9.4 T) [10, 11]. Taking into account the linear worsening of SNR with the reduction of voxel volume, spatial resolutions in the order of hundreds of microns are only achievable through the use of MRI units with high magnetic field intensities. The requisite of segmenting temporally the BOLD response to increasing specificity and spatial resolution clearly poses even more serious problems for the investigation of the neurophysiology of neuronal columns, since it requires keeping the temporal resolution high enough to

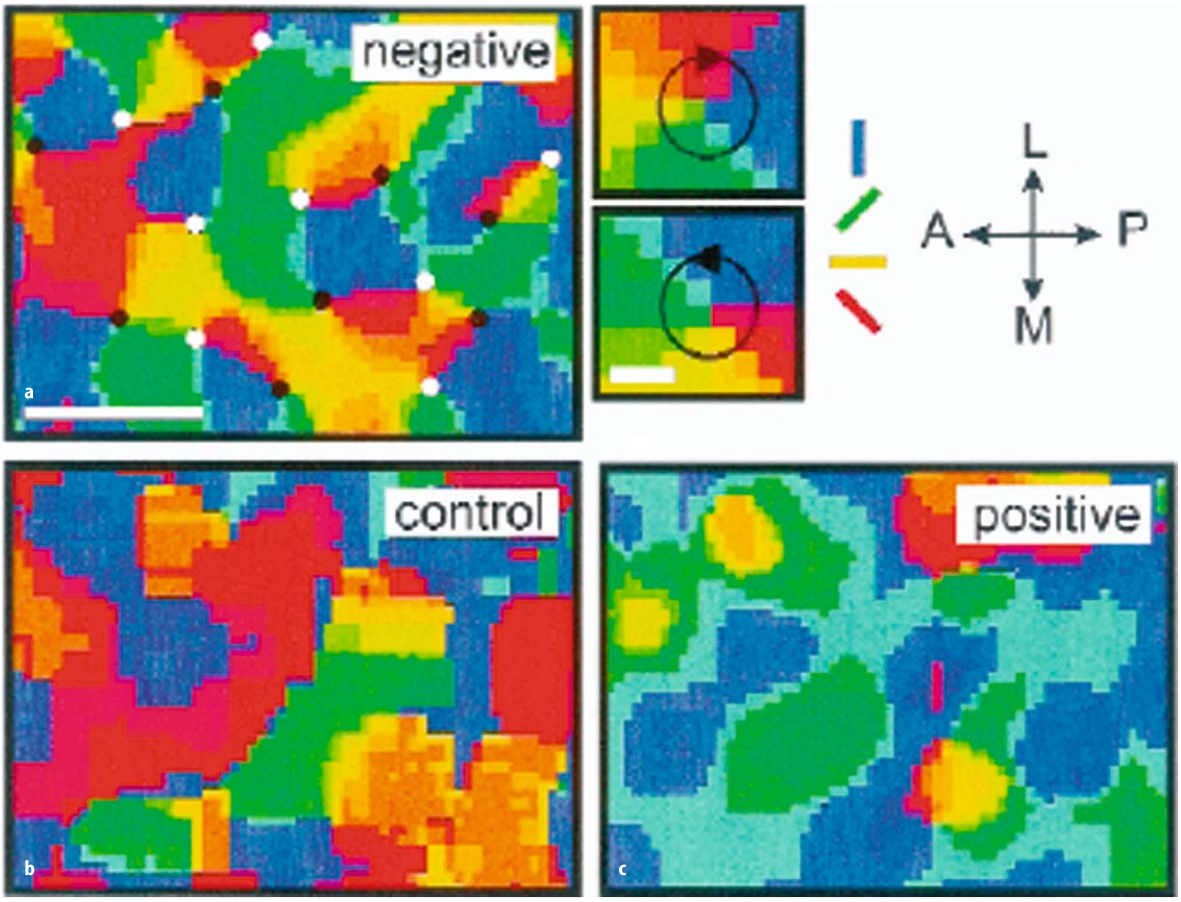

Fig. 10.2 a–c. fMRI-based composite angle maps of cat area 18 on the lateral gyrus (reprinted from [10] with permission). **a** The composite angle map obtained through pixel-by-pixel vector addition of the four single iso-orientation maps based on negative signal changes. The *colour key* next to **a** was used for colour coding the resulting orientation preferences. Overall continuity of the orientation preferences is interrupted at the orientation pinwheels where the cortical columns for different orientations are circularly arranged. The *white and black circles* in **a** depict clockwise and counterclockwise pinwheels, respectively. Two such pinwheels are enlarged *on the right* (**a**). *Scale bar for the enlarged pinwheels* 200 μm. As a control, the composite maps based on MR signals obtained before stimulus onset (**b**) and during positive BOLD signals (**c**) are also displayed. Maps in **b** and **c** were obtained from the same cortical region as in **a**. The control maps are devoid of topological structures characteristic of genuine composite angle maps (*A* anterior, *P* posterior, *M* medial, *L* lateral). *Scale bars* (**a, c**) 1 mm

observe and separate in time the different phases of the BOLD dynamics. This introduces a strict interdependence between spatial and temporal resolution.

The importance of achieving higher spatial resolution with higher field strength may extend beyond functional localization. In fact, the correlations between the time courses of multiple adjacent voxels in very high spatial resolution fMRI signals may contain valuable physiological information, which can be used to produce maps of neuronal-like connectivity [16]. By grouping neighbouring voxels in relation to the degree of temporal cross-correlation between their time courses, it is possible to generate a vector field for each voxel that, for very high spatial resolution data, may present the voxel average local neuronal connectivity within its vicinity. In a rat study [17], it has been shown that while the amplitude changes upon stimulation of these vectors, reflecting a strengthening of local neuronal connectivity, changes in their orientation may represent the altered internal neuronal communication. Again this potential is strictly related to the capability of high-field fMRI of reducing the mixing of multiple tissue-specific signal sources for each voxel.

10.2 High-Field and Temporal Resolution

The information about neuronal phenomena that fMRI extracts from the BOLD effect represents the convolution of the temporal envelope of local brain activity with the so-called haemodynamic input function [15].

The general effect of this convolution consists in the blurring of the functional information in space and in its dispersion in time. Thus, as is the case for the spatial resolution, the limit of temporal resolution is generally set by factors intrinsic to the local brain haemodynamics, and specifically by its time constants, rather than by technical factors. So, even if a theoretical time resolution of a few tens of milliseconds is easy to reach with modern fMRI gradient systems, the dispersion in time of functional information operated by the local haemodynamics does not permit the discrimination of two successive co-localized brain phenomena occurring at time intervals separated by less than 3–4 s [13]. This does not hold true in the case of the initial dip: paradoxically, this early functional phenomenon takes advantage of the haemodynamic delay in order to be separable from the large positive BOLD signal change. The initial dip has been interpreted as being due to an „inverse uncoupling" between metabolism (regional cerebral metabolic rate for oxygen – $rCMRO_2$) and flow (regional cerebral blood flow – rCBF). This early uncoupling, caused by an increase in $rCMRO_2$ in the presence of an unchanged rCBF, can be considered the exact opposite of the later, better known, uncoupling which produces the common BOLD signal through an rCBF increase prevailing over a much less pronounced $rCMRO_2$ change. As a result, the early uncoupling increases the regional deoxygenated haemoglobin and decreases the BOLD signal, while the later uncoupling produces opposite effects giving rise to the positive BOLD response [14].

As discussed above, the examination of the transient increase in deoxyhaemoglobin producing the negative signal change of the initial dip is controversial, even if it is very interesting since it overcomes some of the intrinsic limitations of the spatiotemporal resolution of the BOLD effect. The controversy, involving both fMRI and optical imaging [19, 20], originated from the failure of several laboratories to detect the effect in studies carried out at 1.5 T, probably determined by both the intrinsically reduced sensitivity of lower field strength units, and by a low contrast-to-noise ratio due to the reduced extent of the temporal window where the effect is visible [20]. Even if the initial dip poses considerable problems in its use as a general approach for high-resolution fMRI, it appears clear that the dip is the most promising way actually available for this purpose. In fact, the dip corresponds much better than the positive BOLD effect to the localization of neural phenomena as described by the gold standard of electrical activity recording [20]. If these concepts are accepted, then high magnetic field strength units are to be pursued as the only way of detecting the „elusive" initial dip.

With regard to the „positive" (conventional) haemodynamic response, advanced post-processing techniques such as „deconvolution" [22] or temporal independent component analysis (ICA) [23] are able to extract temporally more sophisticated functional information from high temporal resolution fMRI time-series. Provided that a reasonable signal-to-noise ratio in the functional time-series is present, particularly with the use of high magnetic field strength, a decomposition in the time domain can produce interesting neurophysiological information. In the auditory domain, an ICA decomposition in time and space has been successfully used for the qualitative and quantitative spatiotemporal analysis of BOLD dynamics in the neural processing of sound information [24, 25].

In „true" event-related studies conducted at high temporal resolution, the responses to each repetition of the task generate an fMRI signal which can be retrospectively reduced to a small set of fitted haemodynamic parameters like the onset or duration of the responses. These parameters, when correlated with variations in the experimental performances of the subjects [3, 26, 27] or compared across different areas for single [28] or averaged trial responses [29], enable the investigation of BOLD temporal dynamics on the temporal scale of hundreds of milliseconds. Also in this application, the essential requisite is to operate at a sufficient signal-to-noise ratio, as is usually permitted only by the use of high-field units. This is particularly true if the analysis is aimed at producing superior neurophysiological results, which generally require the simultaneous achievement of high spatial and temporal resolution.

A major technological improvement in MR hardware is represented by the use of multiple radiofrequency receiver coils to independently encode spatial information in parallel from multiple regions (parallel imaging [30, 31]). These techniques are capable of accelerating data acquisition, allowing high temporal resolution functional imaging. Theoretical considerations have shown [32] that the maximum acceleration factor consistent with an acceptable SNR increases linearly with main magnetic field strength.

10.3 High-Field and BOLD Signal Behaviour

It has been clear from the very first experiences that the strength of the main magnetic field (B_0) is a major factor in determining the amplitude of BOLD dependent fMRI signal changes [33] (Fig. 10.3). The physical reasons for the field dependence are inherent in the mechanisms producing the BOLD effect. In fact, the bulk magnetic susceptibility difference between blood containing paramagnetic deoxyhaemoglobin and surrounding diamagnetic tissue, on which difference the BOLD effect is based, increases with the main magnetic field strength, determining larger MR signal changes

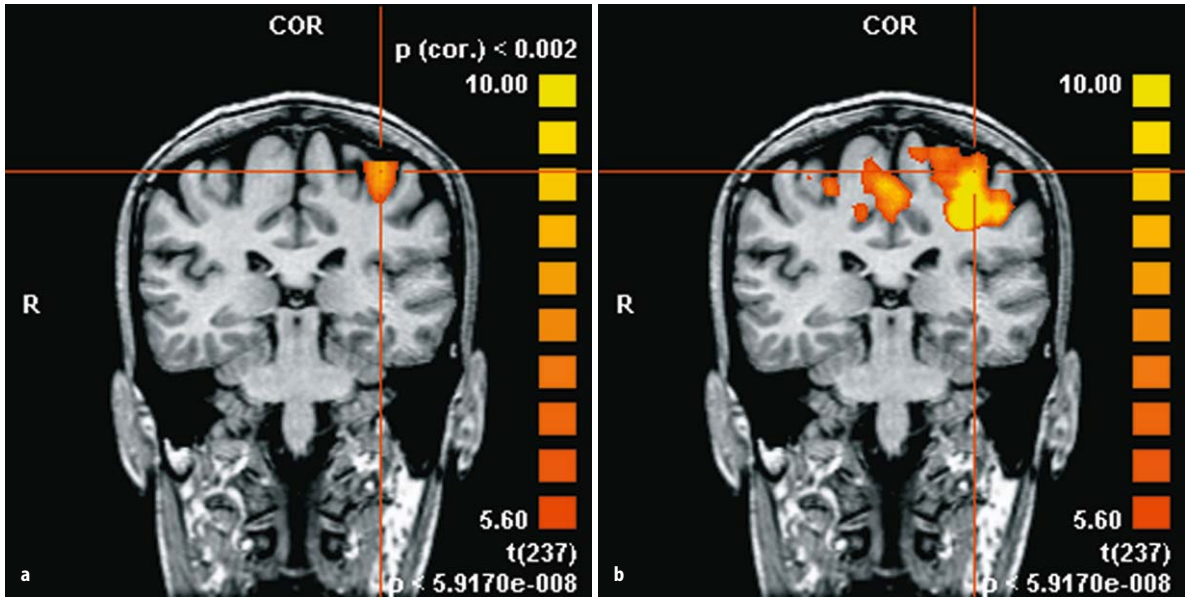

Fig. 10.3. Coronal fMRI maps of motor function obtained at 1.5 T (**a**) and at 3 T (**b**) during a block design experiment with a button press at a 0.5 Hz frequency. The maps have been elaborated with Brain Voyager using a General Linear Model Analysis after undergoing a motion correction and a spatial smoothing pre-processing step. The map obtained at 3 T shows clear advantages in the spatial extension of the activation (sensitivity) particularly in the supplementary motor region, and a better correspondence of the activation with the anatomy of the motor system (specificity). The intensity of fMRI signal (BOLD %) doubles on passing from 1.5 and 3 T

between baseline and activated states if high-field strength units are used [34]. As for the magnitude of the field dependence of the BOLD effect, it has been considered to vary from linear to quadratic [34–36], showing an inhomogeneous spatial distribution, principally depending on the relationship between dimension of voxels and dimension of blood vessels contained in them. Studies on the field dependence of the apparent transverse relaxation rate [36] showed that the BOLD effect is proportional to B_0 if the voxels contain large vessels (venules and veins; $d > 10$ μm), dropping to less than linear if vessels are larger than voxels. The relationship rises to more than linear in voxels containing a mixture of brain tissue, capillaries and venules with a small diameter (less than voxel dimension), and reaches quadratic behaviour (B_0^2) for voxels containing smaller vessels (capillaries and venules; $d < 10$ μm). The biophysical model explaining this complex signal behaviour requires taking into account two basically different modalities of spin dephasing in the extravascular space, known as dynamic and static averaging regimes [35]. The dynamic averaging is caused by the diffusion of water molecules during the time span preceding echo readout, through the inhomogeneous magnetic field determined by the presence of a blood vessel in a given voxel. The degree of inhomogeneity is strongly conditioned by the vessel diameter. At a distance equal to the diameter of the vessel, the perturbation induced by the local magnetic field ($\Delta\omega 0$) is reduced to the 25 % of the $\Delta\omega 0$ measured at the vessel boundary. The maximum effect of the dynamic averaging regime will be experienced when vessel dimensions are in the range of the typical diffusion distances for a given echo time, so ranging between 2 and 10 μm in the common conditions posed by the fMRI experiment. Its effects will be visible in a spin-echo experiment through the changes in T2 [35].

For larger vessels (> 10 μm), complete dynamic averaging for the entire voxel will not be possible.

The diffusion processes will generate only local dynamic averages over a subsection of the volume spanned by the magnetic field gradients produced by the blood vessel, in the so-called static averaging regime. A signal loss in the voxel will be in any case induced by the static averaging regime and will be visible in a gradient echo experiment in the absence of refocusing radiofrequency pulses [35].

The distinction between dynamic and static averaging regimes is fundamental to explaining the field dependence of BOLD with respect to vessel dimensions. In the regime of dynamic averaging, the BOLD effect is expected to vary as the square of the external magnetic field, while in the static averaging regime the dependence is linear. Even for the smallest vessels, the quadratic dependence of extravascular BOLD effect on the external magnetic field is not expected to persist forever with the increasing B_0. At some very high external magnetic field strength, predicted by the theory but not

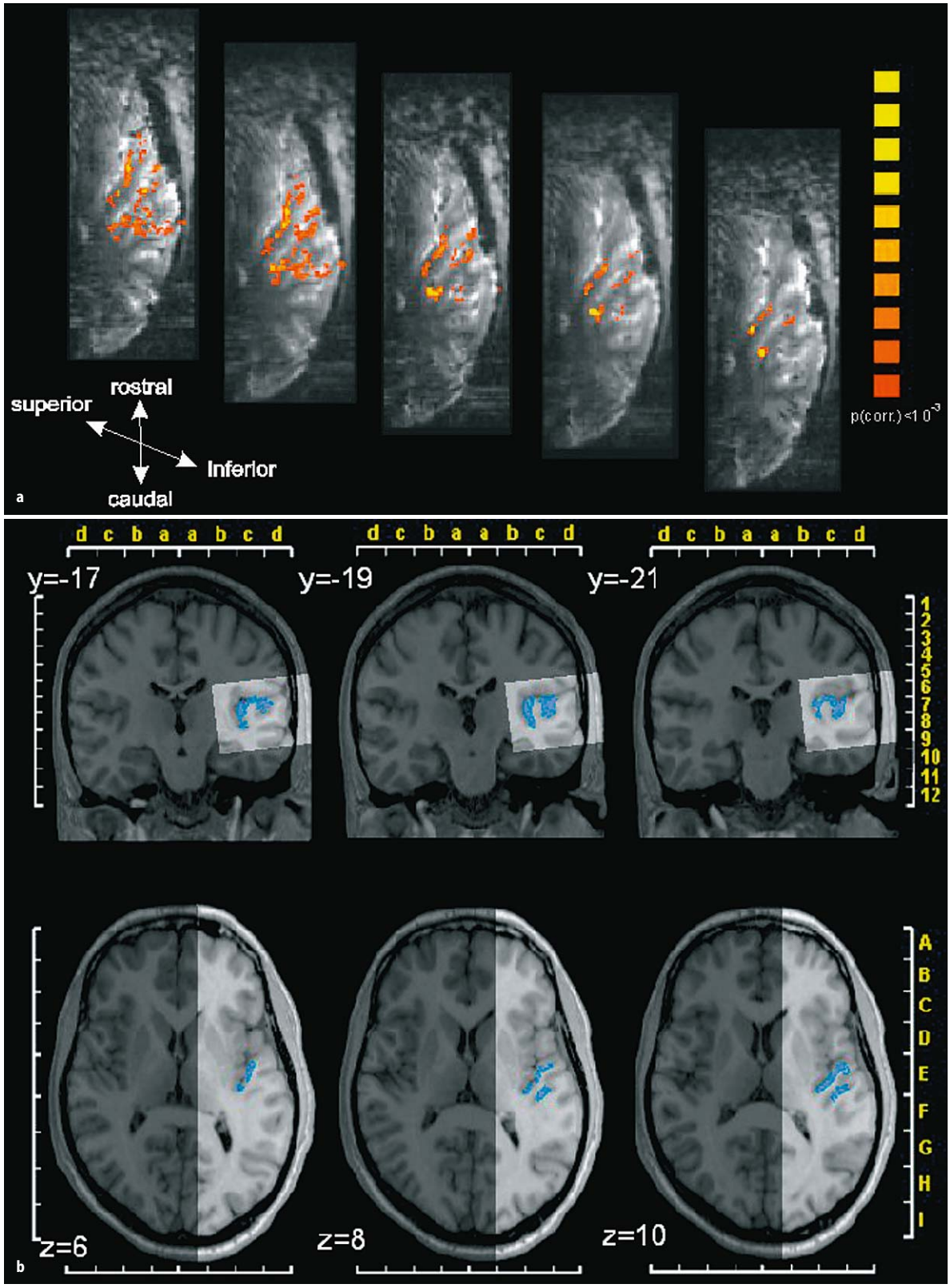

Fig. 10.4 a, b. High resolution fMRI of human auditory cortex obtained at high-field strength (7 T) (reprinted from [45] with permission). Despite the use of very small voxel dimensions, the 7 T EPI series presents a high enough signal to noise ratio to produce a very high „anatomical" detail of functional information

yet verified experimentally, even the extravascular space surrounding the capillaries will behave as in the static averaging regime.

In any case, whatever the exact dependence on the field strength, the BOLD signal from a time-series at high magnetic field strength will gain inherent sensibility and specificity to microcirculation with the increasing B_0 (Figs. 10.4, 10.5). Interestingly, the possibility of operating at a higher spatial resolution will further enhance the spatial specificity of fMRI towards local neuronal activity either because of the greater weight of small vessel contribution and because of the greater capability to separate the large vessel contribution in an imaging voxel. The effects on fMRI spatial resolution can be remarkable. Paralleling the potential for reducing voxel dimensions due to the improved signal to noise ratio, the increasing contribution to the BOLD effect coming from the capillary bed can push the effective spatial resolution towards and beyond the ideal physiological limit of 1 mm^2. In fact, if the initial dip is taken into account, its potential for improving spatial resolution converges with the improvement of signal to noise ratio and with the preferential sensitivity to capillary bed effects, further enhancing spatial resolution even below the millimetre range [8, 9].

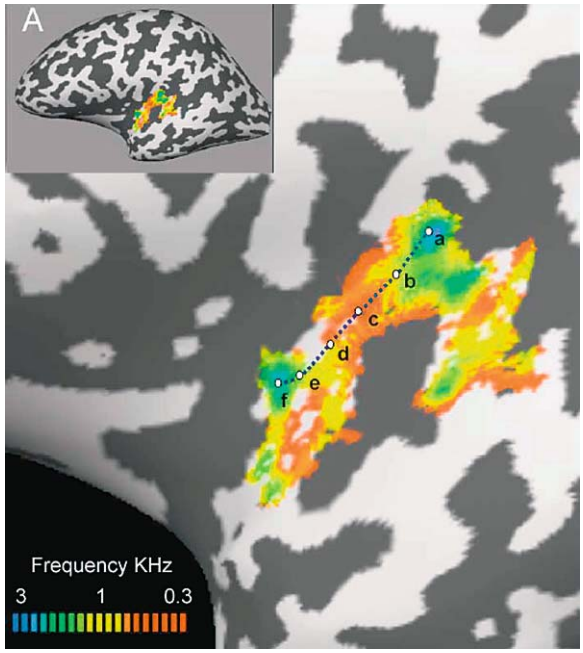

Fig. 10.5. High resolution fMRI of human auditory cortex obtained at high-field strength (7 T) (reprinted from [45] with permission). Owing to the high spatial resolution it becomes possible to map brain functions at the level of tiny clusters *within* larger functional areas. In the auditory cortex, as an example, it is possible to single out the cortical location of the highest sensitivity to different frequencies of a tonal stimulation

10.4 High-Field, Noise and Data Processing Issues

In evaluating the sensitivity and accuracy of BOLD based fMRI experiments, it appears evident that these parameters are ultimately conditioned by the functional contrast-to-noise ratio (CNR=$\Delta S/N$) between the activation-induced signal fluctuation and a „noise" term (N) including random noise, instrument instabilities and physiological fluctuations.

Because of the origin of the BOLD effect, the maximum available CNR at different magnetic field strengths is not univocal, but appears inhomogeneous in space due to different ΔS values depending on the proportion of vessels and brain tissue in the voxel and on the vessel diameter.

Specifically, as stated above, voxels containing vessels larger than the voxel itself present a signal change which varies less than linearly with field strength, while voxels containing capillaries and veins/venules with a diameter less than that of the voxel itself vary greater than linearly [34].

Nonetheless, the contribution of noise and particularly of physiological signal sources within the noise term is also crucial for the CNR. The physical nature and temporal behaviour of physiological signal sources can be very similar in targeting functional source signals and are thus similarly affected by an increase in the magnetic field strength [36]. This means that a substantial increase in the noise arising from physiological sources can be determined by increasing B_0, potentially paralleling the increase in BOLD signal and, thus, reducing the convenience of using high magnetic field strengths.

As a consequence, while several researchers observed a large (three- to fivefold) increase in BOLD signal changes in single slice (2D) fMRI experiments performed at 4.0 T compared to 1.5 T, the ultimate benefit of high-field strength for fMRI will be dependent on the contrast-to-noise ratio and is likely to be much smaller [41]. A study on field strength dependence of CNR (taking into account the background signal fluctuations related to scanner noise and physiologic fluctuations) has demonstrated a smaller (around 40%) improvement when the field strength is increased from 1.5 to 3.0 T [42]. Confounding factors in these studies are a lack of information regarding the level of the physiological background noise and the effects of inflow [41].

With advanced understanding of the sources of physiological noise it is conceivable that the physiological noise contributions that are temporally different from signal will be reduced, so that the ratio of signal to total noise will scale at least linearly with B_0.

Other studies compared CNR values for fMRI experiments performed at 1.5 and 4.0 T, suppressing inflow

effects by performing 3D acquisitions and using spiral readout gradients in order to minimize instabilities related to physiologic fluctuations. When comparing fMRI experiments with the same total scan time, performed on six subjects, and with acquisition parameters optimized for each field strength, the 4.0 T scanner proved to give superior results, with a 70 % greater number of activated voxels and a 20 % higher average *t* score for the activated voxels.

However, there are also noise-related problems that are specific for high-field applications. fMRI time-series recorded at high fields may become more sensitive to motion effects [43]. Moreover, parametric statistical analyses of BOLD fMRI data often assume that the data are normally distributed, the variance is independent of the mean, and the effects are additive. BOLD fMRI data acquired at high-field strengths (4 T) showed a strong departure from normality with the consequence that high-field BOLD fMRI data may need to be suitably transformed before classical parametric statistical analyses are applied [44].

Multivariate data analysis techniques can help to separate the physiological noise from the signal sources, allowing definitely higher CNRs. This is evident for the application of independent component analysis (ICA) to fMRI data-sets [32]. For example, Esposito et al. [33] showed how improvements in CNR are helpful for an ICA-based separation of functional signals from other sources of signal fluctuation. Hence, it is to be expected, although not yet shown by a direct comparison, that, at higher magnetic field strengths, despite the increased contribution to variance of signal and physiological noise components, the capability of ICA algorithms to separate them will be improved.

10.5 Conclusions

The use of high magnetic field strength fMRI units has the potential for improving considerably the sensitivity and specificity of functional studies. As a result of the high-field studies, fundamental neural dynamics taking place at a very small dimensional scale in specific laminar, columnar and multicolumnar domains have become directly visible. The advantages in terms of spatial resolution, temporal resolution, BOLD signal changes and noise behaviour depend on the acquisition sequence and on the practical combination of the acquisition parameters with the local microscopic brain structure. Nevertheless, high-field units can be expected to improve significantly the quality of the fMRI results and the level of neurophysiological information it is possible to gather from the data. The concurrent use of tailored processing strategies can make even more convenient the use of high-field systems.

References

1. Di Salle F, Formisano E, Linden DEJ, et al. (1999) Exploring brain function with magnetic resonance imaging. Eur J Radiol 30:84 – 94
2. Thulborn KR (1999) Clinical rationale for very-high-field (3.0 Tesla) functional magnetic resonance imaging. Top Magn Reson Imaging 10:37 – 50
3. Sereno MI, Dale AM, Reppas JB, et al. (1995) Borders of multiple visual areas in humans revealed by functional magnetic resonance imaging. Science 268:889 – 893
4. Kim S-G, Ugurbil K (1997) Functional magnetic resonance imaging of the human brain. J Neurosci Methods 74:229 – 243
5. Richter W, Somorjai R, Summers R, et al. (2000) Motor area activity during mental rotation studied by time-resolved single-trial fMRI. J Cogn Neurosci 12:310 – 320
6. Pfeuffer J, van de Moortele PF, Yacoub E, et al. (2002) Zoomed functional imaging in the human brain at 7 Tesla with simultaneous high spatial and high temporal resolution. Neuroimage 17:272 – 286
7. Kim S-G, Lee S-P, Goodyear B, Silva AC (1999) Spatial resolution of BOLD and other fMRI techniques. In: Moonen CTW, Bandettini PA (eds) (1999) Functional MRI. Springer-Verlag, Heidelberg, pp 195 – 204
8. Frahm J, Merboldt KD, Henicke W (1993) Functional MRI of brain activation at high spatial resolution. Mag Reson Med 29:139 – 144
9. Menon RS, Ogawa S, Strupp JP, Ugurbil K (1997) Mapping ocular dominance columns in V1 using fMRI. J Neurophysiol 77:2780 – 2787
10. Kim DS, Duong TQ, Kim SG (2000) High-resolution mapping of iso-orientation columns by fMRI. Nat Neurosci 3: 164 – 169
11. Duong TQ, Kim DS, Ugurbil K, Kim SG (2001) Localized cerebral blood flow response at submillimeter columnar resolution. Proc Natl Acad Sci USA 98:10904 – 10909
12. Logothetis NK, Merkle H, Augath M, et al. (2002) Ultrahigh resolution fMRI in monkeys with implanted RF Coils. Neuron 35(2):227 – 242
13. Logothetis NK, Pauls J, Augath M, et al. (2001) Neurophysiological investigation of the basis of the fMRI signal. Nature 412:150 – 157
14. Cheng K, Waggoner RA, Tanaka K (2001) Human ocular dominance columns as revealed by high-field functional magnetic resonance imaging. Neuron 32:359 – 374
15. Villringer A (1999) Physiological changes during brain activation. In: Moonen CTW, Bandettini PA (eds) Functional MRI. Springer-Verlag, Heidelberg, pp 3 – 13
16. Cordes D, Haughton VM, Arfanakis K, et al. (2001) Frequencies contributing to functional connectivity in the cerebral cortex in „resting-state" data. Am J Neuroradiol 22(7):1326 – 1333
17. Goelman G (2004) Radial correlation contrast – a functional connectivity MRI contrast to map changes in local neuronal communication. Neuroimage 23(4):1432 – 1439
18. Bandettini PA (1999) The temporal resolution of functional MRI. In: Moonen CTW, Bandettini PA (eds) Functional MRI. Springer-Verlag, Heidelberg, pp 205 – 220
19. Hu X, Yacoub E, Le TH, Cohen ER, Ugurbil K (1999) Functional MRI signal decrease at the onset of stimulation. In: Moonen CTW, Bandettini PA (eds) Functional MRI. Springer-Verlag, Heidelberg, pp 243 – 252
20. Ugurbil K, Toth L, Kim D-S (2003) How accurate is magnetic resonance imaging of brain function? Trends Neurosci 26(2):108 – 114
21. Goodyear BG, Menon RS (2001) Brief visual stimulation allows mapping of ocular dominance in visual cortex using fMRI. Hum Brain Mapp 14:210 – 217

22. Glover GH (1999) Deconvolution of impulse response in event-related BOLD fMRI. Neuroimage 9(4):416 – 429
23. Calhoun VD, Adali T, Pearlson GD, Pekar JJ (2001) Spatial and temporal independent component analysis of functional MRI data containing a pair of task-related waveforms. Hum Brain Mapp 13(1):43 – 53
24. Seifritz E, Esposito F, Hennel F, et al. (2002) Spatiotemporal pattern of neural processing in the human auditory cortex. Science 297:1706 – 1708
25. Seifritz E, Esposito F, Neuhoff JG, Di Salle F (2003) Response: sound analysis in auditory cortex – from temporal decomposition to perception. Trends Neurosci 26(5):231 – 232
26. Richter W, Ugurbil K, Georgopoulos A, Kim SG (1997) Time-resolved fMRI of mental rotation. Neuroreport 8(17): 3697 – 3702
27. Kim SG, Richter W, Ugurbil K (1997) Limitations of temporal resolution in functional MRI. Magn Reson Med 37(4):631 – 636
28. Formisano E, Linden DE, Di Salle F, et al. (2002) Tracking the mind's image in the brain I: time-resolved fMRI during visuospatial mental imagery. Neuron 35(1):185 – 194
29. Bellgowan PS, Saad ZS, Bandettini PA (2003) Understanding neural system dynamics through task modulation and measurement of functional MRI amplitude, latency, and width. Proc Natl Acad Sci USA 100(3):1415 – 1419
30. Sodickson DK, Griswold MA, Jakob PM (1999) SMASH imaging. Magn Reson Imaging Clin N Am 7(2):237 – 254
31. Pruessmann KP, Weiger M, Scheidegger MB, Boesiger P (1999) SENSE: sensitivity encoding for fast MRI. Magn Reson Med 42(5):952 – 962
32. Wiesinger F, Pruessmann KP, Boesiger P (2002) Potential and limitations of parallel imaging at high field strength. MAGMA 15(Suppl 1):447
33. Ogawa S, Lee T-M, Kay AR, Tank DW (1990) Brain magnetic resonance imaging with contrast dependent on blood oxygenation. Proc Natl Acad Sci USA 87:9868 – 9872
34. Gati JS, Menon RS, Rutt BK (1999) Field strength dependence of functional MRI signals. In: Moonen CTW, Bandettini PA (eds) Functional MRI. Springer-Verlag, Heidelberg, pp 277 – 282
35. Ogawa S, Menon RS, Tank DW, et al. (1993) Functional brain mapping by blood oxygenation level-dependent contrast magnetic resonance imaging. A comparison of signal characteristics with a biophysical model. Biophys J 64:803 – 812
36. Gati JS, Menon RS, Ugurbil K, Rutt BK (1997) Experimental determination of the BOLD field strength dependence in vessels and tissue. Magn Reson Med 38(2):296 – 302
37. Hennig J, Speck O, Koch MA, Weiller C (2003) Functional magnetic resonance imaging: A review of methodological aspects and clinical applications. J Magn Reson Imaging 18(1):1 – 15
38. Kruger G, Kastrup A, Glover GH (2001) Neuroimaging at 1.5 T and 3.0 T: comparison of oxygenation-sensitive magnetic resonance imaging. Magn Reson Med 45(4):595 – 604
39. McKeown MJ, Makeig S, Brown GG, et al. (1998) Analysis of fMRI data by blind separation into independent spatial components. Hum Brain Mapp 6(3):160 – 188
40. Esposito F, Formisano E, Seifritz E, et al. (2002) Spatial independent component analysis of functional MRI time-series: to what extent do results depend on the algorithm used? Hum Brain Mapp 16(3):146 – 157
41. Yang Y, Wen H, Mattay VS, et al. (1999) Comparison of 3D BOLD functional MRI with spiral acquisition at 1.5 and 4.0 T. Neuroimage 9:446 – 451
42. Bandettini PA, Wong EC, Jesmanowicz A, et al. (1994) MRI of human brain activation at 0.5T, 1.5T, and 3.0T: Comparison of DR2* and functional contrast to noise ratio. Abstr Proc Soc Magn Reson 2:434
43. Caparelli EC, Tomasi D, Ernst T (2005) The effect of small rotations on R2* measured with echo planar imaging. Neuroimage 15:1164
44. Lewis SM, Jerde TA, Tzagarakis C, et al. (2005) Logarithmic transformation for high-field BOLD fMRI data. Exp Brain Res 15
45. Formisano E, Kim D-S, Di Salle, et al. (2003) Mirror-symmetric tonotopic maps in human primary auditory cortex. Neuron 40: 859 – 869

Recent Developments and Prospects in High-Field MR

11

A. Bacci, R. Agati, M. Leonardi

During recent years much effort has been put into detecting and classifying disease states, and MR imaging has been a very important tool in this respect. Up to now, increasing the gradient strength has been the only strategy for meeting the increasing demands of advanced diagnostic imaging applications. This strategy is limited by physical, economic, and medical considerations: increasing gradient strength is technically difficult, and is associated with significant hardware costs and with the risk of inducing unwanted side effects such as peripheral neurostimulation.

The main advantage of high-field MR is the improved signal-to-noise ratio, which scales approximately linearly with field strength from 1.5 T to 3 T. This signal can be used to generate more accurate spatial representation or to speed up imaging times, depending on the specific application. Higher field strengths change tissue contrast parameters. T1 relaxation time is increased by approximately 30 %, whereas T2 and T2* relaxation times are decreased by about 15 % [37]. Increasing the field strength from 1.5 T to 3 T also doubles chemical shift and susceptibility. MR spectroscopy benefits considerably from the improved spectral resolution possible with high-field MR, and images acquired on 3 T MR demonstrate enhanced sensitivity to the blood oxygen level-dependent (BOLD) effect [77]. On the other hand, tissue heating induced by radiofrequency power is a disadvantage with the use of 3 T MR. In fact, specific RF absorption rate approximately quadruples when field strength increases from 1.5 T to 3 T. The most recent attempt to circumvent these limitations is parallel imaging MRI.

11.1 Parallel Imaging

Parallel imaging offers a number of advantages, like faster examination times, when applied to standard MR protocols. Rather than relying on rapid gradient switching to speed acquisition, parallel imaging uses clever algorithms and radiofrequency technology to acquire smaller data sets, specifically by undersampling *k*-space [30, 54, 56, 66].

The basis of parallel imaging is the use of the spatial information of the radiofrequency field that is associated with the individual elements of an RF coil array and the use of this information in concert with conventional gradient-based image encoding. Therefore fewer phase-encoding steps have to be performed. It improves data acquisition speeds beyond what can be achieved with conventional non-parallel approaches without imposing additional stress on the gradients (Fig. 11.1). With this method, fully encoded images are reconstructed from undersampled data sets, yielding large savings in scan time. On the other hand, the reductions in scan time incur a cost in both the complexity of the scan and the signal-to-noise ratio (SNR) of the final image [45]. The complexity of the scan arises from the fact that all parallel MRI techniques rely on the knowledge of coil sensitivities, which necessitates some form of calibration. In addition, the SNR loss of every image takes place for two reasons. First, there is a reduction in the temporal averaging of noise associated with the fact that fewer *k*-space points are used in the reconstruction. This leads to an SNR loss proportional to the square root of the reduction in scan time. This has the same effect as in conventional imaging with rectangular FOV [3]. Second, there is amplification of noise because, unlike in conventional Fourier imaging, the transformations used in coil-encoded image reconstruction are not unitary. This leads to an additional spatially dependent source of SNR loss that is quantified by the so-called geometry factor [49]. It is this geometry-associated loss that can be ameliorated through good coil array design and complex algorithms of reconstruction.

Parallel imaging (PI) methods can be categorized into two groups. In the first the missing *k*-space lines are calculated before Fourier transforming the data and this kind of algorithm is called Simultaneous Acquisition of Spatial Harmonics (SMASH) [67]. It can be truly considered to be the start of a new approach in MRI technology. The third generation of this algorithm is the GeneRalized Auto-calibrating Partially Parallel Acquisition (GRAPPA) that is now available for clinical routine imaging. The second type of PI method first reconstructs images with reduced FOV for all receiver

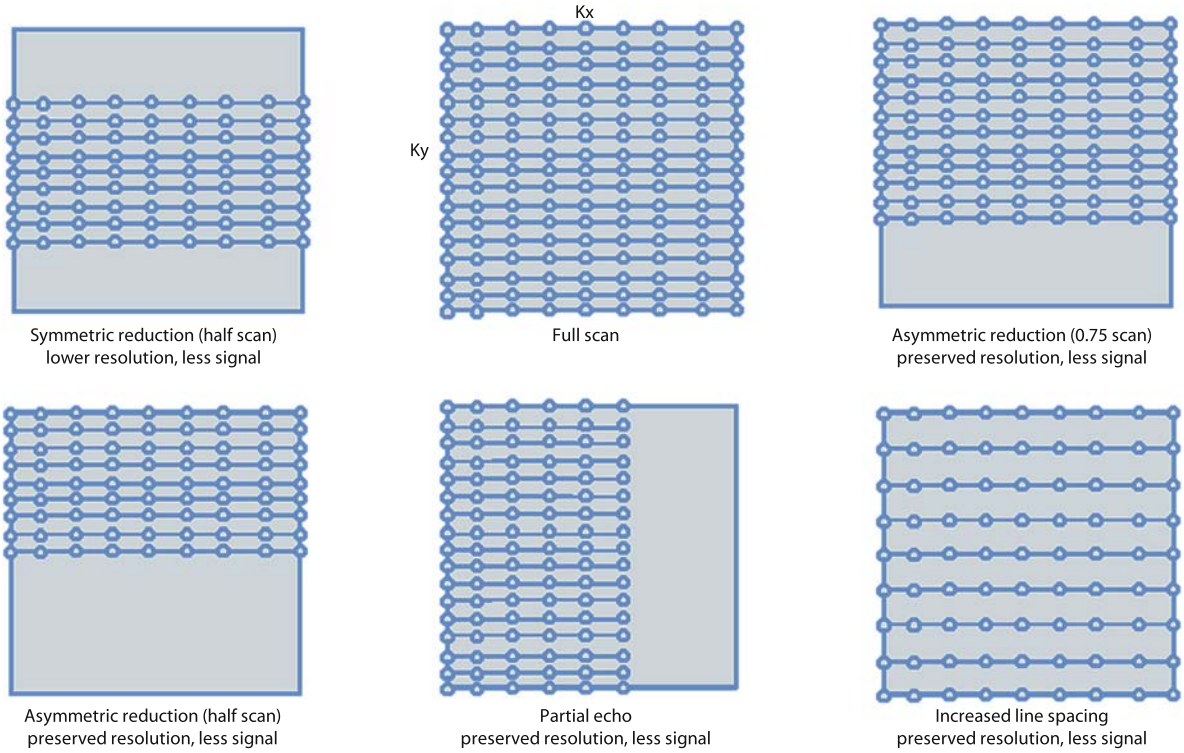

Fig. 11.1. Basics of *k*-space for faster MRI: MRI can be performed faster by acquiring fewer *k*-lines per MR image. (Courtesy of GE Healthcare Technologies)

coil elements and then blends these different images, by utilizing the knowledge of the spatial distribution of individual coil sensitivity, into one image with full FOV. The algorithm of this second type is called SENSitive Encoding (SENSE) and the modified algorithm mSENSE is also available as packages on clinical scanners.

Parallel imaging, regardless of in which domain image reconstruction is performed, requires some additional information about the spatial coil sensitivities; in other words providing information about which part of the FOV is covered by each coil element or from which area the coil does receive its MR signal. A homogeneous sample will present itself with a different signal intensity depending on the distance from the coil (principle of reciprocity) [31]. For PI the coil sensitivity information can be acquired as a separate scan or, typical for the GRAPPA and mSENSE algorithm, by additionally acquiring some of the missing data lines in the centre of *k*-space (so-called reference or auto-calibration lines) integrated into the acquisition [3].

In parallel imaging the acceleration of imaging is due to the reduced number of phase encoding lines that need to be acquired to form an image at a given FOV and resolution. The lines are replaced by exploiting the spatial information that is inherent in the spatially variable sensitivity of an array of surface coils. The number of receiver elements determines the maximum time reduction factor (R), which indicates the level of improvement to acquisition speed [38]. With an acceleration factor of 2, only every other line in *k*-space is acquired and the imaging is virtually cut in half.

Several different techniques for parallel imaging have been proposed by different MR system vendors (ASSET, IPAT, SENSE); they currently allow a reduction of phase encoding steps by a reduction factor of 2 to 6 (and recently even higher). We can try to examine them separately.

Sensitivity encoding (SENSE) is a parallel imaging technique that trades signal-to-noise for speed. Just as S/N is reduced by 40 % whenever the number of excitations is halved in a conventional spin-echo image, the same is true of SENSE: A SENSE factor of 2 halves the acquisition time and reduces the S/N by 40 %. SENSE is therefore most useful when there is excess S/N, such as at 3 T. It requires the use of phase-array coils, and the number of coil elements determines the theoretical limit on the SENSE factor. SENSE works by intentionally reducing the field-of-view and the number of phasing encoding steps, which in turn reduces the acquisition time [5]. This would normally lead to wraparound artefact, or „aliasing“, but because the local sensitivity of each coil in the phase array is known, the aliasing can be unwrapped.

SENSE uses the knowledge of coil intensity (sensitivity) profiles to reconstruct undersampled data sets, post-Fourier transform [53]. Sensitivity assessment re-

quires that low-resolution, fully Fourier-encoded reference images are obtained with each array element and with a body coil prior to parallel imaging. Element-wise division of the array references by the body coil references yields raw sensitivity maps. This means that body coil homogeneity forms the basis of homogeneity correction accomplished by SENSE reconstruction [38]. Raw sensitivity maps are refined by a fitting procedure that performs noise elimination and sensitivity extrapolation. Regions that do not contribute signal, according to the references, are automatically excluded from SENSE reconstruction (Fig. 11.2). Another form of SENSE is Modified SENSE (mSENSE). The difference is that mSENSE uses autocalibration and does not require a reference scan to calculate sensitivity maps [74]. This is achieved by splitting *k*-space into two regions: a central, fully sampled region from which information about coil sensitivities is derived, and an outer undersampled region as in generic SENSE.

The other technique is GRAPPA (generalized autocalibrating partially parallel acquisition); it performs reconstruction in the *k*-space domain [25]. GRAPPA acquires autocalibration signal (ACS) lines along with the reduced data set, and no reference scan is required. The scanner uses the signal lines to estimate a series of weighting functions, which are used to calculate the unacquired lines. When all lines are reconstructed for a particular coil, a Fourier transform can be used to generate the uncombined image for that coil. This process is repeated for each coil of the array to produce a full set of uncombined images, which can then be combined using a normal „sum of squares“ reconstruction. GRAPPA uses several blocks of data to fit each missing line. Additional acquired calibration lines can also be included to improve image quality.

The advantages of using this kind of technique are considerable. The SENSE-mediated reduction of acquisition time can be traded for improved temporal and spatial resolution of any given pulse sequences, without change of image contrast. In addition to the mere increase in image acquisition speed, the reduction of phase-encoding steps brings two further advantages [35]: First, in single-shot EPI applications that are usually used for diffusion imaging, diffusion tensor imaging or functional BOLD-contrast MR studies, SENSE helps to shorten the echo train length in proportion to the reduction factor. The shorter echo train also reduces the phase errors during the EPI readout and the susceptibility effects such as image distortions and blurring. In addition, the shorter echo train translates into a significantly higher SNR.

PI helps to shorten the length of the echo train without loss of spatial resolution in single-shot turbo/fast spin echo (HASTE, SSFSE) too [25]. These sequences

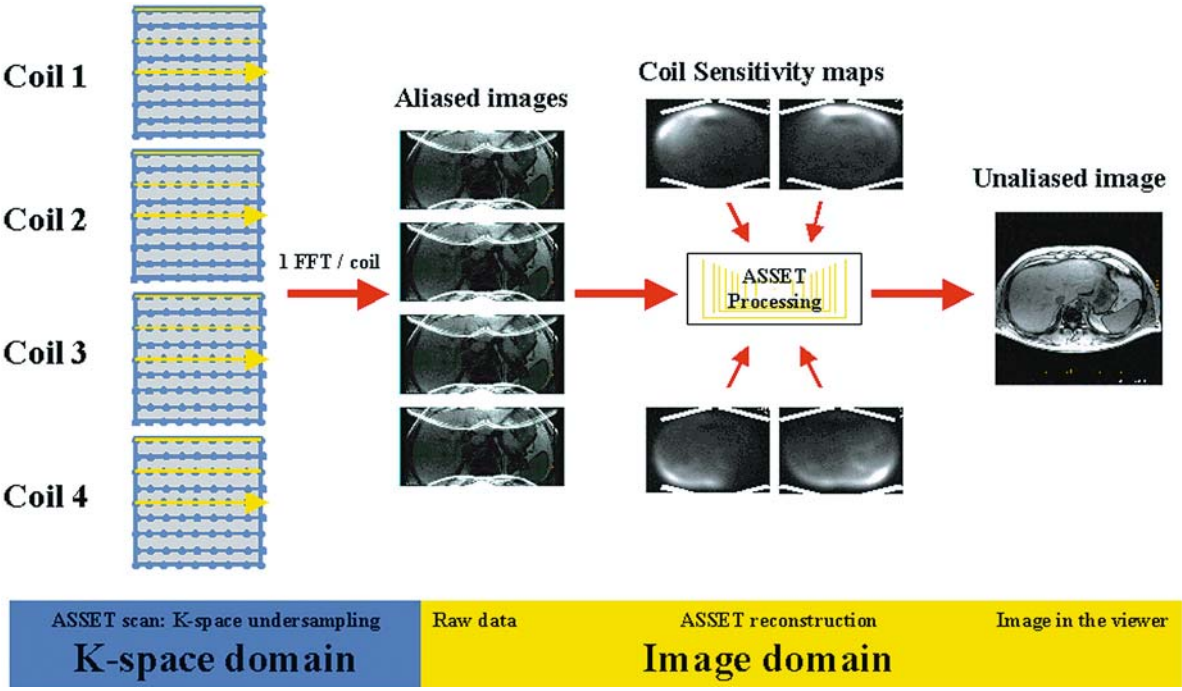

Fig. 11.2. ASSET, SENSE, and IPAT use the knowledge of coil intensity (sensitivity) profiles to reconstruct undersampled data sets, post-Fourier transform. Element-wise division of the array references by the coil references yields raw sensitivity maps. Raw sensitivity maps are refined by a fitting procedure that performs noise elimination and sensitivity extrapolation. Regions that do not contribute signal, according to the references, are automatically excluded from reconstruction. (Courtesy of GE Healthcare Technologies)

often suffer from image artefacts because of their long echo train and can appear blurred because of the T2-related signal decay during the readout of echo train. Second, SENSE helps to reduce RF deposition (regular phase encoding requires an RF pulse for every step). This is extremely helpful for high-field imaging where specific absorption rate (SAR) increases with the square of B_0. The higher the field strength, the more energy patients absorb with excessive heating of the patient. In fact SENSE can also decrease the number of echoes in TSE sequences at a given spatial resolution and thus reduce the specific absorption rate. Acceleration factors of up to six are feasible because of the intrinsically high SNR obtained at 3 T [21]. The combination of SENSE with 3 T makes an ideal partnership for optimized high-field MR protocols [77].

The shorter examination time obtained with parallel imaging is therefore useful for claustrophobic patients and patients who find it difficult to remain still.

Using GRAPPA it is possible to take cervical scans with fewer motion artefacts, because GRAPPA provides a greater signal and less ghosting than mSENSE [38].

While the maximum number of parallel receive channels on clinical scanners is currently in the vicinity of eight, Zhu et al. [79] presented a 32-element receive-coil array and a volumetric paradigm that address the SNR challenge at high accelerations. Each system represents the integration of multiple sets of MR electronics, including analog-to-digital converters and digital data pipelines, into a single system. All receivers in the system multiple sets of electronics were synchronized to each other, which in effect expanded the number of parallel receivers to a total of 32. Pulse sequences were adapted to work with the synchronization mechanism, and custom software was developed to facilitate scan control and data communication.

Parallel imaging facilitates tradeoffs between acquisition time, spatial coverage and image SNR, which has significant implications for the volumetric paradigm. While acquisition time tends to increase linearly with the expansion of volume coverage using a multislice approach, a more manageable time increase can be expected of the same expansion using a parallel imaging-based volumetric approach [79].

11.1.1 Parallel Imaging Applications

11.1.1.1 1024 MR Angiography

Another application of parallel imaging is in MR angiography, where the use of phase-array coils has the advantage of a higher *S*/*N* than standard quadrature RF coils. The greater *S*/*N* of these coils and the higher field strength of 3 T MR can be traded for speed or higher spatial resolution at the same acquisition time. This leads to 1024 MR angiography. The acquisition time for 3D time-of-flight MRA is TR × Np × Ns, and increasing the number of phase-encoding steps (Np) to 1024 would either lead to an excessively long acquisition time or mandate a reduction in TR. On the other hand, a very low TR limits the time available for inflow of unsaturated blood and reduces flow-related enhancement, which is the basis for TOF MRA. Increasing the matrix size from 512 to 1024 along one axis decreases *S*/*N* by 50 % (assuming FOV is held constant). Halving pixel dimension along both the phase and frequency axes reduces *S*/*N* to 25 %. For all these causes the use of 3 T MR and the latest generation of phase-array coils with a rectangular FOV allows the same spatial resolution to be achieved, reducing the acquisition time. If we add a SENSE factor [5], we can halve the time acquisition from 14 min, 12 s to 7 min, 6 s (spoiled GRASS sequence with TR 31/TE 6). Although the spatial resolution of MRA can surpass that of DSA, the latter has the advantage of temporal information. Use of the techniques of Temporally Resolved 3D Contrast MRA allows temporal phases to be obtained from an MR angiogram. They eliminate the traditional trade-off between spatial and temporal resolution in vascular imaging.

11.1.1.2 Temporally Resolved 3D Contrast MRA

We know that the major advantages of intra-arterial digital subtraction angiography are high-spatial-resolution images and temporal information regarding delayed filling of the vasculature of interest. Time-of-flight magnetic resonance (MR) angiography has proved to be accurate in the depiction of vascular pathologic conditions in the peripheral vasculature. However, long acquisition times and flow-related artefacts have hindered its widespread application [61]. Contrast-material enhanced MR angiography is an alternative that has been shown to be less susceptible to the saturation effects that are common with time-of-flight imaging. To optimize image contrast, the maximum concentration of gadolinium should be present during acquisition of central *k*-space lines during peak arterial enhancement [40]. This is normally achieved by using a test bolus injection and fluoroscopic or automated triggering [28]. A final approach has been to collect 3D image data sets rapidly enough (typically 1 – 10 s per

▷

Fig. 11.3. Intracranial AVM. TRICKS images (3D TOF SPGR, TR 3.7, TE 1.3). Matrix 224 × 192, Thk 1.8 mm, FOV 28, temporal res. 2.5 s, 8 phases. They show multiple vascular phases (contrast enhancement of arteries, capillaries and veins). No coordination of contrast agent arrival and image acquisition was required

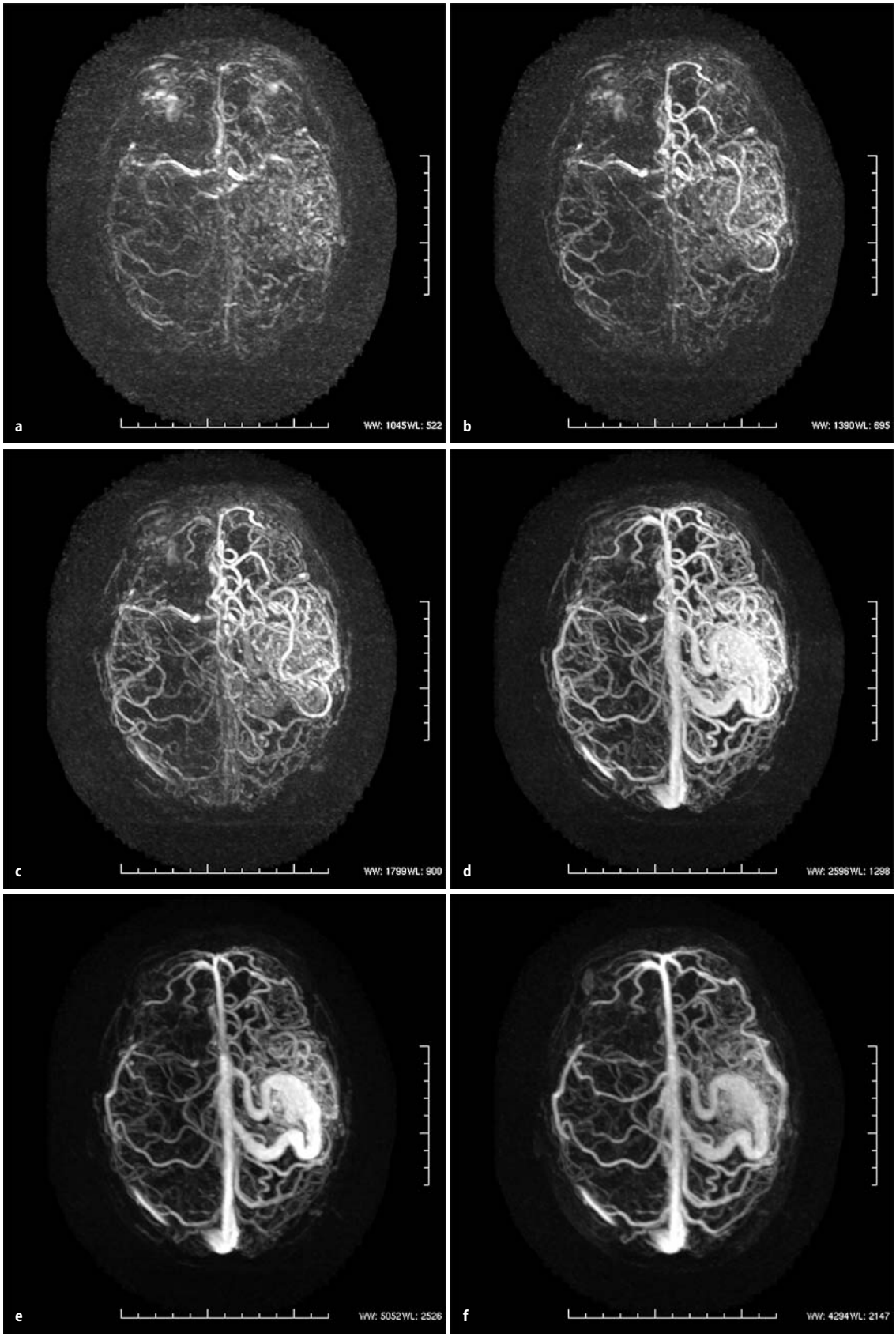
a
WW: 1045 WL: 522
b
WW: 1390 WL: 695
c
WW: 1799 WL: 900
d
WW: 2596 WL: 1298
e
WW: 5052 WL: 2526
f
WW: 4294 WL: 2147

acquisition) that at least one data acquisition is aligned with the arterial phase of the contrast material bolus [52]. Besides eliminating the timing problem, such a new „time resolved" approach provides temporal information about relative rates of contrast enhancement of arteries, parenchymal tissue, and veins [72]. With time-resolved techniques, bolus timing is no longer necessary, as multiple vascular phases are obtained without any predetermined timing, contrast injection and simultaneous beginning of scanning (Fig. 11.3). The operator simply selects the desired image set afterwards: pure arterial phase, maximum venous, etc. The most straightforward way to accelerate acquisition time is simply by scanning faster. This can be done using some combination of limiting the imaging volume, decreasing the resolution, decreasing TR, or using a parallel imaging technique such as SENSE [40]. Recent developments in gradient system allow TR's of < 2 ms in many systems. Even if the temporal resolution is insufficient for isolating the desired vascular phase, post-processing techniques such as correlation analysis can be used to synthesize images of pure arterial versus pure venous phase.

Using 3D TRICKS (time resolved imaging of contrast kinetics) and its variants it is possible to obtain simultaneous high spatial resolution and high temporal resolution over a large field of view.

The basis of this technique is to combine the repeated sampling of the low-spatial-resolution *k*-space views with temporal interpolation to produce a series of time-resolved imaging of contrast kinetics (TRICKS) three-dimensional MR angiographic images. Three-dimensional TRICKS images reveal the dynamics of contrast material arrival and obviate a timing image [34]. The prescribed *k*-space is divided into a number of regions in a TRICKS acquisition [12]. According to Caroll and Vigent [11, 73], the regions can be three (A, B, C) or four (A, B, C and D), and the regions are divided along the phase-encoding (*ky*) direction. The central region (A) contains the lowest one-third of spatial frequencies in the phase encoding direction, and successive regions correspond to higher spatial frequencies in this direction. During each TRICKS time frame, a segment of *k*-space corresponding to one region is acquired. Central *k*-space, which contributes most to overall image contrast, is repeatedly collected every 2 – 8 s in an alternating fashion, with other frames of more peripheral *k*-space collected less frequently. Images are then „synthesized" at high temporal resolution by piecing together each unique block of central *k*-space with a linear interpolation of the remaining *k*-space frames acquired in closest temporal proximity. In this way a high-resolution reference image is collected with N phase encoding steps dimension. The *k*-space segment acquisition time ΔT (and reconstructed frame period) is proportional to the acquired spatial resolution [73]. Temporal resolution is characterized by both the repetition time ΔT of each *k*-space segment and the width of the acquisition window necessary to reconstruct an image set [73].

Two parameters are more important to the understanding of the TRICKS acquisition: the *frame rate* and the *temporal aperture* [12]. The *frame rate* is the rate at which TRICKS segments are acquired and it is calculated as $TR \times Nz \times (Ny/Nr)$, where TR is repetition time, Ny is the number of phase-encoding values, Nz is the number of sections, and Nr is the number of TRICKS regions. It is possible to acquire the highest spatial resolution with a time between acquisition of a region A no greater than the time between arterial and venous enhancement. This ensures that region A is acquired vein-free and combined with regions, which are acquired later. The time during which data for a single frame are acquired is the *temporal aperture*. It is used to determine the length of the contrast agent injection. The largest temporal aperture, which corresponds to the acquisition of all regions of *k*-space [12], is calculated using $TR \times Nz \times (Ny/Nr) \times (Nr+1)$. A high variation in the arrival time of the contrast agent curve can introduce ringing and blurring artefacts, increased by the temporal interpolation [13]. It is much better for a low injection rate, which provides a longer contrast agent bolus to increase imaging time in order to improve spatial resolution, to acquire a greater number of arterial phases and to reduce intravenous concentration. TRICKS does not need a very precise synchronization between acquisition and bolus arrival, providing that the mask is not corrupted by contrast. The TRICKS technique, in fact, uses the combination of an integrated mask and complex subtraction and the detection of the peak arterial frame for selective reconstruction [11]. Since the integrated mask image subsequently removes contrast material already present in the veins from the previous injection, a clean arterial frame can be obtained. In addition, with the application of the peak arterial time-frame technique, the signal intensity in the temporally acquired *k*-space regions is analysed and those frames with increasing signal intensity are used for reconstruction of a clean arterial frame. This procedure is performed in *k*-space and not in image space with reduction of post-processing time [27].

Therefore this technique allows greater temporal and spatial resolution/volume coverage than with a conventional sequence and it lends itself to the „video" format, where passage of contrast material can be directly viewed.

The biggest drawback, other than the large number of images generated, is that *k*-space discontinuities, in conjunction with varying intravascular gadolinium concentration, can potentially lead to artefacts. A recent refinement of this strategy is to traverse *k*-space using radial or spiral projections, which allow for slid-

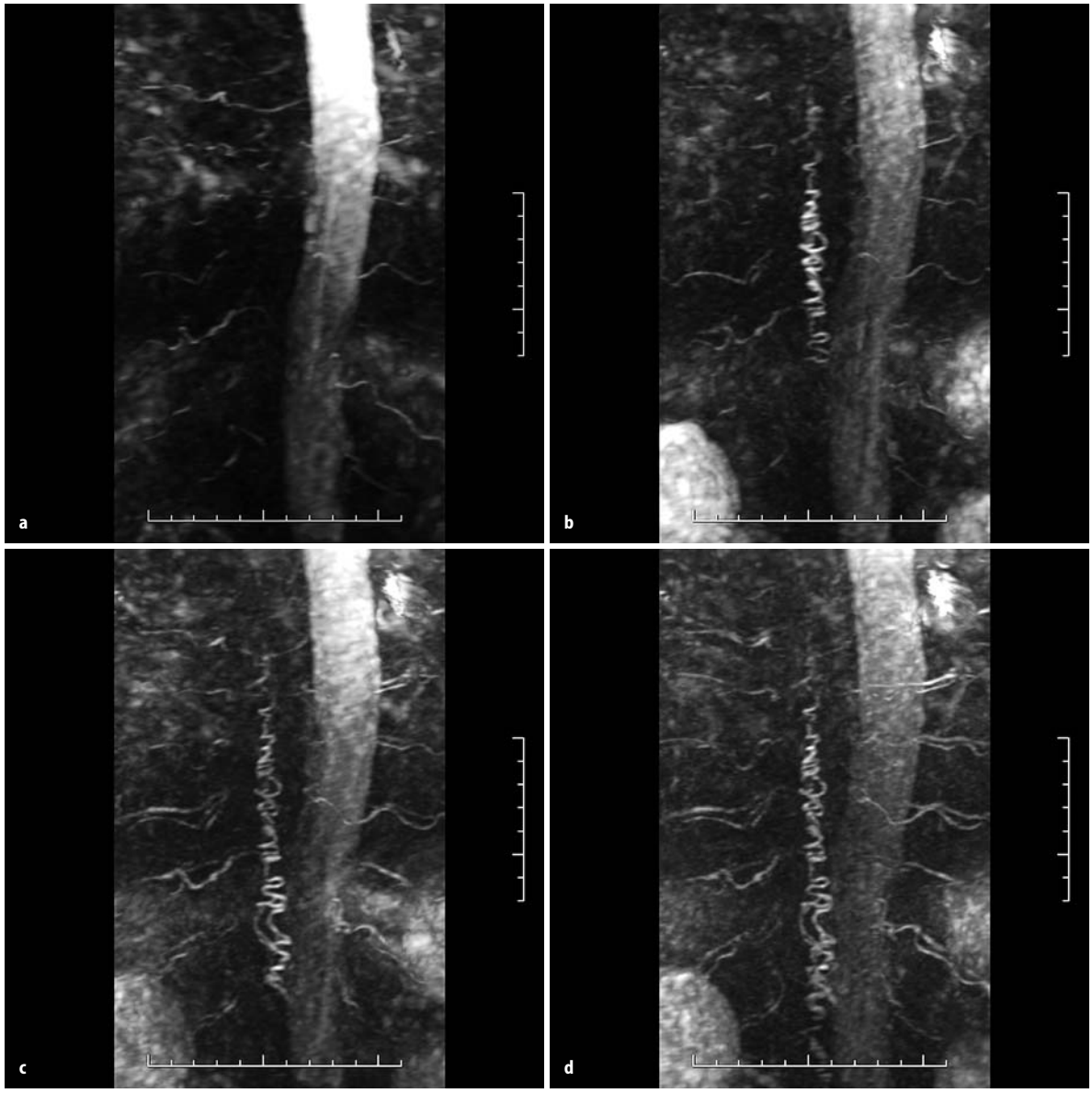

Fig. 11.4. Spinal MRA. Coronal TRICKS images (3D FAST SPGR, TR 4.3, TE 1,1). Matrix 384 × 192, Thk 2 mm, FOV 35, temporal res. 0.04 s, 9 phases. Coronal MIP reconstruction: the images show different enhancing phases of a dural fistula

ing window reconstructions at very temporal and spatial resolutions (Fig. 11.4). One variation, known as isotropic projection reconstruction (VIPR), is particularly promising [40].

The advantages of temporal resolved 3D contrast MRA, like TRICKS, are: to eliminate timing and triggering, to isolate a pure arterial phase even with asymmetric flow, to eliminate venous contamination, to capture flow dynamics, to characterize filling like conventional angiography, and to enable multiple injections through automated complex subtraction. Moreover, the temporal resolution of 3D dynamic imaging is accelerated without sacrificing spatial resolution (Fig. 11.5).

11.1.1.3 Spectroscopy

MR spectroscopic imaging (MRSI) can benefit from both high field strength and parallel imaging techniques. The acquisition of MR spectroscopy (MRSI) allows information to be obtained on the spatial distribution of metabolites in a lesion and surrounding tissue, the determination of the extent of the lesion, and the detection of contralateral lesion. Spectroscopy gains in multiple ways from increased field strength: besides a crucial increase in SNR, the chemical shift difference between different metabolites increases with field strength, allowing for better separation and identifica-

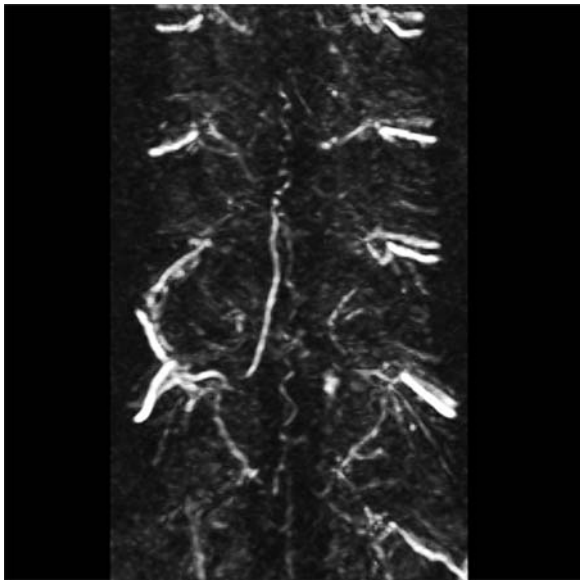

Fig. 11.5. Spinal MRA. Sagittal TRICKS images (3D FAST SPGR, TR 4.3, TE 1,1). Matrix 252×252, Thk 1 mm, FOV 35, temporal res. 0.15 s, 2 phases. Coronal MIP reconstruction: the image shows the Adamkiewicz artery

tion of metabolites. This increased chemical shift difference may be used to obtain higher SNR or additional speed in advanced techniques such as multi-echo spectroscopic imaging (TSI), similar to RARE, FSE or TSE in imaging. This is because in TSI the echo spacing determines the achievable spectral resolution as well as the maximum tolerable number of echoes in the echo train. A field strength of 3 T enables a twofold shorter echo spacing and thus longer echo trains while maintaining the same spectral separation between metabolites as at 1.5 T [17]. The scan time required to achieve acceptable resolution and SNR for MRSI can become too long for practical use in a clinical examination. By using up to six spin-echoes in the echo train, acquisition times for MRSI are reduced significantly. Dydak et al. [15, 16] in two recent works have proposed using the technique of parallel signal acquisition to reduce MRSI scan time and produce metabolite maps in patients with cerebral gliomas. They proposed undersampling the two in-plane phase-encoding dimension of a conventional 2D PRESS MRSI acquisition and using SENSE reconstruction. A reduction factor of 2 was used in each spatial direction, resulting in a net factor of 4 improvement in scan time to achieve a comparable spatial and spectral resolution. It is possible also to achieve a 3D SENSE-MRSI acquisition (24×24×8 slices) within 14 min. The flexibility of parallel imaging techniques allows the combination of two methods, enabling subminute scan times for single slice or a 3 min scan time for 6 slice MRSI scans with high spatial resolution. This will allow in the future the consideration of dynamic or functional MRSI (fMRSI) experiments with good temporal resolution, or the imaging of dynamic metabolic processes covering the whole brain [17].

11.2 PROPELLER

PROPELLER is the PeRiodically Rotated Overlapping ParallEL Lines with Enhanced Reconstruction (PROPELLER) MRI, which is a recent method proposed to reduce motion artefacts. In fact, patient motion is a significant problem in MRI of the brain, leading to a reduction in image quality and loss of diagnostic information. Motion artefacts, loss of resolution, and signal reduction combine to reduce anatomic detail and limit the detection of pathological findings within the brain [18, 59]. The amount of motion artefacts during brain imaging depends on patient cooperation. The patients are often suffering from intracranial pathologies causing confusion, agitation or pain, and 14% of subjects require sedation to obtain satisfactory images [43]. Pipe [49] reported two kinds of artefacts: the type I artefact that arises as a result of tissue displacement during the quiescent period between each data sampling and the following excitation rf; and the type II artefact that arises as a result of spin phase induced by motion through magnetic field gradients between an excitation rf pulse and the subsequent data sampling period. Many methods have been used to resolve these problems. Glover, Pauly and Ahn proposed centre-out imaging methods such as projection-reconstruction [22] and spirals [1] to reduce motion artefacts. These are attributable in part to oversampling of central *k*-space, which reduces artefact in a manner similar to multiple averaging in conventional imaging. In addition, when data collection begins at the centre of *k*-space, in-plane gradient moments are greatly reduced in the central region of *k*-space, minimizing type II artefact. Another method is by use of navigator echoes that collect extra data of measurement of motion or motion-related phase to reduce type I artefact [46]. Navigator echoes may also be used to throw out data collected when there is a significant motion, trading longer data collection times for reduced motion artefacts [58]. Sarty [60] describes a method called single trajectory radial (STAR) imaging. It is a single trajectory *k*-space sampling method that can be made truly radial over most of its trajectory. It is different from previous methods where the acquisition of radial data in *k*-space had to be done line by line with the appropriate TR elapsing between each line acquisition. And it is different from echo planar imaging (EPI) that is capable acquiring complete *k*-space data on a Cartesian grid in a single acquisition along a single trajectory. The basic STAR trajectory consists of radial line segments tangentially joined by circles. The gradients required for the linear part of the trajectory are the obvious combinations of constant

amplitude gradients. Data acquired on the STAR trajectory may be reconstructed by convolution regridding or by a non-uniform Fast Fourier transform. Reconstruction of the mathematical phantom STAR data produced high quality images free from artefact for all cases as was expected.

PROPELLER MRI also permits correction for in-plane displacement and rotation (type I artefact), image phase due to motion (type II artefact), and through-plane motion [49]. PROPELLER MRI acquires data in a series of concentric rectangular strips or blades, each of which rotates through the centre of *k*-space. The central region of *k*-space is sampled for every blade (Fig. 11.6a, b). This allows the correction of spatial inconsistency in position, rotation and phase between strips, and it allows also the rejection of data based on a correlation measure indicating through-plane motion and decreasing motion artefacts through an averaging effect for low spatial frequencies. The method offers major benefits because the central region of *k*-space is sampled multiple times, offering improved artefact suppression, and data within this central region can be compared between each blade. If motion has occurred between the acquisition of each blade, then data can be transposed to its estimated stationary position, prior to final image reconstruction. Every PROPELLER-correct image is derived using data that has been corrected for in-plane rotation and translation [50]. Central *k*-space data from the first blade was chosen as the stationary data set and compared to corresponding data from each PROPELLER blade. Data

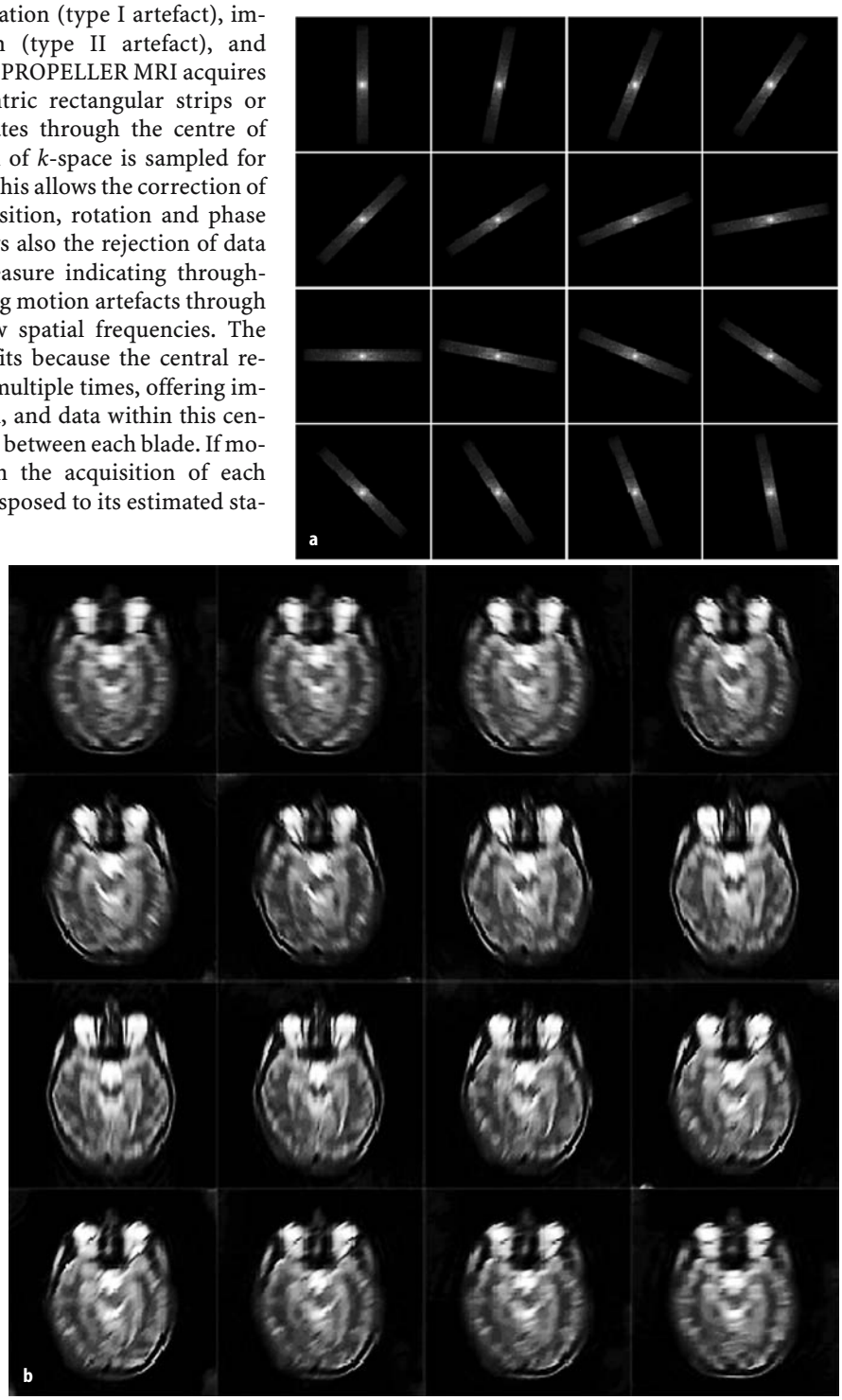

Fig. 11.6 a, b. Propeller blade comparison. For each TR, one fast spin echo train collects all the phase-encoded lines for a blade. Every blade has a low-resolution image. The blades can be compared, and those that do not match can be discarded or, in the case of T2 and T2 FLAIR, a correction can be attempted. (Courtesy of GE Healthcare Technologies)

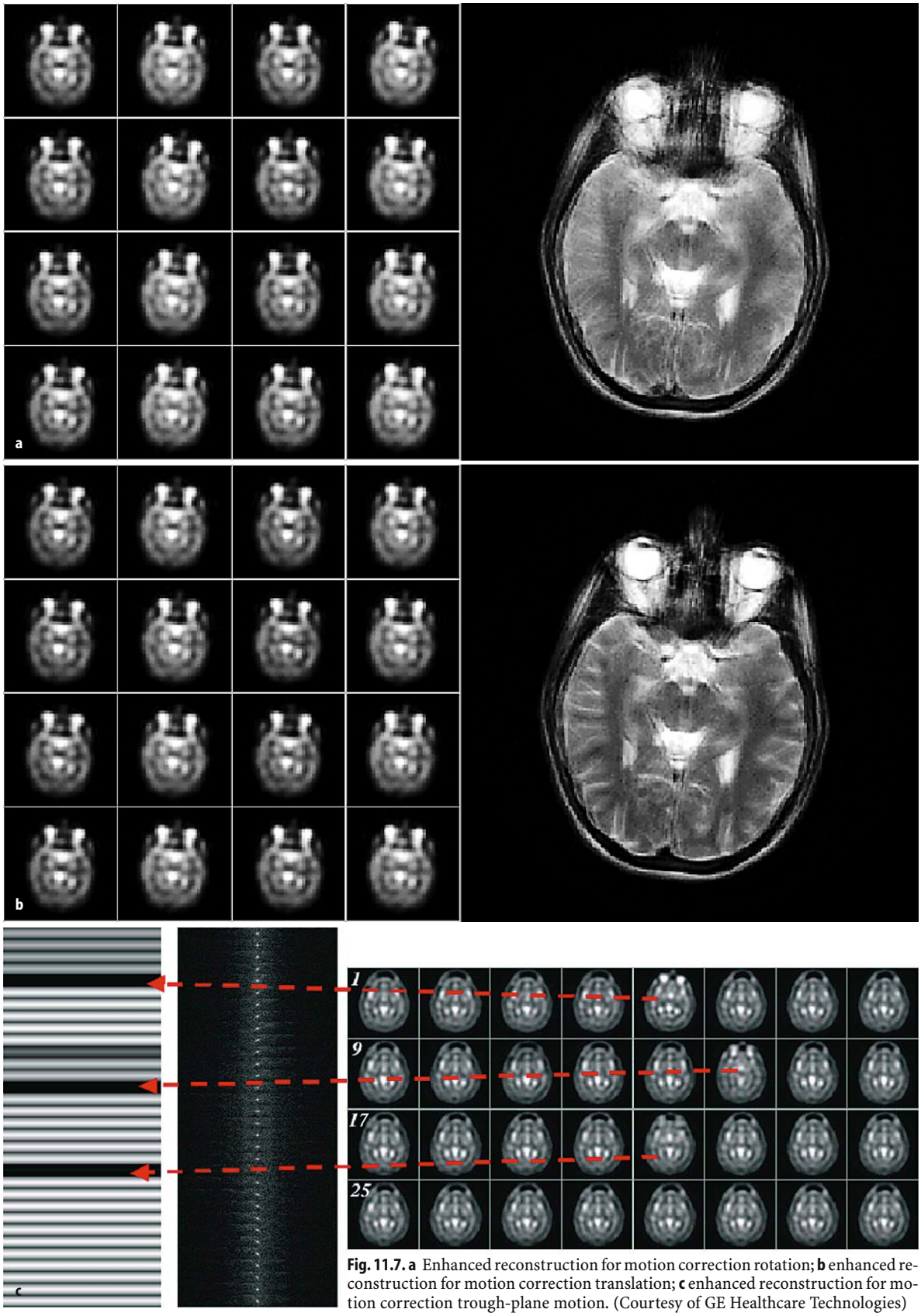

Fig. 11.7. a Enhanced reconstruction for motion correction rotation; **b** enhanced reconstruction for motion correction translation; **c** enhanced reconstruction for motion correction trough-plane motion. (Courtesy of GE Healthcare Technologies)

were correlated with the stationary data set, first by rotation of the blade, using data magnitude in *k*-space, and then by translation using the complex data in *k*-space (Fig. 11.7a, b). The process was then repeated using the average of all corrected blades as the stationary data set with improving image quality (Fig. 11.4c). The amount of motion correction (mm per degrees) was calculated for each PROPELLER blade and the standard deviation was calculated for each image slice [20]. According to Pipe [49], PROPELLER MRI may be implemented with any method that collects data along parallel lines, including standard spin and gradient echo, echo-planar, grase, and magnetization prepared turbo-spin-echo and turbo gradient echo sequences. It reduces motion artefacts in cooperative patients too. Forbes et al. [20] reported that minimal head motion worsened image quality by more than 5 %. The major disadvantage of PROPELLER MRI is an increase in image reconstruction time of approximately 2 – 3 min per scan. This is due to redundant sampling of *k*-space.

The advanced use of PROPELLER MRI is that proposed by Pipe et al. [51] in multishot diffusion-weighted FSE. The clinical utility of diffusion-weighted imaging (DWI) is well established and most DWI data are obtained by single-shot EPI imaging. The extreme variability in phase between applications of diffusion gradients creates significant motion artefacts in the presence of magnetic field inhomogeneities. The authors propose the use of a PROPELLER method which has inherent 2D navigator information in each FSE echo train. FSE data collection is used, which provides greater immunity against geometric distortion than that obtained with EPI sequences and reduces the signal instability present in all diffusion-weighted FSE methods by varying the phase of refocusing pulses. Navigator information is also used to correct data between shots and by a radial sequence, where uncorrected errors are expressed in a rather benign fashion. The authors have found that in the regions of homogeneous B_0, the PROPELLER image has a similar contrast to that of EPI. In regions near significant susceptibility-induced field gradients (e.g. skull base, temporal lobes), PROPELLER DWI exhibits a far superior image quality, lacking the geometric warping and bright-signal artefacts common to EPI. PROPELLER reduces artefacts due to metallic implants and non-removable dental fittings because it is an FSE-based sequence. One other benefit of PROPELLER is its immunity to image warping from eddy currents, which is useful for PROPELLER DTI. There is a 50 % increase in minimum image time over conventional FSE due to the oversampling in the centre of *k*-space.

PROPELLER MRI therefore offers the possibility of a diagnostic study in patients with significant head movement, where a repeat examination with sedation or general anaesthesia would be required, and an improvement of image quality in the presence of inhomogeneity of magnetic field in DWI and DTI sequences. These sequences could easily be added to routine imaging.

11.3 New Prospects

11.3.1 Integration Between Different Functional Techniques

New prospects include the integration of different functional techniques to obtain more complex information about the working of cerebral structures. A major challenge for neuroscience is to understand brain function in terms of connectional anatomy and the dynamic flow of information across neuronal networks.

In white matter, water diffusion is highly directional (anisotropic), with preferential diffusion along the long axis of fibre tracts. With application of large magnetic field gradients during image acquisition, MR images can be sensitized to the diffusion water molecules within the voxel, and from these images we can compute the local direction of greatest diffusion. With these principle diffusion directions, the organization of major fibre tracts can be mapped. Furthermore, a major limitation of this method is that it does not distinguish between efferent and afferent projection.

A complementary approach is concerned with establishing the ways in which information is transmitted and integrated across brain networks. These are dynamic, context-dependent processes, in which variations in task demands lead to the preferential recruitment of some networks over others. Methods for analysis of these processes are based on the premise that functionally interacting regions will show correlated patterns of activity [55]. The advantage of functional neuroimaging methods is that they can be used to detect activity not just in a limited set of areas but across the entire brain simultaneously. This makes it possible to examine the statistical relationship between the activities of several areas across the brain. Ramnani et al. [55] describe new strategies for use of functional MRI data in the analysis of functional connectivity in the human brain. They use diffusion tractography and functional mapping to highlight the possibility that future strategies for understanding interactions between regions of human brain will benefit from integrating anatomically informed models of functional interactions.

The brain is uniquely suited for functional MR imaging with the potential for extensive clinical application and benefit for the patient. Although neurological applications for functional MRI, particularly blood oxygen level dependent (BOLD) imaging, have been in experimental use since the early 1990s, its widespread clinical application is a relatively recent phenomenon.

Recent advances in functional imaging have allowed fMRI to be applied to a broad range of clinical disease processes. The combination of conventional BOLD Imaging with Diffusion Tensor Imaging and other physiologic techniques such as drug challenges holds great promise for understanding neuronal processes and the development of clinically meaningful diagnostic tests. Clinical applications of fMRI have largely relied on block style BOLD fMRI techniques to answer relatively simple questions regarding motor and language mapping in patients. These techniques have been applied most broadly in preoperative evaluations in the setting of brain tumours and epilepsy. More recent techniques such as event related paradigms and combinations of event and block style paradigms have allowed for better study of more sophisticated cognitive processes. These paradigms not only produce more complete assessments of cognitive processes presurgically, but they also open up the potential for non-invasive clinical evaluation of cognition for neurodegenerative processes such as multiple sclerosis, Parkinson's disease, and Alzheimer's disease [55, 63]. fMRI has also been recently applied to the study of the efficacy of therapy for disease processes using drug challenges during fMRI and with fMRI performed during deep brain stimulation.

The combination of fMRI with DTI provides the most comprehensive presurgical mapping available, clearly delineating the relationship of tumours or other pathology to both eloquent cortex and critical white matter pathways. The application of these combined techniques to multiple sclerosis suggests that a new pathway/network driven approach to the assessment of neurological diseases is now possible [48]. Functional MRI has great potential both for mapping brain function and as part of a more comprehensive assessment of neural pathways and networks.

In different preliminary reports we can see the possibility of exploring the connectivity between cerebral regions. Kim et al. [32] use DTI fibre tracking to follow separately the connectivity of central and peripheral fields in the human visual system. Central and peripheral fibres showed different patterns of connectivity with higher visual areas. Areas showing category-specific fMRI responses showed higher connectivity with regions representing central visual field. Upadhyay et al. [70] used DTI fibre tracking and fMRI to understand the functional connectivity that underlies low level auditory stimuli processing in healthy subjects. They found that haemodynamic responses vary in distinct primary auditory cortex regions upon presentation of specific frequency sounds and that tonotopic organization can be revealed using fMRI. Activation was predominantly present along Heschel's gyrus and the sylvian fissure. Using the activation maps, grey matter ROI seeding points were created in DTI data sets to characterize axonal projections within the auditory cortex.

Schonberg et al. [63] used fMRI and DTI in a patient with brain lesions. The brain lesions, especially space occupying lesions, often involve the white matter and alter the known anatomical path in which the fibres pass. Nonetheless in many of these cases only a partial or functional deficit is observed, leading to the assumption that the fibres are still partially functionally intact even if deviated. In such cases, white matter mapping using seed ROI based on known normal anatomical locations might be misleading. In their work they used fMRI driven seed ROI, choosing a procedure in patients with space occupying lesions where probable deviation of white matter tracts was observed. They used analysis of the principal diffusivities to characterize the displaced white matter. Functional MRI activations were used as landmarks to choose seed regions of interest for fibre tracking. Fibre tracking was used to mark areas of displaced white matter and from which DTI measures were extracted. DTI measures of the displaced fibre tracts revealed several significant changes compared to the opposite healthy hemisphere within each patient. Detailed analysis of the DTI measures showed that the displaced fibres were characterized by increased FA, decreased radial diffusivity and increased parallel diffusivity. Lowe et al. [39] demonstrated that the diffusivity of water transverse to the direction of the fibre was reduced in the interhemispheric pathways connecting bilateral motor regions in patients with multiple sclerosis, when compared to a control population. In this study they demonstrated that fibre tracts can be identified and isolated using DTI and fibre tracking algorithms. They adopted a method to compare the diffusion tensor in a subset of axons connecting bilateral motor regions of the brain. This was done using fMRI methods to identify cortical motor regions and DTI-based fibre tracking to select the axonal regions connecting the motor regions. The transverse diffusion was measured specifically along the tracts traversing the corpus callosum and connecting the bilateral motor regions.

One other way to use diffusion gradient is by using spectroscopy (DW-MRS). The diffusion gradient, in fact, produces a decrease in the signal intensity, which is more marked for the molecules diffusing faster. In DW-MRS, diffusion gradients are used to measure the diffusion coefficient of different metabolites. DW-MRS gives information on the size and possibly on the shape of the compartment in which the metabolite is contained and on the shape and size of cells [44].

In another study, Upadhyay et al. [71] used DTI combined with spectroscopy. They considered that in diffusion tensor imaging the degree of directed movement or anisotropic diffusion of water molecules is exploited to characterize the local neuronal microstructure and white matter fibre projections. One confounding issue of the DTI technique arises from the fact that

there are intracellular and extracellular components, which contribute to the overall diffusivity, thus leading to an ambiguity in determining the underlying cause of diffusion properties in a region of interest. Of particular interest is the contribution of the intracellular and the extracellular pools to the fractional anisotropy. Anisotropic diffusion is believed to stem from restrictions imposed on diffusion by barriers such as cell walls, and thus the FA is intimately connected with the tissue structure. The *N*-acetylaspartate (NAA), a solely intracellular constituent, has diffusion properties and it is a possible alternative for probing neuronal structure properties. Upadhyay et al. [71] combined DTI and NMR spectroscopy to characterize the diffusion of NAA and water molecules in a normal subject. Diffusion spectroscopy data was obtained from a voxel positioned in the anterior region of the corpus callosum. The fractional anisotropy value obtained for NAA was significantly larger than the fractional anisotropy value obtained for water in the same VOI. In their opinion this could indicate that intracellular space contributes most significantly to anisotropic diffusion in neural tissue. In a study by Tang et al. [69], they found that in patients with schizophrenia NAA and DTI anisotropy indices were significantly correlated. NAA was significantly reduced in the medial temporal regions and DTI-anisotropy indices were also reduced in the same regions. This implied that there was a white matter abnormality in patients with schizophrenia and the biochemical abnormality as detected in MRS was consistent with the DTI results.

Therefore DTI-MRS may become a promising tool in the investigation of tissue structure through intracellular diffusion properties and biochemical abnormalities.

Another possibility of multimodality imaging is the combination of high-resolution PA (phase-array coils) imaging at 3 T with the spatial localized neural activity at high temporal resolution provided by magnetoencephalography (MEG) and information on abnormal activity provided by the simultaneous EEG recording. Grant [23] describes the increased ability to detect lesions, define their extent and determine their character by phase-array coils and 3 T imaging in patients with focal epilepsy. She uses diffusion tensor imaging to study changes in white matter organization that can play a role in epileptogenesis and seizure propagation. The author also combines these structural imaging advances with coregistered neurophysiological information obtained with magnetoencephalography and with simultaneous EEG recordings. Magnetoencephalography (MEG) is an emerging methodology for detection of extracranial magnetic fields associated with the electrical current of neuronal activity. Mathematical modelling of the source of such activity, combined with anatomical registration to MR imaging, allows the formation of magnetic source images (MSI or functional maps). Since MEG has a submillisecond temporal resolution, these maps have the potential to display the spatiotemporal dynamics of neuronal activity and signal propagation, as well as revealing temporal signatures in evoked responses. To date, the principal clinical success of magnetic source imaging has been the identification of somatosensory cortex in patients scheduled for neurosurgical resection of mass lesions [57]. A number of centres routinely incorporate MSI data into the neuronavigational systems used to guide operative procedures, such that MSI is used not only for presurgical planning, but also for intraoperative guidance.

11.3.2 Molecular Imaging

Developments in cellular and molecular biology are extending the horizon of medical imaging from gross anatomic description towards delineation of cellular and biochemical signalling processes. The emerging fields of cellular and molecular imaging aim to non-invasively diagnose disease based on the in vivo detection and characterization of complex pathologic processes, such as induction of inflammation or angiogenesis. Molecular imaging can briefly be defined as the remote sensing of cellular and molecular processes in vivo. Although molecular imaging is a biology-driven enterprise (it is the underlying biological question rather than the modality that determines which methods are used), it is currently bound by the existing techniques of optical, radionuclear, MR, and ultrasonographic imaging. These techniques are complementary in the sense that they measure processes with different sensitivities and resolutions. Each is beginning to find a niche in molecular imaging research. Each is capable of truly molecular detection in vivo, although only the radionuclear techniques and MR spectroscopy are currently applied in humans. MRI is a particularly advantageous modality for molecular and cellular imaging given its high spatial resolution and the opportunity to extract both anatomic and physiologic information simultaneously [26–76]. In molecular imaging the intrinsic contrast can be augmented by the use of targeted contrast agents in both the experimental and clinical setting. The evolving field of molecular imaging requires the development of a novel class of MR-detectable agents that are better able to provide image contrast to target specific disease processes. Strategies for generating targeted contrast can be broadly categorized [4] as: (1) where the CA (contrast agent) macromolecule is directed to a specific receptor using a high-affinity ligand such as a monoclonal antibody (MAb), (2) where the number of MR reporter molecules increases with enzymatic activity, resulting in signal amplification, and (3) where the presence of a targeted probe is detected through a de-

crease in the bulk water signal due to chemical exchange between protons of bulk water and those of the probe [47]. The high detection sensitivity of the latter is due to numerous water molecules interacting with a single molecule of the probe [4].

Currently, two major classes of contrast agents exist: paramagnetic (gadolinium based) and superparamagnetic agents [75]. The paramagnetic agents shorten both T1 and T2 relaxation, but preferentially T1. They create a hyperintense contrast on conventional T1-weighted spin-echo images. The second class of agents is based on ultrasmall superparamagnetic iron oxide (SPIO) particles. In view of the small size of these particles, the magnetic moments are unhindered by lattice orientation. In a magnetic field, the net magnetic moment is several orders of magnitude greater than that with the paramagnetic agents. This creates extremely large microscopic field gradients for dephasing nearby protons [7] and results in a dramatic shortening of the relaxation properties of the tissue. Recently, contrast probes have been designed to potentially demonstrate changes in gene expression or other cellular processes [2]. The imaging protocols are critically important for SPIO detection by MRI. The susceptibility artefacts created by accumulation of SPIO are most sensitively imaged T2*-weighted imaging sequences. T1-weighted and proton density imaging with sequences are far less sensitive to the susceptibility artefacts induced by SPIO uptake in tissue [33]. The T2*-weighted sequences typically utilize gradient echo techniques with long echo times. The long echo time accentuates signal loss due to the presence of SPIO, but these sequences also tend to suffer from a low signal-to-noise ratio (SNR). Often, highly specialized coils, such as phased array coils or application-specific surface coils, are employed in order to maximize the available SNR [33]. In addition to the imaging protocol itself, the choice of imaging time post SPIO injection is critically important. The long circulating half-life of SPIO nanoparticles is necessary to achieve adequate loading into inflammatory cells, but it can also interfere with obtaining high quality images. Up to 24 h after SPIO administration, the blood concentration is high enough to create image artefacts. On the other hand, too long of a delay (72 h) after SPIO injection can result in no detectable susceptibility artefacts [62].

An alternative approach is to use polymerized vesicles conjugated to monoclonal antibodies for the highly accessible targets in endothelial receptors [68]. These agents consist of a derivitized gadolinium diethylene-tri-aminepentaacetic acid (DTPA) polymerizable lipid, a biotinylated lipid for antibody conjugation, and a diacetylene phosphatidylcholine filler lipid. This approach has been successful in two areas: targeting β integrin upregulation on the endothelium in tumours by using MR imaging to help define regions of abnormal angiogenesis and in an animal model of experimental allergic encephalomyelitis [64, 65]. By incorporating a vast quantity of paramagnetic complex onto each particle, the signal enhancement possible for each binding site is magnified dramatically. The increased paramagnetic influence arises from two mechanisms: the relaxivity per particle increases linearly with respect to the number of gadolinium complexes and the relaxivity of each gadolinium increases due to the slower thumbing of the molecule when attached to the much larger particle. On studying dilutions of nanoparticles in water, T1 relaxivity increased with increasing gadolinium payloads [19]. The chemistry employed to bind the targeted ligand to the particle surface can also dramatically affect the efficacy of the final contrast agent. In some cases, the active binding site of the ligand may become occupied or obscured after attachment to the nanoparticle. Obviously, such agents would yield poor molecular imaging results. In addition, the incorporation of flexible polymer spacers, i.e. polythylene glycol, between the targeting ligand and the nanoparticle surface may improve targeting efficiency. These flexible „tethers“ permit a wider range of motion for the targeting ligand, potentially increasing the likelihood of encountering and binding to the target of interest [78]. In addition to the number of gadolinium ions per particle, the number of targeting ligands per particle must also be optimized. A nanoparticle with numerous bindings ligands tends to provide a more efficacious contrast agent. In contradistinction to SPIO agents, which are designed to increase the T2* relaxation of targeted tissue, paramagnetic compounds are typically used to increase T1 relaxation. The T2* effect employed with SPIO is usually visualized as decreased image intensity with T2*-weighted MRI. Paramagnetic agents will produce increased tissue signal when interrogated with T1-weighted MRI. Therefore, the contrast effects of SPIO and paramagnetic agents are very different, and the MRI pulse sequences and parameters are also distinct for the two methods. On the T1-weighted image, the contrast between two tissues with different T1 relaxation times can be maximized by imaging at the optimum value of TR. Altering the TR by 300 – 400 ms away from the optimum value can reduce the SNR by up to 25 % [42].

An alternative method to define inflammatory events after stroke is to tag cells with MR-detectable agents [8]. The avidity in which ultrasmall SPIOs are phagocytosed by cells of the mononuclear phagocytic system has been used to study the role of macrophage infiltration into the brain in neurodegenerative and inflammatory diseases of the central nervous system. Studies in animal models of stroke, brain tumours, and experimentally induced allergic encephalomyelitis have demonstrated the phagocytic activity of microglial cells and haematogenous macrophages in the lesions

[14]. These studies demonstrate the feasibility of labelling specific inflammatory cell lines.

The existence of a regenerating mechanism in the CNS has emphasized the potential of MR molecular imaging in particular [6]. Although the endogenous activation and recruitment of neuronal progenitors after brain injury remains an elusive goal, an alternative approach has been the administration of transplanted cells in the form of either stem cells or neuronal progenitor cells [41]. For stem cells to be visualized and tracked with MR imaging, they need to be tagged so that they can be detected on MR images. At present two types of contrast agents are available: the gadolinium analogues and the iron oxide nanoparticles. Several approaches have been deployed to enhance cell labelling, to allow in vivo cell tracking by conjugating MR imaging contrast agents to a range of ancillary molecules to enhance their uptake. This can be achieved by coating nanoparticles with internalizing monoclonal antibodies [9], HIV-Tat peptide [36], or transfection agents including dendrimers [10], poly-L-lysine, and lipofection agents [29]. An essential methodological feature of these types of studies is the validation of the imaging findings with histologic techniques.

A wealth of spatial and temporal information on tumour vasculature, metabolism, and physiology can be obtained from non-invasive MRI and MRSI methods. Recent advances in the development of targeted CAs have increased the versatility of MR molecular imaging and will make it an invaluable technique for understanding a complex disease such as cancer.

References

1. Ahn CB, Kim HH, Cho ZH (1986) High-speed spiral-scan echo planar NMR imaging I. IEEE Trans Med Imaging 5:2
2. Artemov D, Mori N, et al. (2003) Magnetic resonance molecular imaging of the HER-2/neu receptor. Cancer Res 63:2723 – 2727
3. Bammer R, Schoenberg SO (2004) Current concepts and advances in clinical parallel magnetic resonance imaging. Top Magn Reson Imaging 15:129 – 158
4. Bhujwalla MZ (2005) Molecular imaging of cancer. Proc Intl Soc Magn Reson Med (in press)
5. Bradley WG (2004) Use of 1024 MRA at 3T enhances neuroscan. Diagn Imaging Eur 10:25 – 27
6. Buchan A, Barber PA (2004) From bench to bedside: evolving experimental MR imaging technology for cerebral ischemia. ASNR 133 – 137
7. Bulte JWM, Brooks RA, et al. (1999) Relaxometry and magnetometry of the MR contrast agent MION-46L. Magn Reson Med 42:379 – 384
8. Bulte JWM, Duncan ID, et al. (2002) In vivo magnetic resonance tracking of magnetically labelled cells after transplantation. J Cereb Blood Flow Metab 22:899 – 907
9. Bulte JWM, Zhang S, et al. (1999) Neurotransplantation of magnetically labelled oligodendrocyte progenitors: magnetic resonance tracking of cell migration and myelination. Proc Natl Acad Sci USA 96:15256 – 15261
10. Bulte JWM, Douglas T, et al. (2001) Magnetodendrimers allow endosomal magnetic labeling and in vivo tracking of stem cells. Nat Biotechnol 19:1141 – 1147
11. Carroll TJ, Korosec FR, et al. (2000) Method for rapidly determining and reconstructing the peak arterial frame from a time-resolved CE-MRA exam. Magn Reson Med 44:817 – 820
12. Carroll TJ, Korosec FR, et al. (2001) Carotid bifurcation: evaluation of time-resolved three-dimensional contrast-enhanced MR angiography. Radiology 220:525 – 532
13. Carroll TJ, et al. (2002) Time-resolved three dimensional contrast enhanced MR angiography of the peripheral vessels. Radiology 225:43 – 52
14. Dousset V, Delalande C, et al. (1999) In vivo macrophage activity imaging in the central nervous system detected by magnetic resonance. Magn Reson Med 41:329 – 333
15. Dydak U, Weiger M, et al. (2001) Sensitivity-encoded spectroscopic imaging. Magn Reson Med 46:713 – 722
16. Dydak U, Pruessmann KP, et al. (2003) Parallel spectroscopic imaging with spin echo trains. Magn Reson Med 50:196 – 200
17. Dydak U (2004) Advanced MR spectroscopic imaging techniques. ASNR Proceedings: 182 – 183
18. Ehman RL, McNamara MT, et al. (1986) Influence of physiologic motion on the appearance of tissue in MR images. Radiology 159:177 – 182
19. Flacke S, Fischer S, et al. (2001) Novel MRI contrast agent for molecular imaging of fibrin: implications for detecting vulnerable plaques. Circulation 104:1280 – 1285
20. Forbes KPN, Pipe JG, et al. (2001) PROPELLER MRI: Clinical testing of a novel technique for quantification and compensation of head motion. J Magn Reson Imaging 14: 215 – 222
21. Gieseke J, Manka C, et al. (2003) Diffusiongewichtete MRT Aufnahmen mit SENSE bei 3 T. Fortschr Roentgenstr 175: 202
22. Glover GH, Pauly JM (1992) Projection reconstruction techniques for reduction of motion effects in MRI. Magn Reson Med 28:275 – 289
23. Grant PE (2004) Structural MR imaging. Epilepsia 45(4): 4 – 16
24. Griswold MA, Jakob PM, et al. (1999) Resolution enhancement in single-shot imaging using simultaneous acquisition of spatial harmonics (SMASH). Magn Reson Med 41:1236 – 1245
25. Griswold MA, Jakob PM, et al. (2002) Generalized autocalibrating partially parallel acquisition (GRAPPA). Magn Reson Med 47(6):1202 – 1210
26. Gupta H, Weissler R (1996) Targeted contrast agents in MR imaging. Magn Reson Imaging Clin N Am 4:171 – 184
27. Hany TF, Carroll TJ, et al. (2001) Aorta and runoff vessels: single-injection MR angiography with automated table movement compared with multiinjection time-resolved MR angiography – initial results. Radiology 221:266 – 272
28. Ho VB, Foo TK (1998) Optimization of gadolinium-enhanced magnetic resonance angiography using an automated bolus-detection algorithm (MR SmartPrep). Invest Radiol 33:515 – 523
29. Hohen M, Kustermann E, et al. (2002) Monitoring of implanted stem cell migration in vivo: a highly resolved in vivo magnetic resonance imaging investigation of experimental stroke in rat. Proc Natl Acad Sci USA 99:16267 – 16272
30. Hutchinson M, Raff U (1988) Fast MRI data acquisition using multiple detectors. Magn Reson Med 6(1):87 – 91
31. Insko EK, Elliott MA, et al. (1998) Generalized reciprocity. J Magn Reson 131:111 – 117
32. Kim M, Ducros M, et al. (2005) Topography of high-order human object areas measured with DTI and fMRI. Proc Intl Soc Magn Reson Med 13:737

33. Kooi ME, Cappendijk VC, et al. (2003) Accumulation of ultrasmall superparamagnetic particles of iron oxide in human atherosclerotic plaques can be detected by in vivo magnetic resonance imaging. Circulation 107:2453 – 2458
34. Korosec FR, Frayne R, et al. (1996) Time-resolved contrast enhanced 3D MR angiography. Magn Reson Med 36:345 – 351
35. Kuhl CK (2004) Parallel imaging in neuroradiology. ASNR Proceedings: 181 – 182
36. Lewin M, Carlesso N, et al. (2000) Tat-peptide-derivatized magnetic nanoparticles allow in vivo tracking and recovery of progenitor cells. Nat Biotechnol 18:410 – 414
37. Lin C, Bernstein M, et al. (2001) In-vivo and in-vitro measurements of T1 relaxation at 3.0 T. Presented at ISMRM 9th annual meeting, Glasgow, UK, 21 – 27 April 2001, p 1391
38. Little MW, Mcrobbie DW (2004) Parallel imaging improves scan speed. Diagn Imaging Eur 5:29 – 35
39. Lowe MJ, Marrie R, et al. (2005) Increased transverse diffusivity of water observed in transcallosal motor fiber tracts in multiple sclerosis. Proc Intl Soc Magn Reson Med 13:1056
40. Maki JH, Prince MR (2005) Principles and optimization of contrast-enhanced 3D MR angiography. Syllabus Intl Soc Magn Reson Med 13
41. McKay R (2000) Stem cells: hype or hope? Nature 406:361 – 364
42. Morawski AM, Winter PM, et al. (2004) Targeted nanoparticles for quantitative imaging of sparse molecular epitopes with MRI. Magn Reson Med 51:480 – 486
43. Murphy KJ, Brunberg JA (1997) Adult claustrophobia, anxiety and sedation in MRI. Magn Reson Med 15:51 – 54
44. Nicolay K, Braun KP, et al. (2001) Diffusion NMR spectroscopy. NMR Biomed 14(2):94 – 111
45. Ohlinger MA, Grant AK, et al. (2003) Ultimate intrinsic signal-to-noise ratio for parallel MRI: Electromagnetic field considerations. Magn Reson Med 50:1018 – 1030
46. Ordidge RJ, Helpern JA, et al. (1994) Correction of motional artifacts in diffusion-weighted MR images using navigator echoes. Magn Reson Med 12:455 – 460
47. Pathak AP, Gimi B, et al. (2004) Molecular and functional imaging of cancer: advances in MRI and MRS. Methods Enzymol 386:3 – 60
48. Phillips MD (2005) Functional neuro MRI. Proc Intl Soc Magn Reson Med 13:562
49. Pipe JG (1999) Motion correction with PROPELLER MRI: Application to head motion and free-breathing cardiac imaging. Mag Reson Med 42:963 – 969
50. Pipe JG (2001) Improved in-plane motion correction for PROPELLER MRI. Proc Intl Soc Magn Reson Med 9:743
51. Pipe JG, Farthing VG, Forbes KP (2002) Multishot diffusion-weighted FSE using PROPELLER MRI. Magn Reson Med 47:42 – 52
52. Prince MR, Grist TM, et al. (1997) 3D contrast MR angiography. Springer-Verlag, Berlin
53. Pruessmann KP, Weiger M, et al. (1999) SENSE: sensitivity encoding for fast MRI. Magn Reson Med 42(5):952 – 962
54. Ra JG, Rim CY (1993) Fast imaging using subencoding data sets from multiple detectors. Magn Reson Med 30(1): 142 – 145
55. Ramnani N, Beherens TEJ, et al. (2004) New approaches for exploring anatomical and functional connectivity in the human brain. Biol Psychiatry 56:613 – 619
56. Roemer PB, Edelstein WA, et al. (1990) The NMR phase array. Magn Reson Med 16(2):192 – 225
57. Roberts TPL (2004) Clinical magnetic source imaging. ASNR Proceedings: 223
58. Sachs T, Meyer CH, et al. (1995) The diminishing variance algorithm for real-time reduction of motion artifacts in MRI. Magn Reson Med 34:412 – 422
59. Schultz CL, Alfidi RJ, et al. (1984) The effect of motion on two-dimensional Fourier transformation magnetic resonance images. Radiology 152:117 – 121
60. Sarty GE (2001) Single trajectory radial (STAR) imaging. Proc Intl Soc Magn Reson Med 9:1806
61. Schiebler ML, Listerud J, et al. (1992) Magnetic resonance angiography of the pelvis and lower extremities: works in progress. Invest Radiol 27:90 – 96
62. Schmitz SA, Coupland SE, et al. (2000) Superparamagnetic iron oxide-enhanced MRI of arteriosclerotic plaques in Watanabe hereditable hyperlipidemic rabbits. Invest Radiol 35:460 – 471
63. Schonberg T, Pianka P, et al. (2005) Characterization of displaced white matter tracts using DTI and fMRI. Proc Intl Soc Magn Reson Med 13:468
64. Sipkins DA, Cheresh DA, et al. (1998) Detection of tumour angiogenesis in vivo by $\alpha v \beta$ 3-targeted magnetic resonance imaging. Nat Med 4:623 – 626
65. Sipkins DA, Gilbels K, et al. (2000) ICAM-1 expression in autoimmune encephalitis visualized using magnetic resonance imaging. J Neuroimmunol 104:1 – 9
66. Sodickson DK, Manning WJ (1999) Simultaneous acquisition of spatial harmonics (SMASH): Fast imaging with radiofrequency coil arrays. Magn Reson Med 42(5):952 – 962
67. Sodickson DK (2000) Tailored SMASH image reconstruction for robust in vivo parallel MR imaging. Magn Reson Med 44:243 – 251
68. Storrs RW, Tropper FD, et al. (1995) Paramagnetic polymerised liposomes as new recirculating MR contrast agents. J Magn Reson Imaging 5:719 – 724
69. Tang C, Friedman J, et al. (2005) Correlations between diffusion tensor imaging (DTI) and magnetic resonance spectroscopy (1H MRS) in schizophrenic patients and normal controls. Proc Intl Soc Magn Reson Med 13:1384
70. Upadhyay J, Lindgren KA, et al. (2005) Function and connectivity in human auditory cortex: A combined fMRI and DTI study at 3T. Proc Intl Soc Magn Reson Med 13:1467
71. Upadhyay J, Kim D-S, et al. (2005) Characterization of intracellular diffusion properties with diffusion tensor spectroscopy. Proc Intl Soc Magn Reson Med 13:582
72. Van Hoe L, De Jaegere T, et al. (2000) Breath-hold contrast-enhanced three-dimensional MR angiography of the abdomen: Time-resolved imaging versus single-phase imaging. Radiology 214:149 – 156
73. Vigen KK, Peters DC, et al. (2000) Undersampled projection-reconstruction imaging for time-resolved contrast-enhanced imaging. Magn Reson Med 43:170 – 175
74. Wang J, Kluge T, et al. (2001) Parallel acquisition techniques with modified SENSE reconstruction mSENSE. Presented at the First Würzburg Workshop on Parallel Imaging, Würzburg, Germany, 7 – 10 November 2001, p 92
75. Weinmann HJ, Ebert W, et al. (2003) Tissue-specific MR contrast agents. Eur J Radiol 46:33 – 44
76. Weissleder R (1999) Molecular imaging: exploring the next frontier. Radiology 212:609 – 614
77. Willinek WA (2004) 3 T systems display rich clinical promise. Diagn Imaging Eur 4:29 – 33
78. Winter PM, Caruthers SD, et al. (2005) Molecular imaging of vascular targets. Proc Intl Soc Magn Reson Med (in press)
79. Zhu Y, Hardy CJ, et al. (2004) Highly parallel volumetric imaging with a 32-element RF coil array. Magn Reson Med 52:869 – 877

3.0 T Brain MRI: A Pictorial Overview of the Most Interesting Sequences

12

T. Popolizio, V. d'Alesio, T. Scarabino

In this chapter we present a series of 3.0 T MR images of the normal whole brain, illustrating 8 different sequences with 16 slices for each sequence: spin echo (SE) T1 (Fig. 12.1a–p), fast gradient echo (FGE) T1 (Fig. 12.2a–p), inversion recovery (IR) (Fig. 12.3a–p), fluid attenuated inversion recovery (FLAIR) T1 (Fig. 12.4a–p), fast spin echo (FSE) T2 (Fig. 12.5a–p), FSE T2 with inverted contrast (Fig. 12.6a–p), gradient echo (GE) T2 (Fig. 12.7a–p), and FLAIR T2 (Fig. 12.8a–p). The whole brain is studied by each sequence from base to top in 16 slices (from „a" to „p"). Therefore for each brain level there are 8 images, one for each sequence.

Tables 12.1 and 12.2 provide a short description of the technical parameters used.

Acknowledgements. We would like to thank the following technical staff for their help: C. Bocci, T. Cassano, I. Di Maggio, G. Fraticelli, A. Lombardi, A. Mazza, G. Miscio (Department of Radiology, IRCCS „Casa Sollievo della Sofferenza", San Giovanni Rotondo) and G.W. Antonucci and P. Colasuonno (Department of Radiology, ASL BA/1, Hospital of Andria).

Table 12.1. T1 images

SE TR/TE 360/9 5 mm thk 512×256 FOV 22×22	**FGE** TR/TE/FA 275/2.5/75 5 mm thk 512×256 FOV 22×22
IR TR/TE/TI 2,040/28/700 5 mm thk 512×256 FOV 22×22	**FLAIR** TR/TE/TI 2,320/27.4/auto 5 mm thk 256×256 FOV 22×22

Table 12.2. T2 images

FSE TR/TE/ETL 4,840/75.7/15 5 mm thk 448×320 FOV 22×22	**FSE with inverted contrast** TR/TE/ETL 4,840/75.7/15 5 mm thk 448×320 FOV 22×22
GE TR/TE/FA 325/20/20 5 mm thk 256×192 FOV 22×22	**FLAIR** TR/TE/TI 11,002/135/2,250 5 mm thk 288×192 FOV 22×22

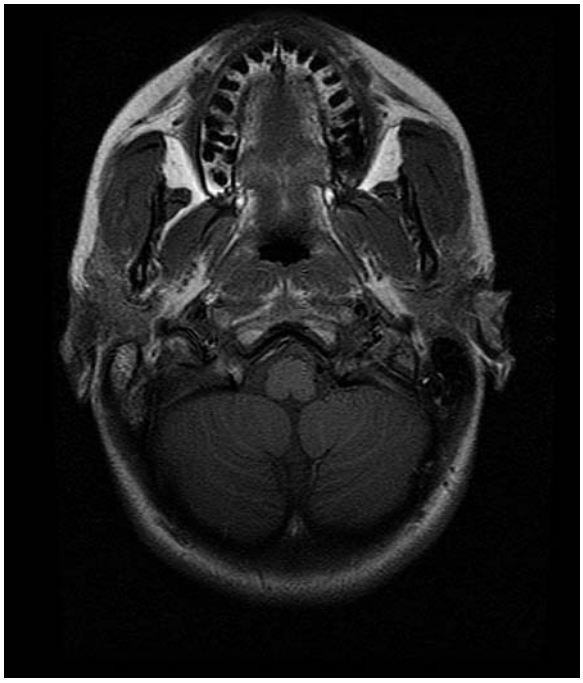

Fig. 12.1 a. SE

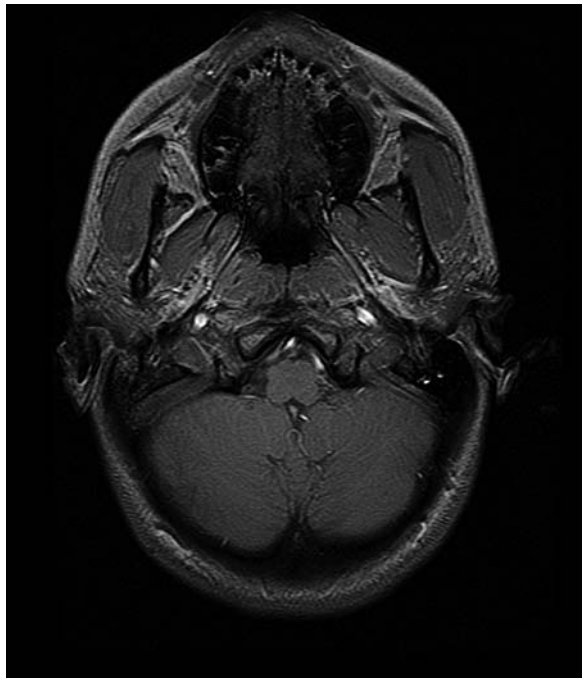

Fig. 12.2 a. FGE

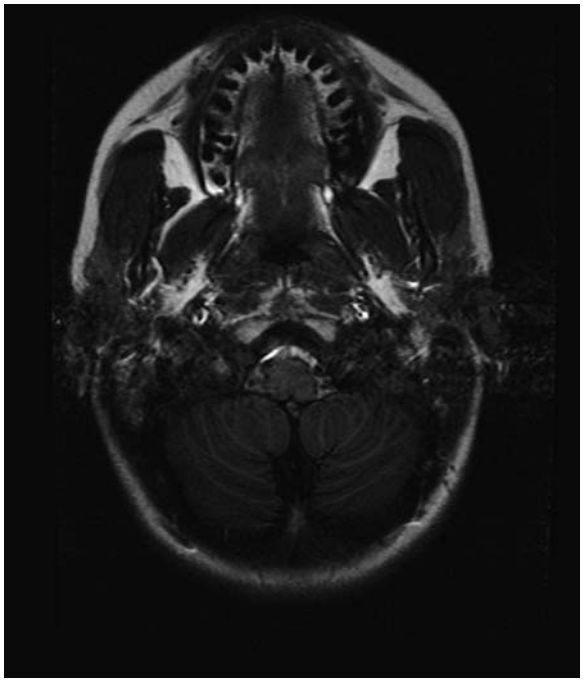

Fig. 12.3 a. IR

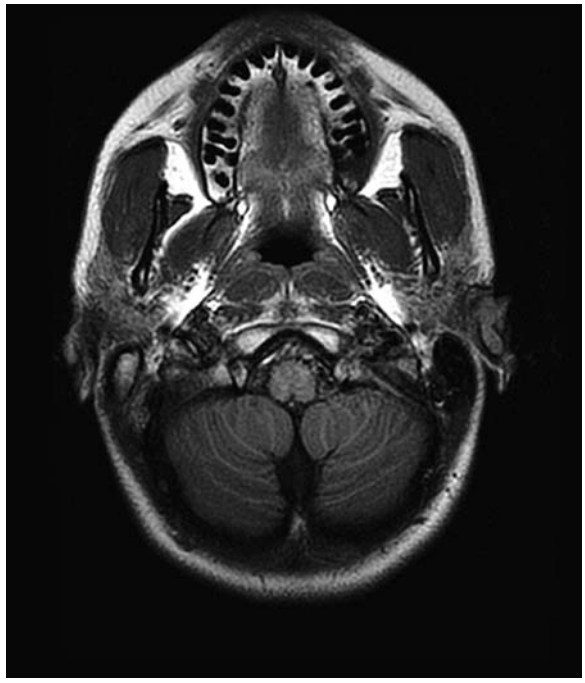

Fig. 12.4 a. FLAIR

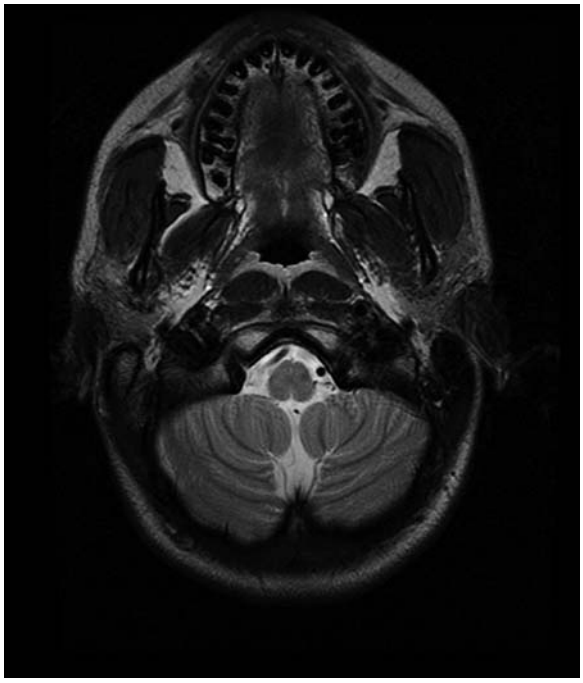

Fig. 12.5 a. FSE

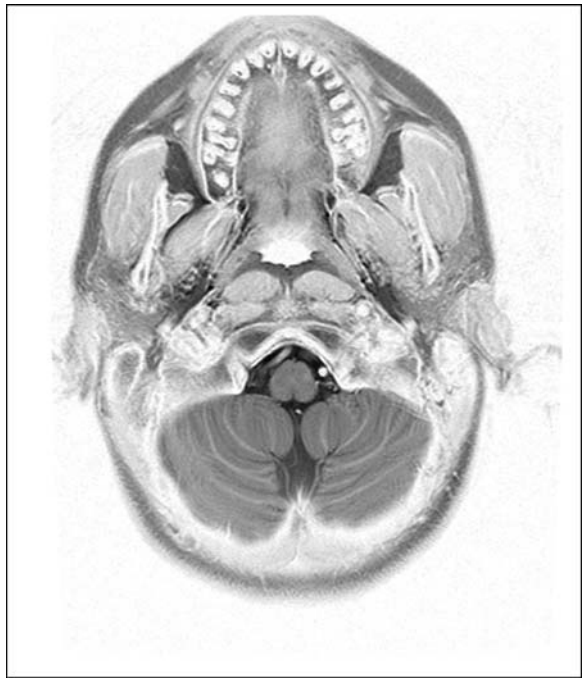

Fig. 12.6 a. FSE with inverted contrast

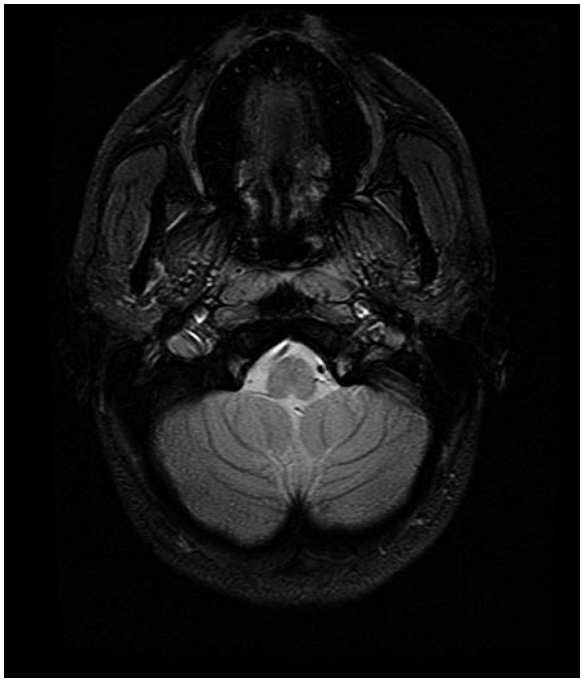

Fig. 12.7 a. GE

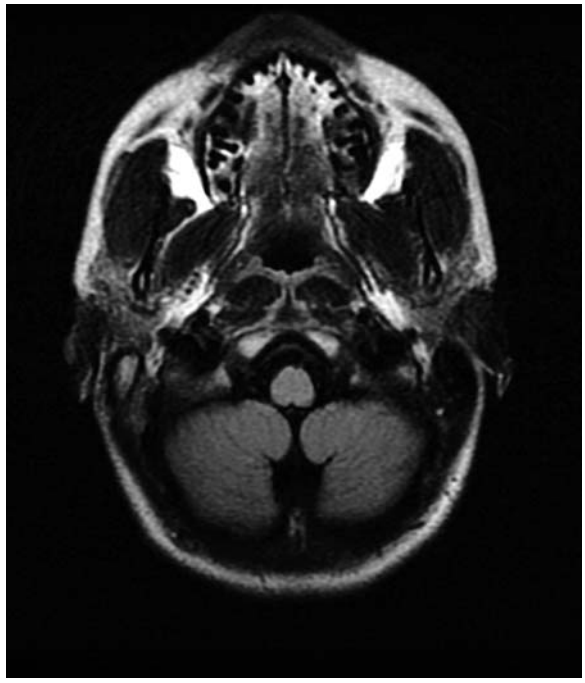

Fig. 12.8 a. FLAIR

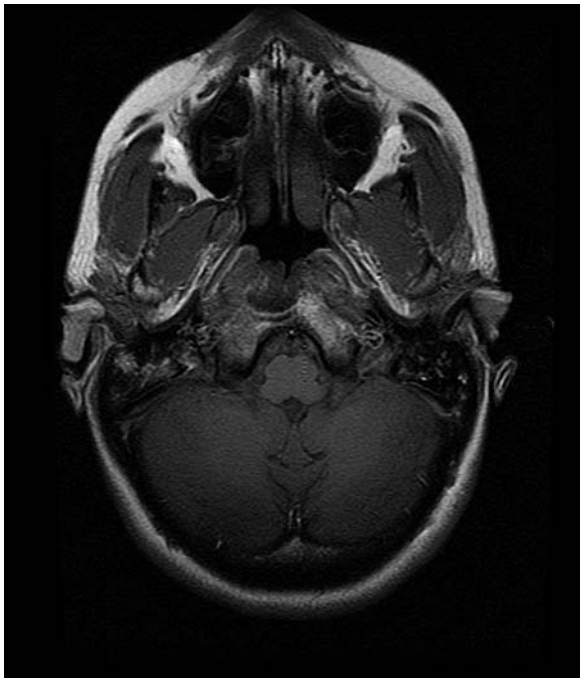

Fig. 12.1 b. SE

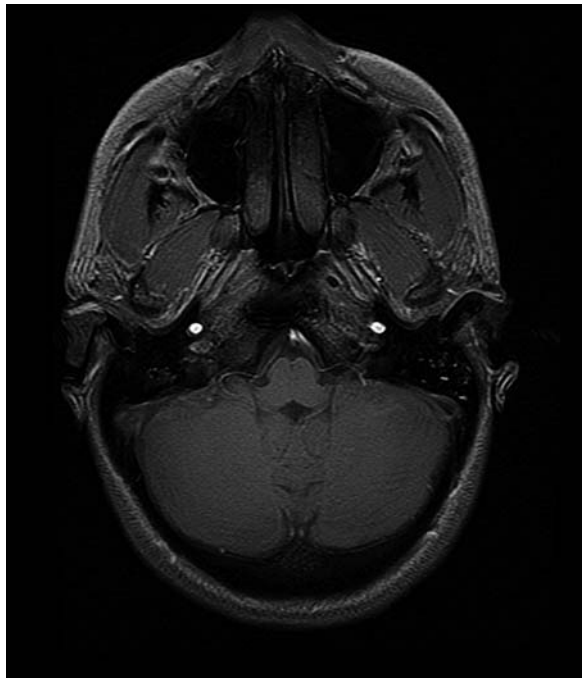

Fig. 12.2 b. FGE

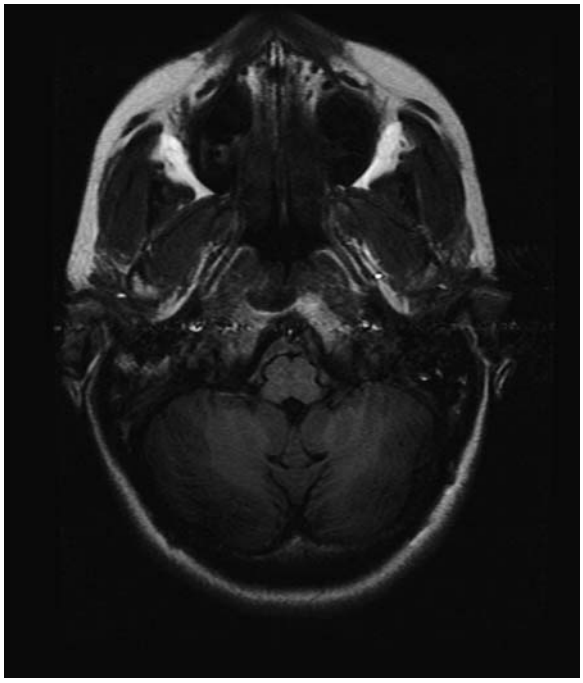

Fig. 12.3 b. IR

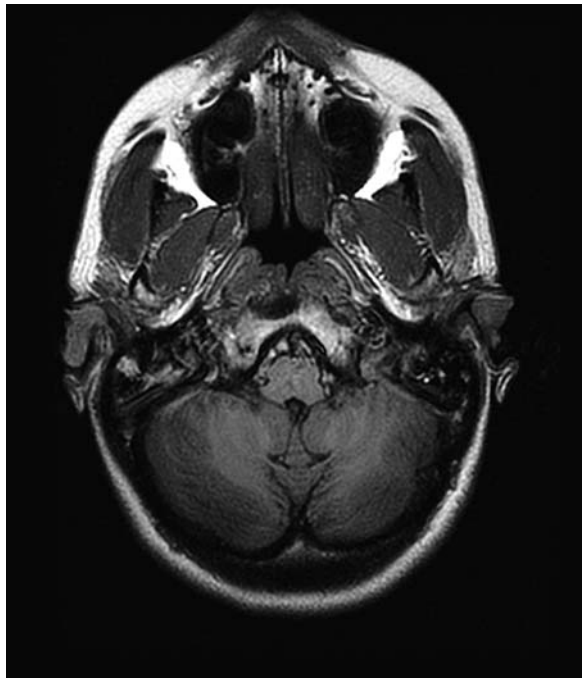

Fig. 12.4 b. FLAIR

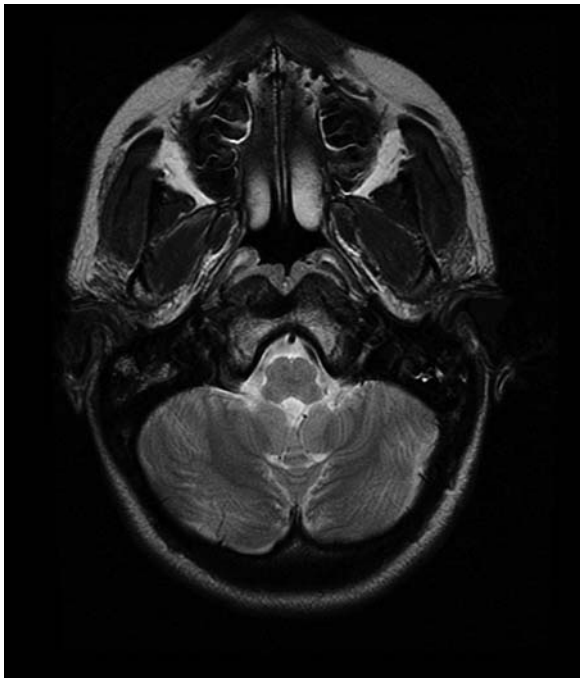

Fig. 12.5 b. FSE

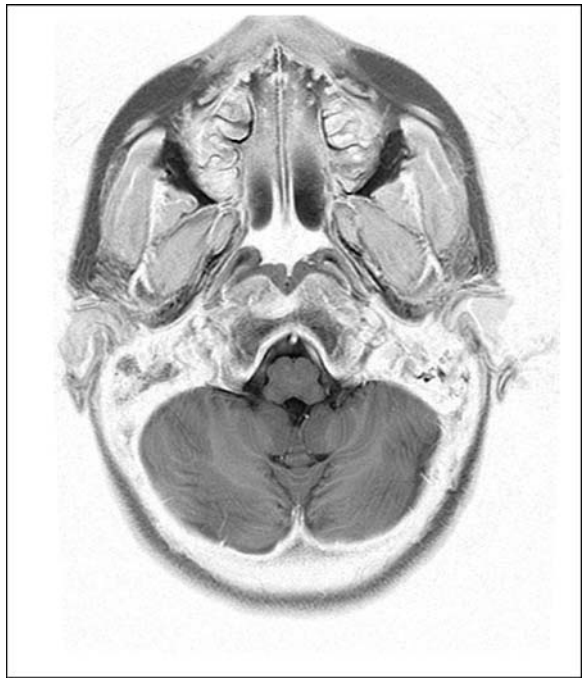

Fig. 12.6 b. FSE with inverted contrast

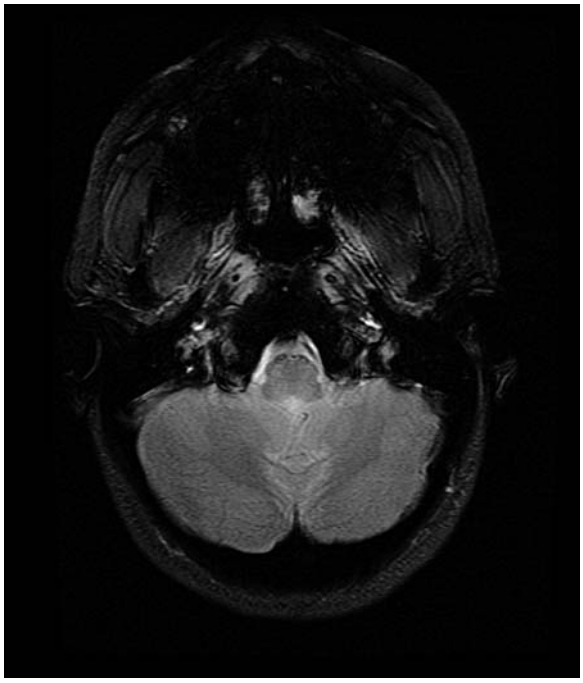

Fig. 12.7 b. GE

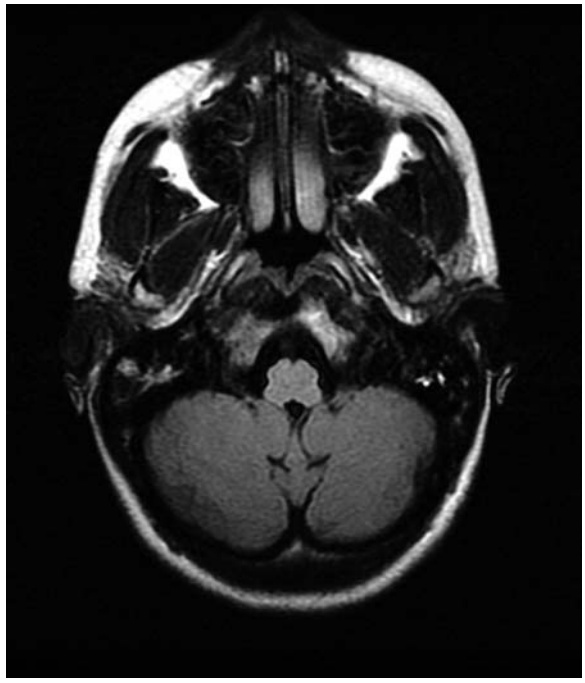

Fig. 12.8 b. FLAIR

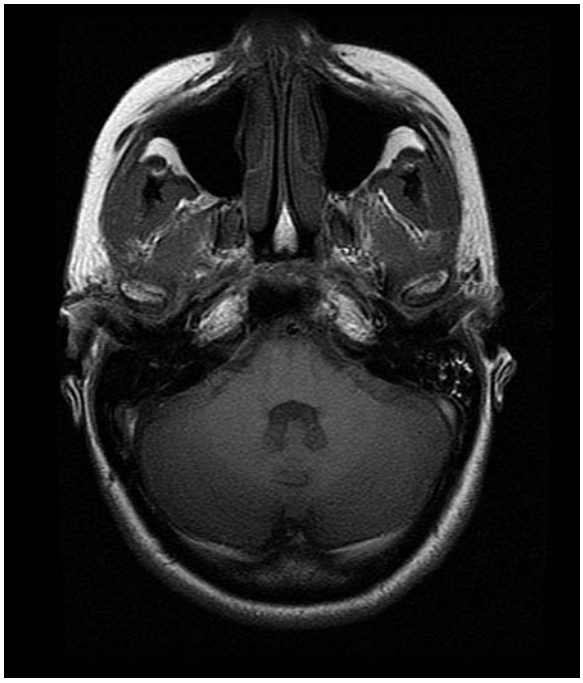

Fig. 12.1 c. SE

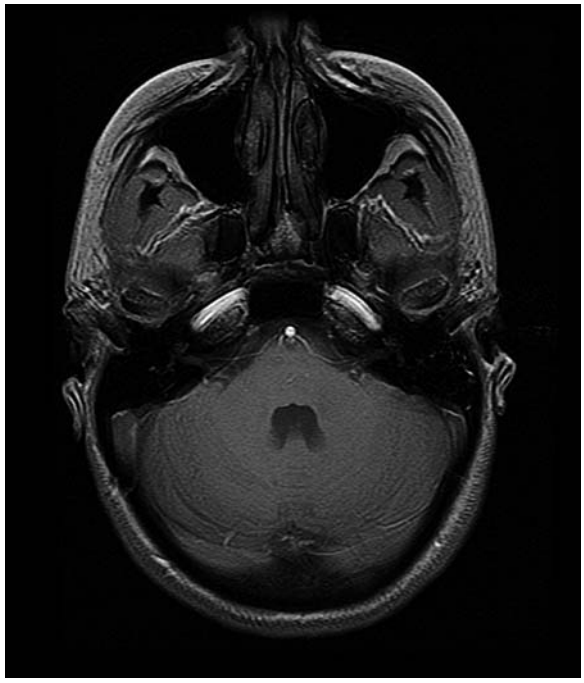

Fig. 12.2 c. FGE

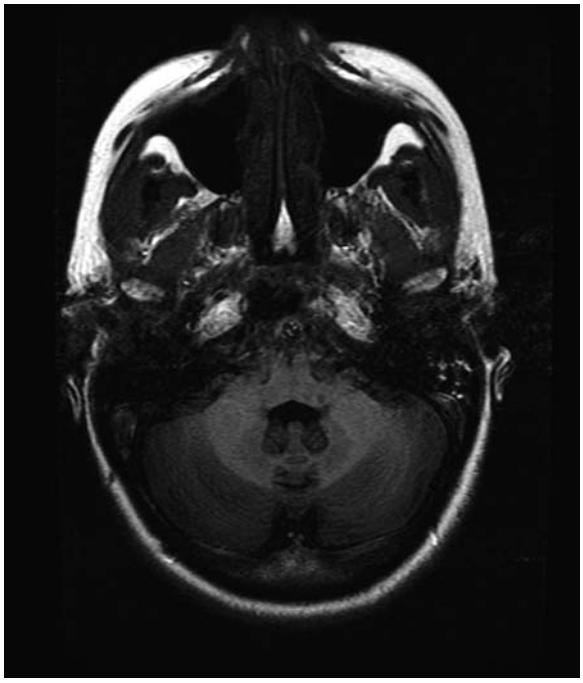

Fig. 12.3 c. IR

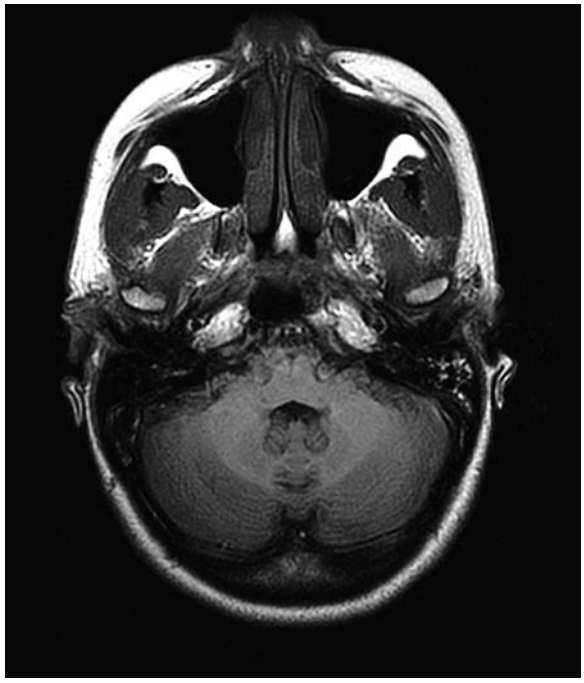

Fig. 12.4 c. FLAIR

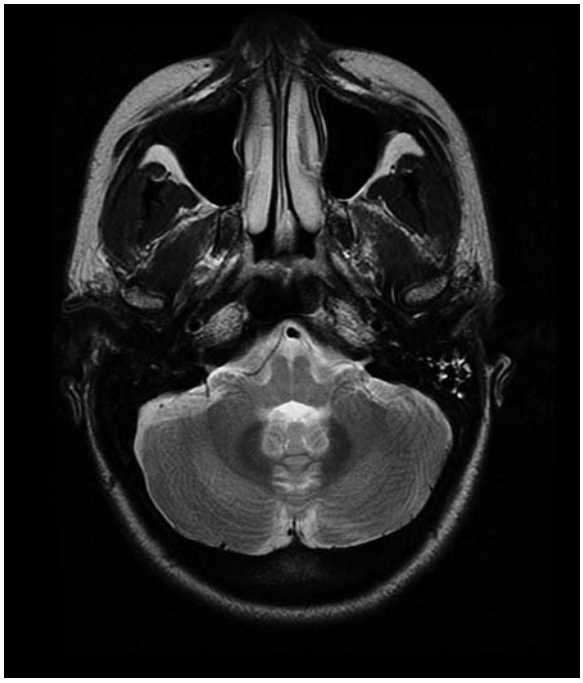

Fig. 12.5 c. FSE

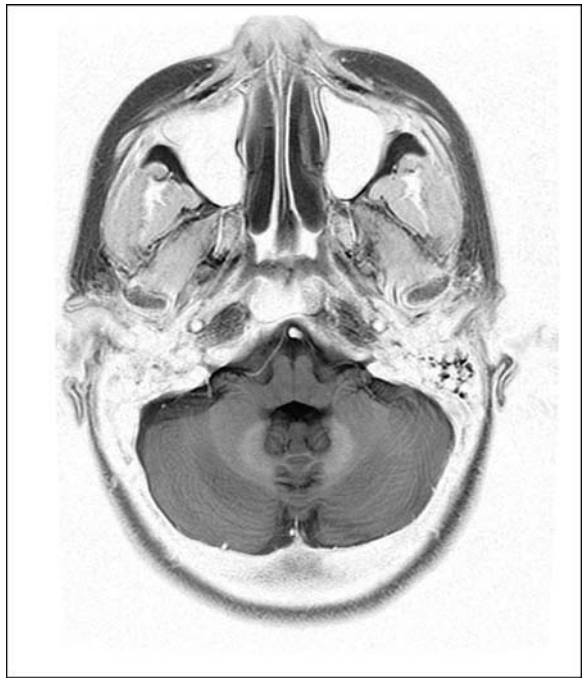

Fig. 12.6 c. FSE with inverted contrast

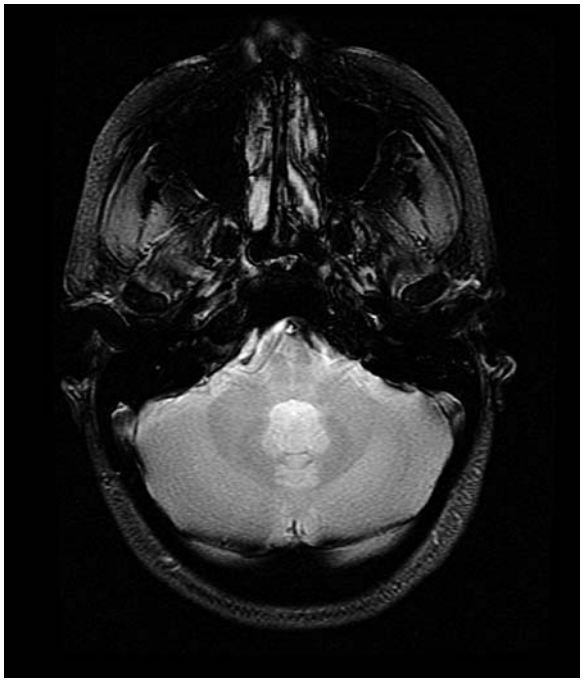

Fig. 12.7 c. GE

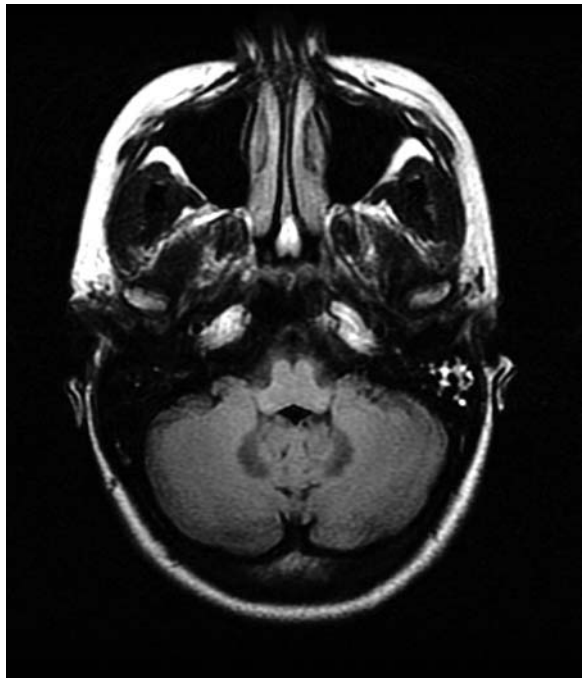

Fig. 12.8 c. FLAIR

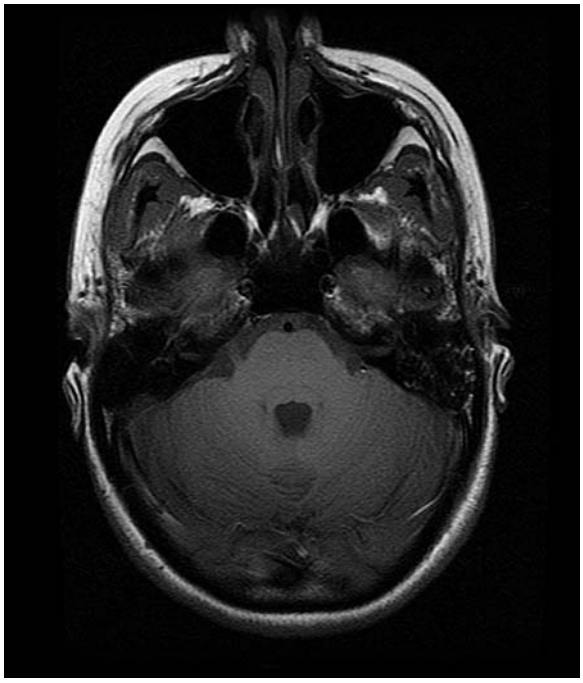

Fig. 12.1 d. SE

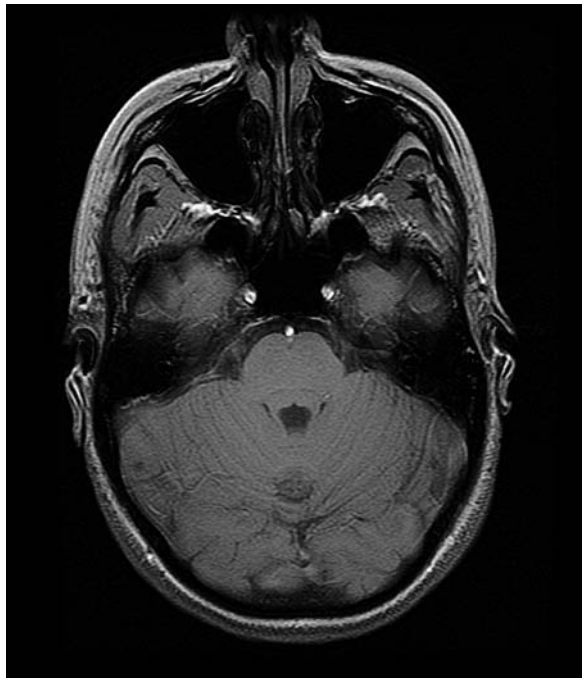

Fig. 12.2 d. FGE

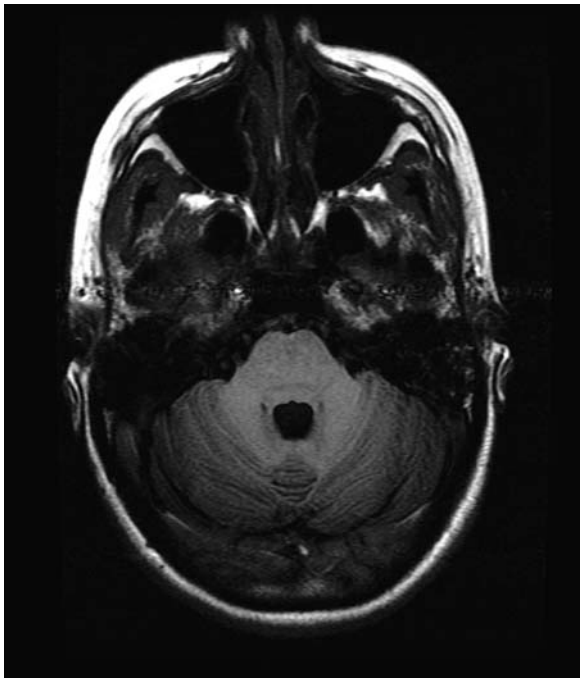

Fig. 12.3 d. IR

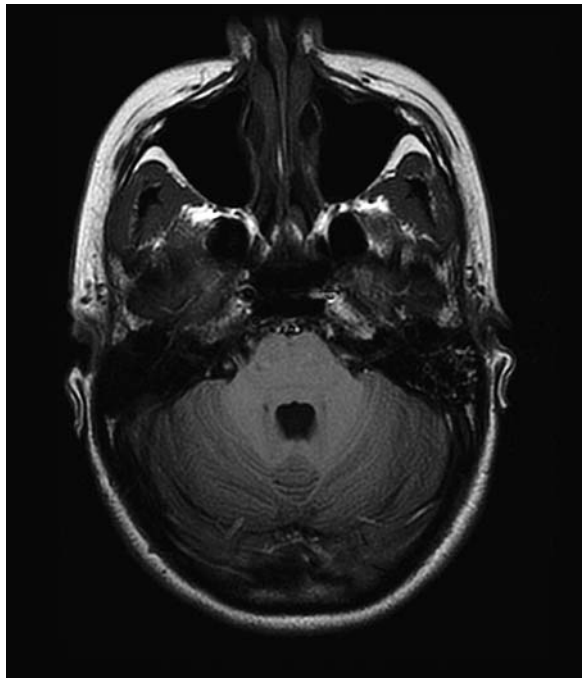

Fig. 12.4 d. FLAIR

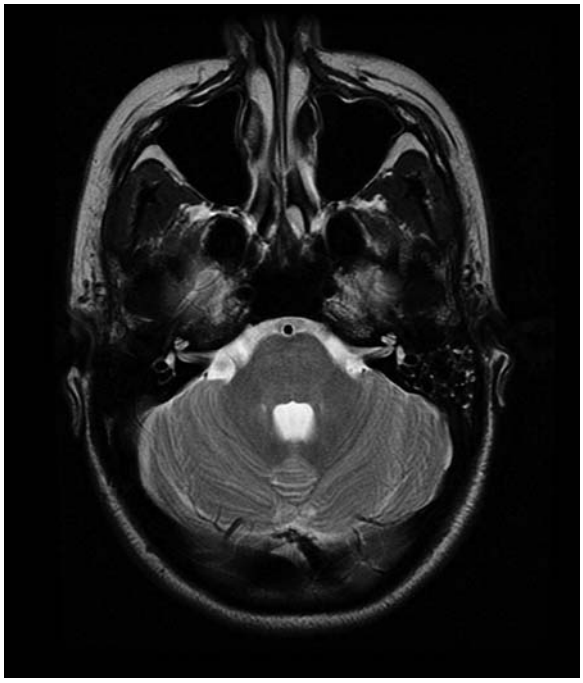

Fig. 12.5 d. FSE

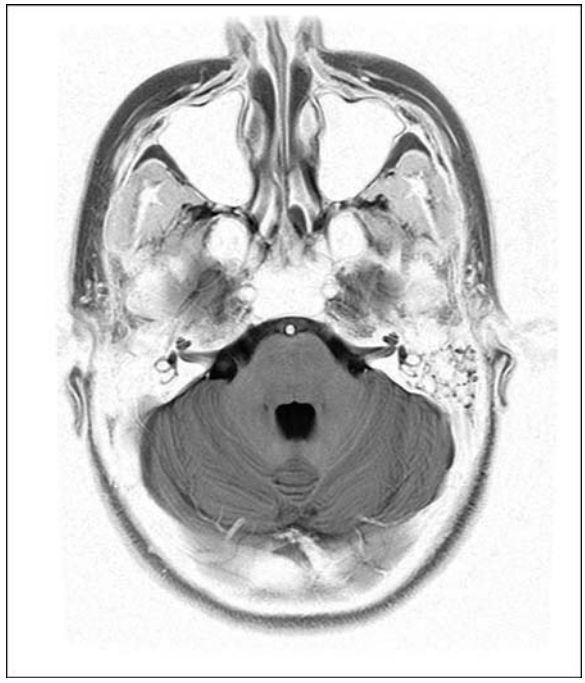

Fig. 12.6 d. FSE with inverted contrast

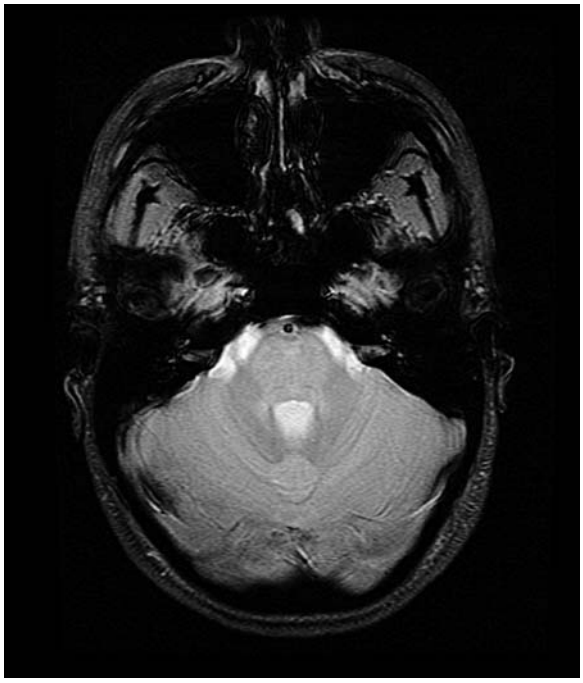

Fig. 12.7 d. GE

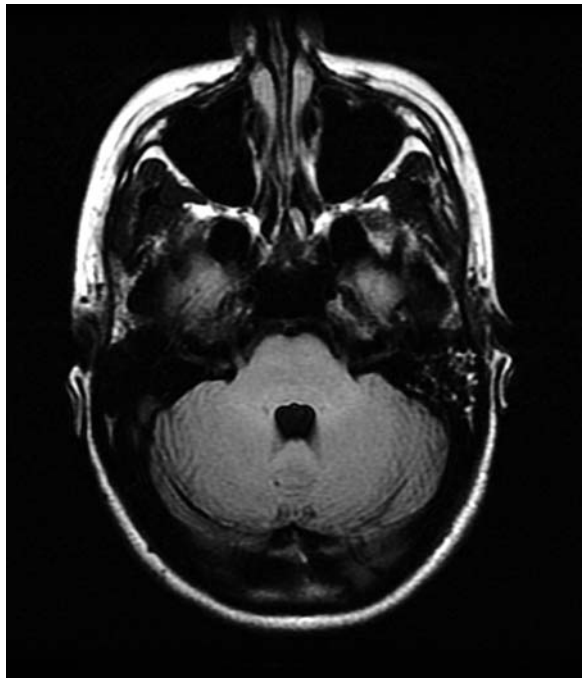

Fig. 12.8 d. FLAIR

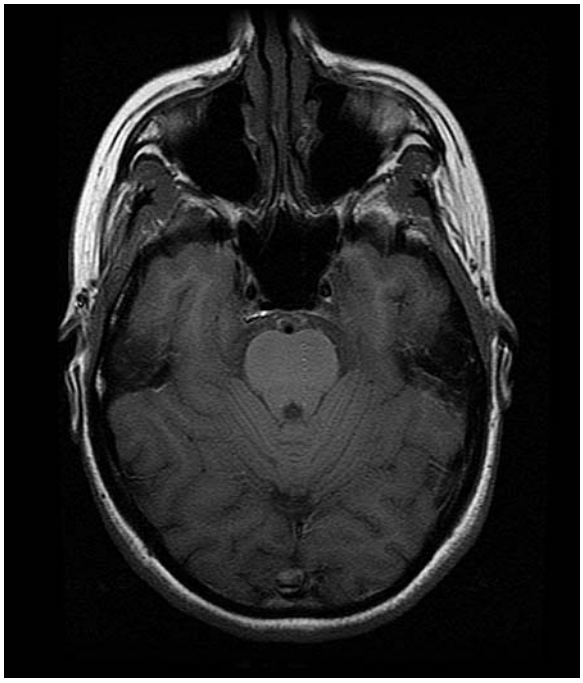

Fig. 12.1 e. SE

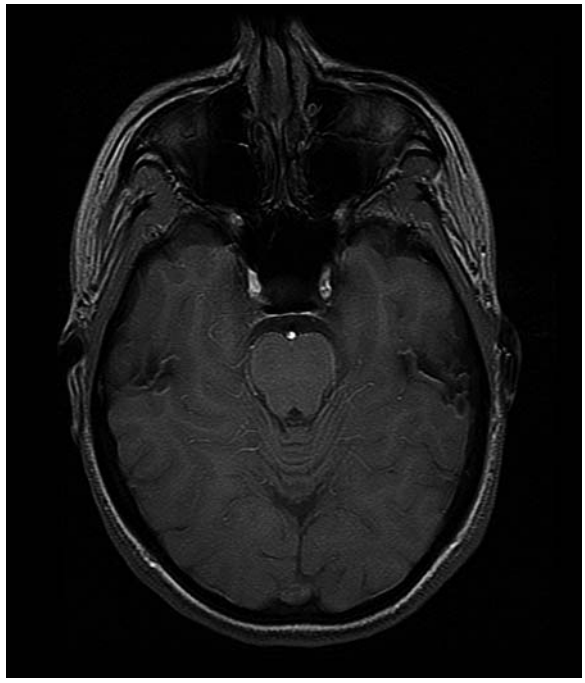

Fig. 12.2 e. FGE

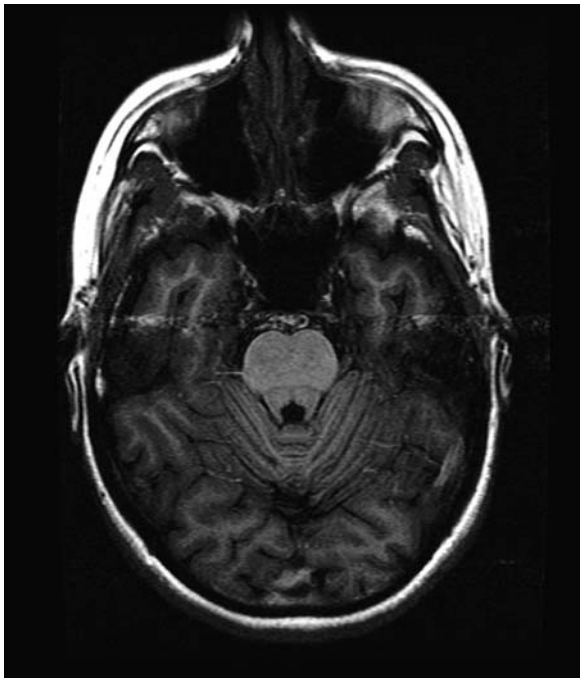

Fig. 12.3 e. IR

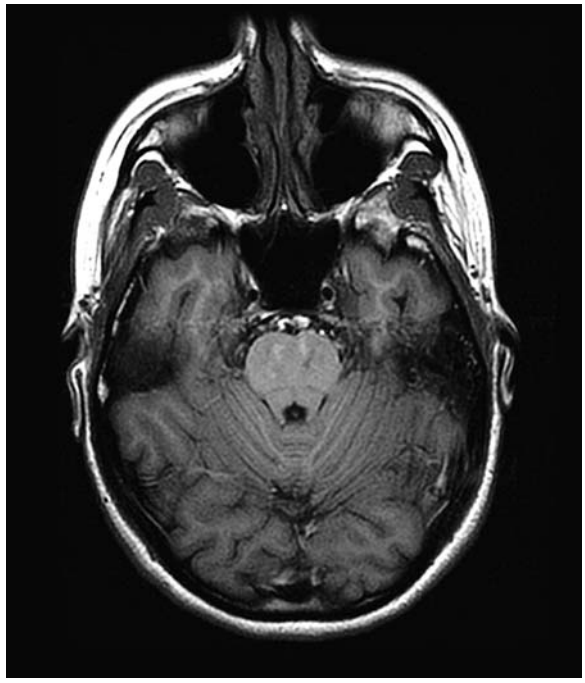

Fig. 12.4 e. FLAIR

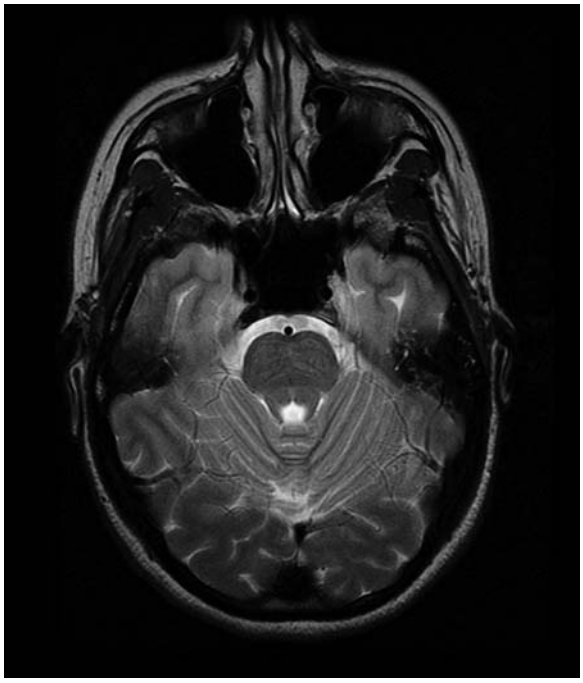

Fig. 12.5 e. FSE

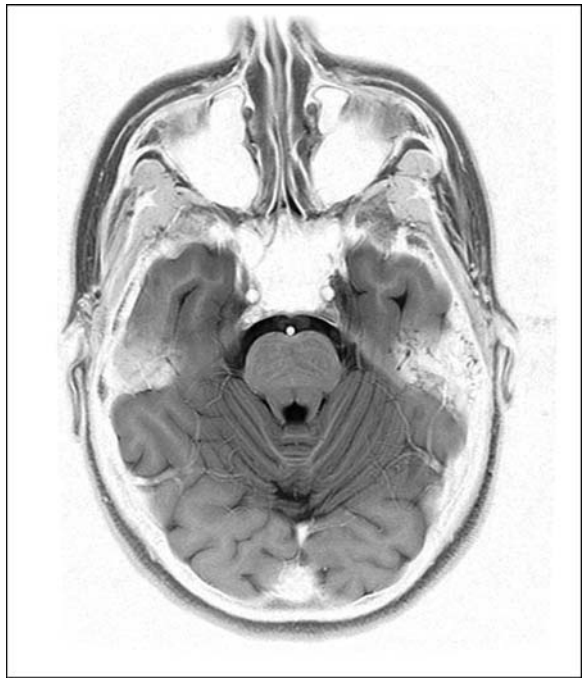

Fig. 12.6 e. FSE with inverted contrast

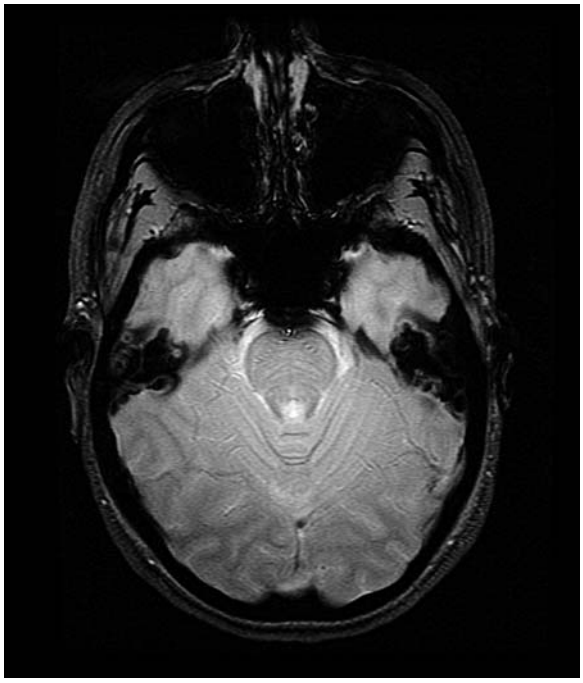

Fig. 12.7 e. GE

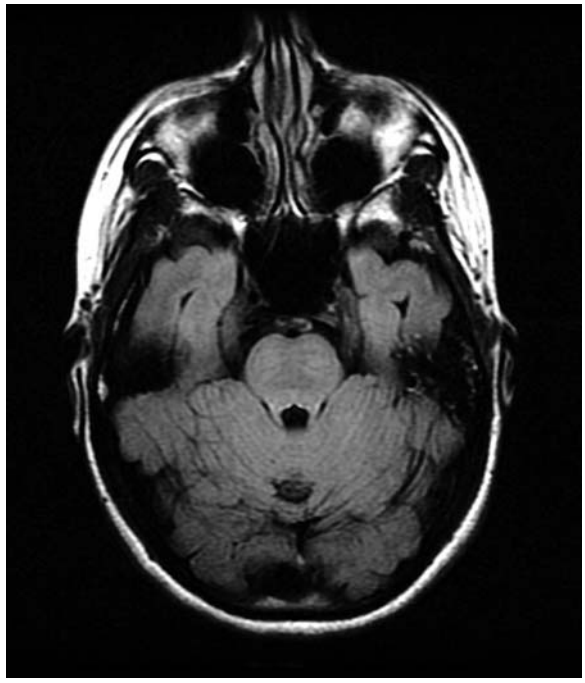

Fig. 12.8 e. FLAIR

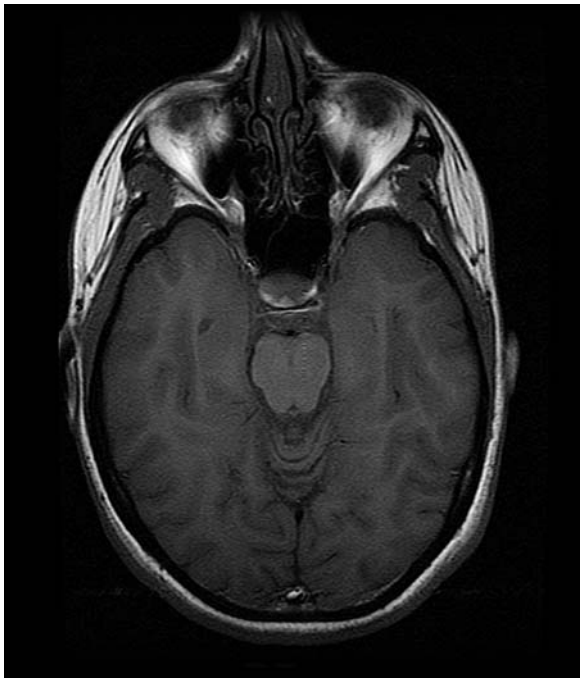

Fig. 12.1 f. SE

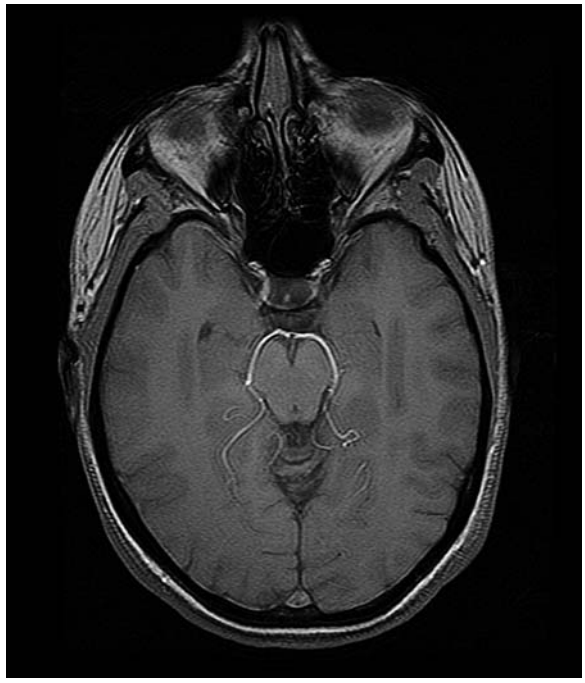

Fig. 12.2 f. FGE

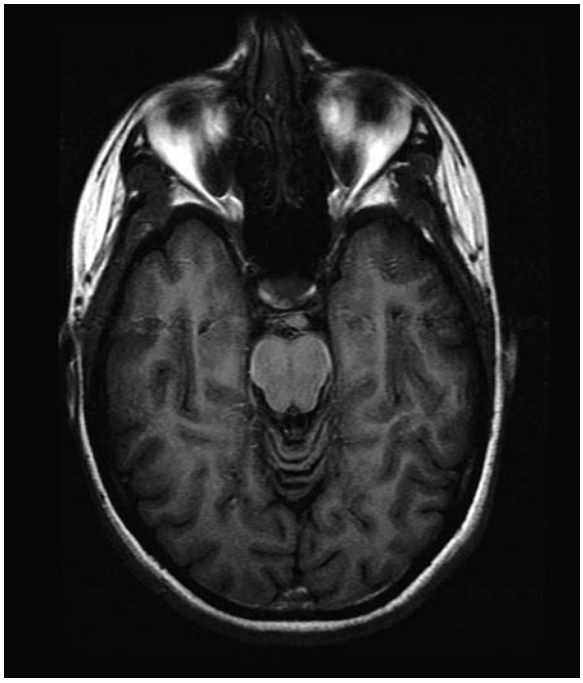

Fig. 12.3 f. IR

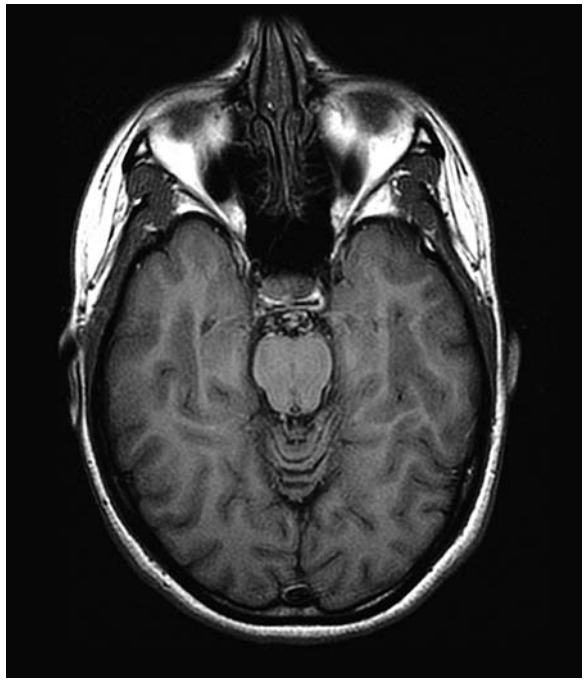

Fig. 12.4 f. FLAIR

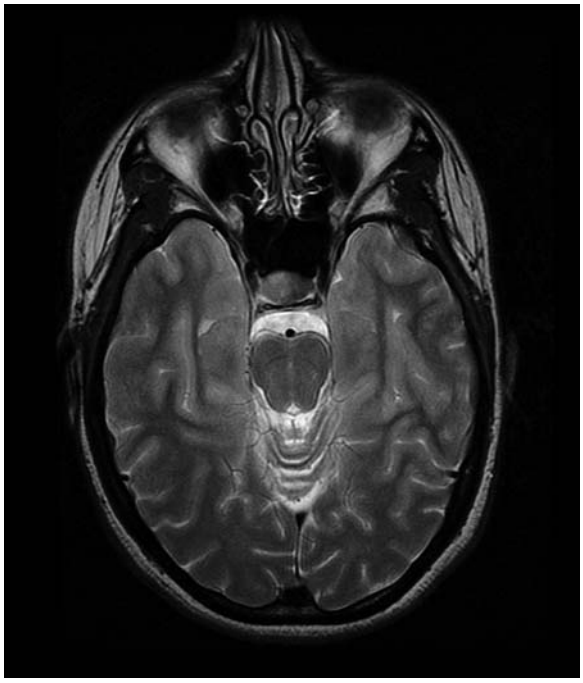

Fig. 12.5 f. FSE

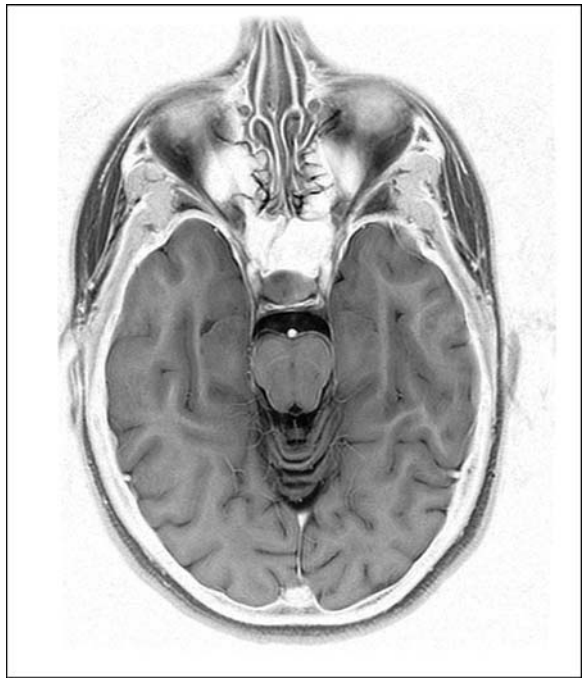

Fig. 12.6 f. FSE with inverted contrast

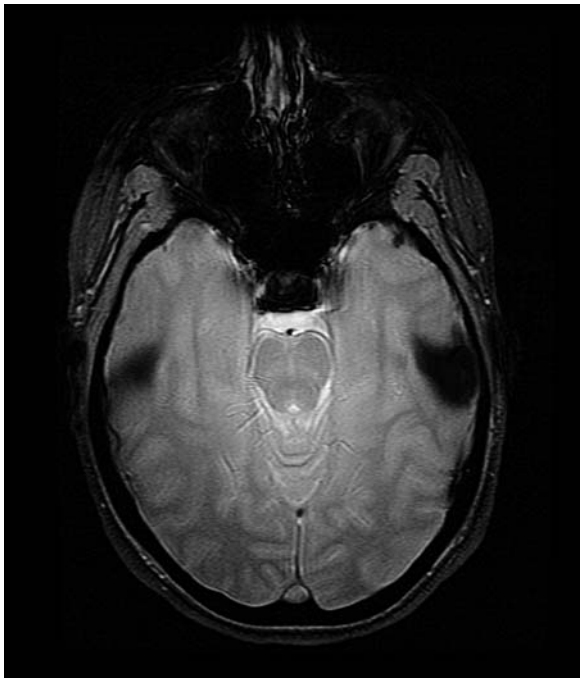

Fig. 12.7 f. GE

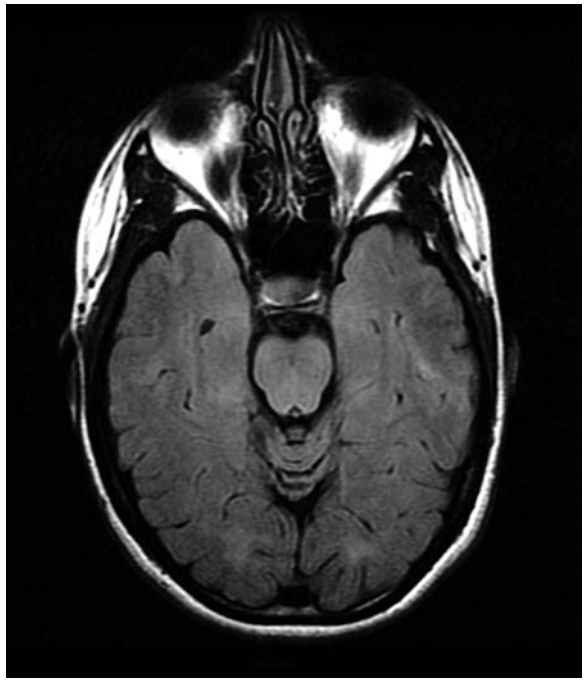

Fig. 12.8 f. FLAIR

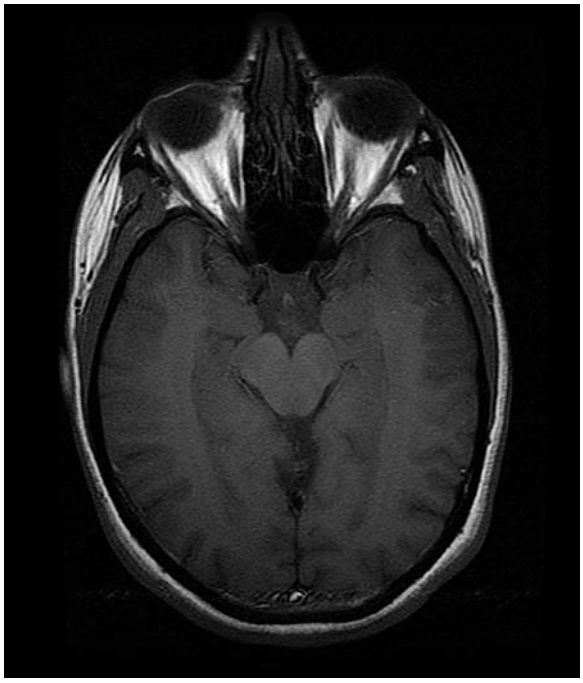

Fig. 12.1 g. SE

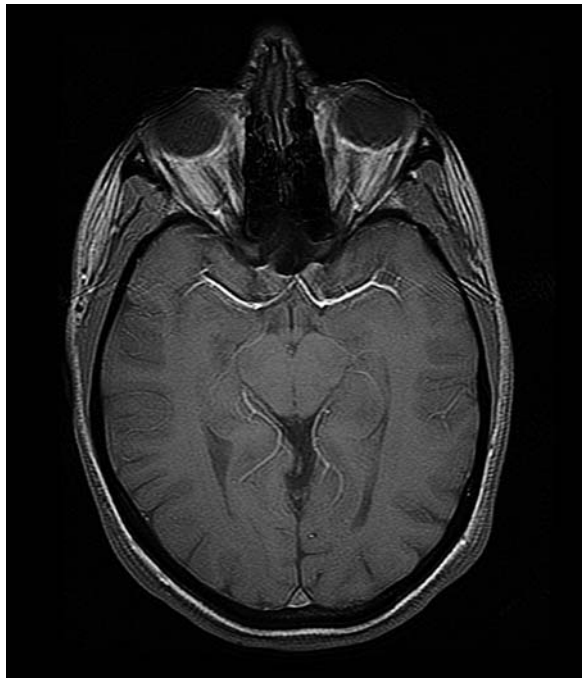

Fig. 12.2 g. FGE

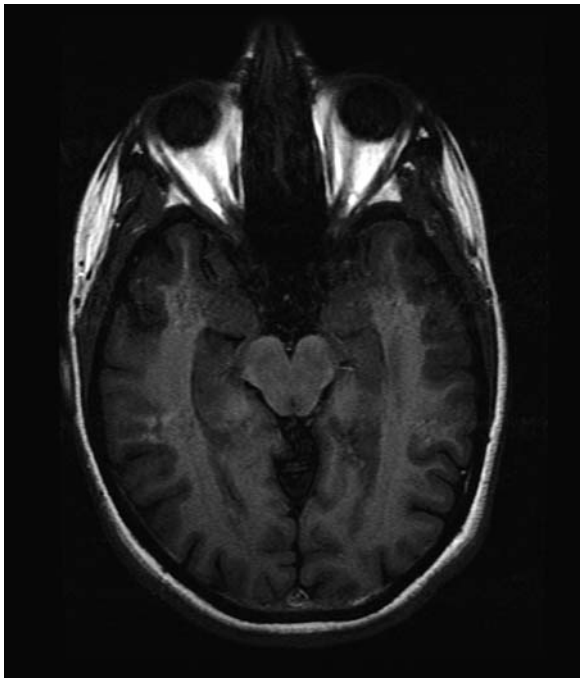

Fig. 12.3 g. IR

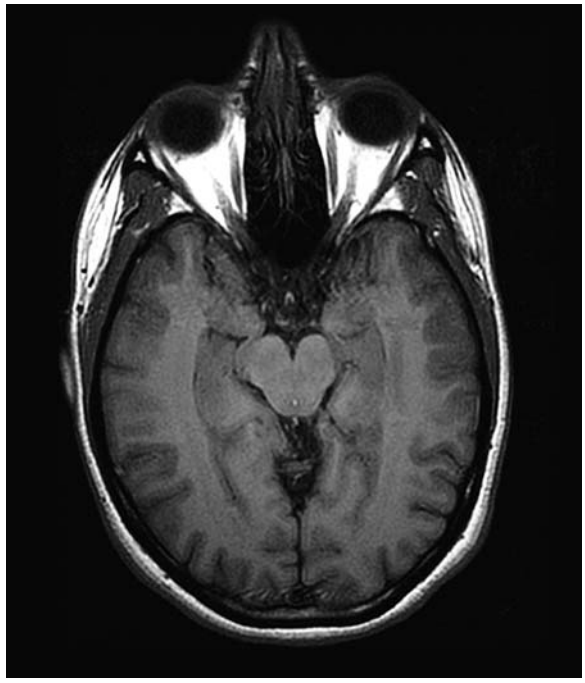

Fig. 12.4 g. FLAIR

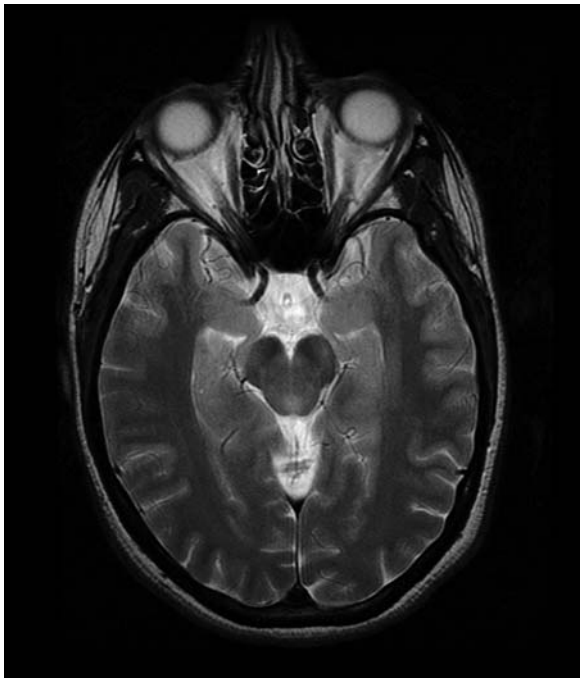

Fig. 12.5 g. FSE

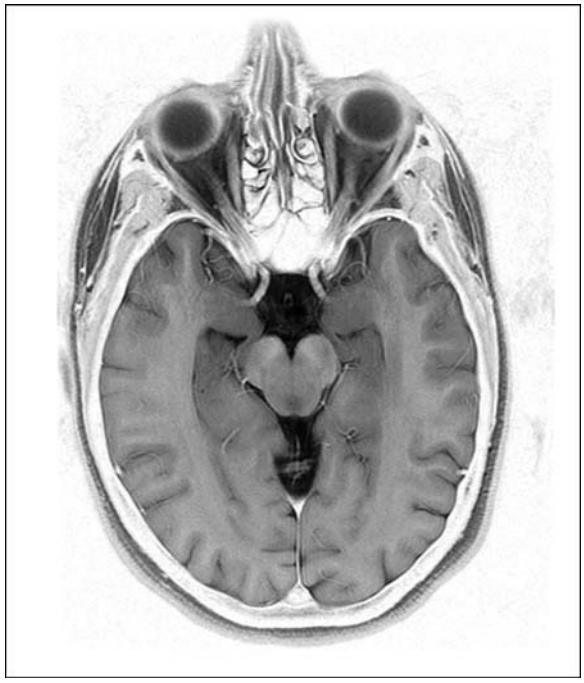

Fig. 12.6 g. FSE with inverted contrast

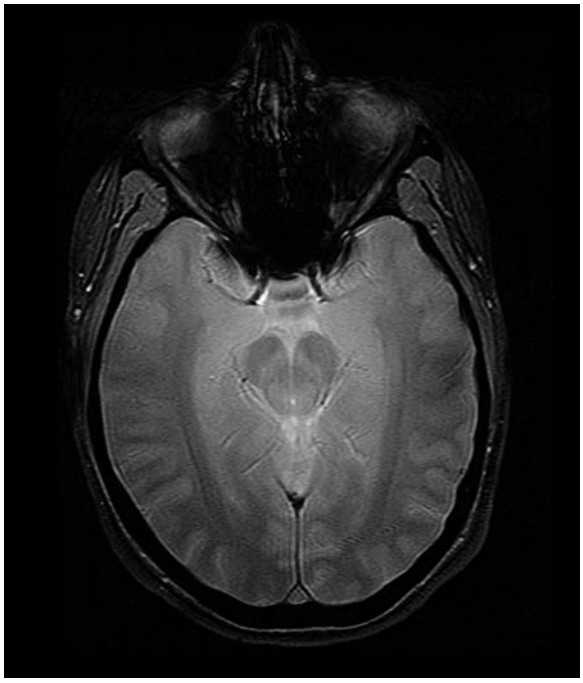

Fig. 12.7 g. GE

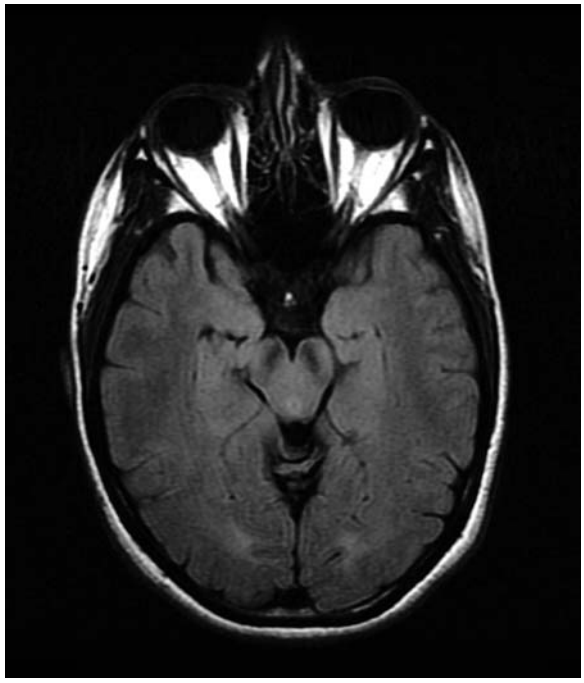

Fig. 12.8 g. FLAIR

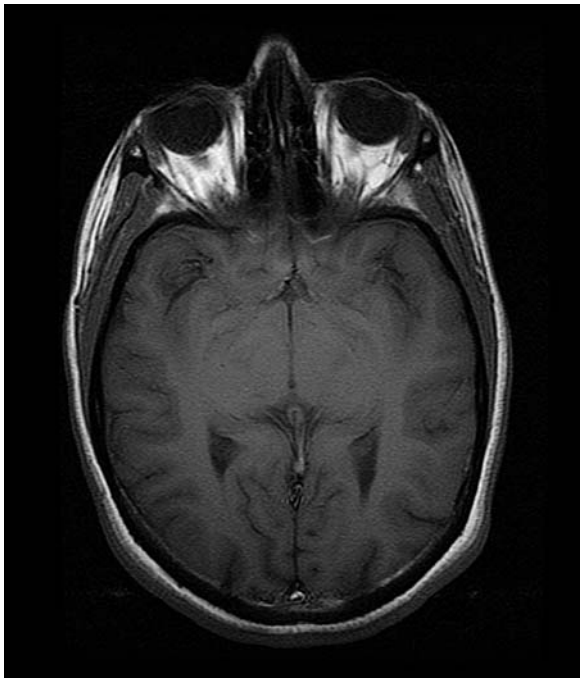

Fig. 12.1 h. SE

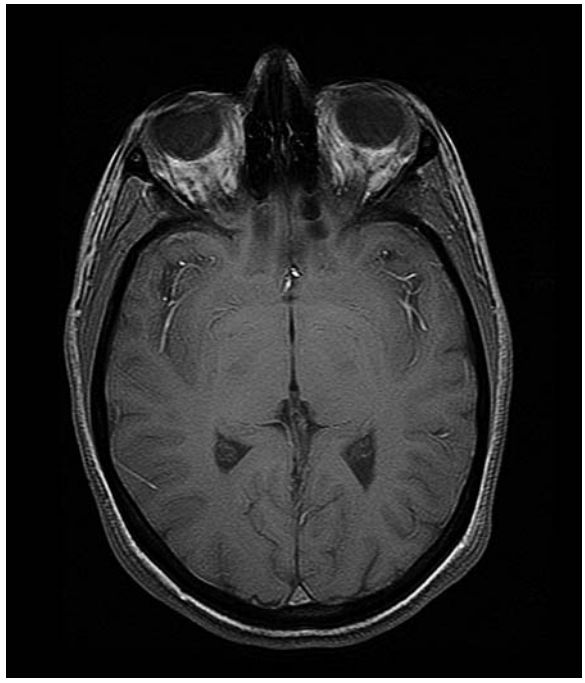

Fig. 12.2 h. FGE

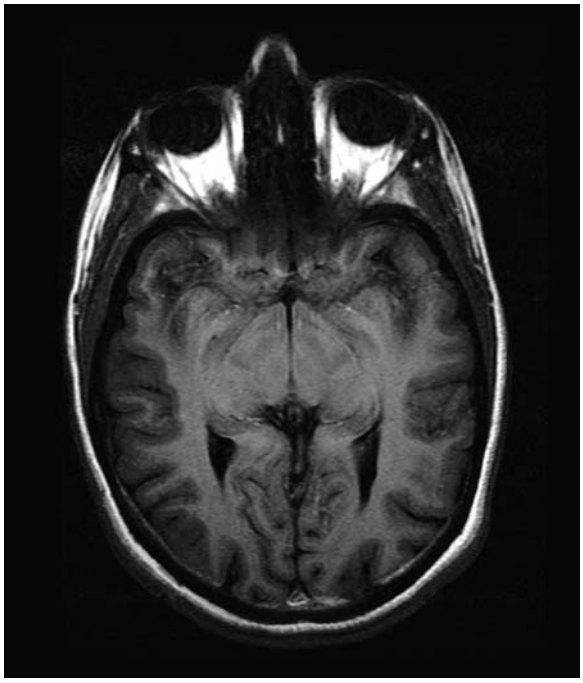

Fig. 12.3 h. IR

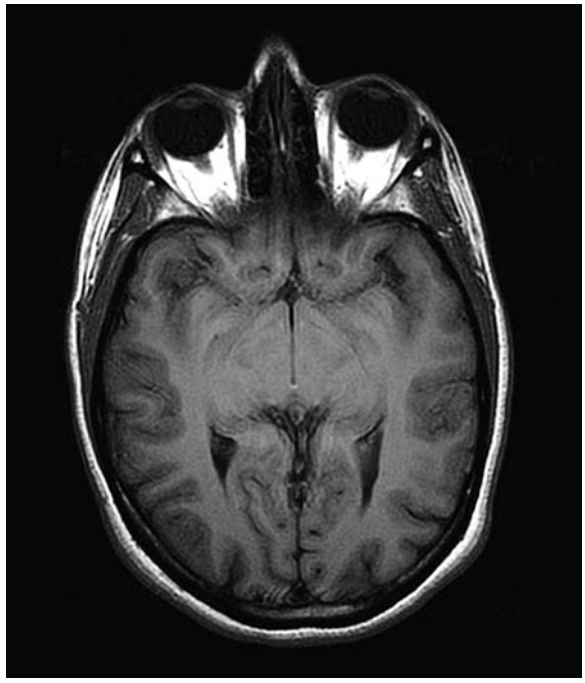

Fig. 12.4 h. FLAIR

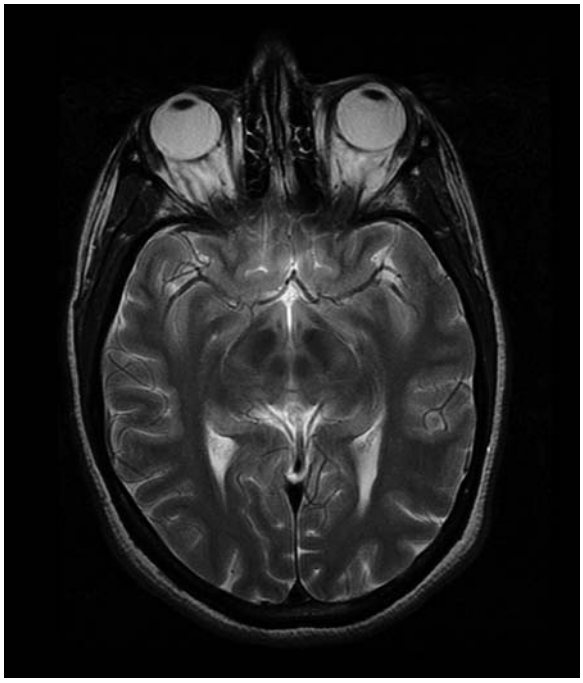

Fig. 12.5 h. FSE

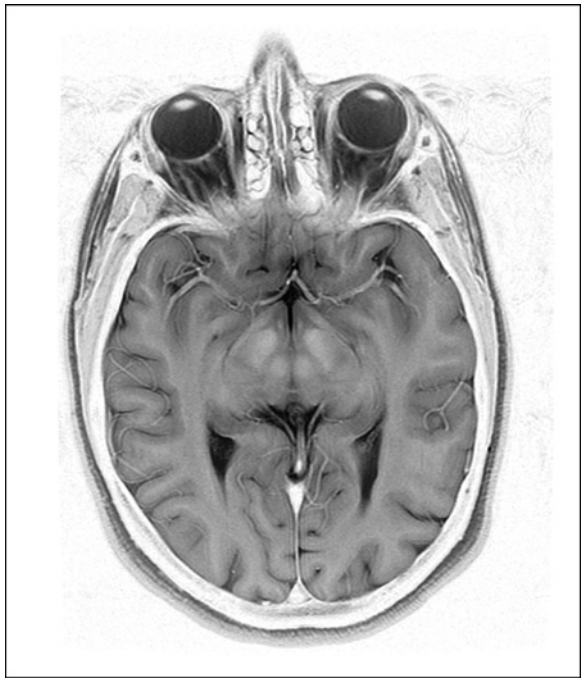

Fig. 12.6 h. FSE with inverted contrast

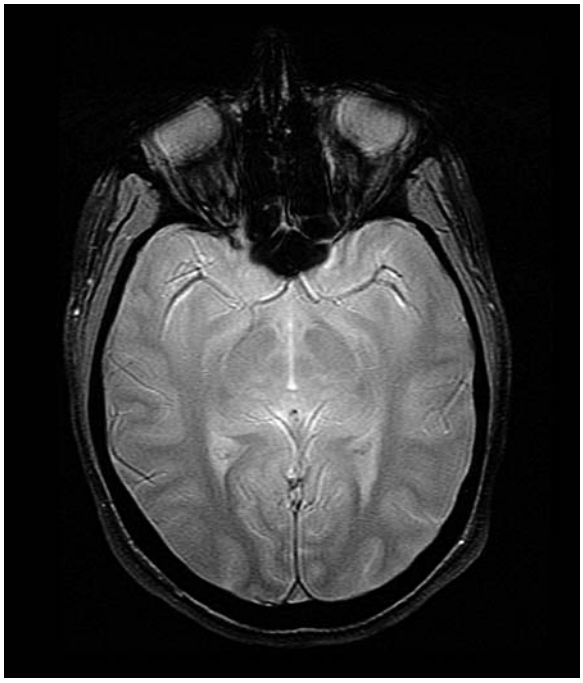

Fig. 12.7 h. GE

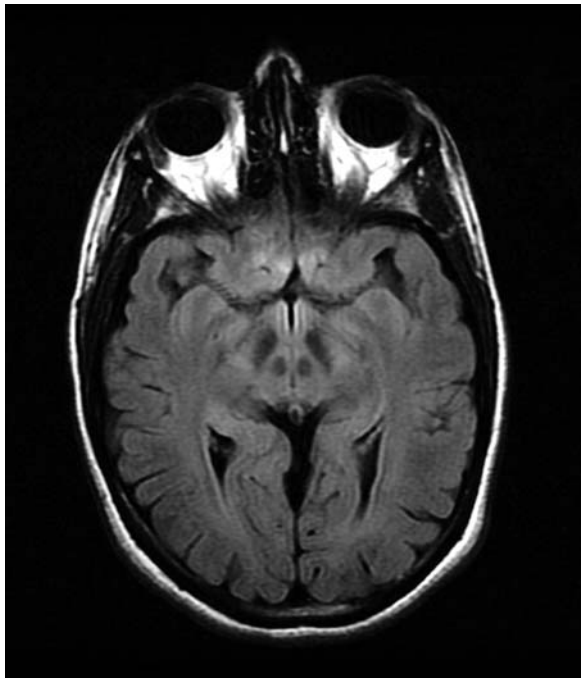

Fig. 12.8 h. FLAIR

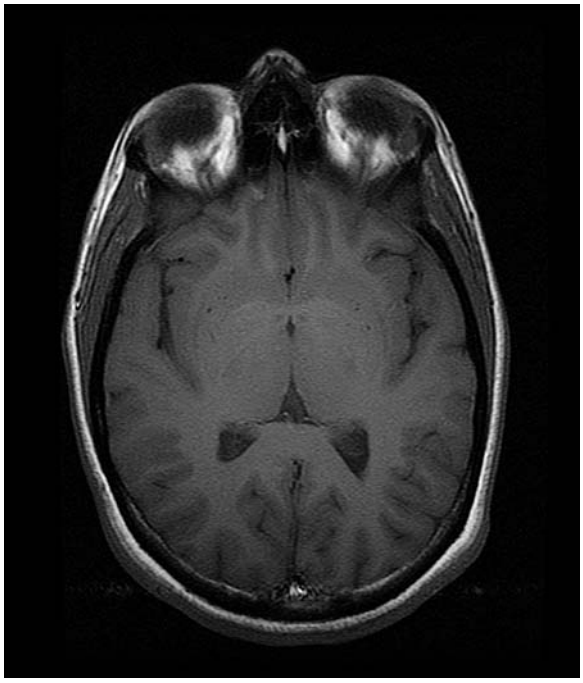

Fig. 12.1 i. SE

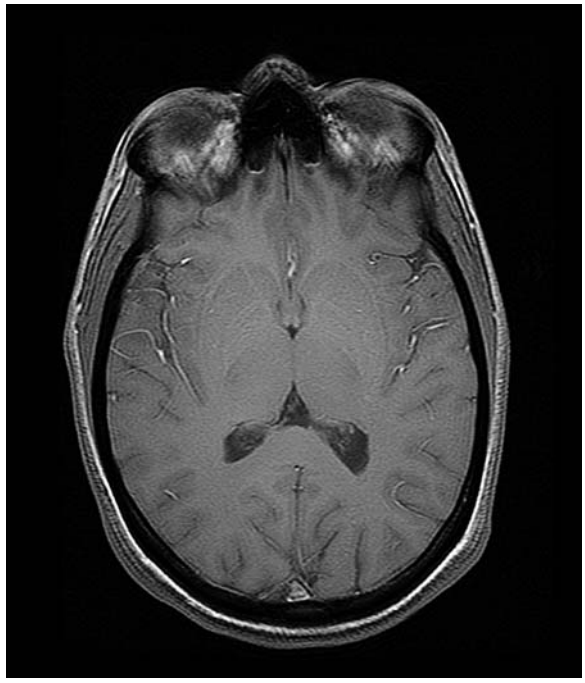

Fig. 12.2 i. FGE

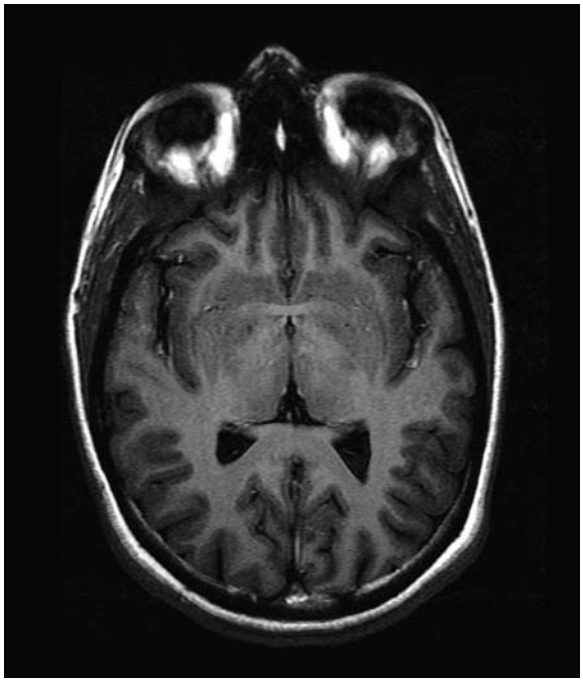

Fig. 12.3 i. IR

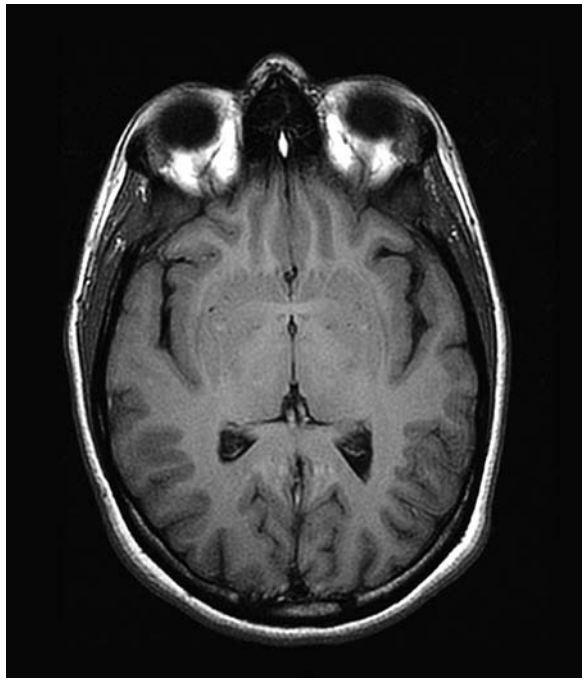

Fig. 12.4 i. FLAIR

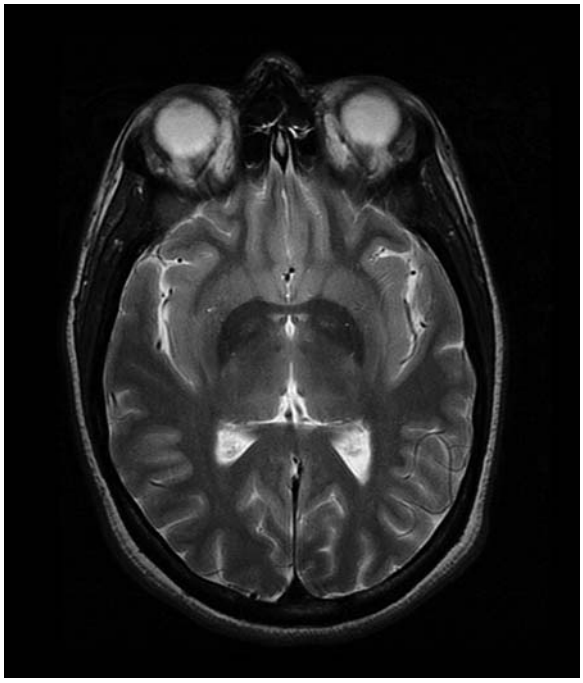

Fig. 12.5 i. FSE

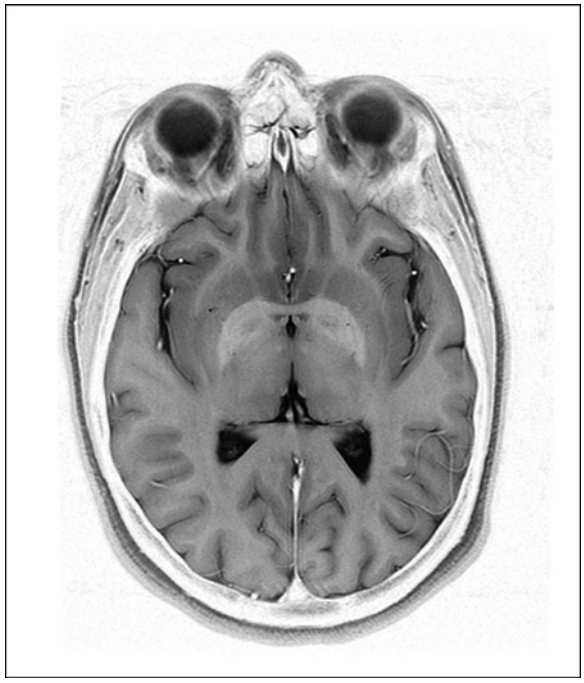

Fig. 12.6 i. FSE with inverted contrast

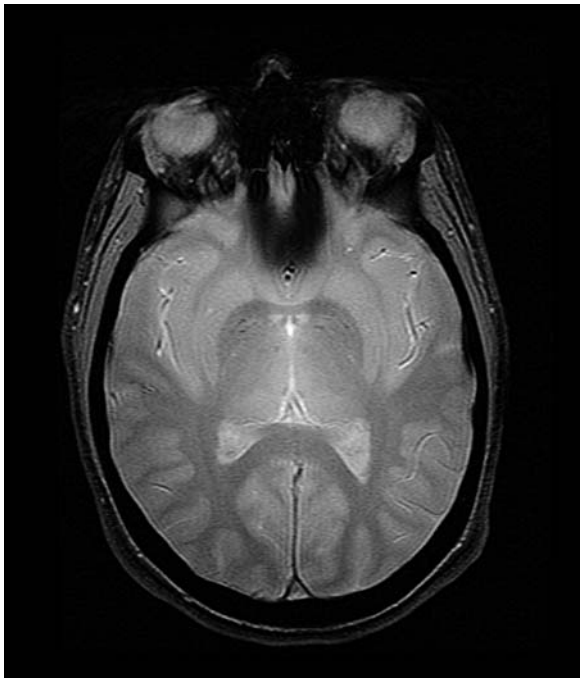

Fig. 12.7 i. GE

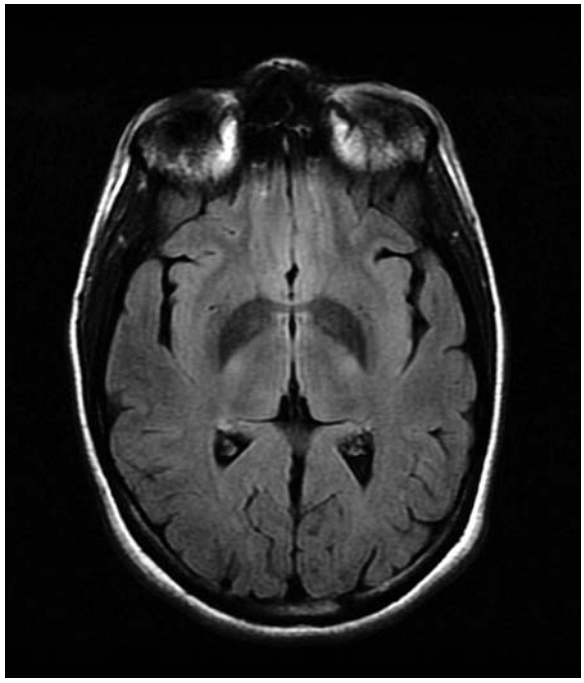

Fig. 12.8 i. FLAIR

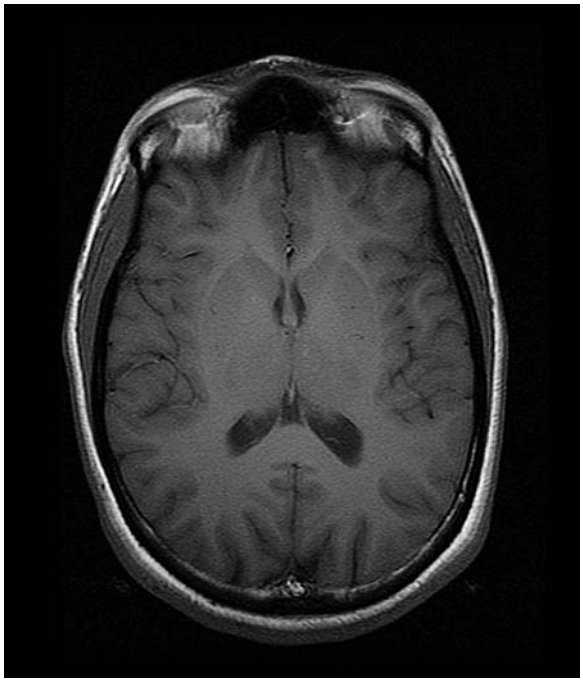

Fig. 12.1 j. SE

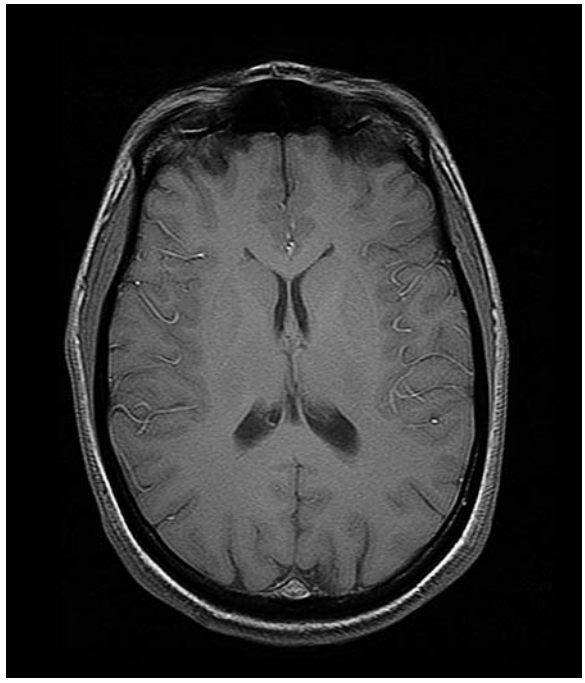

Fig. 12.2 j. FGE

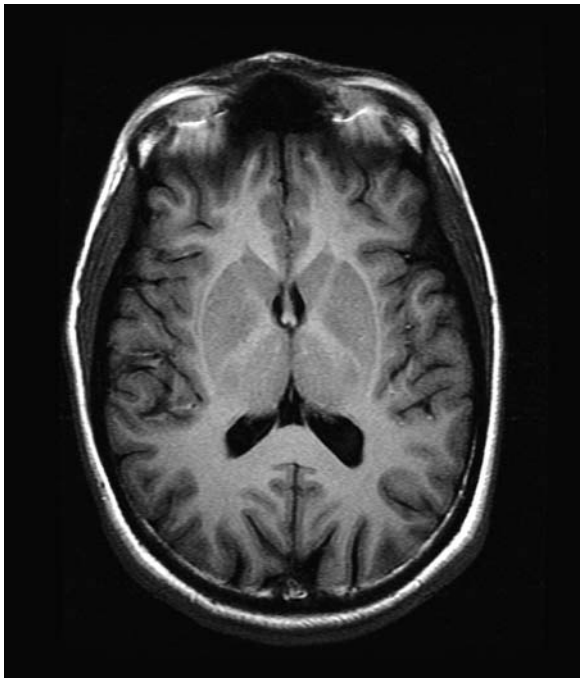

Fig. 12.3 j. IR

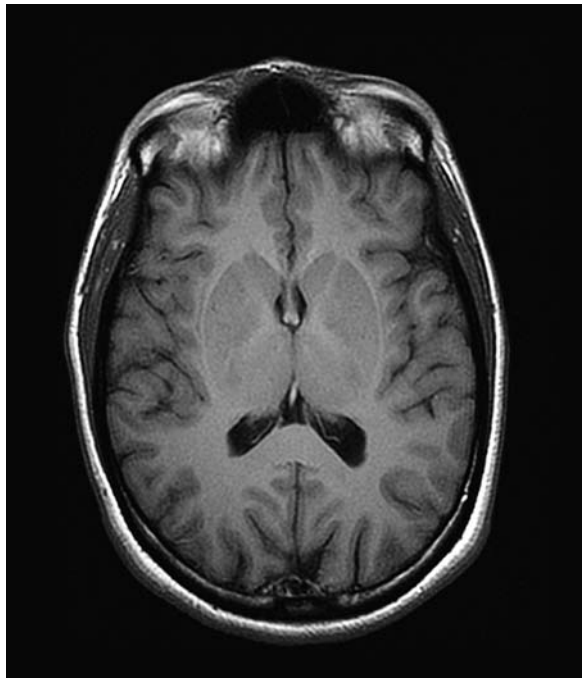

Fig. 12.4 j. FLAIR

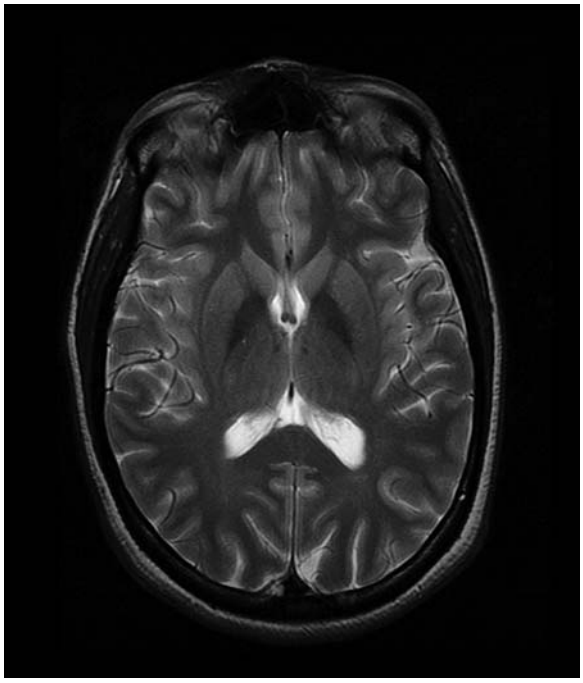

Fig. 12.5 j. FSE

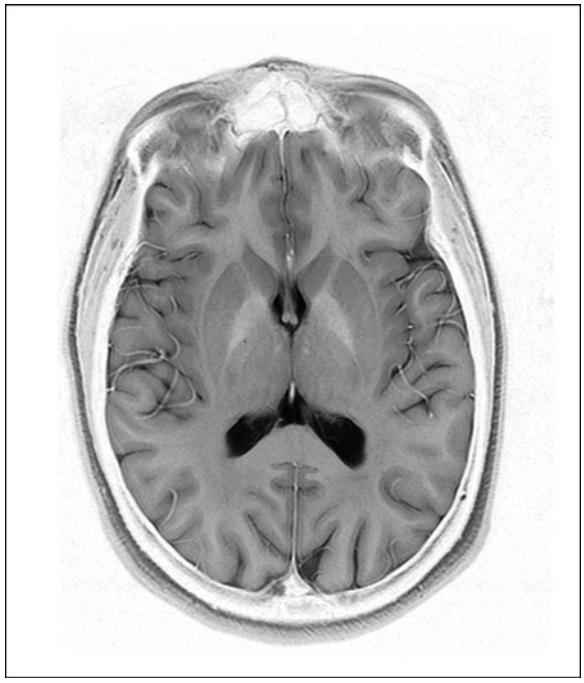

Fig. 12.6 j. FSE with inverted contrast

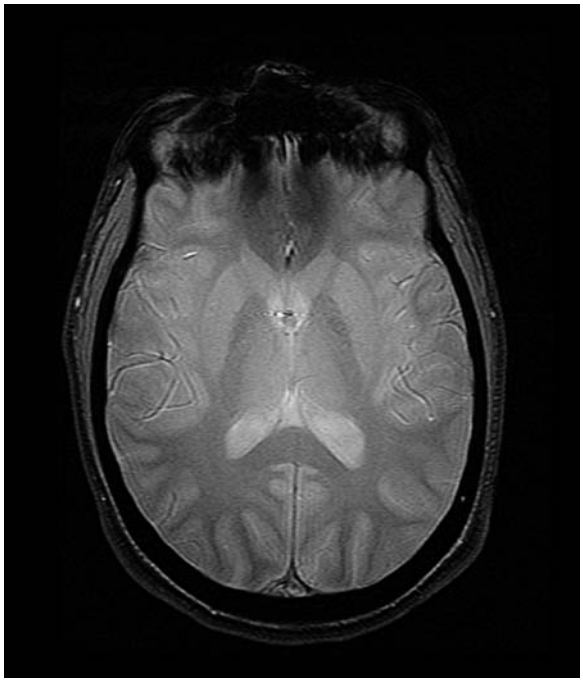

Fig. 12.7 j. GE

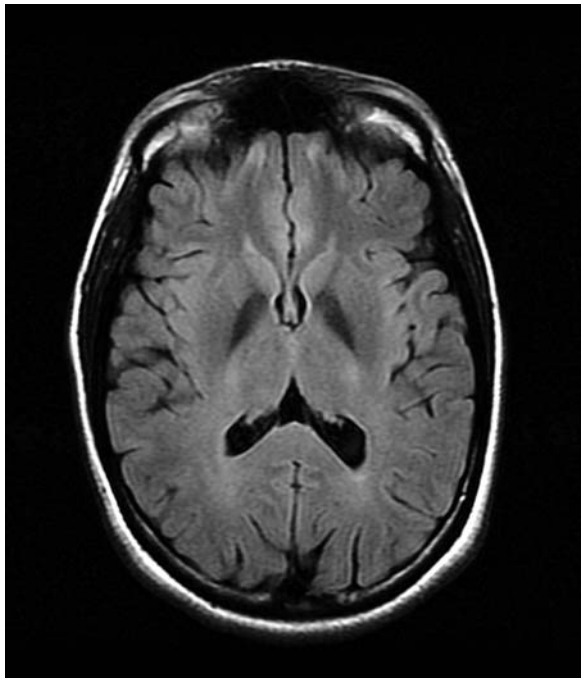

Fig. 12.8 j. FLAIR

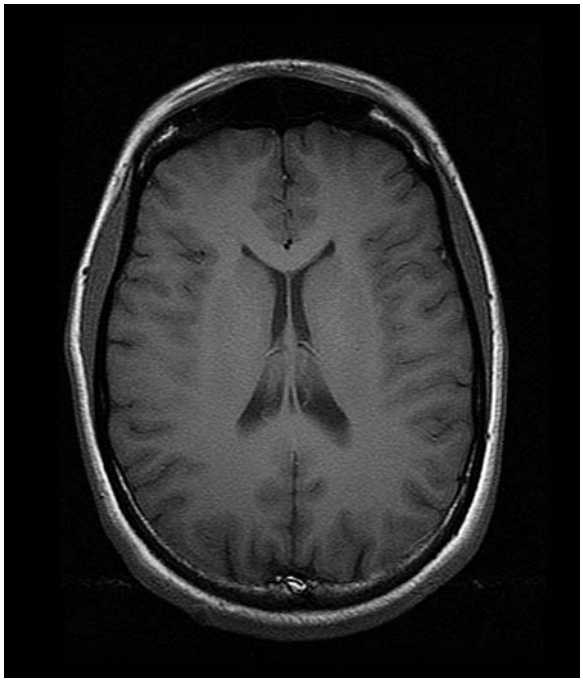

Fig. 12.1 k. SE

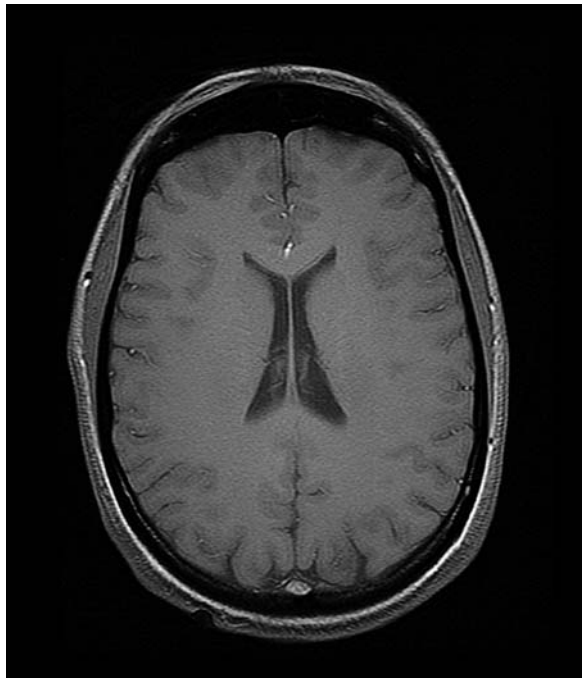

Fig. 12.2 k. FGE

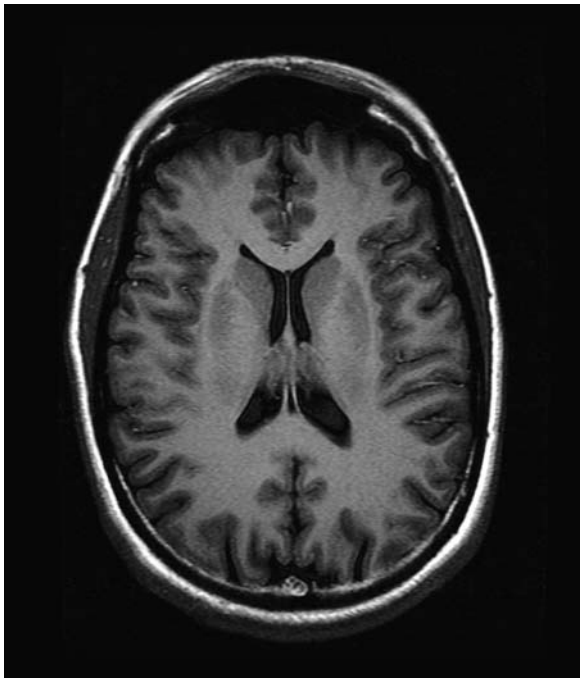

Fig. 12.3 k. IR

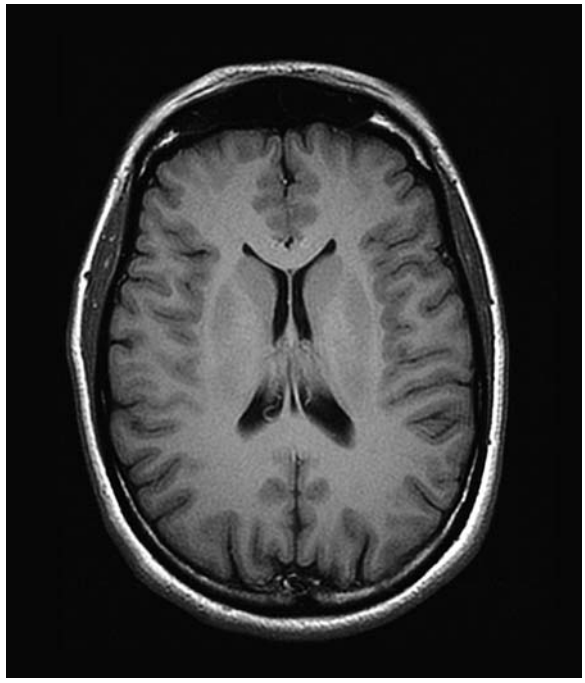

Fig. 12.4 k. FLAIR

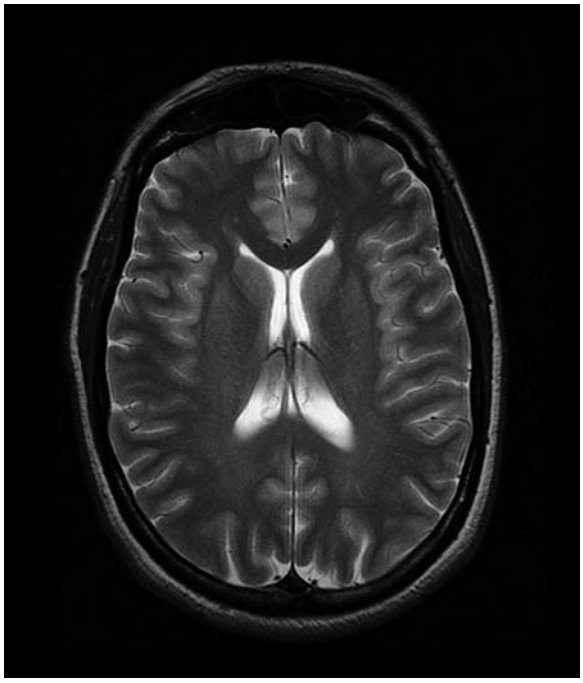

Fig. 12.5 k. FSE

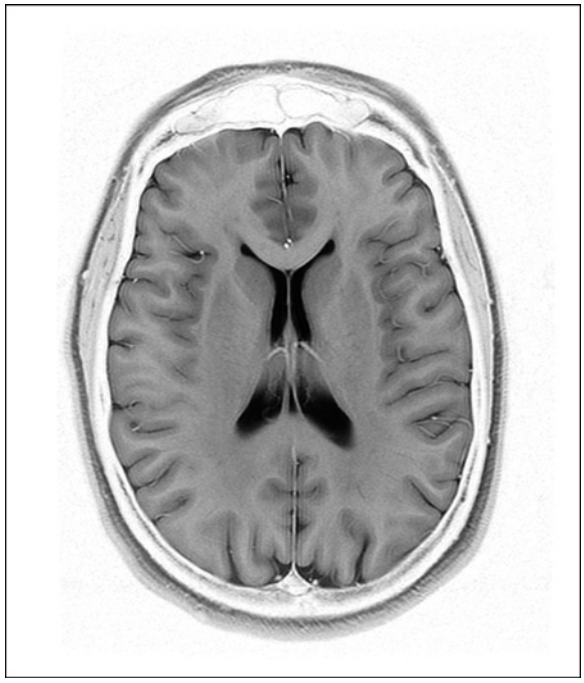

Fig. 12.6 k. FSE with inverted contrast

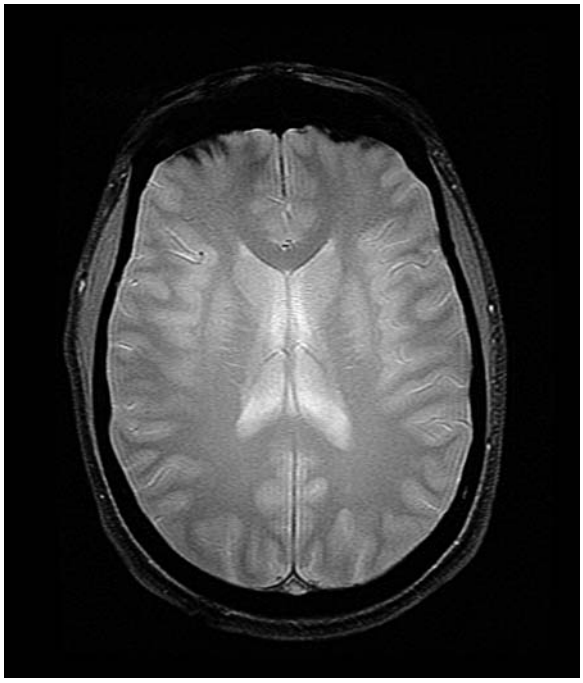

Fig. 12.7 k. GE

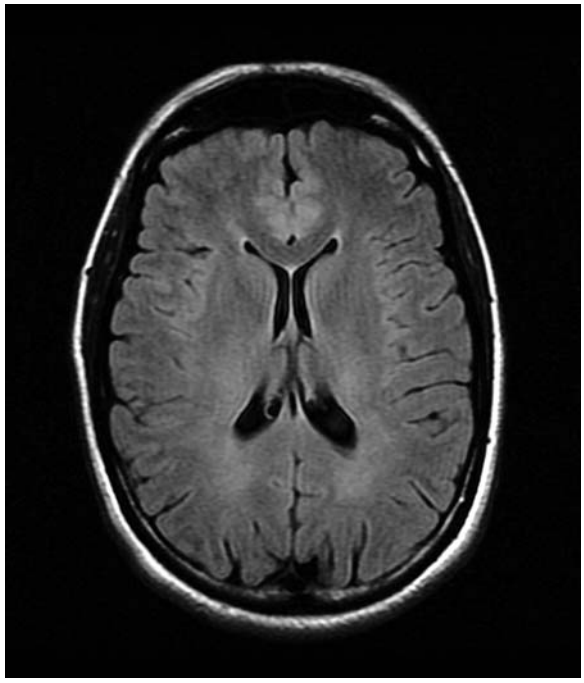

Fig. 12.8 k. FLAIR

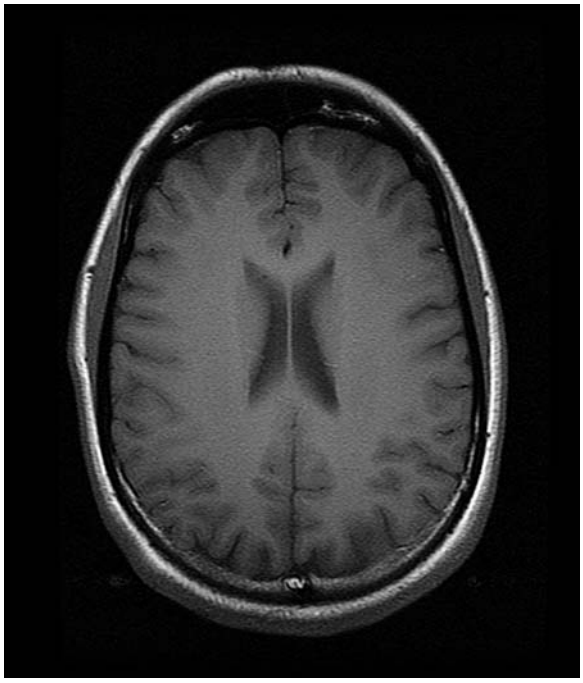

Fig. 12.1 l. SE

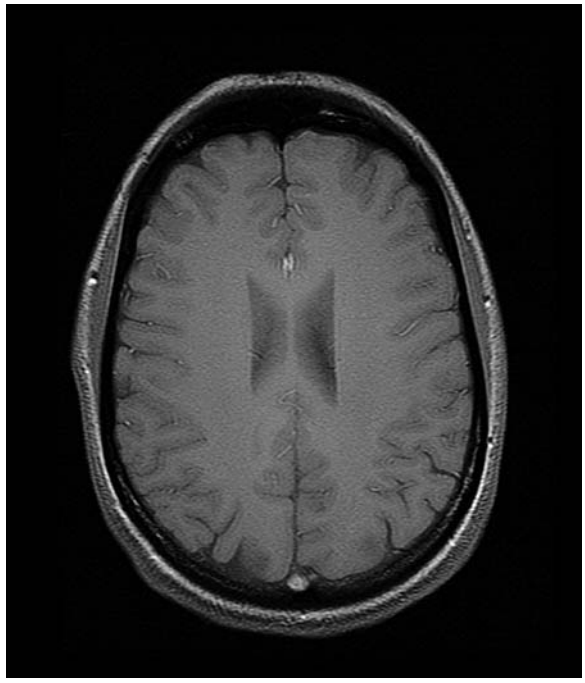

Fig. 12.2 l. FGE

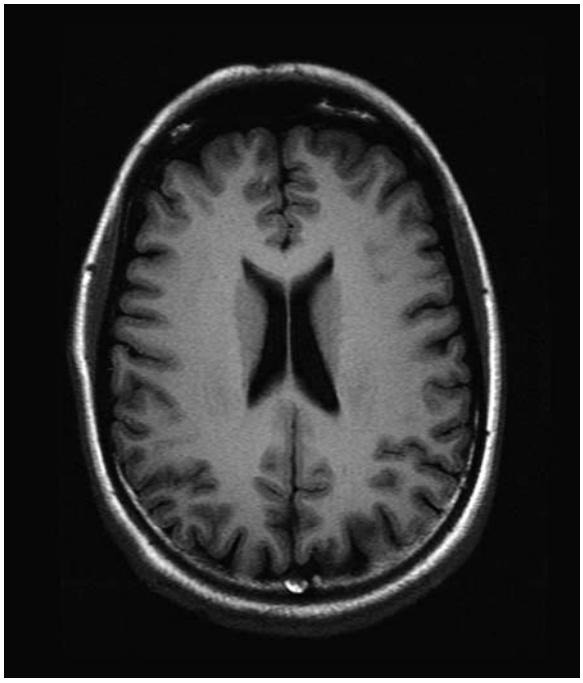

Fig. 12.3 l. IR

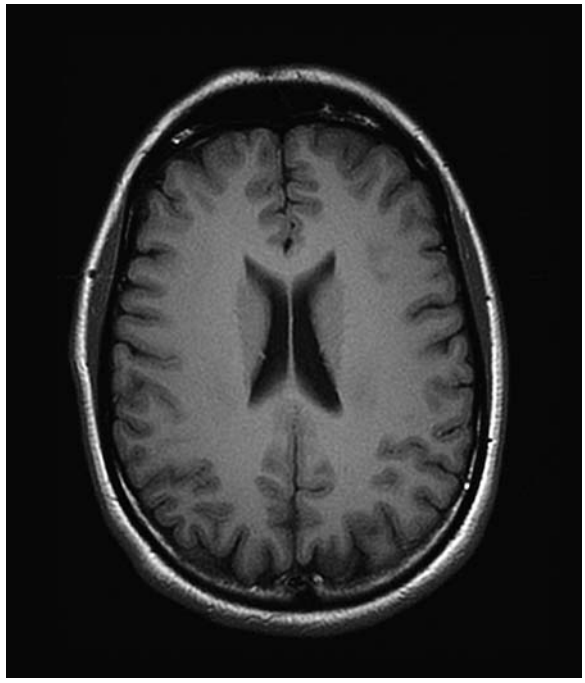

Fig. 12.4 l. FLAIR

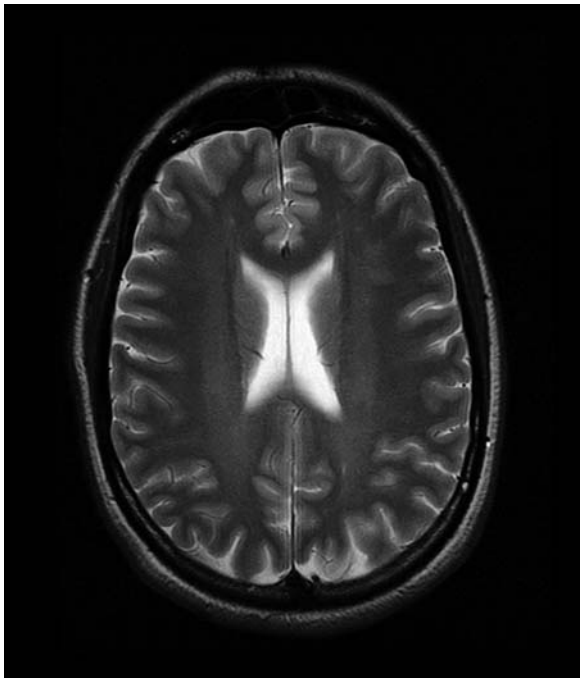

Fig. 12.5 l. FSE

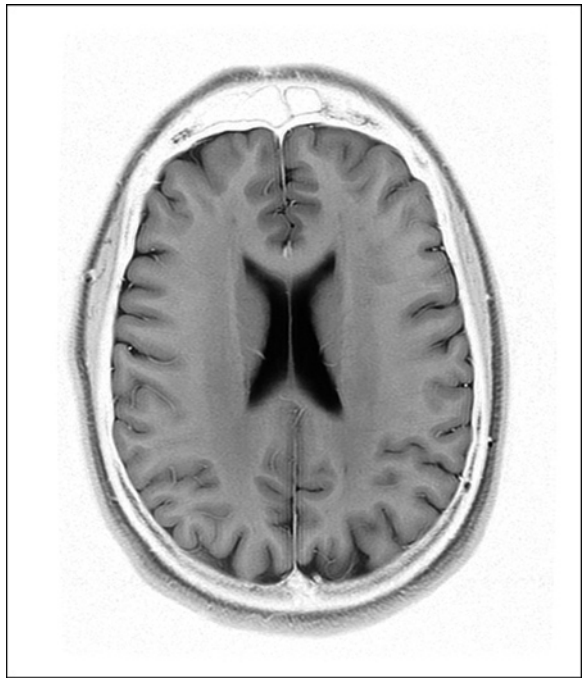

Fig. 12.6 l. FSE with inverted contrast

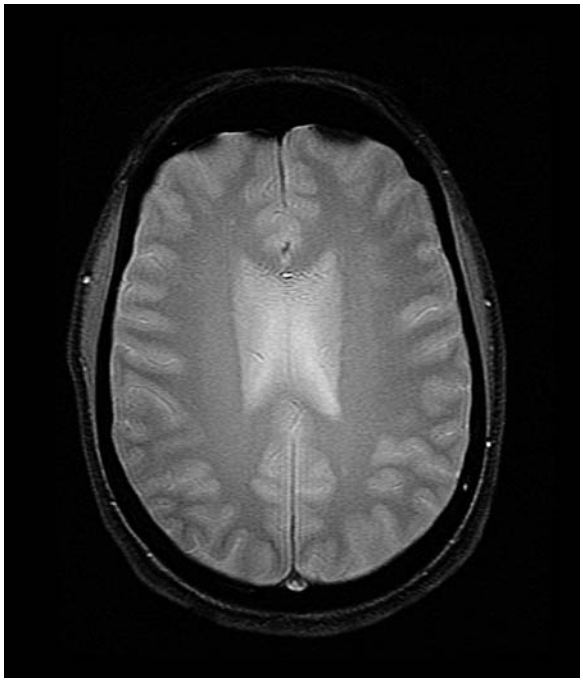

Fig. 12.7 l. GE

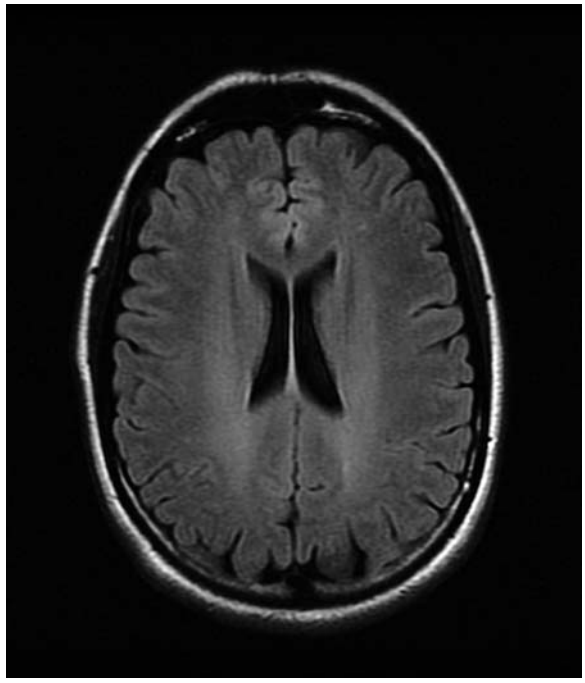

Fig. 12.8 l. FLAIR

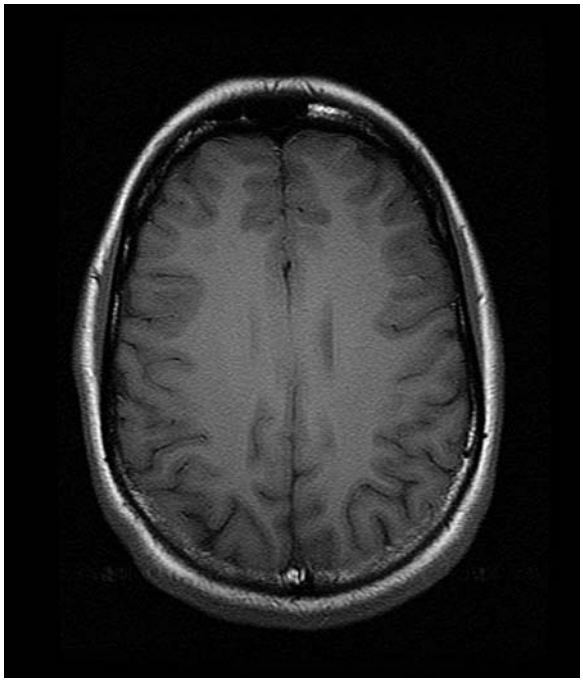

Fig. 12.1 m. SE

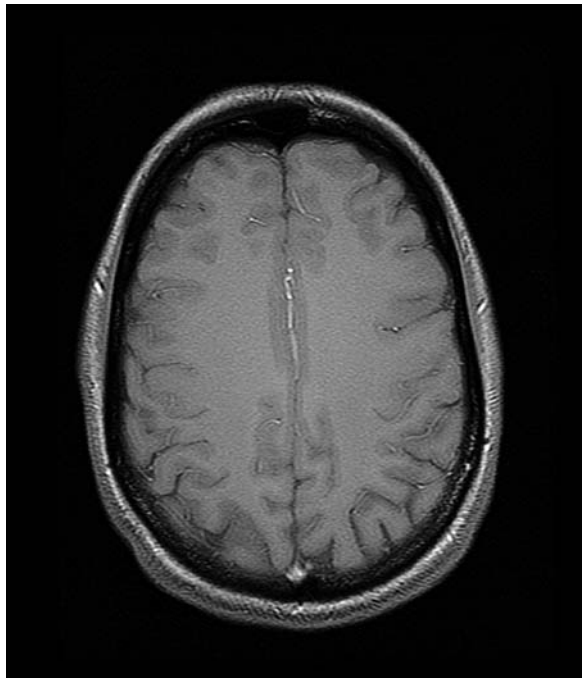

Fig. 12.2 m. FGE

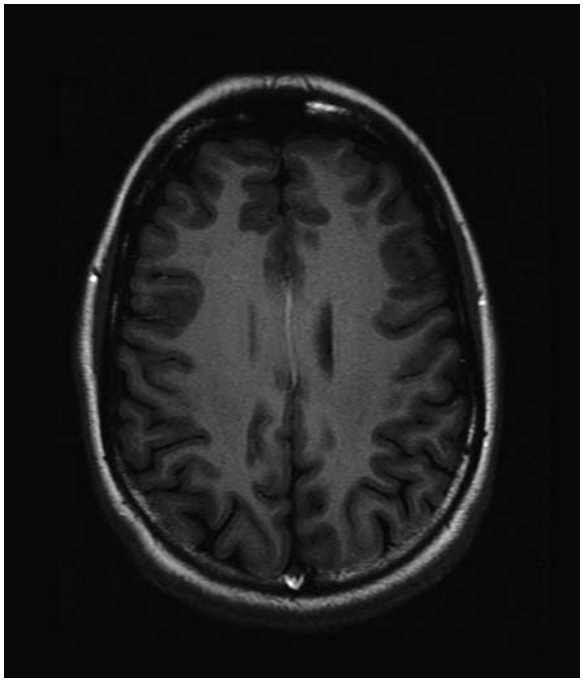

Fig. 12.3 m. IR

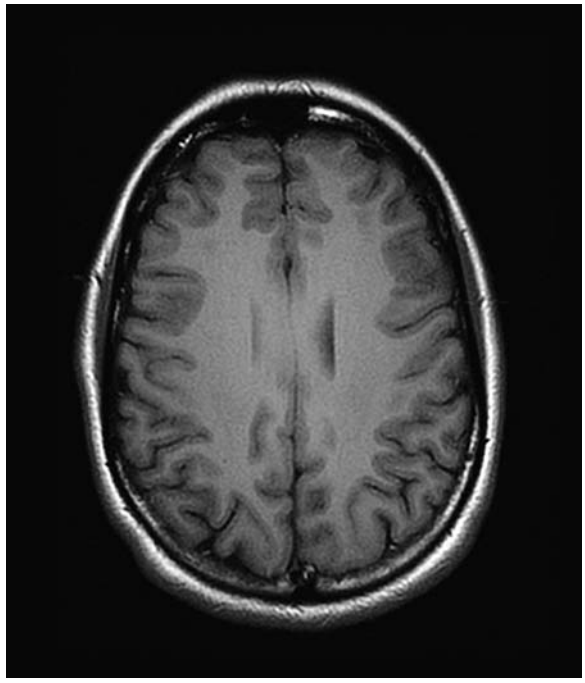

Fig. 12.4 m. FLAIR

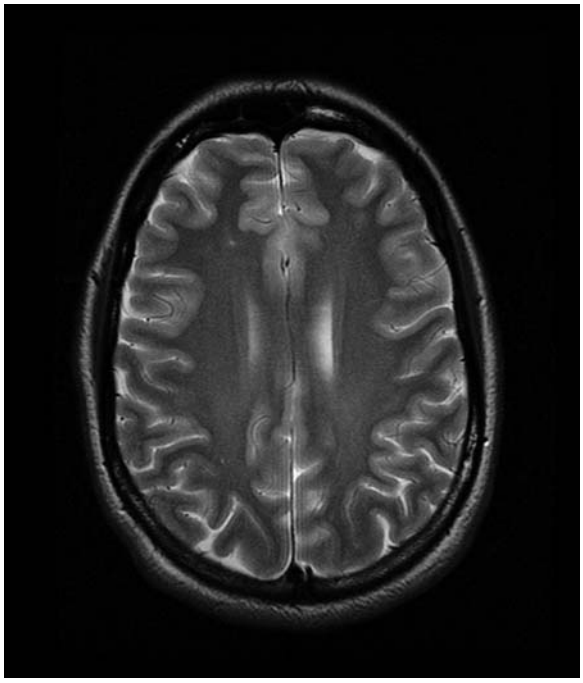

Fig. 12.5 m. FSE

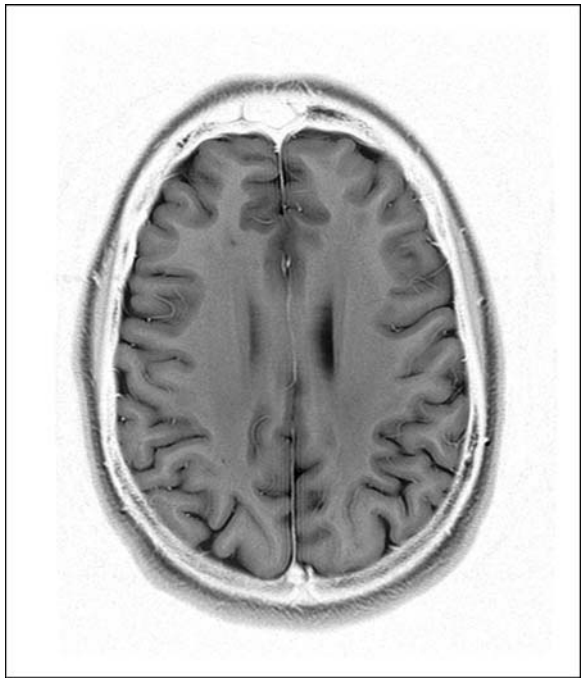

Fig. 12.6 m. FSE with inverted contrast

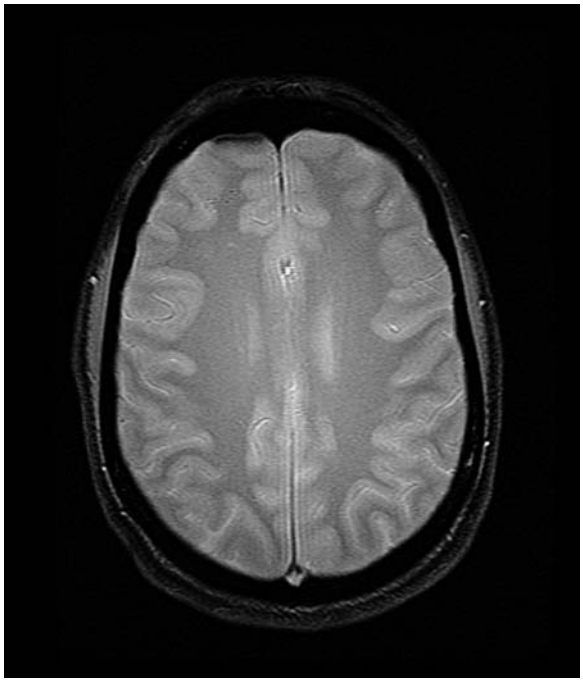

Fig. 12.7 m. GE

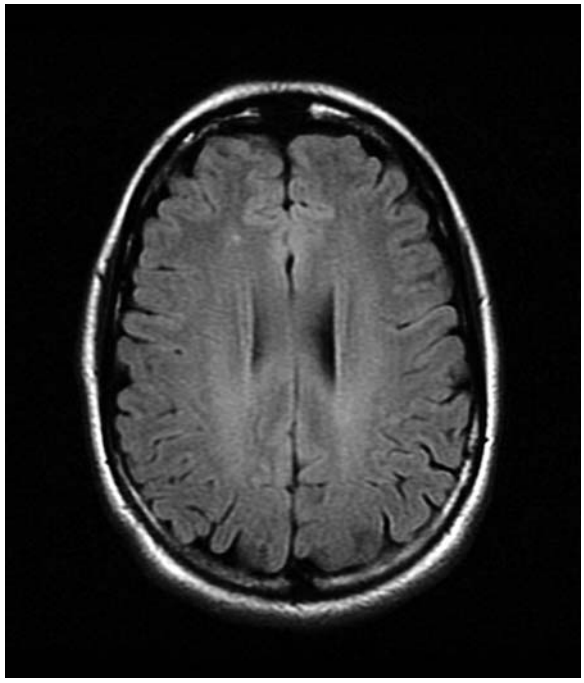

Fig. 12.8 m. FLAIR

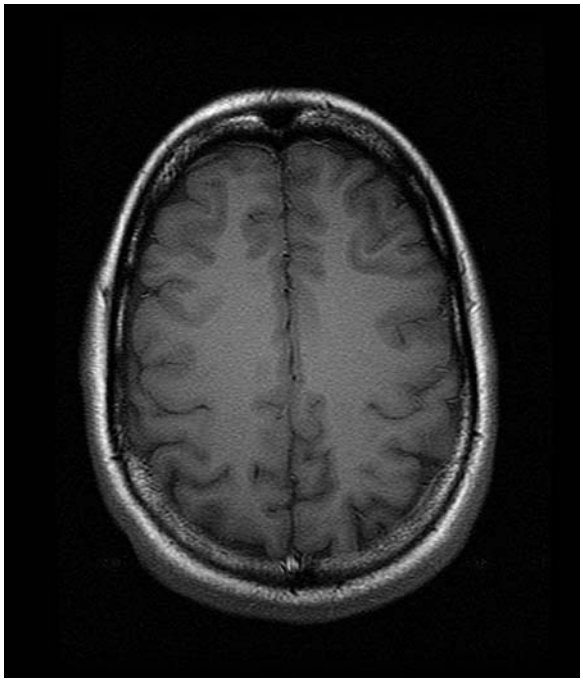

Fig. 12.1 n. SE

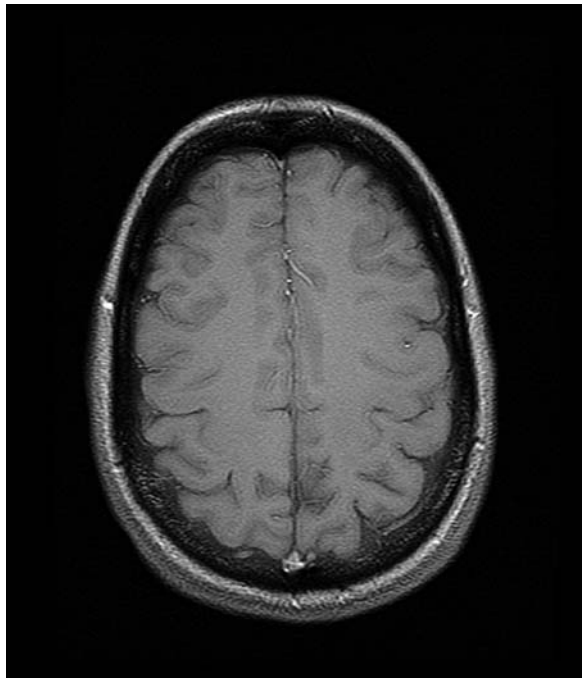

Fig. 12.2 n. FGE

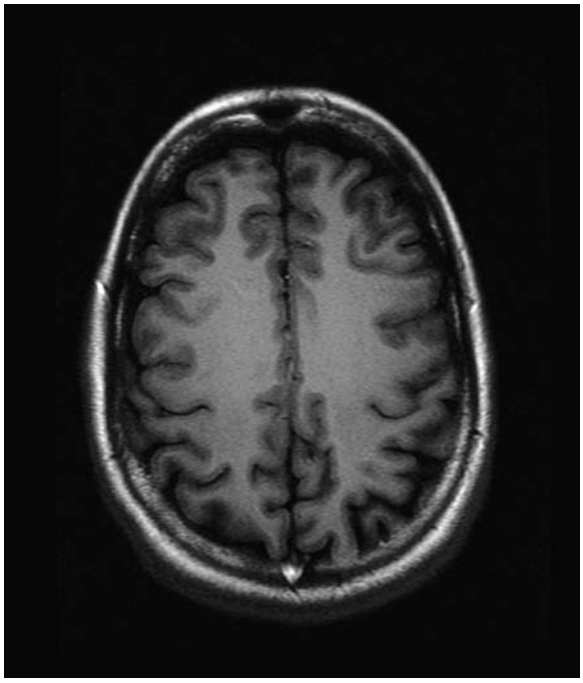

Fig. 12.3 n. IR

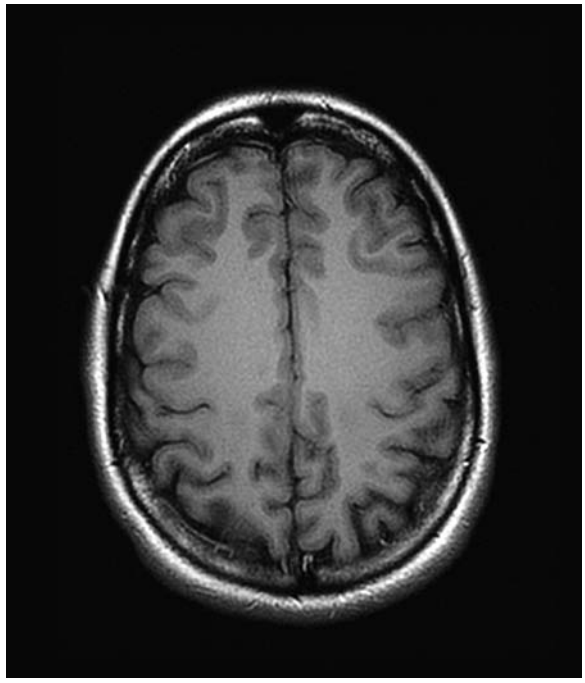

Fig. 12.4 n. FLAIR

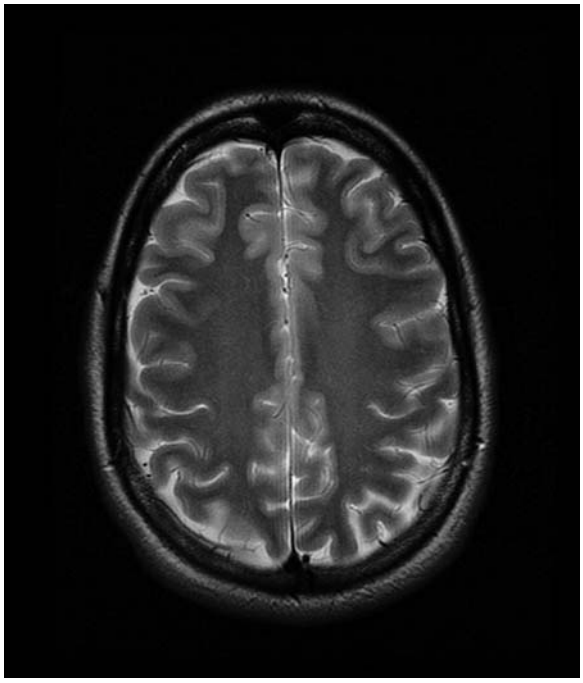

Fig. 12.5 n. FSE

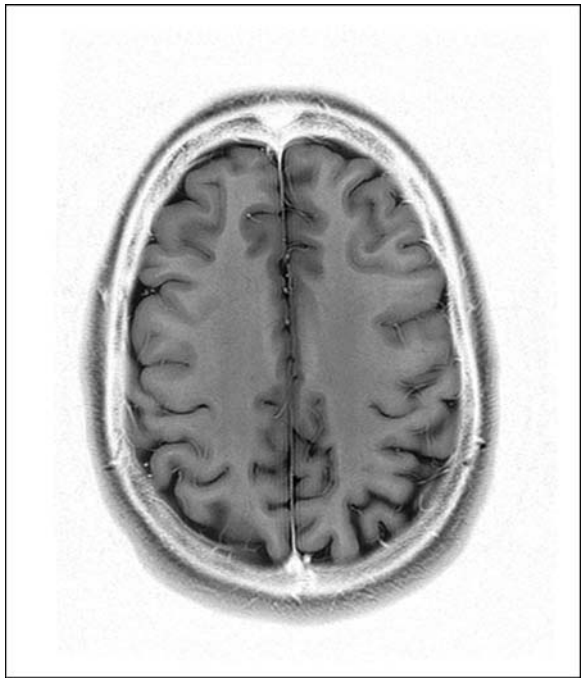

Fig. 12.6 n. FSE with inverted contrast

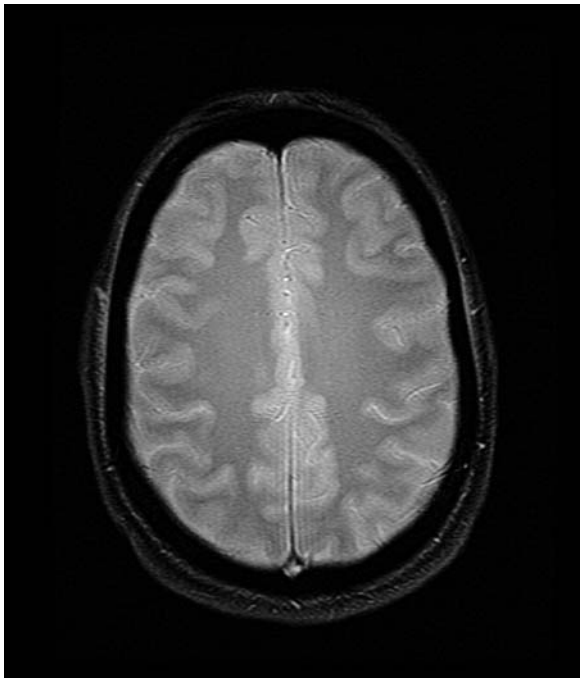

Fig. 12.7 n. GE

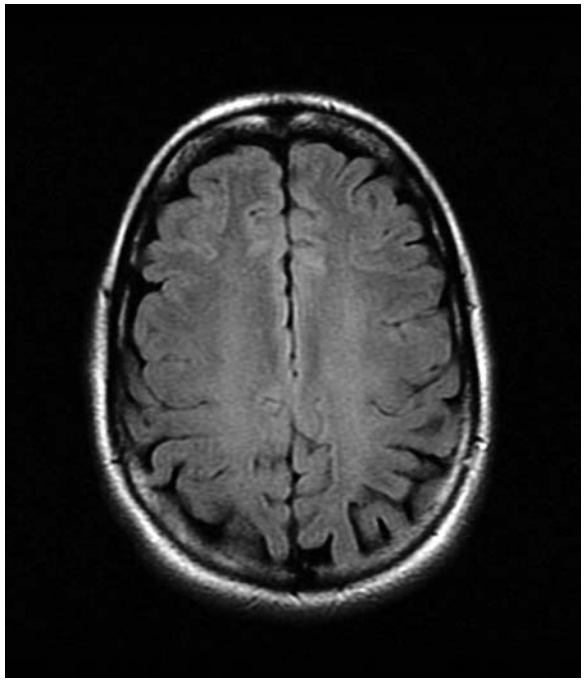

Fig. 12.8 n. FLAIR

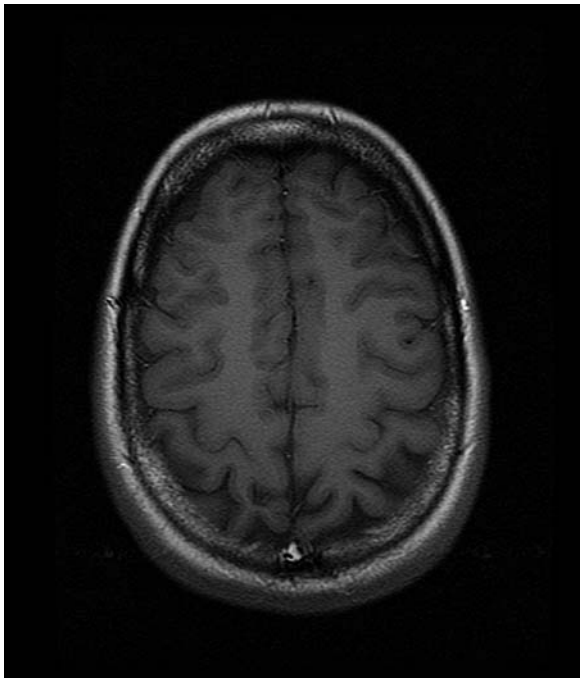

Fig. 12.1 o. SE

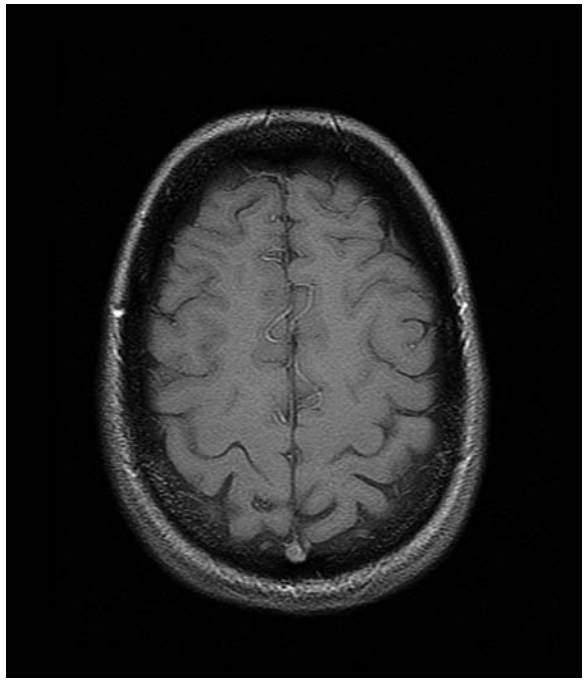

Fig. 12.2 o. FGE

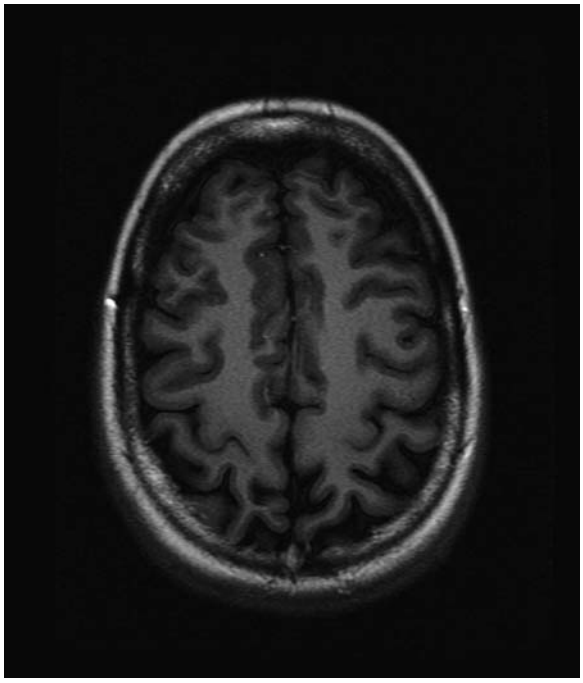

Fig. 12.3 o. IR

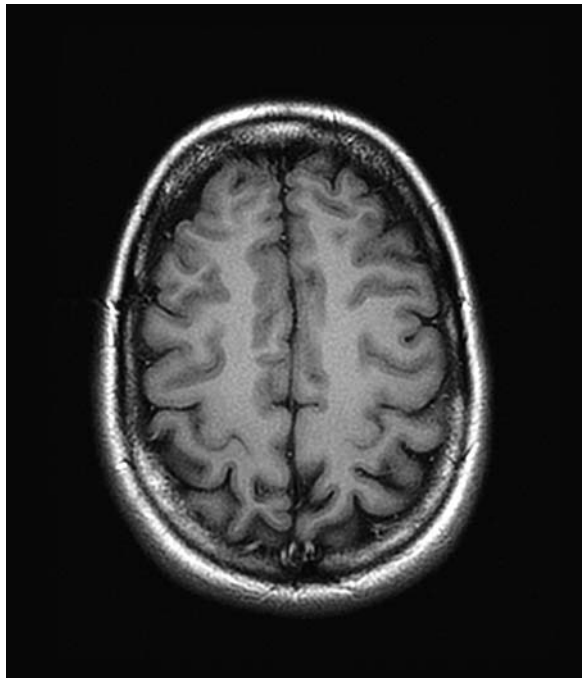

Fig. 12.4 o. FLAIR

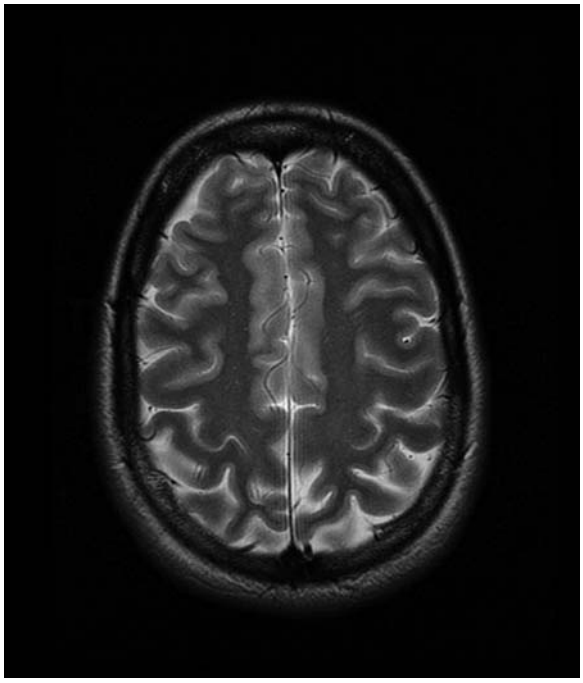

Fig. 12.5 o. FSE

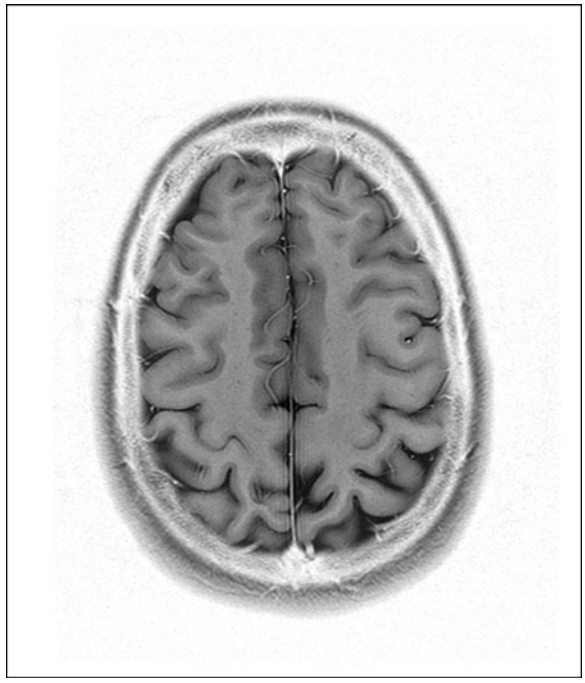

Fig. 12.6 o. FSE with inverted contrast

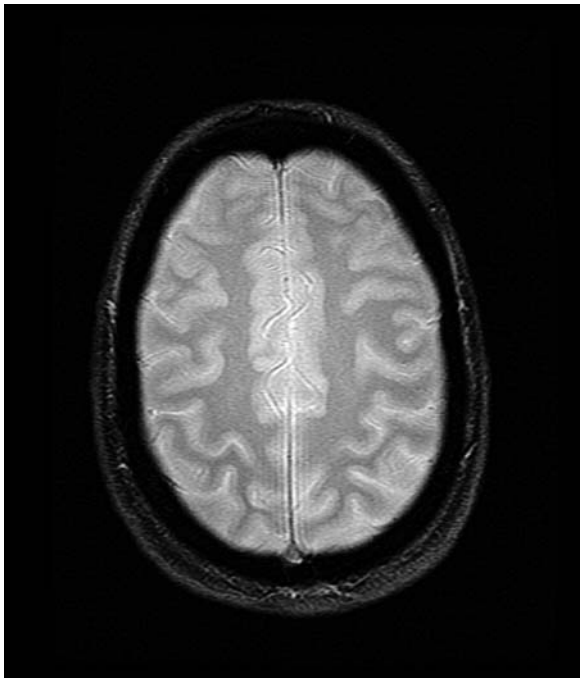

Fig. 12.7 o. GE

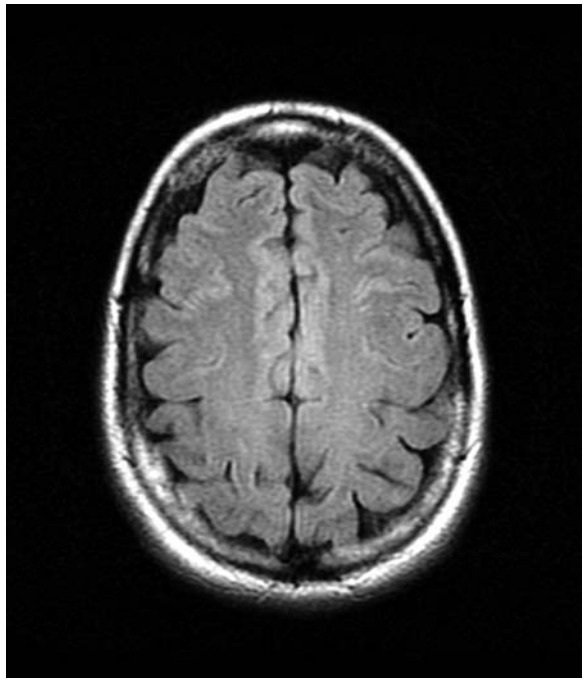

Fig. 12.8 o. FLAIR

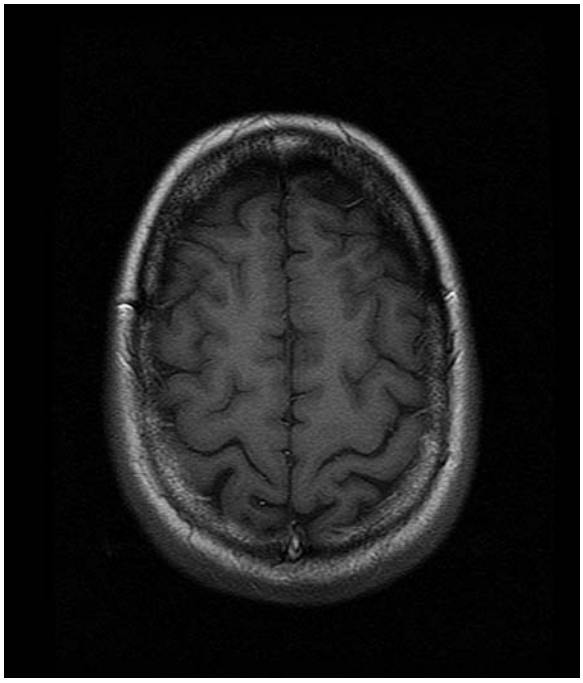

Fig. 12.1 p. SE

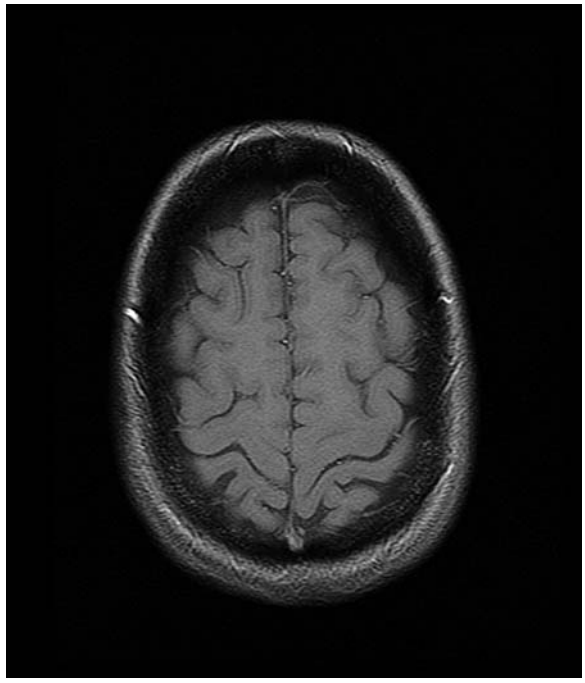

Fig. 12.2 p. FGE

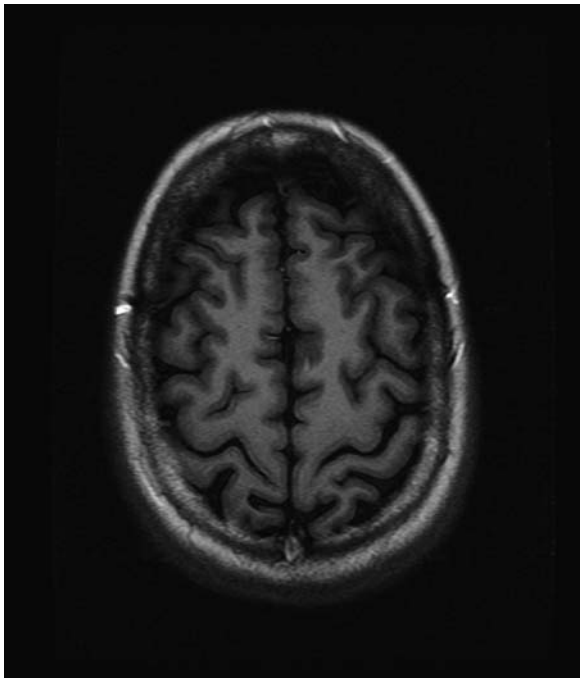

Fig. 12.3 p. IR

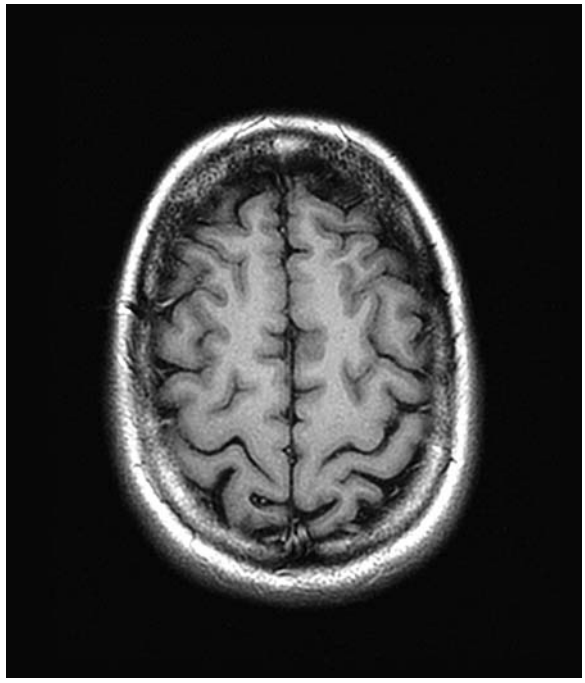

Fig. 12.4 p. FLAIR

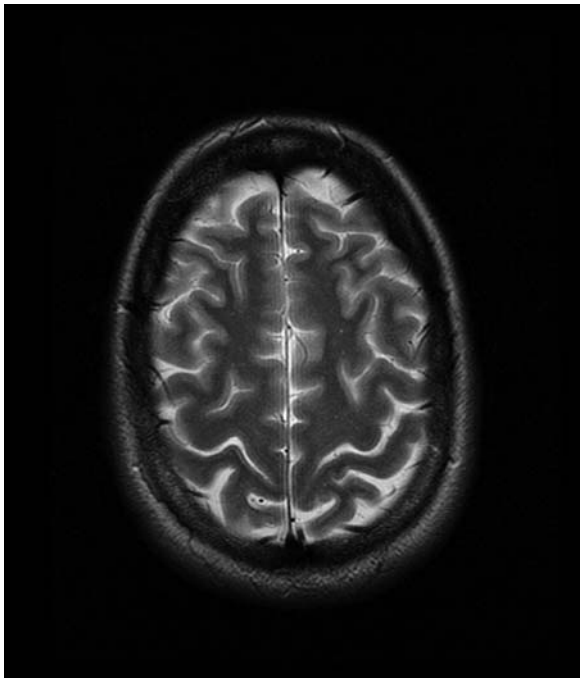

Fig. 12.5 p. FSE

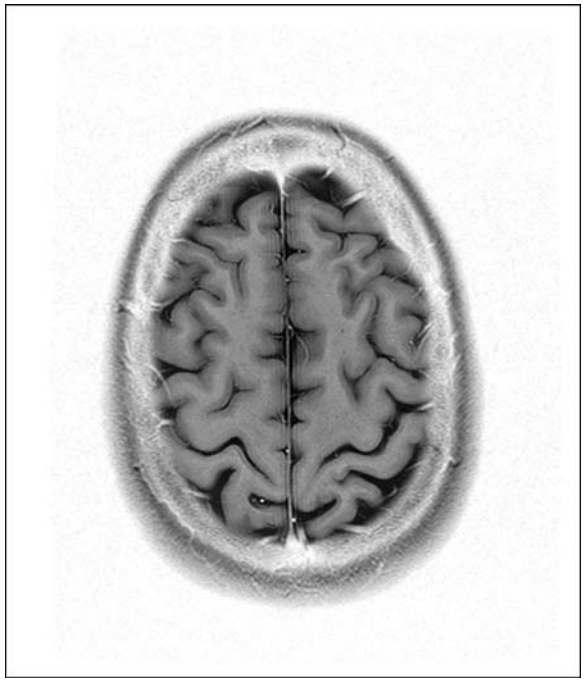

Fig. 12.6 p. FSE with inverted contrast

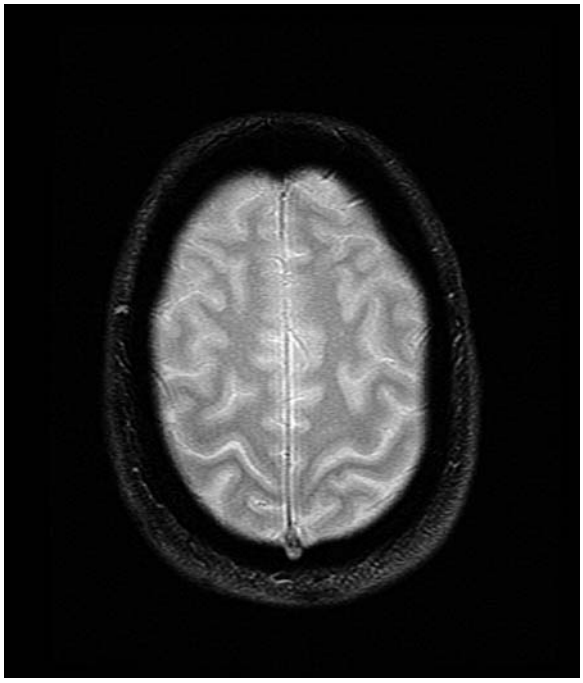

Fig. 12.7 p. GE

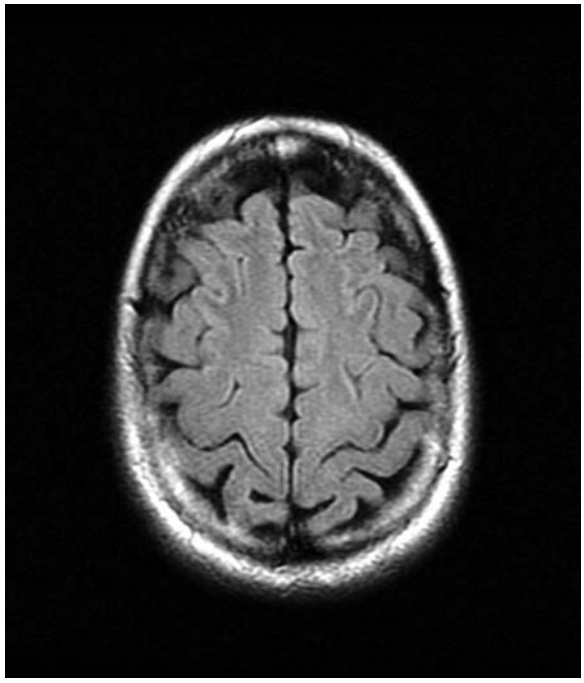

Fig. 12.8 p. FLAIR

Applications

II

High-Field Neuroimaging in Traumatic Brain Injury

13

E. Giugni, G. Luccichenti, G. E. Hagberg, A. Cherubini, F. Fasano, U. Sabatini

Magnetic resonance (MR) is the imaging technique of choice for the study of traumatic brain injury (TBI) in clinically stable patients, both in the acute and in the chronic phase, and is beginning to erode the role of computed tomography (CT) also in clinically unstable trauma patients [1 – 3].

In the latter the role of MR is still to be established. Despite its high sensitivity to focal traumatic lesions, the correlations among MR parameters, clinical picture and prognosis are not wholly satisfactory. Partly, this stems from the fact that the scales used for the clinical evaluation of the acute patient, such as the Glasgow Coma Scale (GCS) [4], are not suitable to predict prognosis in trauma patients, who exhibit a wide range of complex neuropathological conditions [5]. The sparce distribution of MR machines in hospital structures, the difficulty of monitoring vital signs in the tunnel, suboptimal accuracy in depicting fractures, acquisition times and cost are further disadvantages.

Current guidelines consider CT as the imaging technique of choice in unstable patients, where the primary goal is rapid detection of haematomas and other lesions requiring surgery [6]. However, the availability of high-field MR, which enables short times of acquisition with conventional sequences as well as use of ultrafast sequences very sensitive to magnetic susceptibility, like echo-planar (EPI) [7, 8] and turbo-proton echo-planar spectroscopy (t-PEPSI) [9, 10], is expected to make this technique the method of choice also to image clinically unstable patients. Indeed, high-field MR (e.g. 3.0 T) is both more sensitive to focal lesions containing blood components and exhibits an enhanced ability to detect structural and metabolic changes in apparently intact white and grey matter by use of advanced techniques such as diffusion tensor (DTI) and spectroscopy (MRS). These techniques are expected to improve the currently poor correlations with the clinical picture and to become indispensable tools in predicting outcome.

13.1 Rationale for MR Imaging of Patients with TBI

In the acute phase of TBI, secondary ischaemic injury induced by hypotension and oedema or by haemorrhage may be superimposed on the primary, blunt or penetrating, parenchymal injury. In these patients the focal injury is studied using T2-weighted and Fluid Attenuated Inversion Recovery (FLAIR) sequences, the ischaemic injury with diffusion-weighted sequences (DWI), and haemorrhage using T1-, T2*-weighted and FLAIR sequences: in all cases the examination time should be as short as possible.

In the chronic phase, patients exhibit focal lesions with or without haemoglobin degradation products (i.e. diffuse axonal injury, DAI) and phenomena of anatomical and/or functional deafferentation. The MR protocol for clinically stabilized patients thus aims at detecting focal lesions such as signs of stationary tissue distress and DAI using sequences sensitive to gliosis (T2-weighted and FLAIR) and to haemoglobin degradation products (T2*-weighted sequences), and at evidencing direct or indirect signs of deafferentation.

Current guidelines mandate the use of a number of technical features when imaging patients with TBI, including acquisitions in at least two spatial planes, because structures such as corpus callosum and brainstem are better appreciated in sagittal and coronal planes; slice thickness not greater than 5 mm; spin echo (SE)-turbo SE (TSE), proton density (PD) and T2-weighted; SE-TSE, T1-weighted; and gradient echo (GE) T2*-weighted and FLAIR sequences.

T2- and PD-weighted sequences afford optimal visualization of oedema, which is found in the majority of patients with TBI. T1-weighted sequences are useful to document recent intra- and extra-axial blood extravasation. T2-weighted FLAIR sequences are very sensitive to thin extracerebral blood collections in brain contusion, DAI and subarachnoid haemorrhage [11, 12]. T2*-weighted sequences, which are particularly sensitive to the effects of magnetic susceptibility induced by haemoglobin degradation products, are superior to T2-weighted sequences in identifying lesions with a haemorrhagic component, such as contusion

and DAI [13–15]. A recently proposed ultrafast multi echo-planar sequence (time of acquisition 4 s), t-PEPSI [9, 10], is sensitive to static magnetic field inhomogeneities and is optimized for functional neuroimaging as an alternative to T2*-weighted sequences [16]. In this study, these two sequences did not detect a significantly different total number of DAI lesions; the T2*-weighted sequence proved to be significantly superior to t-PEPSI in depicting temporal lesions, as could be expected from the presence in the EPI sequences of geometric distortion and magnetic susceptibility artefacts due to anatomical structures such as the petrous bone in this region. Ultrafast multi EPI sequences thus dramatically reduce imaging time, and their application should be recommended for the study of clinically unstable or uncooperative patients.

Medium-field magnets like those currently employed in clinical practice (1.5 T) allow the acquisition of a protocol with these features in about 20 min.

13.1.1 Results Obtained with Low- and Medium-Field MR

Despite the high sensitivity of MR to focal traumatic lesions, the correlations between clinical picture and MR parameters are not satisfactory. Gentry et al. documented an inverse correlation between GCS score at the time of trauma and number of DAI lesions detected on MR; a low GCS score was also associated with DAI lesions in corpus callosum and brainstem. A low correlation was obtained between GCS score and cerebral contusion and epidural and subdural haematoma [17–20]. Evaluation of these data must however account for the above-mentioned limitations of the clinical scales and for the use of lesion load as the sole MR parameter in TBI patients.

Implementation of volumetric techniques in longitudinal studies directed at improving the correlation between MR parameters and clinical picture showed that neuron loss progresses in the weeks and months following the trauma resulting in focal brain atrophy, which is associated with a more severe outcome [21, 22].

13.2 High-Field MR in Patients with TBI

The potential advantages of high-field MR in routine clinical practice are increased spatial contrast, and spectral and temporal resolution, which are greater with the more advanced techniques. In principle, the performance of a 3.0 T MR imager should be double that of a 1.5 T machine [23]. However, artefacts and technical limitations do not allow this to be achieved in practice. A greater signal/noise ratio (SNR), the main advantage of high-field imaging, can be reduced by local magnetic field variations caused by magnetic field gradient inhomogeneities and will therefore no longer be double as predicted by theory [23–26].

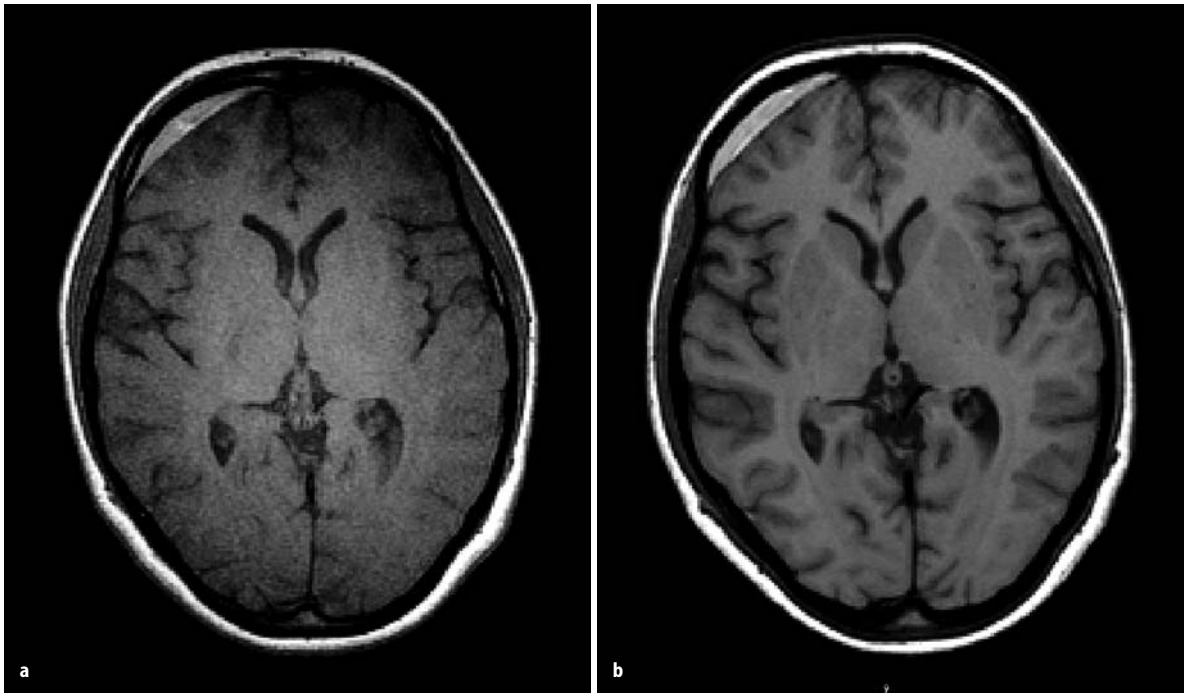

Fig. 13.1. SE T1: comparison between images acquired in the same patient at 3.0 T (Allegra, Siemens) (**a** *left*) and 1.5 T (Vision, Siemens) (**b** *right*). The thin extra-axial right frontal blood collection, indicating a subacute subdural haematoma, is appreciated in both sequences

The reduction in T1 differences among tissue types induces a contrast loss between white and grey matter [27, 28] and can impair detection of lesions like contusion and intraparenchymal haematoma, which in the acute stage are difficult to appreciate also at 1.5 T. The MPRAGE sequence has been introduced to address this problem. Volumetric sequences such as MPRAGE have already been performed at 1.5 T to quantify white and grey matter volume in TBI patients with a view to documenting potential correlations between clinical state and atrophy of specific brain lesions (Fig. 13.1) [22].

As regards T2-weighted images, the greater spatial

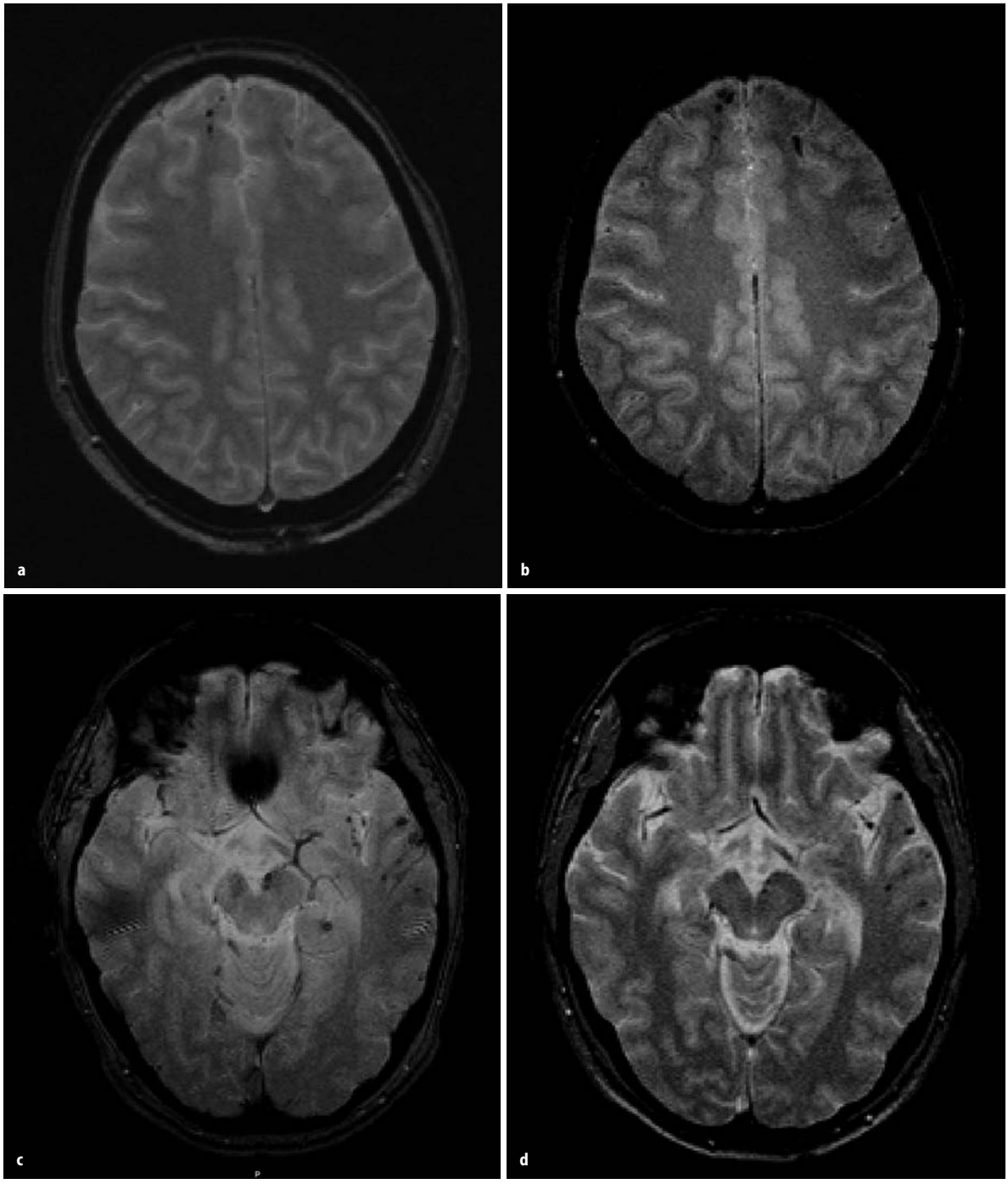

Fig. 13.2. GE T2*: comparison between images acquired in the same patient at 3.0 T (Allegra, Siemens) (**a, c** *left*) and 1.5 T (Vision, Siemens) (**b, d** *right*). Bilateral frontal subcortical (**a, b**) and left temporal and mesencephalic (**c, d**) small focal DAI lesions are more numerous and better visualized at 3.0 T

resolution, resulting in better anatomical detail and contrast due to the greater SNR, allows thicker slices and broader matrices to be used and small lesions such as contusions or DAI to be appreciated. A further advantage of high-field T2-weighted sequences is their ability to depict very small deposits of deoxyhaemoglobin or methaemoglobin as markedly hypointense areas by virtue of magnetic susceptibility effects, which are amplified by the high field [29].

High-field GE T2* sequences are more sensitive to the magnetic susceptibility of haemoglobin degradation products and are thus valuable for detecting DAI. A correlation between number of blood-containing lesions, DAI lesions identified on T2*-weighted sequences and GCS score was confirmed by Scheid et al. [15], whereas no relationship was documented between focal changes appreciable in T2*-weighted sequences and Glasgow Outcome Scale (GOS) scores [30], suggesting that lesion load may not predict prognosis in these patients (Fig. 13.2).

EPI sequences are also more sensitive at 3.0 T than 1.5 T, to the detriment of image geometry. On EPI images distortion is approximately 30% greater at 3.0 T than 1.5 T, but can be reduced to about 1% using SSFSE [31].

Accurate study of intracranial vessels, which is especially useful in patients with TBI and clinically suspected vessel dissection, carotid-cavernous fistula, or dural venous sinus thrombosis, benefits from high-field imaging [32, 33].

13.2.1 Advanced High-Field Techniques in TBI

It is well established that standard MR sequences underestimate traumatic brain injury [6, 15, 34–38]. New MR techniques such as DTI and MRS have been applied to TBI to gain insights into the mechanisms underlying the patient's clinical condition, predict its evolution and thus prognosis, and optimize therapeutic strategies [39–45].

Huisman et al. [42] demonstrated the superior performance of DWI in identifying DAI compared with standard (T2-, T2*-weighted, FLAIR) sequences, but did not address its clinical relevance and thus the potential correlations with prognosis.

DTI is an extension of DWI and provides two essential types of information: a quantitative estimate of anisotropy and its spatial orientation. Tractography uses these microscopic data to track macroscopic axon fibres and is currently the sole method capable of non-invasive in vivo imaging of these structures [24–26]. In DAI, the white matter fibres are typically interrupted; measuring white matter anisotropy with DTI allows the tissue damage to be quantified (Fig. 13.3).

Based on these considerations, Huisman et al. [43] went on to demonstrate that DTI is capable of detecting structural white matter changes, and that these changes correlate with clinical parameters such as GCS score in the acute phase and at discharge. The advantages of applying DTI to patients with head trauma are:

- An ability to gain information on the microscopic brain damage responsible, alone or in association with the macroscopic damage, for the patient's clinical state
- An ability to document and quantify the brain plasticity phenomena underpinning clinical recovery, which may be enhanced using pharmacological and rehabilitation therapies
- The possibility of assessing the therapeutic response even in those patients on whom clinical studies do not provide adequate information; moreover, the quantitative data offered by DTI are not influenced by potential CNS side effects of drug therapy or invasive procedures (e.g. intubation)
- The possibility of using DTI data to predict outcome in trauma patients, since neither standard MR findings nor clinical parameters, such as GCS scores, can predict their future clinical condition

The technical characteristics of high-field MR have enhanced the quality of DTI data, particularly spatial resolution, the spatial deformation induced by magnetic field inhomogeneities and image SNR, thus improving the accuracy of nerve fibre tracking.

The advantage of using 3.0 T MRS consists of an enhancement of the chemical shift with better separation of the metabolite peaks and high SNR [46, 47]. MRS can document a reduction in the *N*-acetylaspartate (NAA) peak, a neuronal and axonal marker, in ostensibly normal white matter free of macroscopic focal changes weeks or months after the trauma, and the extent of this reduction significantly correlates with scores on prognostic measures like GOS and Disability Rating Scale (DRS) [44, 48]. Concomitant elevation of the levels of other metabolites, such as *myo*-inositol (Ins) and choline (Cho), is to be ascribed to glial proliferation or an inflammatory process [49, 50]. Studies of white matter devoid of focal changes have demonstrated that the levels of these metabolites can eventually revert to normal [50] as well as a progressive reduction in NAA associated with increased Cho [49] or decreased Ins peaks [44]. Shutter et al. [45] studied a group of trauma patients in the subacute phase who underwent MRS within a week of the trauma to detect metabolic changes that could predict clinical outcome. Elevation of the levels of metabolites such as glutamate/glutamine (Glx) and Cho in apparently normal white and grey matter was found to be highly predictive of long-term adverse outcome with an accuracy of 89% (Fig. 13.4).

Functional MR imaging (fMRI) currently has a small role in studying trauma patients. It has been proposed for use as a prognostic tool in TBI patients in a coma using medium-field MR. Visual, auditory and so-

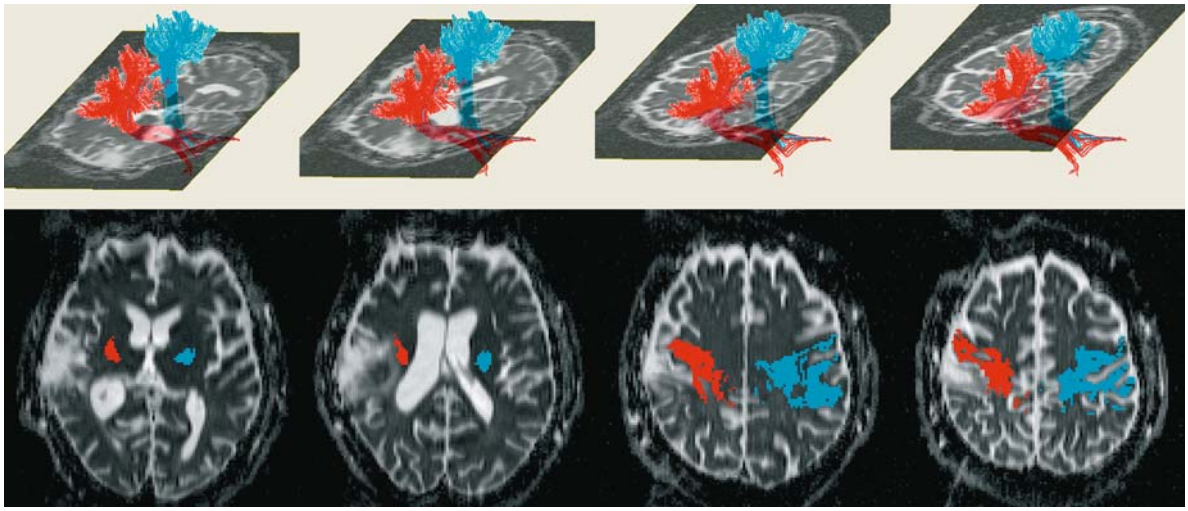

Fig. 13.3. Tractography at 3.0 T (Allegra, Siemens): visualization of motor areas and pyramidal fibres in an extensive right frontal contusion. The right primary motor area and pyramidal fibres are depicted less clearly than in the contralateral area

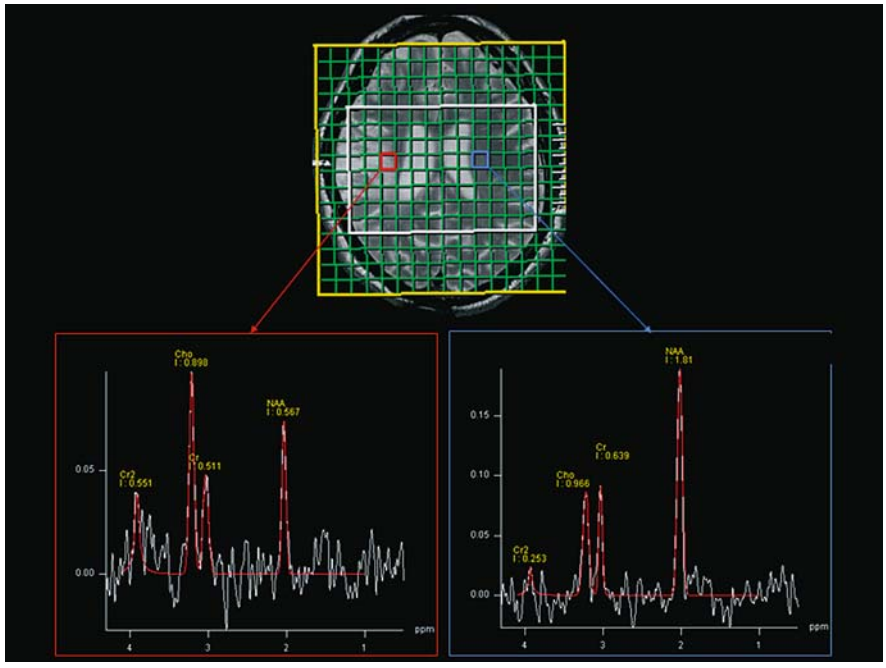

Fig. 13.4. Magnetic resonance spectroscopy with TE = 135 ms. The left spectrum was obtained from a volume of interest located in the right corona radiata, showing reduced NAA/Cr ratio reflecting neuronal loss. The right spectrum obtained from a VOI positioned contralateral to the lesion, is normal

matosensory stimulation during fMRI induced an increment in the haemodynamic response that predicted subsequent recovery, which was confirmed 3 months from trauma by clinical and electrophysiological examination [51]. fMRI has also been proposed to investigate the mechanisms of motor recovery in trauma patients [52, 53]. The effects of trauma on brain tissue have recently been assessed with fMRI, transcranial Doppler and transcranial magnetic stimulation in a TBI patient without tissue damage on conventional MR. This multimodal study demonstrated a dissociation between haemodynamic and functional response [54].

High-field MR, one of whose advantages is a high sensitivity to the BOLD signal, could find applications in the study of the phases of clinical recovery after TBI, as suggested in the literature [52, 53]. In particular, the degree of activation of specific brain areas at fMRI could provide an index of haemodynamic and functional activity in ostensibly healthy tissue in patients with DAI. Longitudinal variations of this index in conjunction with structural parameters and clinical examination could thus assume a prognostic value (Fig. 13.5).

In conclusion, high-field MR has the potential to enhance the accuracy of morphostructural, metabolic

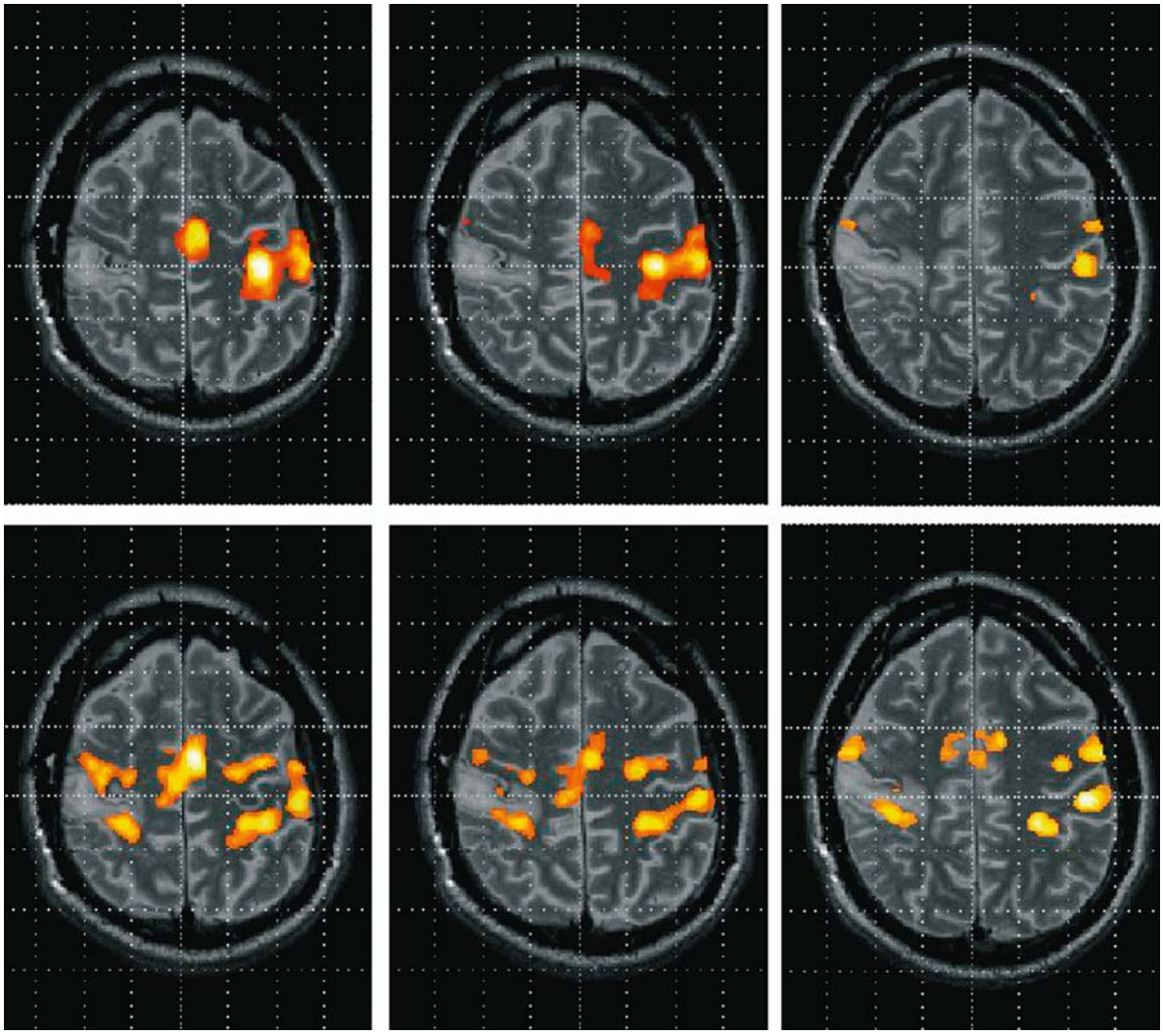

Fig. 13.5. fMRI at 3.0 T (Allegra, Siemens) in a patient with TBI exhibiting an extensive right frontal cortico-subcortical contusion, *top*: activation of left primary and supplementary sensorimotor areas during a motor task (finger tapping, right hand); *bottom*: bilateral activation of primary and supplementary motor areas during the motor task (finger tapping, left hand). Note a low activation of the right primary sensorimotor area and recruitment of the left primary and supplementary sensorimotor areas in the motor task of the clinically affected left hand

and functional studies of the brain parenchyma in trauma patients, advancing the knowledge of the relationships between changes in nerve fibre ultrastructure and clinical symptoms and allowing the quantification of the brain plasticity phenomena that follow spontaneous clinical recovery or administration of pharmacological and rehabilitation therapies.

References

1. Orrison WW, Gentry LR, Stimac GK, et al. (1994) Blinded comparison of cranial CT and MR in closed head injury evaluation. Am J Neuroradiol 15(2):351 – 356
2. Parizel PM, Van Goethem JW, Ozsarlak O, et al. (2005) New developments in the neuroradiological diagnosis of craniocerebral trauma. Eur Radiol 15(3):569 – 581
3. Gentry LR (2002) Head trauma. In: Atlas SW (ed) Magnetic resonance imaging of the brain and spine, 3rd edn. Lippincott, Williams & Wilkins, Philadelphia, pp 1059 – 1098
4. Teasdale TW, Jennett B (1974) Assessment of coma and impaired consciousness: a practical scale. Lancet 11:81 – 84
5. Giannotta SL, Weiner JM, Karnaze D (1987) Prognosis and outcome in severe head injury. In: Cooper PR (ed) Head injury, 2nd edn. Williams & Wilkins, Baltimore, pp 464 – 487
6. Gentry LR (1994) Imaging of closed head trauma. Radiology 297:1 – 17
7. Edelman R, Wielopolski P, Schimitt F (1994) Echo-planar MR imaging. Radiology 192:600 – 612
8. Patel MR, Siewert B, Klufas R, et al. (1999) Echoplanar MR imaging for ultra-fast detection of brain lesions. Am J Roentgenol 173(2):479 – 485
9. Posse S, Wiese S, Gembris D, et al. (1999) Enhancement of BOLD-contrast sensitivity by single-shot multi-echo functional MR imaging. Magn Reson Med 42:87 – 97

10. Hagberg GE, Indovina I, Sanes JN, Posse S (2002) Real-time quantification of T2* changes using multiecho planar imaging and numerical methods. Magn Reson Med 48(5): 877 – 882
11. Ashikaga R, Araki Y, Ispida O (1997) MRI of head injury using FLAIR. Neuroradiology 39:239 – 242
12. Campbell BG, Zimmerman RD (1998) Emergency magnetic resonance of the brain. Top Magn Reson Imaging 9: 208 – 227
13. Kuzma BB, Goodman JM (2000) Improved identification of axonal shear injuries with gradient echo MR technique. Surg Neurol 53:400 – 402
14. Yanagawa Y, Tsushima Y, Tokumaru A, et al. (2000) A quantitative analysis of head injury using T2-weighted gradient-echo imaging. J Trauma 49:272 – 277
15. Scheid R, Preul C, Gruber O, et al. (2003) Diffuse axonal injury associated with chronic traumatic brain injury: evidence from T2*-weighted gradient-echo imaging at 3T. Am J Neuroradiol 24:1049 – 1056
16. Giugni E, Sabatini U, Hagberg GE, et al. (2005) Fast detection of diffuse axonal damage in severe traumatic bran injury: comparison of Gradient-Recalled Echo and Turbo Proton Echo-Planar Spectroscopic Imaging MRI sequences. Am J Neuroradiol 26: 1140 – 1148
17. Gentry LR, Godersky JC, Thompson B, Dunn VD (1988) Prospective comparative study of intermediate-field MR and CT in the evaluation of closed head trauma. Am J Roentgenol 150(3):673 – 82
18. Gentry LR, Godersky JC, Thompson B (1988) MR imaging of head trauma: review of the distribution and radiopathologic features of traumatic lesions. Am J Roentgenol 150(3):663 – 672
19. Gentry LR, Thompson B, Godersky JC (1988) Trauma to the corpus callosum: MR features. Am J Neuroradiol 9: 1129 – 1138
20. Gentry LR, Godersky JC, Thompson B (1989) Traumatic brainstem injury: MR imaging. Radiology 171:177 – 187
21. Smith DH, Chen XH, Pierce JE, et al. (1997) Progressive atrophy and neuron death for one year following brain trauma in the rat. J Neurotrauma 14:715 – 727
22. Tomaiuolo F, Worsley HJ, Lerch J, et al. (2005) Changes in white matter in long-term survivors of severe non-missile traumatic brain injury: a computational analysis of magnetic resonance images. J Neurotrauma 22(1):76 – 82
23. Basser PJ, et al. (2000) In vivo fiber tractography using DT-MRI data. Magn Reson Med 44(4):625 – 632
24. Mori S, van Zijl PC (2002) Fiber tracking: principles and strategies – a technical review. NMR Biomed 15:468 – 480
25. Bammer R, Acar B, Moseley ME (2003) In vivo MR tractography using diffusion imaging. Eur J Radiol 45(3):223 – 234
26. Habas C (2004) Basic principles of diffusion tensor MR tractography. J Radiol 85(3):281 – 286
27. Wansapura JP, Holland SK, Dunn RS, et al. (1999) NMR relaxation times in the human brain at 3.0 T. J Magn Reson Imaging 9:531 – 558
28. Takahashi M, Uematsu H, Hatabu H (2003) MR imaging at high magnetic fields. Eur Radiol 46:45 – 52
29. Allkamper T, Tombach B, Schwindt W, et al. (2004) Acute and subacute intracranial hemorrhages: comparison of MR imaging at 1.5 and 3.0 T – initial experience. Radiology 232:874 – 881
30. Jennett B, Bond M (1975) Assessment of outcome after severe brain damage. Lancet 1:480 – 484
31. Conturo TE, et al. (1999) Tracking neuronal fiber pathways in the living human brain. Proc Natl Acad Sci USA 96(18):10422 – 10475
32. Berneistein MA, Huston J 3rd, Lin C, et al. (2001) High-resolution intracranial and cervical MRA at 3.0 T: technical considerations and initial experience. Magn Reson Med 46:955 – 962
33. Al-Kwifi O, Emery DJ, Wilman AH (2002) Vessel contrast at 3.0 T in time of flight magnetic resonance angiography of the intracranial and carotid arteries. Magn Reson Imaging 20:181 – 187
34. Parizel PM, Ozsarlak O, Van Goethem JW, et al. (1998) Imaging findings in diffuse axonal injury after closed head trauma. Eur Radiol 8:960 – 965
35. Wardlaw JM, Statham PFX (2000) How often is haemosiderin not visible on routine MR following traumatic intracerebral haemorrhage? Neuroradiology 42:81 – 84
36. Blatter DD, Bigler ED, Gale SD, et al. (1997) MR-based brain and cerebrospinal fluid measurement after traumatic brain injury: correlation with neuropsychological outcome. Am J Neuroradiol 18:1 – 10
37. Bigler ED, Anderson CV, Blatter DD, Andersob CV (2002) Temporal lobe morphology in normal ageing and traumatic brain injury. Am J Neuroradiol 23:255 – 266
38. Tomaiolo F, Carlesimo GA, Di Paola M, et al. (2004) Gross morphology and morphometric sequelae in the hippocampus, fornix and corpus callosum of patients with severe non missile traumatic brain injury without macroscopic detectable lesions: a T1-weighted MRI study. J Neurol Neurosurg Psychiatry 59:328 – 331
39. Le TH, Mukherjee P, Henry RG, et al. (2005) Diffusion tensor imaging with three-dimensional fiber tractography of traumatic axonal shearing injury: an imaging correlate for the posterior callosal „disconnection" syndrome: case report. Neurosurgery 56(1):189
40. Naganawa S, et al. (2004) Serial evaluation of diffusion tensor brain fiber tracking in a patient with severe diffuse axonal injury. Am J Neuroradiol 25(9):1553 – 1556
41. Arfanakis K, et al. (2002) Diffusion tensor MR imaging in diffuse axonal injury. Am J Neuroradiol 23(5):794 – 802
42. Huisman TAGM, Sorensen AG, Hergan K, et al. (2003) Diffusion-weighted imaging for the evaluation of diffuse axonal injury in closed head injury. J Computed Assist Tomogr 27:5 – 11
43. Huisman TAGM, Schwamm LH, Schaefer PW, et al. (2004) Diffusion tensor imaging as potential biomarker of white matter injury in diffuse axonal injury. Am J Neuroradiol 25:370 – 376
44. Garnett MR, Blamire AM, Corkill RG, et al. (2000) Early proton magnetic resonance spectroscopy in normal-appearing brain correlates with outcome in patients following traumatic brain injury. Brain 123:2046 – 2054
45. Shutter L, Tong KA, Holshouser BA (2004) Proton MRS in acute traumatic brain injury: role for glutamate/glutamine and choline for outcome prediction. J Trauma 21:1693 – 1705
46. Frayne R, Goodyear BG, Dickhoff P, et al. (2003) Magnetic resonance imaging at 3.0 Tesla: challenges and advantage in clinical neurological imaging. Invest Radiol 38(7):3854–402
47. Juchem C, Merkle H, Schick F, et al. (2004) Region and volume dependencies in spectral line width assessed by 1H 2D MR chemical shift imaging in the monkey brain at 7 T. Magn Reson Imaging 22:1373 – 1383
48. Garnett MR, Corkill RG, Blamire AM, et al. (2001) Altered cellular metabolism following traumatic brain injury: a magnetic resonance spectroscopy study. J Neurotrauma 18:231 – 240
49. Brooks WM, Stidley CA, Petropoulos H, et al. (2000) Metabolic and cognitive response to human traumatic brain injury: a quantitative proton magnetic resonance study. J Neurotrauma 17:629 – 640
50. Friedman SD, Brooks WM, Jung RE, et al. (1999) Quantita-

tive proton MRS predicts outcome after traumatic brain injury. Neurology 52:1384 – 1391
51. Moritz CH, Rowley HA, Haughton VM, et al. (2001) Functional MR imaging assessment of a non-responsive brain injured patient. Magn Reson Imaging 19(8):1129 – 1132
52. Cioni G, Montanaro D, Tosetti M, et al. (2001) Reorganisation of the sensorimotor cortex after early focal brain lesion: a functional MRI study in monozygotic twins. Neuroreport 12(7):1335 – 1340
53. Jang SH, Cho SH, Kim YH, et al. (2005) Motor recovery mechanism of diffuse axonal injury: a combined study of transcranial magnetic stimulation and functional MRI. Restor Neurol Neurosci 23(1):51 – 56
54. Barba C, Formisano R, Sabatini U, et al. (2006) Uncoupling of anatomical and functional motor area damage in a post-traumatic patient revealed by integrated multimodal approach. J Neurol Neurosurg Psychiatry (submitted)

3.0 T Imaging of Ischaemic Stroke

14

T. Popolizio, A. Simeone, G. M. Giannatempo, A. Stranieri, M. Armillotta, T. Scarabino

Ischaemic stroke accounts for 70 % of all acute cerebral vasculopathies and is among the leading causes of death and disability in the Western world. It is most often due to brain vessel atherosclerosis and less commonly to infectious arteritis, emboli from the carotid artery or cardiac pump deficits, resulting in systemic hypoperfusion. A significantly reduced blood flow in the vascular territory supplying the affected vessels induces a metabolic tissue imbalance (hypoxia and hypoglycaemia) that gives rise to variably reversible anatomical injury. Four grades of clinical severity can be distinguished on the basis of the duration of symptoms, which are mainly characterized by a focal neurological deficit:

1 TIA (transient ischaemic attack): a sudden-onset, focal, non-convulsive condition that usually resolves within a few minutes and always within 24 h
2 RIND (reversible ischaemic neurological deficit): symptoms last no more than 48 h and normal conditions are restored within 3 weeks
3 Progressive stroke: progressive onset of clinical symptoms worsening over the first 24 – 48 h and leaving a persistent functional deficit
4 Completed stroke: a stable clinical condition since onset that may improve in time

This classification is not only useful from a clinical point of view, but also from the neuroradiological standpoint, because the duration of parenchymal hypoperfusion, which causes a more or less persistent symptomatology, is related to pathological anatomical characteristics that correspond with distinctive neuroradiological findings. Transient ischaemia damages nerve cells, the elements most sensitive to hypoxia, but not the parenchyma, neither microscopically nor, consequently, „radiologically“. In these patients standard imaging, including high-field MRI, is unable to depict the small hypoperfused area. The cell distress alone can be detected, using functional techniques such as MR diffusion (DWI) and spectroscopic techniques. In ischaemia of longer duration, the glial and mesodermal elements also undergo necrosis and morphostructural changes that can be visualized on standard imaging. In practice, functional DWI, perfusion (PWI) and spectroscopic techniques can identify the affected area in the hours immediately following the stroke, whereas conventional techniques enable evaluation of the later phases.

The recent introduction of fibrinolytic therapies [1] capable of inducing the recanalization of occluded vessels before the tissue damage becomes established has made the early identification of the ischaemic focus extremely important. In the hyperacute phase, besides differentiating ischaemia from haemorrhage, the irreversibly injured tissue must be distinguished from that susceptible to functional recovery.

14.1 Neuropathological Features

Knowledge of the pathological anatomical changes induced by stroke is essential to understand the basic radiological features that reflect the evolution of cellular and tissue changes. On standard MR, only macroscopic neuropathological alterations give rise to signal changes, whereas the technique is scarcely sensitive to early cellular and subcellular injury. Therefore, hyperacute-phase ischaemia is not depicted on standard, even high-field, images.

The biochemical bases of the ischaemic event are not yet completely clear. It has been demonstrated that the ischaemic area shrinks within a few minutes of the event. The hypoxia-induced disruption of anaerobic glycolysis triggers a histopathological cascade, with alteration of the Na^+/K^+ pump and consequent intracellular accumulation of water (cytotoxic oedema). This can be seen microscopically 2 h from the vessel occlusion, during which time the water molecules remain „trapped“ in the intracellular space, with a consequent reduction in their diffusion. The cellular injury caused by water accumulation and progressive microvacuolization is reversible over the first 6 h. After this time, the necrotic process becomes established due to accumulation of lactic acid, pH reduction, damage to the microcirculation, and an increased concentration of excitatory neurotransmitters. Subsequently, damage to the blood-brain barrier (BBB) causes an accumulation of extracellular water, or vasogenic oedema. At 12 – 24 h, the cytotoxic oedema and related cell degeneration

manifest macroscopically as a „pale" area, while the vasogenic oedema can be visualized radiologically. Unlike other organs, in which necrotic tissue is replaced by scar fibrosis, in the brain it is completely removed by macrophages and replaced by a fluid-filled cavity (porencephaly), whose walls are made up of nerve parenchyma exhibiting an intense proliferation of mesodermal elements (fibroblasts, fibrocytes) with formation of new capillaries. In this phase, defined as gliosis, which can last several weeks, the proliferative phenomena result in increasingly sharp borders of the affected area. Finally, months from the stroke, the ischaemic focus develops as a cavity with more or less regular borders that, due to scar retraction, may undergo deformation together with the adjacent parenchyma [2].

14.2 Neuroradiological Protocol

The introduction of thrombolytic therapies capable of reversing the ischaemic injury has changed the neuroimaging protocols, leading to the use of MR also in the emergency workup of these patients. Recent technological advances in hardware (magnet, gradients, coils) and software (ultrafast sequences, post-processing) allow morphological and functional studies to be performed with very short times of acquisition. In clinical practice, functional studies are increasingly being performed in combination with standard MR imaging: DWI and PWI enable identification of the ischaemic area and discrimination of irreversibly damaged tissue from tissue that can respond to treatment instituted in the very first hours from the event [3 – 5].

After CT has ruled out a haemorrhagic stroke, the current emergency neuroradiological protocol envisages a DWI and PWI study directed mainly at planning treatment. Selection of thrombolysis candidates requires morphological evaluation of the vascular district; this is why in the hyperacute phase the MR study may require angiographic (MRA) sequences for aetiopathogenic investigations. In the chronic phase, when the patient's clinical condition has become stable, the neuroradiological protocol envisages a more detailed standard MR study and an MRA investigation to assess outcome and response to therapy.

The hyperacute-phase MR study consists at least of axial T1 sequences, axial FLAIR, DWI, 2D PC MRA (because it is faster than 3D TOF, which only depicts the large vessels of the circle of Willis) and, if a fibrinolytic treatment is envisaged, PWI sequences.

When the patient's condition has become stable, a spectroscopic study can be performed to establish lesion extension and prognosis, while possible recovery and final lesion extension can be investigated with higher-definition morphological and 3D TOF MRA sequences.

14.3 Neuroradiological Diagnostic Imaging

14.3.1 Standard MRI

In ischaemic stroke, the diagnostic role of conventional MR is confined to the subacute and chronic phases, since in the very early hours from the event the changes in interstitial water content (free water) induced by Na^+/K^+ pump alterations are not yet such as to affect the signal in T2-weighted (FSE or FLAIR) sequences, thus yielding a negative MR examination in the hyperacute phase (Fig. 14.1).

Also in MR studies, one of the first signs of ischaemia secondary to arterial occlusion is a signal change in the lumen of the blocked vessel. Whereas in SE sequences vessels normally present a signal void due to arterial and/or turbulent flow (Fig. 14.2), occluded vessels exhibit a characteristic hyperintensity, especially in FLAIR sequences, with an accuracy that is comparable to that of MRA [6, 7].

Even though the cytotoxic oedema does not give rise to signal changes, it can be indirectly detected in cortical areas through gyral swelling, sulcal effacement and a loss of grey-white matter interface definition. Contrast-enhanced sequences, which are not employed routinely, show vascular enhancement due to the slower flow in the occluded or tributary vessel, sometimes associated with tissue enhancement due to local hyperaemia or extravasation of contrast agent through the disrupted endothelium. MR signal changes become evident in the acute phase, when the vasogenic oedema induces hyperintensity in long TR (FSE T2 and FLAIR) sequences (Fig. 14.3) and contrast-enhanced scans may depict a pathological meningeal enhancement [8]. In the subacute phase (3 – 14 days), the signal changes are more marked due to the increasing mass effect and manifest as a signal increase in T2 FSE and FLAIR sequences and hypointensity in T1 SE. On contrast-enhanced scans, enhancement of the infarcted area, which can persist for more than 2 months, is due to the recanalization of the occluded vessel, the opening of collateral circles (luxury perfusion) and BBB changes. In 20 % of cases, rupture of the vascular endothelium following thrombolysis may result in haemorrhage. This phenomenon appears as hypointense foci in T2 and is best seen in GE sequences [9]. In the chronic phase, a very hypointense „haemosiderin tattoo" due to even slight earlier bleeding is consistently detected in all sequences [2].

Chronic-phase MR findings reflect the morphostructural changes induced by the progressive shrinking of the lacunae, which have a cerebrospinal fluid-like content, while the hyperintensity of the adjacent brain parenchyma (particularly evident in FLAIR sequences) is due to reparative gliosis (Fig. 14.4). In this phase,

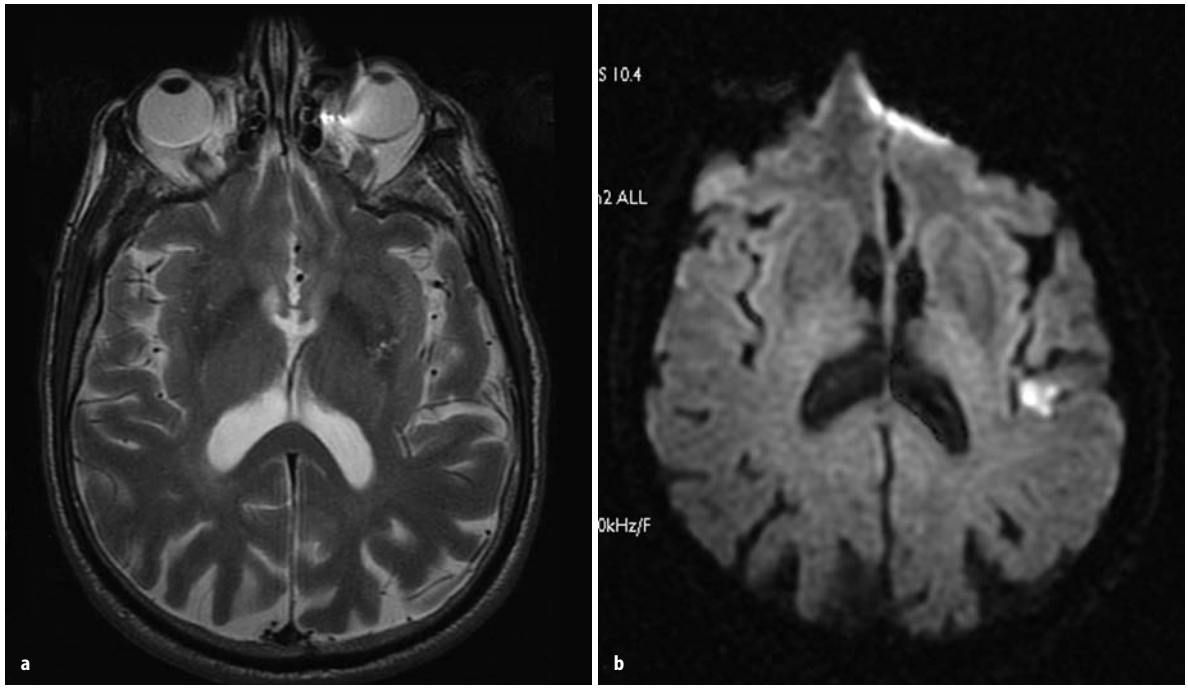

Fig. 14.1. Small hyperacute stroke. The standard MR study (T2 FSE) is negative (**a**). The DWI image shows a hyperintense left subcortical parietal ischaemic focus (**b**)

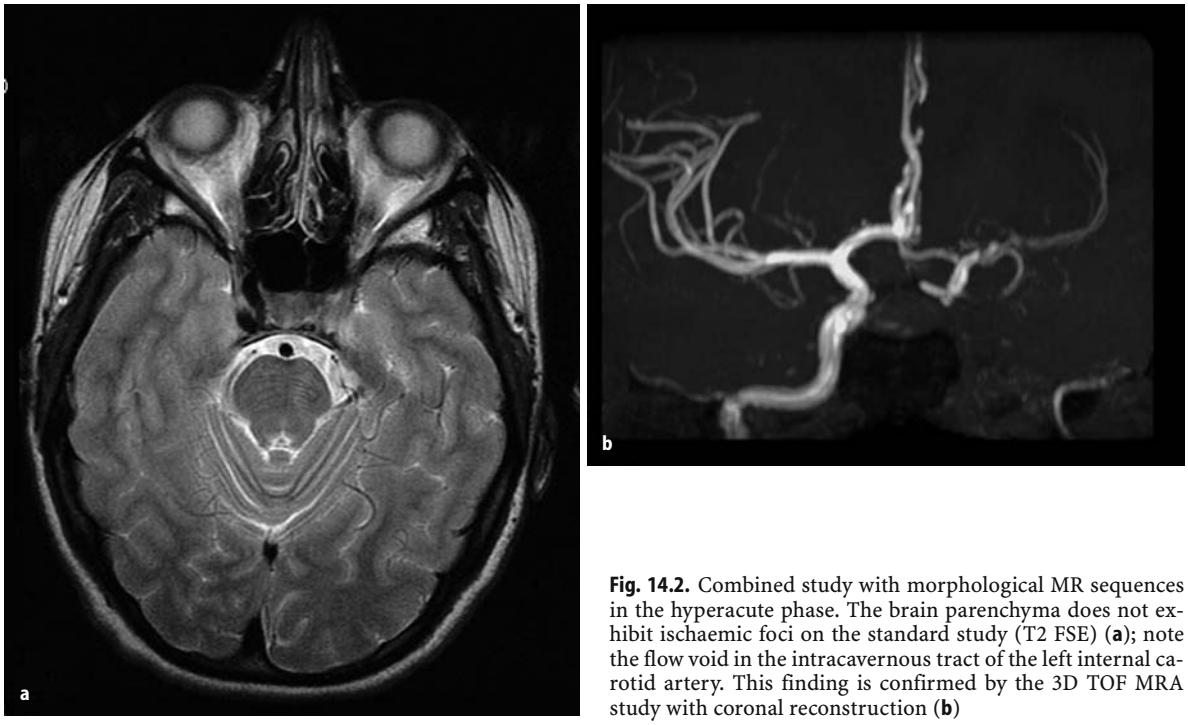

Fig. 14.2. Combined study with morphological MR sequences in the hyperacute phase. The brain parenchyma does not exhibit ischaemic foci on the standard study (T2 FSE) (**a**); note the flow void in the intracavernous tract of the left internal carotid artery. This finding is confirmed by the 3D TOF MRA study with coronal reconstruction (**b**)

signs of Wallerian degeneration of axons (and their myelin sheaths) originating from the infarcted area must be sought. Anterograde axon degeneration, which initially induces degradation of the protein component of myelin while comparatively sparing its lipid component (low signal in FSE T2 sequences), and afterwards reparative gliosis, is depicted on standard MR only in very late phases, i.e. when the axon degeneration has become irreversible. Again, earlier detection of these phenomena can be obtained with DWI [9].

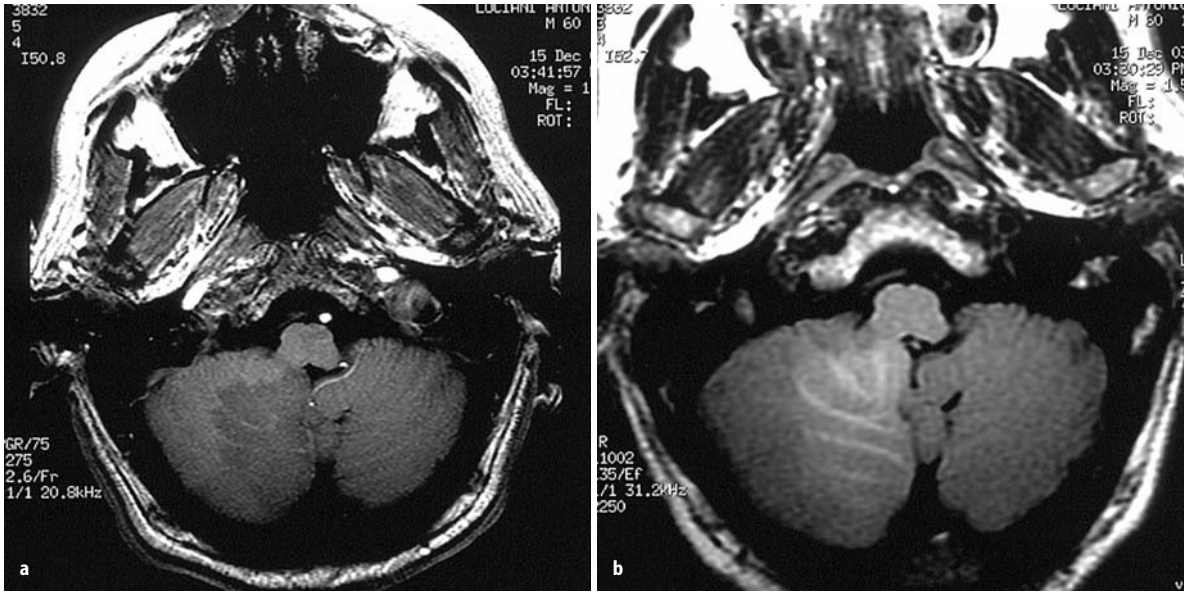

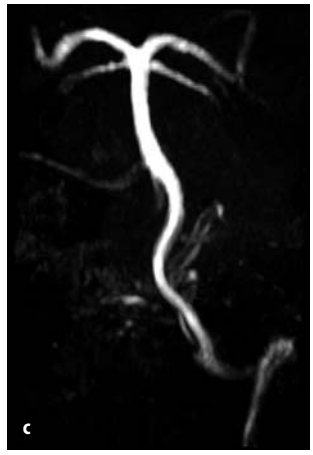

Fig. 14.3. Combined study with morphological MR sequences in the acute phase. Vast right cerebellar stroke. Right cerebellar hypodense area in T1 FSPGR (**a**); ill-defined right hemicerebellar hyperintense area in T2 FSE (**b**). Occlusion of the right vertebral artery in 3D TOF MRA (**c**)

14.3.2 MR Diffusion

DWI is the most sensitive technique to diagnose hyperacute-phase brain ischaemia (Fig. 14.1). Based on the diffusion of water molecules in the cell compartment, their random movement induced by thermal energy can be measured using conventional SE echo-planar sequences acquired with specific weighting. These sequences are sensitive to the movement of H_2O molecules and demonstrate the changes in diffusion induced by pathological events in the form of images and numerical values. In hyperacute ischaemia, the histo-

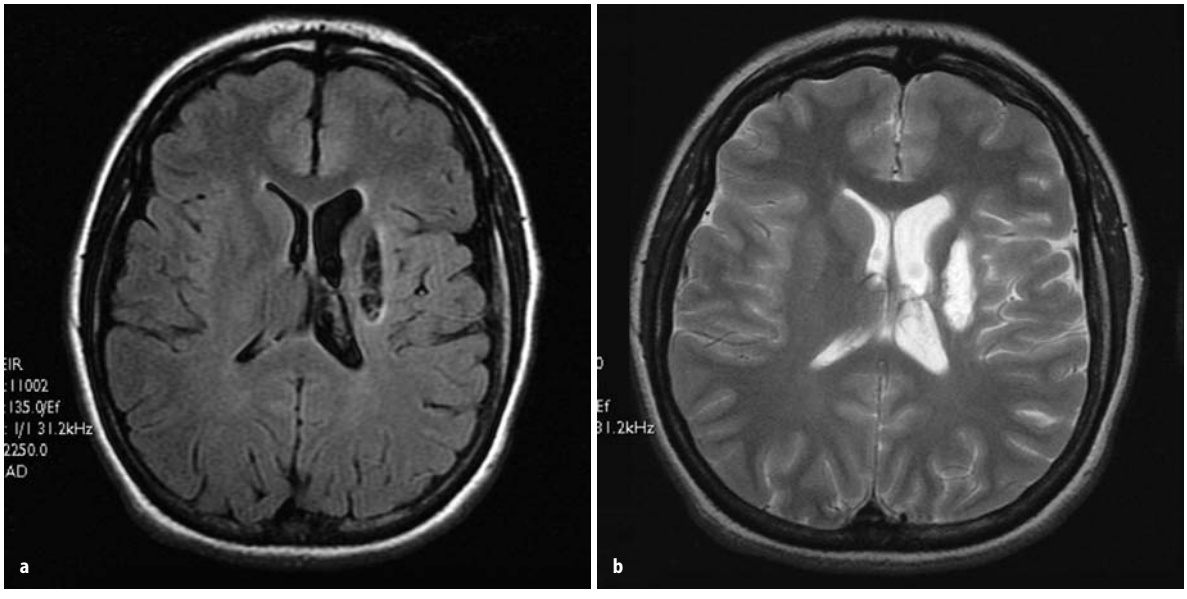

Fig. 14.4. Lacunar sequelae of a left capsular ischaemic stroke in FLAIR (**a**) and T2 FSE (**b**)

pathological injury is the cytotoxic oedema; the H_2O molecules trapped in the cell thus exhibit an impaired diffusion, which is detected in a few minutes as a signal increase in the pathological tissue [10–12].

DWI techniques are sensitive as well as specific (90% and 99%, respectively); these two parameters are directly proportional to the time since disease onset. A negative DWI study does not however exclude a diagnosis of ischaemia. Not all patients with a typical picture of stroke also display an altered DWI signal; this may be due to complete recovery from a TIA, to a non-ischaemic event, or to symptomatic hypoperfusion [13]. Obviously, the DWI study may also have preceded the establishment of an infarcted area, or the lesion may be very small and lie in areas especially difficult to investigate with this method (temporal regions, posterior cranial fossa).

Unlike standard MR, where the hyperintensity of the ischaemic area in long TR sequences corresponds with the expansion of the vasogenic oedema, DWI enables precise evaluation of the injured tissue because the signal hyperintensity peaks within 24 h of clinical onset, and never later. In addition, DWI sequences afford separate visualization of the acute ischaemic area, characterized by strongly reduced diffusion, from the peripheral area, where the apparent diffusion coefficient (ADC) is less affected (although PWI techniques are even more informative; see below) and the tissue damage may be reversed. This is the ischaemic penumbra, which has not sustained a stroke proper, but exhibits the predisposing physiopathological conditions for a new stroke (energy deficit), making it a high-risk area in the subacute phase. Adequate reperfusion often results in functional recovery of the ischaemic penumbra [12].

Another advantage of DWI over standard MRI is that, in patients with multifocal leukoencephalopathy, it allows the identification of the ischaemic lesions responsible for the active symptoms.

14.3.3 MR Perfusion

PWI techniques study changes in blood flow at the level of the microcirculation using ultrafast sequences with a bolus of paramagnetic contrast medium (gadolinium; Gd) [15]. In normal perfusion and intact BBB conditions Gd, though remaining confined to the intravascular space, induces a reduction in T2 signal both in vessels and in the brain parenchyma. In a hypoperfused area (for instance one due to a vascular occlusion), the signal reduction is delayed or attenuated (due to magnetic susceptibility) because of the diminished flow. Since the signal reduction correlates directly with Gd concentration, and thus with cerebral blood volume (CBV), parametric CBV maps of the areas with reduced signal intensity can also be generated.

In stroke patients, the main role of PWI studies is to identify the ischaemic penumbra in the acute phase. Studies of the relationship between cerebral blood flow (CBF) and neuronal disruption have evidenced that there is a short interval related to CBF changes, where neurons, though no longer efficient, are still viable and can be rescued with a suitable therapy. The extension of this area depends both on the duration of the ischaemia and on its entity, because even mild ischaemia, which does not necessarily cause neuronal damage, may induce irreversible injury if protracted.

14.3.4 Combined Diffusion and Perfusion Studies

DWI and PWI studies are more informative in combination than singly, especially in predicting clinical evolution and outcome, and thus in guiding therapy [10, 16–18].

Six different patterns can be identified using combined studies:

1. The area exhibiting reduced perfusion, which also includes the penumbra, is larger than the one exhibiting reduced diffusion (Fig. 14.5). A PWI> DWI mismatch is the most common pattern (55–77% of cases), especially in the hyperacute phase. From the point of view of clinical evolution, early PWI scans depict the maximum size attainable by the infarcted area and, in absence of further vessel occlusion or closure of collateral circles, the worst clinical outcome
2. Similar pathological areas with both methods (Fig. 14.6)
3. A smaller pathological area on PWI (PWI< DWI mismatch)
4. Presence of diffusion, not perfusion, deficits
5. Presence of perfusion, not diffusion, deficits (usually associated with a transient neurological deficit)
6. Negative diffusion and perfusion studies despite an evident clinical alteration

Combined studies can be useful to predict clinical evolution, assess prognosis and evaluate the response to therapy [1, 19]. Patterns #1 and #5 are managed with reperfusion treatment using fibrinolytic agents, the others with neuroprotective drugs.

14.3.5 MR Spectroscopy

MR spectroscopy enables non-invasive in vivo study of some phases of brain metabolism. It is based on the same principles as conventional MR, except that it envisages signal processing during and after sequence acquisition. Whereas in standard MR the signal intensity is the sum of the signals from all the hydrogen-contain-

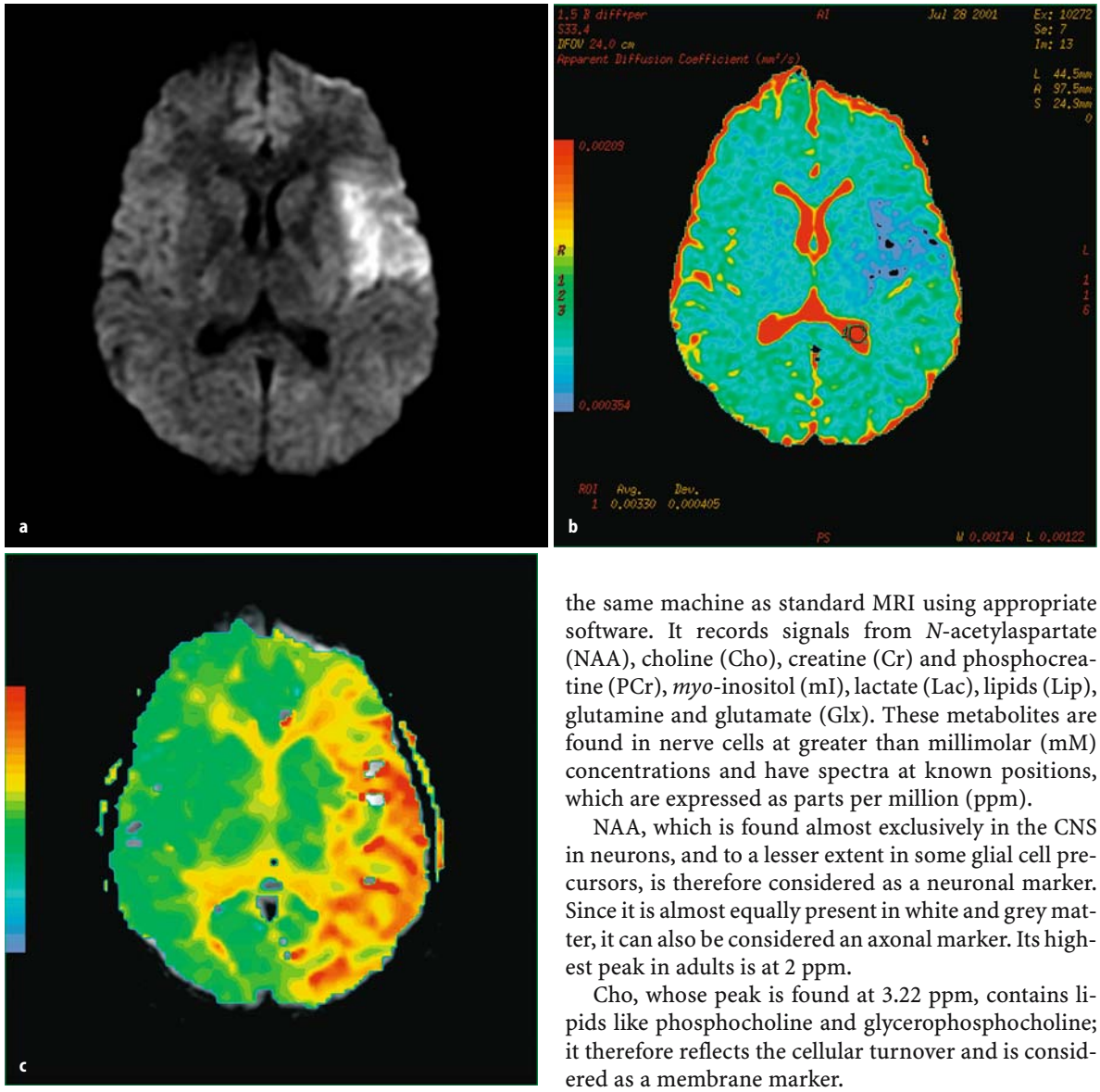

Fig. 14.5. Combined functional study with DWI < PWI mismatch. DWI (**a**), ADC map (**b**), regional CBV map (**c**). Note that the hypoperfused area (**c**) is broader on PWI (**a, b**)

ing molecules in a given volume, in spectroscopy the signal from a given nucleus is separated into its chemical components. The physical principle underpinning the change in the resonance frequency of nuclei is the chemical shift. This is influenced by the magnetic field generated by the cloud of electrons that surrounds the nuclei as well as by the clouds of electrons of nearby atoms, which interact with the main magnetic field. An atom is thus subject to different chemical shifts as a function of the molecule in which it is found, thus enabling identification of the molecule containing it. Hydrogen spectroscopy is currently the most widely used of these techniques, because it can be performed with the same machine as standard MRI using appropriate software. It records signals from *N*-acetylaspartate (NAA), choline (Cho), creatine (Cr) and phosphocreatine (PCr), *myo*-inositol (mI), lactate (Lac), lipids (Lip), glutamine and glutamate (Glx). These metabolites are found in nerve cells at greater than millimolar (mM) concentrations and have spectra at known positions, which are expressed as parts per million (ppm).

NAA, which is found almost exclusively in the CNS in neurons, and to a lesser extent in some glial cell precursors, is therefore considered as a neuronal marker. Since it is almost equally present in white and grey matter, it can also be considered an axonal marker. Its highest peak in adults is at 2 ppm.

Cho, whose peak is found at 3.22 ppm, contains lipids like phosphocholine and glycerophosphocholine; it therefore reflects the cellular turnover and is considered as a membrane marker.

Cr and PCr exhibit a single peak at 3.02 ppm that pools the signal from the high-energy phosphates involved in the energy metabolism. Since its peak is stable also in pathological conditions, it is used as a control value.

Myo-inositol, considered as a specific glial marker, is found at 3.3 – 3.6 ppm.

When present, Lac exhibits a doublet peak at 1.32 ppm. It reflects the production of energy in conditions of altered oxygen supply, a situation that takes place when a partial vessel occlusion activates the enzymatic pathway, which leads to anaerobic glycolysis. Lactate can also accumulate due to infiltration of Lac-containing macrophages, or because it has remained trapped and has not been removed.

Lip, which are mainly found in necrotic processes, resonate at 0.8, 1.2, and 1.5 ppm.

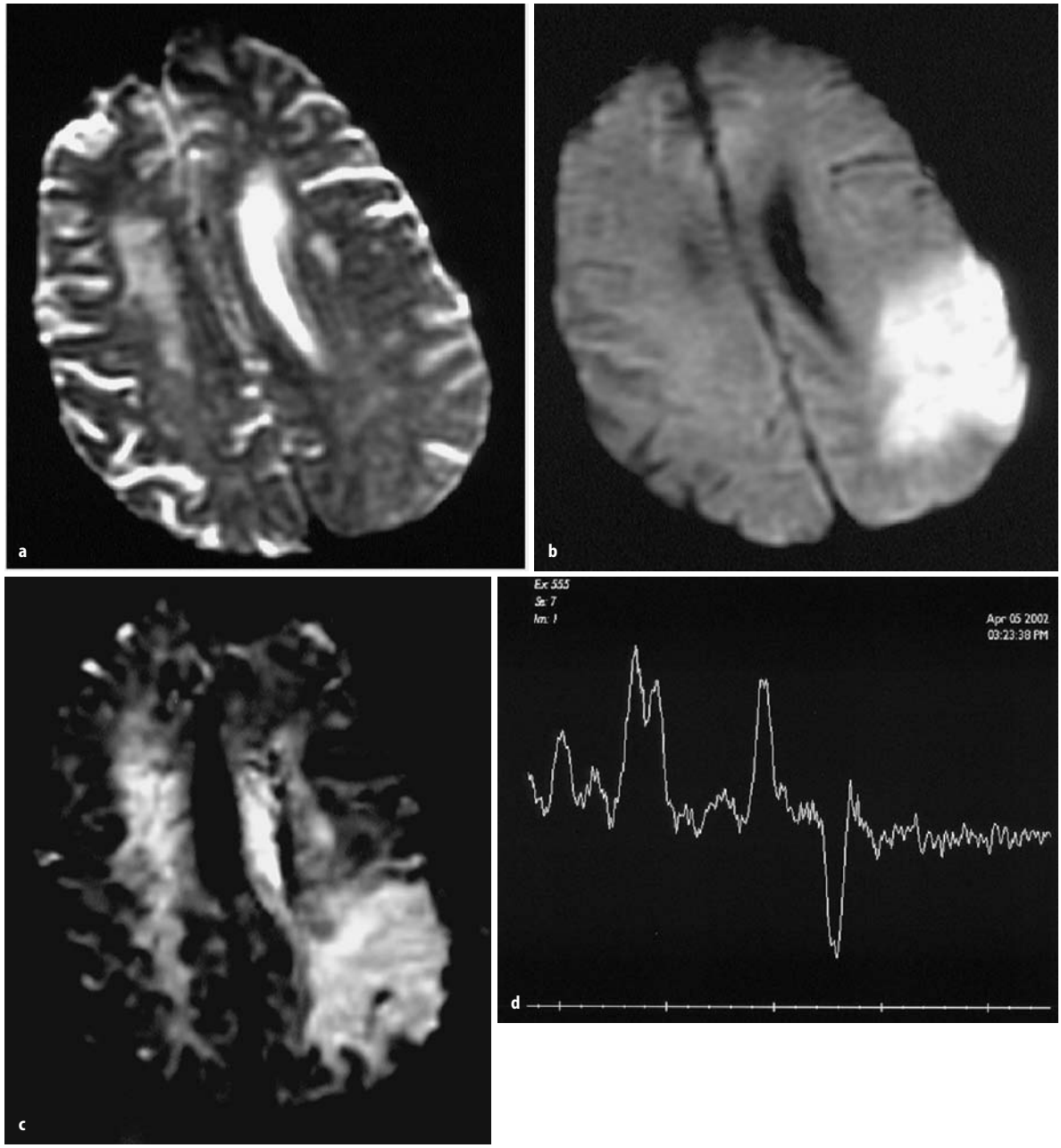

Fig. 14.6. Combined functional study without mismatch (DWI = PWI). Vast right parieto-occipital ischaemic stroke in the hyperacute phase. Ischaemic multifocal leukoencephalopathy without recent ischaemic lesions in T2 EPI (**a**). Marked hyperintensity of the infarcted area in DWI (**b**). Right parietal-occipital signal hyperintensity in PWI (**c**) indicating reduced perfusion of the ischaemic area of similar extension as the one shown in DWI. The spectroscopic single-volume short-TE image shows a marked reduction in the NAA, Cho and Cr peaks, and a Lac peak at 1.3 ppm (**d**)

Finally, Glx exhibits peaks at 2.1 – 2.5 and 3.6 – 3.8 ppm, and pools the signal from neurotransmitters such as glutamate and glutamine.

In CNS ischaemic disease, spectroscopy can be used for the early detection and characterization of ischaemic lesions (Fig. 14.6), to monitor the response to therapy, and especially to distinguish the infarcted area from the ischaemic penumbra [20 – 22]. The necrotic area is characterized by a reduction in NAA (50 % over the first 6 h), whereas the penumbra displays an increased Lac peak without significant changes in NAA [23]. A marked NAA reduction and a strong Lac increase in the acute phase predict an unfavourable outcome.

14.4 3.0 T MRI

The dramatic reduction in imaging times obtained with the fast gradients of high-field MR is especially useful in patients with cerebral ischaemia, who often exhibit a severe clinical condition and may be unable to cooperate.

The parameters used for the standard sequences are reported in Table 14.1.

In the hyperacute phase, the total imaging time for axial T1, coronal or axial FLAIR, DWI and 3D PC MRA is approximately 8 min. A PWI sequence lasting only around 0.44 s will also be performed in thrombolysis candidates.

T2 FSE sequences in different planes of acquisition, a T2* GRE sequence to detect possible blood components, 3D TOF MRA and spectroscopy are performed in the later phases, when longer examination times are better tolerated.

An important advantage of high-field DWI in stroke patients is that it enables a greater anatomical coverage than 1.5 T MR. Another significant difference is its high diagnostic sensitivity in hyperacute ischaemia also at low *b* values (500, rather than 1,000 as in 1.5 T systems), thus reducing gradient stress (Fig. 14.7) [14].

The high-field PWI technique most frequently used in ischaemic stroke is dynamic susceptibility contrast (DSC) with a contrast agent as an exogenous tracer. DSC is faster and is the most widely used technique in clinical practice. It yields a much greater signal change with high-field compared with 1.5 T magnets, resulting in more reliable images [24].

The high signal/noise ratio of 3.0 T MR systems enables data collection using smaller voxels (greater spatial resolution) at shorter intervals (greater temporal resolution). The gradients are so fast that, even using short TE, temporal resolution is in the order of 1 s, the time required to follow the passage of the contrast bolus through the brain and its vessels. In addition, the greater sensitivity of 3.0 T machines to magnetic susceptibility allows a much smaller dose of paramagnetic contrast agent to be used than in lower-field PWI to obtain the same result. Use of higher concentrations of the agent (1 mol) allows to reduce the dose to 1/4.

Table 14.1. Parameters used for standard sequences

Sequence	TE	TR	Other parameters (IT, FA, ETL)	FOV	Th/Sp	NEX	No. of slices	Matrix	Time (min:s)
T1 FSPGR	Min	275	FA 75	22	4/1	1	25	512×256	1:50
FLAIR	130	11,000	IT 2,250	22	4/1	1	24	288×192	2:56
T2 FSE	81	4,840	ETL 15	22	4/1.5	2	24	448×320	2:39
Axial GRE T2*	Min	525.0	FA 20	22	4/1	4	25	512×224	5:56
DWI	Min	11,000	*b* values 1,000	22	4/1	1	26	128×128	0:44
GE-EPI DWI	48	1,700	FA 90	32	5/1	1	12	164×164	0:44
3D PC MRA	30		FA 20	22	35	6		256×224	2:41
3D TOF MRA	Min	26	FA20 ZIP 512 ZIP 2	16	1.4	1	60	288×224	5:53
H-MRS Press 30–144	30 144	2,000		24	Voxel = 20	8	1		4:45

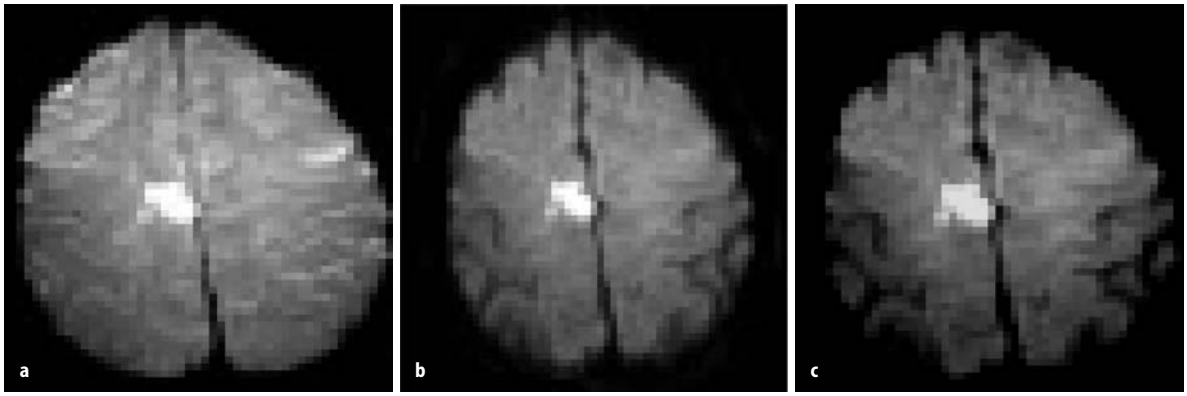

Fig. 14.7. Acute-phase ischaemic stroke studied with DWI with different *b* values (500 in **a**, 1,000 in **b**, 2,000 in **c**). Optimum depiction of the ischaemic area is also obtained with low *b* values (**a**)

14.5 Conclusions

Several neuroradiological techniques can be used to assess ischaemic stroke patients. At facilities where thrombolytic therapies are available, the ideal diagnostic workup in the hyperacute phase is a morphological and functional MR study associated with MRA sequences. However, where this is not feasible (because these techniques are not available, the patient has come to observation in a late phase or is particularly restless, or, signally, a thrombolytic therapy is not indicated), the basic method is CT with serial follow-up studies to monitor disease evolution and the possible complications. At a later time, when this is possible, a conventional MR study with MRA sequences should be performed.

References

1. Hacke W, Kaste M, Fieschi C, et al. (1995) Intravenous thrombolysis with recombinant tissue plasminogen activator for acute hemispheric stroke. The European Cooperative Acute Stroke Study (ECASS). JAMA 274:1017 – 1025
2. Cirillo S, Caranci F, Stella L, et al. (2001) Cranio: infarto ed emorragia. In: Giancarlo Dal Pozzo, UTET. Compendio di Risonanza Magnetica: cranio e rachide, pp 478 – 515
3. Altieri M, Metz RJ, Muller C, et al. (1999) Multiple brain infarcts: clinical and neuroimaging patterns using diffusion-weighted magnetic resonance. Eur Neurol 42(2):76 – 82
4. Baird AE, Warach S (1998) Magnetic resonance imaging of acute stroke. J Cereb Blood Flow Metab 18:583 – 609
5. Yoshiura T, Wu O, Sorensen AG (1999) Advanced MR techniques: diffusion MR imaging, perfusion MR imaging, and spectroscopy. Neuroimaging Clin N Am 9(3):439 – 453
6. Schellinger P, Chalela JA, Kang D, et al. (2005) Diagnostic and prognostic value of early MR imaging vessel signs in hyperacute stroke patients imaged <3 hours and treated with recombinant tissue plasminogen activator. AJNR 26(3): 618 – 624
7. Atlas SW (1994) MR angiography in neurologic disease. Radiology 193:1 – 16
8. Simon J, Czechowsky D, Hill M, et al. (2004) Fluid-attenuated inversion recovery preparation: Not an improvement over conventional diffusion-weighted imaging at 3 T in acute ischemic stroke. AJNR 25:1653 – 1658
9. Maeda M, Abe H, Yamada H, et al. (1999) Hyperacute infarction: a comparison of CT and MRI, including diffusion-weighted imaging. Neuroradiology 41(3):175 – 178
10. Cosnard G, Duprez T, Grandin C, et al. (2000) Diffusion and perfusion-weighted MR imaging during the hyperacute phase of stroke. J Radiol 81(8):858 – 869
11. Lovblad KO, Laubach HJ, Baird AE, et al. (1998) Clinical experience with diffusion-weighted MR in patients with acute stroke. AJNR 19:1061 – 1066
12. Ay H, Buonanno FS, Rordorf G, et al. (1999) Normal diffusion-weighted MRI during stroke-like deficits. Neurology 52(9):1784 – 1792
13. Lutsep HL, Albers GW, DeCrespigny A, et al. (1997) Clinical utility of diffusion-weighted magnetic resonance imaging in the assessment of ischemic stroke. Ann Neurol 41:574 – 580
14. Kuhl CK, Textor HJ, Simon B, et al. (2002) Determine optimum *b*-value for diffusion imaging of acute ischemic stroke at high magnetic fields (3.0 T). Radiology 225:278
15. Detre JA, Leigh JS, Williams DS, et al. (1992) Perfusion imaging. Magn Reson Med 23:37 – 45
16. De Boer JA, Folkers PJM (1997) MR perfusion and diffusion imaging in ischaemic brain disease. Medica Mundi 41:20
17. Ueda T, Yuh WT, Taoka T (1999) Clinical application of perfusion and diffusion MR imaging in acute ischemic stroke. J Magn Reson Imaging 10(3):305 – 309
18. Ueda T, Yuh WT, Maley JE, et al. (2000) Outcome of acute ischemic lesions evaluated by diffusion and perfusion MR imaging. AJNR 20(6):983 – 989
19. Weber J, Mattle HP, Heid O, et al. (2000) Diffusion-weighted imaging in ischaemic stroke: a follow-up study. Neuroradiology 42(3):185 – 191
20. Federico F, Simone IL (1996) Prognostic significance of metabolic changes detected by proton magnetic resonance spectroscopy in ischaemic stroke. J Neurol 243:241 – 247
21. Federico F, Simone IL (1998) Prognostic value of proton magnetic resonance spectroscopy in ischaemic stroke. Arch Neurol 55:489 – 494
22. Mathews VP, Barker PB, Blackband SJ, et al. (1995) Cerebral metabolites in patients with acute and subacute strokes: a serial MR and proton MR spectroscopy study. AJR 165:633 – 638
23. Graham GD, Blamire AM (1992) Proton magnetic resonance spectroscopy of cerebral lactate and other metabolites in stroke patients. Stroke 333 – 340
24. Frayne R, Goodyear BG, Dickhoff P, et al. (2003) Magnetic resonance imaging at 3.0 Tesla: challenges and advantages in clinical neurological imaging. Invest Radiol 38(7):385 – 402

15 High-Field Strength MRI (3.0 T or More) in White Matter Diseases

A. Charil, M. Filippi, A. Falini

The great majority of magnetic resonance imaging (MRI) studies of white matter diseases have been conducted so far on 1.5 T MR scanners. This is likely to change over the next few years with the increased availability of high-field MR scanners. With a magnetic field strength of 3.0 T or higher, a variety of exciting improvements in clinical and research applications are expected. First exclusively employed for research, more than a hundred of these 'new generation' high-field MR scanners are now in use worldwide and are likely to become the next 'gold standard' in the clinical practice.

The aim of the present chapter is to review some of the latest research that has taken advantage of high-field MR scanners for the study of white matter diseases such as multiple sclerosis (MS).

15.1 The Quest for Improved Image Quality and Shorter Acquisition Times

Over the past two decades the contribution of MRI to medical practice has been unrivalled, and a review of the breakthroughs achieved with this in vivo imaging technique would be beyond the scope of this chapter. Research and development in the field of MR imaging have been fuelled by the constant need, among other things, for better pictures of the brain and spinal cord with a higher signal-to-noise ratio (SNR) in order to better visualize and quantify the pathological changes imputable to white matter diseases. While increasing the number of acquisitions (number of excitations, NEX) can improve the SNR of the images, this comes at a cost of time. In fact, the SNR is proportional to the square root of the number of acquisitions. Therefore, in order to double the SNR, the acquisition time will be four times longer. Although in theory this seems interesting, in clinical practice longer acquisition times are prohibitive, and could result in an increased likelihood of image degradation due to motion artefacts, especially in the case of patients having trouble lying still in the scanner for relatively long periods of time.

The main advantage of 3.0 T over lower field MR scanners is a better SNR, which increases roughly linearly with the strength of the magnetic field. Therefore, the SNR of a 3.0 T MRI scanner is theoretically twice as much as the SNR obtained at 1.5 T. Consequently, imaging at 3.0 T enables higher resolution scans with higher imaging matrices and/or thinner slices to be obtained that permit visualization of more detailed anatomical structures while keeping the scan time virtually unchanged. These advantages come at a trade-off of an increased sensitivity to field inhomogeneities and changes in relaxation times, which in turn produce changes in image contrast. At comparable acquisition times, images obtained at 3.0 T have a higher quality with an improved resolution than images obtained at 1.5 T. Alternatively, 3.0 T MRI can be used to obtain acceptable images, similar to those obtained at 1.5 T, but at a fraction of the time, thus reducing potential motion artefacts and improving patients' comfort.

15.2 3.0 T MRI Studies of Multiple Sclerosis

15.2.1 Role of MRI in Multiple Sclerosis

Multiple sclerosis (MS) is an idiopathic inflammatory demyelinating disease of the central nervous system (CNS) characterized by the presence of widely disseminated lesions throughout the brain and spinal cord [11].

Complementary to the clinical assessment, conventional MRI (cMRI) techniques, such as dual-echo, fluid attenuated inversion recovery (FLAIR), and T1-weighted (with and without post-contrast), provide helpful information for the diagnosis and prognosis of MS, as well as for monitoring disease evolution and therapeutic response to disease-modifying drugs [34, 45]. In MS, obtaining MR images of an optimal quality, in terms of resolution and contrast, is a paramount need knowing that, for instance, the diagnostic work-up of patients is based on the ability to identify lesions on MR scans [33].

In addition to the cMRI techniques that are routinely used in clinical practice, a number of non-conventional techniques have been developed in an attempt to overcome the limitations of cMRI [15], such as the lack of specificity to the various pathological substrates of the disease and the inability to quantify the microstruc-

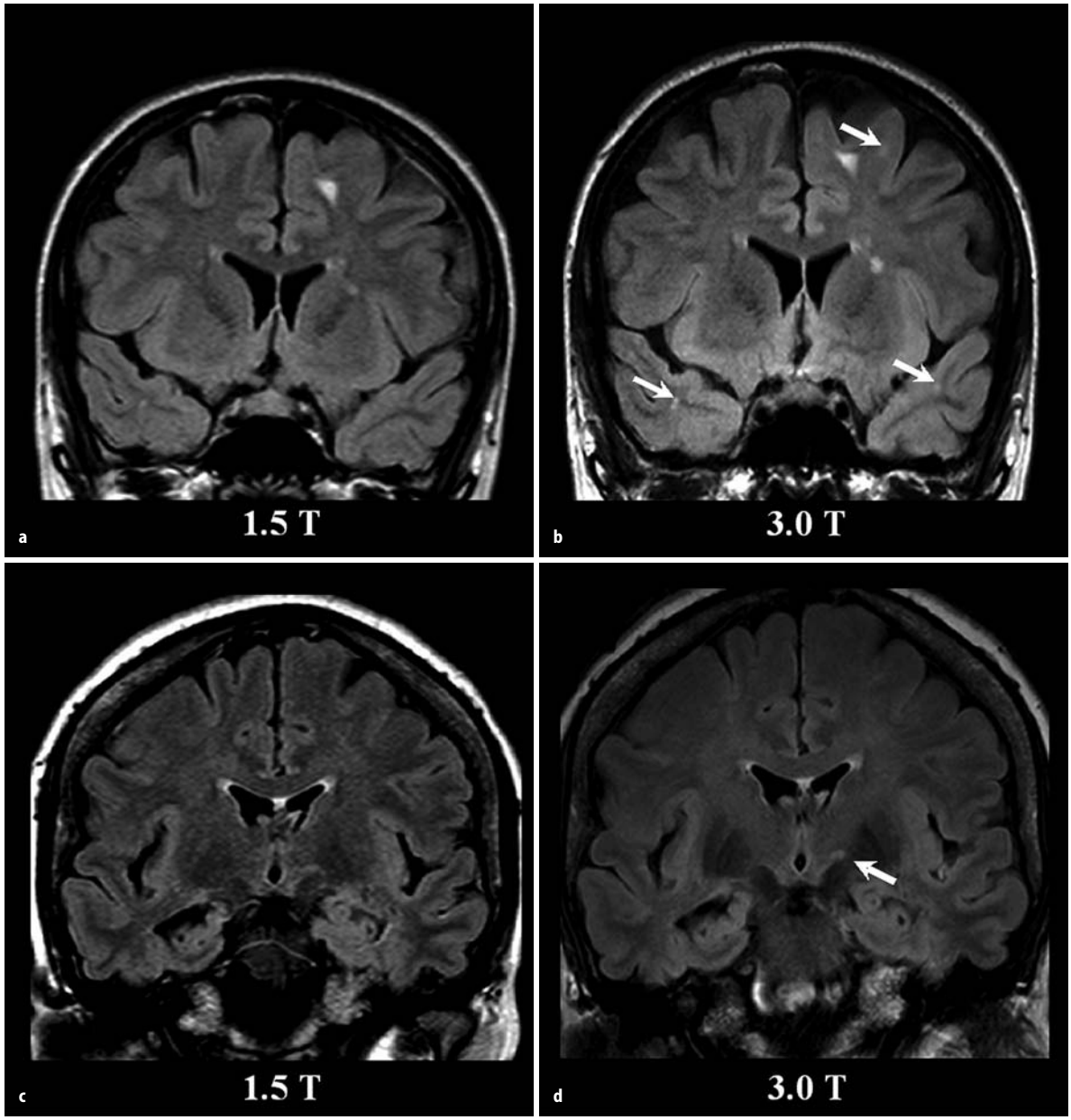

Fig. 15.1. Comparison of 3-mm coronal FLAIR images obtained at 1.5 (**a, c**) and 3.0 T (**b, d**) in patients with secondary progressive MS. Both cortical-subcortical (**a, b**) and deep internal capsule (**c, d**) demyelinating lesions are more clearly detectable at 3.0 T (*white arrows*). Studies were performed on a 1.5- and a 3.0-T MR scanner (Intera, Philips Medical System, Best, The Netherlands)

tural damage that is 'occult' to cMRI. These non-conventional techniques include proton magnetic resonance spectroscopy (^{1}H-MRS), magnetization transfer (MT) imaging, diffusion weighted (DW) imaging, diffusion tensor (DT) imaging with fibre tracking, and functional MRI (fMRI). Relative to the currently widely available 1.5 T MR scanners, higher field MRI at 3.0 T or more will likely improve the quality of these conventional and non-conventional techniques resulting in advances in the management and understanding of MS and other white matter diseases.

15.2.2 Conventional MRI Techniques: Better Lesion Identification and Quantification at Higher Fields

The use of 3.0 T in the clinical practice holds promise regarding image quality improvements which will help identify MS lesions more accurately (Figs. 15.1, 15.2), resulting in a better diagnostic work-up, especially at the earliest stages of the disease when the demonstration of the dissemination of lesions in time and space is vital [33]. Nevertheless, it is legitimate to ask whether there is a real advantage in using 3.0 T MR scanners in

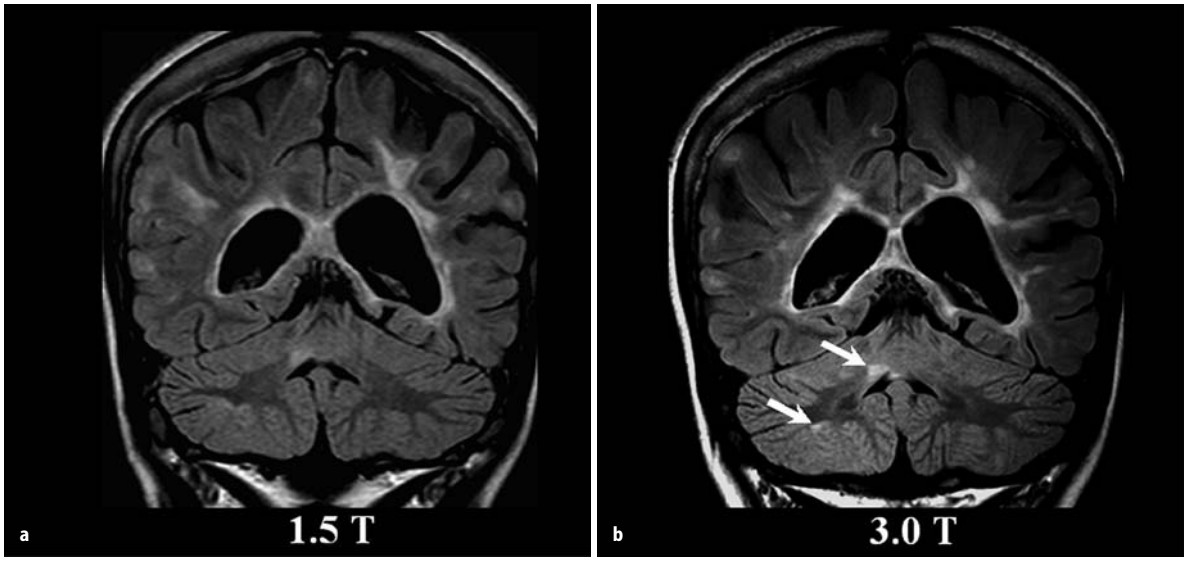

Fig. 15.2. Comparison of 3-mm coronal FLAIR images obtained at 1.5 (**a**) and 3 T (**b**) in a patient with secondary progressive MS. Infratentorial lesions are brighter and more sharply defined at 3.0 T (*white arrows*). Studies were performed on a 1.5- and a 3.0-T MR scanner (Intera, Philips Medical System, Best, The Netherlands)

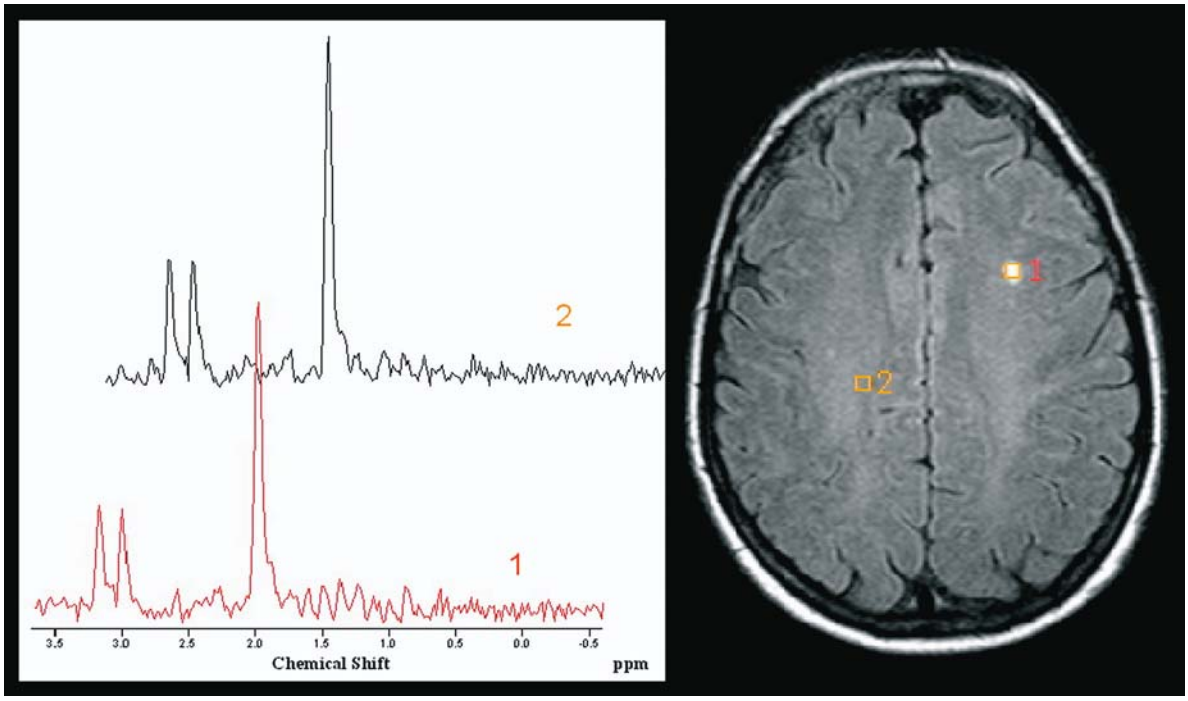

Fig. 15.3. Chemical shift imaging ^{1}H-MRS in a patient with migraine. *N*-Acetylaspartate decrease and choline increase can be measured both in volumes of interest with lesions (*1*) and NAWM (*2*). Study performed on a 1.5- and a 3.0-T MR scanner (Intera, Philips Medical System, Best, The Netherlands)

the routine clinical practice of MS considering their higher cost and the risk of 'false positive' lesions. Several studies have addressed this issue by comparing image quality, lesion detection and diagnostic value of higher (3.0 – 4.0 T) and lower (1.5 T) field strength MR scanners in MS [3, 13, 26, 48].

The study by Keiper and colleagues [26] was the first to compare the ability to detect white matter abnormalities in MS with conventional fast spin-echo imaging of the brain at 1.5 T and 4.0 T. Within a 1-week period, 15 clinically definite MS patients were scanned at both field strengths. Images were evaluated for lesion identi-

fication, size, characterization, and subjective resolution. An average of 88 additional lesions were found on images obtained at 4.0 T. Twenty-five lesions identified by consensus on 4.0 T images were not seen on 1.5 T images. Moreover, 4.0 T images showed 56 additional consensually identified lesions, which were indistinct and seen only in retrospect on 1.5 T images. Also, normal perivascular spaces and small perivascular lesions were more easily visualized on 4.0 T images [26]. Bachmann and colleagues [3] compared the diagnostic efficiency of 3.0 T to 1.5 T MRI scanners in a group of 11 patients with MS. Scan times were similar at both field strengths, but at 3.0 T the sequence was modified to take advantage of the increased SNR and consequently acquire more and thinner slices. Qualitatively, 3.0 T was found to be superior to 1.5 T for lesion conspicuity and overall diagnostic value. However, as expected when increasing the magnetic field, more artefacts were present at 3.0 T than at 1.5 T. Significantly more white matter lesions were detected at 3.0 T ($n = 162$) than at 1.5 T ($n = 117$) [3]. Using identical acquisition conditions at 1.5 T and 3.0 T, Sicotte and colleagues [48] evaluated the relative sensitivity of MR scanning for MS. Twenty-five MS patients were scanned at both field strengths using fast spin echo, and T1-weighted spoiled gradient recalled acquisition with and without gadolinium contrast injections. Relative to scanning at 1.5 T, the 3.0 T scans showed a 21% increase in the number of detectable contrast enhancing lesions, a 30% increase in enhancing lesion volume, based on quantification of lesions visible on both scanners, and a 10% increase in total lesion volume, measured on proton density weighted images [48]. Comparing the total lesion volume and individual lesions observed at 1.5 T and 4.0 T images, Erskine et al. [13] found a 46% increase in the total number of lesions detected and a 60% increase in the total lesion volume with 4.0 T versus 1.5 T imaging in a group of eight MS patients. Several individual lesions observed at 1.5 T coalesced into larger areas of white matter abnormality in the 4.0 T scans [13].

Together these studies show that higher field MR scanners are able to depict white matter lesions in MS patients that are undetectable at 1.5 T through higher resolution with comparable SNRs and imaging times. Even when the scanning protocols were not optimized to take full advantage of the higher field, 3.0 T scans showed more sensitivity in detecting both Gd-enhancing and non-enhancing white matter lesions. Monitoring the clinical evolution or the therapeutic response to drugs in MS patients is also likely to benefit from the use of higher field MR scanning by enabling the acquisition of images with improved resolution, resulting in increased lesion detection and better quantification. Finally, increased sensitivity for the detection and quantification of MS lesions could improve the correlation between findings on MR scans and clinical manifestations of the disease that have been so far disappointing [6, 8].

15.2.3 High-Field Magnetic Resonance Spectroscopy: Improved Measurements of Brain Metabolites

^{1}H-MRS is an in vivo technique able to provide metabolic information about the tissues. In MS, measures of *N*-acetylaspartate (NAA) concentrations are used as a marker of axonal and neuronal damage [1]. Brain NAA is reduced in MS patients relative to healthy controls [18]. The distance between peaks of different chemical species, identified by ^{1}H-MRS, increases linearly with the resonance frequency. Increased SNR allows for shorter scan times, and wider peak separation (spectral resolution), which in turn results in a more accurate peak definition and quantification [39, 47].

^{1}H-MRS allows us to measure the concentrations of the more common metabolites (NAA, choline and creatine) at 1.5 T, but metabolites that are present at lower concentrations, such as glutamine, glutamate and GABA, can be better quantified at higher fields [32].

Using a ^{1}H-MRS technique that isolates the glutamate resonance at 3.0 T, Srinivasan and colleagues [49] compared the levels of glutamate between normal subjects and MS patients in different regions of the brain. Glutamate concentrations were significantly higher in acute lesions and normal-appearing white matter (NAWM), but not in chronic lesions. In contrast, levels of NAA were significantly lower in chronic than in acute lesions and NAWM. The choline level was significantly higher in acute than in chronic lesions. Finally increased glial activity was found in MS, with significantly higher *myo*-inositol levels in acute lesions compared with control white matter. These results support the hypothesis that altered glutamate metabolism is present in MS [49], which might serve as an additional marker of 'destructive' pathological damage. Another study demonstrating the use of high-field ^{1}H-MRS in MS was performed by Wylezinska and colleagues [58], who studied 14 patients with relapsing-remitting (RR) MS and 14 age-matched healthy controls with the aim to define the extent of neuronal injury and loss in thalamic grey matter. Both structural and spectroscopy data were acquired on a 3.0 T MR system. A significant 11% decrease in NAA concentrations and a 25% decrease in normalized thalamic volume were found in MS patients relative to controls. Decreases in thalamic NAA concentration correlated with thalamic volume loss, reflecting the neurodegenerative component of MS [58]. These are just some examples that illustrate the potential role of high-field ^{1}H-MRS in the study of metabolic changes in MS and future ^{1}H-MRS studies in MS might be preferentially conducted at 3.0 T or higher.

15.2.4 Diffusion Tensor Imaging and Fibre Tractography

DT MRI exploits the molecular diffusion of water within biological tissues [29]. Diffusion properties are influenced by the characteristics of the surrounding medium. In MS, the technique is used to detect microscopic abnormalities in the NAWM [5, 17, 20, 55], grey matter [37], cervical cord [53], as well as inside lesions [5, 7, 27, 55].

Current DT MRI acquisitions on 1.5 T MR scanners can take up to 15 min, which represents a considerable amount of time during which the patient has to remain still. Studies have emphasized the value of DT MRI in MS [7, 17, 20, 27, 37, 53] and its potential role as a surrogate marker of disease evolution in clinical trials. However, in order to make DT MRI a viable clinical modality, it is important to be able to acquire this additional sequence in a reasonable amount of time without compromising the overall quality of the images. High-field MR scanners are able to reduce the whole brain DT MRI acquisition time to less than 6 min using a single-shot echo planar method [19]. Fibre tractography is a newly developed technique that uses DT MRI to reconstruct white matter fibre tracts [35]. High-field DT MRI will allow better fibre tractography by increasing the resolution of DT images. Reductions in voxel size will also result in a better differentiation of crossing fibres within a voxel. These improvements in fibre tractography will reinforce the role of this technique in the investigation of diseases affecting the white matter [19].

15.2.5 Anatomical and Physiological Imaging of the Optic Chiasm

Optic neuritis is frequently the initial manifestation of MS. Routine imaging of the optic nerves is a complex task due to the small size of the optic nerve, nerve physiological movement, contamination of the signal from the surrounding tissue (fat, bone, and cerebrospinal fluid), as well as susceptibility effects due to air in neighbouring structures [54]. Higher field MR scanners are likely to overcome at least partially some of these limitations.

In a recent study by Vinogradov and colleagues [54], anatomical, DT and MT MRI at 3.0 T with a custom-designed four-channel head coil were used to study the optic nerve, optic chiasm, and optic tract with the aim of visualizing axonal damage in MS. MT MRI is based on the exchange of magnetization between the protons bound to macromolecules and the protons in free water [57]. Oblique fast spin echo anatomic images were obtained with an in-plane resolution of 0.39×0.52 mm. MT-enhanced 3D gradient-echo time-of-flight images and line scan diffusion images were obtained with an in-plane resolution of 0.78×0.78 mm. Full DT analysis was performed, and apparent diffusion coefficient, fractional anisotropy, and fibre direction maps were obtained. This multimodality approach resulted in high-resolution anatomical and physiological images of the anterior visual pathways that are much harder to obtain at 1.5 T [54].

15.2.6 Pathological Iron Deposition

Several studies suggest that pathological iron deposition in MS could serve as a potential surrogate marker of the destructive disease process [4, 12, 31, 52]. At 3.0 T iron-dependent contrast intrinsic to the brain is much more prominent than at 1.5 T [46], which suggests that future studies aimed at imaging brain iron will be performed on high-field MR systems.

15.2.7 The Future of High-Field Functional MRI in MS

Functional MRI studies at 1.5 T have been conducted in MS patients to study the motor system [30, 40, 42, 44], the visual system [56] and cognition [2, 10, 50]. The increased magnetic susceptibility that comes with higher field magnets enhances the blood oxygenation level dependent (BOLD) effect, and the higher SNR strengthens the signal [9]. As a consequence, increased spatial resolution contributes to mapping additional areas and submillimetre structures. Although no study has been published to date on the use of fMRI at 3.0 T in patients with MS, there is no doubt that future functional investigations will be performed at this field strength to study baseline circuitry and connectivity in the MS brain, as well as the mechanisms of neuronal plasticity and compensation related to the extent and location of brain injury [14].

15.2.8 Very High-Field MRI in MS

Although the advantages of MRI performed at 3.0 or 4.0 T relative to those conducted at 1.5 T are already apparent, it is likely that the future of MRI resides in the use of even higher magnetic field MR scanners, despite the associated technological challenges, as has already been done in normal subjects [23, 36, 43] and MS patients [24] at field strengths as high as 8.0 T. The use of an 8.0 T MR scanner allowed Kangarlu and colleagues [24] to show, in vivo, a clear relationship between the demyelinating lesions and the deep venous system, and more precisely that MS plaques are centred on the microvasculature in the white matter [24]. Previously, these observations were only possible on contrast-enhanced MR [51] or on pathological examination of postmortem specimens [16]. Additionally, the cortical

microanatomy and location and characteristics of cortical lesions can be visualized at these field strengths in brain samples of newly deceased MS patients [25].

15.3 Other White Matter Diseases

The use of MR systems at 3.0 T or higher is relatively new and although several studies have already been conducted on MS, the literature on the use of higher field MR scanners for the study of other white matter diseases is still scarce. Table 15.1 summarizes some of the recent work that has been done so far to assess white matter damage in diseases such as frontotemporal dementia [28], aging [22, 41], Alzheimer's disease [21], and adrenoleukodystrophy [38] with 3.0 or 4.0 T MR scanners. The assessment of white matter changes in neurodegenerative conditions is likely to bring insights into the understanding of white matter diseases where the presence of a neurodegenerative component is increasingly being accepted. Admittedly, normal aging is not a disease; however, again work done with ^{1}H-MRS at 4.0 T [22] and DT MRI at 3.0 T [41] might ultimately help understand some of the processes occurring in the pathological brain.

During the past few years, the application of advanced MR techniques for the assessment of patients with migraine has shown that, similarly to what has been described in other chronic vascular affections, including leukoaraiosis, cerebral autosomal dominant arteriopathy with subcortical infarcts and leukoencephalopathy (CADASIL), brain damage extends beyond the resolution of conventional imaging and diffusely involves the normal-appearing brain tissue (NABT). In a preliminary study using ^{1}H-MRS at 3.0 T, we found that NAA is reduced in white matter lesions as well as in the NAWM of patients with migraine (Fig. 15.3). Concentrations of choline follow an opposite trend, with increased concentrations in the NAWM and lesions. Preliminary findings obtained with DT MRI at 3.0 T also suggest the presence of occult damage in the NABT of patients suffering from migraine.

Table 15.1. Summary of some of the recent work done so far to assess white matter damage in diseases such as frontotemporal dementia, aging, Alzheimer's disease, and adrenoleukodystrophy with 3.0 or 4.0 T MR scanners

Author, year	Disease	Technique	Field strength	Subjects	Findings
Hattori et al., 2002 [21]	AD	^{1}H-MRS	3.0 T	9P, 12C	In patients, the *N*-acetyl group (NA)/creatine + phosphocreatine (Cr) ratios were decreased in both the GM of the posterior cingulate gyrus and the precuneus, and the parieto-occipital WM regions. A decrease in the glutamate + glutamine (Glx)/Cr ratio and a correlation between the NA/Cr and Glx/Cr ratios were detected in the GM, but not in the WM. NA and Glx metabolism are simultaneously affected in AD; however, metabolic changes in Glx are more profound in the GM than in the WM
Oz et al., 2005 [38]	ALD	^{1}H-MRS	4.0 T	17P, 26C	Detection of early neurochemical changes in lesion formation prior to detection of abnormalities by conventional MRI. Creatine and choline containing compounds were the weakest markers of cerebral disease while *N*-acetylaspartate, glutamine, and lipids + lactate were the strongest
Larsson et al., 2004 [28]	FTD	CMRI, DTI	3.0 T	1P (p-m)	In this postmortem investigation of brain tissue by MRI, DTI and histopathology, frontotemporal atrophy as well as bilateral frontal WM abnormalities were seen. The WM changes were slightly more extensive on DTI than on conventional MRI. Correlation with histopathology of the corresponding regions revealed typical frontal lobe degeneration of non-Alzheimer type, with mild frontotemporal degeneration in the outer cortical layers and a moderate frontal WM gliosis with demyelination
Kaiser et al., 2005 [22]	Normal aging	^{1}H-MRS	4.0 T	24C	Comparisons between old and young subjects showed higher concentration of scyllo-inositol and *myo*-inositol in older subjects and a trend for a correlation between scyllo-inositol and *myo*-inositol levels across subjects
Pfefferbaum et al., 2005 [41]	Normal aging	DTI	3.0 T	20C	Selective decline in frontal WM anisotropy and high bulk mean diffusivity in healthy older compared with younger adults. However, posterior systems are largely preserved with age. The study highlights the potential implication of a microstructural WM mechanism for the commonly observed decline in frontally based functions

AD Alzheimer's disease, *ALD* adrenoleukodystrophy, *FTD* frontotemporal dementia, *DTI* diffusion tensor imaging, *MRS* magnetic resonance spectroscopy, *CMRI* conventional MRI, *P* patients, *C* controls, *p-m* postmortem, *GM* grey matter, *WM* white matter

15.4 Conclusions

In white matter conditions, high-field MRI does the same as lower field MRI, but does it better. Although this simplified description might be correct, it would not reflect the full range of advantages and exciting possibilities that come with the development of higher field MR systems. MRI has been, and still is, an invaluable tool to study MS in vivo. High-field MRI will certainly further strengthen the role of MRI as the most sensitive paraclinical tool available for early diagnosis of MS. Both conventional and non-conventional MR techniques will take advantage of the use of high-field MR systems to study MS, as well as other white matter diseases.

References

1. Arnold DL, Wolinsky JS, Matthews PM, Falini A (1998) The use of magnetic resonance spectroscopy in the evaluation of the natural history of multiple sclerosis. J Neurol Neurosurg Psychiatry 64 Suppl 1:S94 – 101
2. Au Duong MV, Boulanouar K, Audoin B, et al. (2005) Modulation of effective connectivity inside the working memory network in patients at the earliest stage of multiple sclerosis. Neuroimage 24(2):533 – 538
3. Bachmann R, Reilmann R, Kraemer S, et al. (2003) Multiple sclerosis: comparative MR-imaging at 1.5 and 3.0 Tesla [abstract 1465]. Presented at: Radiological Society of North America RSNA 2003 89th Scientific Assembly and Meeting; December 5, 2003; Chicago
4. Bakshi R, Benedict RH, Bermel RA, et al. (2002) T2 hypointensity in the deep gray matter of patients with multiple sclerosis: a quantitative magnetic resonance imaging study. Arch Neurol 59(1):62 – 68
5. Bammer R, Augustin M, Strasser-Fuchs S, et al. (2000) Magnetic resonance diffusion tensor imaging for characterizing diffuse and focal white matter abnormalities in multiple sclerosis. Magn Reson Med 44(4):583 – 591
6. Barkhof F (2002) The clinico-radiological paradox in multiple sclerosis revisited. Curr Opin Neurol 15(3):239 – 245
7. Castriota-Scanderbeg A, Fasano F, Hagberg G, et al. (2003) Coefficient D(av) is more sensitive than fractional anisotropy in monitoring progression of irreversible tissue damage in focal nonactive multiple sclerosis lesions. AJNR Am J Neuroradiol 24(4):663 – 670
8. Charil A, Zijdenbos AP, Taylor J, et al. (2003) Statistical mapping analysis of lesion location and neurological disability in multiple sclerosis: application to 452 patient data sets. Neuroimage 19(3):532 – 544
9. Chen W, Ugurbil K (1999) High spatial resolution functional magnetic resonance imaging at very-high-magnetic field. Top Magn Reson Imaging 10(1):63 – 78
10. Chiaravalloti N, Hillary F, Ricker J, et al. (2005) Cerebral activation patterns during working memory performance in multiple sclerosis using FMRI. J Clin Exp Neuropsychol 27(1):33 – 54
11. Compston A, Coles A (2002) Multiple sclerosis. Lancet 359(9313):1221 – 1231
12. Craelius W, Migdal MW, Luessenhop CP, et al. (1982) Iron deposits surrounding multiple sclerosis plaques. Arch Pathol Lab Med 106(8):397 – 399
13. Erskine MK, Cook LL, Riddle KE, et al. (2005) Resolution-dependent estimates of multiple sclerosis lesion loads. Can J Neurol Sci 32(2):205 – 212
14. Filippi M, Rocca MA (2003) Disturbed function and plasticity in multiple sclerosis as gleaned from functional magnetic resonance imaging. Curr Opin Neurol 16(3):275 – 282
15. Filippi M, Rocca MA, Comi G (2003a) The use of quantitative magnetic-resonance-based techniques to monitor the evolution of multiple sclerosis. Lancet Neurol 2(6):337 – 346
16. Fog T (1965) The topography of plaques in multiple sclerosis. Acta Neurol Scand 15:1 – 161
17. Gallo A, Rovaris M, Riva R, et al. (2005) Diffusion-tensor magnetic resonance imaging detects normal-appearing white matter damage unrelated to short-term disease activity in patients at the earliest clinical stage of multiple sclerosis. Arch Neurol 62(5):803 – 808
18. Gonen O, Moriarty DM, Li BS, et al. (2002) Relapsing-remitting multiple sclerosis and whole-brain *N*-acetylaspartate measurement: evidence for different clinical cohorts initial observations. Radiology 225(1):261 – 268
19. Hasan KM, Narayana PA (2005) DTI parameter optimization at 3.0 T: potential application in entire normal human brain mapping and multiple sclerosis research. Medica Mundi 49(1):30 – 45
20. Hasan KM, Gupta RK, Santos RM, et al. (2005) Diffusion tensor fractional anisotropy of the normal-appearing seven segments of the corpus callosum in healthy adults and relapsing-remitting multiple sclerosis patients. J Magn Reson Imaging 21(6):735 – 743
21. Hattori N, Abe K, Sakoda S, Sawada T (2002) Proton MR spectroscopic study at 3 Tesla on glutamate/glutamine in Alzheimer's disease. Neuroreport 13(1):183 – 186
22. Kaiser LG, Schuff N, Cashdollar N, Weiner MW (2005) Scyllo-inositol in normal aging human brain: 1H magnetic resonance spectroscopy study at 4 Tesla. NMR Biomed 18(1):51 – 55
23. Kangarlu A, Burgess RE, Zhu H, et al. (1999) Cognitive, cardiac, and physiological safety studies in ultra high field magnetic resonance imaging. Magn Reson Imaging 17(10): 1407 – 1416
24. Kangarlu A, Rammohan KW, Bourekas EC, Chakeres DW (2002) In-vivo microscopic imaging of multiple sclerosis with high field MRI. In: Filippi M, Comi G (eds) New frontiers of MR-based techniques in MS. Springer, Berlin Heidelberg New York
25. Kangarlu A, Rammohan KW, Bourekas EC, RayChaudhry A (2004) Imaging of cortical lesions in multiple sclerosis. Proceedings of 12th Meeting of the International Society of Magnetic Resonance in Medicine. Kyoto, Japan
26. Keiper MD, Grossman RI, Hirsch JA, et al. (1998) MR identification of white matter abnormalities in multiple sclerosis: a comparison between 1.5 T and 4 T. AJNR Am J Neuroradiol 19(8):1489 – 1493
27. Larsson HB, Thomsen C, Frederiksen J, et al. (1992) In vivo magnetic resonance diffusion measurement in the brain of patients with multiple sclerosis. Magn Reson Imaging 10(1):7 – 12
28. Larsson EM, Englund E, Sjobeck M, et al. (2004) MRI with diffusion tensor imaging post-mortem at 3.0 T in a patient with frontotemporal dementia. Dement Geriatr Cogn Disord 17(4):316 – 319
29. Le Bihan D, Mangin JF, Poupon C, et al. (2001) Diffusion tensor imaging: concepts and applications. J Magn Reson Imaging 13(4): 534 – 546
30. Lee M, Reddy H, Johansen-Berg H, et al. (2000) The motor cortex shows adaptive functional changes to brain injury from multiple sclerosis. Ann Neurol 47(5):606 – 613
31. Levine SM, Chakrabarty A (2004) The role of iron in the pathogenesis of experimental allergic encephalomyelitis and multiple sclerosis. Ann N Y Acad Sci 1012:252 – 266

32. Mason GF, Pan JW, Ponder SL, et al. (1994) Detection of brain glutamate and glutamine in spectroscopic images at 4.1 T. Magn Reson Med 32(1):142 – 145
33. McDonald WI, Compston A, Edan G, et al. (2001) Recommended diagnostic criteria for multiple sclerosis: guidelines from the International Panel on the diagnosis of multiple sclerosis. Ann Neurol 50(1):121 – 127
34. Miller DH (1996) Guidelines for MRI monitoring of the treatment of multiple sclerosis: recommendations of the US Multiple Sclerosis Society's task force. Mult Scler 1(6):335 – 338
35. Mori S, van Zijl PC (2002) Fiber tracking: principles and strategies – a technical review. NMR Biomed 15(7 – 8): 468 – 480
36. Novak P, Novak V, Kangarlu A, et al. (2001) High resolution MRI of the brainstem at 8 T. J Comput Assist Tomogr 25(2):242 – 246
37. Oreja-Guevara C, Rovaris M, Iannucci G, et al. (2005) Progressive gray matter damage in patients with relapsing-remitting multiple sclerosis: a longitudinal diffusion tensor magnetic resonance imaging study. Arch Neurol 62(4): 578 – 584
38. Oz G, Tkac I, Charnas LR, et al. (2005) Assessment of adrenoleukodystrophy lesions by high field MRS in non-sedated pediatric patients. Neurology 64(3):434 – 441
39. Pan JW, Hetherington HP, Vaughan JT, et al. (1996) Evaluation of multiple sclerosis by 1H spectroscopic imaging at 4.1 T. Magn Reson Med 36(1):72 – 77
40. Pantano P, Iannetti GD, Caramia F, et al. (2002) Cortical motor reorganization after a single clinical attack of multiple sclerosis. Brain 125(7):1607 – 1615
41. Pfefferbaum A, Adalsteinsson E, Sullivan EV (2005) Frontal circuitry degradation marks healthy adult aging: Evidence from diffusion tensor imaging. Neuroimage 26(3): 891 – 899
42. Reddy H, Narayanan S, Woolrich M, et al. (2002) Functional brain reorganization for hand movement in patients with multiple sclerosis: defining distinct effects of injury and disability. Brain 125(12):2646 – 2657
43. Robitaille PM, Abduljalil AM, Kangarlu A (2000) Ultra high resolution imaging of the human head at 8 tesla: 2K × 2K for Y2K. J Comput Assist Tomogr 24(1):2 – 8
44. Rocca MA, Gallo A, Colombo B, et al. (2004) Pyramidal tract lesions and movement-associated cortical recruitment in patients with MS. Neuroimage 23(1):141 – 147
45. Rovaris M, Filippi M (1999) Magnetic resonance techniques to monitor disease evolution and treatment trial outcomes in multiple sclerosis. Curr Opin Neurol 12(3): 337 – 344
46. Schenck JF, Zimmerman EA (2004) High-field magnetic resonance imaging of brain iron: birth of a biomarker? NMR Biomed 17(7):433 – 445
47. Schubert F, Seifert F, Elster C, et al. (2002) Serial 1H-MRS in relapsing-remitting multiple sclerosis: effects of interferon-beta therapy on absolute metabolite concentrations. MAGMA 14(3): 213 – 222
48. Sicotte NL, Voskuhl RR, Bouvier S, et al. (2003) Comparison of multiple sclerosis lesions at 1.5 and 3.0 Tesla. Invest Radiol 38(7):423 – 427
49. Srinivasan R, Sailasuta N, Hurd R, et al. (2005) Evidence of elevated glutamate in multiple sclerosis using magnetic resonance spectroscopy at 3 T. Brain 128(5):1016 – 1025
50. Staffen W, Mair A, Zauner H, et al. (2002) Cognitive function and fMRI in patients with multiple sclerosis: evidence for compensatory cortical activation during an attention task. Brain 125(6):1275 – 1282
51. Tan IL, van Schijndel RA, Pouwels PJ, et al. (2000) MR venography of multiple sclerosis. AJNR Am J Neuroradiol 21(6): 1039 – 1042
52. Tjoa CW, Benedict RH, Weinstock-Guttman B, et al. (2005) MRI T2 hypointensity of the dentate nucleus is related to ambulatory impairment in multiple sclerosis. J Neurol Sci 234(1 – 2):17 – 24
53. Valsasina P, Rocca MA, Agosta F, et al. (2005) Mean diffusivity and fractional anisotropy histogram analysis of the cervical cord in MS patients. Neuroimage 26(3):822 – 828
54. Vinogradov E, Degenhardt A, Smith D, et al. (2005) High-resolution anatomic, diffusion tensor, and magnetization transfer magnetic resonance imaging of the optic chiasm at 3T. J Magn Reson Imaging 22(2):302 – 306
55. Werring DJ, Clark CA, Barker GJ, et al. (1999) Diffusion tensor imaging of lesions and normal-appearing white matter in multiple sclerosis. Neurology 52:1626 – 1632
56. Werring DJ, Bullmore ET, Toosy AT, et al. (2000) Recovery from optic neuritis is associated with a change in the distribution of cerebral response to visual stimulation: a functional magnetic resonance imaging study. J Neurol Neurosurg Psychiatry 68(4):441 – 449
57. Wolff SD, Balaban RS (1994) Magnetization transfer imaging: practical aspects and clinical applications. Radiology 192(3):593 – 599
58. Wylezinska M, Cifelli A, Jezzard P, et al. (2003) Thalamic neurodegeneration in relapsing-remitting multiple sclerosis. Neurology 60(12):1949 – 1954

16 High-Field Neuroimaging in Parkinson's Disease

P. Péran, G. Luccichenti, A. Cherubini, G. E. Hagberg, U. Sabatini

Until recently, standard neuroimaging techniques have had a marginal role in the diagnosis and follow-up of Parkinson's disease (PD). The diagnosis of PD is essentially based on clinical data (neurological examination and evaluation of therapeutic response) (UK Parkinson's Disease Brain Bank criteria). In the early phase the magnetic resonance (MR) examination may be negative. In other words MR is not sufficiently sensitive to the damage caused by PD. One-fourth of patients with a clinical diagnosis of idiopathic PD are subsequently found to have other degenerative disorders [11]. Like clinical examination, standard MR is scarcely specific and has a secondary role that is in fact limited to gross differential diagnosis with other neurological disorders.

The increasing prevalence of PD, partly as a consequence of population ageing, the introduction of experimental therapeutic strategies, and technological advances in MR hardware and software have stimulated the development of MR techniques with a potential for greater sensitivity and specificity for early diagnosis and the quantification of the pathological process. In particular, the introduction of high static magnetic field (3.0 T) imagers has provided promising results in the study of degenerative neurological diseases by using advanced techniques that have also been recently proposed for clinical application.

We examine the rationale of standard MR diagnostic imaging, the more advanced quantification techniques and the advantages and drawbacks of 3.0 T magnetic fields in PD.

16.1 Rationale

Illustration of the rationale of diagnostic imaging in PD requires a brief description of the pathological and consequent functional changes induced by the disease. Idiopathic PD is a degenerative disorder characterized by progressive and focal loss of the dopaminergic neurons of substantia nigra (SN), or pars compacta. Their depletion induces functional changes in the circuit of the basal ganglia (dopaminergic deafferentation), whose activity is modulated by SN, and eventually functional deafferentation of frontostriatal circuits [2]. The anatomical and functional changes induced by PD can be represented as a three-level system: (1) mesencephalic (neuroaxonal degeneration); (2) basal ganglia (dopaminergic deafferentation); and (3) cortical (functional deafferentation) (Fig. 16.1).

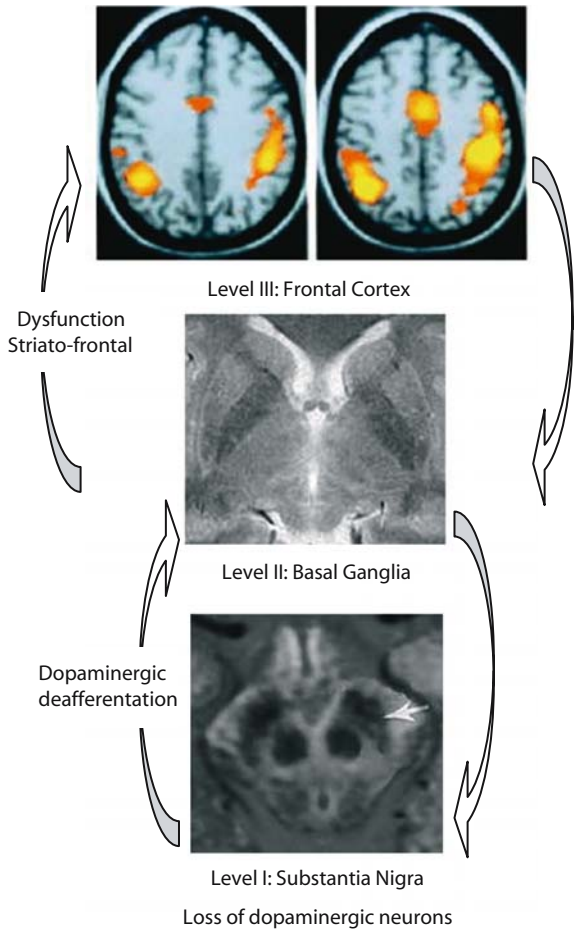

Fig. 16.1. Representation of the anatomical and functional changes of PD. The changes are observed at three levels: *I* mesencephalic (EPI diffusion-weighted image); *II* basal ganglia (spin-echo T2-weighted image); *III* cortical (functional MR, motor task)

At each of these three levels MR can further and significantly contribute to evidencing the anatomical and functional changes induced by PD.

MR imaging is particularly difficult in PD patients owing to the technical limitations of the scanners due to the intrinsic characteristics and the reduced size of the structures involved. As regards the former, the high intracellular iron content of SN dopaminergic neurons, which is an essential element of their metabolic processes [31], helps to enhance the contrast between the structures and surrounding tissue. However, the iron deposits also play a significant role in the cascade of events that lead to apoptotic cell death [32]. With regard to the small size of the structures, the mesencephalon contains important bundles of ascending and descending myelin fibres, nuclear structures such as red nuclei and the third pair of cranial nerves, SN and reticular substance. In normal individuals, SN usually measures a few square millimetres, emphasizing the crucial importance of spatial resolution for its precise quantification.

Data obtained using low-, medium- and high-field MR are presented below in relation to each anatomical and functional level involved in PD and the potential of 3.0 T MR imaging is illustrated.

16.1.1 Mesencephalic Level

16.1.1.1 Low- and Medium-Field MR

The mesencephalon, in particular SN, is the area where focal neuronal degeneration electively takes place. Several acquisition techniques have been applied using low- and medium-field magnets to try and define the parameters for the identification and quantification of SN. These studies, performed in a small number of patients, have demonstrated that identification of the borders and dimension of SN is difficult in healthy as well as PD subjects. These modest results have discouraged large-scale application of such methods in clinical practice, but have had the merit of demonstrating that the integrated use of multiple acquisition techniques capable of enhancing and showing the different mesencephalic component structures is essential to identify and quantify SN.

Hutchinson et al. [12, 13] used T1-weighted inversion recovery with two different inversion times to suppress the mesencephalic white and grey matter signal, respectively. The ratio of the signals obtained with the two inversion times allowed the quantification of SN in healthy subjects and the assessment of focal neuron loss in PD patients. Being based on a semiautomatic method, these investigations, which were performed in a small number of subjects and patients, have proved difficult to reproduce. Hu et al. [10] demonstrated that positron emission tomography (PET) with (18)F-dopa was more effective than MR with inversion recovery in discriminating patients with PD from controls in only 83 % of cases.

Oikawa et al. [17], using dual-echo spin-echo and short inversion time inversion recovery sequences, failed to show significant differences in SN dimension between PD patients and control subjects. Other studies have been unable to find significant differences in SN volume using diffusion-weighted (DWI) sequences [1, 26]. Finally, indices of SN neuron depletion were calculated in healthy and PD individuals using magnetization transfer ratio (MTR), an MR parameter that is based on the energy transfer from protons bound to macromolecular structures like myelin to free-water protons [7]; other researchers have proposed using the measurement of brain iron by means of T2* maps obtained using gradient-echo sequences [4, 8].

Due to their spatial resolution, these low- and medium-field MR studies have demonstrated limited accuracy in SN evaluation. The slice thickness used was 3 – 4 mm, which is insufficient to measure the modest quantitative differences induced by the loss of dopaminergic neurons.

16.1.1.2 High-Field MR

One of the main advantages of high-field MR is its high spatial resolution and consequent greater and more accurate anatomical definition. In addition, magnetic susceptibility artefacts due to the iron selectively deposited in SN are enhanced by the higher magnetic field. Spin-echo sequences allow the acquisition of proton density- and T2-weighted images with $0.9 \times 0.9 \times 2\ mm^3$ voxels in a few minutes (Fig. 16.2) and the quantification of iron deposits using relaxometry, a technique that greatly benefits from the high magnetic field.

The nigrostriatal degeneration characteristic of PD induces a change in functional connectivity between SN and basal nuclei. This change is held to be associated with a reduction in anatomical connectivity. Fibre tracking techniques allow the reconstruction of the course of axon bundles on DWI images by estimating the preferential direction of the diffusion of water molecules. The fibre tracking technique benefits from a high signal-to-noise ratio (SNR) and therefore from high field intensities (Fig. 16.3). Use of this method, which shows considerable potential in the study of connectivity among brain regions, is limited in the mesencephalon by its scarce sensitivity to the minimum deviations of fibre bundles that are found in PD and by susceptibility artefacts induced by the anatomical area, which is adjacent to the air-filled cavities of the splanchnocranium and petrous bones.

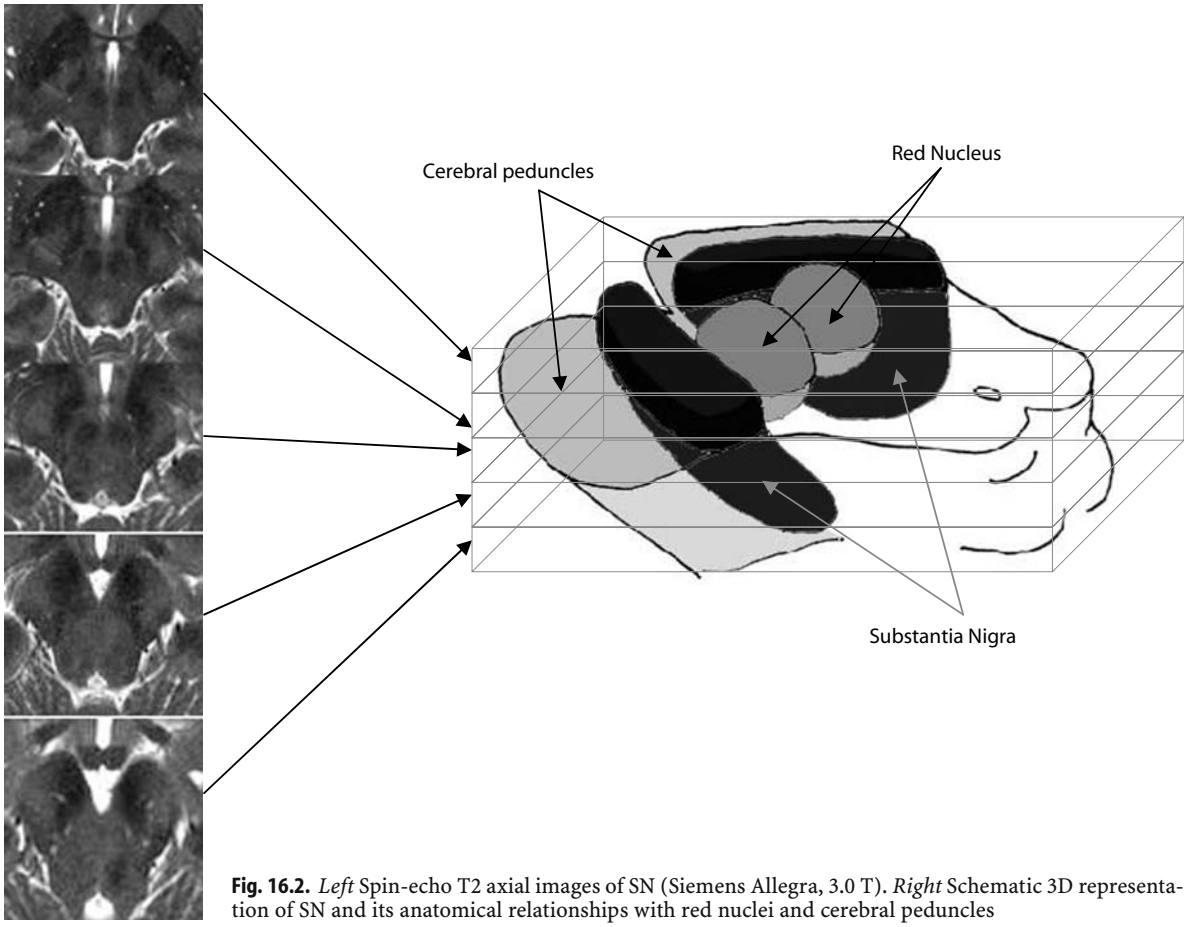

Fig. 16.2. *Left* Spin-echo T2 axial images of SN (Siemens Allegra, 3.0 T). *Right* Schematic 3D representation of SN and its anatomical relationships with red nuclei and cerebral peduncles

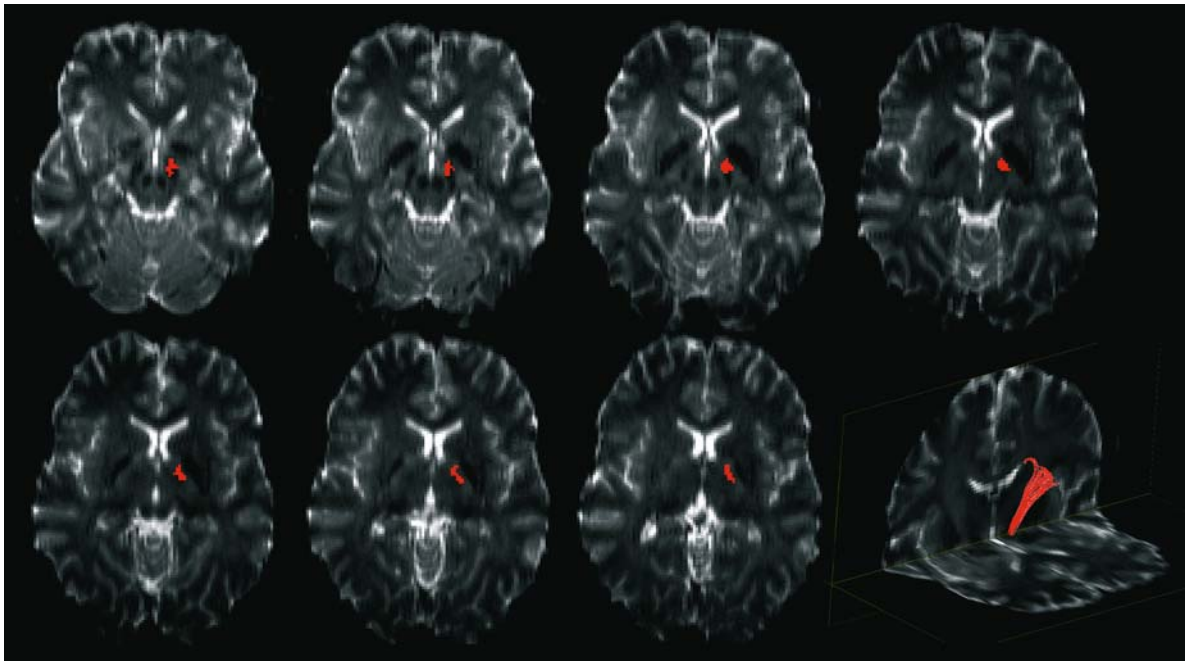

Fig. 16.3. Nigrostriatal tractography. Tractographic images are superimposed on EPI T2-weighted slices (Siemens Allegra, 3.0 T)

Due to their technical characteristics, 3.0 T MR imagers are thus a promising tool to assess the neuronal and axonal depletion that characterizes PD.

16.1.2 Basal Ganglia Level

16.1.2.1 Low- and Medium-Field MR

Since PD induces nigrostriatal axon degeneration, dopaminergic deafferentation and pre- and postsynaptic disruption of the basal ganglia, the latter do not undergo neuron depletion but synaptic and metabolic alterations. At this level, nuclear medicine-based techniques such as PET and single photon emission tomography (SPECT) employed with specific tracers selectively binding to pre- or postsynaptic dopaminergic receptors have demonstrated their progressive loss, which is related to disease severity [5].

As regards MR, studies of the basal ganglia (globus pallidus, caudatus and putamen) based on morphological evaluation, size, and metabolic parameters such as iron deposition, have yielded contradictory results. Quantification of the iron deposits, which provides a metabolic index of the pre- and postsynaptic disruption of the basal ganglia, has until now been the main goal of the largest number of studies of PD (see [32] for a review). In MR, the presence of iron in brain parenchyma induces a reduction in transverse relaxation times that can be measured on T2- and T2*-weighted sequences. When comparing PD patients with a control group, this reduction was mainly observed at the level of globus pallidus [4, 30] and putamen [3, 4, 30]. However, Graham et al. observed increased putaminal transverse relaxation times induced by the reduction in iron content in patients with PD [8, 22]. In a recent study, Kosta et al. confirmed these data by demonstrating an increase in T2 transverse relaxation times in globus pallidus and putamen. In patients who have had the disease for more than 5 years the putaminal surface was also increased compared with patients with a shorter disease duration, presumably reflecting gliotic neuroreparative phenomena [15].

MR diffusion techniques have been applied to assess subcortical neurodegenerative disorders such as PD and multisystem atrophy (MSA). Schocke et al. showed that analysis of the apparent diffusion coefficient (ADC) in the basal ganglia allowed PD patients to be distinguished from MSA patients [25] based on a greater ADC – an indirect measure of neuronal depletion and of associated reactive gliosis – in the putamen of the latter [25–27]. Seppi et al. documented an ADC increment in globus pallidus and putamen in patients with progressive supranuclear paralysis (PSP) compared with PD patients [28]. MR diffusion techniques are thus effective in discriminating PD from other subcortical diseases (MSA, PSP), but are unable to differentiate PD patients from control subjects of comparable age without neurological disorders [26, 27].

Magnetization transfer imaging (MTI), or the study of MTR maps, is another technique capable of quantifying the degree of myelination [19] and has been used by Eckert et al. to assess neuronal depletion in basal ganglia [7]. The authors observed significant differences in globus pallidus between PD patients and control subjects in 75–80% of cases. This technique has not been further applied to PD, and these data have not been reproduced in other studies.

The main investigations into basal ganglia dopaminergic deafferentation in PD have used various MR techniques with contrasting results. None of the methods used at low and medium fields can reliably differentiate PD patients from control subjects.

16.1.2.2 High-Field MR

There are no available studies of the effects of dopaminergic deafferentation on the basal ganglia circuit. Also with reference to these structures, however, measurement of the iron deposits should benefit from the advantages of high magnetic fields (Fig. 16.4). Compared with SN, where iron deposition is characteristic of the physiological activity of dopaminergic neurons [8, 15], in the basal ganglia these deposits are an indirect parameter of the neuronal metabolic changes induced by dopaminergic deafferentation.

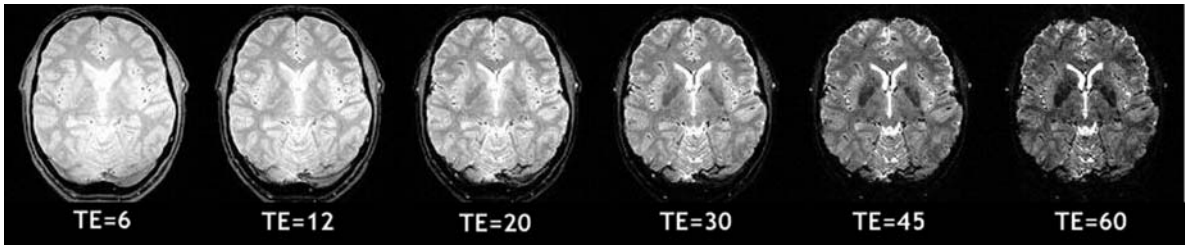

Fig. 16.4. Relaxometry using GE with different echo times [6, 12, 20, 30, 45, 60]

Also in this area, DWI sequences allow the estimation of local axonal depletion and provide the data required to track SN dopaminergic fibres, as recently proposed in medium-field MR studies [16]. Also at this level, tractographic techniques suffer from scarce spatial resolution and from susceptibility artefacts induced by surrounding structures and by the iron deposits themselves, which reflect disease progression.

16.1.3 Cortical Level

16.1.3.1 Low- and Medium-Field MR

As illustrated above, the prefrontal cortical changes induced by PD are essentially functional and are a consequence of dopaminergic deafferentation in the basal ganglia. The altered cortical activity, i.e. the functional deafferentation due to the dysfunction of striatofrontal circuits, would be the cause of the motor and cognitive deficits characteristic of PD. The classic scheme of Alexander et al. describes the different parallel, independent and recurrent striatofrontal circuits connecting specific prefrontal cortical areas with specific striatal and pallidal regions [2]. Evidence of dementia-like cognitive deterioration in some PD patients in the course of disease suggests that the functional changes in the striatocortical circuits progress towards brain atrophy. The recent introduction of cerebral cortex quantification techniques (voxel-based morphometry) using volumetric acquisitions has not provided univocal data in PD patients in terms of factors predictive of dementia. For instance, some researchers have observed a reduction in the volume of the frontal cortex [6] and others of the hippocampal cortex, superior temporal gyrus and cingulum in non-demented PD patients [29]. MR morphological studies of the cortex are therefore scarcely informative in this disorder, whereas functional investigations using PET, SPECT and functional MR imaging (fMRI) have confirmed the hypothesis of motor and cognitive cortical functional deafferentation.

The early fMRI studies of patients with PD performing a simple motor task have clearly demonstrated reduced activation (reflected in reduced regional cerebral blood flow) at the level of the main cortical regions that receive afferents from the basal ganglia: supplementary motor area (SMA) [14, 18, 20, 21], dorsolateral prefrontal cortex [14, 18, 24] and anterior cingulate gyrus [14, 18]. In the same patients, other cortical areas, functionally related to the former, exhibited increased activation: primary sensorimotor, lateral premotor, and parietal cortex [18]. It has been demonstrated that reduction in SMA activity is sensitive to dopaminergic drugs in that it is detected in PD patients not receiving treatment and regresses with therapy administered in the acute phase [20], whereas it is not observed in those receiving chronic dopaminergic treatment [21]. In the first fMRI study of PD patients [23], the authors documented a complex cortical activation during a motor task, confirming on the one hand the results obtained with nuclear medicine techniques [18, 20] showing reduced activation of the rostral portion of SMA, and on the other evidencing increased activation in the caudal portion of SMA, anterior cingulum and primary sensorimotor cortex and parietal cortical areas. This pattern of cortical activation was reversible with administration of L-dopa both at the level of the rostral SMA and of the other cortical areas, such as primary sensorimotor cortex, lateral premotor and parietal cortex [9].

Overall, these studies have demonstrated the hypothesis of reversible functional deafferentation induced by altered striatal modulation in prefrontal cortical area; this in turn is associated with a complex pattern of cortical activation with reorganization of the areas involved in the planning and execution of movements.

16.1.3.2 High-Field MR

High-field MR has opened up new prospects for the study of the functioning of striatofrontal circuits in PD. On the one hand, fMRI with EPI sequences affords greater spatial and temporal resolution (e.g. 38 slices 2 mm in thickness are acquired in 2.4 s). This enables cortical activation during simple or complex motor tasks to be studied more easily in PD patients (Fig. 16.5). In addition, fMRI data can be correlated to structural studies using dedicated protocols both at the level of the mesencephalon and of the basal ganglia (Fig. 16.5). Identification of activated cortical areas during fMRI can allow the course of corticostriatal circuit fibres to be tracked and their possible depletion in PD to be quantified. Other techniques for the quantification of the extent of deafferentation, like relaxometry and MR spectroscopy, can exploit the better SNR afforded by 3.0 T fields.

16.2 Conclusions

By virtue of greater signal intensity, susceptibility artefacts and chemical shift, 3.0 T MR imagers with advanced techniques have provided promising results for the study of PD that could not be obtained with standard magnets. Microstructural, metabolic and functional data will, as never before, contribute to the early diagnosis and follow-up of PD.

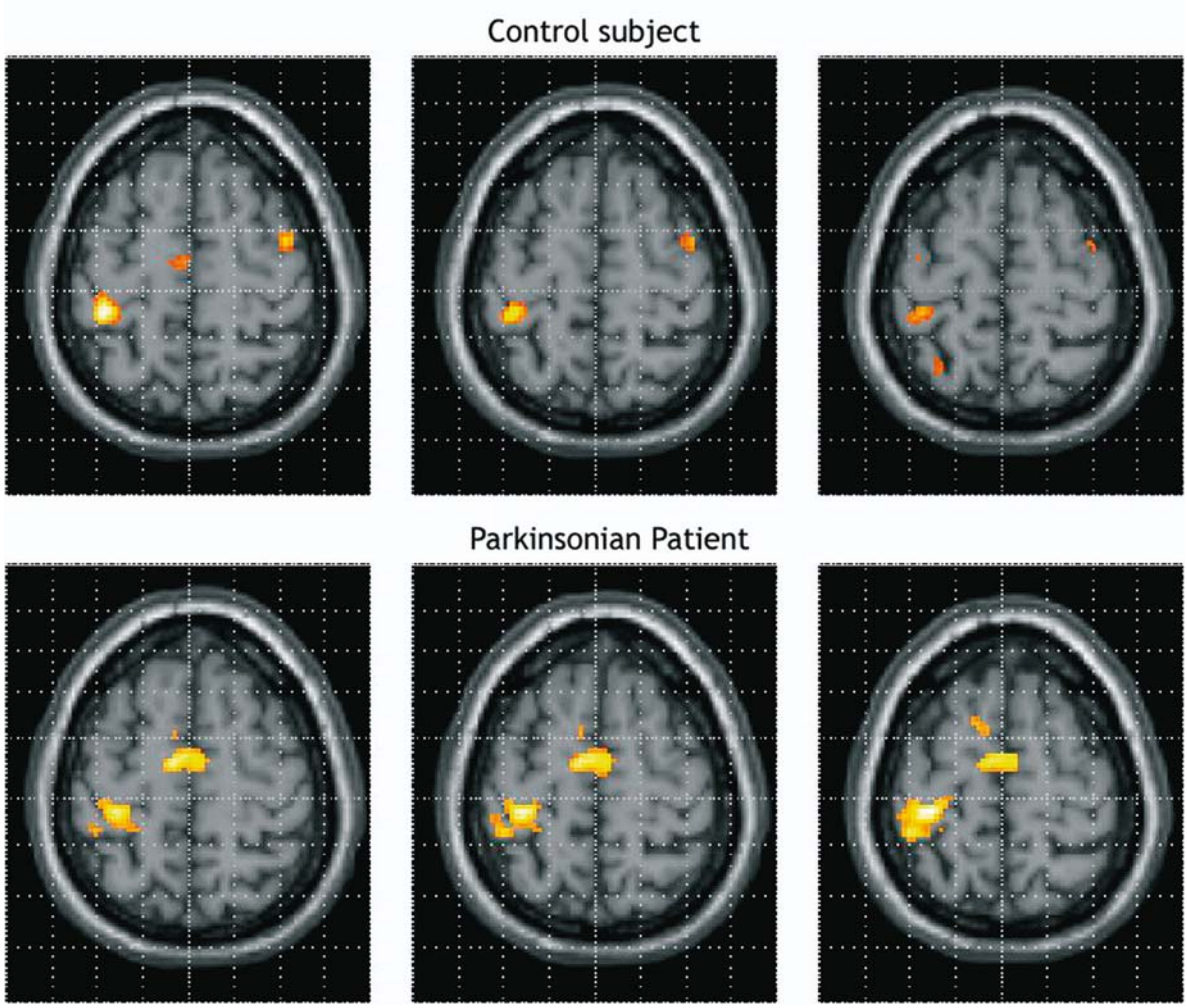

Fig. 16.5. fMRI with motor task (Siemens Allegra, 3.0 T). Hyperactivation of contralateral SMA, primary sensorimotor and premotor areas in a PD patient receiving dopaminergic therapy compared with a control subject

References

1. Adachi M, Hosoya T, Haku T, et al. (1999) Evaluation of the substantia nigra in patients with Parkinsonian syndrome accomplished using multishot diffusion-weighted MR imaging. Am J Neuroradiol 20:1500 – 1506
2. Alexander GE, DeLong MR, Strick PL (1986) Parallel organization of functionally segregated circuits linking basal ganglia and cortex. Annu Rev Neurosci 9:357 – 381
3. Antonini A, Leenders KL, Meier D, et al. (1993) T2 relaxation time in patients with Parkinson's disease. Neurology 43:697 – 700
4. Bartzokis G, Cummings JL, Markham CH, et al. (1999) MRI evaluation of brain iron in earlier- and later-onset Parkinson's disease and normal subjects. Magn Reson Imaging 17:213 – 222
5. Brooks DJ (2004) Neuroimaging in Parkinson's disease. NeuroRx 1:243 – 254
6. Burton EJ, McKeith IG, Burn DJ, et al. (2004) Cerebral atrophy in Parkinson's disease with and without dementia: a comparison with Alzheimer's disease, dementia with Lewy bodies and controls. Brain 127:791 – 800
7. Eckert T, Sailer M, Kaufmann J, et al. (2004) Differentiation of idiopathic Parkinson's disease, multiple system atrophy, progressive supranuclear palsy, and healthy controls using magnetization transfer imaging. Neuroimage 21:229 – 235
8. Graham JM, Paley MN, Grunewald RA, et al. (2000) Brain iron deposition in Parkinson's disease imaged using the PRIME magnetic resonance sequence. Brain 123(12): 2423 – 2431
9. Haslinger B, Erhard P, Kampfe N, et al. (2001) Event-related functional magnetic resonance imaging in Parkinson's disease before and after levodopa. Brain 124:558 – 570
10. Hu MT, White SJ, Herlihy AH, et al. (2001) A comparison of (18)F-dopa PET and inversion recovery MRI in the diagnosis of Parkinson's disease. Neurology 56:1195 – 1200
11. Hughes AJ, Daniel SE, Kilford L, Lees AJ (1992) Accuracy of clinical diagnosis of idiopathic Parkinson's disease: a clinico-pathological study of 100 cases. J Neurol Neurosurg Psychiatry 55:181 – 184
12. Hutchinson M, Raff U (2000) Structural changes of the substantia nigra in Parkinson's disease as revealed by MR imaging. Am J Neuroradiol 21:697 – 701
13. Hutchinson M, Raff U, Lebedev S (2003) MRI correlates of pathology in parkinsonism: segmented inversion recovery ratio imaging (SIRRIM). Neuroimage 20:1899 – 1902

14. Jahanshahi M, Jenkins IH, Brown RG, et al. (1995) Self-initiated versus externally triggered movements. I. An investigation using measurement of regional cerebral blood flow with PET and movement-related potentials in normal and Parkinson's disease subjects. Brain 118(4):913 – 933
15. Kosta P, Argyropoulou MI, Markoula S, Konitsiotis S (2005) MRI evaluation of the basal ganglia size and iron content in patients with Parkinson's disease. J Neurol (in press)
16. Lehericy S, Ducros M, Van de Moortele PF, et al. (2004) Diffusion tensor fiber tracking shows distinct corticostriatal circuits in humans. Ann Neurol 55:522 – 529
17. Oikawa H, Sasaki M, Tamakawa Y, et al. (2002) The substantia nigra in Parkinson disease: proton density-weighted spin-echo and fast short inversion time inversion-recovery MR findings. Am J Neuroradiol 23: 1747 – 1756
18. Playford ED, Jenkins IH, Passingham RE, et al. (1992) DJ impaired mesial frontal and putamen activation in Parkinson's disease: a positron emission tomography study. Ann Neurol 32:151 – 161
19. Rademacher J, Engelbrecht V, Burgel U, et al. (1999) Measuring in vivo myelination of human white matter fiber tracts with magnetization transfer MR. Neuroimage 9: 393 – 406
20. Rascol O, Sabatini U, Chollet F, et al. (1992) Supplementary and primary sensory motor area activity in Parkinson's disease. Regional cerebral blood flow changes during finger movements and effects of apomorphine. Arch Neurol 49:144 – 148
21. Rascol O, Sabatini U, Chollet F, et al. (1994) Normal activation of the supplementary motor area in patients with Parkinson's disease undergoing long-term treatment with levodopa. J Neurol Neurosurg Psychiatry 57:567 – 571
22. Ryvlin P, Broussolle E, Piollet H, et al. (1995) Magnetic resonance imaging evidence of decreased putamenal iron content in idiopathic Parkinson's disease. Arch Neurol 52: 583 – 588
23. Sabatini U, Boulanouar K, Fabre N, et al. (2000) Cortical motor reorganization in akinetic patients with Parkinson's disease: a functional MRI study. Brain 123(2):394 – 403
24. Samuel M, Ceballos-Baumann AO, Boecker H, Brooks DJ (2001) Motor imagery in normal subjects and Parkinson's disease patients: an $H_2{}^{15}O$ PET study. Neuroreport 12:821 – 828
25. Schocke MF, Seppi K, Esterhammer R, et al. (2002) Diffusion-weighted MRI differentiates the Parkinson variant of multiple system atrophy from PD. Neurology 58:575 – 580
26. Schocke MF, Seppi K, Esterhammer R, et al. (2004) Trace of diffusion tensor differentiates the Parkinson variant of multiple system atrophy and Parkinson's disease. Neuroimage 21:1443 – 1451
27. Seppi K, Schocke MF, Donnemiller E, et al. (2004) Comparison of diffusion-weighted imaging and [^{123}I]IBZM-SPECT for the differentiation of patients with the Parkinson variant of multiple system atrophy from those with Parkinson's disease. Mov Disord 19:1438 – 1445
28. Seppi K, Schocke MF, Esterhammer R, et al. (2003) Diffusion-weighted imaging discriminates progressive supranuclear palsy from PD, but not from the Parkinson variant of multiple system atrophy. Neurology 60:922 – 927
29. Summerfield C, Junque C, Tolosa E, et al. (2005) Structural brain changes in Parkinson disease with dementia: a voxel-based morphometry study. Arch Neurol 62:281 – 285
30. Ye FQ, Allen PS, Martin WR (1996) Basal ganglia iron content in Parkinson's disease measured with magnetic resonance. Mov Disord 11:243 – 249
31. Youdim MB, Riederer P (2004) A review about brain iron in normal and pathological conditions. In: Encyclopedia of neuroscience. Elsevier, Amsterdam
32. Zecca L, Youdim MB, Riederer P, et al. (2004) Iron, brain ageing and neurodegenerative disorders. Nat Rev Neurosci 5:863 – 873

High-Field 3 T Imaging of Alzheimer Disease 17

G. Luccichenti, P. Péran, A. Cherubini, E. Giugni, T. Scarabino, G. E. Hagberg, U. Sabatini

Alzheimer disease (AD) is a neurodegenerative disease with neuronal loss, leading to dementia and neurological impairment [1]. Metabolic alterations are the basis of histological changes, occurring several years before cognitive impairment. In mild cognitive impairment (MCI) functional disability is absent; conversely, in Alzheimer dementia, disease progression is faster and disability occurs.

Accurate assessment of AD is crucial for early treatment, proper differential diagnosis, prediction of disease progression and quantification of response to therapy. It should be emphasised that these four aspects are critical for development of new therapies. Currently, AD is assessed by defining dementia and neurological signs. However, these signs are non-specific and might be caused by several factors. Histology is invasive, and cannot be proposed routinely. Neuroimaging potentially represents a valuable tool for early diagnosis and follow-up [2]. Diagnostic imaging techniques for dementia are magnetic resonance (MR), and nuclear medicine techniques, such as single photon emission tomography (SPECT) and positron emission tomography (PET). These latter techniques allow brain metabolism to be assessed, which has been shown to be correlated with neuronal loss. Nuclear imaging techniques are expensive, invasive, with poor spatial resolution and will not be mentioned in this paper.

Interesting results have been obtained by conventional and advanced neuroimaging techniques for differential diagnosis and estimation of disease progression, although these results refer to groups of patients and cannot be transferred for assessing single patients [3]. Hence, it should be pointed out that two different approaches for discussing results of AD neuroimaging are possible. The first one is to discuss results obtained from groups of patients in experimental settings. The second approach is to discuss the clinical applications of these techniques.

Magnetic resonance represents the most practical tool for assessing dementia. MR allows quantitative estimation of brain features in a non-invasive way through conventional and advanced techniques, such as brain morphometry, volume estimation, diffusion weighted imaging (DWI), diffusion tensor imaging (DTI), magnetization transfer, relaxometry, perfusion weighted imaging (PWI), MR spectroscopy, and functional MR. These advanced techniques are affected by the amount of information which is provided by the scanner (e.g. signal to noise ratio, SNR) and require data post-processing. In MR, signal depends on the amount of protons recruited by the magnetic field. The larger the amount of recruited protons, the greater the increase in signal with higher SNR (keeping other parameters constant). The development of high-field scanners has seen increased interest in the medical community, and they have been proposed for routine clinical imaging.

The aim of this paper is to describe neuroimaging in MCI and AD and the potential role of high-field 3 T MR scanners in research and clinical applications.

17.1 Rationale in Imaging Neurodegenerative Diseases

In order to focus on problems of imaging neurodegenerative diseases, it might be useful to start from some basic observations on such diseases, correlating pathology with diagnostic imaging.

Generally, neuropsychological impairment of neurodegenerative diseases is due to biochemical alterations, structural abnormalities and circuit impairment, which are interrelated. Biochemical changes occur earlier than histological and macroscopic alterations, preceding clinical symptoms. In AD, neuronal loss is more prominent in temporal and parietal lobes, particularly in entorhinal cortex, hippocampus and amygdala, with volume reduction of brain and enlargement of cerebrospinal fluid spaces (CSF) [4]. Areas of neuronal loss vary according to the underlying disease: AD patients have significantly smaller left temporal lobes and parahippocampal gyri than those with dementia with Lewy bodies [5–7]. In addition, volume loss and cognitive impairment have been shown to be associted with genotype, particularly with APOE epsilon4 allele [8–12]. Volume loss of hippocampal formation, which correlates with functional impairment, has been observed in preclinical AD patients, and volume loss rate is predictive of disease progression [13–18].

The volume of entorhinal cortex predicts development of AD [19–21]. In addition, and as a consequence of neuronal loss, there is a deafferentation with degeneration of white matter (WM) and reduction of connectivity between cerebral regions. Basal ganglia ferritin iron levels are increased in AD [22].

In clinical settings, a standard MR protocol in neurodegenerative disease includes T1, proton density (PD) and T2 weighted images in at least axial and coronal planes. Fast-fluid inversion recovery (fast FLAIR) sequences can replace PD images. Three-dimensional T1-weighted scans, as magnetization prepared gradient echo (MPRAGE) sequences, are essential for assessing brain atrophy.

Routine MR imaging investigates gross structural changes only, allowing the assessment of brain atrophy and differential diagnosis with other diseases causing dementia. MR is crucial for excluding tumours, infectious and inflammatory diseases, providing two items of information: whether chronic ischaemic damage is present, which is included in the differential diagnosis of dementia, and a qualitative appraisal of brain atrophy by visually assessing enlargement of perivascular and subarachnoid spaces (Fig. 17.1). Visual assessment has been proven to be specific in differential diagnosis between AD and other dementia, particularly if combined with neuropsychological assessment [23]. However, in assessing single individuals, visual estimation of brain atrophy in the early stages may be not sensitive and specific enough, because atrophy occurs when dementia signs are already present. In addition, in single patients, brain atrophy is not predictive of disease progression and does not provide an accurate quantification of potential response to therapy. Hypointense signal in basal ganglia is often present in gradient echo and PD-T2 images due to accumulation of calcium and iron. Subcortical hyperintense lesions in T2-weighted images can be present and should be considered as ischaemic damage, which is superimposed on brain atrophy, and are not associated with but contribute to cognitive impairment [24–26]. Periventricular hyperintense areas in T2-weighted images should be considered as atrophic damage and are not associated with vascular risk and dementia [25, 27].

In summary, in single individuals conventional MR does not allow early and accurate diagnosis, prediction of disease progression or quantification of potential response to therapy. Based on such findings, indications for conventional MR imaging can be as follows:

1. To do differential diagnosis with other dementia.
2. To identify concurrent diseases that may induce dementia.

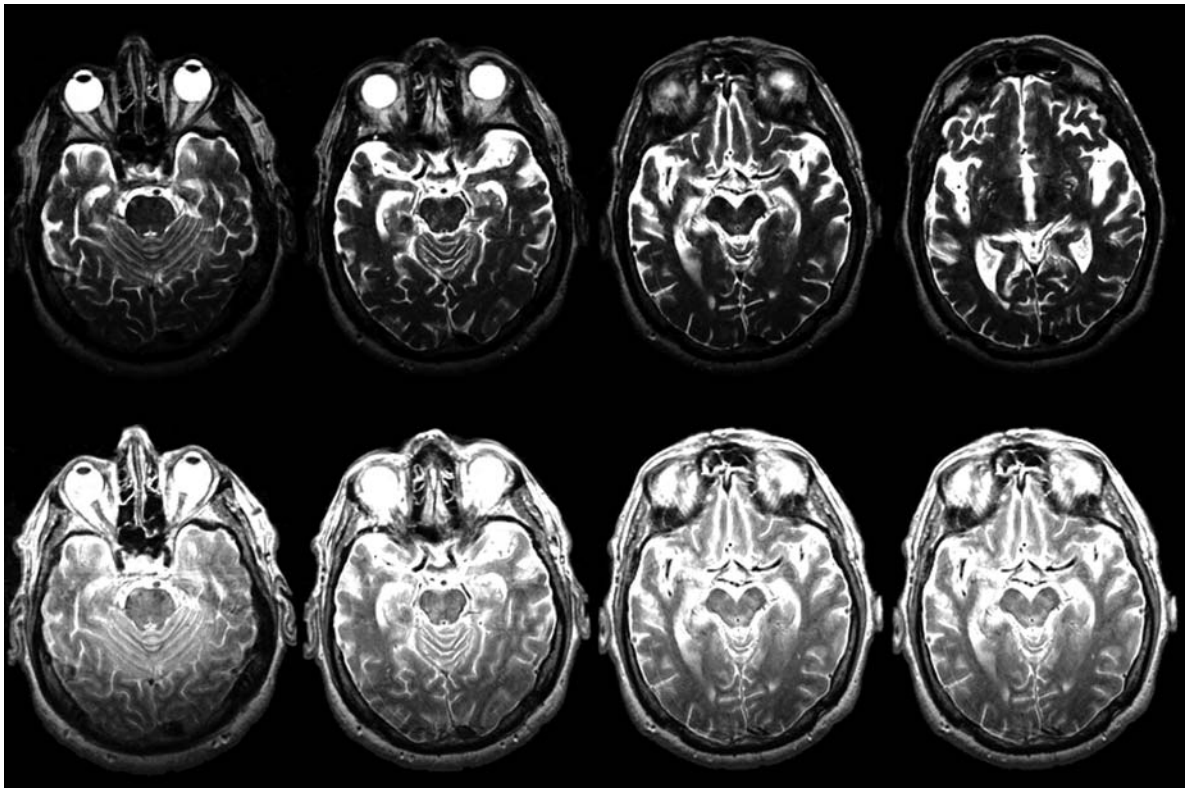

Fig. 17.1. Axial T2-weighted images obtained with a 3 T MR scanner at different levels showing moderate brain atrophy with enlargement of subarachnoid spaces and ventricles

3. To quantify brain atrophy. This is performed in daily practice by subjective visual estimation but precise estimation can also be carried out using automated tools.
4. To perform early diagnosis of degenerative disease.

The latter aim is challenging because early changes in degenerative diseases are clinically silent and patients undergo MRI only if at least mild cognitive impairment (MCI) is present. On the other hand, conventional techniques have a low sensitivity for mild volume loss: only gross structural changes are assessed in routine practice. As a result, routine MR neuroimaging is unsuitable for the latter points.

17.2 Advanced Magnetic Resonance Techniques

Subtle changes in several different indicators can be investigated through the use of advanced MR techniques.

Molecular and metabolic imaging with MR spectroscopy quantifies several biochemical markers. AD is associated with decreased metabolism of the brain. MR spectroscopy (Fig. 17.2) shows a reduction of *N*-acetylaspartate over time before volume reduction occurs [28–31], and an increase in *myo*-inositol [32, 33], suggesting these markers are predictors of cognitive impairment [34]. However, MRS techniques are limited by poor spatial resolution, and precise quantification is cumbersome. In addition, unless absolute quantification is performed, no references exist and the voxel values are expressed through ratios within and between voxels.

Diffusion weighted imaging depicts random motion of water molecules, which varies according to the number of microscopic structures hindering this motion. Diffusion is restricted in cytotoxic oedema, in which water goes from interstitium to intracellular spaces, where diffusion is hindered, reducing the size of the interstitium. Diffusion is abnormal in AD due to neuronal loss [35, 36], although this finding has not always been confirmed [37]. In addition to simple quantification of water motion, gradient-encoded sequences measure water diffusion in several directions. Using these spatially encoded diffusion weighted images, preferential diffusion direction (diffusion anisotropy) can be obtained. From these data, a diffusion tensor for each voxel can be generated. This technique is called diffusion tensor imaging and is the basis of fibre tracking techniques. Fibre tracking techniques reconstruct nervous pathways by connecting tensors, assuming that preferential direction of water diffusion is parallel to nervous bundles. In degenerative diseases, diffuse degeneration has at least two effects. The first is to reduce the size of the nerve bundles, which are then represented using a lower number of „virtual fibres“. The second is that interstitial space size is slightly increased, thus reducing structure density, causing anisotropic diffusion. In AD diffusion anisotropy is reduced [38]. The reduction of diffusion anisotropy reduces the capability of fibre tracking to identify pathways and to connect cerebral areas. In other words, connectivity measured through fibre tracking techniques may represent a surrogate indicator of brain connectivity [39]. Theoretically, after functional impairment, microanatomical connectivity between cerebral regions is the next alteration before clear cerebral atrophy occurs.

Magnetic resonance perfusion is based on signal changes during the passage of contrast material or

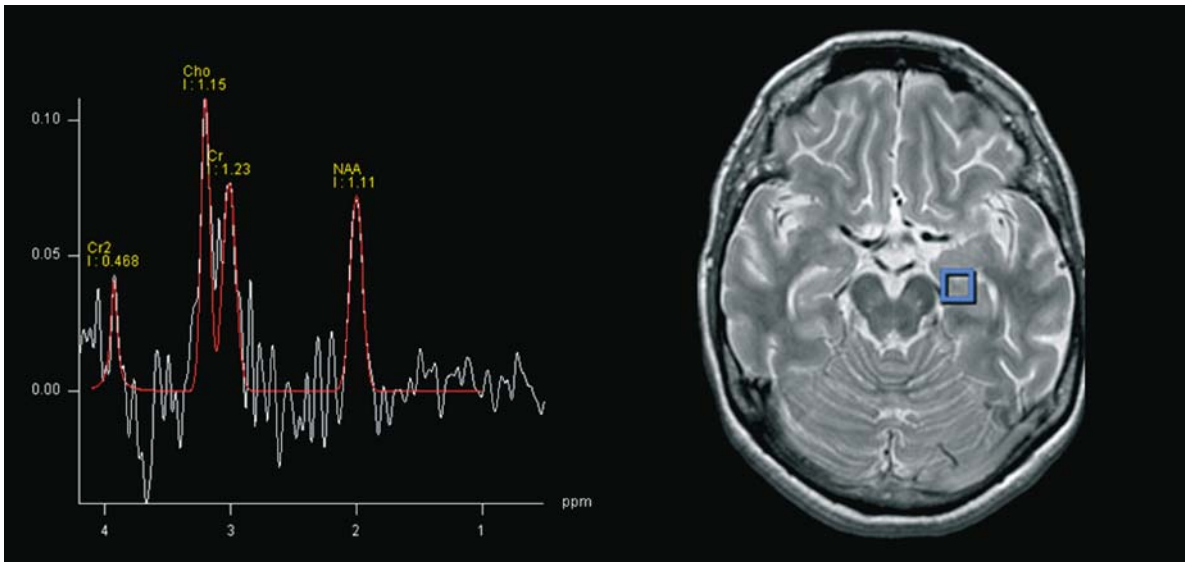

Fig. 17.2. MR spectroscopy obtained with a 3 T MR scanner with a TE=135 ms sequence, clearly showing the reduction of *N*-acetylaspartate/creatine peak ratios compared to normal individuals

spin-labelled protons through a slice with a T2* weighted scan. A significant blood flow reduction has been observed in AD patients in respect to healthy controls [40, 41].

Several other MR techniques might be useful indicators of microstructural changes. Magnetization transfer is based on signal loss induced by macromolecules. MT ratios in the hippocampus and cortical grey matter are significantly lower in patients with AD than in those with non-AD dementia and in control subjects [35, 42 – 44].

Absolute T1 and T2 maps may be useful to increase reproducibility and to perform comparisons over time. In addition, relaxation values have been used for automatic segmentation of brain structures, which is particularly useful for quantifying atrophy.

Estimation of brain atrophy and volume of entorhinal cortex, hippocampus and amygdala have been extensively investigated though a variety of techniques [45 – 50]. In fact, this is a post-analysis technique, requiring a suitable image data set. These data sets are represented by conventional morphological high resolution images. Three-dimensional gradient echo-based sequences are used. Image weightening varies according to the structure being studied. For instance, amygdala has been defined on high-resolution T1-, T2- or diffusion weighted images; these latter have been shown to be the most suitable ones for identifying the layers of this small inner structure [51]. Manual segmentation is practical for assessing the volume of amygdala, which is reduced in AD. Semiautomatic and automatic segmentation procedures are under investigation in order to increase reproducibility [52, 53]. There is a very high correlation between hippocampal volumes measured through MR and neuronal numbers in histology, showing that accurate volumetric measurements of the whole hippocampal formation can be obtained by using MR [54]. Voxel-based morphometry (VBM), based on T1 images (MPRAGE sequence), estimates, using a statistical approach, areas in which neuronal loss is prominent by comparing patients with a reference control group [55]. In addition, patients can be monitored over time in order to assess atrophy progression rate [56 – 58]. Components of the brain (white matter, grey matter, cerebrospinal fluid and other tissues) are segmented automatically and relative volume loss is assessed for brain areas [59 – 61]. Corrections with intracranial total volume can be done in order to reduce interindividual variability, although intracranial volume is not associated with AD [62, 63]. Estimation of brain atrophy can help to predict conversion from MCI to AD [57, 64]. Comparison over time of atrophy after registration of serial MRI has been shown to be a potentially powerful method with which to monitor progression of AD in clinical trials [65, 66]. Cortical pattern matching (CPM) is a more accurate method, in which homologous areas of the brain are compared between two groups. CPM uses brain sulci as references for defining homologous areas of the brain, overcoming interindividual variability of brain anatomy [67].

Differences of extension and signal intensity of cortical activation in fMRI were observed between MCI, AD patients and control groups [68, 69], and between groups of patients with different phenotypes [8, 70]. Functional MRI might provide substantial information for assessing disease progression in groups and predicting neuromodulation and effects of drugs. However, group analysis results can hardly be transferred in single individuals for clinical routine. Hardware should be suitable for such investigations, operators should be experienced in fMRI, and image scanning and analysis are expensive for uncertain responses.

17.3 Advantages of 3 T Scanning

By recruiting a larger amount of protons, a high magnetic field strength supplies more signal, in keeping other scan parameters constant. Put in simple words, 3 T scanners have the following three advantages over conventional magnets: (1) they increase signal, spatial resolution or scan time, respectively, by keeping other parameters constant; (2) they enhance susceptibility effects (T2* effects), which are useful for assessing blood products and for the blood oxygenated level dependent (BOLD) technique (on which fMRI is based); and (3) they increase the chemical shift effect, which is the basis of MR spectroscopic techniques.

As shown in the previous paragraph, subjective assessment of conventional MR imaging of gross anatomy supplies information for differential diagnosis, but neither quantification nor preclinical diagnosis is possible. On the other hand, increasing spatial resolution with 3T does not supply additional information concerning changes which might be useful for quantification or preclinical diagnosis. For instance, by keeping constant other scanning parameters, voxel volume can be reduced by half, which is far from the spatial resolution that is theoretically required for imaging microstructures.

Three-tesla scanners, by enhancing T2* effects, might be more sensitive in depicting deposits of iron and calcium, which are frequent in neurodegenerative disorders; however, no work has been carried out to assess how this theoretical advantage may be useful in clinical routine, keeping in mind that quantification and sensitivity are the ultimate aims. Biochemical and structural changes in AD are associated with functional impairment, which can be investigated through fMRI. Functional MRI benefits from increased SNR and T2* effects: the BOLD technique is more sensitive

and sampling frequency can be increased, allowing more accurate event-related experiments.

Enhancing chemical shift phenomenon increases spectral resolution, which is the capability to discern two metabolites in MRS. Biochemical alterations occur early in disease before atrophy, and change more rapidly than morphology. Hence MRS may represent a sensitive and specific tool for assessing early disease and early response to therapy. Potential drawbacks of high-field magnets are represented by magnetic field inhomogeneity in specific regions that are close to air interfaces, such as in the temporal lobe region, which is close to petrous bone and sphenoid sinuses.

Three-tesla scanners allow advanced imaging of degenerative diseases to be performed faster than conventional 1.5 T magnets, thus potentially allowing the assessment with combined techniques [71]. High-field systems enhance the capabilities of advanced imaging techniques, thus increasing the sensitivity and specificity for early diagnosis and quantification of therapy response. Furthermore, 3 T scanners might potentially be useful for transferring results obtained from group studies in experimental settings to routine clinical settings.

References

1. McKhann G, Drachman D, Folstein M, et al. (1984) Clinical diagnosis of Alzheimer's disease: report of the NINCDS-ADRDA Work Group under the auspices of Department of Health and Human Services Task Force on Alzheimer's Disease. Neurology 34:939 – 944
2. Chetelat G, Baron JC (2003) Early diagnosis of Alzheimer's disease: contribution of structural neuroimaging. Neuroimage 18:525 – 541
3. Celsis P (2000) Age-related cognitive decline, mild cognitive impairment or preclinical Alzheimer's disease? Ann Med 32:6 – 14
4. Callen DJ, Black SE, Gao F, et al. (2001) Beyond the hippocampus: MRI volumetry confirms widespread limbic atrophy in AD. Neurology 57:1669 – 1674
5. Harvey GT, Hughes J, McKeith IG, et al. (1999) Magnetic resonance imaging differences between dementia with Lewy bodies and Alzheimer's disease: a pilot study. Psychol Med 29:181 – 187
6. Barber R, Ballard C, McKeith IG, et al. (2000) MRI volumetric study of dementia with Lewy bodies: a comparison with AD and vascular dementia. Neurology 54:1304 – 1309
7. Barber R, McKeith IG, Ballard C, et al. (2001) A comparison of medial and lateral temporal lobe atrophy in dementia with Lewy bodies and Alzheimer's disease: magnetic resonance imaging volumetric study. Dement Geriatr Cogn Disord 12:198 – 205
8. Bookheimer SY, Strojwas MH, Cohen MS, et al. (2000) Patterns of brain activation in people at risk for Alzheimer's disease. N Engl J Med 343:450 – 456
9. Juottonen K, Lehtovirta M, Helisalmi S, et al. (1998) Major decrease in the volume of the entorhinal cortex in patients with Alzheimer's disease carrying the apolipoprotein E epsilon4 allele. J Neurol Neurosurg Psychiatry 65:322 – 327
10. Geroldi C, Laakso MP, DeCarli C, et al. (2000) Apolipoprotein E genotype and hippocampal asymmetry in Alzheimer's disease: a volumetric MRI study. J Neurol Neurosurg Psychiatry 68:93 – 96
11. Moffat SD, Szekely CA, Zonderman AB, et al. (2000) Longitudinal change in hippocampal volume as a function of apolipoprotein E genotype. Neurology 55:134 – 136
12. Hashimoto M, Yasuda M, Tanimukai S, et al. (2001) Apolipoprotein E epsilon 4 and the pattern of regional brain atrophy in Alzheimer's disease. Neurology 57:1461 – 1466
13. Fox NC, Warrington EK, Freeborough PA, et al. (1996) Presymptomatic hippocampal atrophy in Alzheimer's disease. A longitudinal MRI study. Brain 119(6):2001 – 2007
14. Jack CR Jr, Petersen RC, Xu Y, et al. (2000) Rates of hippocampal atrophy correlate with change in clinical status in aging and AD. Neurology 55:484 – 489
15. Mizuno K, Wakai M, Takeda A, Sobue G (2000) Medial temporal atrophy and memory impairment in early stage of Alzheimer's disease: an MRI volumetric and memory assessment study. J Neurol Sci 173:18 – 24
16. Petersen RC, Jack CR Jr, Xu YC, et al. (2000) Memory and MRI-based hippocampal volumes in aging and AD. Neurology 54:581 – 587
17. Gosche KM, Mortimer JA, Smith CD, et al. (2002) Hippocampal volume as an index of Alzheimer neuropathology: findings from the Nun Study. Neurology 58:1476 – 1482
18. Jack CR Jr, Dickson DW, Parisi JE, et al. (2002) Antemortem MRI findings correlate with hippocampal neuropathology in typical aging and dementia. Neurology 58: 750 – 757
19. Killiany RJ, Hyman BT, Gomez-Isla T, et al. (2002) MRI measures of entorhinal cortex vs hippocampus in preclinical AD. Neurology 58:1188 – 1196
20. Du AT, Schuff N, Zhu XP, et al. (2003) Atrophy rates of entorhinal cortex in AD and normal aging. Neurology 60: 481 – 486
21. Du AT, Schuff N, Kramer JH, et al. (2004) Higher atrophy rate of entorhinal cortex than hippocampus in AD. Neurology 62:422 – 427
22. Bartzokis G, Sultzer D, Cummings J, et al. (2000) In vivo evaluation of brain iron in Alzheimer disease using magnetic resonance imaging. Arch Gen Psychiatry 57:47 – 53
23. Wahlund LO, Julin P, Johansson SE, Scheltens P (2000) Visual rating and volumetry of the medial temporal lobe on magnetic resonance imaging in dementia: a comparative study. J Neurol Neurosurg Psychiatry 69:630 – 635
24. Hirono N, Kitagaki H, Kazui H, et al. (2000) Impact of white matter changes on clinical manifestation of Alzheimer's disease: A quantitative study. Stroke 31:2182 – 2188
25. Barber R, Gholkar A, Scheltens P, et al. (2000) MRI volumetric correlates of white matter lesions in dementia with Lewy bodies and Alzheimer's disease. Int J Geriatr Psychiatry 15:911 – 916
26. Mungas D, Jagust WJ, Reed BR, et al. (2001) MRI predictors of cognition in subcortical ischemic vascular disease and Alzheimer's disease. Neurology 57:2229 –2235
27. Smith CD, Snowdon DA, Wang H, Markesbery WR (2000) White matter volumes and periventricular white matter hyperintensities in aging and dementia. Neurology 54: 838 – 842
28. Adalsteinsson E, Sullivan EV, Kleinhans N, et al. (2000) Longitudinal decline of the neuronal marker *N*-acetyl aspartate in Alzheimer's disease. Lancet 355:1696 – 1697
29. De Stefano N, Mortilla M, Federico A (1999) Proton magnetic resonance spectroscopy of the brain in dementia. Ital J Neurol Sci 20:S258 – 264
30. Jessen F, Block W, Traber F, et al. (2000) Proton MR spectroscopy detects a relative decrease of *N*-acetylaspartate in the medial temporal lobe of patients with AD. Neurology 55:684 – 688

31. Schuff N, Capizzano AA, Du AT, et al. (2002) Selective reduction of *N*-acetylaspartate in medial temporal and parietal lobes in AD. Neurology 58:928 – 935
32. Huang W, Alexander GE, Chang L, et al. (2001) Brain metabolite concentration and dementia severity in Alzheimer's disease: a (1)H MRS study. Neurology 57:626 – 632
33. Valenzuela MJ, Sachdev P (2001) Magnetic resonance spectroscopy in AD. Neurology 56:592 – 598
34. Kantarci K, Smith GE, Ivnik RJ, et al. (2002) 1H magnetic resonance spectroscopy, cognitive function, and apolipoprotein E genotype in normal aging, mild cognitive impairment and Alzheimer's disease. J Int Neuropsychol Soc 8:934 – 942
35. Bozzali M, Franceschi M, Falini A, et al. (2001) Quantification of tissue damage in AD using diffusion tensor and magnetization transfer MRI. Neurology 57:1135 – 1137
36. Kantarci K, Jack CR Jr, Xu YC, et al. (2001) Mild cognitive impairment and Alzheimer disease: regional diffusivity of water. Radiology 219:101 – 107
37. Bozzao A, Floris R, Baviera ME, et al. (2001) Diffusion and perfusion MR imaging in cases of Alzheimer's disease: correlations with cortical atrophy and lesion load. AJNR Am J Neuroradiol 22:1030 – 1036
38. Takahashi S, Yonezawa H, Takahashi J, et al. (2002) Selective reduction of diffusion anisotropy in white matter of Alzheimer disease brains measured by 3.0 Tesla magnetic resonance imaging. Neurosci Lett 332:45 – 48
39. Rose SE, Chen F, Chalk JB, et al. (2000) Loss of connectivity in Alzheimer's disease: an evaluation of white matter tract integrity with colour coded MR diffusion tensor imaging. J Neurol Neurosurg Psychiatry 69:528 – 530
40. Alsop DC, Detre JA, Grossman M (2000) Assessment of cerebral blood flow in Alzheimer's disease by spin-labeled magnetic resonance imaging. Ann Neurol 47:93 – 100
41. Johnson NA, Jahng GH, Weiner MW, et al. (2005) Pattern of cerebral hypoperfusion in Alzheimer disease and mild cognitive impairment measured with arterial spin-labeling MR imaging: initial experience. Radiology 234:851 – 859
42. Hanyu H, Asano T, Iwamoto T, et al. (2000) Magnetization transfer measurements of the hippocampus in patients with Alzheimer's disease, vascular dementia, and other types of dementia. AJNR Am J Neuroradiol 21: 1235 – 1242
43. Hanyu H, Asano T, Sakurai H, et al. (2001) Magnetization transfer measurements of the hippocampus in the early diagnosis of Alzheimer's disease. J Neurol Sci 188:79 – 84
44. Kabani NJ, Sled JG, Chertkow H (2002) Magnetization transfer ratio in mild cognitive impairment and dementia of Alzheimer's type. Neuroimage 15:604 – 610
45. Xu Y, Jack CR Jr, O'Brien PC, et al. (2000) Usefulness of MRI measures of entorhinal cortex versus hippocampus in AD. Neurology 54:1760 – 1767
46. Frisoni GB, Geroldi C, Beltramello A, et al. (2002) Radial width of the temporal horn: a sensitive measure in Alzheimer disease. AJNR Am J Neuroradiol 23:35 – 47
47. Hsu YY, Schuff N, Du AT, et al. (2002) Comparison of automated and manual MRI volumetry of hippocampus in normal aging and dementia. J Magn Reson Imaging 16:305 – 310
48. Gunter JL, Shiung MM, Manduca A, Jack CR Jr (2003) Methodological considerations for measuring rates of brain atrophy. J Magn Reson Imaging 18:16 – 24
49. Desphande NA, Gao FQ, Bakshi SN, et al. (2004) Simple linear and area MR measurements can help distinguish between Alzheimer's disease, frontotemporal dementia, and normal aging: the Sunnybrook dementia study. Brain Cogn 54:165 – 166
50. Stoub TR, Bulgakova M, Leurgans S, et al. (2005) MRI predictors of risk of incident Alzheimer disease: a longitudinal study. Neurology 64:1520 – 1524
51. Adachi M, Kawakatsu S, Hosoya T, et al. (2003) Morphology of the inner structure of the hippocampal formation in Alzheimer disease. AJNR Am J Neuroradiol 24:1575 – 1581
52. Gosche KM, Mortimer JA, Smith CD, et al. (2001) An automated technique for measuring hippocampal volumes from MR imaging studies. AJNR Am J Neuroradiol 22: 1686 – 1689
53. Barra V, Frenoux E, Boire JY (2002) Automatic volumetric measurement of lateral ventricles on magnetic resonance images with correction of partial volume effects. J Magn Reson Imaging 15:16 – 22
54. Bobinski M, de Leon MJ, Wegiel J, et al. (2000) The histological validation of post mortem magnetic resonance imaging-determined hippocampal volume in Alzheimer's disease. Neuroscience 95:721 – 725
55. Pennanen C, Testa C, Laakso MP, et al. (2005) A voxel based morphometry study on mild cognitive impairment. J Neurol Neurosurg Psychiatry 76:11 – 14
56. Fox NC, Crum WR, Scahill RI, et al. (2001) Imaging of onset and progression of Alzheimer's disease with voxel-compression mapping of serial magnetic resonance images. Lancet 358:201 – 205
57. Chetelat G, Landeau B, Eustache F, et al. (2005) Using voxel-based morphometry to map the structural changes associated with rapid conversion in MCI: A longitudinal MRI study. Neuroimage (in press)
58. Schott JM, Price SL, Frost C, et al. (2005) Measuring atrophy in Alzheimer disease: a serial MRI study over 6 and 12 months. Neurology 65:119 – 124
59. Baron JC, Chetelat G, Desgranges B, et al. (2001) In vivo mapping of gray matter loss with voxel-based morphometry in mild Alzheimer's disease. Neuroimage 14:298 – 309
60. Thompson PM, Mega MS, Woods RP, et al. (2001) Cortical change in Alzheimer's disease detected with a disease-specific population-based brain atlas. Cereb Cortex 11:1 – 16
61. Karas GB, Burton EJ, Rombouts SA, et al. (2003) A comprehensive study of gray matter loss in patients with Alzheimer's disease using optimized voxel-based morphometry. Neuroimage 18:895 – 907
62. Whitwell JL, Crum WR, Watt HC, Fox NC (2001) Normalization of cerebral volumes by use of intracranial volume: implications for longitudinal quantitative MR imaging. AJNR Am J Neuroradiol 22:1483 – 1489
63. Edland SD, Xu Y, Plevak M, et al. (2002) Total intracranial volume: normative values and lack of association with Alzheimer's disease. Neurology 59:272 – 274
64. Killiany RJ, Gomez-Isla T, Moss M, et al. (2000) Use of structural magnetic resonance imaging to predict who will get Alzheimer's disease. Ann Neurol 47:430 – 439
65. Fox NC, Cousens S, Scahill R, et al. (2000) Using serial registered brain magnetic resonance imaging to measure disease progression in Alzheimer disease: power calculations and estimates of sample size to detect treatment effects. Arch Neurol 57:339 – 344
66. Crum WR, Scahill RI, Fox NC (2001) Automated hippocampal segmentation by regional fluid registration of serial MRI: validation and application in Alzheimer's disease. Neuroimage 13:847 – 855
67. Ballmaier M, O'Brien JT, Burton EJ, et al. (2004) Comparing gray matter loss profiles between dementia with Lewy bodies and Alzheimer's disease using cortical pattern matching: diagnosis and gender effects. Neuroimage 23:325 – 335
68. Johnson SC, Saykin AJ, Baxter LC, et al. (2000) The relationship between fMRI activation and cerebral atrophy:

comparison of normal aging and Alzheimer disease. Neuroimage 11:179 – 187
69. Machulda MM, Ward HA, Borowski B, et al. (2003) Comparison of memory fMRI response among normal, MCI, and Alzheimer's patients. Neurology 61:500 – 506
70. Bondi MW, Houston WS, Eyler LT, Brown GG (2005) fMRI evidence of compensatory mechanisms in older adults at genetic risk for Alzheimer disease. Neurology 64:501 – 508
71. Back T, Mockel R, Hirsch JG, et al. (2003) Combined MR measurements of magnetization transfer, tissue diffusion and proton spectroscopy. A feasibility study with neurological cases. Neurol Res 25:292 – 300

18 3.0 T Imaging of Brain Tumours

A. Di Costanzo, F. Trojsi, T. Popolizio, G. M. Giannatempo, A. Simeone, S. Pollice, D. Catapano, M. Tosetti, N. Maggialetti, V. A. d'Angelo, A. Carriero, U. Salvolini, G. Tedeschi, T. Scarabino

Conventional MRI, or CT scanning if MRI is not available or contraindicated, is the method of choice for the non-invasive assessment of suspected intracranial tumours, but has limited sensitivity and specificity [1, 2]. In the past 20 years, there have been great advances in diagnostic imaging procedures with increasing accuracy of preoperative assessment of brain neoplasms. Proton magnetic resonance spectroscopic imaging, diffusion-weighted imaging and perfusion-weighted imaging all have contributed to an improvement of sensitivity and specificity in the diagnosis and monitoring of primary brain tumours.

Proton MR spectroscopic imaging (^{1}H-MRSI) is a non-invasive technique that provides metabolic information from living tissues [3, 4]. Of the main metabolites of interest, choline (Cho) is found to be increased in areas of active membrane turnover, as in brain gliomas; *N*-acetylaspartate (NAA) is regarded as a marker of neuronal damage, destruction and/or dysfunction, and it is decreased whenever neurons are replaced by other cells; creatine (Cr) comprises signals from both phosphocreatine and creatine and is involved in energy metabolism; and lactate and/or lipids (LL) usually indicate necrosis [3, 4]. Several studies have demonstrated that ^{1}H-MRSI can be used to guide surgical resection or biopsies, to define radiotherapy planning and monitor treatment effects, and to identify recurrence and progression of brain gliomas [3–10].

Diffusion-weighted imaging (DWI) is an MR technique sensitive to molecular motion of water within brain tissue, and provides information about compositional, structural, and organizational features of biological tissues [11]. A number of studies suggest that maps of the diffusion parameter called apparent diffusion coefficient (ADC), deriving information from cellularity and structural integrity, may play a role in the evaluation of brain tumours [12–17]. However, data about the distinction between different tumour types and grades [12, 15, 16], or between tumour infiltration and vasogenic oedema [12, 17], are still conflicting.

Perfusion-weighted imaging (PWI) is an MR technique that looks into the haemodynamics of tumour tissue. The PWI measurement more frequently used is the relative cerebral blood volume (rCBV), which is directly correlated with microvessel density and tumour grade [18]. A number of studies have successfully used this technique in the preoperative classification and grading of brain tumours [18–22].

So far, all the above-mentioned MR techniques have been performed mainly using magnetic field strengths of 1.5 T. Higher magnetic field MR is expected to take advantage of the higher signal-to-noise ratio (SNR), and the improved spatial, temporal and spectral resolution [23, 24].

18.1 Glial Neoplasms

Gliomas are the most common brain tumours [25] and are divided into astrocytomas, oligodendrogliomas and ependymomas. Astrocytomas are the most frequent type of glioma and present different grades of malignancy: grades I–IV. Grades I and II are classified as low-grade gliomas, while grades III (anaplastic astrocytomas) and IV (glioblastomas) are classified as high-grade gliomas. Malignant astrocytomas (grades III and IV) are the most common subtypes, and glioblastoma multiforme, in particular, represents approximately 51 % of all CNS tumours [26]. Gliomas are extremely heterogeneous in terms of imaging appearance. They are infiltrative lesions with margins often poorly defined on both T1- and T2-weighted images [27]. Low-grade gliomas are typically non-enhancing after injection of gadolinium and are identified as a region of hypointensity on T1-weighted images and of hyperintensity on T2-weighted images. Grade III gliomas have large regions of hypointensity on T1-weighted images but may also have regions which appear bright on postcontrast T1-weighted images. Grade IV gliomas may be non-enhancing, but more frequently they have substantial regions of contrast enhancement with a central area of hypointensity that corresponds to necrosis. However, gadolinium-enhancing lesion is not always a reliable indicator of active tumour. This is due partly to the existence of tumour tissue which does not enhance, and partly to the presence of contrast-enhancing necrosis [28]. Of the astrocytic tumours, gliomatosis cerebri is a peculiar clinical and histopatholog-

ical entity, characterized by diffuse overgrowth of glial elements with infiltration of at least two and sometimes three contiguous areas of brain [29]. The distinction between gliomatosis cerebri and other diffuse infiltrating gliomas, such as multicentric glioma, has been debated [30]. However, gliomatosis cerebri refers to tumour with contiguous involvement of different regions, whereas multicentric glioma is defined as distinct foci of tumour in different sites [31]. Furthermore, gliomatosis cerebri typically lacks features found in high-grade gliomas, especially vascular proliferation and necrosis, and shows no mass effect [32].

In recent years, the combination of ^{1}H-MRSI, DWI and/or PWI in addition to conventional MRI has improved the ability to differentiate solid tumour from other intratumoral or peritumoral components [33–36]. Most of these studies have been performed at a magnetic field strength of 1.5 T. We applied such a multiparametric MR approach using a 3 T MR scanner to better characterize the large heterogeneity of brain gliomas. We evaluated 30 patients, 20 with high- and 10 with low-grade gliomas, before undergoing surgery and histologic confirmation. Normalized metabolite signals, including choline (Cho), *N*-acetylaspartate (NAA), creatine (Cr) and lactate/lipids (LL), were obtained by ^{1}H-MRSI; apparent diffusion coefficient (ADC) by DWI; and relative cerebral blood volume (rCBV) by PWI. We carefully examined the regions of interest (ROIs) surrounding the enhanced margins of tumours (perienhancing ROIs) and those surrounding the non-enhancing tumours (peritumoral ROIs), identifying peculiar multiparametric MR patterns. We divided perienhancing ROIs into two groups: ROI with abnormal signal on conventional MRI (perienhancing abnormal ROIs) and normal-appearing ROIs (perienhancing normal ROIs). The first group was further divided into three groups: presumed tumour or tumour-infiltrated („tumour“) ROIs, presumed vasogenic oedema („oedema“) ROIs and presumed tumour-infiltrated oedema („tumour/oedema“) ROIs. Perienhancing and peritumoral normal-appearing ROIs were further divided into two groups: presumed tumour-infiltrated („infiltrated“) ROIs and „normal“ ROIs.

In high-grade gliomas, „tumour“ ROIs showed an abnormal Cho/NAA ratio (> 1), with an ADC lower and rCBV higher than „oedema“ ROIs. These latter showed a normal Cho/NAA ratio, low or normal metabolite levels, and an ADC higher and rCBV lower than „tumour“ ROIs. „Tumour/oedema“ ROIs showed an abnormal Cho/NAA ratio, low metabolite levels and intermediate ADC and rCBV values (Figs. 18.1, 18.2). „Tumour“, „tumour/oedema“ and „oedema“ patterns were frequently present in the same tumour. In effect, regions of altered signal outside the enhancing margins of high-grade gliomas represent a variable combination of vasogenic oedema and infiltrating tumour cells [37]. The predominance of tumour cells produces spectra with the typical tumour pattern (i.e. with high Cho peaks and abnormal Cho/NAA ratios) [5–8], reduces ADC because of augmented cellularity [12], and increases rCBV because of incremented size and/or number of vessels [38]. If vasogenic oedema is prominent, the increase of interstitial water in normal brain [39] „dilutes“ the signal of metabolites producing normal spectra with reduced metabolite peaks [34], increases the extracellular spaces and the diffusion of water [40], and compresses the blood vessels reducing rCBV [34]. If vasogenic oedema and neoplastic cells are both predominant, spectra have the typical tumour pattern, but the metabolite signals are „diluted“, and ADC and rCBV assume intermediate values. „Infiltrated“ ROIs showed the typical tumour spectra with a high Cho and/or abnormal Cho/NAA ratio (Fig. 18.2). The finding of perienhancing tumour-infiltrated ROIs is in agreement with neuropathological studies showing tumour cells in areas well beyond the tumour margins as depicted on conventional MRI [8].

In low grade gliomas, the mass usually showed all metabolite peaks except for LL, but Cho and less frequently Cr were generally higher and NAA lower than normal (Figs. 18.3, 18.4). Peritumour „infiltrated“ ROIs showing a high Cho peak and/or an abnormal Cho/NAA and no abnormalities on conventional MRI (Fig. 18.3) were found in three patients.

We also observed a case of gliomatosis cerebri in a 43-year-old patient (Figs. 18.5, 18.6). The tumour appeared on T2-weighted images as a diffuse hyperintensity that involved the splenium of corpus callosum, and the cortex and white matter of mesial temporal lobes. In the affected ROIs, ^{1}H-MRSI showed spectra with the typical „tumour“ pattern (Fig. 18.5). After 3 months, the lesion acquired the features of malignant glioma in the right occipital lobe, with diffuse contrast enhancement and evidence of necrotic core. The multiparametric approach, with ^{1}H-MRSI, DWI and PWI, allowed the identification of areas with „tumour“ and „oedema“ patterns (Fig. 18.6).

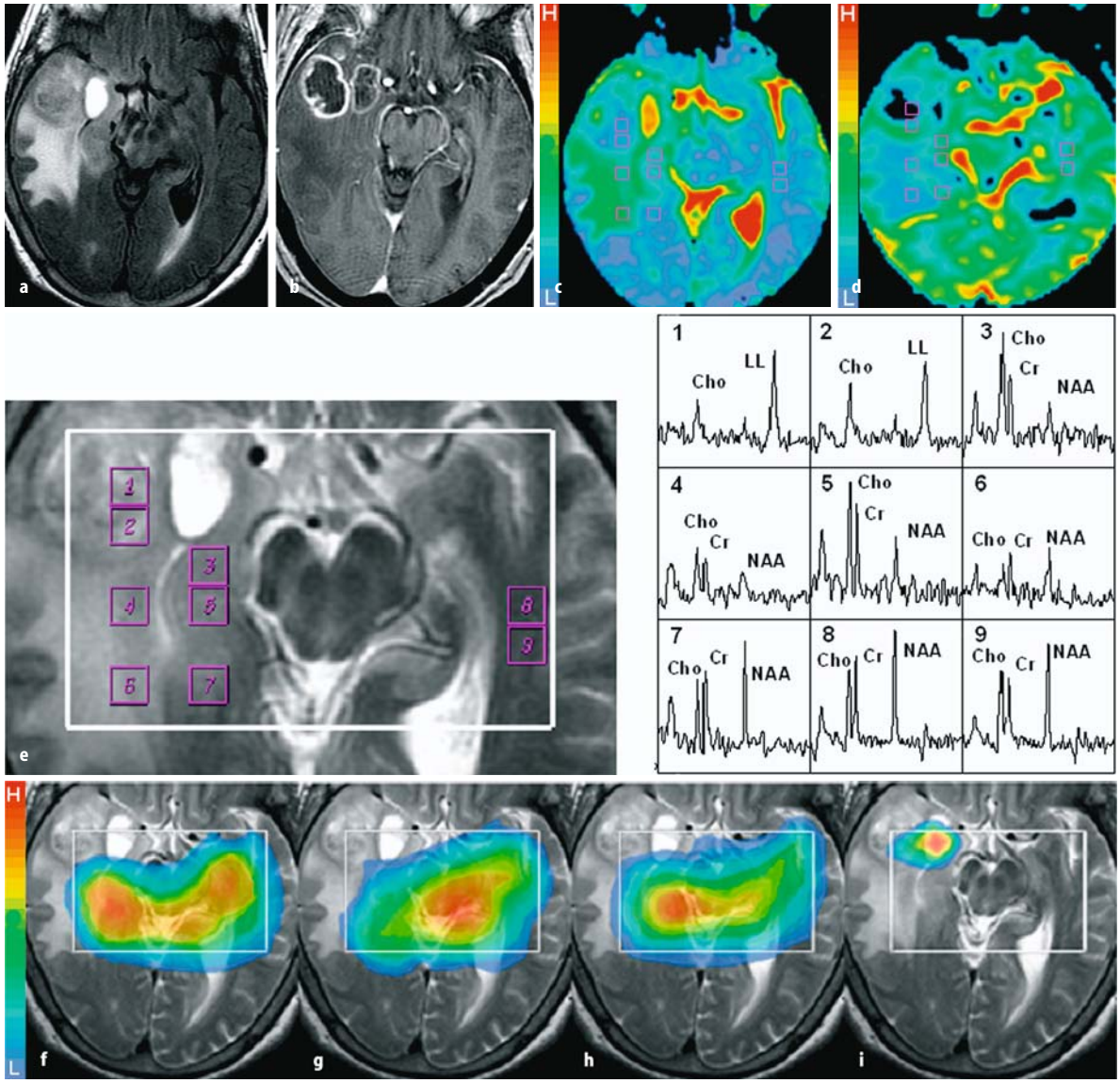

Fig. 18.1. FLAIR (**a**), contrast-enhanced T1-weighted (**b**) and T2-weighted (**e**) images, ADC (**c**), rCBV (**d**), Cho (**f**), NAA (**g**), Cr (**h**) and LL (**i**) maps, and proton MR spectra (*1–9*) from selected ROIs in a 58-year-old woman with a right temporal glioblastoma. ROIs are those with a necrotic aspect (*1, 2*); perienhancing ROIs with abnormal signal on T2-weighted images and „tumour" (*3, 5*), „tumour/oedema" (*4*) and „oedema" (*6*) multiparametric patterns; and homolateral (*7*) and contralateral (*8, 9*) normal ROIs. On the colour scale, *H* indicates the strongest signal intensity and *L* the weakest (*Cho* choline, *NAA N*-acetylaspartate, *Cr* creatine, *LL* lactate and/or lipids, *ADC* apparent diffusion coefficient, *rCBV* relative cerebral blood volume). The lesion shows two apparently necrotic regions surrounded by a ring enhancement (**b**): the medial region, which presents high signal intensity on T2-weighted and FLAIR images (**e**) and high ADC (**c**), likely represents a colliquative necrosis. Note that „tumour" ROIs show an abnormal Cho/NAA ratio (>1), Cho and rCBV higher, and ADC lower than „oedema" ROI, while „tumour/oedema" ROI presents an abnormal Cho/NAA ratio, low metabolite peaks and intermediate ADC and rCBV; necrotic ROIs show a variable level of Cho and a high LL peak

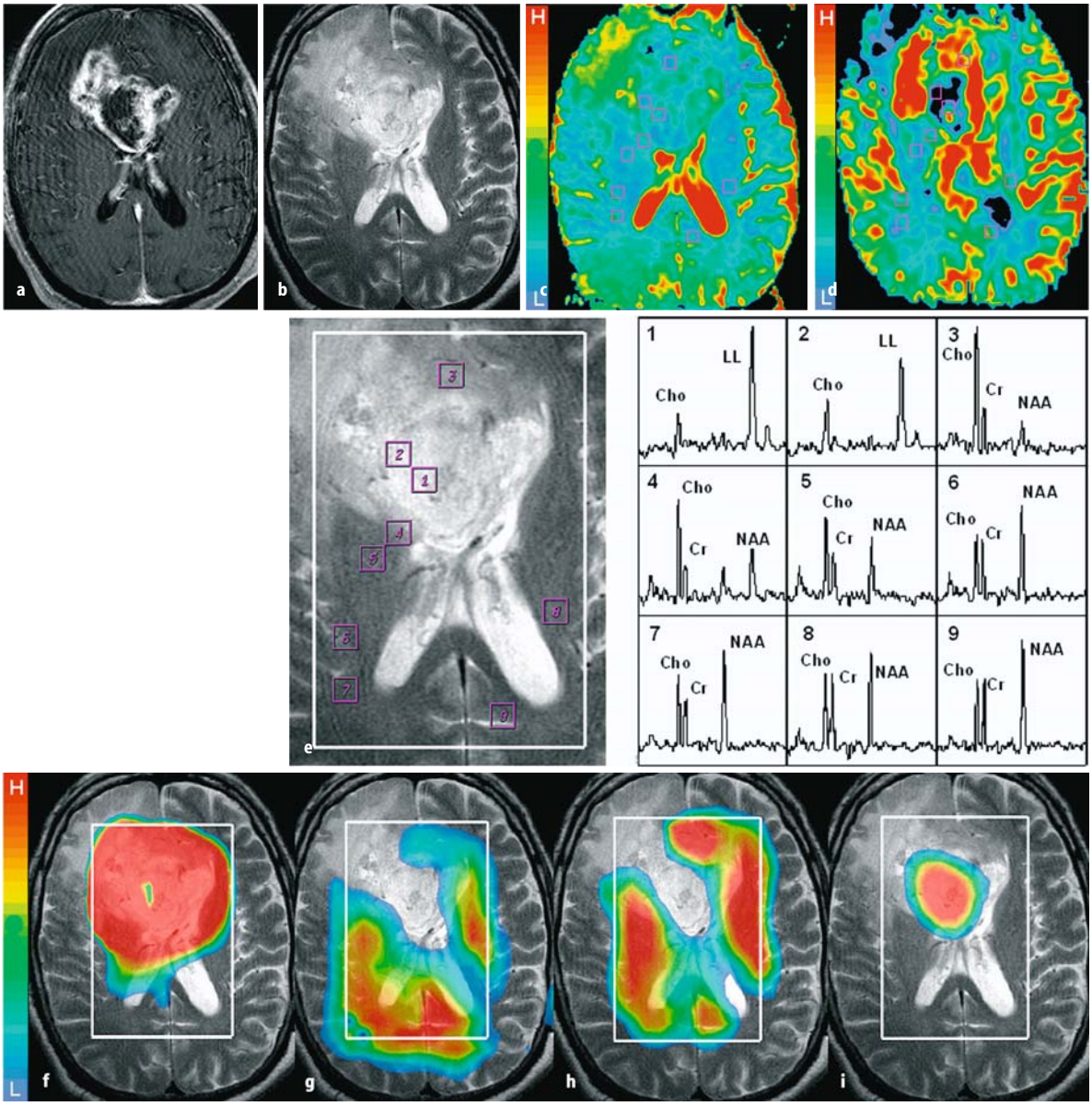

Fig. 18.2. Contrast-enhanced T1-weighted (**a**) and T2-weighted **(b, e)** images, ADC (**c**), rCBV (**d**), Cho (**f**), NAA (**g**), Cr (**h**) and LL (**i**) maps, and proton MR spectra (*1 – 9*) from selected ROIs in a 64-year-old man with a right frontal glioblastoma. ROIs are those with a necrotic aspect (*1, 2*); tumour margin (*4*); perienhancing ROIs with „tumour" (*3*) and „infiltrated" (*5*) pattern; and homolateral (*6, 7*) and contralateral (*8, 9*) normal ROIs. On the colour scale, *H* indicates the strongest signal intensity and *L* the weakest (*Cho* choline, *NAA N*-acetylaspartate, *Cr* creatine, *LL* lactate and/or lipids, *ADC* apparent diffusion coefficient, *rCBV* relative cerebral blood volume). Note that the „tumour" ROI presents multiparametric MR characteristics similar to „tumour" ROIs in Fig. 18.1 (i.e. high Cho peak, abnormal Cho/NAA ratio, low ADC and high rCBV) and an abnormal signal on T2-weighted image; the „infiltrated" ROI presents an abnormal Cho/NAA ratio (> 1), a Cho peak higher than normal ROIs and no signal abnormality on T1- and T2-weighted images; necrotic ROIs show a variable level of Cho and a high LL peak

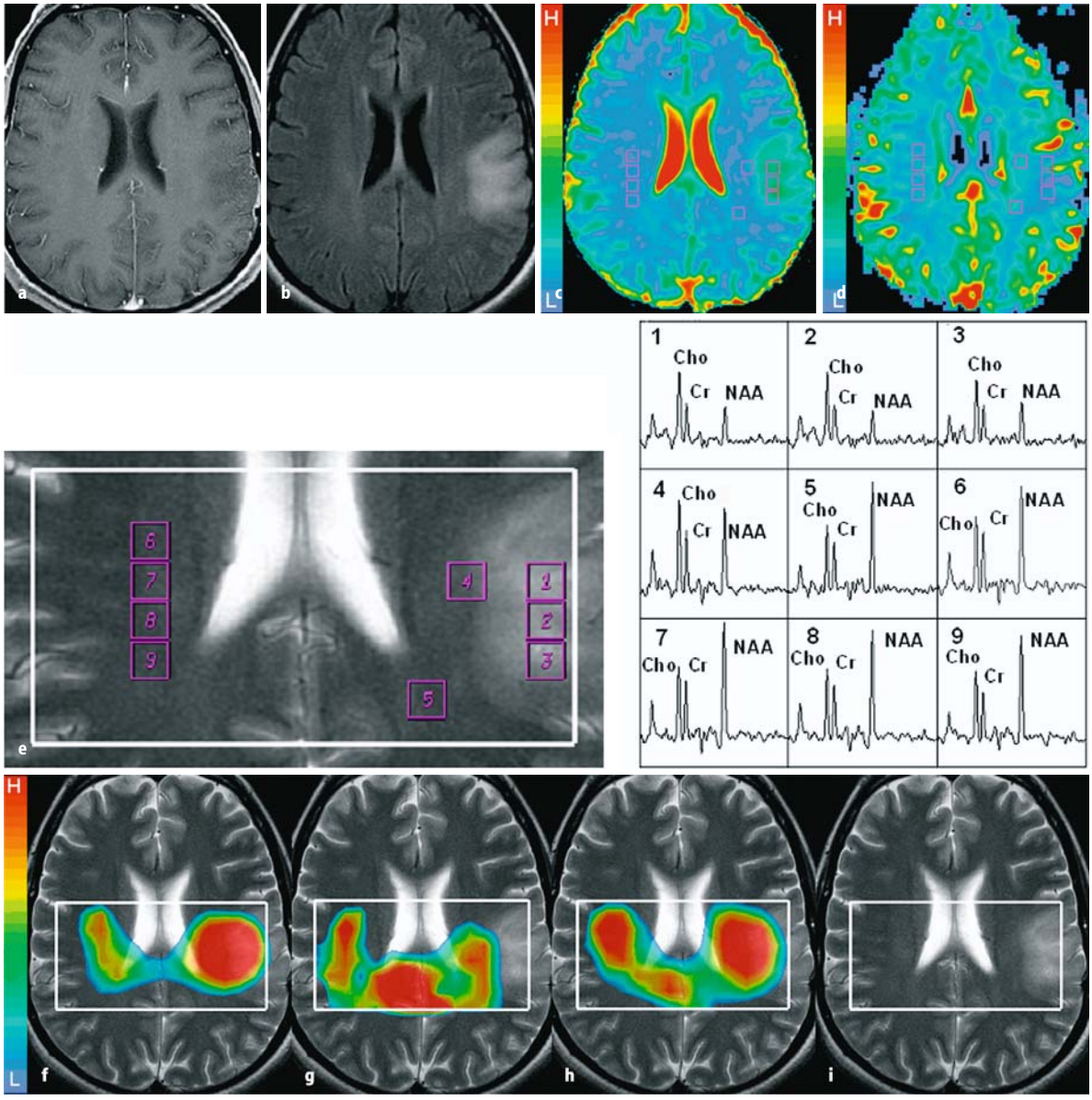

Fig. 18.3. Contrast-enhanced T1-weighted (**a**), FLAIR (**b**) and T2-weighted (**e**) images, ADC (**c**), rCBV (**d**), Cho (**f**), NAA (**g**), Cr (**h**) and LL (**i**) maps, and proton MR spectra (*1 – 9*) from selected ROIs in a 36-year-old woman with a grade II fronto-parieto-temporal oligodendroglioma. ROIs are tumour mass (*1 – 3*), peritumour „infiltrated" ROI (*4*), homolateral (*5*) and contralateral (*6 – 9*) normal ROIs. Note that the „infiltrated" ROI presents an abnormal Cho/NAA ratio (> 1), a Cho peak higher than normal ROIs and no signal abnormality on T1- and T2-weighted images; the tumour mass shows all the metabolite peaks, except LL, and an abnormal Cho/NAA ratio; ADC values are higher than and rCBV values are similar to those of normal white matter

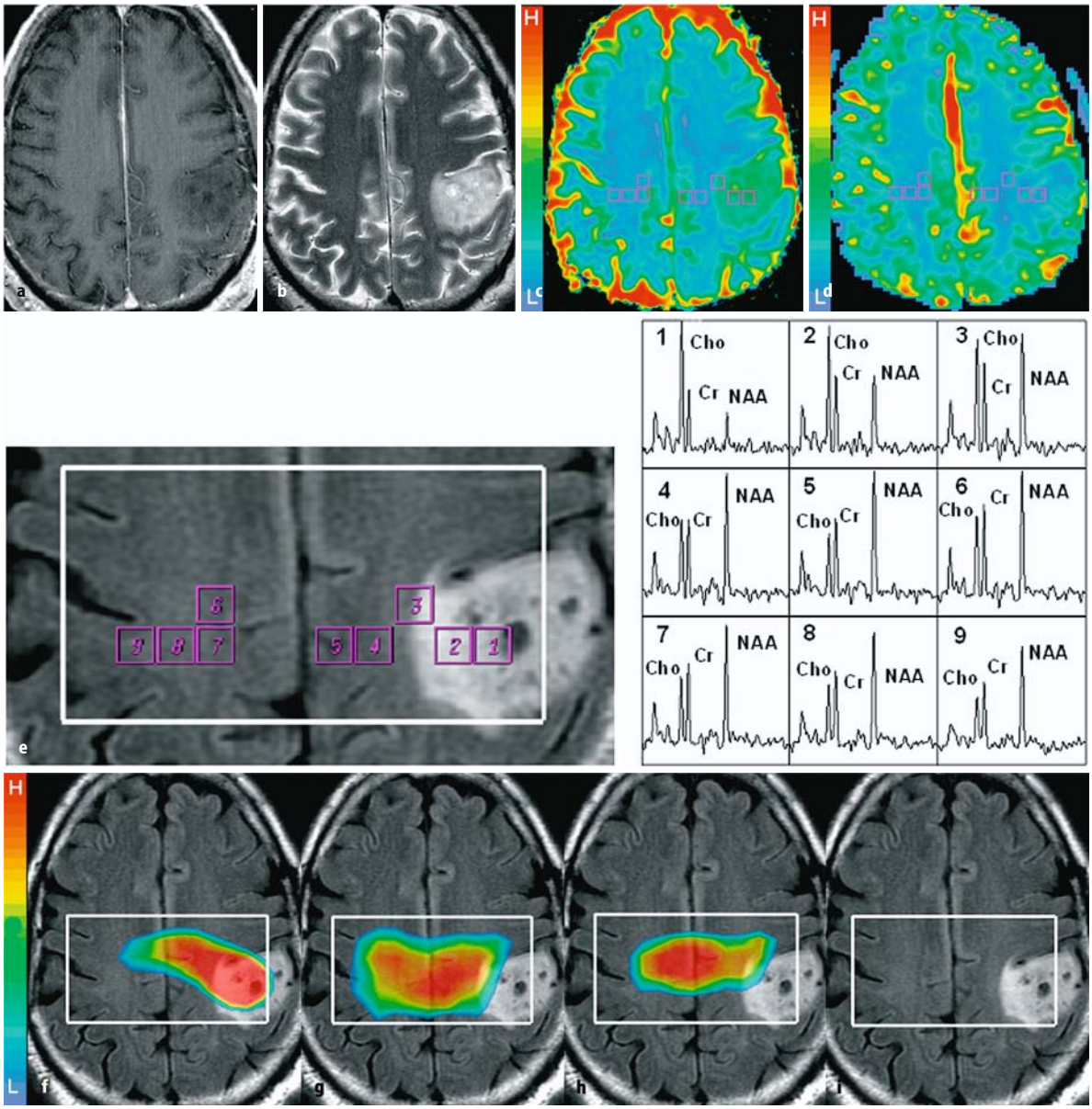

Fig. 18.4. Contrast-enhanced T1-weighted (**a**), T2-weighted (**b**) and FLAIR (**e**) images, ADC (**c**), rCBV (**d**), Cho (**f**), NAA (**g**), Cr (**h**) and LL (**i**) maps, and proton MR spectra (*1 – 9*) from selected ROIs in a 49-year-old man with parietal fibrillary astrocytoma of grade II. ROIs are tumour mass (*1, 2*) and margin (*3*), homolateral (*4, 5*) and contralateral (*6 – 9*) normal ROIs. Note in the tumour mass the presence of all the metabolite peaks except LL, and the abnormal Cho/NAA ratio; ADC values are higher than and rCBV values are similar to those of normal white matter

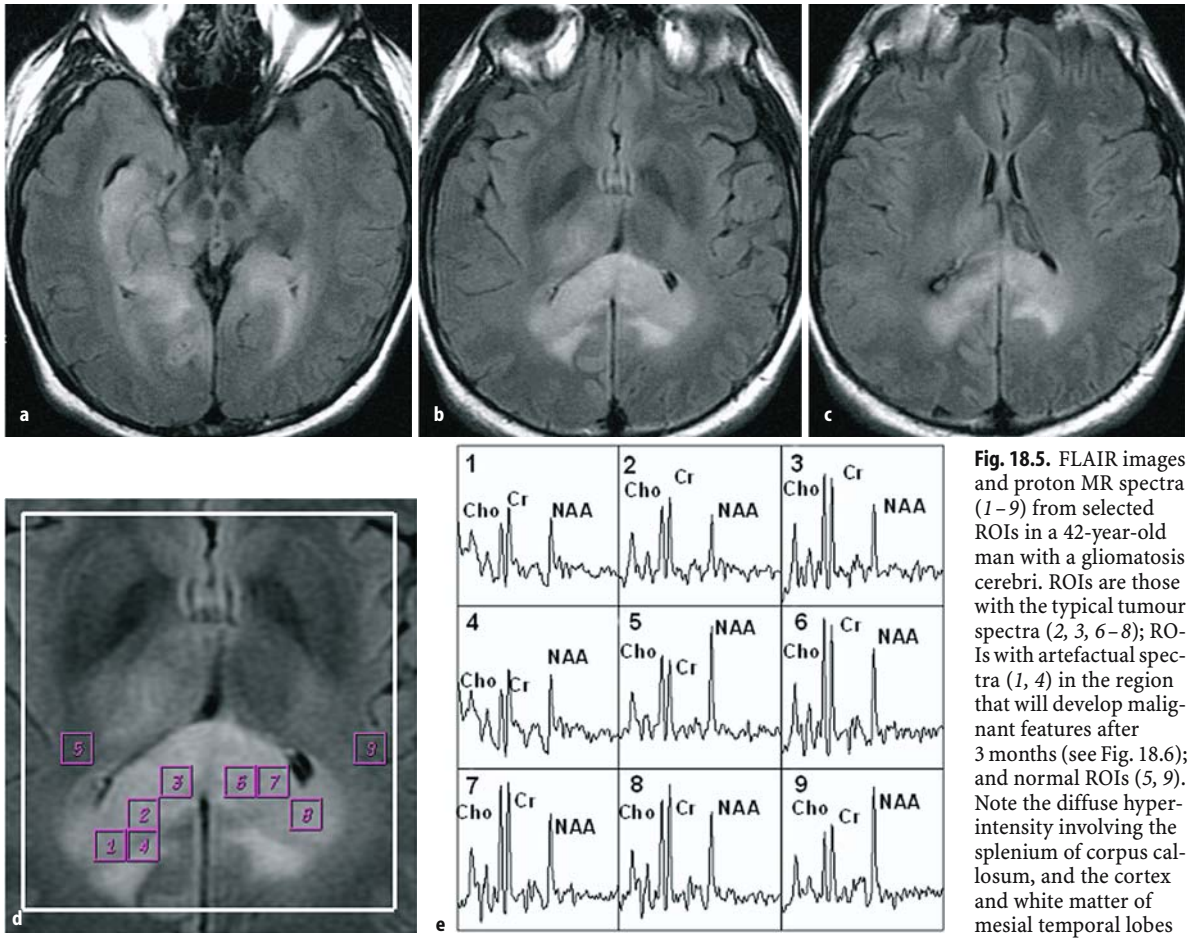

Fig. 18.5. FLAIR images and proton MR spectra (*1 – 9*) from selected ROIs in a 42-year-old man with a gliomatosis cerebri. ROIs are those with the typical tumour spectra (*2, 3, 6 – 8*); ROIs with artefactual spectra (*1, 4*) in the region that will develop malignant features after 3 months (see Fig. 18.6); and normal ROIs (*5, 9*). Note the diffuse hyperintensity involving the splenium of corpus callosum, and the cortex and white matter of mesial temporal lobes

18.2 Meningiomas

The most common extra-axial brain tumours are meningiomas, although haemangiopericytomas, sarcomas, lymphomas and metastasis are also frequent. They account for 20 – 25 % of all intracranial tumours and are found approximately twice as often in women as in men [41]. Meningiomas are classified as WHO grade I, grade II or atypical meningiomas, and grade III or anaplastic meningiomas. Atypical variant has increased mitotic activity, high cellularity and foci of necrosis. The distinction between typical and atypical variant is clinically relevant, because benign meningiomas recur in about 7 – 20 % of cases, whereas atypical variants recur in 29 – 41 % of cases [42, 43]. There are characteristic MRI features that distinguish meningiomas from intra-axial neoplasms, such as buckling of adjacent cortex, widening of cerebrospinal fluid spaces, and displacement of subarachnoid veins [41 – 43]. Although meningiomas are extra-axial and usually benign, they are often accompanied by brain oedema that causes clinical symptoms and is one of the most serious complications in the management of these tumours. The pathogenetic mechanism of oedema is not clear. However, oedema is correlated with large tumour size, disappearance of peritumoral rim, irregular tumour margins, and hyperintensity on T2 images. The disappearance of peritumoral rim and the irregularity of tumour margins indicate cortical penetration of the tumour, which can favour the extent of oedema into white matter [44]. ^{1}H-MRSI, DWI and PWI represent useful tools in the distinction of typical from atypical variants [43] and in the differentiation of meningiomas from other tumoral lesions [18, 45 – 47]. ^{1}H-MRSI generally shows marked reduction or absence of NAA and Cr and a variable amount of Cho (Fig. 18.7). The multiplet signal from glutamate and glutamine (Glx) is considered a prominent feature of meningiomas, as well as the signal from glutathione (GSH). Cho and LL levels relate directly to the malignancy of meningiomas [3, 46]. ADC values in meningioma are similar to or slightly higher than those of normal white matter, while in peritumoral hyperintense regions, generally consisting of vasogenic oedema, they are significantly higher [47]. rCBV may be grossly estimated due to the complete lack of blood-brain barrier in tumour capillaries. Meningio-

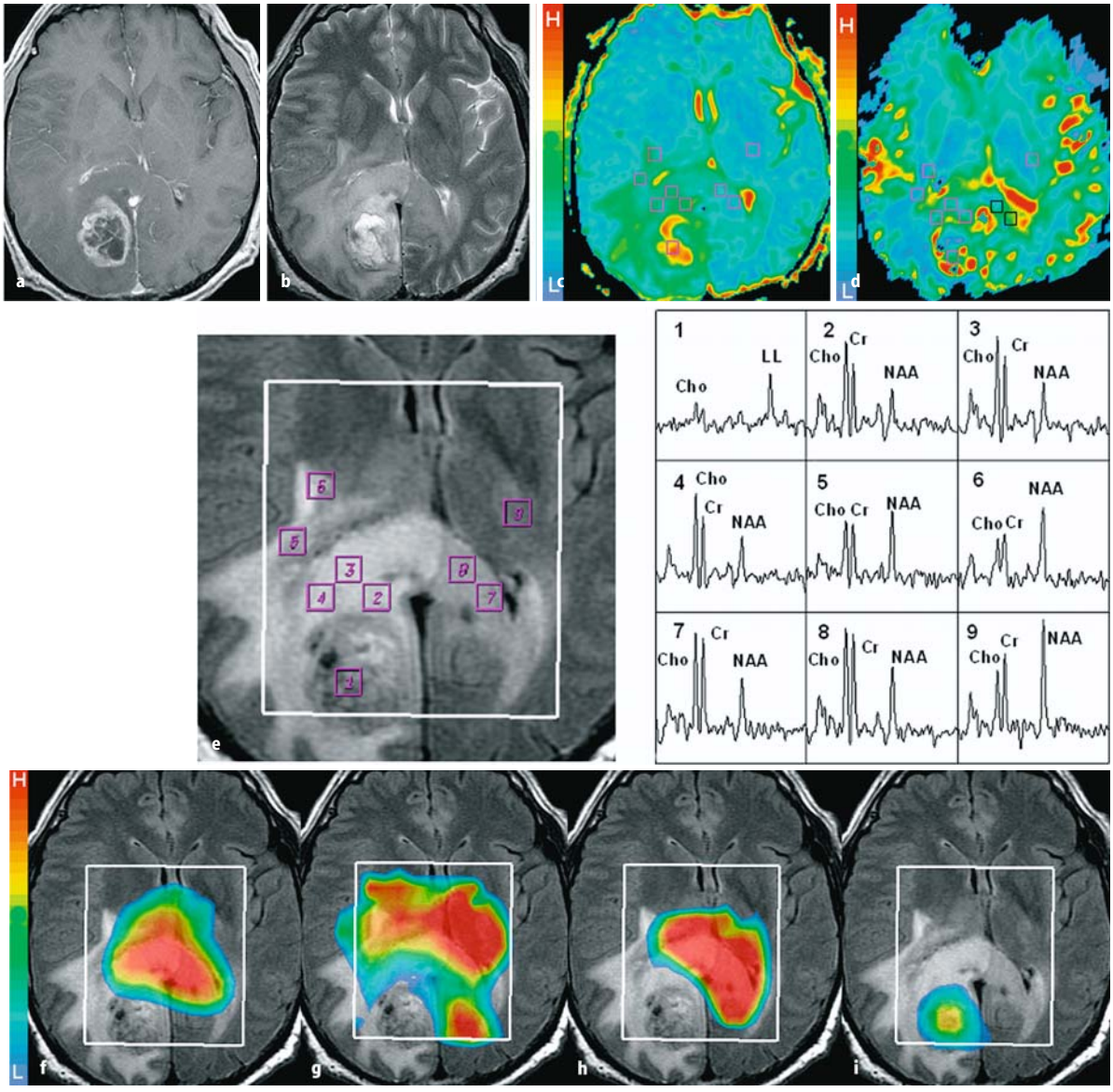

Fig. 18.6. Contrast-enhanced T1-weighted (**a**), T2-weighted (**b**) and FLAIR (**e**) images, ADC (**c**), rCBV (**d**), Cho (**f**), NAA (**g**), Cr (**h**) and LL (**i**) maps, and proton MR spectra (*1 – 9*) from selected ROIs in the same patient as Fig. 18.5, after 3 months. Note that in the right occipital lobe the lesion has acquired the features of malignant glioma, with diffuse contrast-enhancement and evidence of necrotic core. ROIs are ROI with necrotic aspect (*1*); perienhancing ROIs with „tumour" (*2 – 4*) and „oedema" (*5, 6*) pattern; ROIs in the remaining lesion (*8, 7*) without relevant modification compared to previous examination (Fig. 18.5); and contralateral (*8, 9*) normal ROIs. Note: the low level of Cho and the high LL peak in the necrotic core; the abnormal Cho/NAA ratio in tumoral ROIs; the normal Cho/NAA ratio and the lower metabolite levels in the „oedema" ROI, as compared to the contralateral normal ROI; and the similarity of spectra in ROIs *8* and *7*, as compared to ROIs *6* and *7* in Fig. 18.5

mas are highly vascular and their capillaries are highly leaky and permeable. The latter produces the immediate contrast agent leakage, during the first-pass contrast agent bolus, without any substantial recovery of T2* signal loss back to the baseline, and renders the intravascular compartmentalization of contrast agent impossible [48].

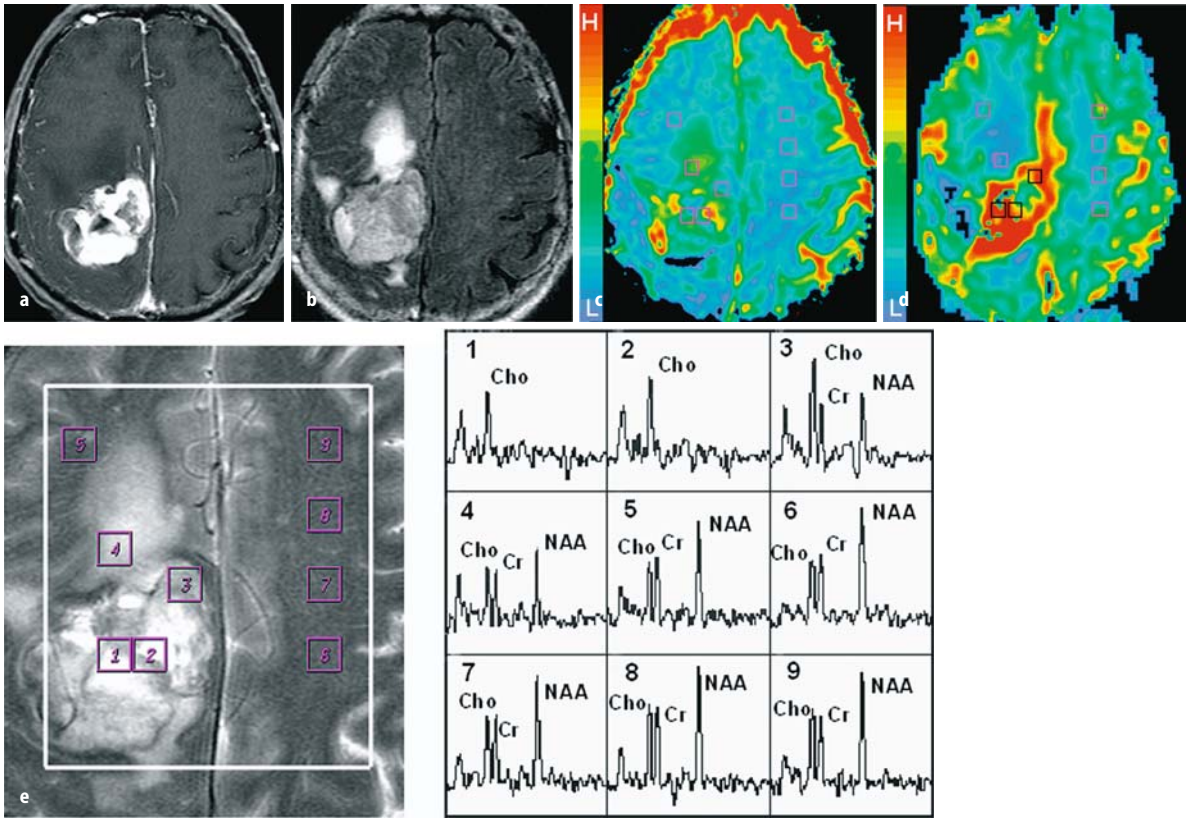

Fig. 18.7. Contrast-enhanced T1-weighted (**a**), FLAIR (**b**) and T2-weighted (**e**) images, ADC (**c**) and rCBV (**d**) maps, and proton MR spectra (*1 – 9*) from selected ROIs in a 54-year-old man with a grade II frontoparietal meningioma. ROIs are tumour mass (*1, 2*) and margin (*3*), vasogenic oedema (*4*), homolateral (*5*) and contralateral (*6 – 9*) normal ROIs. Note that the vasogenic oedema ROI presents a normal Cho/NAA ratio, metabolite peaks lower than mirrored normal ROIs (*7, 8*), and an ADC higher and an rCBV lower than contralateral normal white matter; rCBV in meningioma mass is overestimated due to the leakage phenomenon during the first pass of contrast agent bolus

18.3 Primary Central Nervous System Lymphomas

CNS lymphomas may be either primary or secondary. Secondary involvement occurs in 25 – 30 % of non-Hodgkin's lymphomas and is exceptional in Hodgkin's disease. Secondary lymphomas tend to infiltrate the leptomeninges and spare the parenchyma, while primary lymphoma typically presents deep in the brain parenchyma, sparing the leptomeninges [49, 50]. In immunocompetent patients, primary CNS lymphomas (PCNSL) are generally non-Hodgkin's lymphomas of germinal B-cell origin [51], and arise and remain restricted to the CNS in more than 85 % of cases. They constitute between 1 % and 6 % of all malignant tumours of the CNS and 3 – 5 % of all extranodal non-Hodgkin's lymphomas [49, 50]. PCNSL extensively infiltrate the brain, and individual tumour cells are seen in otherwise normal brain with intact blood-brain barrier because no neovascularization accompanies this infiltrative disease [49, 50]. The most frequent location of PCNSL is the cerebral hemispheres, basal ganglia and thalamus, and less frequently the corpus callosum and choroid plexus [52]. On conventional MRI, lymphomas are characterized by prominent contrast enhancement, and reappearance of contrast-enhancing lesion after treatment is usually a sign of recurrence. T2 and FLAIR images reveal homogeneous areas iso- or hypointense to cortex [52]. However, radiological diagnosis of PCNL remains a challenge because MR imaging findings can be similar to those of other intracranial tumours or demyelinating lesions [52, 53]. ^{1}H-MRSI, DWI and PWI have been applied in combination with conventional neurimaging to ameliorate the differential diagnosis. In contrast-enhancing areas, ^{1}H-MRSI generally reveals spectra with a marked increase of Cho and LL, and a conspicuous decrease of Cr and NAA (Fig. 18.8), or an absence of metabolite signals [53]. DWI generally shows an ADC lower than or similar to normal white matter [53], and rCBV is higher than contralateral normal ROIs [18, 54]. The ability of PWI to detect tumour angiogenesis can be useful in differentiating high-grade gliomas from PCNL. Hartmann et al. [54] reported a maximum rCBV in PCNSL significantly lower than in glioblastomas. These results are in agree-

ment with histopathological evidence showing low neovascularization in lymphomas, although vascular abnormalities and tumour invasion of endothelial cells and vessel lumen are often seen [55]. In two cases of PCNSL, in addition to ROIs with a „tumour" pattern, we could identify ROIs with an „oedema" multiparametric pattern. In one case, according to the neuropathological findings showing diffuse tumour infiltration in tissues surrounding the PCNSL mass [55], we identified ROIs with an „oedema/tumour" multiparametric pattern (Fig. 18.8).

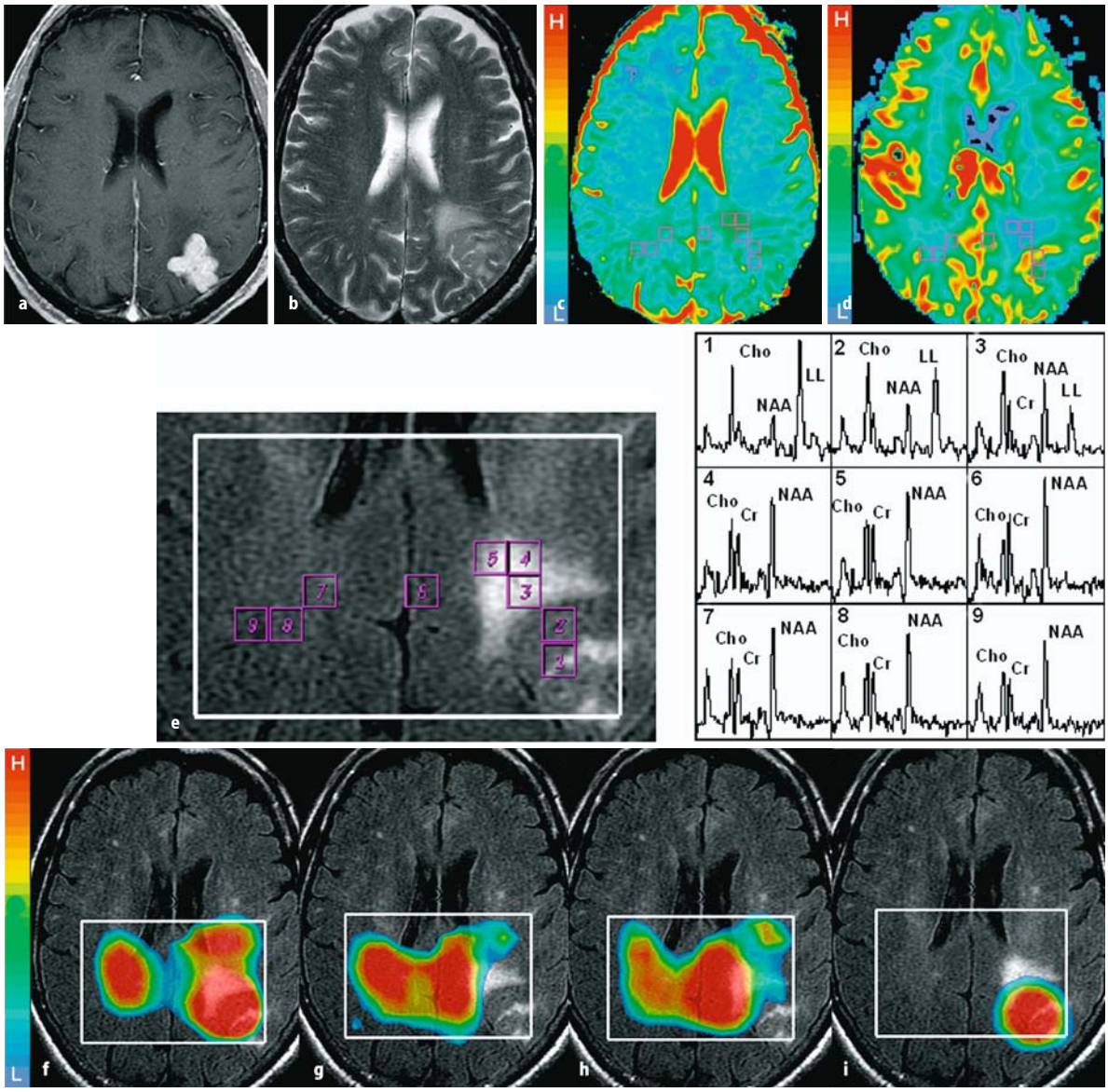

Fig. 18.8. Contrast-enhanced T1-weighted (**a**), T2-weighted (**b**) and FLAIR (**e**) images, ADC (**c**), rCBV (**d**), Cho (**f**), NAA (**g**), Cr (**h**) and LL (**i**) maps, and proton MR spectra (*1 – 9*) from selected ROIs in a 73-year-old man with a primary CNS lymphoma in the left parietal lobe. ROIs are tumour mass (*1, 2*), ROIs with „tumour/oedema" (*3*) and „oedema" (*4, 5*) pattern, homolateral (*6*) and contralateral (*7 – 9*) normal ROIs. Note: the high levels of Cho and LL in the tumour mass; the abnormal Cho/NAA ratio and the presence of LL in the „tumour/oedema" ROI; the normal Cho/NAA ratio in the „oedema" ROIs; the values of ADC and rCBV in the „tumour/oedema" ROI, which are respectively, lower and higher than in the „oedema" ROIs

18.4 Metastases

Metastatic tumours are actually more common than primary brain tumours and their incidence is increasing [56, 57]. They occur in middle-aged and older adults and can originate from almost any systemic cancers, although carcinomas of lung, breast, skin and kidneys, and melanomas are the most common causes of brain metastases [57]. On conventional MRI, most brain metastases are seen as multiple, nodular, well-circumscribed enhancing lesions, often at the grey-white matter junction, with central necrosis or haemorrhage and surrounding vasogenic oedema [58]. The diagno-

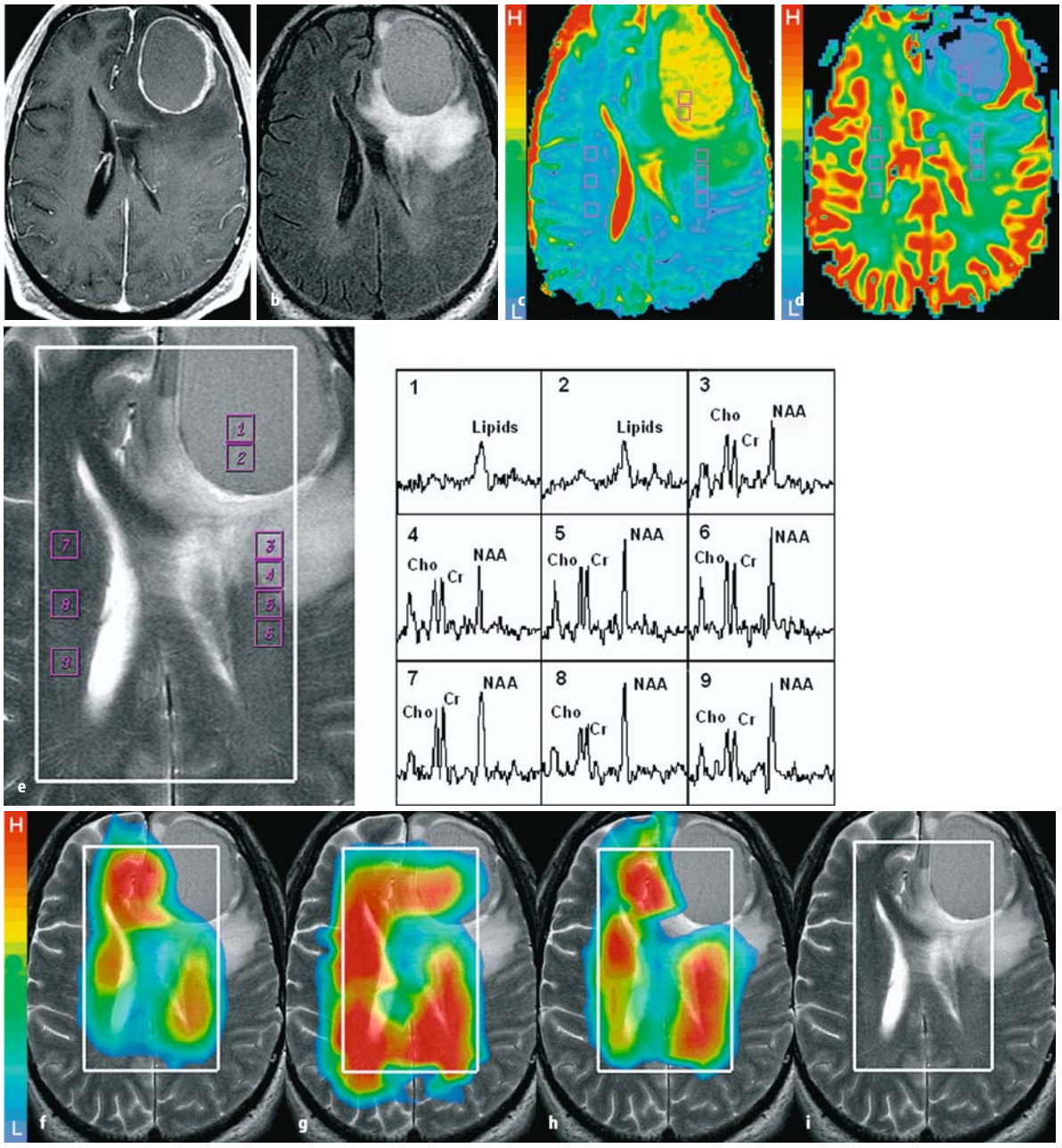

Fig. 18.9. Contrast-enhanced T1-weighted (**a**), FLAIR (**b**) and T2-weighted (**e**) images, ADC (**c**), rCBV (**d**), Cho (**f**), NAA (**g**), Cr (**h**) and LL (**i**) maps, and proton MR spectra (*1 – 9*) from selected ROIs in a 60-year-old man with a left frontal solitary metastasis from a thyroid carcinoma. ROIs are a necrotic core surrounded by a thin ring-like enhancement (*1, 2*); vasogenic oedema (*3, 4*); homolateral (*5, 6*) and contralateral (*7 – 9*) normal ROIs. Note: the absence of Cho, Cr and NAA, and the presence of lipid resonance at 2.02 ppm in the spectra of the necrotic core; the lower levels of metabolites, and the higher ADC and lower rCBV in oedema ROIs as compared to normal ROIs

sis of intracranial metastases on conventional imaging is usually uncomplicated and straightforward. However, differentiation between solitary metastases, which occur in 30–50% of cases, and high-grade gliomas is difficult because both may exhibit oedema, mass effect and central necrosis, especially if there is no history of systemic cancer [54]. It is also difficult on conventional imaging to distinguish among metastases from different origins. ^{1}H-MRSI usually shows an absence of metabolites or high LL peak in the necrotic core, and a variable amount of Cho and LL along the enhanced margins; NAA and Cr are absent or markedly reduced [3]. Perienhancing regions of metastasis show Cho and rCBV lower [34, 36] and ADC higher [36, 59] than those of high-grade gliomas. Perienhancing regions of metastasis, in fact, represent pure vasogenic oedema since it does not contain infiltrating tumour cells [39], while those of high-grade gliomas contain tumour cells infiltrating along the perivascular spaces [37]. ^{1}H-MRSI, DWI and PWI may be helpful then to distinguish preoperatively solitary metastases from high-grade gliomas (Fig. 18.9). PWI may also allow the distinction of hypervascular metastases, such as those from renal carcinoma or melanoma, from other types of metastases [60].

18.5 Conclusion

Combining metabolic, diffusion and haemodynamic information from ^{1}H-MRSI, DWI and PWI with morphological information from conventional MRI undoubtedly improves the assessment of intracranial tumours, increasing the capability to discriminate between different tissues. Furthermore, using high-field MR can allow shorter imaging times for a given resolution, a higher resolution for a given imaging time, or a combination of both, due to the higher SNR. A short acquisition time is preferable for the fast imaging of ill and sometimes poorly cooperative subjects, especially if long MR protocols are used. High spatial resolution allows high quality imaging and therefore additional diagnostic information. We suggest that the multiparametric MR approach, including ^{1}H-MRSI, DWI and PWI in addition to conventional MRI, at 3 T may provide a non-invasive fast and accurate tool for the formulation of diagnosis and prognosis, the planning of treatment and the monitoring of therapeutic response in patients with brain tumours.

References

1. Behin A, Hoang-Xuan K, Carpentier AF, Delattre J-Y (2003) Primary brain tumours in adults. Lancet 361:323–331
2. Grant R (2004) Overview: brain tumour diagnosis and management. Royal College of Physicians guidelines. J Neurol Neurosurg Psychiatry 75 (Suppl 2):18–23
3. Howe FA, Opstad KS (2003) ^{1}H MR spectroscopy of brain tumor and masses. NMR Biomed 16:123–131
4. McKnight TR (2004) Proton magnetic resonance spectroscopic evaluation of brain tumor metabolism. Semin Oncol 31:605–617
5. Li X, Lu Y, Pirzkall A, McKnight T, Nelson SJ (2002) Analysis of the spatial characteristics of metabolic abnormalities in newly diagnosed glioma patients. J Magn Reson Imaging 16:229–237
6. Burtscher IM, Skagerberg G, Geijer B, et al. (2000) Proton MR spectroscopy and preoperative diagnostic accuracy: an evaluation of intracranial mass lesions characterized by stereotactic biopsy findings. Am J Neuroradiol 21:84–93
7. Dowling C, Bollen AW, Noworolski SM, et al. (2001) Preoperative proton MR spectroscopic imaging of brain tumors: correlation with histopathologic analysis of resection specimens. Am J Neuroradiol 22:604–612
8. Croteau D, Scarpace L, Hearshen D, et al. (2001) Correlation between magnetic resonance spectroscopy imaging and image-guided biopsies: semiquantitative and qualitative histopathological analyses of patients with untreated glioma. Neurosurgery 49:823–829
9. Rabinov JD, Lee PL, Barker FG, et al. (2002) In vivo 3-T MR spectroscopy in the distinction of recurrent glioma versus radiation effects: initial experience. Radiology 225:871–879
10. Tedeschi G, Lundbom N, Raman R, et al. (1997) Increased choline signal coinciding with malignant degeneration of cerebral gliomas: a serial proton magnetic resonance spectroscopy imaging study. J Neurosurg 87:516–524
11. Sener RN (2001) Diffusion MRI: apparent diffusion coefficient (ADC) values in the normal brain and a classification of brain disorders based on ADC values. Comput Med Imaging Graph 25:299–326
12. Kono K, Inoue Y, Nakayama K, et al. (2001) The role of diffusion-weighted imaging in patients with brain tumors. Am J Neuroradiol 22:1081–1088
13. Asao C, Korogi Y, Kitajima M, et al. (2005) Diffusion-weighted imaging of radiation-induced brain injury for differentiation from tumor recurrence. Am J Neuroradiol 26:1455–1460
14. Muti M, Aprile I, Principi M, et al. (2002) Study on the variations of the apparent diffusion coefficient in areas of solid tumor in high grade gliomas. Magn Reson Imaging 20:635–641
15. Yamasaki F, Kurisu K, Satoh K, et al. (2005) Apparent diffusion coefficient of human brain tumors at MR imaging. Radiology 235:985–991
16. Lam WWM, Poon WS, Metreweli C (2002) Diffusion MR imaging in glioma: does it have any role in the pre-operation determination of grading of glioma? Clin Radiol 57:219–225
17. Tien RD, Felsberg GJ, Friedman H, et al. (1994) MR imaging of high-grade cerebral gliomas: value of diffusion-weighted echoplanar pulse sequences. Am J Roentgenol 162:671–677
18. Cha S, Knopp EA, Johnson G, et al. (2002) Intracranial mass lesions: dynamic contrast-enhanced susceptibility-weighted echo-planar perfusion MR imaging. Radiology 223:11–29
19. Maia ACM, Malheiros SMF, da Rocha AJ, et al. (2005) MR cerebral blood volume maps correlated with vascular endothelial growth factor expression and tumor grade in nonenhancing gliomas. Am J Neuroradiol 26:777–783
20. Law M, Yang S, Babb JS, et al. (2004) Comparison of cerebral blood volume and vascular permeability from dynamic susceptibility contrast-enhanced perfusion MR imaging with glioma grade. Am J Neuroradiol 25:746–755

21. Lev MH, Ozsunar Y, Henson JW, et al. (2004) Glial tumor grading and outcome prediction using dynamic spin-echo MR susceptibility mapping compared with conventional contrast-enhanced MR: confounding effect of elevated rCBV of oligodendrogliomas. Am J Neuroradiol 25:214 – 221
22. Cha S, Tihan T, Crawford F, et al. (2005) Differentiation of low-grade oligodendrogliomas from low-grade astrocytomas by using quantitative blood-volume measurements derived from dynamic susceptibility contrast-enhanced MR imaging. Am J Neuroradiol 26:266 – 273
23. Frayne R, Goodyear BG, Dickhoff P, et al. (2003) Magnetic resonance imaging at 3.0 Tesla: challenges and advantages in clinical neurological imaging. Invest Radiol 38:385 – 402
24. Di Costanzo A, Trojsi F, Tosetti M, et al. (2003) High-field proton MRS of human brain. Eur J Radiol 48:146 – 153
25. Counsell CE, Grant R (1998) Incidence studies of primary and secondary intracranial tumours: a systematic review of their methodology and results. J Neurooncol 37:241 – 250
26. Prados M (2000) Neoplasms of the central nervous system. In: Bast R, Kufe D, Pollock R, Weichselbaum R, Holland J, Frei E (eds) Cancer medicine, 5th edn. BC Decker, Hamilton, Ontario, pp 1055 – 1082
27. Yuh WT, Nguyen HD, Tali ET, et al. (1994) Delineation of gliomas with various doses of MR contrast material. Am J Neuroradiol 15:983 – 989
28. Pirzkall A, McKnight TR, Graves EE, et al. (2001) MR-spectroscopy guided target delineation for high-grade gliomas. Int J Radiat Oncol Biol Phys 50:915 – 928
29. Kleihues P, Cavenee WK (eds) Pathology and genetics of tumours of the nervous system. IARC Press, Lyon, France
30. Fallentin E, Skriver E, Herning M, et al. (1997) Gliomatosis cerebri: an appropriate diagnosis? Case reports. Acta Radiol 38:381 – 390
31. Barnard RO, Geddes JF (1987) The incidence of multifocal cerebral gliomas: a histologic study of large hemisphere sections. Cancer 60:1519 – 1531
32. Artigas J, Cervos-Navarro J, Iglesias JR, et al. (1985) Gliomatosis cerebri: clinical and histological findings. Clin Neuropathol 4:135 – 148
33. Castillo M, Smith JK, Kwock L, Wilber K (2001) Apparent diffusion coefficients in the evaluation of high-grade cerebral gliomas. Am J Neuroradiol 22:60 – 64
34. Law M, Cha S, Knopp EA, et al. (2002) High-grade gliomas and solitary metastases: differentiation by using perfusion and proton spectroscopic MR imaging. Radiology 222: 715 – 721
35. Tzika AA, Astrakas LG, Zarifi MK, et al. (2003) Multiparametric MR assessment of pediatric brain tumors. Neuroradiology 45:1 – 10
36. Chiang IC, Kuo Y-T, Lu C-Y, et al. (2004) Distinction between high-grade gliomas and solitary metastases using peritumoral 3-T magnetic resonance spectroscopy, diffusion, and perfusion imagings. Neuroradiology 46:619 – 627
37. Strugar JG, Criscuolo GR, Rothbart D, Harrington WN (1995) Vascular endothelial growth/permeability factor expression in human glioma specimens: correlation with vasogenic brain edema and tumor-associated cysts. J Neurosurg 83:682 – 689
38. Cha S, Johnson G, Wadghiri YZ, et al. (2003) Dynamic, contrast-enhanced perfusion MRI in mouse gliomas: correlation with histopathology. Magn Reson Med 49:848 – 855
39. Strugar J, Rothbart D, Harrington W, Criscuolo GR (1994) Vascular permeability factor in brain metastases: correlation with vasogenic brain edema and tumor angiogenesis. J Neurosurg 81:560 – 566
40. Eis M, Els T, Hoehn-Berlage M (1995) High resolution quantitative relaxation and diffusion MRI of three different experimental brain tumors in rat. Magn Reson Med 34:835 – 844
41. Black PM (1993) Meningiomas. Neurosurgery 32:643 – 657
42. Mahmood A, Caccamo DV, Tomecek FJ, et al. (1993) Atypical and malignant meningiomas: a clinicopathological review. Neurosurgery 33:955 – 963
43. Maier H, Ofner D, Hittmair A, et al. (1992) Classic, atypical, and anaplastic meningioma: three histopathological subtypes of clinical relevance. J Neurosurg 77:616 – 623
44. Nakano T, Asano K, Miura H, et al. (2002) Meningiomas with brain edema. Radiological characteristics on MRI and review of the literature. Clin Imaging 26: 243 – 249
45. Yang S, Law M, Zagzag D, et al. (2003) Dynamic contrast-enhanced perfusion MR imaging measurements of endothelial permeability: differentiation between atypical and typical meningiomas. Am J Neuroradiol 24:1554 – 1559
46. Cho Y-D, Choi G-H, Lee S-P, Kim J-K (2003) ^{1}H-MRS metabolic patterns for distinguishing between meningiomas and other brain tumors. Magn Reson Imaging 21:663 – 672
47. Provenzale JM, McGraw P, Mhatre P, et al. (2004) Peritumoral brain regions in gliomas and meningiomas: investigation with isotropic diffusion-weighted MR imaging and diffusion-tensor MR imaging. Radiology 232:451 – 460
48. Cha S (2004) Perfusion MR imaging of brain tumors. Top Magn Reson Imaging 15:279 – 289
49. Jellinger KA, Paulus W (1992) Primary central nervous system lymphomas – an update. J Cancer Res Clin Oncol 119:7 – 27
50. Lai R, Rosenblum MK, DeAngelis LM (2002) Primary CNS lymphoma. A whole-brain disease? Neurology 59:1557 – 1562
51. Larocca LM, Capello D, Rinelli A, et al. (1998) The molecular and phenotypic profile of primary central nervous system lymphoma identifies distinct categories of the disease and is consistent with histogenetic derivation from germinal center-related B cells. Blood 92:1011 – 1019
52. Buhring U, Herrlinger U, Krings T, et al. (2001) MRI features of primary central nervous system lymphomas at presentation. Neurology 57:393 – 396
53. Küker W, Nägele T, Korfel A, et al. (2005) Primary central nervous system lymphomas (PCNSL): MRI features at presentation in 100 patients. J Neurooncol 72:169 – 177
54. Hartmann M, Heiland S, Harting I, et al. (2003) Distinguishing of primary cerebral lymphoma from high-grade glioma with perfusion-weighted magnetic resonance imaging. Neurosci Lett 338:119 – 122
55. Onda K, Wakabayashi K, Tanaka R, Takahashi H (1999) Intracranial malignant lymphomas: clinicopathological study of 26 autopsy cases. Brain Tumor Pathol 16:29 – 35
56. Deangelis LM (2001) Brain tumors. N Engl J Med 344:114 – 123
57. Jeyapalan S, Batchelor T (2000) Diagnostic evaluation of neurologic metastases. Cancer Invest 18:381 – 394
58. Hwang T, Close T, Grego J, et al. (1996) Predilection of brain metastasis in grey and white matter junction and vascular border zones. Cancer 77:1551 – 1555
59. Krabbe K, Gideon P, Wagn P, et al. (1997) MR diffusion imaging of human intracranial tumours. Neuroradiology 39:483 – 489
60. Kremer S, Grand S, Berger F (2003) Dynamic contrast-enhanced MRI: differentiating melanoma and renal carcinoma metastases from high-grade astrocytomas and other metastases. Neuroradiology 45:44 – 49

Use of fMRI Activation Paradigms: A Presurgical Tool for Mapping Brain Function

19

D. Cevolani, R. Agati, M. Leonardi

Until not many years ago, the only reliable ways of mapping of brain eloquent areas were invasive methods, such as intraoperative cortical stimulation and somatosensory evoked potentials. Invasive methods are accurate, but time-consuming during the surgical procedure, often reducing the mapping analysis to „just sufficient" knowledge to enable to surgeon to proceed [36].

Obviously, the goal of neurosurgery is to maximize resection while preserving important brain functions. With this aim, it is important to provide the surgeon with all the available information to identify the eloquent cortex preoperatively; it is a well-known phenomenon that many tumours and their surrounding oedema cause a significant mass effect, which may markedly distort the cortical anatomy and make classical anatomical landmarks useless.

The presurgical use of functional magnetic resonance imaging (fMRI) paradigms enables the neurosurgeon to be given a complete mapping of brain eloquent areas before surgery, thus making the surgeon aware of the actual situation. Consequently, the surgeon may plan the surgery and decide the strategy of approach preoperatively, including the question of whether to operate or not [13].

The fMRI technique has a high spatial and temporal resolution, a non-invasive character and is safe (the source of the signal is endogenous and MRI has no known risks), thus also allowing the patient follow-up. It enables a correct definition of the relationships between, for instance, a tumour and the adjacent eloquent cortex. It is noteworthy that, sometimes, the intraoperative mapping by direct cortical stimulation is unsuccessful, especially when testing higher cognitive functions such as language, which requires the patient to be awake and not sedated as during the surgery [15]. In these cases, fMRI information becomes not only an invaluable help, but also avoids the chance of a „surprise" during the surgical procedure [3].

Finally, fMRI can detect functional cortical reorganization and plasticity, namely the displacement of brain function from one location to another [14, 27]. This phenomenon has clear-cut implications for the surgical management of the patient.

In this paper, we focus our attention on: the phenomena at the root of eloquent brain maps, the description of some activation paradigms, and their main presurgical application.

19.1 The BOLD Phenomenon

Mapping eloquent areas by MRI is based on the blood oxygenation level-dependent (BOLD) contrast phenomenon. This is due to the paramagnetic properties of deoxyhaemoglobin. When a pool of neurons pass from a rest state to an activation state, the increased discharge of spikes induces a rise in regional oxygen consumption rate. This event brings two main effects: a regional increase in the absolute number of deoxyhaemoglobin molecules and a local vasodilation, due to the flow autoregulatory mechanism, which is characteristic of the brain circulation. The increase in blood regional flow largely overwhelms the amount of oxygen extracted by the activated neurons and leads to a relative decrease of deoxyhaemoglobin concentration. The resulting net effect is a local rise in oxyhaemoglobin and a local drop in deoxyhaemoglobin. The drop in paramagnetic deoxyhaemoglobin leads to an increased signal intensity in T2*- and T2-weighted images. The mapping of eloquent areas, then, is achieved by acquiring T2*- or T2-weighted images consecutively, while the subject is performing the task or is at rest. Finally, the difference between the performing condition and the resting condition is calculated [16].

19.2 3 T vs 1.5 T

In the past 10 – 15 years, 1.5 T systems have been the most commonly used field strength in everyday clinical use. The advances in technology and the increased availability of higher fields have opened the door to a variety of exciting improvements in clinical and research application of MRI. In particular, 3 T systems have continued to gain wide acceptance as one of the main field strengths used for clinical and research studies [22]. The reasons for this acceptance are many.

One of the main advantages of high field imaging is the improvement of the signal to noise ratio (SNR). It has been shown [22] that the signal is expected to increase by a factor of 4 at 3 T, with respect to 1.5 T. Unfortunately, the noise also increases by a factor of 2. As a consequence, there is a twofold improvement in SNR, which may have profound clinical implications. (1) *Shortening of data acquisition times*. It is possible to decrease the total data acquisition times by a factor of 4 at 3 T, while maintaining a SNR comparable to that obtained at 1.5 T. This time reduction shortens the overall exam length and could minimize patient motion artefacts. (2) *Improving spatial resolution*, while keeping acquisition times similar to 1.5 T. Spatial resolution improves differently according to the acquisition approach used. Therefore, depending on the structures in exam and the imaging sequences used, it is possible to improve SNR to optimize the visualization of relevant details of interest.

Another effect observed with high field imaging is an *increasing susceptibility*. fMRI is probably one of the best examples of converting artefacts into useful physiological information [22]. Signal changes due to BOLD effects are directly proportional to the magnetic field strength. The higher the field strength, the more sensitive the sequence will be to BOLD effects. Assuming the changes in the deoxyhaemoglobin concentration remain identical, the percentage signal changes are expected to increase twofold at 3 T when compared with that obtained from 1.5 T. However, since the absolute signal changes are small (~10 % with a 3 T system), appropriate task paradigms must be planned.

19.3 The „Ideal" Paradigm

Before starting any routine clinical application of fMRI on patients, it is useful to perform a survey of the literature in the search for the „ideal" paradigm. In our opinion, a reliable paradigm should have the following characteristics: (1) The activation induced should be *specific*. Specificity refers to the ability to localize a function: a high specific paradigm should have a high localizing power, i.e. the ability to select and discover all and only the areas appertaining to that function considered. This way, evoked eloquent areas are defined unambiguously as to anatomical location and extent. (2) The activation induced should be *reproducible:* evoked eloquent areas have to remain unchanged as to location and extent, through different trials, made in the same and/or in different sessions, thus allowing patient follow-up. (3) The paradigm should be *easy* to learn by patients having different social and cultural backgrounds. If a patient does not understand clearly what to do or what will happen, he or she obviously will not perform the paradigm correctly and the result will be a suboptimal activation. (4) The paradigm should be *short-lasting*. The length of time of a paradigm should enable the patient to maintain a high attention level all through the trial; otherwise, again a suboptimal activation will result. Unfortunately, an optimal duration is only a compromise between the time spent by the patient in the magnet and the need to acquire enough data for statistically significant mapping. Usually, an fMRI session includes more than one paradigm and lasts for almost an hour.

A Few Words on Sensitivity. Sensitivity is the ability to detect low signals and/or to respond to small physical amounts or differences. As we have just seen („3 T vs 1.5 T") and will see soon („Experimental Design"), sensitivity does not depend only on the biological phenomena at the base of the BOLD contrast effect, but also on the characteristics of acquiring equipment (magnetic field strength, kind of sequence acquired, artefacts, etc.), as well as on the experimental design applied. Unfortunately, sensitivity and specificity are often in inverse relation. As a consequence, caution is needed in comparing results obtained by using different equipment and experimental designs.

It is useful, after the choice from the literature of the paradigms having the above characteristics, to select from them those producing the widest activation areas, with the aim, in a presurgical perspective, to spare as much eloquent tissue as possible. The result of such an operation is to obtain a set of paradigms, which, on the whole, constitute an adequate tool with which to explore the main eloquent cortical areas (cf. [7] for review). After this, a safe strategy to set up the system is to implement and apply all paradigms to healthy volunteers, before proceeding with the routine clinical application on patients. Finally, each patient has to receive a personalized set of paradigms, which are selected on the basis of the specific localization and extension of the existing pathology.

19.4 Stimulating Apparatus

Usually, there is the need with some tools to apply a proper stimulation. For instance, we used goggles, earphones and a push-button panel (ten push buttons), to monitor patient response (Visual Stim XGA Digital Stereo Commander XG, Resonance Technology).

Stimuli could be administrated in different ways, but a careful procedure is to perform this step by software as automatically as possible. For instance, we use the Stim2 and Presentation software and a dedicated PC. The same PC synchronizes the beginning of stimulation to the beginning of acquisition using a radiofrequency pulse.

19.5 Experimental Design

The main limitation with fMRI experimental design planning arises from the fact that the signal changes being measured are very small. Thus, fMRI can be used only for determining *relative* signal intensity changes within a single image session [25]. There are two main methods of planning an fMRI experimental design: block design and event-related design.

A typical *block design* consists of two alternating situations: the „activation condition" and the „resting condition", which often have the same duration. Each condition is considered as a mean static value across the whole period. The principles of BOLD data processing are based on the subtraction of the rest from the active periods; thus rest behaves as a baseline with respect to activation. The resulting difference between the two signals is the specific activation effect we are dealing with. It follows that the rest condition is very important, as much as the active condition, and is more important the smaller the eloquent area to be revealed. Finally, the rest condition is not always the absence of anything, but may also consist of another task, which may differ in the different paradigms.

An *event-related design* considers the time course of the event, and not a time-integrated averaging procedure. Each trial is considered separately as being time-locked to the beginning of the stimulus and signal changes are explored in relation to the onset of the event generated by the trial. Event-related signal averaging requires the repetition of trials and the alignment of the data to a reference point, such that repeated time-locked epochs of data can be recorded and subsequently averaged together. In this way, event-related design can explore the temporal shape of the event and discover if there is a temporal evolution, e.g. if a transient signal change is followed by a sustained signal change (in a block paradigm the transient and sustained signal changes would not be resolved, because activity is mediated over each condition) [8].

With respect to event related design, block design, besides being simpler, has a higher power in signal detection, i.e. has a higher sensitivity, due to the intrinsic characteristics of the method (to find significant differences between means). So a block design seems a more convenient way to perform presurgical fMRI paradigms [23].

19.6 Data Processing

Once data have been acquired, they need to be *pre-processed*. The purpose of this procedure is to remove various kinds of artefacts in order to maximize the sensitivity for later statistical analysis.

After reconstructing row data into images, looking like brain slices, *slice-timing correction* occurs. Actually, each slice is acquired at slightly different times, but further analysis needs to adjust the data so that it appears that all voxels within one volume have been acquired at exactly the same time. *Motion correction* follows: by using rotation and translocation, each volume is transformed to be aligned with all the others [39]. Often but not always, a *spatial blurring* of each volume is taken into account, with the aim of reducing noise without significantly affecting the activation signal. Afterwards, overall intensity level is adjusted so that all volumes have the same mean intensity (*intensity normalization*) [34]. The final step is the filtering of each time series of voxels by linear or non-linear tools, in order to reduce low and high frequency noise. Now data are ready for statistical data processing [35].

A detailed description of statistical analysis is beyond the purpose of this paper, so only a few general points will be described and single subject data only are referred to. Statistical analysis is carried out to determine which voxels are activated by the stimulation. Various possible methods may be used to compute the significance level of these activated voxels. The principle is a model-based method (e.g. [10]), where an expected response is generated and compared with the data. Commonly, each time series of voxels is analysed independently (*univariate analysis*), in a *General Linear Model (GLM)*. To get the best fit of the model to the data, the „stimulus function", which is often a sharp on/off waveform, is smoothed, delayed and converted into the haemodynamic response function (HRF) [41]. Once the model fits the data, an estimate of the „*goodness of fit*" is found, expressed as a parameter estimate (the estimated β value), which is converted, dividing it by the standard error, into the t value. Proper standard statistical transformations convert the t value into P (probability) or Z statistics, which contain the same statistical information: how significant the data are [40]. An important issue concerning these methods is the arbitrary establishment of the statistical *threshold*, above which the activity is significant, and below which data are rejected. If the significant (P) threshold is applied to every voxel in the brain, the huge amount of resulting voxels makes the number of false positives too high to be accepted; in this case a Bonferroni's correction is used (the significance level at each voxel is divided by the number of voxels, to correct the number of comparisons to be made). Otherwise, one may take into

account clusters of activated voxels before estimating the significance. This method is more sensitive to activation but more arbitrary. Whatever the choice, the resulting output is a statistical map, which indicates those points where the brain has activated in response to the stimulus.

The above analysis concerns the low-resolution fMRI series, acquired during the performance of the task. An fMRI experiment typically includes also a single high quality structural series, useful to better localize anatomically the task-related regions of increased signal. This isovolumetric morphological series needs in turn to be pre-processed [34], segmented [20] and coregistered with fMRI series, which, at last, are superimposed on the volumetric acquisition. In this way, activation areas may be viewed in the context of a good quality brain image (Fig. 19.1).

19.7 Software

The most commonly used packages are SPM and Brain Voyager; both import DICOM data, perform 2D and 3D statistical analysis and process single- or multi-subject data. Brain Voyager also has a real time utility, Turbo Brain Voyager. There is no need to describe this well-known software in detail, suffice it to say that, at the beginning, fMRI was used only for research purposes and the software was targeted at this goal. With the increasing diffusion of this technique and its clinical application, manufacturers of magnetic equipment entered the market and began the production of new software. An example is the newly introduced GE software, *BrainWave*, which cannot process multi-subject data, but is very convenient and has many advantages so that we chose it as the software for fMRI analysis in the routine clinic. The package consists of two parts: Real Time and Post-Acquisition. *Real Time* allows visualization of statistical *t*-maps during the acquisition; as the acquisition proceeds, statistical activation maps are processed and superimposed in real time on the fMRI series just acquired. This way, it is possible to monitor the situation and the activating effects from the very beginning of the acquisition. The *Post-Acquisition* package per-

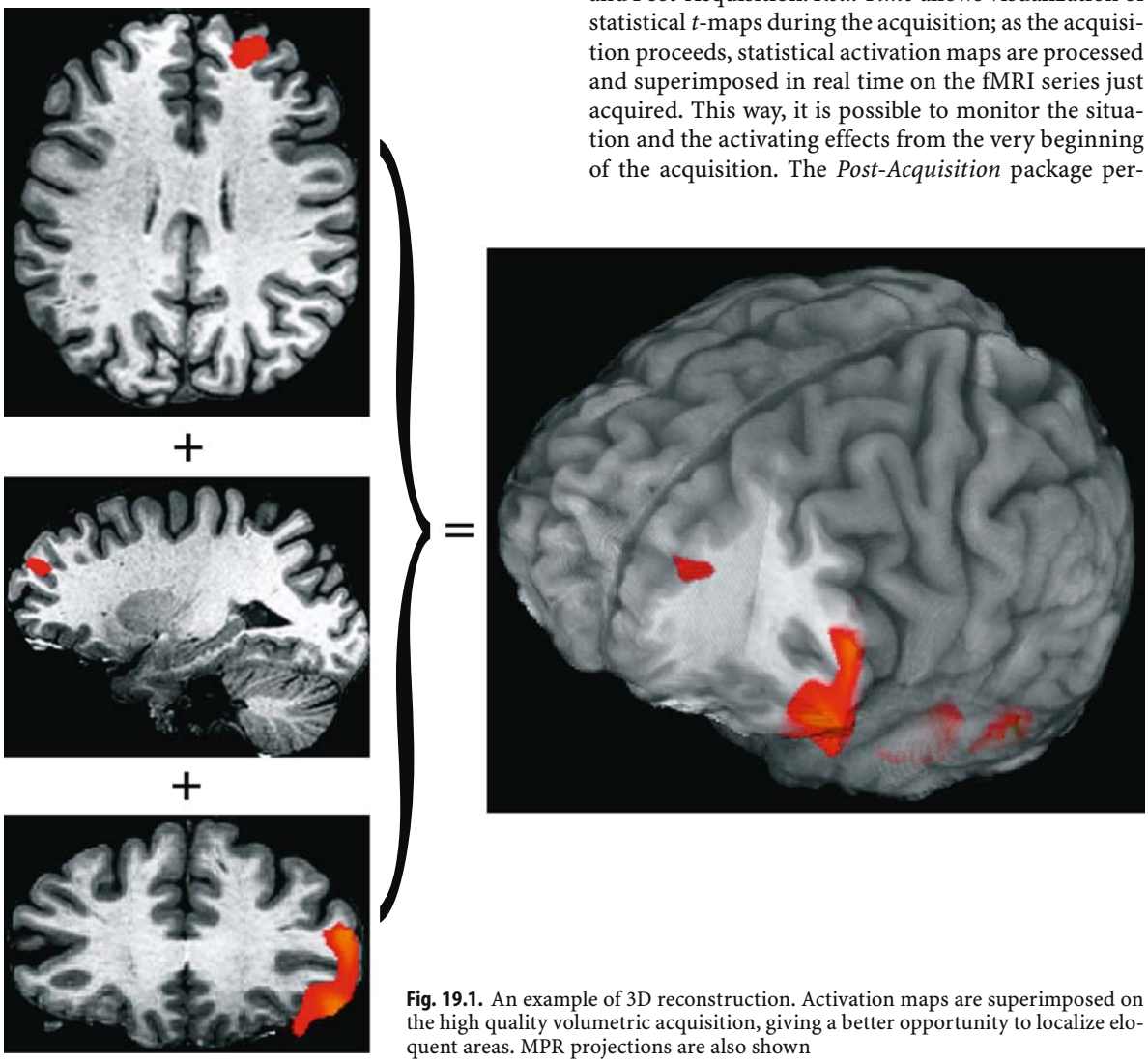

Fig. 19.1. An example of 3D reconstruction. Activation maps are superimposed on the high quality volumetric acquisition, giving a better opportunity to localize eloquent areas. MPR projections are also shown

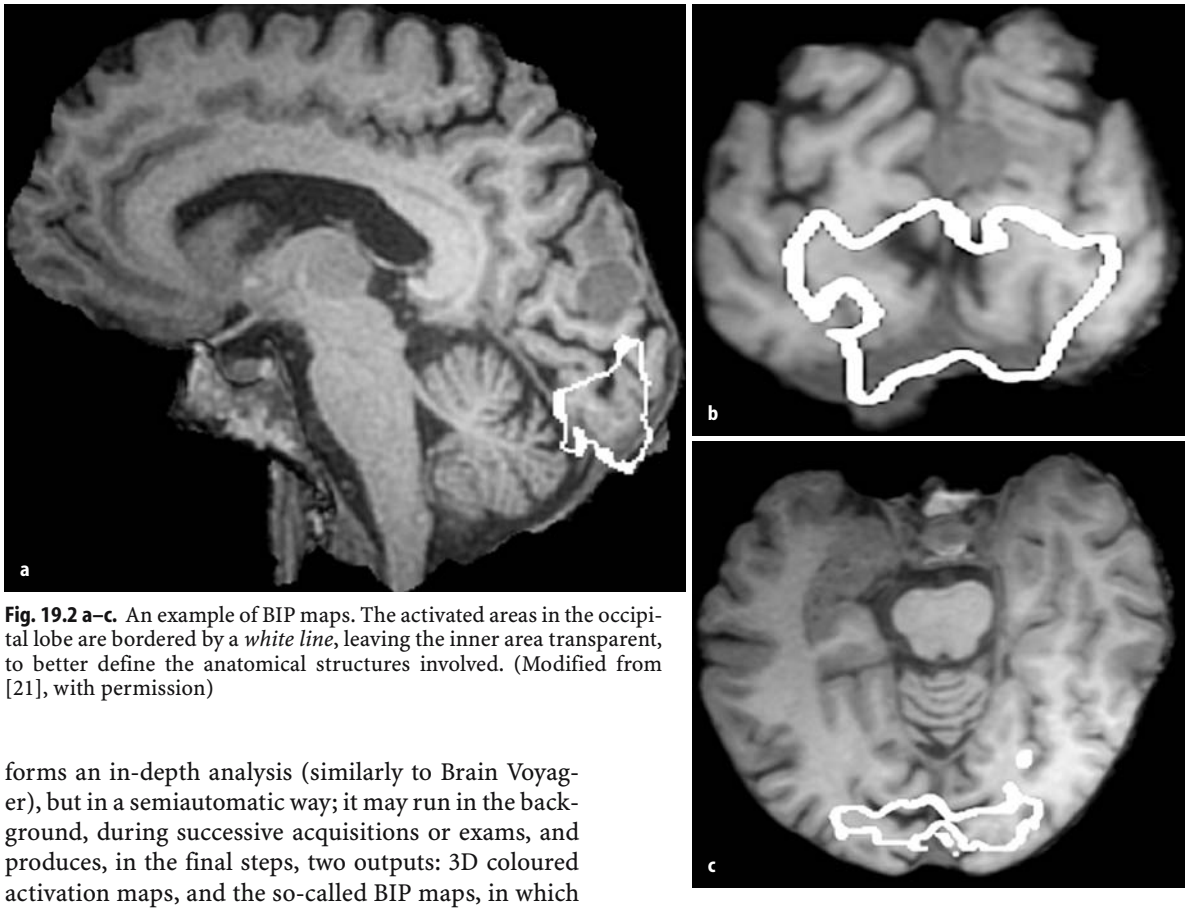

Fig. 19.2 a–c. An example of BIP maps. The activated areas in the occipital lobe are bordered by a *white line*, leaving the inner area transparent, to better define the anatomical structures involved. (Modified from [21], with permission)

forms an in-depth analysis (similarly to Brain Voyager), but in a semiautomatic way; it may run in the background, during successive acquisitions or exams, and produces, in the final steps, two outputs: 3D coloured activation maps, and the so-called BIP maps, in which the activated areas, bounded by a white contour, are superimposed on the 3D structural isovolumetric sagittal acquisition. BIP maps are a DICOM output; they can be represented, in turn, in the three planes of the space (MPR) and, sent to the neuronavigator, are invaluable to the neurosurgeon (Fig. 19.2).

19.8 Paradigms

19.8.1 Motor Paradigms

Motor and sensory paradigms were the first to be implemented, both because of the ease with which they can be performed in the scanner with no additional equipment and their easy validation by preoperative and intraoperative cortical monitoring. The good correlation between cortical monitoring and fMRI results made fMRI motor tasks the method of choice for the presurgical evaluation of patients.

There are many motor tasks described in the literature. Owing to the cortical distortion of the sensorimotor homunculus, the wider areas of fingers, hands, tongue and lips are the most frequently explored to produce the highest BOLD signal. Furthermore, hands/fingers and lips/tongue are very important anatomical effectors, involved, respectively, in day-to-day manual activities and speaking. As a consequence, hand and lip movements are the most often used tasks to explore the activity of the primary motor cortex. When the lesion is located near the convexity of the brain, movements of the foot are also used.

As regards the hand movements, there is a wide spectrum of paradigms ranging from the simple opening and closing of the hand or squeezing a sponge, to the more complex sequential tapping of fingers in predetermined fixed order or repetitive opposition of the thumb and each of the remaining fingers. Simple and complex hand motor tasks bring about different cortical activation patterns.

Simple hand movements activate only the contralateral primary motor cortex, the superior part of the precentral gyrus, in an area called the „precentral knob“, otherwise named inverted Ω, which may also be divided by a sulcus in the middle and in that case is called horizontal ε [43, 44]. Complex hand movements activate not only the contralateral primary motor cortex, but also the ipsilateral motor cortex, the supplementary motor area, the premotor and the somatosensory cortex bilaterally [38]. There are different fundamental

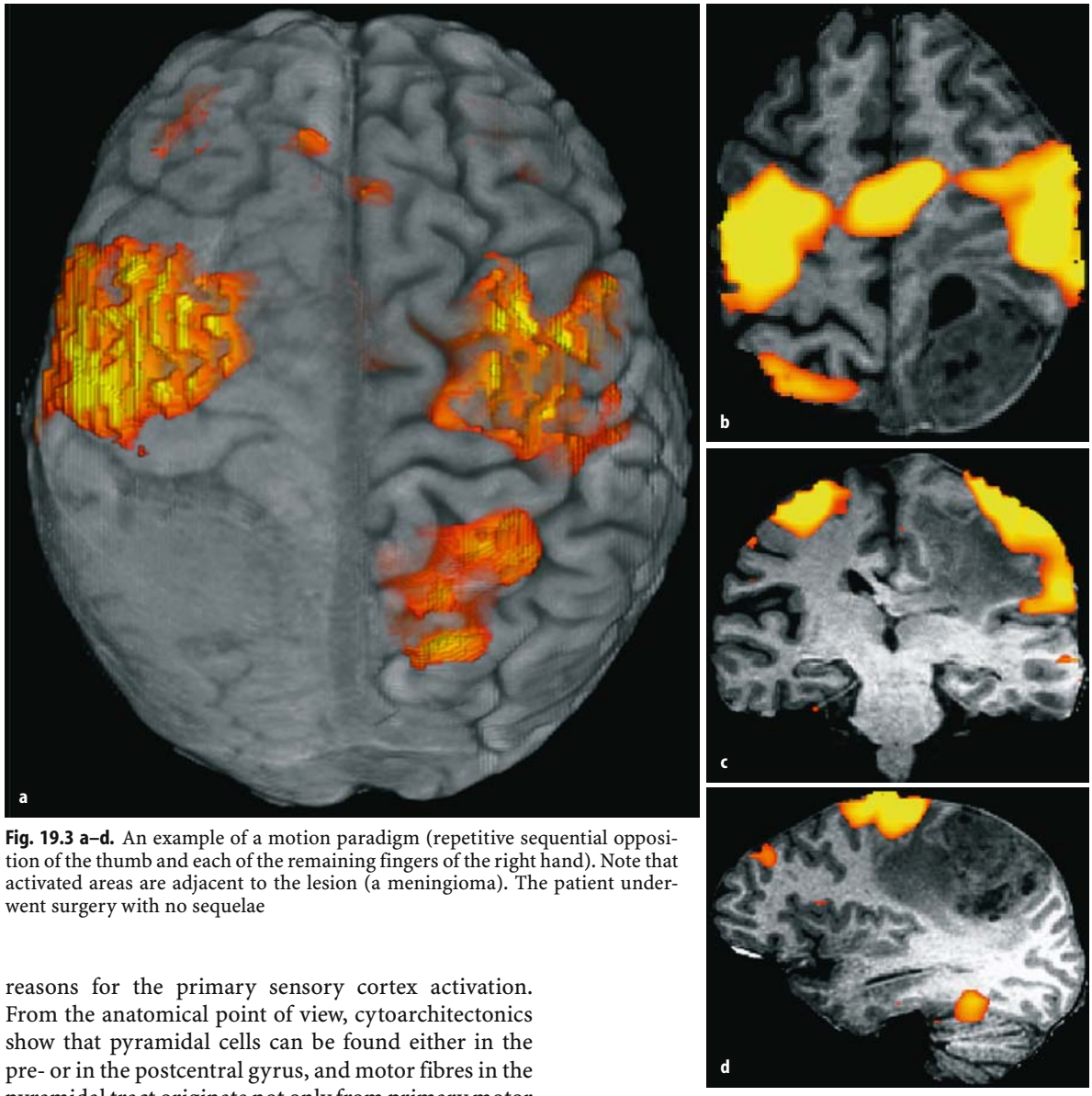

Fig. 19.3 a–d. An example of a motion paradigm (repetitive sequential opposition of the thumb and each of the remaining fingers of the right hand). Note that activated areas are adjacent to the lesion (a meningioma). The patient underwent surgery with no sequelae

reasons for the primary sensory cortex activation. From the anatomical point of view, cytoarchitectonics show that pyramidal cells can be found either in the pre- or in the postcentral gyrus, and motor fibres in the pyramidal tract originate not only from primary motor areas (Ms I) but also from primary sensitive areas (Sm I). According to classical neurophysiology, it is possible to elicit motor responses by electrically stimulating the precentral gyrus, as well as the postcentral gyrus, with a partial overlapping of the homunculi of cortical motor and sensory representation. Finally, both sensory proprioceptive and esteroceptive afferents can be activated by positional changes during the performance of motor tasks.

When the motor task is complex, there is also an asymmetry in lateralization, as regards the dominant hemisphere. In right-handed subjects, finger movements of the right hand substantially activate the dominant (left) hemisphere with almost no activation in the non-dominant (right) hemisphere [17]. In left-handed subjects, the activation pattern may show a high degree of variability, but often both left and right hand movements produce activations comparable between dominant and non-dominant hemispheres [33]. Obviously, all these differences must be taken into account in analysing an activation pattern.

Figure 19.3 shows an example of eloquent areas evoked by the repetitive sequential opposition of the thumb and each of the remaining fingers of the right hand.

19.8.2 Sensory Paradigms

Sensory paradigms are used less often than motor paradigms, but have the advantage of being a passive task,

which may also be performed on uncooperative patients (anaesthetized, unconscious, neurologically impaired, disabled, aged, babies, etc.). In this last case, they could be the only way to identify the sensorimotor cortex for surgical planning.

The most common way to perform a sensory paradigm is by tactile stimulation of the skin of the hand or, less frequently, of the foot or face. Simple plastic toothbrushes, blunt nails, air puffs and even the examiner's fingertips may accomplish this kind of stimulation.

Results show eloquent areas in both the postcentral and the precentral gyri [42]. The situation is similar to that which we have seen in motor paradigms: there is an anatomical cytoarchitectonic reason (i.e. the presence of granular cells not only in Sm I but also in Ms I) together with numerous connections through corticocortical or thalamocortical relays [42]; moreover, a direct cortical stimulation of the motor cortex in humans evokes sensory experiences [4]. The concept of a narrow, discrete, pre-Rolandic motor cortex separated from post-Rolandic sensory strip, although pervasive, has been challenged by evidence of a broad overlapping sensorimotor cortex [37].

19.8.3 Visual Paradigms

Before the introduction of fMRI, the most common way to obtain functional information about important anatomical visual areas, such as the fibre system of the optic radiations, the lateral geniculate nucleus and the striate/extrastriate cortices, was by perimetric examination of the visual field. This technique, however, provides only a subjective determination, at each point, of the functional variation in time and lacks direct anatomical information. Conventional neuroradiological imaging, on the other hand, simply outlines lesion location and its gross extent, but it is often difficult to establish if the presence of oedema or structural alterations of local anatomy imply neuronal death. A better understanding of the function-structure correlation of striate organization has been provided by functional PET imaging studies, but the associated radiation exposure and the limited availability of PET units have restricted its application for routine evaluation of patients with visual field defects to those described in a few clinical reports [18].

The enhanced spatial and temporal resolution of non-invasive fMRI, together with its safety and availability, have provided new and valuable information in understanding the organization and functional properties of visual areas in the human cortex. For instance, fMRI has been a precious method in confirming cortical retinotopy and quantitatively defining cortical extension of the central foveal vision [18, 32], results that, otherwise, could only have been obtained in an invasive manner. fMRI imaging can detect objective visual field deficits, caused by lesions not only producing destruction of the primary visual cortex, but also interrupting visual pathways and creating a lack of sensory input, without destroying neurons in the occipital cortex [18].

Visual stimulation may be delivered in plenty of modes: frequently used stimuli are flashing of white or coloured lights at certain frequencies, or alternating checkerboards, stripes or bands. Stimuli may be presented by a video screen or by goggles. This last device is often preferred, because it allows different kinds of stimulations (e.g. monocular, different mixes of hemifields, quadrants) and allowed us to explore cortical visual retinotopy. Moreover, it provides a better concentration for the patient, who cannot see anywhere but into the goggles. The resting condition is frequently characterized by a black screen with a fixation point in the centre. We implemented visual paradigms in our department by using goggles and alternating (500 ms period) black and red vertical bands (Fig. 19.4).

19.8.4 Language and Lateralization Paradigms

Since the classical works of Wernicke and Broca, the location and definition of brain language areas have been a goal and a challenge for researchers. Language areas

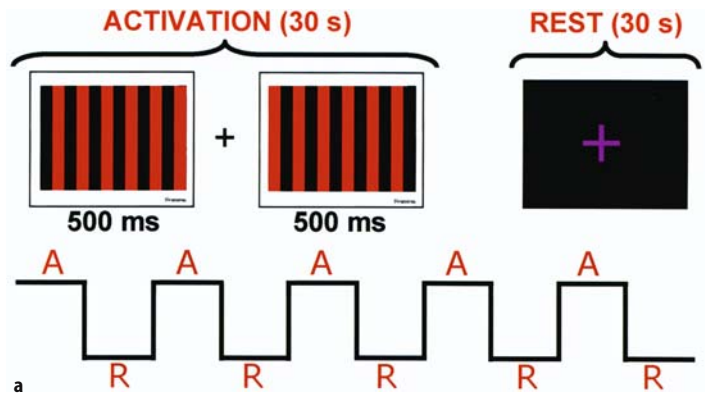

Fig. 19.4. An example of a visual paradigm. **a** Stimulation (alternating black and red vertical bars with a period of 500 ms) and rest alternating every 30 s. Stimulation may involve full visual fields bilaterally (**b**) or superior/inferior right quadrants (**c, d**, respectively). Cortical retinotopy is respected. Note the small meningioma in the left hemisphere. (Modified from [21], with permission)

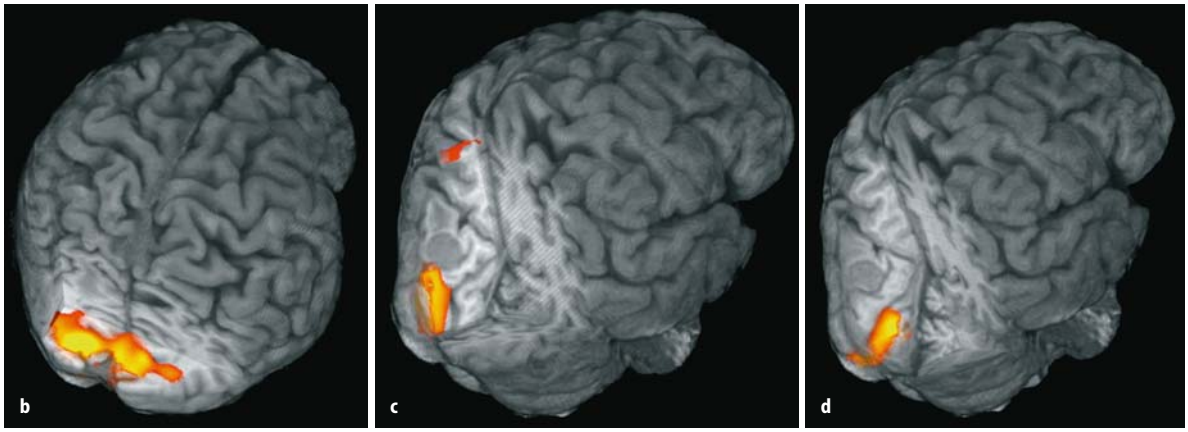

Fig. 19.4 (Cont.)

have traditionally ascribed to two discrete regions: Wernicke's area, which is responsible for the receptive aspects of language (comprehension), and Broca's area, which controls the expressive aspects of language (production). The former is located in the left posterior temporal lobe, the latter in the left inferior frontal lobe, anterior to the central fissure; both are interconnected by the arcuate fasciculus that allows information exchange between the two.

Language areas are usually located in only one hemisphere, more frequently the left, but lateralization may not remain constant: translocation of single Wernicke's [27] or single Broca's [14] areas to the contralateral hemisphere has been demonstrated in right-handed patients, when, for instance, a slowly growing tumour allows brain plasticity mechanisms to come into play.

Owing to the complexity of language-related functions, the exact location of these functional areas is somewhat variable and cannot be predicted on the basis of anatomy alone. Of course these areas are of great importance to the private and social life of the patient and sparing them is essential when a surgical approach is required.

Before the arrival of PET and fMRI and for approximately half of the previous century, the Wada test represented the „gold standard" and the task routinely used to assess the language-dominant hemisphere. Briefly, the Wada test requires the catheterization of both the internal carotid arteries, the successive injection, for each side, of amobarbital (125 mg), followed by hemispheric anaesthetization, to exclude one hemisphere at a time; the final step is the study of the awake hemisphere to establish persistence or disruption of language functions. Of note, the Wada test is possible only when there are no vascular abnormalities allowing arterial crossflow between the two hemispheres.

The advent of fMRI has changed the approach to language exploration. As one can easily infer, the Wada test has many disadvantages with respect to fMRI: invasiveness, higher risk, higher cost, and very short amounts of time (5 – 10 min) available to explore the awake hemisphere. fMRI, in addition to being non-invasive and cheaper, is not affected by underlying supply patterns, can be easily repeated, if necessary, without additional risk and affords the examiner sufficient time to test a range of cortical functions. Moreover, owing to the fact that the entire brain is examined simultaneously, results are not confounded by difficulties in reproducing test conditions separately for each hemisphere, as in the Wada test. As a consequence, several studies have compared fMRI to the Wada test and have shown a significant correlation between results from both modalities in most cases. fMRI studies typically identify more language regions than direct electrocortical stimulation mapping and the Wada test, suggesting that fMRI not only identifies areas that are critical for language processing, but also areas that participate in a less critical manner in networks that sustain language function. The result is a wider availability of information.

Plenty of paradigms have been used in the literature (cf. [5] for an exhaustive review) to define lateralization and locate language areas. On the whole, language paradigms may be classified into two main categories: the ones exploring receptive language and the ones exploring expressive language.

Receptive Language Paradigms. This kind of task explores the comprehension aspect of language and elicits eloquent areas corresponding to Wernicke's areas proper (the posterior part of the superior temporal gyrus, posterior BA22) and the surroundings (the anterior-superior and middle temporal gyri, anterior BA22, the midsuperior temporal sulcus, midportion of BA21 and BA22), with the adjacent angular (BA39) and supramarginal (BA40) gyri, in the dominant hemisphere.

Receptive language paradigms are mainly divided into *reading comprehension* (visual input) and *auditory comprehension* (auditory input). The most common

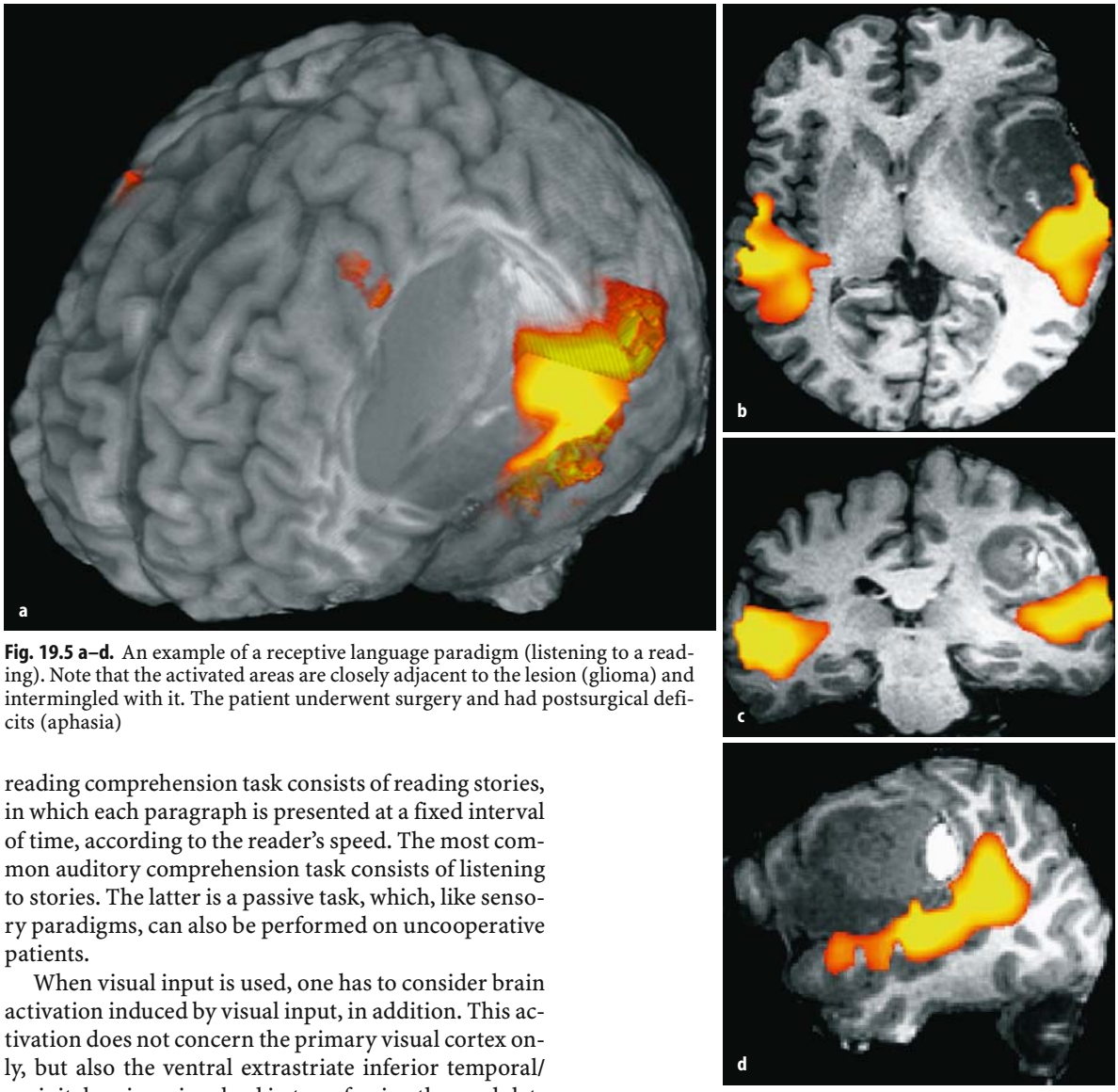

Fig. 19.5 a–d. An example of a receptive language paradigm (listening to a reading). Note that the activated areas are closely adjacent to the lesion (glioma) and intermingled with it. The patient underwent surgery and had postsurgical deficits (aphasia)

reading comprehension task consists of reading stories, in which each paragraph is presented at a fixed interval of time, according to the reader's speed. The most common auditory comprehension task consists of listening to stories. The latter is a passive task, which, like sensory paradigms, can also be performed on uncooperative patients.

When visual input is used, one has to consider brain activation induced by visual input, in addition. This activation does not concern the primary visual cortex only, but also the ventral extrastriate inferior temporal/occipital regions, involved in transferring the modulated inputs to the Wernicke's area. Otherwise, when auditory input is used, this will produce an auditory response in the adjacent auditory cortices of the superior temporal gyri. To isolate Wernicke's area and delete visual/auditory responses, other visual/auditory stimuli (e.g. uppercase/lowercase letters or backward text, respectively) may be used in the contrasting control task. However, this is not the case for presurgical purposes, because auditory/visual areas also have to be spared from the surgery.

Figure 19.5 shows an example of receptive language paradigm (listening to a reading).

Expressive Language Paradigms. This kind of task explores the production aspect of language and elicits eloquent areas corresponding to Broca's area proper (the pars opercularis, BA44, and the posterior portion of the pars triangularis, posterior BA45, of the inferior frontal gyrus), plus the precentral gyrus of the insula, in the dominant hemisphere.

Most of the numerous existing paradigms can be classified into two main categories: *verbal fluency* and *semantic decision*. The main difference between the two is that semantic decision tasks do not explore language production only, but also some working memory functions; the result is the activation of other areas in addition to expressive language ones (see below).

Verbal fluency tasks rely on the ability to produce words in different ways. Worth noting is that the patient is requested to generate words covertly (inner speech), to avoid possible artefacts caused by movements of the lips, tongue and head in active word generation. When the task is of the phonological kind, the patient is visu-

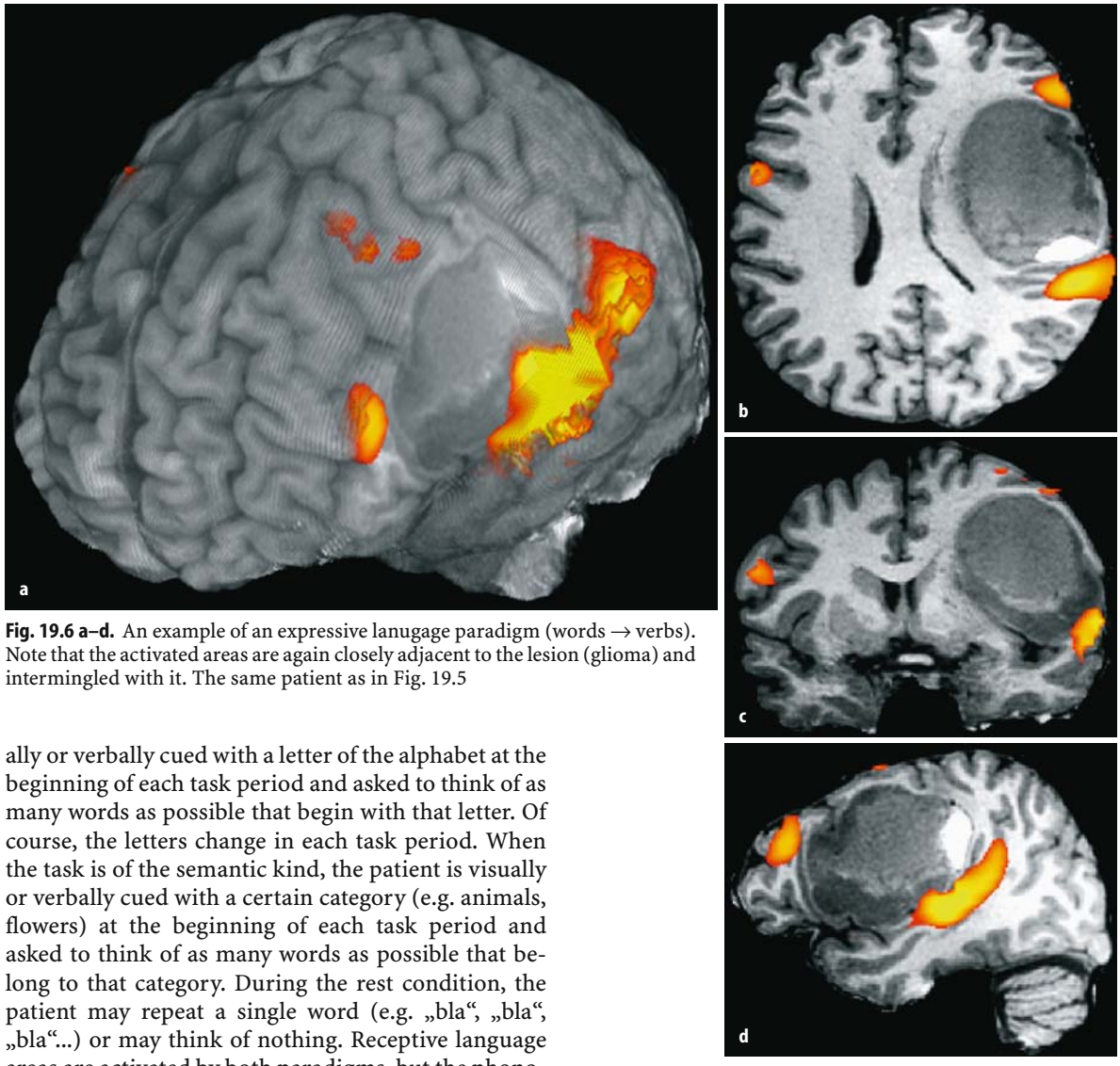

Fig. 19.6 a–d. An example of an expressive lanugage paradigm (words → verbs). Note that the activated areas are again closely adjacent to the lesion (glioma) and intermingled with it. The same patient as in Fig. 19.5

ally or verbally cued with a letter of the alphabet at the beginning of each task period and asked to think of as many words as possible that begin with that letter. Of course, the letters change in each task period. When the task is of the semantic kind, the patient is visually or verbally cued with a certain category (e.g. animals, flowers) at the beginning of each task period and asked to think of as many words as possible that belong to that category. During the rest condition, the patient may repeat a single word (e.g. „bla", „bla", „bla"...) or may think of nothing. Receptive language areas are activated by both paradigms, but the phonological task gives a more clear-cut activation than the semantic one [29].

A verbal fluency task which is very well used and reliable in disclosing lateralization is verb generation from words. A sequence of words is aurally or visually presented to the patient, who has to think of a verb corresponding to each word (e.g. piano → to play), whereas the rest condition consists of silence. In addition to Broca's area, other eloquent areas may be activated in the dominant hemisphere: the pars orbitalis of the inferior frontal gyrus, BA47, the middle frontal gyrus, BA46 and 9, and the prefrontal and posterior temporal cortices.

Semantic Decision Tasks. In this kind of task, a couple of words are sequentially presented to the patient, who has to decide if the couple appertain to a certain semantic category stated previously (e.g. synonyms vs. antonyms, abstract vs. concrete, living vs. non-living, etc.). Rest conditions differ according to whether the task is given aurally or visually. In the first case, couples of tones are presented and the patient has to decide if they are identical or not. In the second case, couples of letter are shown and the patient has to decide if they are written in uppercase or in lowercase. As already mentioned, these tasks activate other areas, besides Broca's area, and these are: the middle and the inferior temporal gyri, fusiform and parahippocampal gyri, the cingulate cortex (BA32) and the superior frontal region (BA8) in the dominant hemisphere.

Figure 19.6 shows an example of an expressive language paradigm (words → verbs).

19.9 Presurgical Applications of fMRI

19.9.1 fMRI and Brain Tumours

Certainly, fMRI takes pride of place in the presurgical evaluation of brain tumours. As stated in the introduction, fMRI is of inestimable value in locating eloquent areas when normal relationships between anatomy and function are lost (e.g. when a mass effect distorts the anatomical landmarks or when functional areas may be relocated to other areas in the brain). However, in some situations, fMRI activation in and around tumours must be interpreted with caution.

Schreiber et al. [31] found that fMRI activation is reduced near glial tumours, but is usually not affected by non-glial tumours. They suggested that this phenomenon might be explained by the fact that glial tumours grow in a more infiltrative manner and thus alter the cellular architecture, whereas non-glial tumours show more delineation from normal tissue, leaving the cellular architecture intact.

Primary brain tumours, especially low-grade tumours, have been shown to have functional tissue preserved within the lesion itself. Negative findings may represent language cortex working, but having an activity level below the sensitivity of the technique and thus not being detected. Moreover, it is known, from both angiographic and MR studies, that tumour vasculature in malignant gliomas loses the ability to autoregulate. If the brain's ability to autoregulate the flow of blood is lost in brain tissue, which is still functioning, then this area may not respond to increased neural activity by a corresponding increase in blood flow [15]. Another reason adduced by the same authors is the mass effect. Venous structures are normally under low pressure and are easily compressible. The increased tumour mass effect compresses the venules and larger veins, thereby speeding the egress of deoxyhaemoglobin-laden blood from the area of activation. This leads to a decrease in the relative concentration of deoxyhaemoglobin in the area of activation, which in turn results in an effective decrease in the difference in concentration of deoxyhaemoglobin between the resting and active states. This would lead to a decreased ability of fMR imaging to detect changes between the resting and active states [15].

However, intraoperative cortical mapping confirmed most of the fMRI findings and showed that the possible limitations of technique concerned only some selected cases and did not impede the successful identification of the eloquent cortex in the vast majority of patients of this kind.

19.9.2 fMRI and Epilepsy

Another important field of fMRI application is the presurgical evaluation of patients with refractory epilepsy. It is well known that about 90 % of well-selected patients become seizure-free after surgical treatment [11]. As far as the surgical outcome is concerned, fMRI becomes an important tool for selecting and better characterizing these patients.

fMRI in fact plays a significant role not only in defining the lateralization of language functions, but also in localizing the specific language areas. As to this last point, it has been shown that patients with epilepsy tend to have more „bilateral" activation: they reveal a significantly higher recruitment of contralateral homologous language areas, compared to the normal controls. Moreover, the earlier the onset of dominant temporal lobe seizure foci, the more widespread and atypical the distribution of language areas; expressive and receptive language skills can also dissociate in people with brain lesions occurring early in life [2]. In this context, fMRI becomes an invaluable help in mapping clinically relevant language functions in the epilepsy surgery population.

Another advantage of fMRI use is the possibility of defining the seizure spatially and temporally. Krings et al. [19] performed fMRI on a patient, who happened to experience a simple partial seizure; the seizure was associated with changes in MR signal in different regions, showing the spatiotemporal course of spreading. fMRI data correlated with EEG-determined seizure foci. Hence, it is possible to use fMRI not only to detect the cortical location of activations associated with the seizure, but also to define the epileptogenic focus in the originally activated area. The recent development of EEG-triggered fMRI allows interpretable electroencephalographic data to be recorded during MRI scanning. In this way, it is possible to combine the spatial resolution of MRI with the temporal resolution of electrophysiology in the seizure localization. EEG-linked fMRI acquisition is a promising technique in the field of epilepsy.

19.9.3 fMRI and AVM

The presurgical evaluation of arteriovenous malformations (AVMs) is another interesting and controversial application of fMRI. They are the most common of cerebrovascular malformations and consist of a coiled mass of arteries and veins, without an intervening capillary network, lying in a bed formed by displacement rather than invasion of normal brain tissue. Functionally, they are direct arteriovenous communications causing a shunt of blood from the arterial to the venous

side. The high flow volume shunted through an AVM fistula appears as „voids" within the structure in morphological MR images and may induce a decrease in cerebral perfusion pressure in the downhill artery [24].

The surgical importance of AVMs is related to their high probability of bleeding and giving epileptic crisis. In such situations, the localization of eloquent cortices near AVMs becomes important not only presurgically, but also during possible embolization procedures, because, when there is doubt that an AVM is close to eloquent tissue, particular care must be exercised to avoid devascularizing these functional areas.

The debate about the use of fMRI in AVMs revolves around the peculiar haemodynamics of this pathology. AVMs produce high velocity, low resistance blood-flow and induce feeding artery hypotension and draining vein hypertension, with a potential net reduction in cerebral perfusion pressure in neighbouring territories. Chronic hypotension does not necessarily result in loss of neuronal function in brain tissues surrounding AVMs, but haemodynamic perturbations may reduce or impede the BOLD signal in adjacent eloquent cortex, obscuring activation where neuronal function may be present.

More specifically, there is a possible disagreement with respect to the presence or absence of significant activation within and around the nidus. The nidus represents the area, interposed between the distal segments of feeding arteries and the emerging proximal segments of draining veins, where arteriovenous shunting occurs. As revealed by histopathological findings, the nidus excludes intervening brain, whereas feeding and draining vessels are separated by brain parenchyma. Therefore, shunted blood within the nidus should not take part in metabolic changes occurring during neuronal activity, including oxygen consumption. Considering that the origin of the fMRI signal is the BOLD phenomenon, activation should not be measurable within the nidus of an AVM. The conflicting results in the literature may derive from the morphological difficulty in distinguishing the exact border of the nidus from the adjacent complex and variably dilated vessels on MR images. Intervening brain between distal feeding and proximal draining vessels could be mistaken for intranidal activation [1].

The above haemodynamic problems occur when there are severe flow anomalies; yet many patients have only moderate or any flow alterations at all. In these cases, a high correlation has been shown between fMRI mapping and electrocortical stimulation mapping [28].

Finally, Cannestra et al. propose the subdivision of MAVs into three groups on the basis of fMRI results. In group I (minimal risk), AVM and eloquent areas are disjoined by at least one gyrus free from activation; in group II (high risk) AVM and eloquent areas are intimately associated; in group III (indeterminate risk) AVM and eloquent areas are adjacent to each other. Group I patients may undergo direct surgical excision of the AVMs solely on the basis of fMRI maps. Group II patients are considered inoperable and are referred for radiosurgery. In group III patients, eloquent areas are too close to the AVMs (less than 1 cm) to allow estimation of risk; these patients are considered candidates for intraoperative electrocortical stimulation [6].

19.9.4 fMRI and Other Pathologies

fMRI is rapidly moving into the clinical setting, including being used for traumas, vascular diseases, inflammations, multiple sclerosis, Alzheimer disease, developmental disorders, learning disabilities and many other conditions [13].

One good example is the presurgical evaluation of a hydrocephalus case, which had a temporo-occipital cyst as an EEG documented source of epilepsy. The surgical question was the removal of the temporo-occipital cyst, in a patient with nearly normal full visual fields. fMRI revealed the existence of an eloquent area medial to the cyst, a result that documented a functional reorganization of the visual cortex. This way of presurgically defining visual cortex plasticity called for a conservative resection of the temporo-occipital region, with sparing of the medial aspect of the cyst [9].

19.9.5 fMRI and Presurgical Risk

The presurgical evaluation of patients with cerebral lesions involves the evaluation of the risk of post-surgery sequelae. Of course it is imperative for the patients to know the kind of deficit they are going to meet, as well as the probability this deficit will actually occur. In other words, the methodological approach to the risk assessment should be qualitative and quantitative. The qualitative aspect examines which function is at risk of being damaged and refers to the location of eloquent areas concerning that function (e.g. motor cortex for motion, Wernicke's and Broca's areas for language, etc.). The quantitative aspect is far more difficult to evaluate. Many studies have investigated this problem (cf. [36] for review) and the resultant quantitative best parameter to evaluate this risk is the distance between eloquent areas and lesions. The outcome of such a kind of analysis gives the following resulting values: when the distance lesion-eloquent areas exceeded 2 cm, surgical resection was considered safe and no sequelae occurred in patients. As the distance decreased, the risk of deficits increased: when the value was between 1 and 2 cm, 33 % of patients showed postoperative deficits. Finally, when the distance was less than 1 cm, 50 % of patients experienced postoperative sequelae. Similar re-

sults were obtained by Haglund et al. [12] some years previously. These authors, by intraoperative cortical stimulation, showed no sequelae for distances over 2 cm, 17 % sequelae for distances between 0.7 and 1 cm, and 43 % sequelae for distances under 0.7 cm. Many authors (cf. [36] for review) also compared fMRI mapping of eloquent areas with results obtained by direct cortical mapping and a good spatial correlation between the two methods was shown.

These results indicate a reliability of fMRI not only in defining the anatomical locations of an explored function, but also in determining the presurgical risk. In this way, the patient are given reliable information on possible postoperative loss of function, making them clearly and fully aware at the moment of informed consent, and, at the same time, it is possible to set up a process of proper presurgical planning.

19.9.6 Our Experience

We received our 3 T GE Signa Excite MRI system in February 2004, but our experience with fMRI dates only from October 2004, when we received the stimulating apparatus. From October 2004 to June 2005, we performed fMRI on 27 patients with the following pathologies: 15 tumours, 4 AVMs, 4 cavernous angiomas, 2 dysplasias, 1 Parkinson's disease and 1 aphasia. Of these patients, 12 did not undergo surgery, 2 because of non-surgical pathologies (aphasia and Parkinson) and the other 5 because fMRI showed eloquent areas strictly adjacent to the lesions. The remaining 15 patients underwent surgery. Again, of these, 7 did not show activation areas adjacent to the lesions and had no post-surgical sequelae (cf. e.g. Fig. 19.3), whereas the last 8 had eloquent cortices adjacent to the lesions. Of these, 3 (37.5 %) experienced post-surgical sequelae (1 serious deficit and 2 moderate deficits, cf. e.g. Figs. 19.5, 19.6). The above percentage values are in good agreement with the previously described values of presurgical risk (cf. 33 % in [36]).

19.10 Conclusions

fMRI has proved to be a reliable, safe, reproducible method with which to presurgically define eloquent areas. This technique gives us the opportunity to know in advance the actual situation of a lesion so that the surgeons may plan their approach strategy. This technique also allows the establishment of a presurgical evaluation of risk and enables the patient to be fully aware at the moment of informed consent. Despite the increase in its clinical applications, fMRI is still underused in the clinical field and should be performed almost routinely before surgery.

References

1. Alkadhi H, Kollias SS, Crelier GR, et al. (2000) Plasticity of the human motor cortex in patients with arteriovenous malformations: a functional MR imaging study. AJNR 21: 1423 – 1433
2. Baxendale S (2002) The role of functional MRI in the presurgical investigation of temporal lobe epilepsy patients: a clinical perspective and review. J Clin Exp Neuropsychol 24:664 – 676
3. Bogomolny DL, Petrovich NM, Hou BL, et al. (2004) Functional MRI in the brain tumor patients. Top Magn Reson Imaging 14:325 – 335
4. Baumgartner C, Barth DS, Levesque MF, et al. (1992) Human hand and lip sensorimotor cortex as studied on electrocorticography. Electroencephalogr Clin Neurophysiol 84:115 – 126
5. Cabeza R, Nyberg L (2000) Imaging cognition II: an empirical review of 275 PET and fMRI studies. J Cogn Neurosci 12:1 – 47
6. Cannestra AF, Pouratian N, Forage J, et al. (2004) Functional magnetic resonance imaging and optical imaging for dominant-hemisphere perisylvian arteriovenous malformations. Neurosurgery 55:804 – 814
7. Cevolani D, Agati R, Albini Riccioli L, et al. (2004) Pre-surgical use of functional paradigms in brain fMRI mapping: our initial 3T experience. Rivista di Neuroradiologia 17: 836 – 848
8. Donaldson DI, Buckner RL (2004) Effective paradigm design. In: Jezzard P, Matthews PM, Smith SM (eds) Functional MRI. An introduction to methods. Oxford University Press, Oxford
9. Fried I, Nenov VI, Ojermann SG, et al. (1995) Functional MR and PET imaging of rolandic and visual cortices for neurosurgical planning. J Neurosurg 83:854 – 861
10. Friston K, Holmes A, Poline J-B, et al. (1995) Analysis of fMRI time series revisited. Neuroimage 2:45 – 53
11. Golby AJ, Poldrack RA, Illes J, et al. (2002) Memory lateralization in medial temporal lobe epilepsy assessed by functional MRI. Epilepsia 43:855 – 863
12. Haglund MM, Berger MS, Mitchel S, et al. (1994) Cortical localization of temporal lobe language sites in patients with gliomas. Neurosurgery 34:567 – 576
13. Holodny AI (2004) Preoperative and postoperative mapping of eloquent regions in the brain. ASNR:33 – 36
14. Holodny AI, Schulder M, Ybasco A, et al. (2002) Translocation of Broca's area to the contralateral hemisphere as the result of the growth of a left inferior frontal glioma. J Comput Assist Tomogr 26:941 – 943
15. Holodny AI, Schulder M, Liu WC, et al. (2000) The effect of brain tumors on BOLD functional MR imaging activation in the adjacent cortex: implications for image-guided neurosurgery. AJNR 21:1415 – 1422
16. Hu X, Norris D (2004) Advances in high-field magnetic resonance imaging. Annu Rev Biomed Eng 6:157 – 184
17. Kim SG, Ashe J, Hendrich K, et al. (1993) Functional magnetic resonance imaging of motor cortex: hemispheric asymmetry and handedness. Science 261:615 – 617
18. Kollias SS, Landau K, Khan N, et al. (1998) Functional evaluation using magnetic resonance imaging of the visual cortex in patients with retrochiasmatic lesions. J Neurosurg 89:780 – 790
19. Krings T, Topper R, Reinges MH, et al. (2000) Hemodynamic changes in simple partial epilepsy: a functional fMRI study. Neurology 54:524 – 527
20. Lemieux L, Hammers A, Mackinnon T, et al. (2003) Automatic segmentation of the brain and intracranial cerebrospinal fluid in T1-weighted volume MRI scans of the head,

and its application to serial cerebral and intracranial volumetry. Magn Res Med 49:872 – 884
21. Leonardi M, Agati R, Cevolani D, et al. (2004) Potential impact of advanced 3 Tesla diagnostics in the management of patients with brain tumours. Rivista di Neuroradiologia 17:849 – 881
22. Lin W, An H, Chen Y, et al. (2003) Practical consideration for 3T imaging. Magn Reson Imaging Clin N Am 11:615 – 639
23. Liu TT, Frank LR, Wong EC, et al. (2001) Detection power, estimation efficiency, and predictability in event-related fMRI. Neuroimage 13:759 – 773
24. Mast H, Mohr JP, Osipov A, et al. (1995) Steal is an unestablished mechanism for the clinical presentation of cerebral arteriovenous malformations. Stroke 26:1215 – 1220
25. Matthews PM (2004) An introduction to functional magnetic resonance in the brain. In: Jezzard P, Matthews PM, Smith SM (eds) Functional MRI. An introduction to methods. Oxford University Press, Oxford
26. Moritz C, Haughton V (2003) Functional MR imaging: paradigms for clinical preoperative mapping. Magn Reson Imaging Clin N Am 11:529 – 542
27. Petrovich NM, Holodny AI, Brennan CW, et al. (2004) Isolated translocation of Wernicke's area to the right hemisphere in a 62-year-man with a temporo-parietal glioma. AJNR 25:130 – 133
28. Pouratian N, Bookheimer SY, Rex DE, et al. (2000) Utility of preoperative functional magnetic resonance imaging for identifying language cortices in patients with vascular malformations. J Neurosurg 97:21 – 32
29. Pujol J, Vendrell P, Deus J, et al. (1996) Frontal lobe activation during word generation studied by functional MRI. Acta Neurol Scand 93:403 – 410
30. Rao SM, Binder JR, Hammeke TA, et al. (1995) Somatotopic mapping of the human primary motor cortex with functional magnetic resonance imaging. Neurology 45: 919 – 924
31. Schreiber A, Hubbe U, Ziyeh S, et al. (2000) The influence of gliomas and non-glial space occupying lesions on blood-oxygen-level-dependent contrast enhancement. AJNR 21:1055 – 1063
32. Sereno MI, Dale AM, Reppas JB, et al. (1995) Borders of multiple visual areas in humans, revealed by functional magnetic resonance imaging. Science 268:889 – 893
33. Singh LN, Higano S, Takahashi S, et al. (1998) Comparison of ipsilateral activation between right- and left-handers: a functional MR imaging study. Neuroreport 9:1861 – 1866
34. Sled JG, Zijdenbos AP, Evans AC (1998) A nonparametric method for automatic correction of intensity nonuniformity in MRI data. IEEE Trans Med Imaging 17:87 – 97
35. Smith SM (2004) Overview of fMRI analysis. In: Jezzard P, Matthews PM, Smith SM (eds) Functional MRI. An introduction to methods. Oxford University Press, Oxford
36. Sunaert S, Yousry TA (2001) Clinical applications of functional magnetic resonance imaging. Neuroimaging Clin N Am 11:221 – 236
37. Uematsu S, Lesser RP, Gordon B (1992) Localization of sensorimotor cortex: the influence of Sherrington and Cushing on the modern concept. Neurosurgery 30:904 – 913
38. Wexler BE, Fulbright RK, Lacadie CM, et al. (1997) An fMRI study of the human cortical motor system response to increasing functional demands. Magn Res Imaging 15: 385 – 396
39. Woods RP, Grafton ST, Holmes CJ, et al. (1998) Automated image registration: I. General methods and intrasubject, intramodality validation. J Comput Assist Tomogr 22:139 – 152
40. Worsley KJ, Marrett S, Neelin P, et al. (1996) A unified statistical approach for determining significant signals in images of cerebral activation. Hum Brain Mapp 4:58 – 73
41. Worsley KJ, Friston KJ (1995) Analysis of fMRI time series revisited – again. Neuroimage 2:173 – 181
42. Yetkin FZ, Mueller WM, Hammeke TA, et al. (1995) Functional magnetic resonance imaging mapping of the sensorimotor cortex with tactile stimulation. Neurosurgery 36:921 – 925
43. Yoursy I, Naidich TP, Yoursy TA (2001) Functional magnetic resonance imaging. Factors modulating the cortical activation pattern of the motor system. Neuroimaging Clin N Am 11:195 – 202
44. Yoursy TA, Schmid UD, Alkadhi H, et al. (1997) Localization of the motor hand area to a knob on the precentral gyrus. Brain 120:141 – 157

Subject Index

Printing and Binding: Stürtz GmbH, Würzburg